博士論文

Characterization of Liquefaction and Seepage Properties under Different Saturation Conditions of Bauxite During Maritime Transport

(船積みボーキサイトの異なる飽和条件下における
液状化特性と透水特性の評価**)**

by

タン・ティアン　ジェイロード　ウイ
Tan Tian Jaylord Uy

A thesis submitted in partial fulfillment
of the requirements for the degree of

Doctor of Philosophy

Department of Civil Engineering
University of Tokyo
Tokyo, Japan
February 2019

Abstract

Similar to liquefaction of soils during earthquakes, liquefaction of a solid bulk cargo can occur when excessive cyclic or dynamic loading, induced by rough seas and vessel vibrations, is transmitted to the cargo. If liquefaction of a solid bulk cargo occurs, it may cause the vessel to capsize and it has been found that from 1988 to 2015, there have been 24 suspected liquefaction incidents reported, which resulted in 164 casualties and the loss of 18 vessels (Munro and Mohajerani, 2016). One of the recent incident occurred in Jan 02, 2015 when 46.4 kilotons (handymax type vessel) of bauxite (primary ore of aluminum) being transported by MV Bulk Jupiter capsized on its way from Malaysia to China.

After the loss of MV Bulk Jupiter, the global bauxite industry was requested by the International Maritime Organisation (IMO) to undertake research into the behavior of bauxites during ocean transportation. The global bauxite industry responded by forming the Global Bauxite Working Group (GBWG) to conduct research on the behavior and characteristics of seaborne traded bauxites to inform the IMO in relation to the safe shipping of bauxites (Global Bauxite Working Group, 2017). One of their findings is that Handymax type carriers experience the largest motions for similar sea state conditions (Global Bauxite Working Group (GBWG), 2017), hence the importance of this study.

In order to reveal the liquefaction potential of bauxite, this thesis was conducted as an independent study from a point view of geotechnical engineering focusing on a type of bauxite assumed to be transported by a Handymax type carrier.

Work had been done by Wang (2014) using two types of iron ore material and one of the key findings was that considering the liquefaction potential of unsaturated zone in analysis is important in the overall understanding of the heap subjected to motions experienced by the Capesize (~150 kDWT) type carrier (Wang, 2014). Hence, it is worth to characterize bauxite and investigate how it would respond since it is a different material, when transported by Handymax (~50 kDWT) type vessel. Also in the process of loading the bulk cargoes into the ship and during transportation, the distribution of water contents on the bulk cargoes varies with respect to depth and changes with duration of travel. This causes some change in boundaries on the saturated zone and unsaturated zone of the heap. Thus, water flow properties are equally important to be dealt with in this study and a way to measure them is necessary. Finally, condition that can potentially cause instability on Handymax carrying bauxite heap was needed to be known.

In view of the conditions stated above, this research was performed (1) to characterize bauxite on its geotechnical properties and compare them with other geomaterials, (2) to develop a testing method to measure permeability of bauxite under different saturation conditions, and (3) identify threshold conditions by numerical simulation of dynamic response at different conditions.

For bauxite, three degrees of compactions (D_c) were prepared, labeled as loose (D_c = 65%), medium dense (D_c = 80%), and dense (D_c = 90%). The densities were assigned from published reports and prepared to the equivalent D_c in the laboratory.

The major outcomes from this study are summarized as follows:

1. Liquefaction resistance of bauxite

Considering the unsaturated condition of the heap of bauxite, the liquefaction resistance of the saturated and unsaturated conditions was studied by conducting undrained cyclic loading tests. The test was performed on a specially manufactured triaxial apparatus, on which the measurement systems of pore air pressure, pore water pressure, volume change of the unsaturated specimens were equipped.

In terms of liquefaction behavior, it was found out that under saturated condition, bauxite behaves similar to other types of geomaterials in terms of liquefaction resistance curve at lower densities and higher densities. The stress paths and strain curves of bauxite were observed to be similar to iron ore and Inagi sand (silty sand), while Toyoura sand was observed different especially at loose case.

For unsaturated case, previous study had been conducted by Wang et al. (2016a) on iron ore to propose a new index called volumetric strain ratio (R_v). Liquefaction Resistance Ratio (LRR), which is the ratio between the Liquefaction Resistance ($R_{L,Unsat}$) of soil under unsaturated case compared to its saturated case ($R_{L,Sat}$), was plotted against R_v and found out to exhibit better correlation than previously correlated parameters such as LRR vs. potential volumetric strain ($\varepsilon^*_{v,air}$) (Okamura and Soga 2006). Conducting experiments for bauxite at saturation degrees of 84% (Sr=84%) and Sr=58%, bauxite followed the trend of the proposed LRR plotted against $R_{v,}$ exhibiting a better correlation than LRR vs. $\varepsilon^*_{v,air}$.

2. Water flow characteristics of bauxite

The property of permeability, which is essential to analyze the seepage, dynamic responses etc. in the heap, was measured for the saturated and unsaturated bauxite. Permeability tests were performed on Triaxial apparatus using a flexible wall.

Previous researches utilize ceramic disks (Goh 2015) placed on top of the specimen and bottom while in this research, membrane filter (Nishimura et al., 2012) was introduced to the top cap and bottom pedestal instead of the traditional ceramic disk for unsaturated specimens. In order to measure the head difference of the fluid flowing through the specimen, a Local Pin-Type Sensor wrapped by membrane filter (same material as that of top and bottom pedestal) was used to measure the head difference directly. The inflow rate was measured by using a Mariotte's bottle which supplies the constant head, placed on a weighing scale in which the mass is received by the computer at a specified interval. The outflow rate, on the other hand was measured by using a differential pressure transducer (DPT). It was found out that the *k* of soils could be measured using the newly developed

Local Pin-Type Sensor at various Sr, where values are obtained by simple average when inflow rate equals outflow rate (steady state condition) and measured head is reasonably stable.

Current tests were done on bauxite (range: $1x10^{-5}$ to $1x10^{-3}$ cm/sec), iron ore (range: $1x10^{-5}$ to $1x10^{-4}$ cm/sec), and Inagi sand (range: $1x10^{-5}$ to $1x10^{-4}$ cm/sec). The local pin-type sensor was found out to be ineffective for Toyoura sand.

Bauxite was found to behave closer to Inagi sand in its permeability properties under saturated and unsaturated conditions.

By utilizing the information obtained from SWRC, indirect method using Van-Genuchten Model (VG Model) was used to evaluate *k* values under unsaturated condition. The experimental data results were compared with VG model and in general, the VG model estimate is an underestimate of the results that can be obtained from the experimental data. This implies that direct measurement of *k* values is necessary.

3. Seepage analysis

From the *k* and SWRC tests data, seepage analysis was carried out using GuSLOPE 2.0 using the experimentally obtained values. The final distribution of water on the heap was simulated to identify the envelope, which indicates the maximum height of water table in the heap for a given initial Sr, and the distribution of Sr in the unsaturated zone.

Initial degree of saturation of 90% (Sr_{init}=90%) was considered for seepage analysis for modeling. Results show that the water distribution is a function of the density of the heap with looser materials having higher wet base in general. The shape of the wet base accumulated is generally ellipsoidal, with the peak at the centerline of the cross section, tapering to the side boundary.

4. Dynamic responses analysis

Upon knowing the material properties and distribution of water on the heap, the two dimensional response of the heap of bauxite was evaluated by employing a commercial software, UWLC Ver. 2. A generalized elasto-plastic model (PZ-model) was employed to simulate the behavior of liquefiable zone of the heap. Two cases, which focus on the effects of liquefaction potential and permeability of the unsaturated zone on the overall response of the heap, were studied. In each case, the response of the heap was examined under different rolling angles from 5° to 30°, under different densities, and then compared with iron ore. From the simulation results, it was found out that bauxite at loose condition ≤5° rolling angle; medium dense: ≤10° rolling angle; and dense: ≤15° rolling angle could withstand a 360 cycle rolling motion. This number was adopted from the narrative of events from the Bahamas Maritime Authority (BMA) report on the case of MV Bulk Jupiter. For iron ore fines, a dense (D_c = 92%) could withstand ≤10° rolling angle.

Like the previous study by Wang (2014), it was also found out that assuming the unsaturated region to be liquefiable decreased the overall resistance of heap of bauxite. Hence, consideration of liquefaction potential of the unsaturated zone in the heap of bauxite for Handymax type carrier is necessary to evaluate the overall liquefaction potential of the heap.

As recommended application, this study provides a qualitative understanding of the behavior of heap of bauxite during maritime transport. While simple assumptions were adopted to describe the kind of motions a ship may experience in a typical voyage, the results suggest thresholds and extents for different heap densities and wet base, which can affect the safety of the carrier.

Although bauxites have large differences in particle size distribution depending on the deposit and subsequent processing, the results in this study can be helpful for other gradations by following similar methodology and approach.

Acknowledgment

All glory and honor to my living God and my Lord and Savior Jesus Christ. It is by His goodness and grace that He has watched over me all these years. I couldn't have done this without Him and I live for His Name.

There are no words to thank my supervisor enough, Professor Junichi Koseki. It is my privilege and honor to be under his guidance in both my MS and PhD. I enjoyed all the classes I took under him because his way of teaching is unmatched. In my research, he was patient in guiding me and he was always available to provide guidance and direction and he never withheld in sharing his deep knowledge about Geotechnical Engineering. His influence to me goes beyond our topics as he also imparted life lessons and disciplined me for my own good. Whether the way I approach things in general, or inappropriate actions I do. I have learned a lot of lessons from him which I can bring with me wherever I go.

To my senior, Dr. Hailong Wang to whom I owe a lot. He was always there when I asked questions and was patient in explaining things to me when I couldn't understand. From the time I stepped in as MS student, until I finished my PhD, he was there to help me in all the ways he could. I couldn't ask for a better Senpai than him and he is the ultimate Senpai.

To Mr. Takeshi Sato, whose work and life experience in itself speak volumes about who he is – a brilliant person dedicated to his craft. He always helped and always came up with brilliant ideas how to make apparatus for conducting tests. It's a privilege to see his work ethics and how he always shared his good cheer to us.

To my research panelists, Prof. Reiko Kuwano, Prof. Takashi Kiyota, Prof. Kenji Watanabe, Prof. Tomoyoshi Nishimura, and Prof. Fei Cai – they all gave important comments and suggestions to improve my work. They gave good questions to challenge my research with the intent of improving it and making it more coherent. Also for the time and patience they gave to me in listening when I consulted to them, as well as explaining to me things I didn't know.

To Prof. Hiroyuki Kyokawa – he gave key suggestions in organizing my thesis and the doctor seminar we had under him was helpful. He sent me journals related to my topic to read and also supported when there is equipment needed to conduct the tests.

To my host mom Mrs. Noriko Saito – I am so privilege to be her son. She's caring, loving, and concerned. She introduced a lot of Japanese cultural things to me, invited me to their annual Golden Week celebration and Christmas celebration at their home. She knows my friends and welcomed them as well with open arms! I am blessed to have her.

The MEXT, who provided the scholarship, I am grateful for the generosity and provision. I was well provided during my stay here because of their support.

I would like to thank my laboratory mates. When experiments were not working well, they were the ones who listened, sympathized, and encouraged. In one way or another, they have made suggestions to improve my work. Indeed, research life became more fun because of my lab mates.

I also want to acknowledge my friends at my church - Tokyo Baptist Church. I have many friends there from different nationalities, background, and life experiences. They are my brothers and sisters and they prayed for me and strengthened me. They are my family here in Japan. They always reminded me of God's goodness and reminded me that God is always there for us.

To my friends in the Philippines - thank you for the encouragements. Despite geographical distance, thanks to social media, they were easy to connect with. They showed support and prayed for me too.

Lastly, I thank God for my family, especially my mother. She has always supported me in what I wish to pursue and just stayed by no matter what. She is patient with me, and caring and loving. I am also privilege to have very good relationships with my siblings. Family is God's gift indeed.

Table of Contents

Chapter 5: Numerical Analysis: Seepage

Chapter 6: Numerical Analysis: Dynamic Response

Chapter 7: Conclusions and Recommendations

Chapter 1
Introduction

Contents

1-1 Background of the Study

Liquefaction is a frequently occurring problem taking place when transporting wet granular solid bulk cargoes on board bulk carriers. Similar to liquefaction of soils during earthquakes, liquefaction of a solid bulk cargo can occur when excessive cyclic or dynamic loading, induced by rough seas and vessel vibrations, is transmitted to the cargo. If liquefaction of a solid bulk cargo occurs, it may cause the vessel to capsize. From 1988 to 2015, there have been 24 suspected liquefaction incidents reported, which resulted in 164 casualties and the loss of 18 vessels (Munro and Mohajerani, 2016).

One of the most recent occurrences is the MV Bulk Jupiter (Fig. 1-1), a Handymax type bulk carrier. The voyage started in Kuantan in Malaysia. Prior to voyage, the east coast of Malaysia had endured record-breaking rainfall over a month of December 2014, recording the highest monthly rainfall in the history of Kuantan at 1806.4 mm over a 22 day period (The Commonwealth of the Bahamas: Report on MV Bulk Jupiter, 2015). The vessel commenced the voyage at 21:24 of December 30, 2014 (local time) to South West Lamma, Hong Kong, in order to bunker prior to continuing on to its final destination of Qingdao, China to discharge 46,400 tons of bauxite (principal ore of aluminum). On the way to its destination, weather forecast notified the vessel of a tropical storm in the region and was provided with alternative waypoints in order to reduce the exposure to gale force winds and waves. At 06:54 on January 02, 2015 (local time), the Japanese Coast Guard received a distress alert and immediately initiated a search and rescue operation. Of the nineteen (19) crew, only the Chief Cook was rescued and sixteen (16) crew members remain missing. A typical voyage of Malaysia to China lasts 9 to 14 days (216 hours to 336 hours), but MV Bulk Jupiter capsized at about 57.5th hour of its voyage (The Commonwealth of the Bahamas: Report on MV Bulk Jupiter, 2015).

The Chief Officer inspected the cargo on the morning of January 05, 2015 and later commented:

> *"to my horror I saw that the cargo in No.4 hold had liquefied and the surface of the cargo was now flat and moving to port and starboard in a jelly-like fashion. There were also pools of water in each corner of the surface of the cargo."* (The Commonwealth of the Bahamas: Report on MV Bulk Jupiter, 2015, section 4.3.14, p.34)

After the loss of the bauxite carrying vessel the Bulk Jupiter in early 2015, the global bauxite industry was requested by the International Maritime Organisation (IMO) to undertake research into the behavior of bauxites during ocean transportation. The global bauxite industry responded by forming the Global Bauxite Working Group (GBWG) to conduct research on the behavior and characteristics of seaborne traded bauxites to inform the IMO in relation to the safe shipping of bauxites (GBWG, 2017). GBWG was commissioned to provide a science based, peer reviewed globally valid criterion for distinguishing Group C and Group A bauxites, and to develop a globally applicable Transportable Moisture Limit (TML) test for Group A bauxites, which can be used to develop a schedule for bauxite fines and amend the schedule for bauxite.

In this research, one type of bauxite was tested and investigated using new techniques for its liquefaction potential properties and water flow characteristics to verify how bauxite heap on Handymax type bulk carrier would respond to dynamic motions. With the aid of computer for numerical simulations, seepage analysis and dynamic analysis were likewise performed.

Work had been done by Wang (2014) on Capesize (~150 kDWT) type carriers with iron ore material and one of the key findings was that considering the liquefaction potential of unsaturated zone in analysis is important (Wang, 2014). While it is also common for bauxite to be carried by Capesize type carrier, Handymax (~50 kDWT) type carrier was used in this study because Handymax vessels experience the largest motions for similar sea state conditions (GBWG, 2017). Besides, MV Bulk Jupiter is a type of Handymax type carrier.

1-2 Main Objectives

The main concern of this study is the potential liquefaction problem of heaps of bauxite during transportation in the ocean. To find a solution of this problem from the standpoint of a geotechnical engineer, the next section 1-3 presents the scope and flow of study and the process of problem simplification and research configuration.

The main objectives of this study are:

1. To characterize geotechnical properties of bauxite on its liquefaction resistance (R_L), soil-water retention curve (SWRC), and permeability (k) at different saturation conditions, and compare it with other geomaterials having similar gradations;

2. To develop a testing method to measure the permeability of bauxite and other geomaterials under different saturation conditions; and

3. To identify threshold conditions by numerical simulation of dynamic response at various densities of bauxite and geomaterials.

The first objective pertains to characterizing bauxite, and comparing the results with iron ore fines, Inagi sand, and Toyoura sand with respect to their geotechnical properties such as liquefaction resistance and water flow characteristics.

The second objective is the development of a new method to measure permeability of geomaterials at different saturation conditions to deteremine their water flow properties.

Lastly, the third objective proposes certain conditions or threshold by which liquefaction is expected to take place by numerical simulation of dynamic response at various densities and geomaterials.

1-3 Scope and Flow of Study

1.3.1. Technical Issues and Scope of Study

There are two main technical issues as underlined below to be addressed in this research:

A. What kind of motions may a ship experience in a typical voyage?

The motions a ship may experience depends mostly on its voyage route (e.g. from Malaysia to China), weather conditions of each zone along the voyage (e.g. a ship may suffer from storm in some seasons at some sea areas), the period of extreme weather condition and how to statistically consider, the normal period, height and mode of ocean waves, the size and arrangement of a ship and so on. Studies have been mentioned in the official report of the Global Bauxite Working Group (2017) on these issues. In this study, instead of finding solutions in these unfamiliar research fields, simple assumptions are adopted base on study results of GBWG and the Bahamas Maritime Authority (BMA) reports and inquiries to related professionals. Assumptions are as follow:

1. Only consider the effect of predominant motion, the rolling motion (six motion components of a ship, Surge, Sway, Heave, Roll, Pitch and Yaw are shown in Fig. 1-2);

2. Only consider the shear stress induced by rolling motion, effect of acceleration is not considered;

3. Assuming the period of rolling motion is 10 second (0.1 Hz) (Global Bauxite Working Group, 2017);

4. A ship/a heap is assumed to experience a certain number of cycles of roll in a voyage;

5. Only analyze response of one heap in a ship (there are 5 holds in a ship for Handymax type bulk carrier; one heap in each hold).

B. How will a heap respond under expected motions?

1. Saturation condition of a heap

Fig. 1-3 shows a typical photo of the heap of bauxite. The material is usually piled up in natural ground without protection from weathering. It usually contains certain amount of water before loading. The water content in a heap is expected to be roughly uniform at the moment right after loading to a ship. The water content distribution is believed to change from a uniform distribution to a non-uniform one because of movement of water in the heap during one voyage (9-14 days). The movement of water results in a time-dependent water distribution in the heap, where a saturated or nearly saturated zone at the lower part and dryer condition at the upper part of the heap may form as shown in Fig. 1-4.

2. Stress applied on a heap

The motion a heap is assumed to suffer from is rolling motion as shown schematically in Fig. 1-5. Because of the rolling motion, a cyclic shear stress is applied on the heap induced by rotation of center of gravity. Under such a shear stress, the whole heap or part of the heap may liquefy.

1.3.2. Flow of Study

The experimental study and numerical simulation are carried out for the evaluation of the response of a heap of bauxite. Basic properties of saturated and/or unsaturated bauxite, such as water retention ability, water permeability and resistance against cyclic shear stress/liquefaction were studied by conducting laboratory element tests; the overall responses of a heap of bauxite, such as time-dependent water distribution in the heap and response of a heap under rolling motion were carried out by numerical simulation. The more detailed works are addressed as follows:

1. Undrained cyclic loading test

Resistance against cyclic shear stress/liquefaction of an element of bauxite provides basic properties for analysis of the response of a heap of bauxite. In this study, tests were conducted on a triaxial apparatus. Considering the unsaturated condition a heap of bauxite may form, proper evaluation of the liquefaction resistance of unsaturated bauxite was one of the agenda of this study. From the work pioneered by Wang (2014), the effects of degree of saturation and fines content on the resistance against liquefaction of bauxite was investigated to verify if it fits the proposed volumetric strain ratio (R_v) proposed by Wang (2014). In order to achieve this, consolidation test to obtain the volumetric change of soils induced by change of confining pressure was also conducted to better understand the effect of fines content on liquefaction resistance.

2. Permeability (k) test under different saturation conditions

Coefficient of permeability (k) of a soil element indicates the water flow velocity in this element. It is an important aspect for estimation of time-dependent water distribution in a heap of bauxite. In this study, efforts are taken to develop testing techniques of permeability test for both saturated and unsaturated soils in a triaxial apparatus. The test was conducted in a triaxial system to reduce the interface effect between the specimen and the confining wall and to freely control the confining stress. Constant water head system was applied to both saturated specimen and unsaturated specimen. Since the used triaxial system is unable to directly measure the water head difference at the two ends of a specimen, a local pin-type sensor intended to measure the head difference between two points is introduced in Chapter 4 of this research. Through testing techniques, k under both saturated and unsaturated states is discussed.

3. Soil-Water Retention Curve (SWRC) test

This test describes a relationship between suction and water content for an unsaturated soil and indicates water retention ability of a soil. As shown an element of an unsaturated soil in Fig. 1-6, pore water in a soil will naturally flow from one place with high elevation potential (P_E) to another place with low P_E. The magnitude of P_E only depends on the position of pore water in the element. On the other hand, there is another component of potential, matric potential (or capillary potential, which usually termed as suction/matric suction=pore air pressure – pore water pressure in geotechnical engineering, osmotic suction is assumed to be 0 herein for simplicity) works on pore water. The magnitude of suction depends on the amount of water in soil matrix (soil skeleton) and property of soil particle, namely, the fewer water in the soil matrix and/or the more hydrophilic the soil particle, the higher the suction in soil becomes to retain the rest of pore water. Suction is of the same meaning as tension T (attraction force between soil particle and pore water induced by meniscus effect as shown in Fig. 1-6). Subsequently, the reduction of pore water driven by P_E induces the increase of T which tries to stop pore water from leaving. As a result, the combined effect of each potential component produces an equilibrium state in the element. SWRC exactly describes the equilibrium state of a soil element. An arbitrary position in the heap of bauxite can be considered as an element like the one in Fig. 1-6. Through proper estimation of suction distribution in the heap and utilization of SWRC of bauxite, the equilibrium water distribution in the heap can be evaluated.

4. Seepage analysis

The analysis of seepage of water in the heap of bauxite is important to estimate the saturation condition in the heap. Saturated zone and unsaturated zone may form during the voyage for the heap with an initially uniform water content. The extent of the saturated zone and the degree of saturation of the unsaturated zone are crucial information for the dynamic analysis of the heap. Numerical tool was utilized to simulate the seepage in the heap of bauxite based on the results of SWRC test and permeability test. Van Genuchten model (Van Genuchten, 1980; Kool et al., 1985 and Parker et al., 1985) was introduced to a FEM code for simulation in comparison with experimental data obtained from *k* tests and SWRC tests. The effects of initial water content, density of bauxite, and boundary on the saturation distribution are discussed. The critical conditions when the maximum height of saturated zone for a given initial degree of saturation are estimated and the distribution of degree of saturation of unsaturated zone in the heap under critical conditions is evaluated.

5. Dynamic response analysis

The final objective of this study is to evaluate the liquefaction potential of the heap of bauxite. The two dimensional response analysis of the heap is performed numerically. The liquefaction potential of both saturated zone and unsaturated zone are taken into consideration. At different densities of bauxite, the areas with high liquefaction potential are plotted out. The liquefaction potential of the heap under different angles of rolling motion is also discussed. The results are compared with iron ore material assuming the same heap.

In terms of flowchart, Fig. 1-7 shows the flow of study of this research.

1-4 Brief Overview of Unsaturated Soil Mechanics

The general field of soil mechanics can be subdivided into that portion dealing with saturated soils and that portion dealing with unsaturated soils. Fig. 1-8 shows the categorization of soil mechanics in terms of pore water pressure drawn in a flowchart. The differentiation between saturated and unsaturated soils becomes necessary due to basic differences in their nature and engineering behavior.

Presently, due to the various studies carried out on saturated soils vast knowledge has been acquired on various aspects of this soil type and its behavior under various conditions. Nevertheless, there are many conditions in which soil does not reach full saturation. Particularly in the arid and semiarid regions of the world unsaturated soils are very common. Most of the behaviors experienced by unsaturated soils are related to volumetric strain.

Unsaturated soils are considered to be safe against cyclic shear due to the high compressibility of the pore air. And though liquefaction is generally associated with loose, saturated, cohesionless soils, there have been cases where even unsaturated soils have been prone to liquefaction when they are underlain by seams of saturated soils. Yoshimi et.al (1989) stated that when the degree of saturation decreases to 90%, the cyclic shear strength is double that of fully saturated soil under ordinary testing conditions in case of fine clean sands. In order to achieve a full liquefaction state in the case of unsaturated soils both the pore air and water pressure must be at the same pressure as the initial mean total confining pressure. At a zero effective stress state, unsaturated soil specimens tend to behave similar to liquids in much the same way as saturated specimens.

Despite the fact that several researchers have written and contributed to the field of knowledge of unsaturated soils such as Fredlund and Rahardjo (1993), Ng and Menzies (2007), Ngo (2009), and Nishimura and Koseki (2009) among others, there is still a great need to better understand the behavior of unsaturated soils subjected to cyclic loading.

1.4.1. Concept of Unsaturated Mechanics

When soils are submerged under water for a period of time, the voids in the soil mass tend to fill up with water, thus causing all the pore air to be pushed out due to hydrostatic pressures and the density difference between the air and the water. This process is similar to what occurs with soil located below the ground water table. Under this condition, the air void ratio is equal to zero and the degree of saturation, Sr is equal to unity ($Sr = 1$) and the soils are termed as 'saturated soils'. Many of the problems which are encountered in saturated soils are closely related to the effective stress, σ' and pore water pressure, u_w.

On the other hand, the term "partly saturated", "partially saturated" or "unsaturated" usually refers to the condition where the voids in the soil mass are filled with both water and air and the soil mass is located above the ground water table. Fig. 1-9 illustrates the different soil conditions that exist and their corresponding pore water pressures. Under each condition the soil is subjected to different types of pore water pressure, thus the stresses

developed in each condition will differ. In the case of the saturated condition, the soil strength is influenced by the effective stress variables and the positive pore water pressure generated in the soil reduces the soils strength by eliminating the interaction between the soil particles. In the case of the unsaturated condition, due to the effect of the contractile skin (i.e. the air-water interface) (Fredlund and Morgenstern, 1977), the soil is subjected to two independent stress state variables namely, net normal stress (σ-u_a) and matric suction (u_a–u_w) (Wulfsohn, Adams and Fredlund, 1996).

Given its origin, unsaturated soils may be natural or artificial. These soils are more abundant in arid and semi-arid regions, where the seasons are marked by prolonged dry periods. Among the many types of unsaturated soils, some are notorious and problematic for engineers.

Apart from natural and geological processes, man-made activities such as excavation, remolding and recompacting may also result in the desaturation of saturated soils and therefore, the formation of unsaturated soils. These natural and man-made materials pose difficulty in being considered and understood, particularly where volume changes are concerned, within the framework of classical saturated soil mechanics.

The most characteristic phenomena of unsaturated soil behavior are those related to its volumetric strain as a result of modifying the degree of saturation (*Sr*). This volumetric strain can be positive (collapse) or negative (expansion). According to Aitchison (1973), both the collapse as well as the expansion can be considered as processes of structural instability, due to the discontinuity in the deformational behavior of the soil while varying the environmental conditions(for example, changes in humidity), without changing the external stress state.

1.4.2. Concept of Suction

The term "soil suction" was used by Schofield (1935) to represent the "pressure deficiency" in the pore water of some soils having the capacity to absorb water if it is added at atmospheric pressure. The term suction signifies the parameter of the stress state that takes into account those surface effects capable of retaining water within the soil structure. Without the incorporation of this parameter it is impossible to define the stress state and to understand the deformational response of unsaturated soils.

The difference between pore air pressure and pore water pressure is defined as matric suction (u_a-u_w). The value of this matric suction depends on the surface tension and the radius of curvature of the meniscus. When the degree of saturation decreases, the meniscus retracts into small pore spaces where the radius of curvature of the meniscus is reduced and, thus, the matric suction increases. Due to the small pores clay soils have higher matric suction than granular soils.

The flow of water through unsaturated soils is controlled by the total water potential gradient. The total water potential can be expressed as the sum of three components:

1. Gravitational potential, caused by rise of the ground water with respect to a reference level;
2. Capillary or matric potential, caused by the effects of surface tension;
3. Osmotic potential, caused by the concentration of dissolved ions in the water (of the soil).

For an unsaturated soil with pore air at atmospheric pressure, the matric potential is given by matric suction, defined previously, multiplied by the unit weight of water. By analogy, the osmotic potential divided by the unit weight of water is called "osmotic suction". The sum of the matric suction and osmotic suction is defined as the total suction.

Experimental evidence suggests that the shear strength and volume change behavior of unsaturated soils are more dependent on matric suction than on the total suction (Alonso et al. 1987). Thus, the stress-strain behavior depends on matric suction while the flow of water depends on the total suction gradient (and gravitational effects).

1.4.3. Volumetric Behavior of Unsaturated Soils

The concept of volume changes in an unsaturated soil can be expressed in terms of deformations or relative movement of the soil phases. It is necessary to establish deformation state variables that are consistent with multiphase continuum mechanics principles. A change in the relative position of points or particles in a body forms the basis for establishing deformation state variables. In the case of a saturated soil specimen the change in void ratio is due to the volume change of the water phase, so the soil volume change can be evaluated purely on the basis of the variation in water volume. Whereas, in the case of unsaturated soils, which can be considered as a four phase soil system (see Fig. 1-10), soil, water, air, and contractile skin, the volume changes occur due to the changes in both the air and the water phases. The total volume change of an unsaturated specimen is equal to the sum of the volume change of water and volume change of air by assuming that the soil skeleton is incompressible.

With respect to the study regarding the deformational behavior of unsaturated soils there are several approaches that consider the soil as an isotropic elastic material. Fredlund and Morgenstern (1976) referring to the solid phase, used different elastic moduli with respect to the stresses and the suction. Justo and Saettersdal (1982) cited by Yuk (1994), presented a review of the elastic methods and analysis of expansive and collapsible soils. Richards (1984) analyzing the stress-strain behavior of expansive soils, proposes a model that incorporates the nonlinear behavior, depending on the applied stress and the suction, hysteresis in the stress-strain behavior and the internal stresses of tension and shear.

1.4.4. Shear Strength of Unsaturated Soils

In the case of saturated soils, one stress state variable is sufficient to describe the behavior of two phases (solid and water/or air) of the soil mass. The stress state variable σ' is defined as $\sigma' = \sigma - u_w$, where σ' is the effective stress, σ is the total stress, and u_w is the pore-water pressure (Terzaghi, 1943).

Matyas and Radhakrishna (1968) mentioned that the principle of effective stress was inadequate to explain the volumetric behavior of unsaturated soils. The use of the effective stress equation proposed by Bishop (1959) for both compression and wetting processes resulted in unusual values of the parameter χ (negative values). Bishop and Blight (1963) and Matyas and Radhakrishna (1968) suggested expressing the soil behavior in terms of two independent stress components rather than in terms of a single effective stress. The two stress state variables defined by these authors were: $(\sigma - u_a)$ and $(u_a - u_w)$.

$$\sigma' = (\sigma - u_a) + \chi(u_a - u_w) \qquad \text{(Eqn. 1-1)}$$

Where, σ' is the effective stress, σ is the total stress, u_a is the pore air pressure, u_w is the pore water pressure, χ is a parameter that depends on the degree of saturation.

Fredlund and Morgenstern (1977) presented a theoretical stress analysis for unsaturated soils based on multi-phase continuum mechanics. They considered the unsaturated soil as a four-phase system. These authors added the contractile skin as a fourth phase and these four phases were used by these two authors in the stress analysis of unsaturated soil on the basis of continuum mechanics. The soil particles were presumed to be incompressible and the soil was considered chemically inert. This analysis determined that any two of three possible variables $(\sigma - u_a)$, $(u_a - u_w)$, and $(\sigma - u_w)$ could be used to describe the state of normal stress in unsaturated soils. Three possible combinations of the proposed variables could be used to express the state of stress of unsaturated soils:

1. $(\sigma - u_a)$ and $(u_a - u_w)$;
2. $(\sigma - u_w)$ and $(u_a - u_w)$; and
3. $(\sigma - u_a)$ and $(\sigma - u_w)$

Any two of the above mentioned stress state variables can be used to describe the shear strength and volume change behavior of unsaturated soils. The components of these variables are physically measurable quantities. The first combination of stress state variables, $(\sigma - u_a)$ and $(u_a - u_w)$, has been the most widely used since the effect of a change in the total normal stress can be separated from the effect caused by a change in the pore-water pressure. In addition, the pore-air pressure is considered to be atmospheric (i.e., zero gauge pressure) for most practical engineering problems (Fredlund et al., 1978; and Fredlund and Rahardjo, 1993). The term $(\sigma - u_a)$ is referred to as the "net normal stress", and the term $(u_a - u_w)$ is referred to as the "matric suction".

Fredlund and Morgenstern (1977) validated the concept of the proposed stress state variables experimentally by running "null" tests. In these tests it was proven that changing the air, water, and the total pressures resulted in no change in the state of the soil as long as the state variables ($(\sigma - u_a)$, $(u_a - u_w)$, and $(\sigma - u_w)$) remain constant. The stress state variables were therefore considered to be valid for describing the mechanical properties of unsaturated soils.

1-5 Organization of the Thesis

This thesis comprises of seven (7) chapters and four (4) appendices.

1.5.1. Chapter Division

The contents of each chapter are as follows:

Chapter 1: Introduction

This chapter gives a brief introduction to the research topic and examines the incident that happened to MV Bulk Jupiter in January 2015. To understand the phenomenon of the capsized MV Bulk Jupiter, the objectives of the research are presented, and scope and technical issued needed to be solved, as well as flow of the study. A general literature review of the aspects relevant to this study with respect to unsaturated soils is presented consisting of an introduction to unsaturated soils, followed by a brief history of unsaturated soils mechanics.

Chapter 2: Test Materials

The second chapter presents the physical properties of the material and material properties employed in this study. The materials used are Bauxite, which is the principal ore of aluminum and the main material used in this study, iron ore fines type B (IOF-B), Inagi sand, and Toyoura sand. Each material is described in terms of its material description, particle size distribution, specific gravity, maximum dry density, and its optimum moisture content.

Chapter 3: Liquefaction Resistance under Different Saturation Conditions

This chapter presents the results of a series of undrained cyclic loading tests performed on both fully saturated and unsaturated sand specimens. The results are discussed by presenting graphs: the axial strain, the volumetric strain, pore-water pressure, and suction vs. time relationship, stress- strain relationship and the relationship between cyclic stress ratio and number of cycles. At the end of the chapter, the results are plotted to the proposed new governing index by Wang (2014) called volumetric strain ratio, R_v to be the governing factor of liquefaction resistance of the unsaturated soil.

Chapter 4: Permeability Tests under Different Saturation Conditions and SWRC Tests

In the fourth chapter, the experimental results are analyzed, discussed and comparisons are then made between specimens under the standard permeameter tests using rigid mold, as compared with new methods to measure head difference by Local Pin-Type Sensors using the triaxial apparatus (flexible wall). The technique is further extended under unsaturated conditions by utilizing a triaxial permeamter system with modification from the one used under saturated condition. Similarly, SWRC tests are performed to describe the relationship between suction and volumetric water content (or saturation degree). Finally results are

compared to an indirect method of estimating permeability of unsaturated soils by Van Genuchten Model (VG Model).

Chapter 5: Numerical Analysis: Seepage

Numerical analysis of seepage using a finite element method (FEM) software called Guslope is utilized to understand the distribution of water on the heap of bauxite. Comparisons are also made to iron ore and Inagi sand.

Chapter 6: Numerical Analysis: Dynamic Response

This chapter obtains the parameter for PZ model (Pastor and Zienkiewicz, 1990) from experimental data of monotonic and cyclic tests by simulating it numerically. PZ model is used in the analysis of liquefaction of heap. The heap material is described by its physical, mechanical, and water distribution properties from the experimental data obtained. Runs are conducted using a commercial software, UWLC Ver. 2.

Chapter 7: Conclusions and Recommendations

Finally, chapter seven summarizes the main results and the related conclusions of this study and also provides recommendations for further studies pertaining to this field of research.

1.5.2. Appendices

Appendix A: Liquefaction Tests

Appendix B: Permeability Tests and SWRC Tests

Appendix C: Seepage Analysis

Appendix D: Dynamic Response Analysis

Image: https://www.marinetraffic.com/en/ais/details/ships/shipid:373826/mmsi:-9339947/imo:9339947/vessel:BULK_JUPITER

Fig. 1–1. MV Bulk Jupiter (Handymax type bulk carrier)

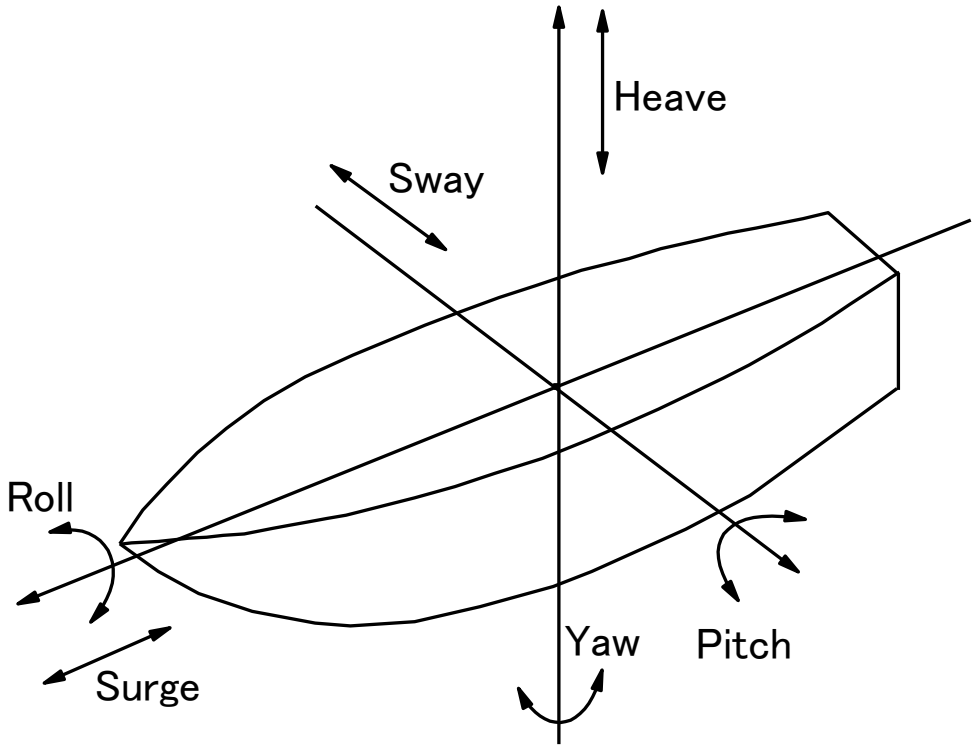

Fig. 1–2. Six motion components of a ship (Wang, 2014)

Fig. 1–3. A typical image of the heap of bauxite

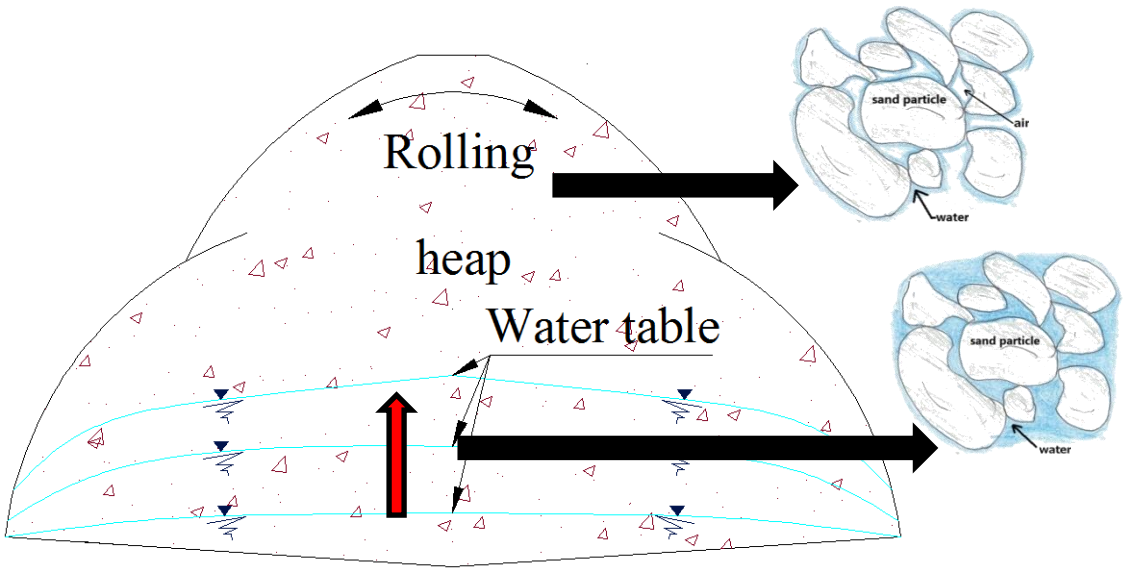

Fig. 1–4. Saturation condition of a heap (Wang, 2014)

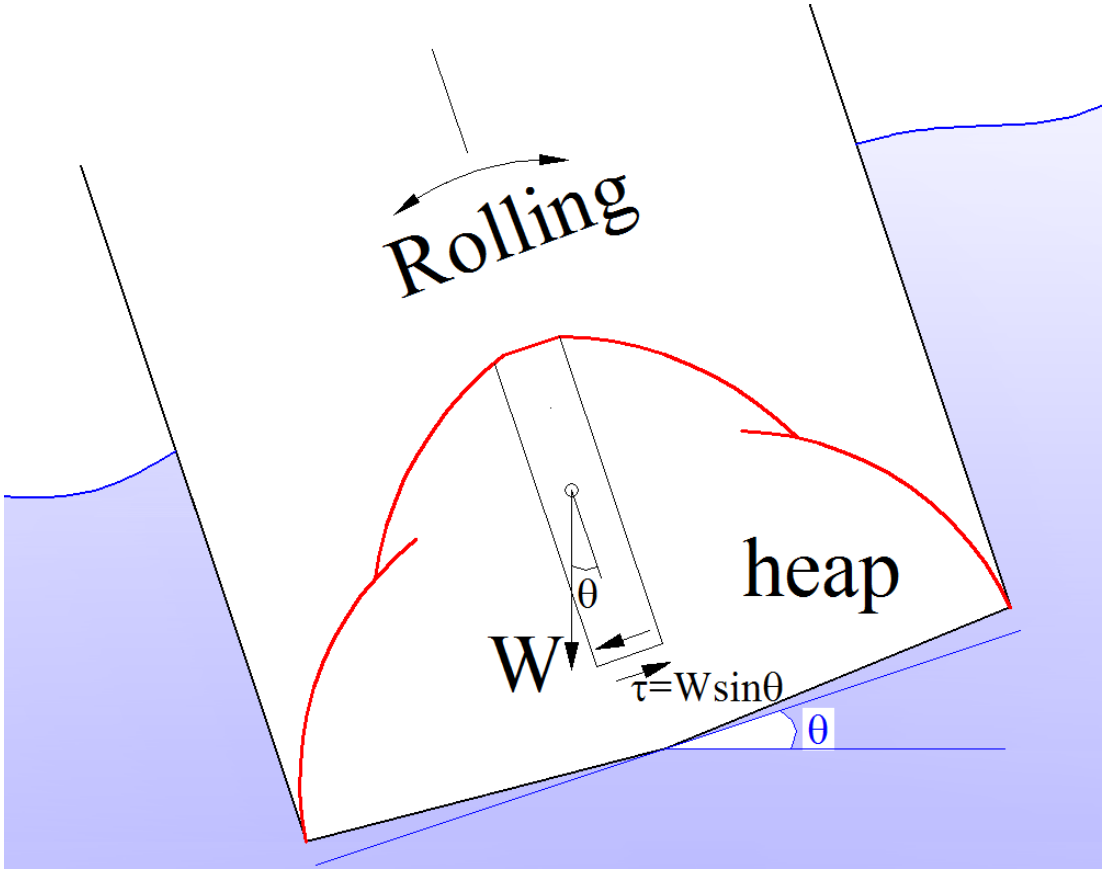

Fig. 1–5. The condition of a heap under rolling motion (Wang, 2014)

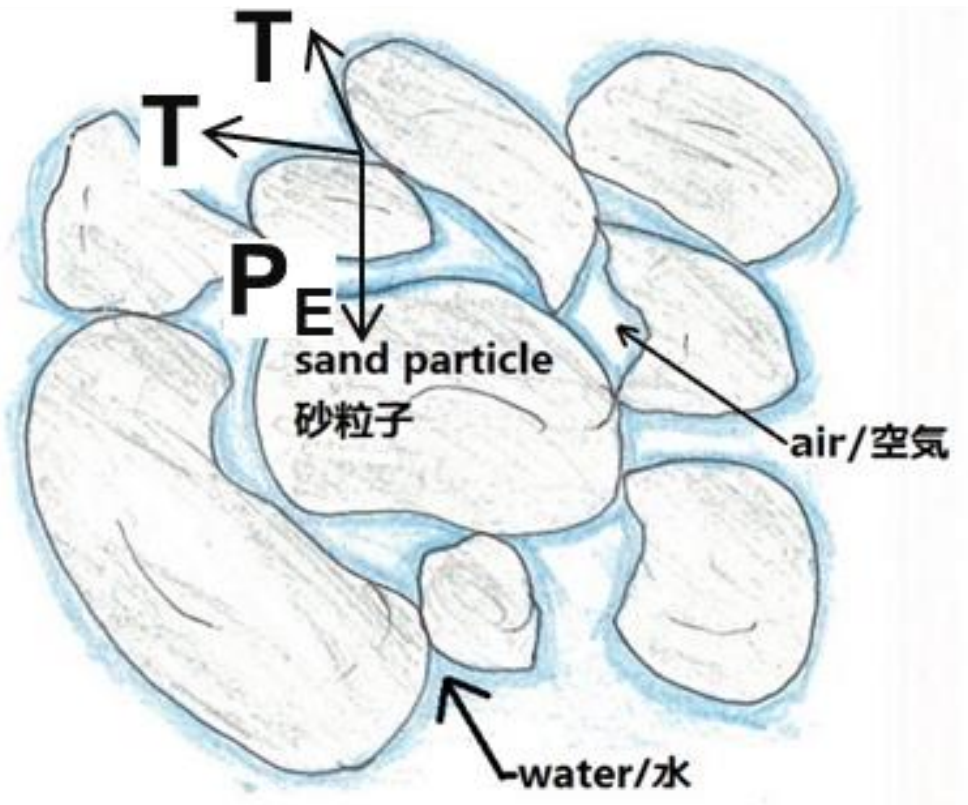

Fig. 1–6. Forces worked on pore water of an unsaturated soil element (Wang, 2014)

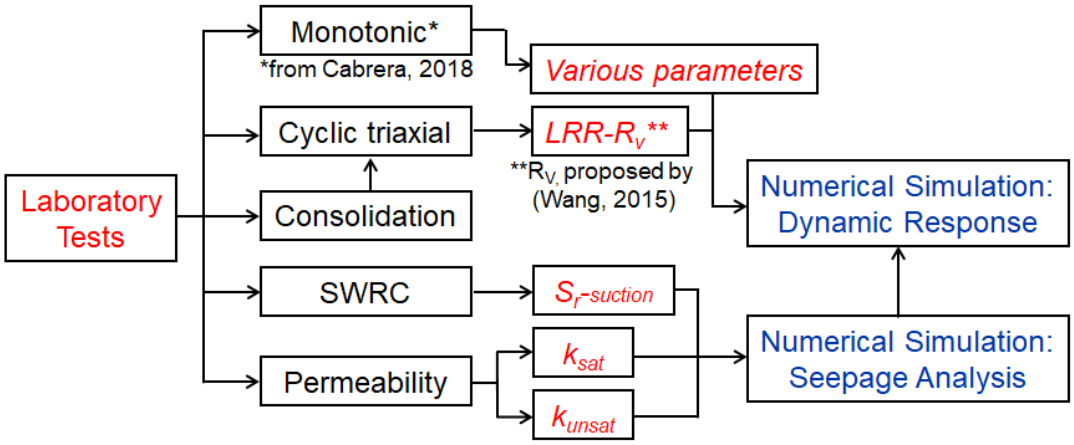

Fig. 1–7. Flow of Study

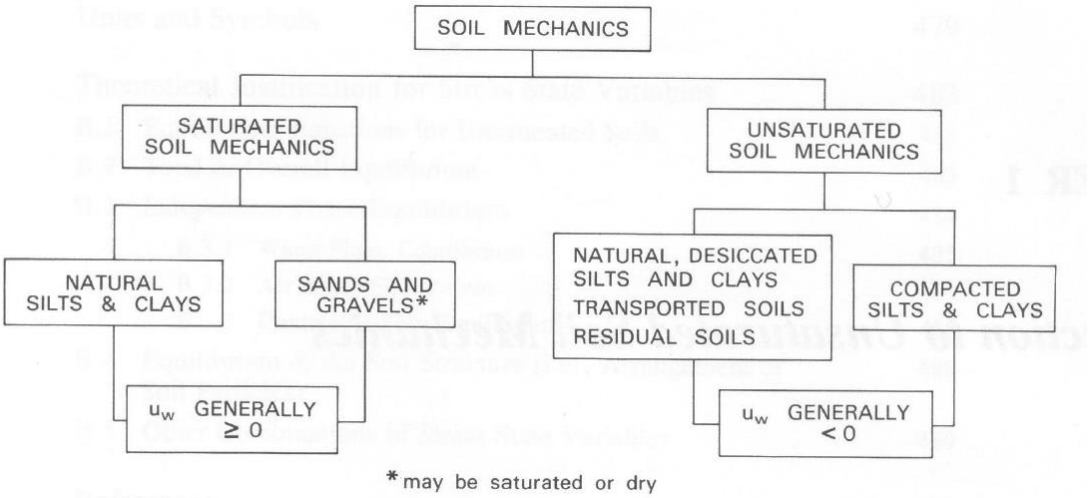

Fig. 1–8. Categorization of Soil Mechanics (Fredlund, 2007)

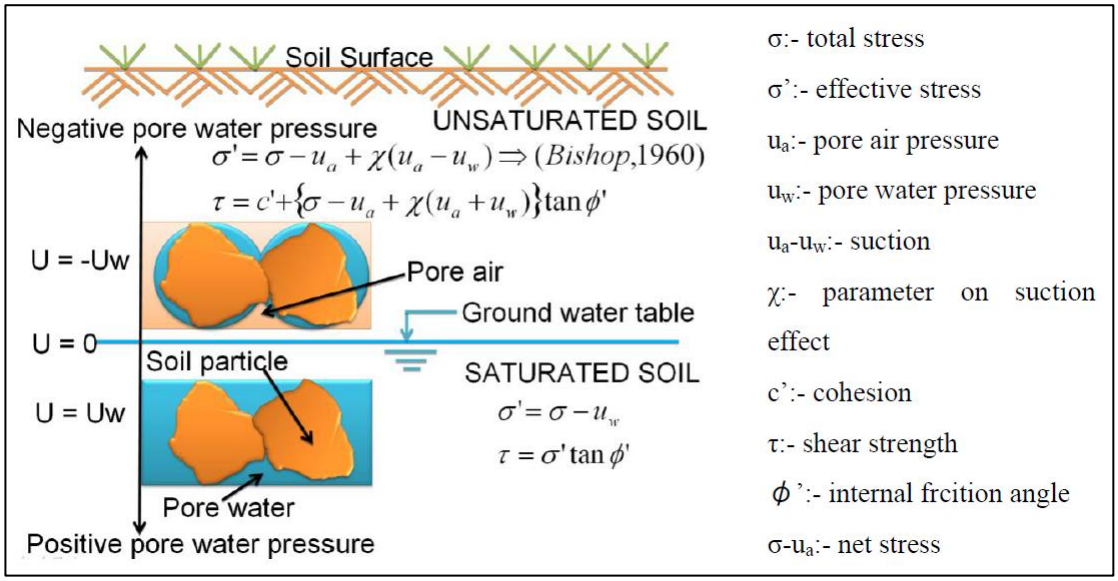

Fig. 1–9. Different Soil Conditions that exist and their corresponding Pore Water Pressure (Fredlund, 2007)

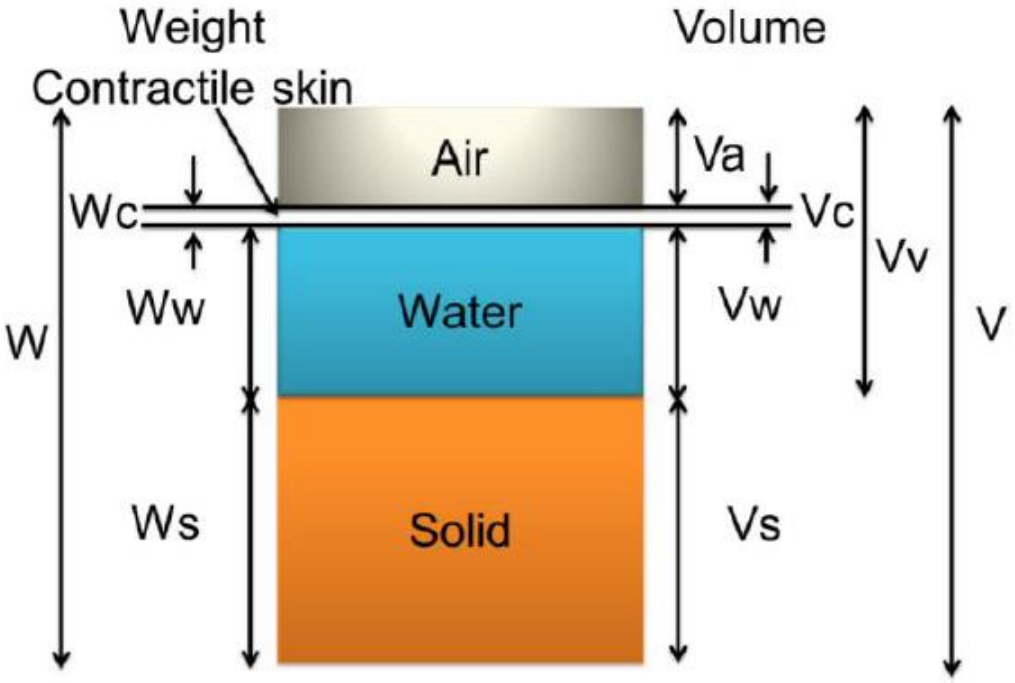

Fig. 1–10. Four-phase Unsaturated Soil System (Fredlund, 2007)

Chapter 2
Test Materials

Contents

2-1. Introduction

In this study, tests were conducted on four types of materials namely: (1) Bauxite, (2) Iron ore fines type B (IOF-B), (3) Inagi sand, and (4) Toyoura sand.

Bauxite is a sedimentary rock with a relatively high aluminum content. It is the principal ore of aluminum. Iron Ore Fines, on the other hand is a mineral where metallic iron can be extracted. Inagi sand is a silty sand while Toyoura sand is a widely used clean sand for conducting experiments in Japan.

Table 2-1 summarizes the material properties of geomaterials and they are utilized in:

1. Bauxite (passing 2 mm sieve): used for all tests in this study;
2. IOF-B: used for all tests in this study, however existing results on undrained monotonic tests and undrained cyclic loading tests were obtained from Wang, 2014;
3. Inagi sand: used mainly for permeability tests (saturated and unsaturated conditions);
4. Toyoura sand: used mainly for permeability tests (saturated condition).

Table 2-1. Properties of materials used

Material	Bauxite (entire gradation)	Bauxite (<2.00 mm)	IOF-B (Wang, 2014)	Inagi Sand (Batch 2007)	Toyoura Sand (Batch J)
Gravel (%)	56.8	-	33.5	0	0
Sand (%)	25.7	59.4	42.9	70.5	99.9
Silt (%)	6.6	28.6	17.1	18.2	-
Clay (%)	11.0	12.0	6.5	11.3	-
Fines Content (%)	17.6	40.6	23.6	29.5	0.1
Specific Gravity, G_S	2.642	2.642	4.444	2.656	2.652
D_{60} (mm)	3.60	0.384	1.382	0.136	-
D_{50} (mm)	2.65	0.200	0.715	0.115	0.16
D_{30} (mm)	0.658	0.054	0.136	0.076	-
D_{10} (mm)	0.036	0.001	0.013	0.004	-
Coefficient of Curvature, U'_c	3.33	6.48	1.0	10.6	-
Coefficient of Uniformity, U_c	99.7	328.9	106.3	34.0	-
Max.void ratio, e_{max}	-	-	-	1.645	0.989
Min.void ratio, e_{min}	-	-	-	0.907	0.611
Max.dry density, $\rho_{d,max}$ (g/cm^3)	1.95*	1.70**	2.79	1.66	-
Optimum moisture content, w (%)	10.7	17.5	12.0	20.7	-

Notes:

1. Gravel, Sand, Silt and Clay: Percentage of particle size in the range of 2-75 mm, 0.075-2 mm, 0.005-0.075 mm and < 0.005 mm, respectively; Fines content: particle size <0.075 mm;
2. D_{60}, D_{50}, D_{30} and D_{10}: sizes passed by 60%, 50%, 30% and 10% of a material by weight, respectively;
3. $U'_C=D_{30}^2/(D_{10}*D_{60})$; $U_C = D_{60}/D_{10}$;
4. Gs: specific gravity; e_{max} and e_{min}: Maximum and minimum void ratio; ρ_{dmax} and ω_{opt}: Maximum dry density and optimum water content obtained from compaction test.
5. $\rho_{d,max}$ was obtained by *Type E compaction method (see Table 2-2) with compaction energy of 18.07 kg*cm/cm^3, while **type A compaction method with compaction energy of 5.63 kg*cm/cm^3.

2-2. Bauxite

2.2.1. Material Description

Bauxite was named after the village Les Baux in southern France, where it was first recognized as containing aluminum and named by the French geologist Pierre Berthier in 1821. Bauxite is the primary aluminum ore for most of the world's production of aluminum, with aluminum being the third most abundant element in the earths' crust (Global Bauxite Working Group, 2017). Bauxite does not have a specific composition as it is a mixture of aluminum hydroxides, clay minerals, and insoluble materials such as quartz, hematite, magnetite, siderite, and goethite. Generally, commercially viable grades of bauxite range up to 50% in aluminium hydroxides, up to 35% silica usually as quartz, and up to 15% hematite/goethite.

Fig. 2-1 shows the appearance of the bauxite used in this experiment. Bauxite is typically a soft, reddish brown material with an earthy luster (Fig. 2-1a). When mortared, the particle size can be as small as fine powder to as huge as greater than 19 mm. It has irregular shape with rough edges. Fig. 2-1b shows the microscopic view of bauxite.

2.2.2. Particle Size Distribution

The particle size analysis of soil involves determining the percentage by mass of particles within the different size ranges. The particle size distribution of a coarse soil is determined by performing a sieve analysis test. This process comprises of passing the soil through a series of standard test sieves having successively smaller mesh sizes. The mass of soil retained in each sieve is then determined and the accumulative percentage by mass passing each sieve is calculated. In the case where there are fine particles present in the soil, the soil sample is treated with a deflocculating agent and washed through the sieves.

The particle size distribution of a fine soil or the fine fraction of a coarse soil can be determined by the sedimentation method. This method is based on Stokes' law which provides the theoretical basis to calculate the relationship between sedimentation velocity and particle size: the larger the particles the greater the settling velocity and vice versa.

Fig. 2-2 shows the gradation curve of bauxite following the Japanese Geotechnical Society (JGS) test method for particle size distribution of soils (JGS 0131-2009). Considering the entire gradation of the specimen, it can be observed that the fines would be around 17.6%. The apparatus used in testing however is designed for a specimen with height of 10 cm and diameter of 5 cm.

In preparing the specimen, the standard code for preparation of soil specimens for triaxial tests (JGS 0520-2009) stipulates in Section 4.2d that "The standard diameter of a specimen shall be at least 20 times the maximum particle size of the sample." Using the entire gradation, the particle was as large as 19 mm or greater, hence the diameter of the specimen that the apparatus can support being 5 cm (i.e 50 mm) would not be suitable. By

utilizing only those passing 2 mm, it would be 25 times, therefore satisfying the standard. The particle size of that passing 2 mm is also shown in Fig. 2-2 and has 40.6% fines.

Fig. 2-3 shows the particle sizes passing at sieves segregated into several pans. It was also tested that the bauxite used in the experiments was non-plastic as Atterberg Limits cannot be obtained.

2.2.3. Specific Gravity, G_S

Specific gravity is the ratio of the density of a substance to the density of a reference substance; equivalently, it is the ratio of the mass of a substance to the mass of a reference substance for the same given volume. The specific gravity of the soil particles (G_s) is given by:

$$G_s = \frac{\rho_s}{\rho_w} \qquad \text{(Eqn 2-1)}$$

where: ρ_s is the density of soil/geomaterial and ρ_w is the density of water at 20°C.

JGS 0111-2009 was followed for the test method for density of bauxite. Three samples were tested, resulting to 2.643, 2.642, and 2.641. The average value, 2.642 was used for all the related calculations for this material.

2.2.4. Maximum Dry Density (MDD) and Optimum Moisture Content (OMC)

Compaction is the process by which the bulk density of an aggregate of matter is increased by driving out air. For any soil, for a given amount of compaction energy, the density obtained depends on the moisture content. At very high moisture contents, the maximum dry density is achieved when the soil is compacted to nearly saturation, where (almost) all the air is driven out. At low moisture contents, the soil particles interfere with each other; addition of some moisture will allow greater bulk densities, with a peak density where this effect begins to be counteracted by the saturation of the soil.

JGS 0711 was used as the test method for soil compaction using a rammer. The standard code specifies several compaction method shown in Table 2-2 extracted from JGS 0711-2009.

Table 2-2. Types of Compaction Method (JGS 0711-2009)

Type	Rammer mass (kg)	Inner φ of mold (cm)	Height of mold (cm)	Number of layers	Number of compactions per layer	Compaction Energy (kg*cm/cm^3)	Allowable max. particle size (mm)
A	2.5	10	12.73	3	25	5.63	19
B	2.5	15	17.50	3	55	4.00	37.5
C	4.5	10	12.73	5	25	25.32	19
D	4.5	15	17.50	5	55	18.01	19
E	4.5	15	17.50	3	92	18.07	37.5

Fig. 2-4 presents the compaction curve of bauxites conducted in two (2) different types of compaction method. However, the specimens were prepared using only those passing 2 mm, Type A compaction method. It is symbolized by the black curve in Fig. 2-4, having a MDD of 1.702 g/m^3 and OMC of 17.5%.

Using the entire gradation, it was necessary to conduct Type E as well to be able to correlate it properly with the bauxite during maritime transport (i.e. not only those passing 2 mm). The blue plot indicates Type E method, resulting to MDD of 1.947 g/m^3 while OMC was 10.7%.

A parameter compaction degree D_c is used to identify the relative density of the specimen prepared to its maximum dry density. It is defined as:

$$D_C = \frac{dry\ density\ of\ specimen}{maximum\ dry\ density\ of\ specimen} \quad \text{(Eqn 2-2)}$$

For bauxite throughout the experiments, three densities were prepared, namely at D_c =65% which is specified as Loose, D_c =80% as Medium Dense, and D_c =90% as Dense.

2-3. Iron Ore fines type B (IOF-B) (Extracted and summarized from Wang, 2014)

2.3.1. Material Description

Fig. 2-5 shows the overall and close-up view of a typical relatively large particle of IOF-B. Large particles of IOF-B are normally covered by dull brownish-yellow fines and possess a multi-layer structure like shale.

2.3.2. Particle Size Distribution

Fig. 2-6 shows the gradation of IOF-B. It is classified as a SFG material containing 33.5% gravel, 42.9% sand, 17.1% silt and 6.5% clay according to the test standard JGS 0131-2009. Non-plastic fines content was about 24%.

2.3.3. Specific Gravity, G_S

Iron ore fines are normally rich in iron oxides, of which the specific gravity is usually higher than other common soils encountered in geotechnical engineering. The average value, 4.444, was used for all the related calculations for this material.

2.3.4. Maximum Dry Density (MDD) and Optimum Moisture Content (OMC)

The compaction test was conducted for IOF-B according to method A. A MDD of 2.79 g/cm^3 was obtained with an OMC of 12.0%. Fig. 2-7 shows the compaction curve of IOF-B.

2-4. Inagi sand

2.4.1. Material Description

Soil can be defined as any uncemented or weakly cemented accumulation of mineral particles formed by the weathering actions of frost, temperature, gravity, wind, rain and in some cases chemicals. On the basis of origin of their constituents, soils can be divided into two large groups: residual soils and transported soils. If the soil particles formed as a result of weathering remain at their original location they constitute a residual soil. If the soil particles are transported and deposited in a different location they constitute a transported soil, the sources of transportation may be gravity, wind, water or glaciers.

Inagi sand belongs to the transported soils category. It is an inland weathered sand widely found in the Tama district. This sand consists of crushable particles and can be classified as silty sand with considerable amount of fines.

2.4.2. Particle Size Distribution

The particle size distribution of inagi sand is shown in Fig. 2-8. It is a material containing 70.5% sand, 18.2% silt and 11.3% clay. Fines content was about 29.5%.

2.4.3. Specific Gravity, G_S and Void Ratio, e

For Inagi sand, G_s used was 2.656 for all cases. Void ratio was also obtained for inagi sand. Void ratio is defined as the ratio of the volume of void space (V_V), and the volume of solids (V_S). It is expressed as:

$$e = \frac{V_V}{V_S} \qquad \text{(Eqn 2-3)}$$

Relevant to void ratio are the maximum void ratio and the minimum void ratio. The obtained maximum void ratio in the experiment was 1.645 while the minimum void ratio was 0.907.

2.4.4. Maximum Dry Density (MDD) and Optimum Moisture Content (OMC)

In the experiments, the maximum dry density obtained was 1.66 g/cm^3 while the optimum moisture content was 20.7% (see Figure 2-9).

2-5. Toyoura Sand

2.5.1. Material Description and Physical Properties

Toyoura sand is widely used clean sand for conducting experiments in Japan. The particle size distribution of Toyoura sand used in the experiments is shown in Fig. 2-10. It is a uniformly graded sand, composed of 99.9% sand particles, with practically very little or no

fines. The G_s obtained for Toyoura sand was 2.647, while the maximum and minimum void ratios obtained were 0.989 and 0.611 respectively.

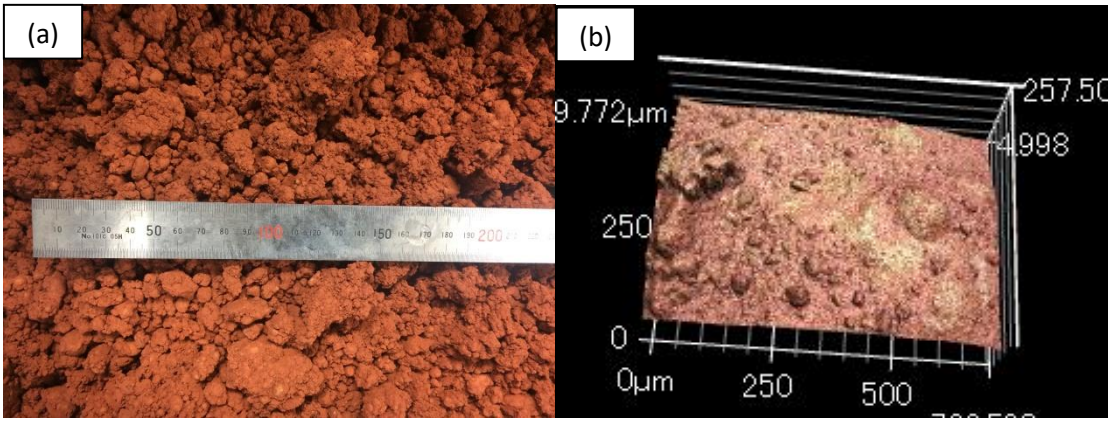

Fig. 2-1. (a) overview appearance and (b) microscopic view of bauxite

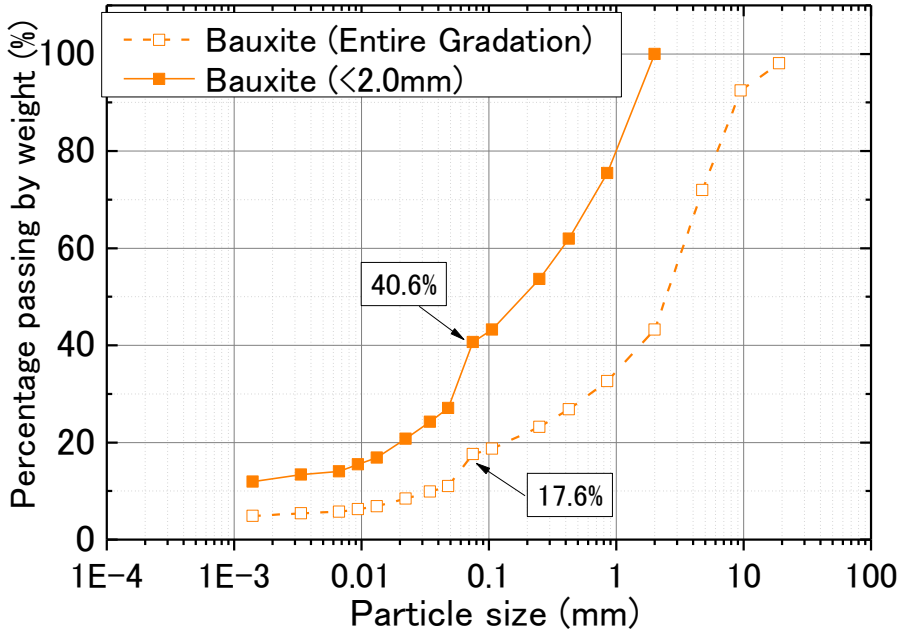

Fig. 2-2. Particle Size Distribution of bauxite

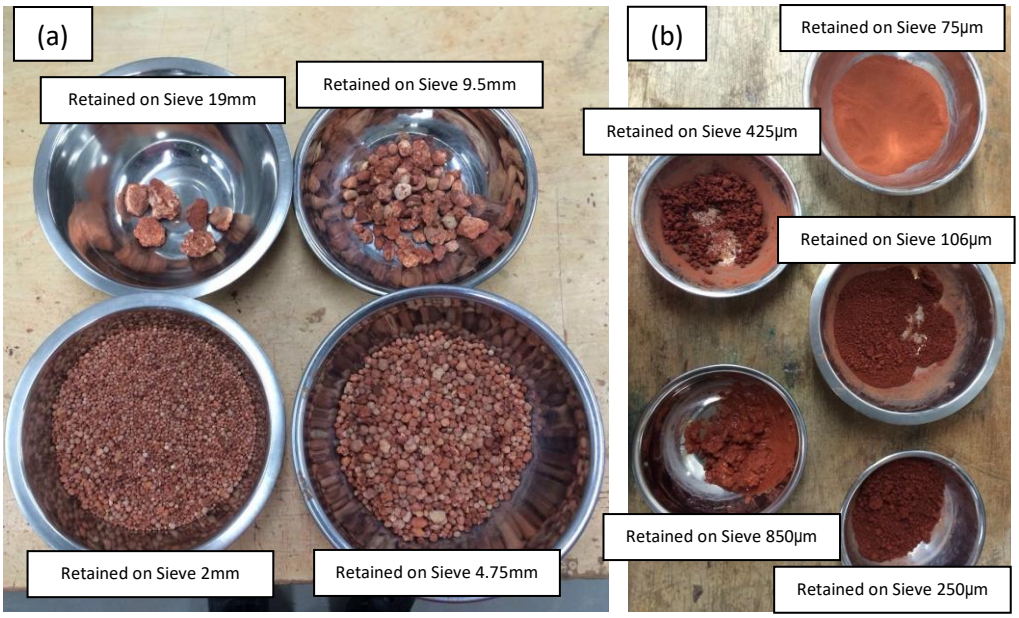

Fig. 2-3. (a) particle size greater than 2 mm and (b) particle sizes less than 2 mm

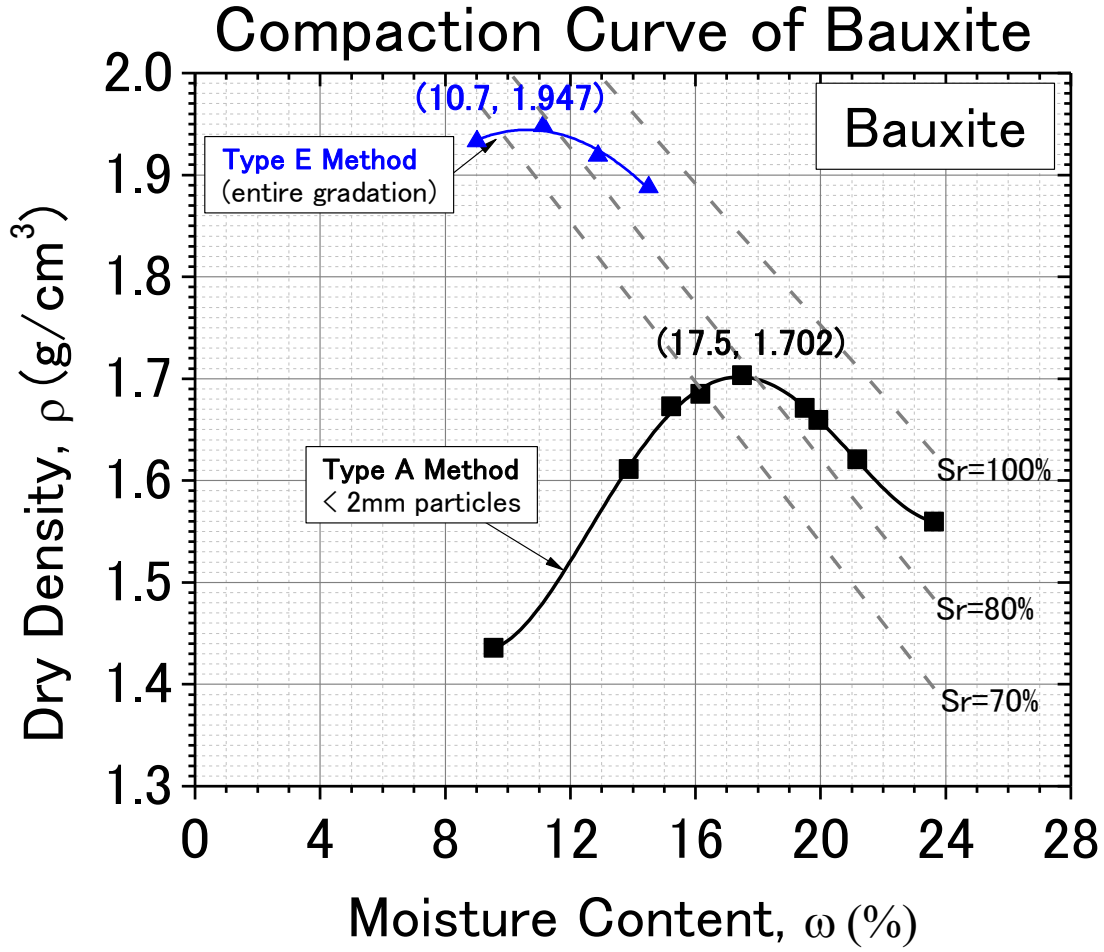

Fig. 2-4. Compaction curve of bauxite

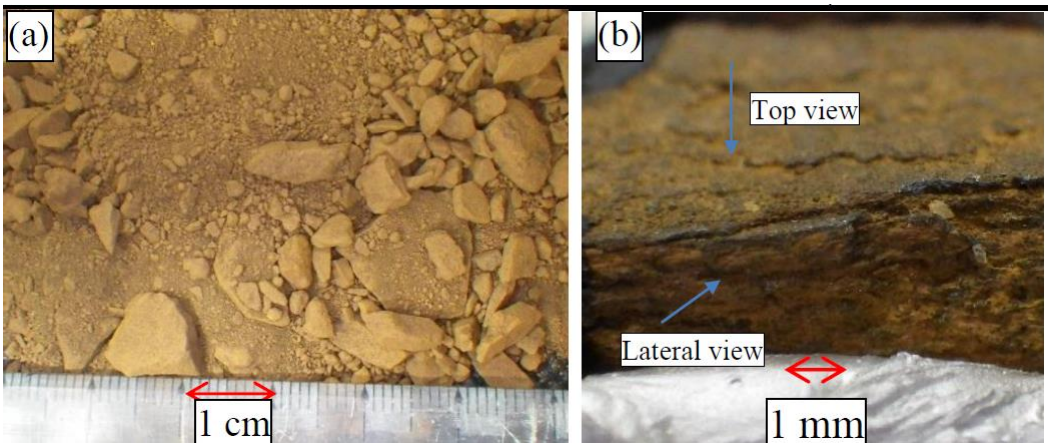

Fig. 2-5. Overall and close-up view of IOF-B (Wang, 2014)

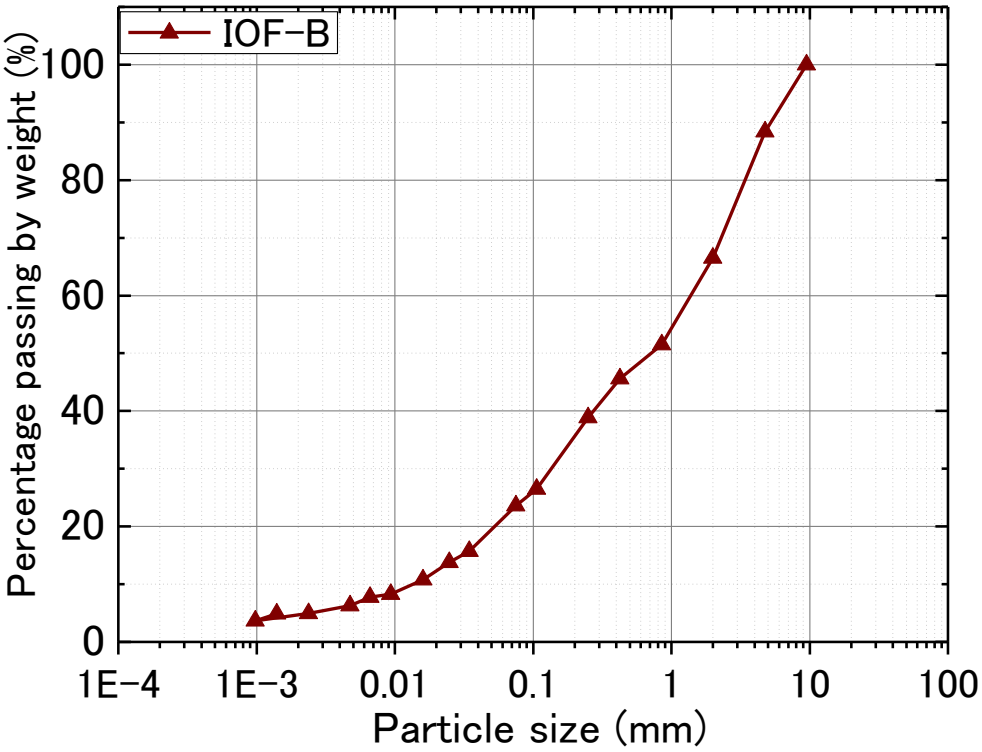

Fig. 2-6. Particle size distribution of IOF-B (Wang, 2014)

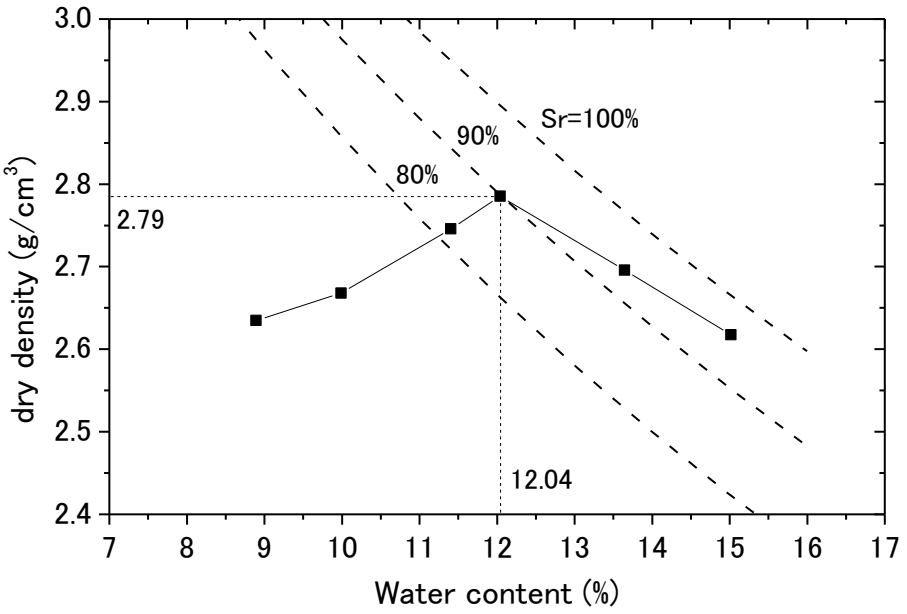

Fig. 2-7. Compaction Curve of IOF-B (Wang, 2014)

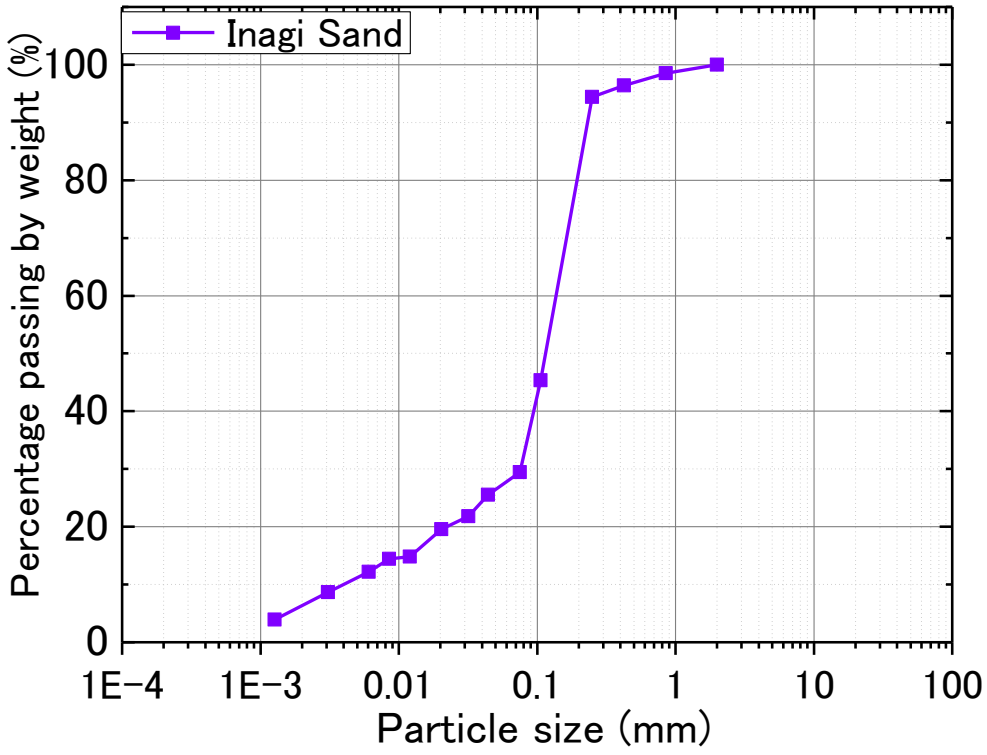

Fig. 2-8. Particle size distribution of Inagi sand

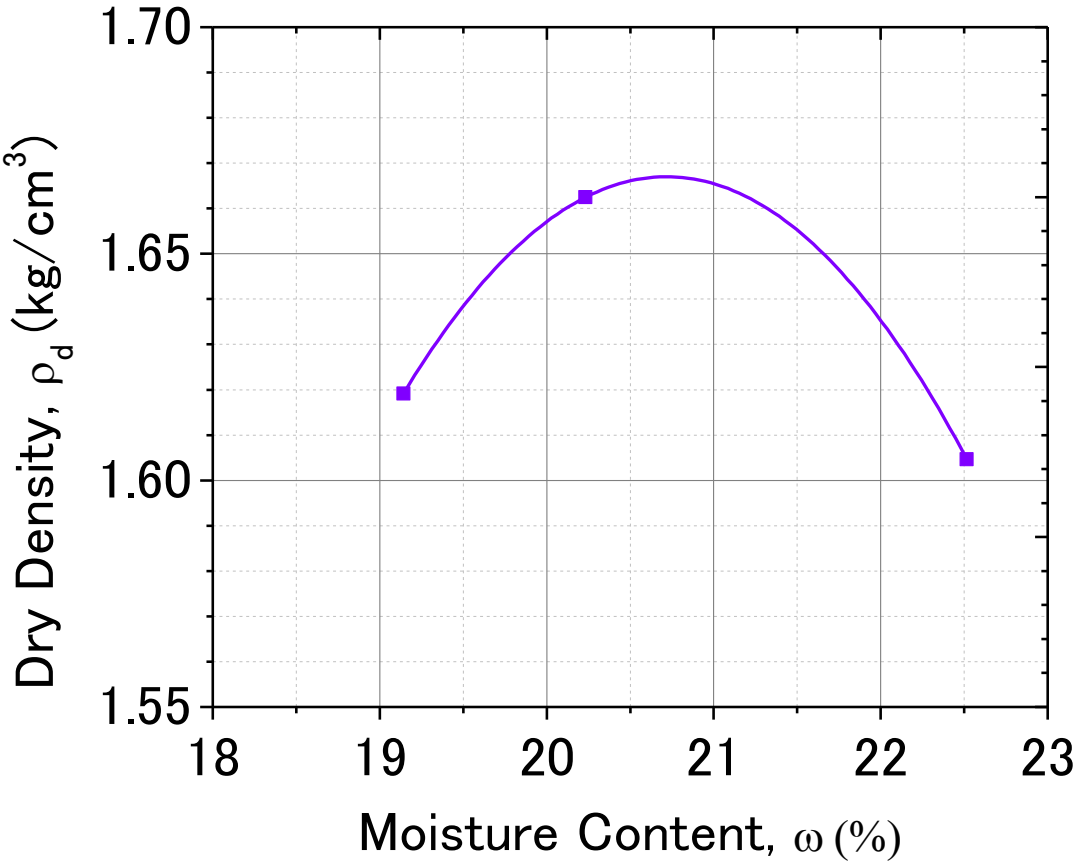

Fig. 2-9. Compaction Curve of Inagi Sand

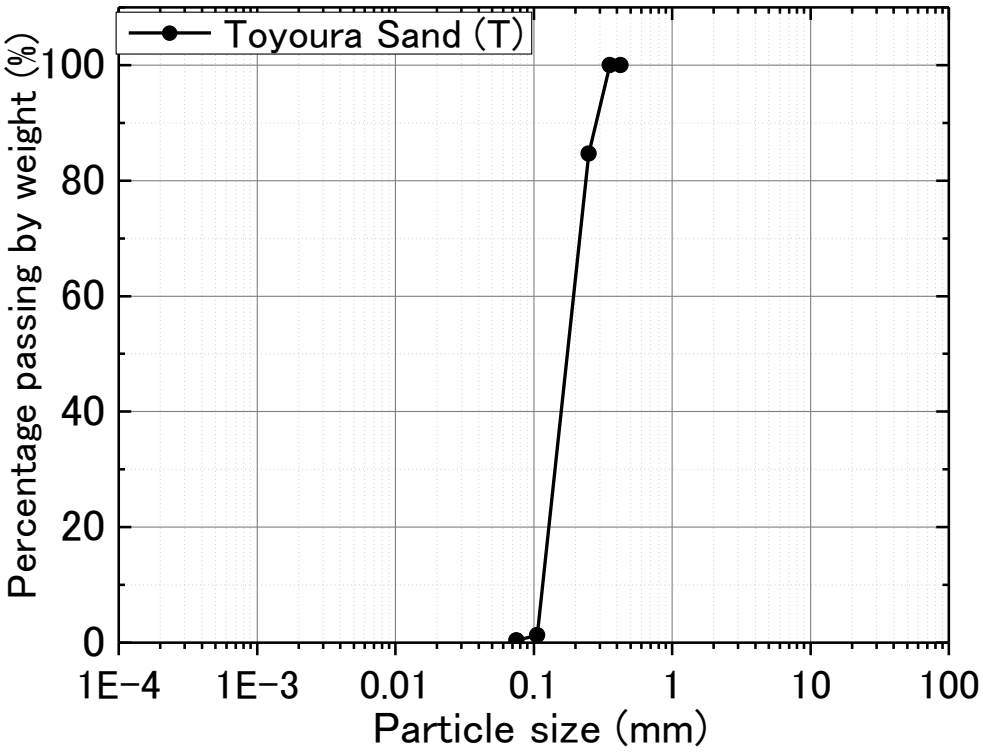

Fig. 2-10. Particle Size Distribution of Toyoura Sand

Chapter 3
Liquefaction Resistance under Different Saturation Conditions

Contents

3-1. Introduction

This chapter describes the liquefaction resistance of bauxite under different saturated conditions and different degrees of compactions. The results for bauxite were compared to iron ore fines tests results and other typical soils.

Undrained tests were conducted using bauxite under saturated case using the stress-controlled Triaxial Apparatus. After which, tests were carried out at unsaturated case at different degrees of saturation (S_r = 58% and S_r = 84%) using the Triaxial Apparatus with Linkage Double Cell System.

The main purpose of this chapter is to determine bauxite on its liquefaction behavior, if it has unique characteristics as compared to other geomaterials used in this study. Accordingly, it is also used to verify if it follows the trend of the proposed liquefaction resistance ratio (LRR) plotted against a new index called volumetric strain ratio (R_v). This new index was proposed by Wang (2014). Discussion of this new index is included in this chapter.

Another purpose is that the test results obtained from the liquefaction tests were used to compare with the numerical simulation results later in Chapter 6: Numerical Analysis: Dynamic Response. The tests were used to obtain parameters to assign for a model used in the simulations.

3.1.1. Liquefaction

The terminology 'liquefaction' was defined by Castro et al. (1977) as a phenomenon wherein a saturated sand loses a large percentage of its shear resistance (due to monotonic or to cyclic loading) and flows in a manner resembling a liquid until the shear stresses acting on the mass are as low as its reduced shear resistance. Seismic liquefaction occurs in loose sandy ground that is saturated with water. When pore water pressure rises during shaking, the effective stress decreases with time. In the extreme case, the effective stress becomes zero. Since the effective stress stands for the contact force at grain-to-grain contacts in sand, the zero effective stress suggests that there is no effective contact between grains. Hence, grains are actually floating in pore water without constraint from surrounding sand particles (Towhata, 2008). After complete loss of effective stress, sand has neither shear modulus nor shear strength, and consequently develops large deformation even under minor shear stress.

It was not until 1964 when liquefaction came to be considered seriously by engineers (Towhata, 2008). In early days, collapse of buildings and failure of slopes were more important and more harmful than liquefaction, because those conventional types of seismic damage caused more human casualties. In contrast, liquefaction does not kill people, although it is hazardous to modern structures. Further, liquefaction occurs in loose sandy deposits that are found in abandoned river channels, young alluvial planes, and human reclamations. These areas of high liquefaction potential were not used by human activity before. Therefore, liquefaction used to be nothing but a geological phenomenon, and it was not threatening to our society.

In recent times, urban development has spread into those areas that were not made use of before. Areas of soft soil used to be agricultural areas, and in particular, rice field: people lived on more stable ground. In many cases, these newly urbanized areas have loose sandy deposit with high ground water level; hence, the liquefaction potential is high as well. Since land reclamation became popular, liquefaction-susceptible ground has been produced. In summary, liquefaction as a natural hazard is a consequence of spreading of urbanization into unsuitable ground conditions.

3.1.2. Cyclic Stress Ratio, CSR

Resistance of sand against liquefaction is determined by running undrained cyclic triaxial tests on soil specimens. Cyclic stress with a constant amplitude is loaded repeatedly, and the number of cycles are counted until the following conditions:

(1) Development of the excess pore water pressure (Δu_w) (or excess pore air pressure (Δu_w) for the specimens with positive suction measurement) to 90% initial confining pressure (Δu = 0.9 σ_0' criterion) for both the saturated and unsaturated specimens; or

(2) peak-to-peak (i.e., double amplitude) axial strain equal to 2.5%, 5%, 10%, and so forth. For all experiments, double amplitude (*DA*) of 5% was selected.

The 100% development of excess pore water/air pressure is called “initial liquefaction” and the strain upon initial liquefaction may not yet be as large as those mentioned above. Thus, liquefaction in laboratory tests is defined in different ways; by pore pressure rise or development of strain. Though both definitions cannot guarantee that the tested materials can reach the state of liquefaction defined by Castro (1975) and Castro and Poulos (1977), they can be conveniently applied to the widely accepted framework proposed by Seed and Idriss (1971) and Seed (1979) to evaluate the resistance against liquefaction (R_L) of the soil.

Since the cyclic shear stress increases with the initial confining pressure, the idea of resistance ratio was defined as Equation 3-1.

$$\text{CSR} = \tau_{max}/\sigma_o' = \sigma_d/2\sigma_o' \qquad \text{(Eqn 3-1)}$$

where τ_{max} is the maximum shear stress, σ_o' is the initial confining stress, and σ_d is the single amplitude of the axial cyclic loading.

3.1.3. Liquefaction Resistance Curve

The number of loading cycles to liquefaction depends on the amplitude of resistance ratio. Therefore, laboratory tests should be run with a variety of stress amplitude, and the varying resistance ratio is plotted against the respective number of cycles needed for liquefaction. Liquefaction here is defined by one of the 90% pore pressure (either Δu_w or Δu_a) development (initial liquefaction), or 5% double (peak-to-peak) amplitudes of axial strain in cyclic triaxial tests. An indicative liquefaction resistance curve is shown in Fig. 3-1.

3-2. Terminology and Formulations

Terminology and formulations used for calculation include:

1. Deviator stress $q = \sigma_a - \sigma_r$: The difference between the axial stress and the radial stress of the specimen.

2. Total mean principal stress p: $p = (\sigma_a - 2\sigma_r)/3 = q/3 + \sigma_r$, where σ_r is equivalent to the cell pressure measured from the cell pressure transducer.

3. Effective mean principal stress $p' = p - u_w$: In the saturated test, it is a common definition to represent the mean value of the effective stress. In the unsaturated test, it is used to represent the difference between the total mean stress p and pore water pressure u_w.

4. Net mean principal stress $p - u_a$: The difference between total mean principal stress p and pore air pressure u_a.

5. Suction: It is equal to $u_a - u_w$.

6. Axial strain ε_a: Change in height divided by height after consolidation.

7. Measured volumetric strain $\varepsilon_{vol.m}$: Calculated according to data measured by the double cell system and the vertical displacement transducer. The volume used for calculation is the volume of the specimen after consolidation under σ_o'.

8. Theoretical volumetric strain $\varepsilon_{vol.air}$: represents the volumetric strain calculated from measured data of u_a based on Boyle's law. Strictly speaking, this value is the theoretical volumetric strain of the specimen caused by air compression. u_w was used for the calculation when u_a was not available. Its maximum value, $\varepsilon^*_{vol.air}$, is calculated by assuming that u_a is equal to the cell pressure.

9. *CSR*: Cyclic stress ratio, $\mathrm{CSR} = \tau_{max}/\sigma_o' = \sigma_d/2\sigma_o'$, where σ_d is single amplitude of the axial cyclic loading.

10. $N_{DA=5\%}$: Number of cycles that induces double amplitude of 5% of axial strain.

11. R_L is evaluated resistance against liquefaction which is defined as the value of *CSR* which causes 5% double amplitude of axial strain or 90% initial confining pressure ($\Delta u = 0.9\ \sigma_0'$) of the specimen at 20th cycle.

3-3. Undrained Cyclic Loading Test Using the Stress-Controlled Triaxial Apparatus

Undrained tests were first conducted on bauxite under saturated case using the stress-controlled Triaxial Apparatus.

3.3.1. Test Apparatus

The test apparatus used for saturated case is shown in Fig. 3–2. The stress-controlled Triaxial Apparatus is composed of the following essential parts:

1. Function Generator
   A function generator is a piece of electronic test equipment or software used to generate different types of electrical waveforms over a wide range of frequencies. Some of the most common waveforms produced by the function generator are the sine, square, triangular and sawtooth shapes. These waveforms can be either repetitive or single-shot (which requires an internal or external trigger source).

   In this experiment, the function generator developed by Tektrokix with Model AFG 3021 was utilized. It has 12 different standard waveforms, although only the sine waves were utilized in the tests conducted. On pulse waveforms, leading and trailing edge time can be set independently. External signals can be connected and added to the output signal. Dual-channel models can generate two identical or completely different signals. This idea will further be explained in the unsaturated case where two function generators were used.

2. Pneumatic Power System
   A double action cylinder was installed to apply cyclic loading. Two sides of the double action cylinder were connected to two pressure regulators, respectively. The pressure at the bottom of the cylinder is kept constant and the pressure at the top of the cylinder is controlled by an E/P regulator converting electric signal to pneumatic signal. The electric signal sent to the E/P regulator is triggered by a function generator. In such a way, the frequency, amplitude etc. of vertical cyclic loading can be precisely applied by adjusting the output electric single of the Function Generator. A relatively small double action cylinder, Fujikura SCD-40-48-B0, having a stroke of 48 mm and a friction free ball bearing (without seal at bearing), is used in this system to further increase the accuracy of the applied loading.

3. Load Cell (LC)
   This is a device is used to measure the deviator stress, q by obtaining the difference between the axial stress and radial stress. The value obtained is divided by the cross sectional area of the specimen to obtain the pressure.

4. Linear Variable Differential Transducer (LVDT)
   LVDT is a type of electrical transformer used for measuring linear displacement (position). It is designed with long slender coils to make the output voltage essentially linear over displacement up to several millimeters long. In this experiment, LVDT developed by Shinkoh-Minebea Co., Ltd. was used with a maximum displacement capacity of 20 mm.

   The LVDT can be used as an absolute position sensor. Even if the power is switched off, on restarting it, the LVDT shows the same measurement, and no positional information is

lost. Its biggest advantages are repeatability and reproducibility once it is properly configured. Also, apart from the uni-axial linear motion of the core, any other movements such as the rotation of the core around the axis will not affect its measurements.

5. Differential Pressure Transducer (DPT)
   In this study, there were two types of DPT used. A high capacity range, called High Capacity Differential Pressure Transducer (HCDPT) was used to measure the pressure difference in water levels between the burette (i.e. the amount of water sucked/expelled from the specimen) and the cell. It has a capacity range of 0 to 320 kPa.

   Another type, which is not used for saturated case but important for unsaturated case, is called the Low Capacity Differential Pressure Transducer (LCDPT). It measures the difference in water levels between the inner and outer cell (i.e., volume change of the specimen) and has a capacity range of 0 to 6 kPa.

6. Pressure Sensors
   This device is used to measure the pressure supplied into the cell, and another one for pore water, and has a maximum capacity of 500 kPa.

7. Bottom Pedestal and Top Cap
   The bottom pedestal is where the specimen is placed. It is also where the filter paper is secured by screws. The top cap, on the other hand, is connected to the load cell. This is to secure the specimen at the top end, and is free to move due to displacements.

8. Filter Paper
   Filter paper is a semi-permeable paper barrier placed perpendicular to a liquid or air flow. It is used to separate fine substances from liquids or air. The filter paper used in the experiments were developed by Toyo Roshi Company under Advantec in Japan.

3.3.2. Test Methodology

The following section describes the detailed methodology in conducting a liquefaction experiment using the stress-controlled Triaxial Apparatus.

1. Preparation of Triaxial Apparatus
   a. Make sure to clean the parts of the triaxial apparatus. There should be no gel and no dust as these may interfere in the results of the tests.
   b. First, measure the dummy specimen height for reference. This is essential so that when an actual specimen is placed, the difference of the dummy specimen height and the actual specimen.
   c. Apply grease on O-ring. Apply grease as well on both the bottom pedestal and top cap to stick with the rubber membrane.
   d. Before placing the rubber membrane cut it into 15 cm or longer (recommended) to provide for 10 cm soil specimen, plus 2.5 cm extra length on each ends to secure to the bottom pedestal and top cap, respectively.

2. Preparation of Specimen
   a. Depending on desired degree of compaction, pre-weigh sample that will fit in the 10 cm height, and 5 cm diameter mold. In this experiment, a degree of compaction D_c = 65% was aimed for loose, D_c = 80% for medium dense, and D_c = 90% for dense were prepared.
   b. Introduce bauxite by 1-dimension consolidation in the mold (See Fig. 3–3).
   c. Place the porous stone and the filter paper on the bottom pedestal.
   d. Transfer the prepared specimen from the mold on top of the porous stone and filter paper on the bottom pedestal.
   e. Balance top pedestal using counterweights such that it can freely move.
   f. Add filter paper at top cap as well.
   g. Connect the load cell cable to the amplitudes to indicate voltage (which was correlated to indicate force). Calibrate the amplitude to have minimal contact force as possible so that when the top cap reaches contact to the specimen, the value would more or less be zero.
   h. Gradually touch top cap to specimen. After which, secure the rubber membrane to the top cap.
   i. Measure the diameter and height of the specimen. The values obtained are the initial condition of the test.

3. Saturation of Specimen
   a. Instead of introducing CO_2, use Double Vacuuming Method (Ampadu and Tatsuoka, 1993) to saturate the specimen. This is more effective since bauxite has fines, which may be difficult to saturate the voids in case of CO_2 flushed by water. Increase back pressure up to -100 kPa while cell pressure up to -80 kPa.
   b. Vacuum specimen for at least 8 hours before saturating the specimen.
   c. The saturation of the specimen takes about 2 hours at least.
   d. After saturation, convert 20 kPa back pressure to 20 kPa cell pressure before proceeding to verify if the specimen has indeed saturated or not.

4. Saturation Check (B-Value)
   a. Connect the (+) side of HCDPT to cell pressure. On the other hand, connect the (-) side of HCDPT to the back pressure (i.e. pressure of specimen. The pressure of the specimen must be connected to the reference tube so that excess pore water pressure can migrate through and from the specimen.
   b. Make sure to saturate all tubes connected to the specimen.
   c. Using the pressure regulator, simultaneously increase the cell pressure to 220 kPa, while the back pressure will also be increased to 200 kPa. The effective confining pressure is maintained at 20 kPa. Make sure to maintain isotropic condition by counter-balance.
   d. Measure the corresponding voltage values:

$$B = \frac{\Delta u_w}{\Delta \sigma_o} \qquad \text{(Eqn 3-2)}$$

   where B = B-value; Δu_w = increment of pore water pressure; and $\Delta \sigma_o$ = increment of total principal stress

B = $\Delta u/\Delta\sigma_o$ = $[(V_2 - V_1)/ (V_2 - V_o)] \geq 0.95$

- V_o = record the voltage value corresponding the 220 kPa
- V_1 = increase to 230 kPa (do not allow water to flow to reference tube so that pressure could be measured if there is air). Record the voltage equivalent to 230 kPa
- V_2 = allow once again for water to flow to reference tube. Record again the voltage equivalent of 230 kPa

e. Increase effective confining pressure to 50 kPa
f. Consolidate for 2 hours.
g. Measure the height of the specimen before conducting the liquefaction test. This is the height of the specimen after consolidation.
h. Measure the volume change from the reference tube. This accounts for the volume change, as well as the cross sectional area of the specimen after consolidation.

5. Liquefaction Test
   a. Using the function generator, the desired parameters can be adjusted. The frequency of cyclic loading is set at 0.1 Hz. The amplitude is also adjusted according to the loading of the specimen after consolidation. The CSR is specified for the test as well.
   b. Place the triaxial apparatus, connected to the double action cylinder.
   c. Press "Start Saving" button to collect data.
   d. Start the input signal for cyclic loading.
   e. Wait for the specimen to liquefy. Stop the test at the instance when the excess pore water pressure is equal to the effective confining pressure (i.e. 50 kPa)

3.3.3. Tests Conducted

This section tabulates the tests conducted under stress-controlled Triaxial Apparatus for bauxite.

Four (4) tests were performed under D_c = 67% (Loose), six (6) tests were conducted under D_c = 82% (Medium Dense), and four (4) tests were carried out under D_c = 88% (Dense).

Table 3-1, Table 3-2, and Table 3-3 present the summary of the test results conducted for loose, medium dense, and dense cases, respectively.

Table 3-1. Saturated Test Conditions of Liquefaction Tests for bauxite, D_c = 67% (Loose)

Test No.	Initial Confining Pressure σ_o' (kPa)	Void ratio, e at σ_o'	Degree of Compaction, D_c (%)	B-value	Liquefaction	
					CSR	$N_{DA=5\%}$
L1	48.7	1.074	68.3	0.997	0.164	5.4
L2	48.7	1.107	67.6	0.989	0.141	8.1
L3	47.7	1.150	66.1	0.995	0.124	48.5
L4	48.2	1.155	66.3	0.992	0.124	27.0

Table 3-2. Saturated Test Conditions of Liquefaction Tests for bauxite, D_c = 82% (M.Dense)

Test No.	Initial Confining Pressure σ_o' (kPa)	Void ratio, e at σ_o'	Degree of Compaction, D_c (%)	B-value	Liquefaction	
					CSR	$N_{DA=5\%}$
M1	49.1	0.932	80.4	0.972	0.156	49.4
M2	48.6	0.857	83.7	0.983	0.181	6.4
M3	49.0	0.839	84.5	0.987	0.173	12.3
M4	48.9	0.891	82.2	0.987	0.163	22.9
M5	48.2	0.865	83.3	0.985	0.191	1.7
M6	50.2	0.911	81.3	0.988	0.165	11.6

Table 3-3. Saturated Test Conditions of Liquefaction Tests for bauxite, D_c = 88% (Dense)

Test No.	Initial Confining Pressure σ_o' (kPa)	Void ratio, e at σ_o'	Degree of Compaction, D_c (%)	B-value	Liquefaction	
					CSR	$N_{DA=5\%}$
D1	49.7	0.746	88.4	0.979	0.266	315.3
D2	48.8	0.749	88.4	0.980	0.356	5.0
D3	49.2	0.757	88.2	0.974	0.336	10.8
D4	49.6	0.760	88.1	0.975	0.297	28.9

All tests were conducted under isotropically consolidated specimens.

3.3.4. Analysis of Test Results

In order to check the isotropy of the the tests, the data were plotted at volumetric strain, ε_{vol} vs axial strain, $\varepsilon_{a.}$ If the deformation is isotropic, it would result to a 3:1 plot since the strain on the axial direction is the same as the radial and cirumferential directions. Fig. 3-4 presents the volumetric strain (ε_{vol}) vs the axial strain (ε_a) plot. Although the results don't necessarily obey the 3:1 plot, the tests can be assessed if it is consistent with other test data in terms of its strain behavior from this plot. Results are perhaps affected by specimen preparation and procedural implementation consistency, among other reasons. From this plot, it can be observed that test L3 has a 11:1 slope and is significantly different from the other three tests under loose case. For medium, dense, test M5 was assessed to be inconsistent with other ε_{vol} vs ε_a plots for medium dense. For dense case, all tests were acceptable.

Fig. 3-5 shows the liquefaction curve for bauxite. Points L3 and M5 were both omitted from the plot since their strain behavior were not consistent with the other tests conducted under the same density condition. Points for IOF-B at D_c = 93% were also plotted on the graph since previous work from Wang (2014) utilized this information to run the numerical simulation of dynamic response at this condition. The dynamic response of bauxite shall eventually be compared to the results of the existing results of IOF-B. Hence, at this point, it is relevant to include the plots obtained from IOF-B as well.

The discussions for typical test results are elaborated in the succeeding sections.

1. Loose, D_c = 67%

Fig. 3-6 plots the time history of excess pore water pressure of test L4. The initial confining pressure for test L4 was 48.2 kPa. In Table 3-1, it can be seen that it took 27 cycles to achieve 5% double amplitude of axial strain. From the time history of excess pore water pressure, taking 90% initial confining pressure (Δu = 0.9 σ_0') which is equal to 43.4 kPa, it also took around 27 cycles for the excess pore water pressure to achieve this condition. From this data, it can be said that the 5% double amplitude of axial strain and excess pore water pressure building up equal to 90% of the initial confining pressure occurred simultaneously. Other test results also show that for saturated case, occurrences of the two conditions do not deviate much in terms of number of cycles. While these two conditions do not necessarily define a "liquefied state", these two conditions were utilized consistently in the tests to evaluate the resistance against liquefaction (R_L) of the soil.

Fig. 3-7 shows the axial strain vs the deviator stress (q) plot. The progression of axial strain under cyclic loading was more or less equal in extension and compression. Development of large deformation even under minor shear stress can be seen once the axial strain of 5% had been exceeded.

Fig. 3-8 presents the stress path that the specimen underwent during cyclic loading. The trend of stress path does not exhibit the sudden decrease of mean principal stress. In other words, as the excess pore water pressure builds up gradually (see Fig 3-6), the effective stress of the specimen also decreased gradually, until liquefaction occurs either by DA=5%, or excess pore water pressure is equal to 90% of the initial confining pressure.

The liquefaction resistance (R_L) from the tests conducted under loose case was 0.125.

2. Medium Dense, D_c = 82%

Fig. 3-9 is a plot of the time history of excess pore water pressure of tests M4. Just like the loose case, the 5% double amplitude of axial strain and the excess pore water pressure building up equal to 90% of the initial confining pressure both occurred almost at the same time at 22.9 cycles.

The trend in Fig 3-10 showing the axial strain vs the deviator stress (q) plot was comparable to the results in loose case. Although test M4's axial strain biased a bit to the compression side under cyclic loading, the development of large deformation under minor shear stress can be observed once the DA=5% had been exceeded.

Fig. 3-11, which is the stress path of test M4 exhibited the same trend as that of loose case. The effective stress of the specimen gradually decreased until it exhibited liquefaction characteristics as defined in these experiments.

The liquefaction resistance (R_L) from the tests conducted under loose case was 0.165.

3. Dense, D_c = 88%

For dense case, one of the notable difference is the comparison with IOF-B liquefaction curve at D_c = 93%. By examining the plot in Fig. 3-5, it can be seen that the curve dramatically changes for IOF-B as the CSR changes as compared to the graph of bauxite. The corresponding R_L for bauxite is 0.317, while that of IOF-B is 0.337 at $N_{DA=5\%}$=20 cycles.

Fig. 3-12 and Fig. 3-13 show the time history of excess pore water pressure of bauxite test D4, and IOF-B at *CSR*=0.300, respectively. One noticeable difference in the dense case compared to the loose and medium dense is that the magnitude of the excess pore water pressure build up is greater. The number of cycles necessary to achieve 90% initial confining pressure was 28 cycles while DA=5% at 28.9 cycles for bauxite. For iron ore, the occurrence of excess pore water pressure build up equaled to 90% initial confining pressure was 30 cycles, while DA=5% at 34.6 cycles. From these typical figures, it is inconclusive to say the difference in the liquefaction curve since both materials exhibited gradual increase in excess pore water pressure build up and the relatively high magnitude.

Fig. 3-14 and Fig. 3-15 show the axial strain vs the deviator stress (q) plot for bauxite and iron ore, respectively. From these plot, the development of the axial strain due to the increase in shear stress biased on the extension side for both types of material. From these plots, the behavior of both materials was also similar.

Lastly, Fig. 3-16 and Fig. 3-17 present the stress paths of bauxite and iron ore respectively. The p'-q plot of both materials decreased gradually, until p reached zero.

4. Comparison with Toyoura sand

Data were extracted from Tan Tian (2016) for the tests conducted for Toyoura sand. The test was conducted at σ_c = 50.6 kPa with relative density (D_r) of 53.4% (loose).

The time history of excess pore pressure is shown in Fig. 3–18. It can be observed that there is a sudden jump in pore pressure at the instance of liquefaction. This behavior is typical of Toyoura Sand, when the soil strength attains peak, and then dramatically decreases to residual strength. Another thing that can be observed is the 100% development of excess pore water pressure almost simultaneously achieved with DA=5%. This behavior was not observed in bauxite tests conducted in this study.

As for the strain curve, the extension side exhibits larger strain than the compression side (see Fig. 3-19). The fluid behavior of strain can also be observed such that minimal change in deviator stress caused axial strain change even up to 6% on the extension side. This was not observed in bauxite tests. This shows that Toyoura sand has higher resistance in compression than in extension.

As for the p-q plot (see Fig. 3-20), the sudden decrease of mean principal stress can be observed. The plot also explains the behavior that Toyoura sand has lower resistance in the

extension side since the stress path is nearer at the extension side failure line, than at the compression side.

5. Comparison with Inagi sand

Data were extracted from Tan Tian (2016) for the tests conducted for Inagi sand. The test was conducted at σ_c = 58.0 kPa with degree of compaction (D_c) of 73.4% (loose).

The time history of excess pore water pressure, strain curve, and *p-q* plot of Inagi sand (test 4) are shown in Fig. 3–21 to Fig. 3–23.

Contrary to Toyoura sand, an abrupt or sudden increase in excess pore water pressure couldn't be observed in Fig. 3-21. The build up was similar to the ones observed in bauxite and iron ore, which is gradual. However, the 100% development of excess pore water pressure can be observed for Inagi sand, while this couldn't be observed in bauxite.

As for the axial strain compared to the deviator stress curve, Fig. 3-22 presents the plot for Inagi sand. The axial strain development is symmetrical in both compression and extension, but the plastic behavior of the strain at minimal increase in deviator stress was not as evident as Toyoura sand. On the other hand, this behavior can be observed to be similar to bauxite at loose case in Fig. 3-7.

Fig. 3–23 presents the stress path. The trend of stress path does not also exhibit the sudden decrease of mean principal stress. In other words, as the excess pore water pressure builds up gradually, the effective stress of the specimen also decreases gradually, until liquefaction occurs either by DA=5%, or excess pore water pressure is equal to the maximum confining pressure.

The next section discusses the implementation of a modified triaxial apparatus called linkage double cell system to measure volume change of specimen under unsaturated condition.

3-4. Undrained Cyclic Loading Test Using the Linkage Double Cell System

Tests were conducted using bauxite under unsaturated case using the Linkage Double Cell System.

3.4.1. Test Apparatus

1. Traditional Double Cell System

Fig. 3-24 schematically illustrates the Traditional Double Cell System specifically designed for testing unsaturated soil. The main components of the system include a vertical displacement transducer (VDT), a top cap, an inner cell, a reference tube and a differential pressure transducer (DPT). The top cap having a constant diameter (D_t) is appositely designed longer than the ordinary one to provide a wider measurement range. Note that, the inner diameter

(D_i) of the upper part of the inner cell is also constant. The DPT is connected to the reference tube and to the inner cell to measure the change in water level in the inner cell (WL_i). The reference tube is placed outside the pressure cell and connected with the pressure cell by a flexible nylon tube.

Fig. 3-24 (b) schematically illustrates the measurement principal of the volume change of the specimen under undrained condition. Suppose there is a vertical movement of the top cap, the volume change of all the substances beneath WL_i (ΔV_{DPT}) can be deduced by the DPT measurements. Part of ΔV_{DPT} is due to the intrusion of the top cap (ΔV_{VDT}) obtained from the measurement of the VDT. Thus, the total apparent volume change of the specimen (ΔV, set positive for volume reduction of the specimen) is obtained:

$$\Delta V = -(\Delta V_{\mathrm{DPT}} - \Delta V_{\mathrm{VDT}}) \qquad \text{(Eqn 3-3)}$$

ΔV has two components, namely the actual volume change of the specimen (ΔV_{sp}) and the apparent volume change (ΔV_{SC}) induced by the system compliance (e.g. meniscus effect etc.). Dividing both sides of Eqn. 3-3 by the initial volume of the specimen (V_0, measured immediately before the cyclic loading), the total apparent volumetric strain (ε_v) can be obtained:

$$\varepsilon_{\mathrm{v}} = \varepsilon_{\mathrm{v,sp}} + \varepsilon_{\mathrm{v,SC}} = \frac{\Delta V_{\mathrm{sp}} + \Delta V_{\mathrm{SC}}}{V_0} = -\frac{\Delta V_{\mathrm{DPT}} - \Delta V_{\mathrm{VDT}}}{V_0} \qquad \text{(Eqn 3-4)}$$

where:

$\varepsilon_{v,sp}$ = actual volumetric strain of the specimen

$\varepsilon_{v,SC}$ = apparent volumetric strain induced by system compliance

There are several technical issues in using the traditional double cell system. Firstly, it was expected that the meniscus effect was the primary factor inducing $\varepsilon_{v,SC}$ in the double cell system shown in Fig. 3–24. However, as described later, the time response delay in the measurement of the DPT was found to have a significant effect on $\varepsilon_{v,SC}$ as well. It was found that the delay in time axis between DPT and VDT (see Fig. 3–25) is generally constant under the sinusoidal loading with different amplitudes (~0.6 sec). A detailed description of the procedure and comprehensive explanation can be accessed through Wang et al. (2016b).

For the strain-controlled monotonic triaxial tests of unsaturated soil specimens, $\varepsilon_{v,SC}$ measured by the traditional double cell system may be reduced to a negligible level by careful calibration (Ng et al., 2002). However, it is much more difficult to significantly reduce $\varepsilon_{v,SC}$ for the stress-controlled cyclic loading tests with relatively prompt loading frequency. Due to this, the step signal delay makes the measurement of ε_v of the unsaturated specimen barely to be used.

2. Linkage Double Cell System

The reason why the delay in time of the DPT induces $\varepsilon_{v,SC}$ is that ε_v relates to the vertical displacement of the top cap as indicated in Eqn. 3–4. The novelty of the linkage double cell

system, as schematically shown in Fig. 3-26, is that a linkage rod moving simultaneously with the loading shaft is introduced to the reference tube, through which ΔV_{VDT} in Eqn. 3-3 ideally becomes zero. The main technical differences of the modified version compared with the traditional double cell system are as follows:

- The height of the top cap is reduced, and a longer stainless steel loading shaft (No. 14 in Fig. 3-26) is installed between the top cap and the load cell. In addition, the diameter of the upper part of the inner cell is also reduced.
- The reference tube (No. 9) having an inner diameter (D_R) equals to that of the upper part of the inner cell (D_R=D_i), is moved into the pressure cell.
- An aluminum plate (No. 11) is fixed on the loading shaft at one end and connected with an acrylic rod (i.e. the linkage rod, No. 10) at the other end. Note that, the outer diameter of the linkage rod (D_r) is the same as that of the loading shaft (i.e. $D_r = D_s$).

Though the modifications above are not a solution of the time delay issue of the DPT, they, as a whole, make the measurement of ε_v is no longer affected by the vertical movement of the loading shaft. Therefore, ε_v is evaluated as follows:

$$\varepsilon_{\mathrm{v}} = \varepsilon_{\mathrm{v,sp}} + \varepsilon_{\mathrm{v,SC}} = \frac{-\Delta V_{\mathrm{DPT}}}{V_0} \qquad \text{(Eqn 3-5)}$$

In addition, the meniscus effect is expected to be reduced due to the synchronized same direction movement between the linkage rod and the loading shaft. The meniscus effect caused by the use of two different materials (i.e. stainless steel for the loading shaft and the acrylic for the linkage rod) is believed to be negligible.

A comparison of the performance of the Traditional Double Cell System and the Linkage Double Cell System can also be referred to Wang et al. (2016b).

3. Key Features of Measuring Unsaturated Specimen

a. Cell pressure (σ_h) control system – to maintain total mean principle stress (p) constant (p-constant condition). By using double function generator, the σ_h can be simultaneously adjusted following the vertical cyclic loading applied by the vertical stress control system. The magnitude of increment of σ_h ($\Delta\sigma_h$) was set as one third of deviator stress (q) as shown schematically in Fig. 3–27, through which p can be kept constant. According to the concepts of pore pressure coefficients A and B, the increment of pore water pressure (Δu_w) of the specimens under the undrained condition can be expressed as:

$$\Delta u_w = B\left[\Delta p + \left(A - \frac{1}{3}\right)\Delta q\right] \qquad \text{(Eqn 3–6)}$$

If we define increment of effective mean principle stress ($\Delta p'$) as:

$$\Delta p' = \Delta p - \Delta u_w = (1 - B)\Delta p + B\left(\frac{1}{3} - A\right)\Delta q \qquad \text{(Eqn 3–7)}$$

It is clear that $\Delta p'$ will be rarely affected by Δp for the saturated specimens which are normally of B values of ≥0.95. However, it is not valid for the unsaturated specimens, of

which B values may reduce sharply with slight reduction in degree of saturation (Sr) (Yoshimi et al, 1989). To remove such an effect, the p-constant condition was applied to the unsaturated specimens in this study (Wang, 2017).

b. Suction measurement system –under relatively high loading frequency (0.1 Hz), it is difficult to measure the suction by using the ceramic disk (Unno et al., 2008). Thus, the membrane filter technique was introduced to measure u_w (Nishimura et al., 2012). The thin membrane filter was fixed by a stainless cover with six screws on the bottom pedestal. Pore air pressure (u_a) was measured by a pressure transducer being connected with the drainage path of the top cap. A hydrophobic filter was glued on the surface of the top cap to reduce the invasion of pore water during the tests (see Fig. 3–28). Suction (S) was calculated by $S=u_a-u_w$.

3.4.2. Test Methodology

The following section describes the detailed methodology in conducting a Liquefaction experiment using the Linkage Double Cell System on Triaxial Apparatus.

1. Preparation of Triaxial Apparatus
   a. Attached the hydrophobic filter paper on the top pedestal using the glue for photo paper. This is different from the membrane filter and the ordinary filter paper. As a rule of thumb, ordinary filter paper is not used for unsaturated case. Paste the glue at the edge.
   b. The small measuring inner cell has the same diameter dimensions as the reference one. It is advisable to put grease around the O-ring surface so that it will be easier to remove later. Also, put some grease inside the connecting inner cell
   c. Remove the entire top portion of the triaxial machine so that the specimen can be prepared. Clean the bottom pedestal. Do not screw yet nor put the membrane filter.
   d. Place the water-tight acrylic pipe for saturating the bottom pedestal. After which, introduce water to the water-tight acrylic pipe before vacuuming (see Figure 3–29).
   e. Simultaneously saturate the tubes connected to the pressure transducer. Allow de-airing for 30 minutes.
   f. After 30 minutes, flush all tubes to saturate.
   g. Calibrate the values to zero at this point, such that when membrane filter and specimen is placed, the suction will be recorded.
   h. Introduce the membrane filter at the bottom pedestal. Secure the bottom pedestal by screwing it appropriately.

2. Preparation of Specimen
   a. Depending on desired degree of compaction, pre-weigh sample that will fit in the 10 cm height, and 5 cm diameter mold.
   b. Introduce bauxite by 1-dimension consolidation in the mold (See Fig. 3–3). It is recommended to apply more compression on the top of the specimen since the bottom one is naturally more compressed due to the self-weight of the specimen, as well as the compaction imposed when the specimen is placed on the mold.

c. Carefully insert the membrane into the specimen.
d. Transfer the prepared specimen from the mold on top of the saturated membrane filter on the bottom pedestal. The pore water pressure should record negative value at this point, since air is exposed to the atmosphere. The difference of pore air pressure and pore water pressure is the suction.
e. Put the top portion of the triaxial machine now. After which, introduce counter balance.

3. Linkage Double Cell Set-up
   a. Simultaneously establish distance to tube and the interaction of the top cap to the specimen.
   b. Connect the load cell. Calibrate to zero. Connect top pedestal tube. This is for the pore air pressure. Then while still open to atmosphere, zero the value. Make sure the pore air pressure is connected to the equipment via the inner cell connection which is connected to the specimen.
   c. Measure diameter and height. No back pressure needed since the specimen can hold itself up.
   d. Install Inner Cell. Fill the inner cell with water.
   e. Adjust reference cell to 10mm to secure distance between the reference and the inner cell. Then lock it (see Figure 3–30)

4. Consolidation of Specimen
   a. The outer cell can be inserted at this point and then introduce water.
   b. Gradually increase the confining pressure up to the desired or target maximum confining pressure. In the tests conducted, it was 50 kPa.
   c. Consolidate for 2 hours.
   d. After consolidation, check again change in volume and height. Record both data and then fill the water inside the inner cell up to the brim once again.

5. Conducting the Test
   a. Set the desired *CSR* value for testing. For the regulator to control the cell pressure, change the phase of the sine wave input to 180 degrees. This is to simulate the plot shown in Figure 3–27.
   b. Convert the cell pressure into impulse from the function generator. For the tests conducted, it is equal to 50 kPa.
   c. The main function regulator is adjusted according to the amplitude and offset through calculations.
   d. Make sure to close the valve for pore air pressure before conducting the test.
   e. Simultaneously input signal on both function generators to trigger impulses.
   f. Make sure to record data.
   g. Wait for the specimen to liquefy. Stop the test at the instance when the excess pore air pressure is equal to the maximum confining pressure (i.e 50 kPa).

6. Cleaning and Determination of Mass of Specimen

a. The actual moisture content of the specimen must be obtained. First, take the specimen on a separate can. This is for the moisture content. On another can, take the remaining sample upon cleaning. The total mass will be the sum of the two separate oven-dried pans.
b. The level of the lock is determined so that the load cell will not hit the inner cell. The other thing is that the when the pneumatic cylinder goes up, the shaft will not hit the top such that the load cell will be damaged. So the plate of the pneumatic cyclic device must be adjusted.

3.4.3. Tests Conducted

This section tabulates the tests conducted under Linkage Double Cell System on Triaxial Apparatus for bauxite. In all tests, the maximum confining pressure applied was 50 kPa in isotropic condition and medium dense degree of compaction (D_c≈80%). The number of cycles to cause the pore air pressure (u_a) to build up equal to 90% of the initial confining pressure was included in the tabulation.

Table 3–4 shows the summary of the conditions of the tests conducted under degree of saturation of 84%-85% (S_r=84%~85%). Table 3-5 on the other hand, presents the summary of the conditions of the tests for S_r=56%~61%.

Table 3-4. Unsaturated Test Conditions of Liquefaction Tests for bauxite, S_r=84%

Test No.	Initial Confining Pressure σ_o' (kPa)	Degree of Saturation, S_r (%)	Degree of Compaction, D_c (%)	Liquefaction		
				CSR	$N_{DA=5\%}$	$N_{0.9\sigma o'}$
a1	49.1	80.7	78.5	0.284*	78.8	103.2
a2	50.0	84.3	78.5	0.322	0.8	3.0
a3	49.1	84.6	78.6	0.279	8.3	8.6
a4	51.1	75.5	78.5	0.277	22.9	27.0
a5	50.0	85.8	77.9	0.259	42.8	42.9
a6	49.8	84.4	78.9	0.268	17.8	18.4

*Initial CSR was 0.230. At 400 cycles, specimen has not yet liquefied. Air was diffused and test was continued using the same specimen

Table 3-5. Unsaturated Test Conditions of Liquefaction Tests for bauxite, S_r=58%

Test No.	Initial Confining Pressure σ_o' (kPa)	Degree of Saturation, S_r (%)	Degree of Compaction, D_c (%)	Liquefaction		
				CSR	$N_{DA=5\%}$	$N_{0.9\sigma o'}$
b1	49.9	56.9	81.0	0.368	5.8	21.0
b2	50.8	61.5	80.8	0.358	5.1	12.0
b3	49.7	57.9	81.4	0.353	113.2	149.0
b4	51.3	56.1	81.0	0.361	37.3	78.4
b5	50.0	56.2	80.1	0.398	12.6	58.0

3.4.4. Analysis of Test Results

Fig. 3-31 presents the volumetric strain (ε_{vol}) vs the axial strain (ε_a) plot. The isotropic plot is 3:1. One of the reasons why 3:1 was unachieved was because of anisotropy. Anisotropy is the property of being directionally dependent, as opposed to isotropy, which implies identical properties in all directions. It is difficult to maintain isotropy during tests, since naturally, the self-weight of the specimen among others would affect the stress. Another reason would be the fluctuation of the voltage due to the impulses sent by the sensors. The numbers are unstable, hence giving different values during time of recording. Lastly, the phenomenon called membrane penetration could affect the isotropy. The membrane usually penetrates to the specimens under certain confining pressure. The membrane penetration results in an uneven surface of the specimens, which makes it difficult to measure the specimen's dimension precisely.

Although the results don't necessarily obey the 3:1 plot, the tests can be assessed if it is consistent with other test data in terms of its strain behavior from this plot. From this plot, it can be observed that tests a1 and a4, as well as tests b1 and b2 were assessed to be different in their strain behavior compared to the other test preparations.

Fig. 3-32 shows the liquefaction curve for bauxite. Points a1, a4, b1, and b2 were all omitted from the plot since their strain behavior were not consistent with the other tests conducted under the same S_r condition. Both $N_{DA=5\%}$ criteria and $N_{0.9\sigma o'}$ criteria were plotted against *CSR.* $N_{DA=5\%}$ and $N_{\Delta u=0.9\sigma 0'}$ for each saturated specimen are similar to each other, while it seems that the development of DA=5% takes place earlier than $\Delta u=0.9\sigma_0'$ as S_r decreases. For S_r = 56-61%, the R_L was 0.279 for DA=5% criteria while R_L was 0.280 for 0.9σo'. However, for S_r = 84-85%, the R_L was 0.385 for DA=5% criteria while R_L was 0.587 for 0.9σo'. This shows the effect of air in the specimen during the unconsolidated cyclic loading. Air is compressible, hence, contributes to the "resistance" of the soil. This concept shall be further expanded in the succeeding discussions.

1. Typical Test Results

Fig. 3–33 shows the plot of pore air pressure, u_a, pore water pressure, u_w, and suction of Test b4. The membrane filter technique could measure negative pore water pressure in a prompt manner and as a result suction of the unsaturated specimens was well monitored under the 0.1 Hz cyclic loading. This is evident in the suction, resulting from $u_a - u_w$, indicated by a dashed blue line up to about 270 seconds (i.e. 27th cycle). The suction became more pronounced after that until the specimen underwent DA=5% at 37.3 cycles. However, the test was further progressed until u_a or u_w reaches 90% initial confining pressure. In this plot shown, it was until 78.4th cycle where the u_a reached 46.2 kPa, which is 90% of the initial confining pressure of 51.3 kPa. Another thing worth pointing out in this graph is the plot of mean principal stress *p* with respect to time indicated in color green. Due to the p-constant condition, the values obtained for *p* were sinusoidal but consistently in the average range of 52 kPa.

The succeeding figures from Fig. 3–34 to Fig. 3–37 present the typical plots for time history of deviator *q*, axial strain vs volumetric strain plot, axial strain vs deviator *q*, and stress path, respectively.

The extension side decreases in strength as the build up of u_a increased as can be seen from Fig. 3–34. In the compression side however, the time history of *q* was consistent throughout the test. By further looking to Fig. 3-35 and Fig. 3-36, the behavior of axial strain during cyclic loading biased on the extension side. This signified the presence of u_a in the specimen such that deformation of particles being compressed was restrained by the air being compressed. This is different from saturated case wherein the voids are fully saturated with water and the water was assumed incompressible.

In Figure 3-37, the green plot signifies the mean principal stress, being maintained at 50 kPa by the double function regulator. This is consistent with the plot in Fig. 3-33 indicated by brown. Unlike in saturated case where the effective stress is defined by the total stress and excess pore water pressure, in unsaturated case, it is comprised of the net normal stress ($\sigma - u_a$) and suction components ($u_a - u_w$) as discussed in Chapter 1 under Shear Strength of Unsaturated Soils. Hence, the net normal stress would not necessarily approach zero, as can be seen from this plot.

2. Volume Change Measurement of Unsaturated Soils

One of the intent of using the Linkage Double Cell System was to improve accuracy in measuring the volume change of the specimen during consolidation and even during cyclic loading. The improvement provided by the Linkage Double Cell System can be understood from Wang et al, (2016b).

Figure 3-38 is the volume measurement, both measured and calculated. The calculated volume is obtained from Boyle's Law. Boyle's Law basically states in mathematical form that:

$$P_o V_o = P_n V_n \qquad \text{(Eqn. 3–8)}$$

Where P_o = initial pressure (in this case atmospheric); V_o = initial volume (in this case directly measured, P_n = measured by pore air transducer; and V_n = being determined

It was surmised that the air tube connected to the top cap must have affected the results, since during consolidation, it is exposed to the air, while during cyclic loading, it is compressed. Hence, the volume of the air tube was determined, and it only accounted for 2.2 ml or 2.2 cm^3. When that volume was taken into account in the calculation, the result of the measured volume was insignificant. There is minimal effect; hence, there must be other factors that could have affected the discrepancy.

It is desired that the calculated and the measured volume are the same or comparable so that the degree of saturation (Sr) can be determined by simply measuring the volumetric

strain of the specimen. However, this is one of the limitation since the obtained measurement and the calculated (theoretical) volumetric strains do not match.

3.4.5. Liquefaction Resistance Ratio (LRR)

To evaluate the effect of S_r on the R_L, liquefaction resistance ratio (LRR) is defined as the ratio of $R_{L,unsat}$ to $R_{L,sat}$ under either the DA=5% criterion ($LRR_{DA=5\%}$) or the $\Delta u=0.9\sigma_0'$ criterion ($LRR_{\Delta u=0.9\sigma 0'}$) for the same soil with otherwise similar conditions. Fig. 3–39 shows the liquefaction curve similar to Fig. 3-32, but indicating the $LRR_{DA=5\%}$ and $LRR_{\Delta u=0.9\sigma 0'}$ of both S_r = 84% and S_r = 58%. It can be seen that the LRR of DA=5% criterion is lower than its $\Delta u=0.9\sigma_0'$ criterion counterpart.

Fig. 3-40 presents the relationship between S_r and $LRR_{DA=5\%}$ for bauxite and other soils used in previous studies by other researchers. Masa sand (Yasuda et al., 1999) and Niigata sand (Ishihara et al., 2001) are clean sands with F_c of less than 5%. Though the figure may imply a monotonic increase trend of liquefaction resistance as the reduction in S_r for all tested soils, the relationship between S_r and $LRR_{DA=5\%}$ is not unique even only for the clean sands under different testing conditions. It also reveals that $LRR_{DA=5\%}$ values of Toyoura sand are much higher than those of materials with considerable fines content (i.e. bauxite, IOF-B, Inagi sand) under the same S_r. In other words, using the S_r and $LRR_{DA=5\%}$ correlation is not sufficient to explain the unsaturated behavior of geo materials.

3.4.6. Potential Volumetric Strain, ($\varepsilon^*_{v,air}$)

Okamura and Soga (2006) considered the effect of compressibility of pore air in the unsaturated soils on $LRR_{DA=5\%}$ and proposed a parameter, potential volumetric strain ($\varepsilon^*_{v,air}$) to correlate $LRR_{DA=5\%}$. $\varepsilon^*_{v,air}$ is regarded as the volumetric stain of the specimens caused by pore air compression when the excess pore air pressure equals the initial confining pressure ($\Delta u_a=\sigma_0'$) and is obtained by applying Boyle's law:

$$\varepsilon^*_{v,air} = \frac{\sigma_0'}{p_b+\sigma_0'}(1-S_r)\frac{e}{1+e} \qquad \text{(Eqn. 3– 9)}$$

where, p_b is the absolute value of back pressure (kPa) and e is the void ratio.

In Fig. 3–41, the relationship between $\varepsilon^*_{v,air}$ and $LRR_{DA=5\%}$ is plotted. It is clear that the relationship between $LRR_{DA=5\%}$ and $\varepsilon^*_{v,air}$ is rather unique for clean sands. However, the data of bauxite sand do not follow the trend curve proposed by Okamura and Soga (2006), distributing under the curve instead.

3.4.7. Volumetric Strains of Saturated and Unsaturated Soils

Volumetric strains of saturated and unsaturated soils under undrained conditions are influenced by the strain due to cyclic shear loading ($\varepsilon_{v,\tau}$), reduction of confining pressure

($\varepsilon_{v,\sigma'}$), and compressibilty of pore air ($\varepsilon_{v,air}$=0 for S_r =100%). The relationship of the three parameters is illustrated in Fig. 3-42 while the mathematical relationship can be written as:

$$\varepsilon_{v,\tau} + \varepsilon_{v,\sigma'} = \varepsilon_{v,air} \quad \text{(Eqn. 3–10)}$$

In Eqn 3-10, it can be said that $\varepsilon_{v,\tau}$ is the motion inducing loss of effective stress, and $\varepsilon_{v,\sigma'}$ and $\varepsilon_{v,air}$ are the motions to recover the effective stress. Hence, the single parameter $\varepsilon^*_{v,air}$, which is the maximum value of $\varepsilon_{v,air}$ as an index may be insufficient to represent the response characteristics of different soils on different test conditions (Wang et al., 2016a). To estimate the reduction of volumetric strain caused by $\varepsilon_{v,\sigma'}$, isotropic consolidation tests were conducted on the saturated specimens. After consolidation up to a specified initial effective confining pressures the effective confining pressure was decreased step by step to simulate the reduction process of effective confining pressure σ' during undrained cyclic loading. The relationship between the ratio σ'/σ_0' and $\varepsilon_{v,\sigma'}$ during the unloading process is shown in Fig. 3-43. Clearly, such relationship is different for different materials. The results also show that the volume of the specimens may expand significantly when σ' reduces to a relatively low value, e.g. less than $0.1\sigma_0'$. A similar plot is shown in Fig. 3-44 to show results for bauxite only, in different densities (i.e. degree of compaction).

3.4.8. Volumetric Strain Ratio, R_v

As another index, the volumetric strain ratio ($R_v=\varepsilon_{v,air}/\varepsilon_{v,\sigma'}$) was proposed to correlate LRR with consideration of volumetric expansion of the specimens due to reduction in confining pressure.

The condition of isotropic consolidation tests is shown in Table 3–6 to calculate R_v. A detailed explanation can be read in Wang et al. (2016a).

Table 3-6. Conditions of isotropic consolidation tests (Bauxite @ σ_0'=50 kPa)

Condition	D_c (%)	$\varepsilon_{v,0.9\sigma'}$	S_r (%)	$R_v=\varepsilon_v^*{}_{,air}/\varepsilon_{v,0.9\sigma'}$	$LRR_{DA=5\%}$	$R_v=\varepsilon_{v,0.9air}/\varepsilon_{v,0.9\sigma'}$	$LRR_{u=0.9\sigma_0'}$
Loose	65	1.279	100	0	1	0	1
			84	2.40	1.69*	2.16	1.70*
			58	6.31	2.33*	5.68	3.56*
M. Dense	80	0.709	100	0	1	0	1
			84	3.64	1.69	3.27	1.70
			58	8.96	2.33	8.07	3.56
Dense	90	0.287	100	0	1	0	1
			84	7.77	1.69*	6.97	1.70*
			58	20.35	2.33*	18.33	3.56*

*Assumed LRR due to absence of experimental data (i.e. assumed to be the same as medium dense case)

Fig. 3-45(a) shows the relationship between R_v, in which $\varepsilon_{v,air}$ is represented by $\varepsilon^*_{v,air}$, and $LRR_{DA=5\%}$ of the three different degrees of compaction of bauxite. Among these points, only medium dense case were obtained from experimental data while the loose case and dense

case were inferred based on the assumption that the LRR is the same as that of medium dense. Compared with $LRR_{DA=5\%}$ vs. $\varepsilon^*_{v,air}$ (Fig. 3–41), R_v exhibited better correlation with $LRR_{DA=5\%}$ (i.e. the effect of soil types is minimized). Since $\varepsilon_{v,0.9\sigma0'}$ is used in the calculation of R_v, it would be more reasonable to use $\varepsilon_{v,0.9air}$, which is $\varepsilon_{v,air}$ when pore pressure equals 90% of σ_0', instead of $\varepsilon^*_{v,air}$ for R_v calculation. Accordingly, $LRR_{\Delta u=0.9\sigma0'}$ would be more appropriate to be used instead of $LRR_{DA=5\%}$. Hence, Fig. 3-45(b) was also plotted, showing an even more improved correlation with LRR.

3-5. Chapter Summary

In this Chapter, the following points can be stated.

1. Undrained tests were conducted using the stress-controlled Triaxial Apparatus under saturated case while a modified system called Linkage Double Cell System (Wang, 2016a) on Triaxial Apparatus was used to perform tests for unsaturated case. Three degrees of compaction (D_c) of bauxite were carried out, namely loose case (D_c=67%), medium dense case (D_c=82%), and dense case (D_c=88%). Iron ore fines type B (IOF-B) at D_c=93% were also extracted from Wang (2014) to compare this study's test results.

2. Under saturated condition, bauxite's behavior during cyclic loading evidenced gradual increase of pore water pressure (u_w), exhibiting liquefaction condition under 5% double amplitude of axial strain (DA=5%) or 90% initial confining pressure (Δu = 0.9 σ_0') simultaneously. In unsaturated condition however, the development of DA=5% takes place earlier than Δu=0.9σ_0' as degree of saturation (S_r) decreases.

3. While the liquefaction curve of IOF-B at D_c=93% shows a different trend than that of bauxite at D_c=88%, the behavior of both materials during cyclic loading exhibited similar characteristics such as u_w building up gradually, or development of the axial strain due to the increase in shear stress biased on the extension side for both types of material. Difference of the curve may be attributed to some other factors such as their physical properties or chemical properties.

4. Comparing bauxite to Toyoura sand at loose condition, it can be said that bauxite's behavior is different than Toyoura sand's behavior. Toyoura sand's behavior is characterized by the sudden increase in excess pore water pressure at the instance of liquefaction, as well as the large increase of axial strains in the extension side with a small increase in deviator stress. On the other hand, bauxite's behavior is closer to that of Inagi sand (silty sand), however 100% development of excess pore pressure couldn't be achieved in some tests in bauxite while it was achieved in Inagi sand.

5. In unsaturated condition, the Linkage Double Cell System improved the volume measurements during consolidation and even during cyclic loading of the specimen. The Linkage Double Cell System helps resolve the meniscus effect caused by the top cap in the Traditional Double Cell System, as well as the time delay in the measurement of DPT. At this point however, the measured volume change and the calculated volume change

during cyclic loading do not agree. Hence, the S_r cannot be directly related to volume change.

6. A new index called volumetric strain ratio (R_v) was proposed to correlated liquefaction resistance ratio (LRR) with various sands (Wang, 2015). Like the previously tested materials such as iron ore and Inagi sand, bauxite follows the trend of the proposed LRR plotted against R_v, which exhibits a better correlation than LRR plotted against $\varepsilon^*_{v,air}$.

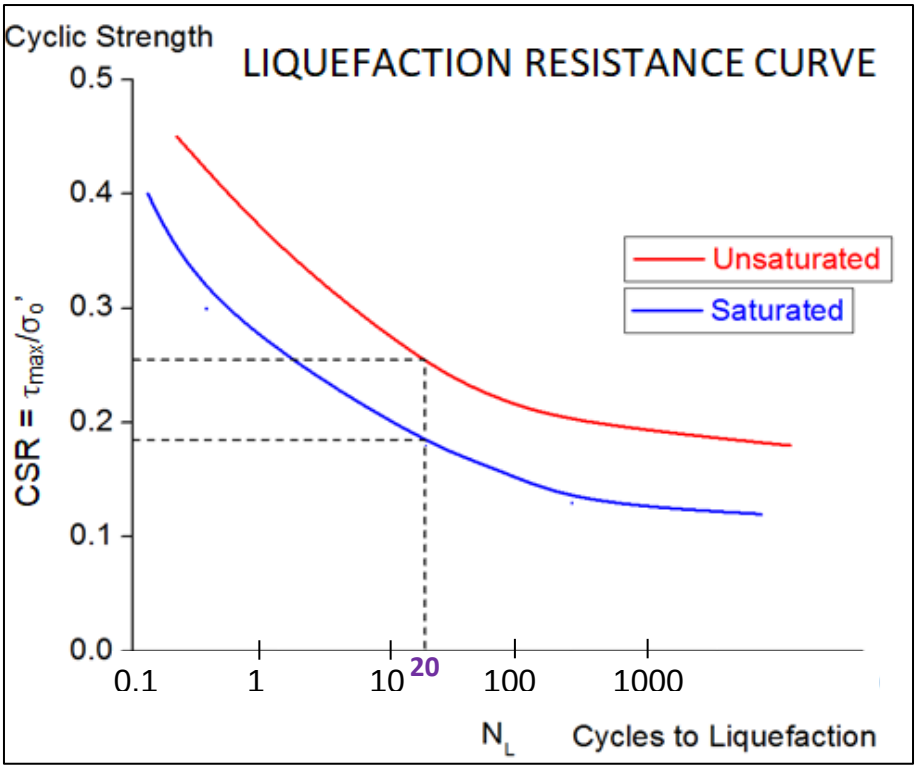

Fig. 3-1. Typical Liquefaction Resistance Curve Plot

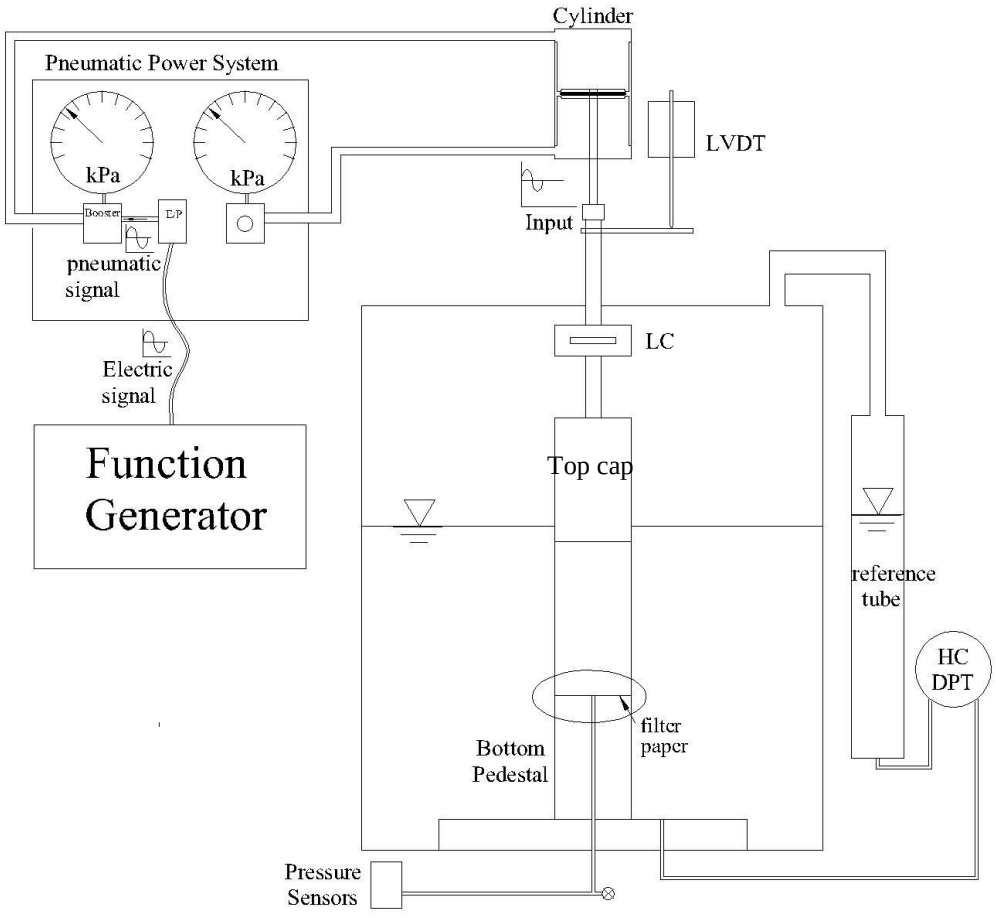

Fig. 3-2. Layout of Stress-controlled Triaxial Apparatus for Saturated Tests (Wang, 2014)

Fig. 3-3. Specimen Preparation by 1-D Consolidation

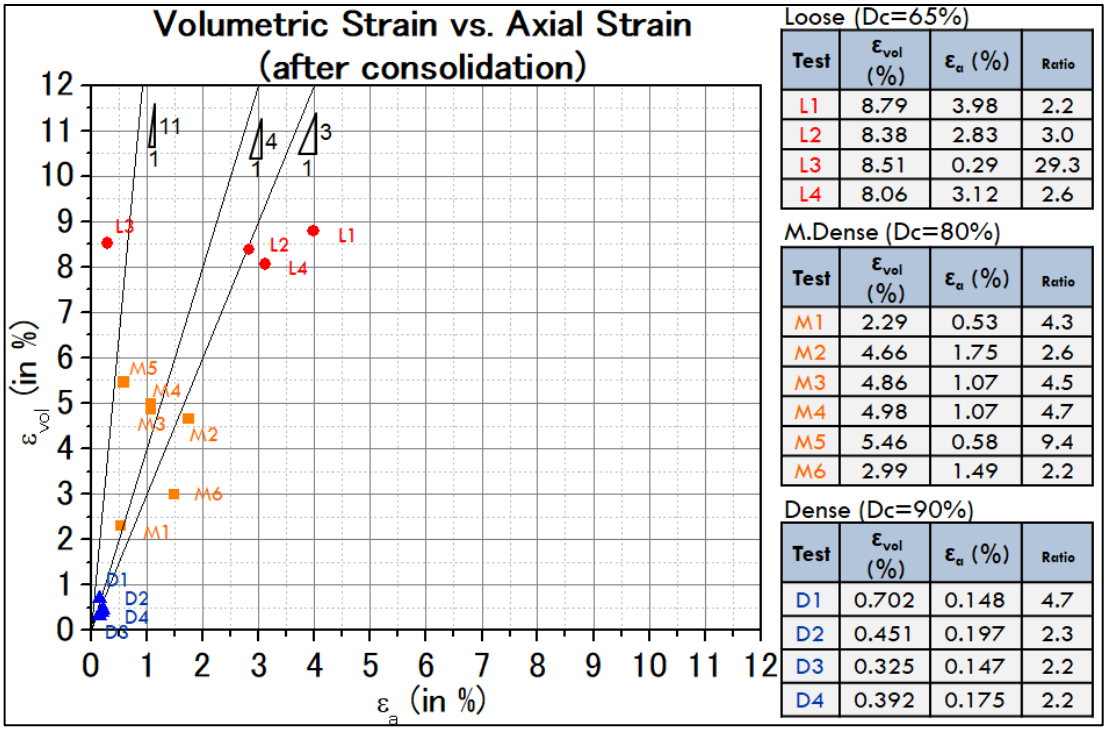

Loose (Dc=65%)

Test	ε_{vol} (%)	ε_a (%)	Ratio
L1	8.79	3.98	2.2
L2	8.38	2.83	3.0
L3	8.51	0.29	29.3
L4	8.06	3.12	2.6

M.Dense (Dc=80%)

Test	ε_{vol} (%)	ε_a (%)	Ratio
M1	2.29	0.53	4.3
M2	4.66	1.75	2.6
M3	4.86	1.07	4.5
M4	4.98	1.07	4.7
M5	5.46	0.58	9.4
M6	2.99	1.49	2.2

Dense (Dc=90%)

Test	ε_{vol} (%)	ε_a (%)	Ratio
D1	0.702	0.148	4.7
D2	0.451	0.197	2.3
D3	0.325	0.147	2.2
D4	0.392	0.175	2.2

Fig. 3-4. ε_{vol} vs. ε_a plot of bauxite (Saturated)

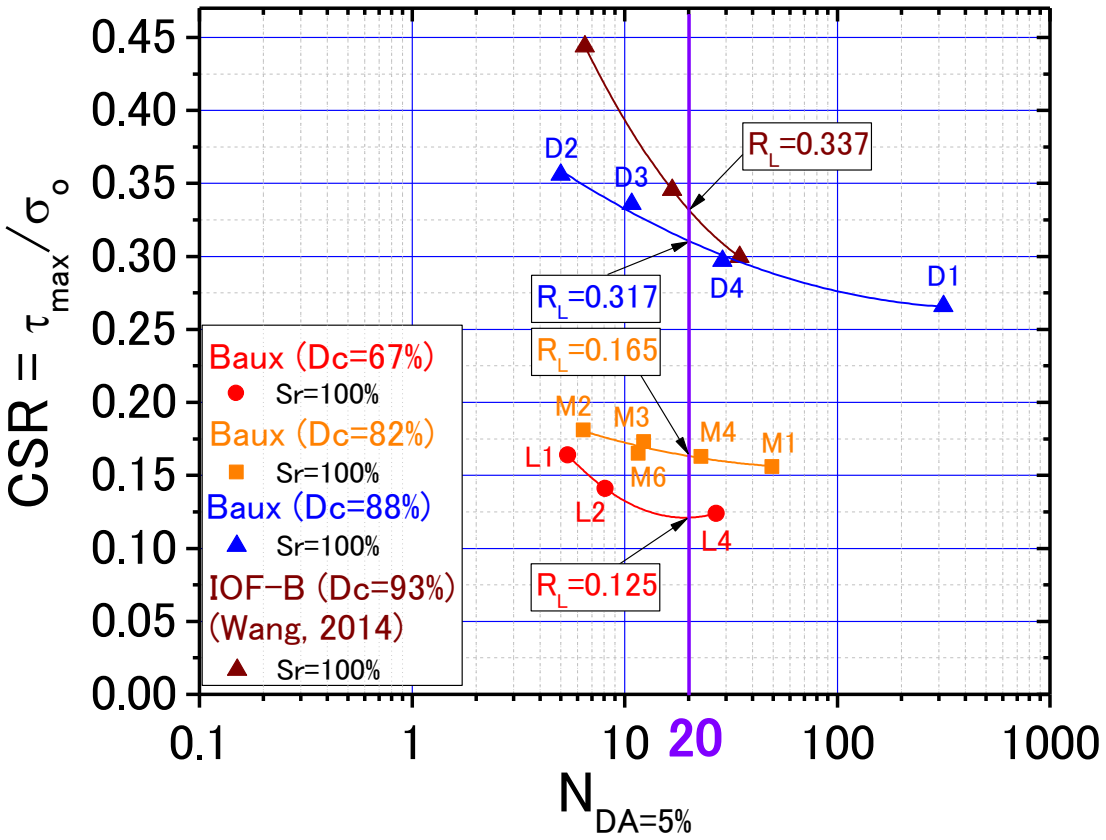

Fig. 3-5. CSR vs $N_{DA=5\%}$ plot of bauxite (Saturated)

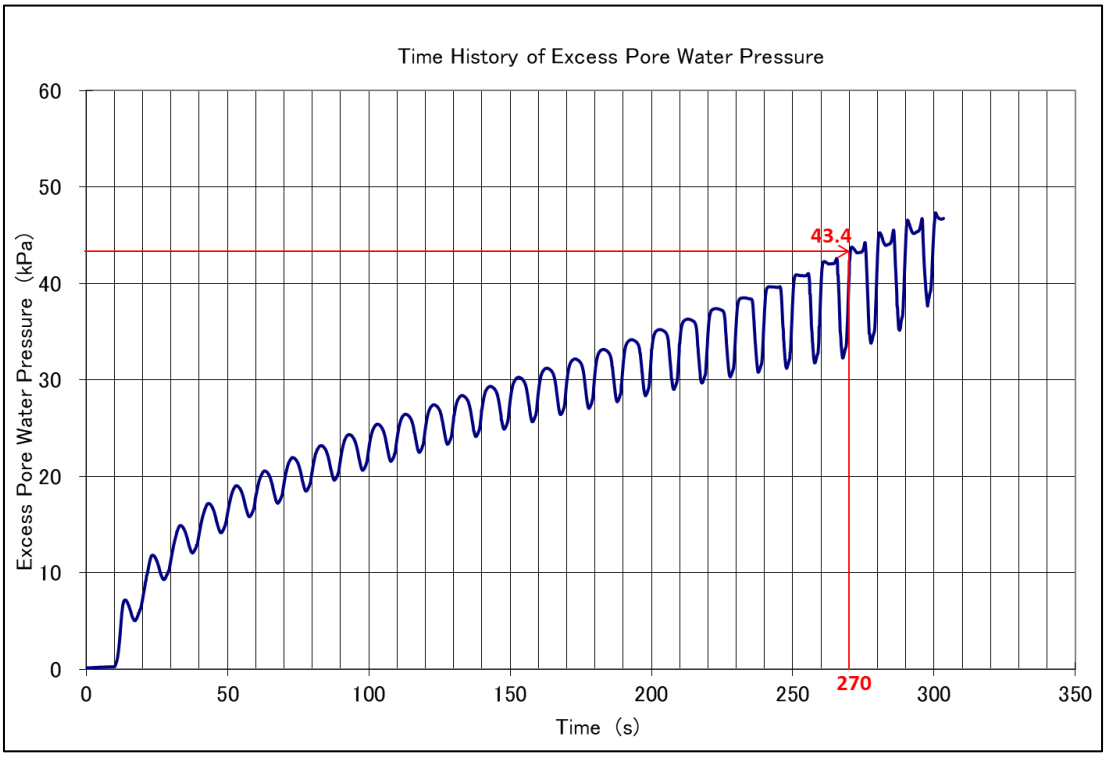

Fig. 3-6. Time History of Excess Pore Water Pressure (Test L4-bauxite, loose case, saturated)

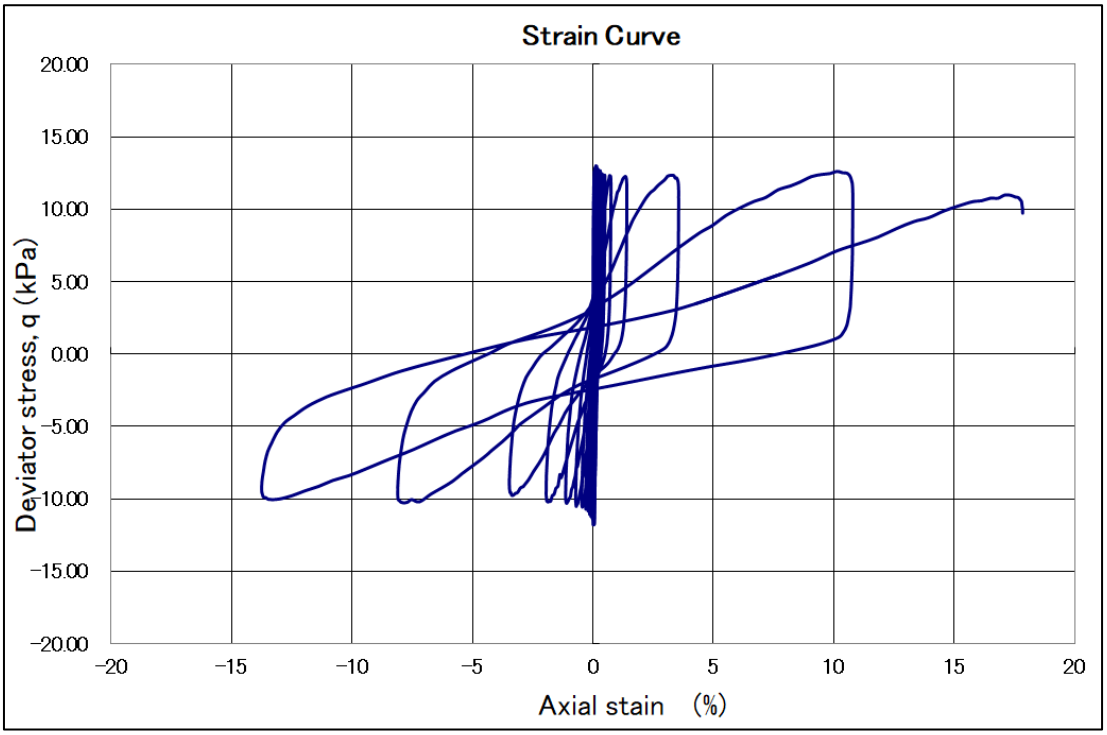

Fig. 3-7. Axial Strain vs. Deviator Stress *q* (Test L4-bauxite, loose case, saturated)

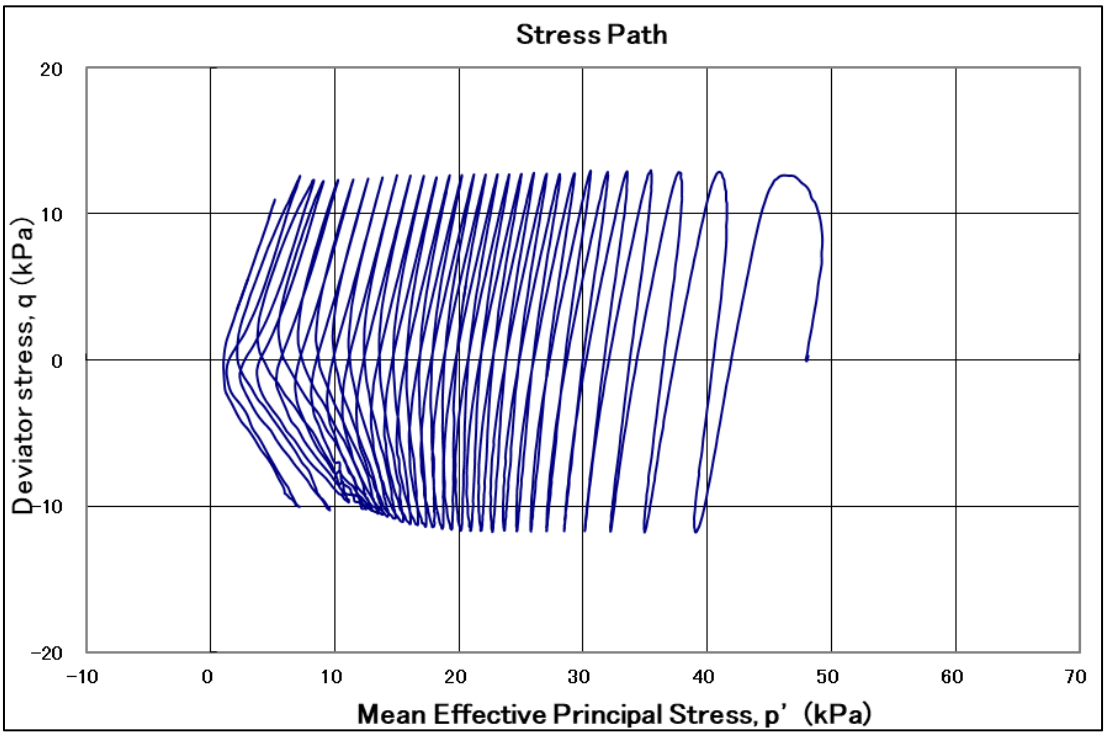

Fig. 3-8. *p* – *q* plot (Test L4-bauxite, loose case, saturated)

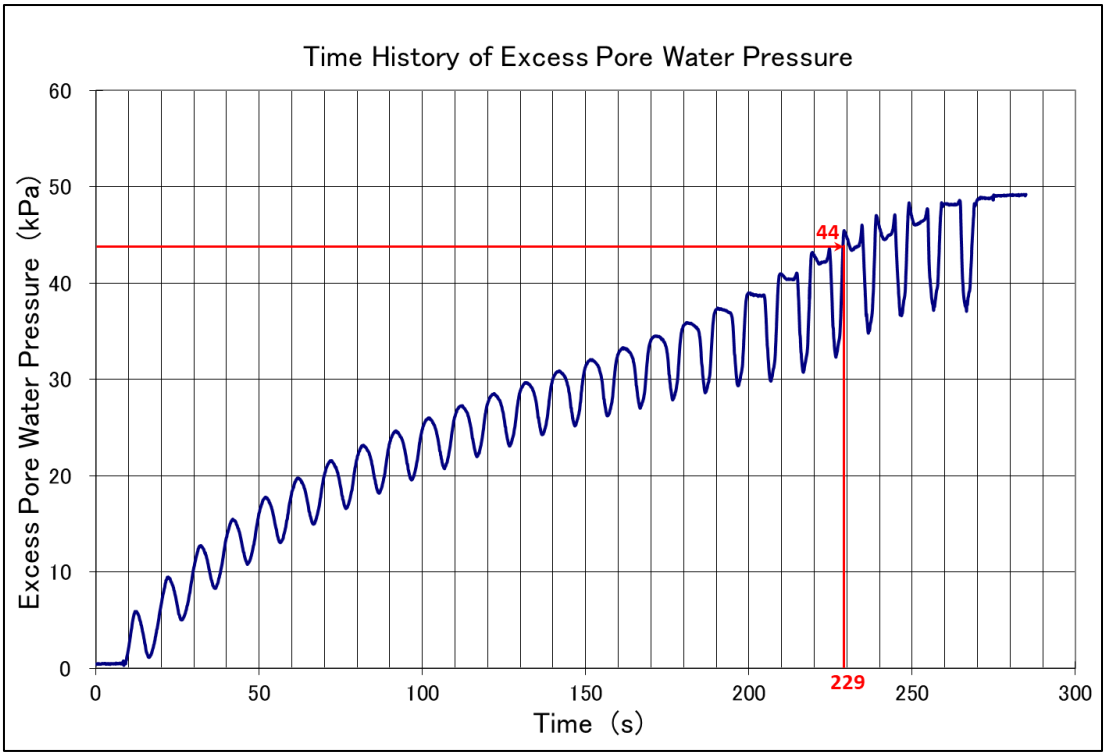

Fig. 3-9. Time History of Excess Pore Water Pressure (Test M4-bauxite, m.dense, saturated)

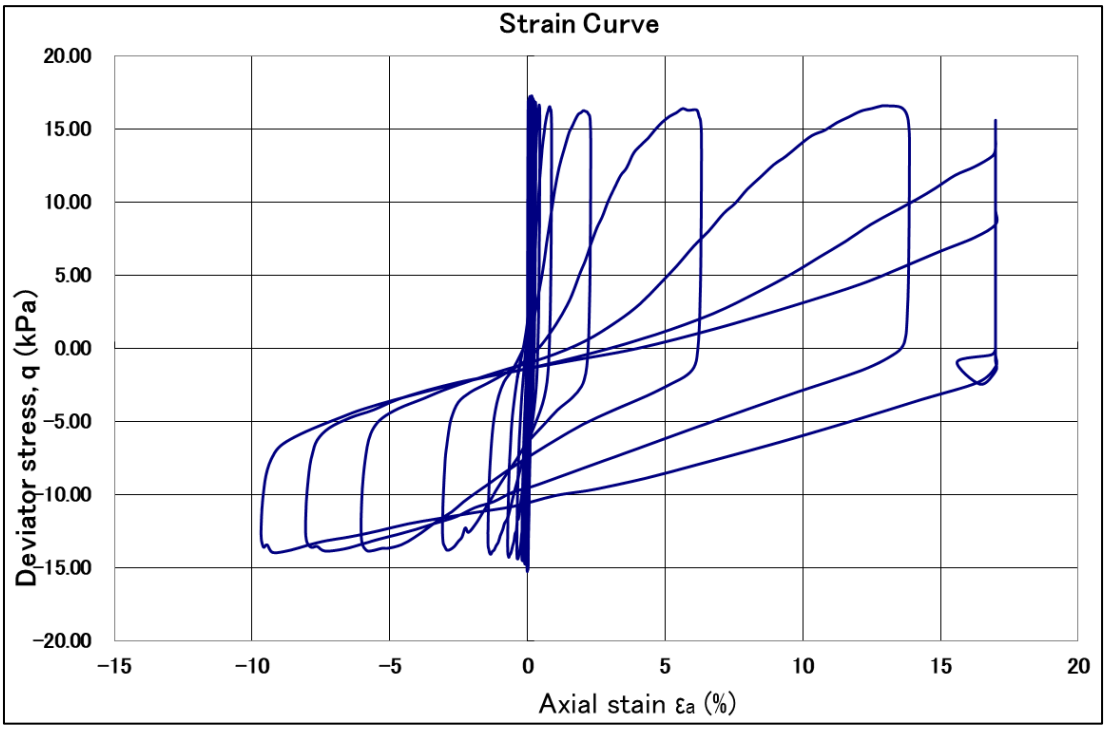

Fig. 3-10. Axial Strain vs. Deviator Stress *q* (Test M4-bauxite, m.dense, saturated)

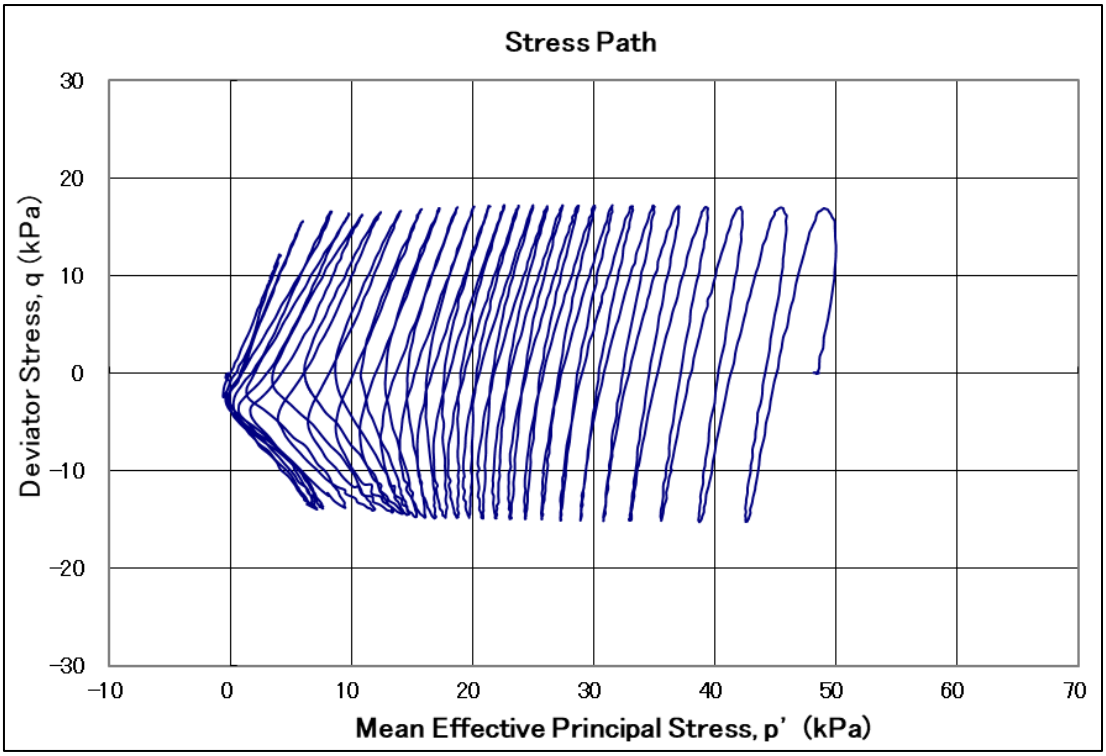

Fig. 3-11. *p* – *q* plot (Test M4-bauxite, m.dense, saturated)

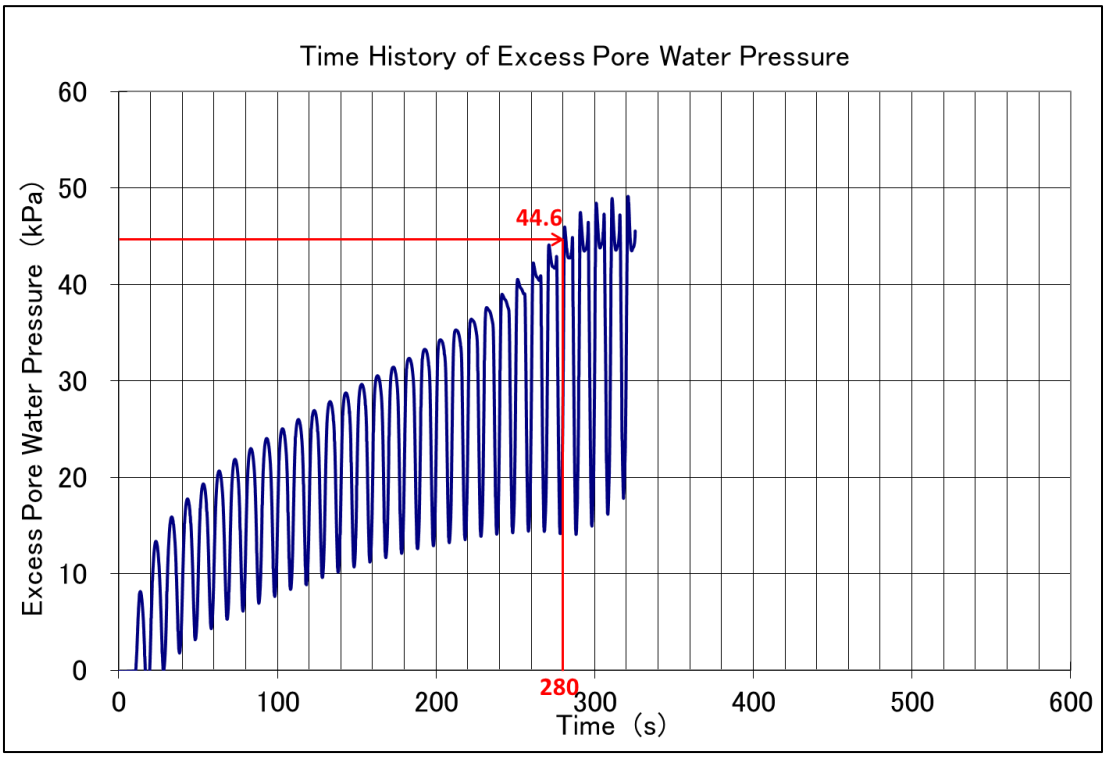

Fig. 3-12. Time History of Excess Pore Water Pressure (Test D4-bauxite, dense, saturated)

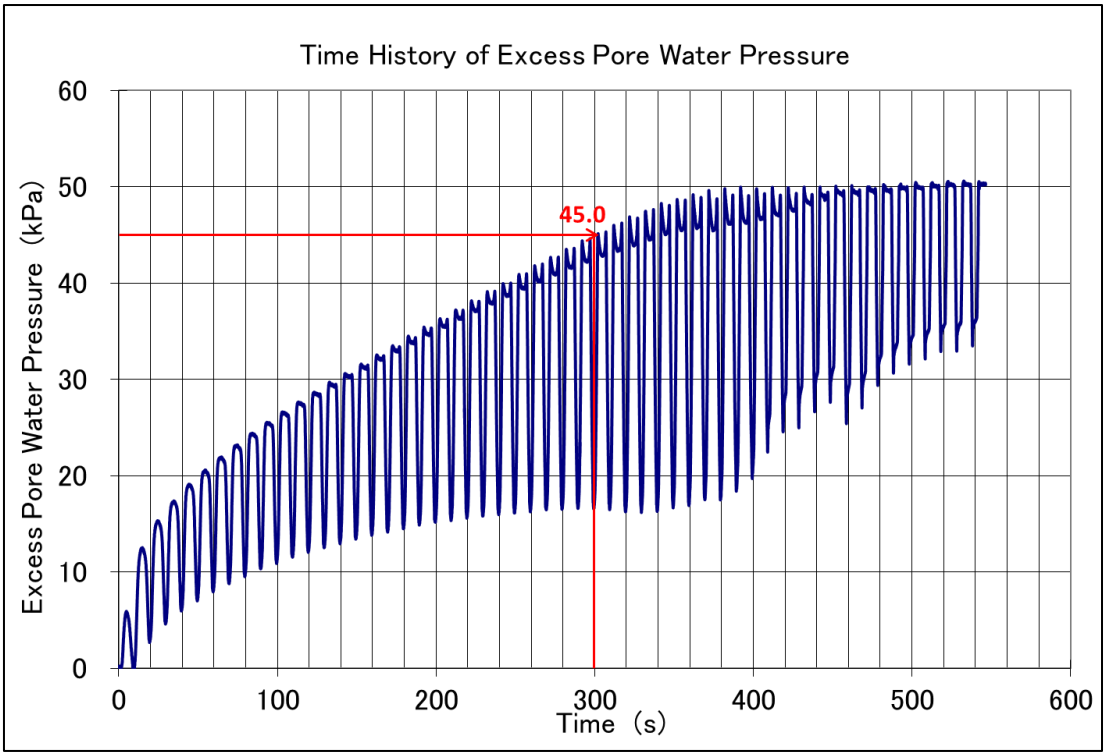

Fig. 3-13. Time History of Excess Pore Water Pressure (iron ore test, dense, saturated)

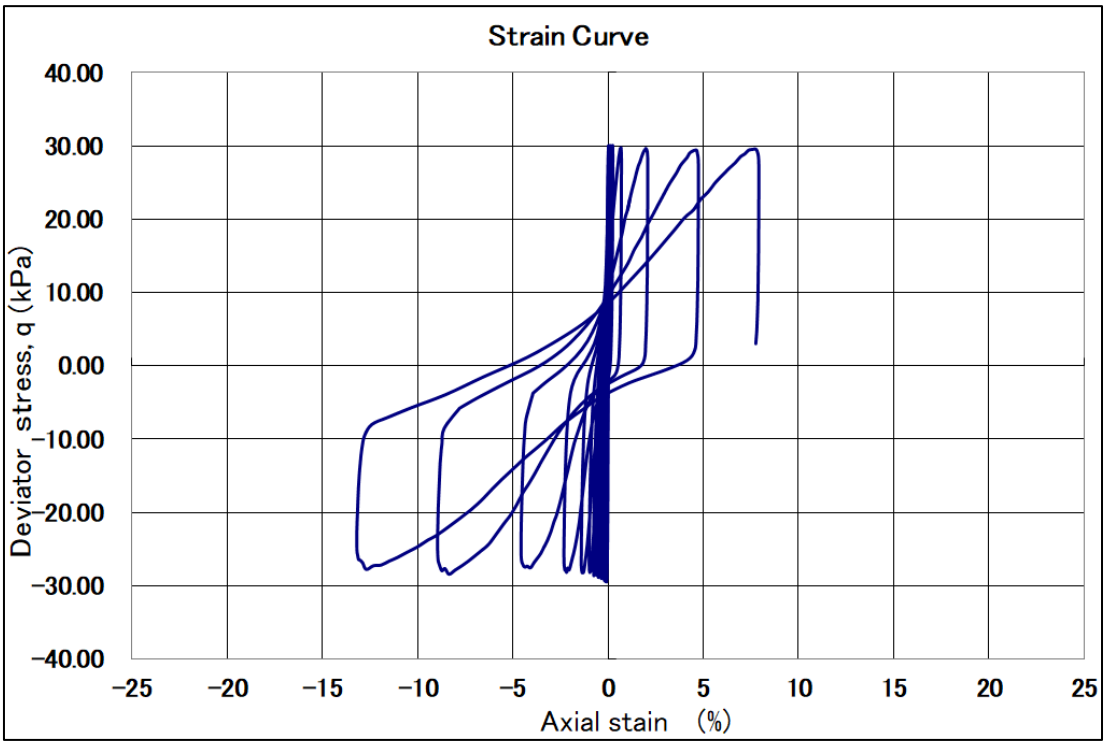

Fig. 3-14. Axial Strain vs. Deviator Stress *q* (Test D4-bauxite, dense, saturated)

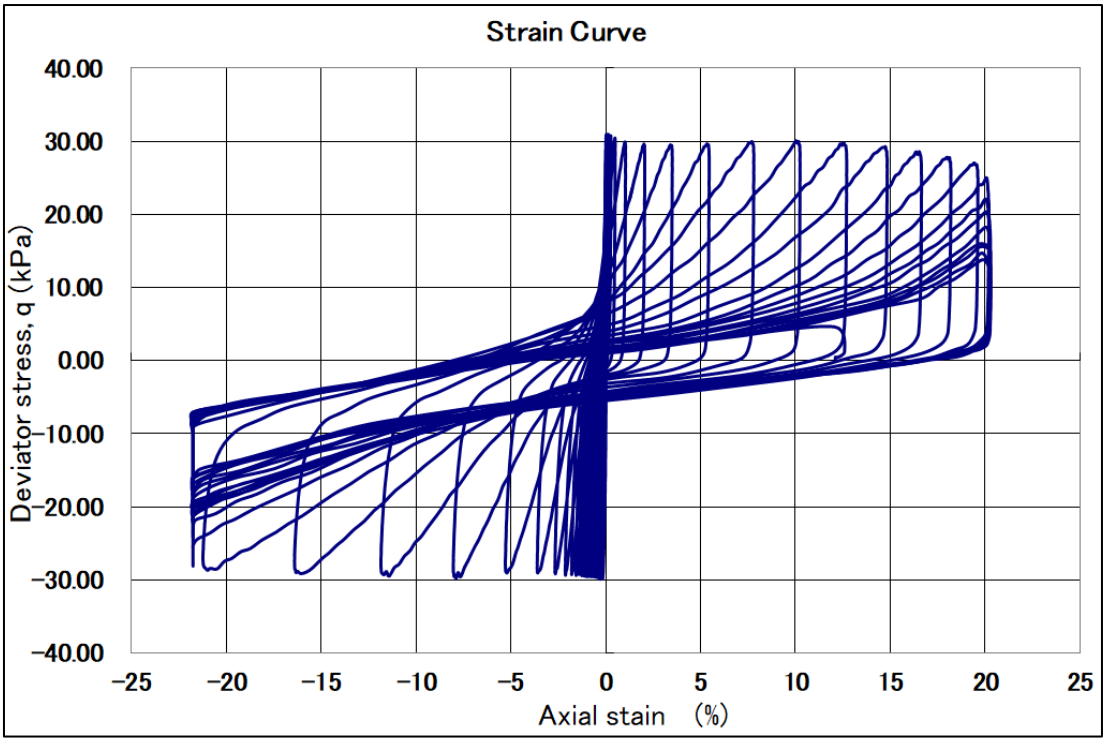

Fig. 3-15. Axial Strain vs. Deviator Stress *q* (iron ore test, dense, saturated)

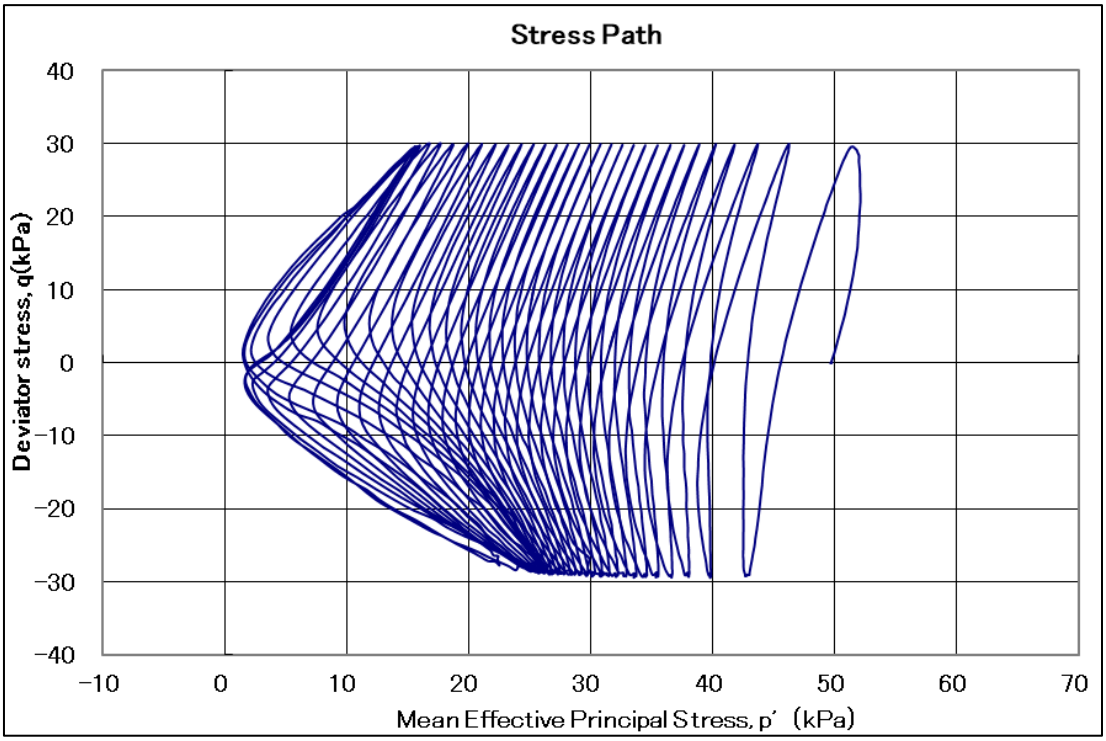

Fig. 3-16. *p* – *q* plot (Test D4-bauxite, dense, saturated)

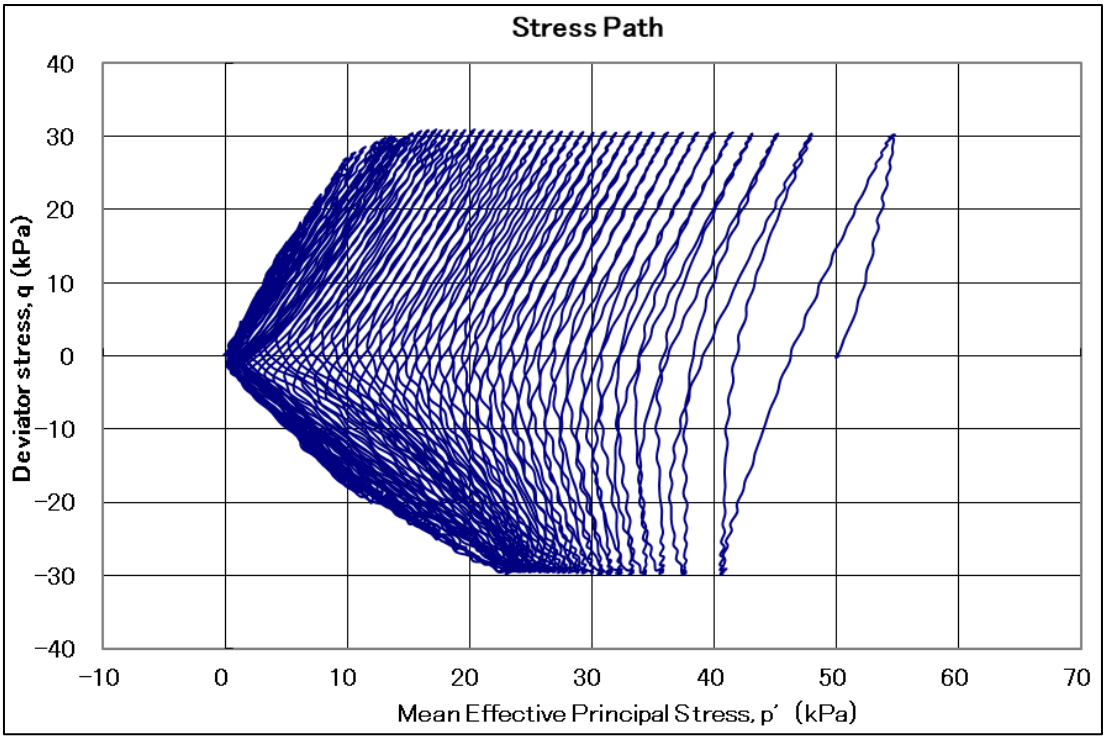

Fig. 3-17. *p* – *q* plot (iron ore test, dense, saturated)

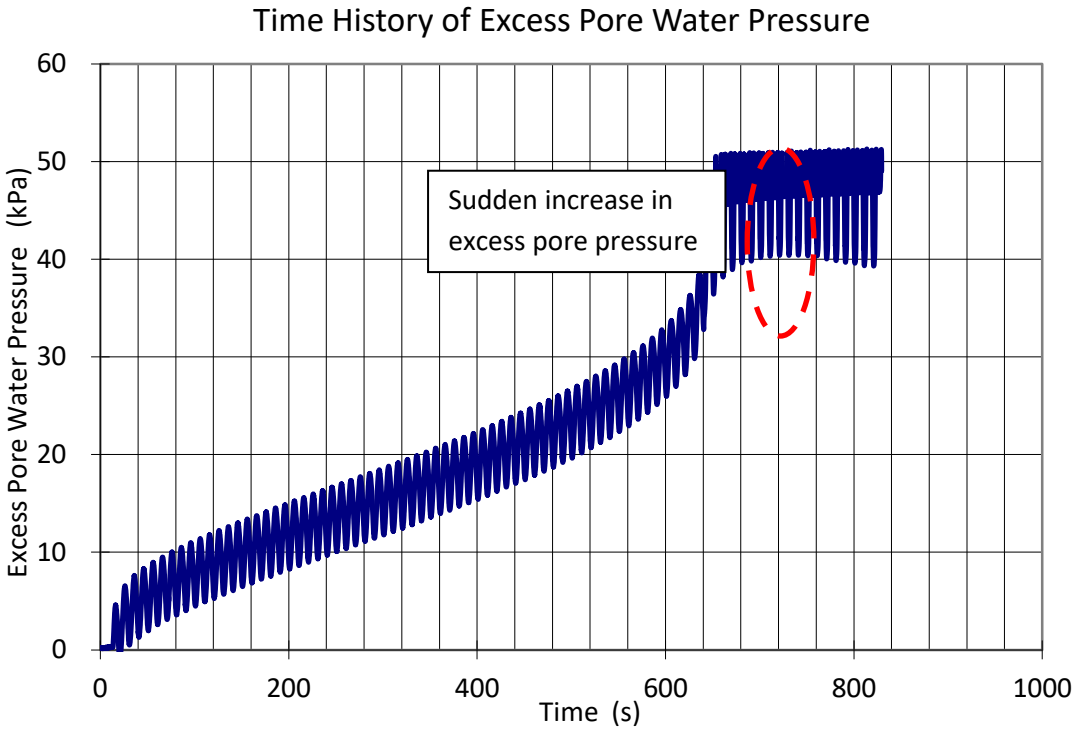

Fig. 3-18. Time History of Excess Pore Water Pressure
(Test 6-Toyoura sand, saturated, extracted from Tan Tian, 2016)

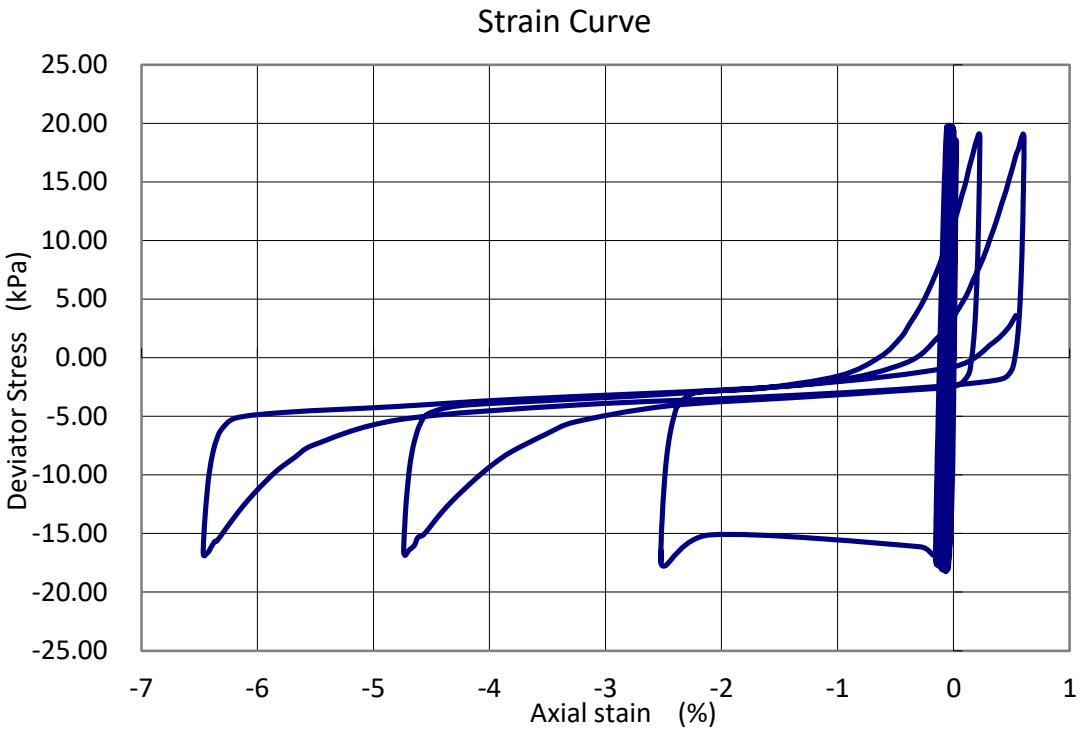

Fig. 3-19. Axial Strain vs. Deviator Stress *q*
(Test 6-Toyoura sand, saturated, extracted from Tan Tian, 2016)

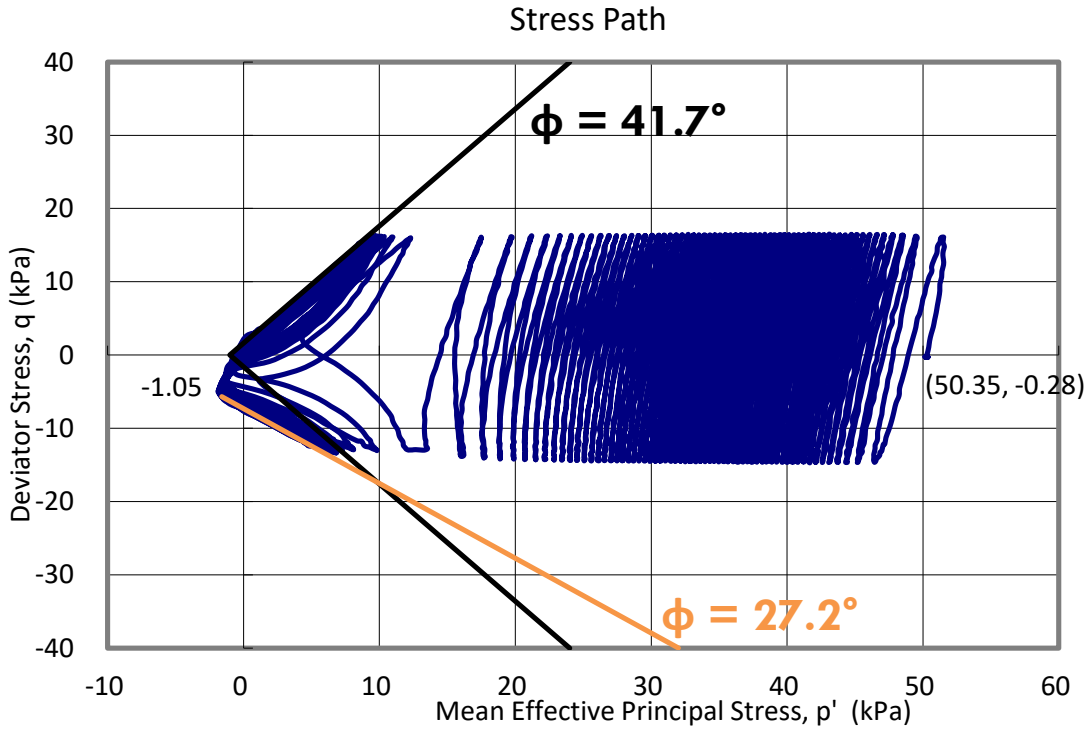

Fig. 3-20. *p* – *q* plot (Test 6-Toyoura sand, saturated, extracted from Tan Tian, 2016)

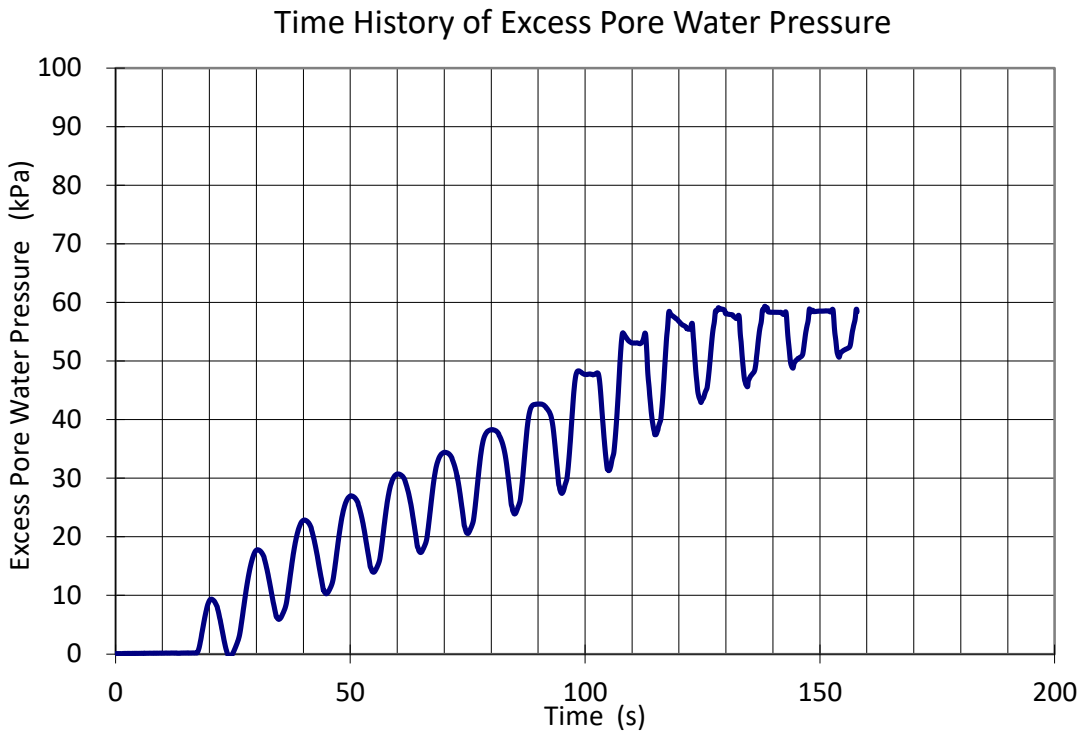

Fig. 3-21. Time History of Excess Pore Water Pressure
(Test 4-Inagi sand, saturated, extracted from Tan Tian, 2016)

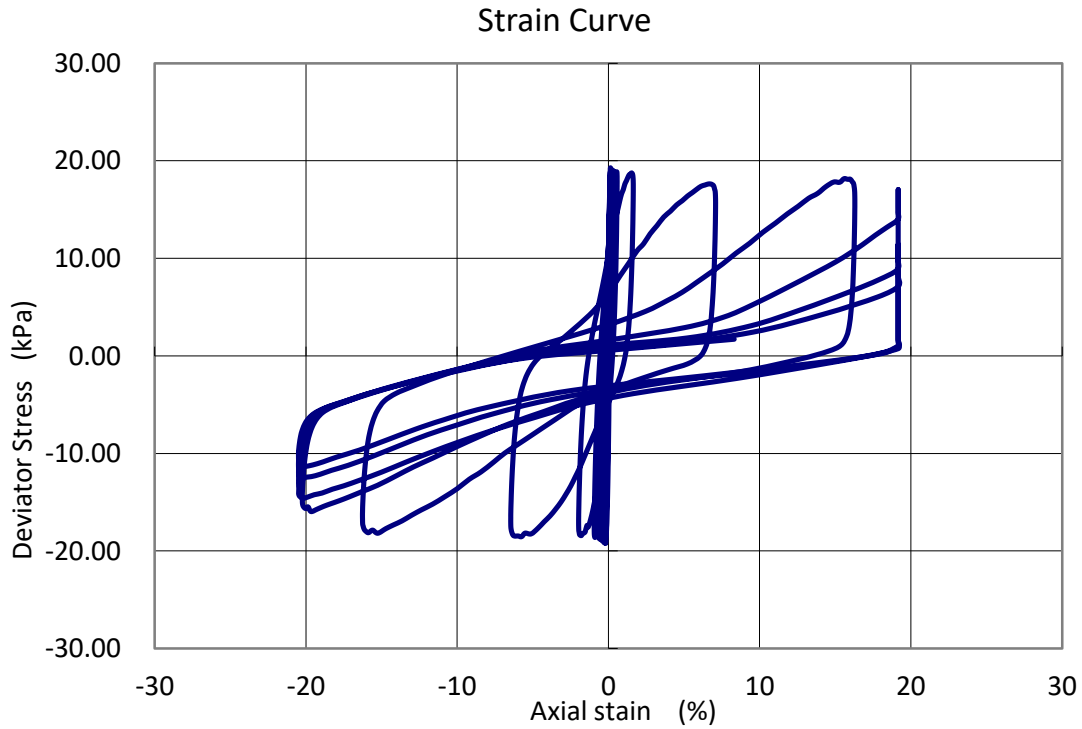

Fig. 3-22. Axial Strain vs. Deviator Stress *q*
(Test 4-Inagi sand, saturated, extracted from Tan Tian, 2016)

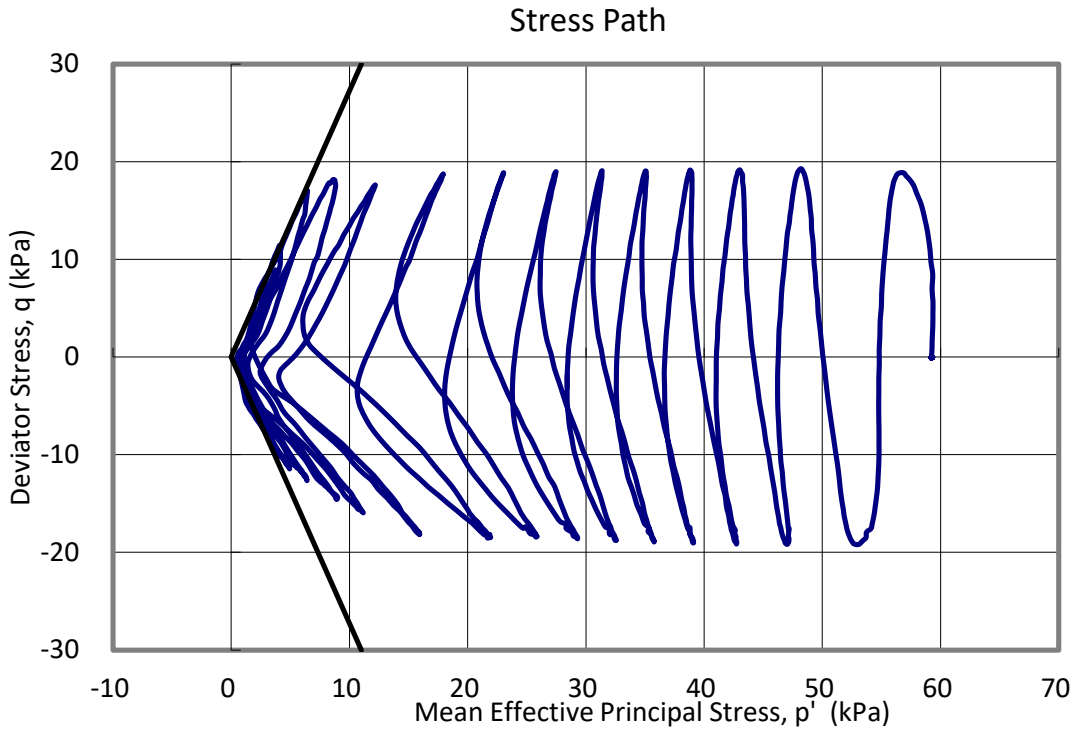

Fig. 3-23. *p* – *q* plot (Test 4-Inagi sand, saturated, extracted from Tan Tian, 2016)

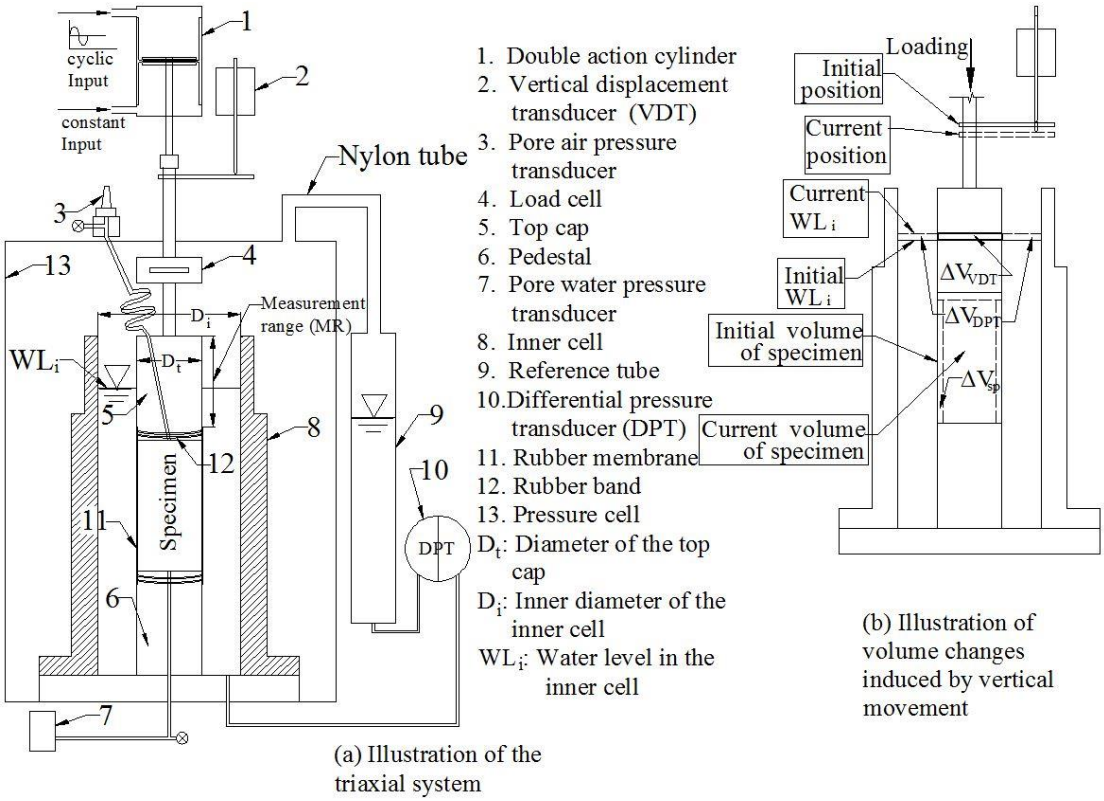

Fig. 3-24. Layout of the Traditional Double Cell System

(Wang, 2015)

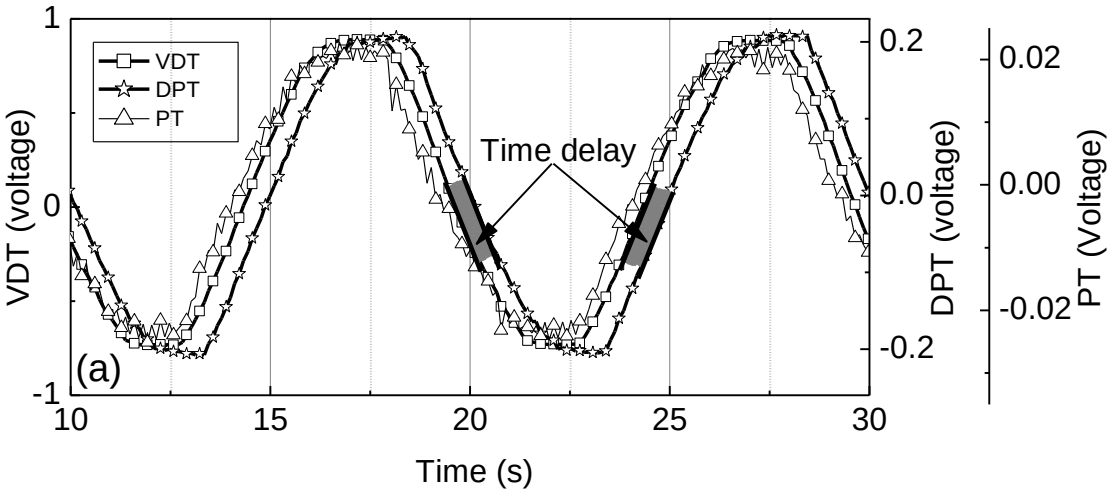

Fig. 3-25. Time Delay between DPT and VDT, PT measurements

(Wang, 2015)

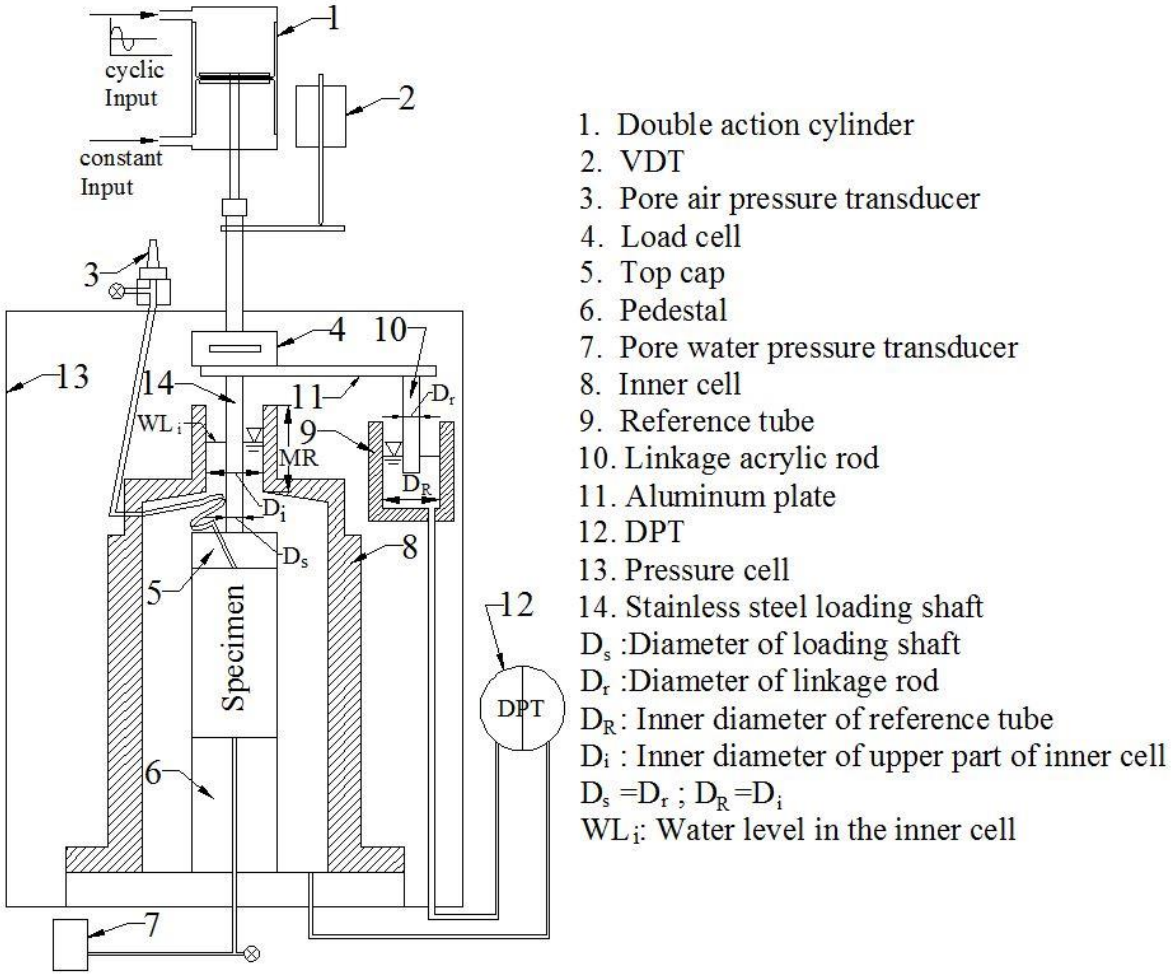

Fig. 3-26. Layout of the Linkage Double Cell System

(Wang, 2015)

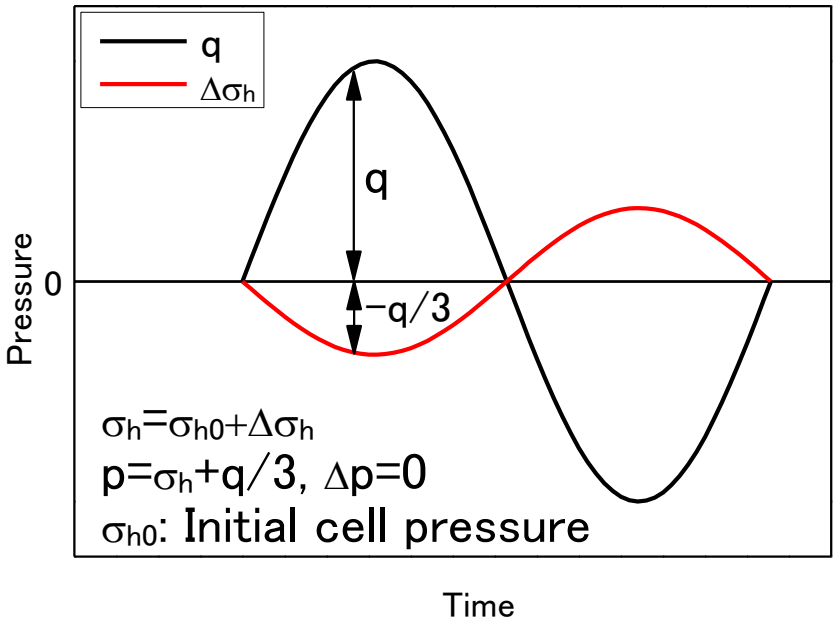

Fig. 3-27. Principle of Cell Pressure Control (Wang, 2015)

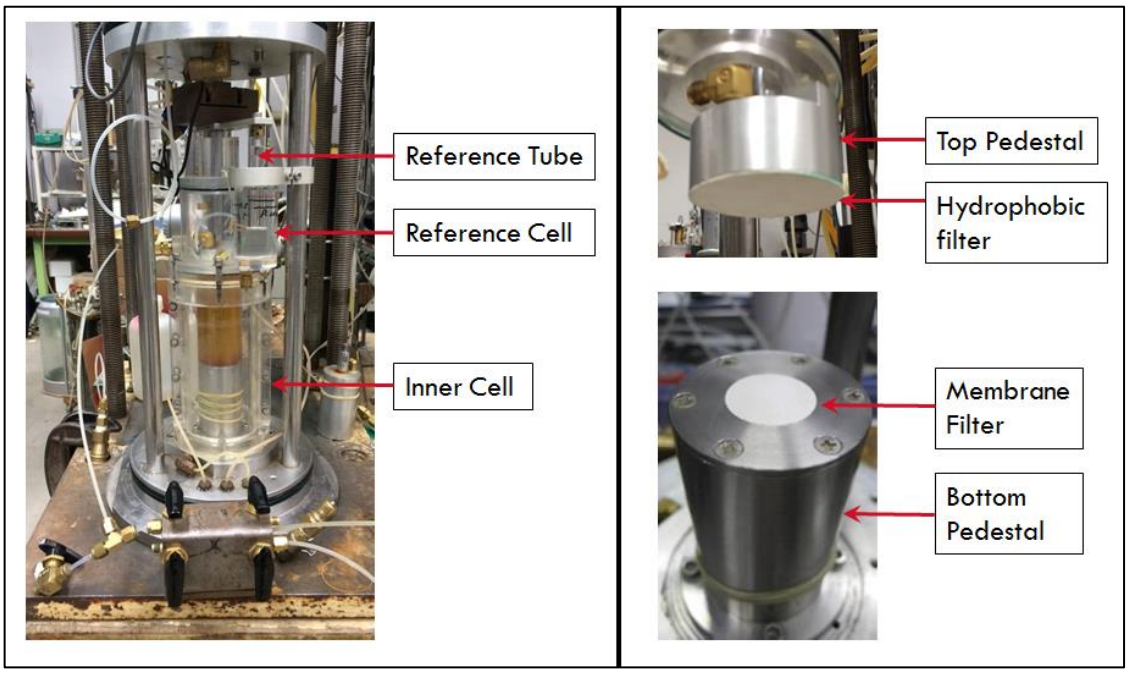

Fig. 3-28. Photo of the Linkage Double Cell System (L); Top Cap and Bottom Pedestal (R)

Fig. 3-29. Water-tight acrylic pipe used to saturate the bottom pedestal

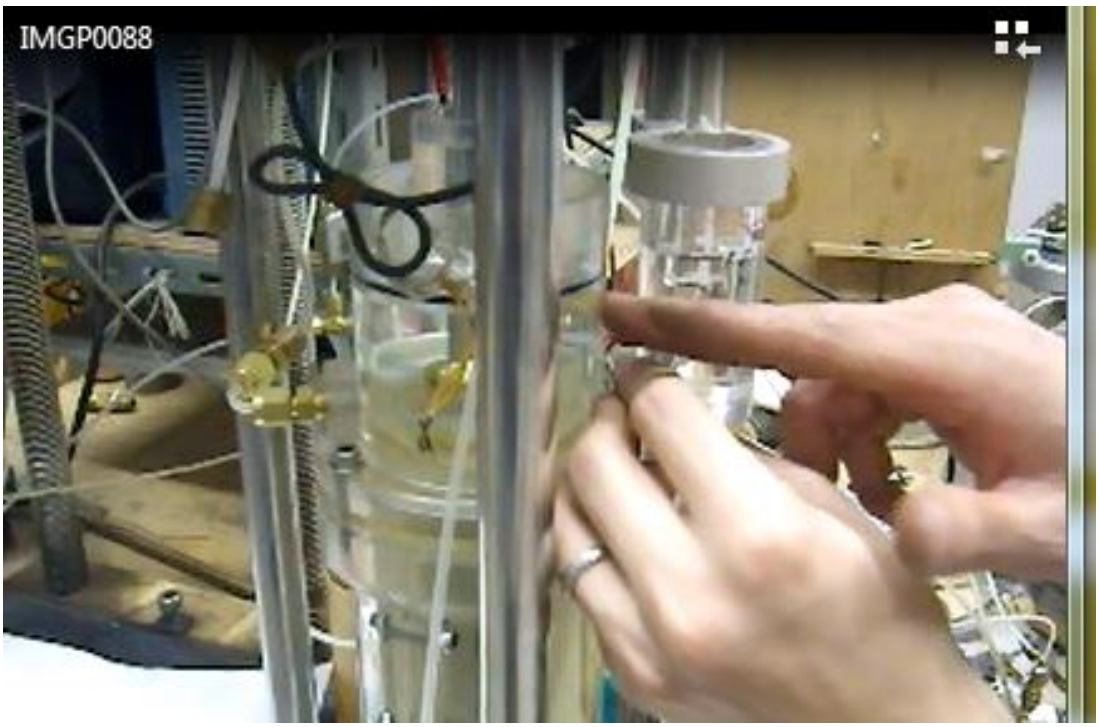

Fig. 3-30. Linkage Double Cell System Set-up. The distance between Inner Cell and Reference Cell is being established.

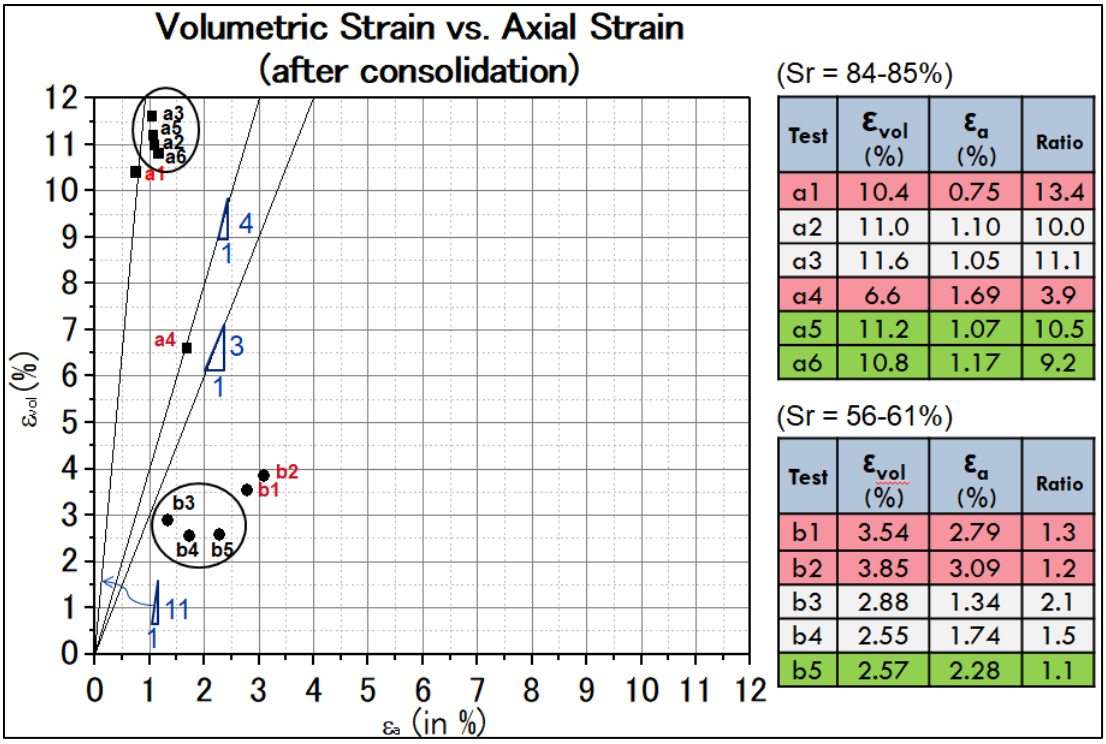

(Sr = 84-85%)

Test	ε_{vol} (%)	ε_a (%)	Ratio
a1	10.4	0.75	13.4
a2	11.0	1.10	10.0
a3	11.6	1.05	11.1
a4	6.6	1.69	3.9
a5	11.2	1.07	10.5
a6	10.8	1.17	9.2

(Sr = 56-61%)

Test	ε_{vol} (%)	ε_a (%)	Ratio
b1	3.54	2.79	1.3
b2	3.85	3.09	1.2
b3	2.88	1.34	2.1
b4	2.55	1.74	1.5
b5	2.57	2.28	1.1

Fig. 3-31. ε_{vol} vs. ε_a plot of bauxite (Unsaturated)

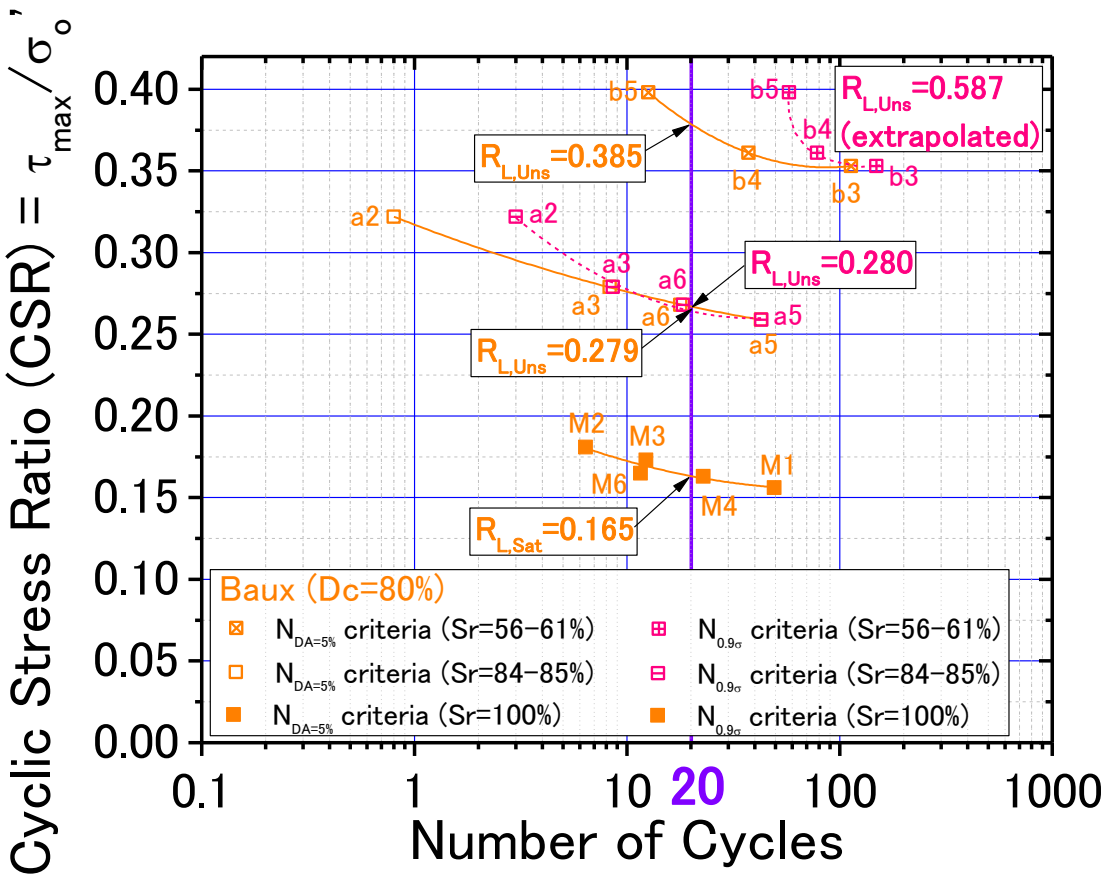

Fig. 3-32. CSR vs Number of Cycles plot of bauxite (Unsaturated)

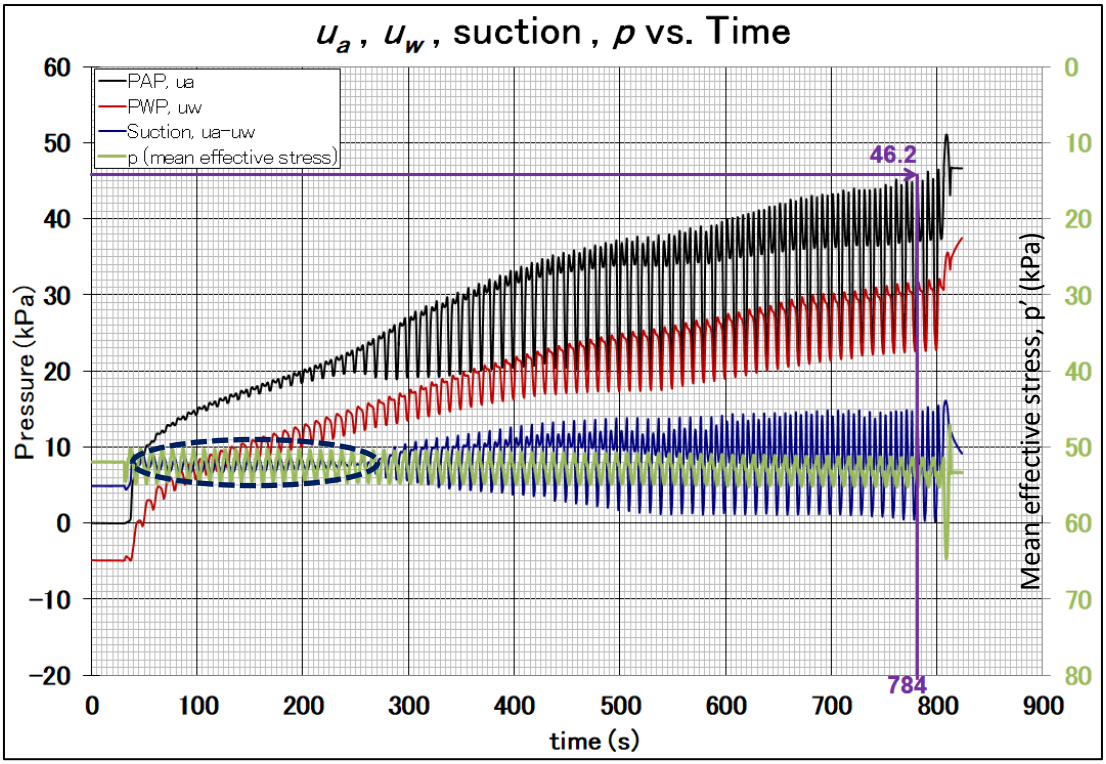

Fig. 3-33. u_a, u_w, Suction, and p behavior (Test b4-bauxite, unsaturated)

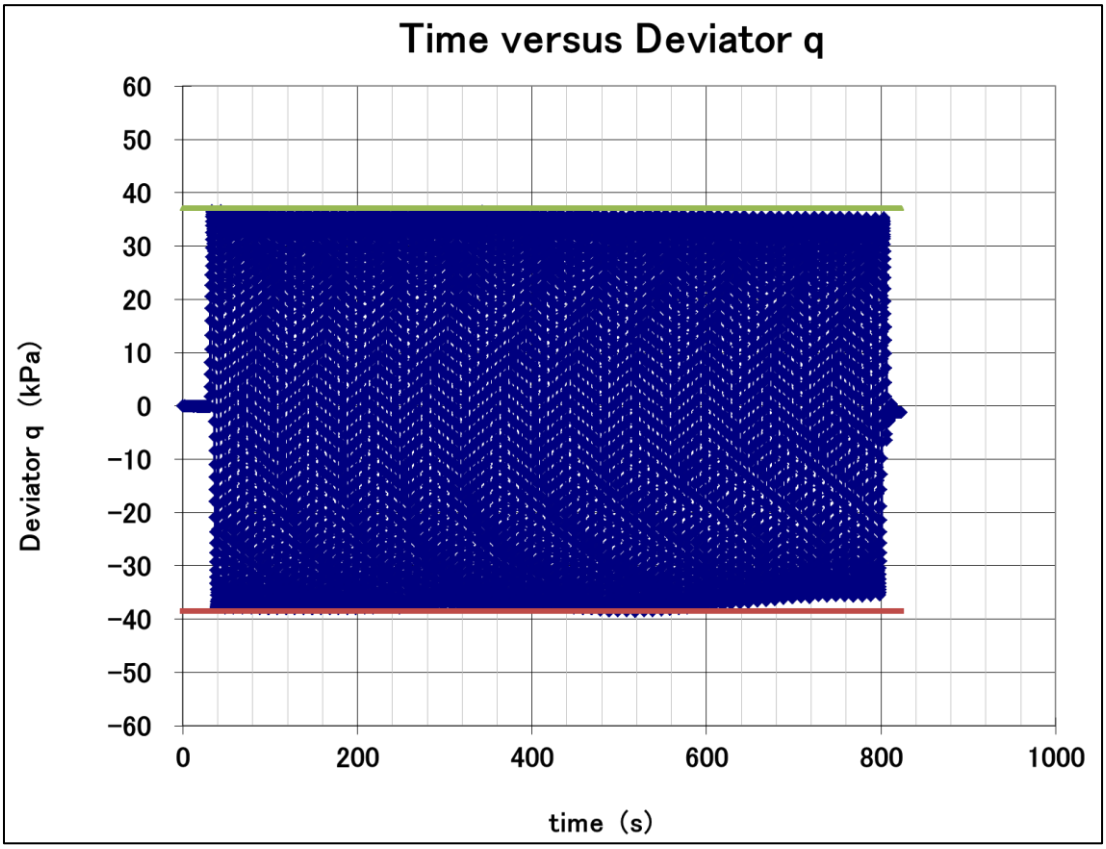

Fig. 3-34. Time history of Deviator Stress q plot (Test b4-bauxite, unsaturated)

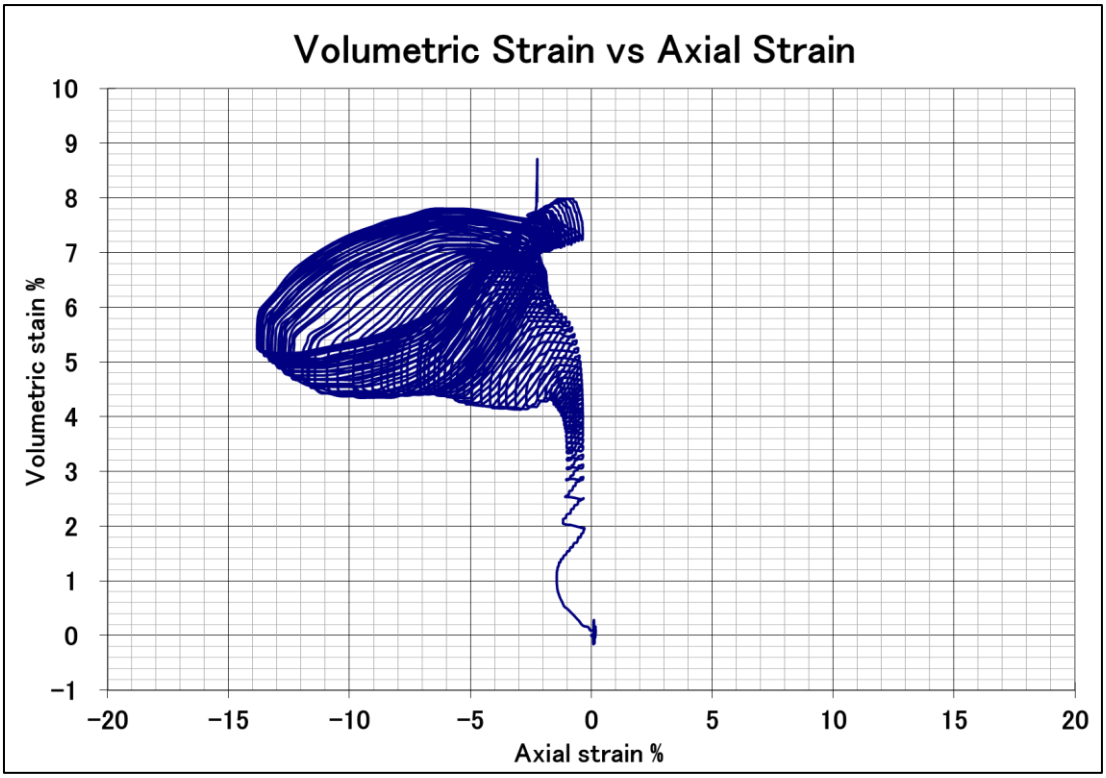

Fig. 3-35. Axial Strain vs. Volumetric Strain (Test b4-bauxite, unsaturated)

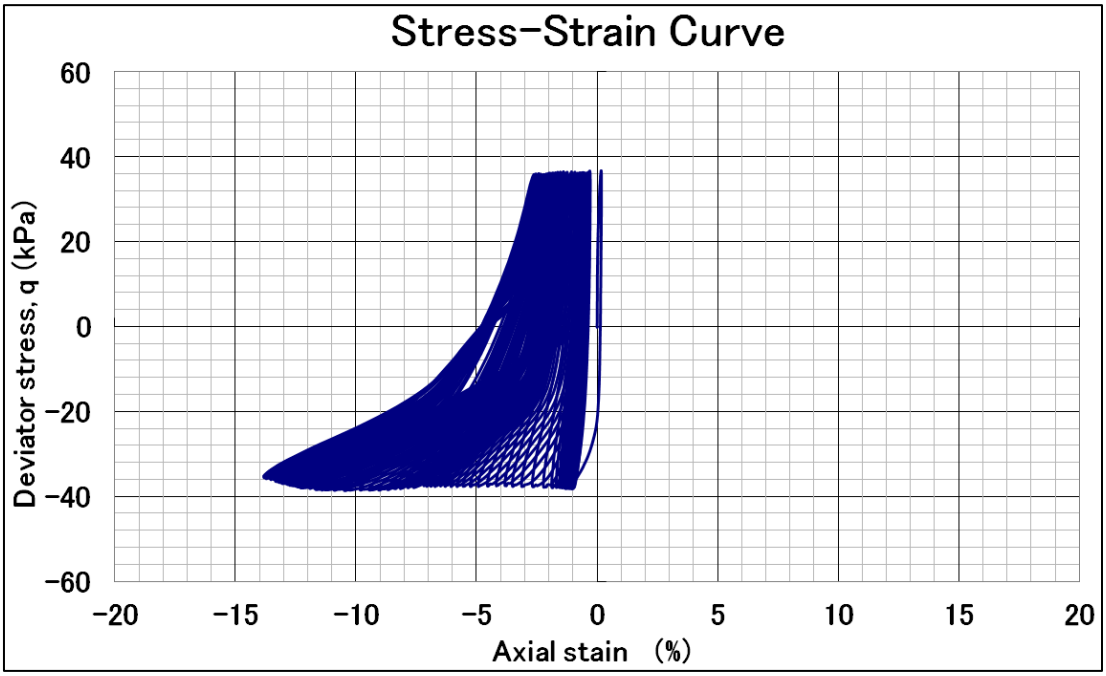

Fig. 3-36. Axial Strain vs. Deviator Stress *q* (Test b4-bauxite, unsaturated)

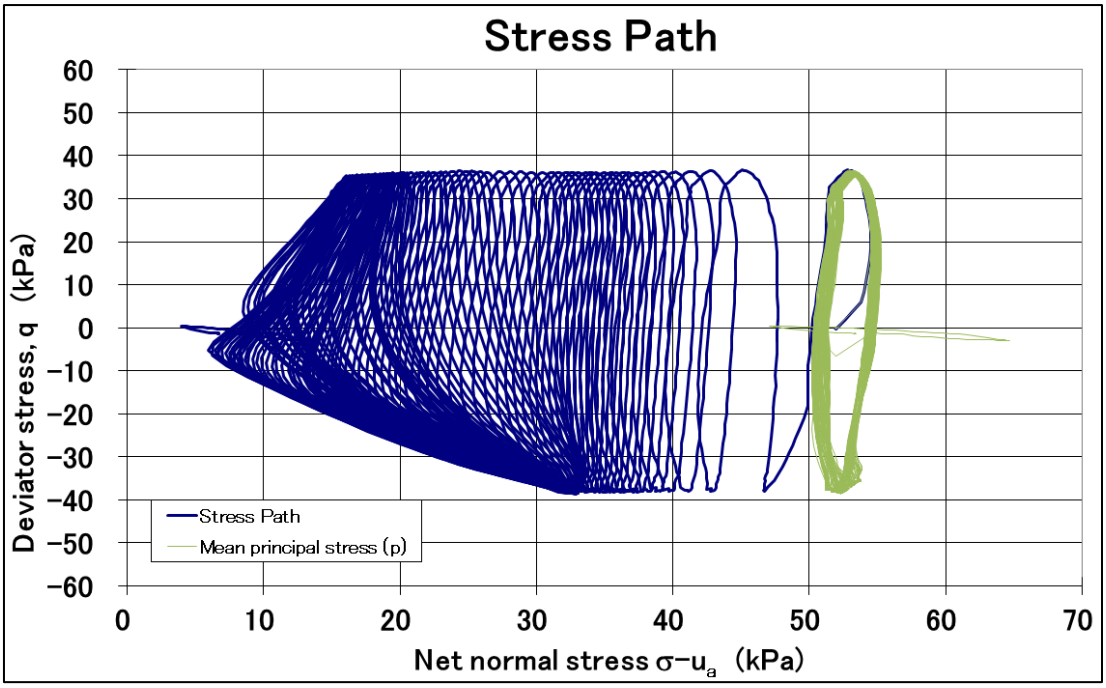

Fig. 3-37. *p* – *q* plot (Test b4-bauxite, unsaturated)

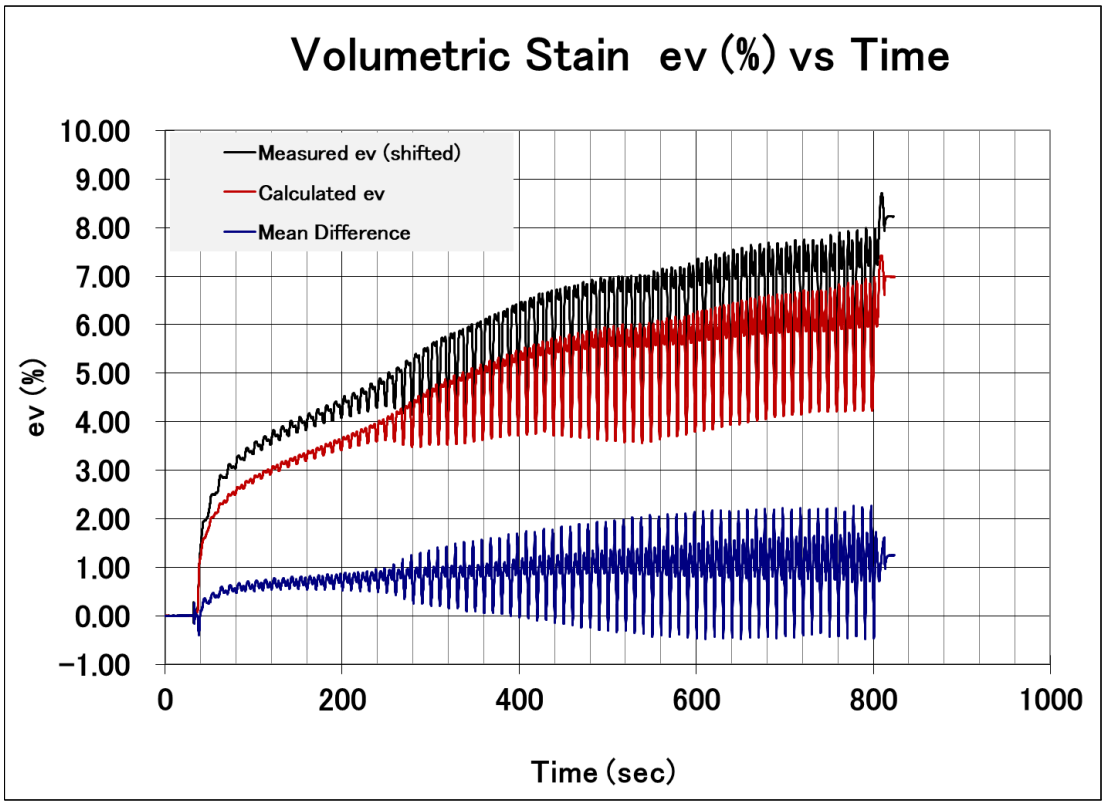

Fig. 3-38. Volumetric Strain – measured and calculated
(Test b4-bauxite, unsaturated; σ'_{max} = 50 kPa)

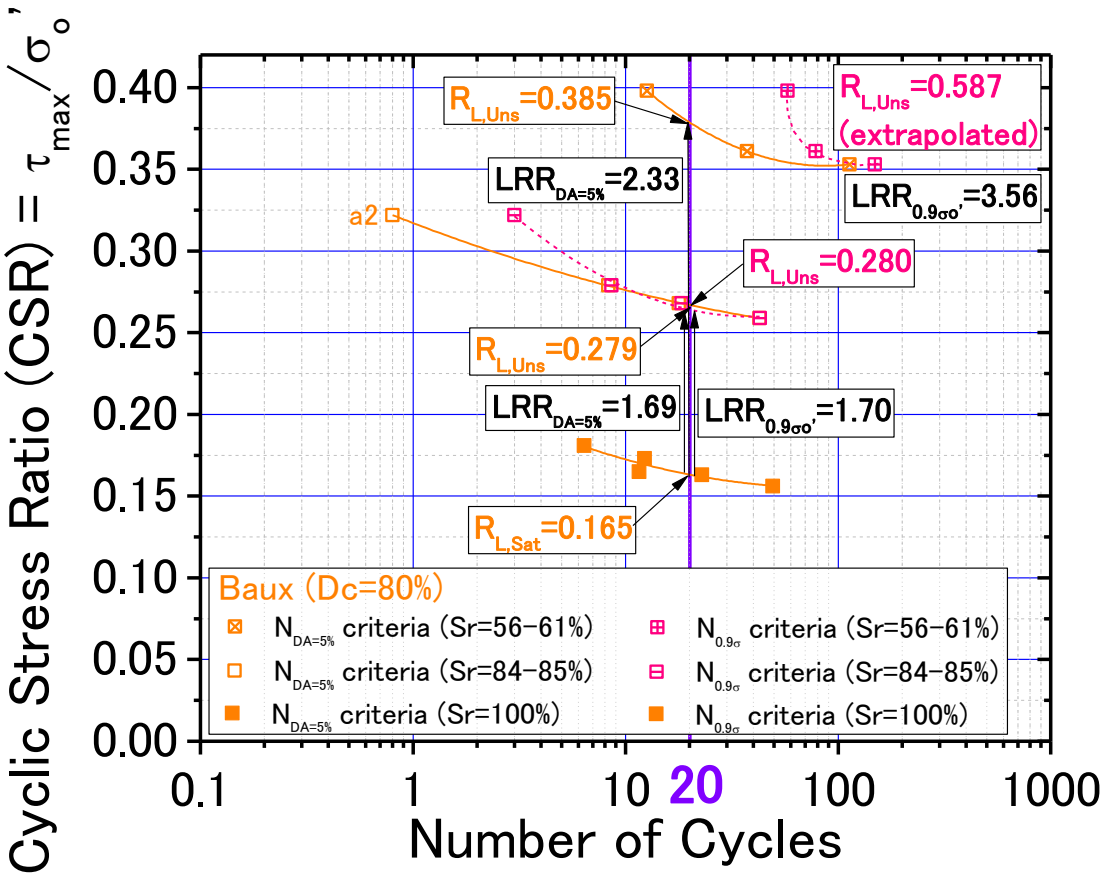

Fig. 3-39. CSR vs Number of Cycles plot of bauxite indicating LRR (Unsaturated)

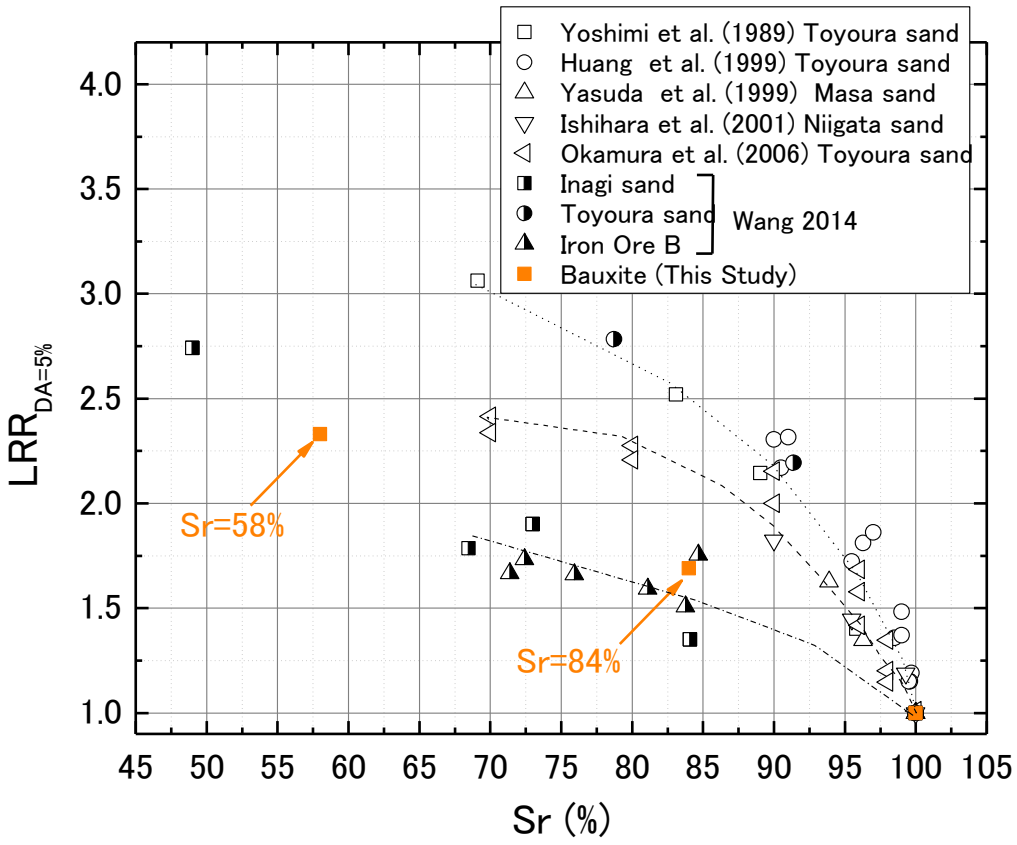

Fig. 3-40. Relationship between Sr and $LRR_{DA=5\%}$

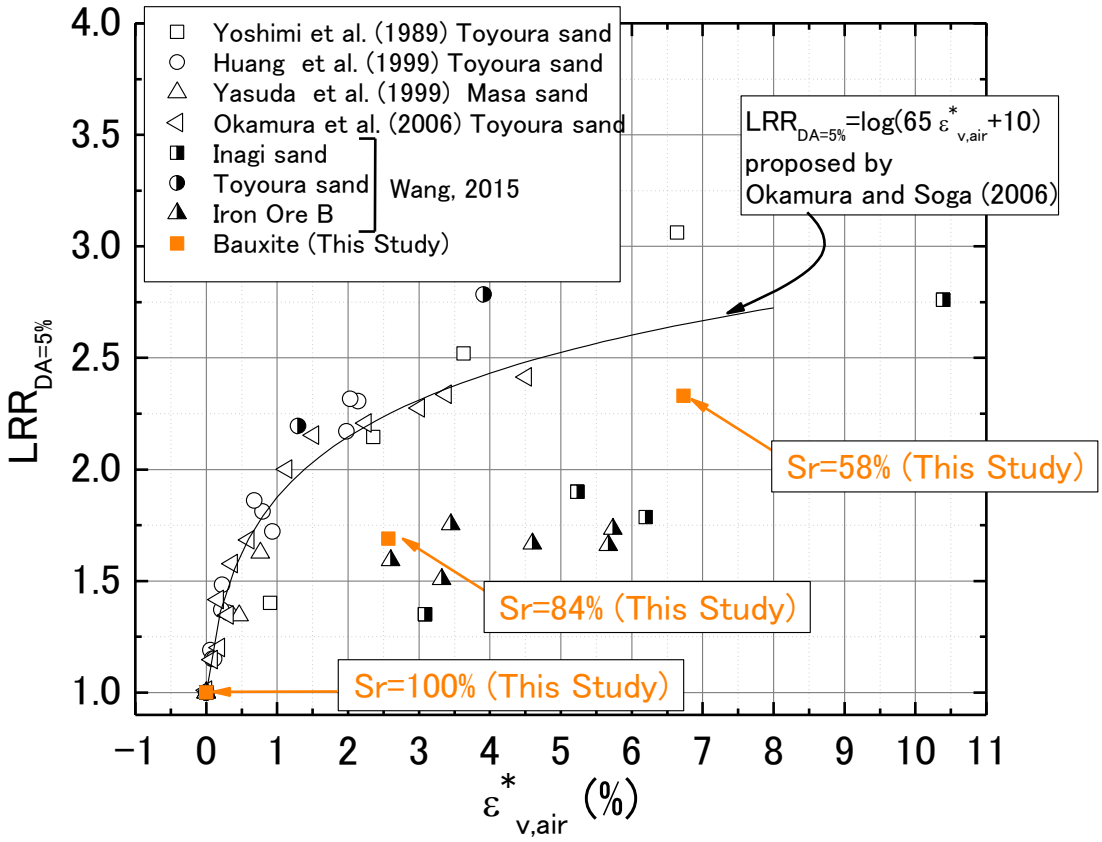

Fig. 3-41. Relationship between potential volumetric strain ($\varepsilon^*_{v,air}$) and $LRR_{DA=5\%}$

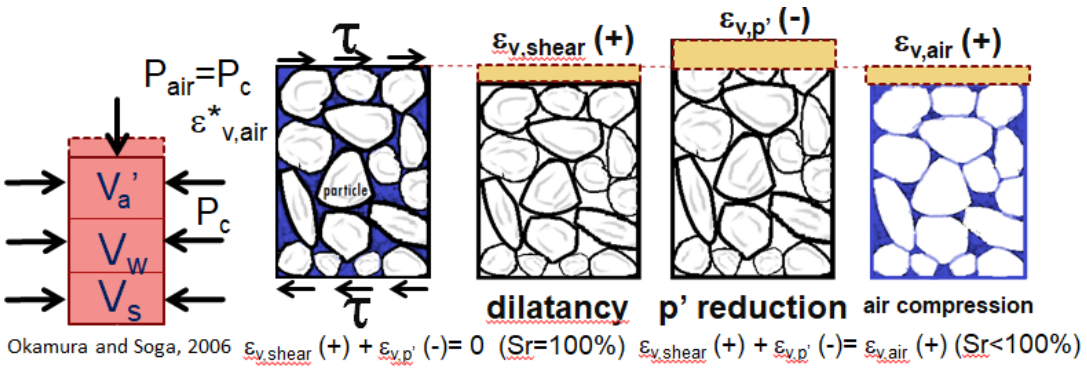

Fig. 3-42. Illustration of $\varepsilon_{v,\tau}$, $\varepsilon_{v,\sigma'}$, and $\varepsilon_{v,air}$ (Wang, 2014)

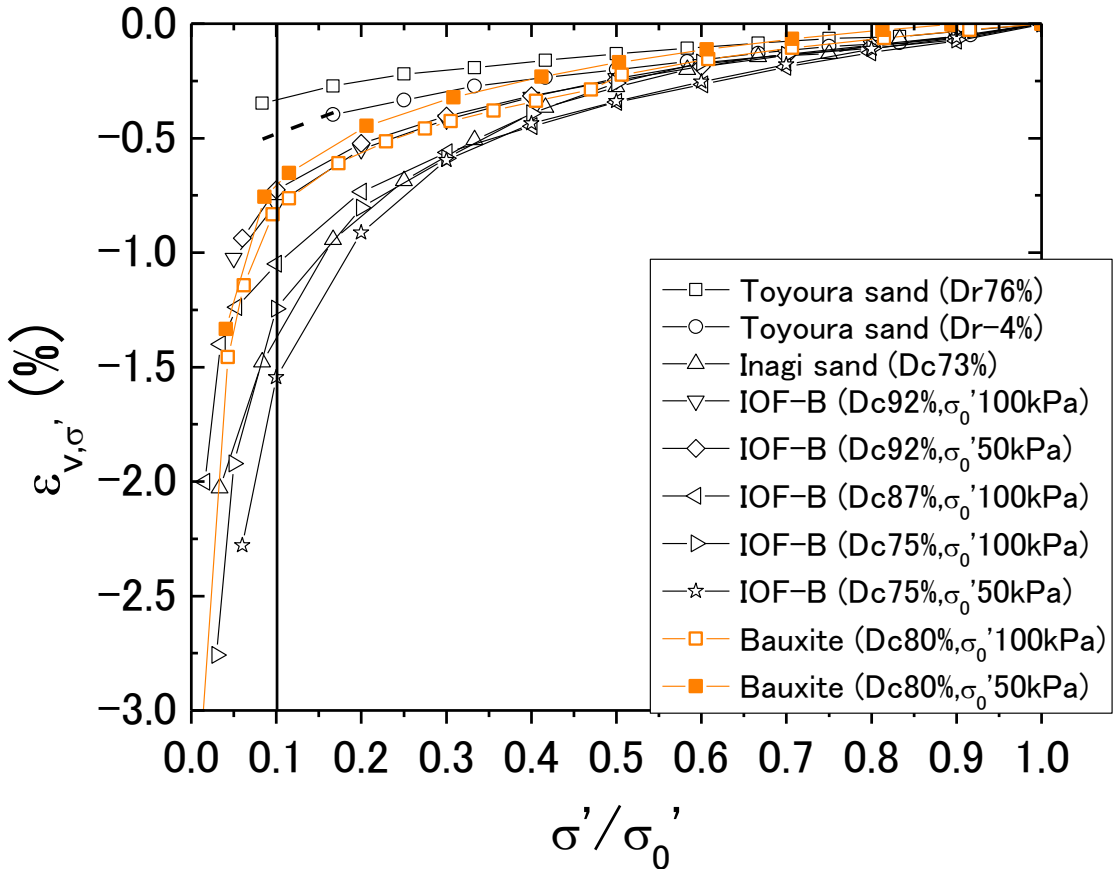

Fig. 3-43. Isotropic Consolidation Test (Unloading) relating σ'/σ_0' and $\varepsilon_{v,\sigma'}$

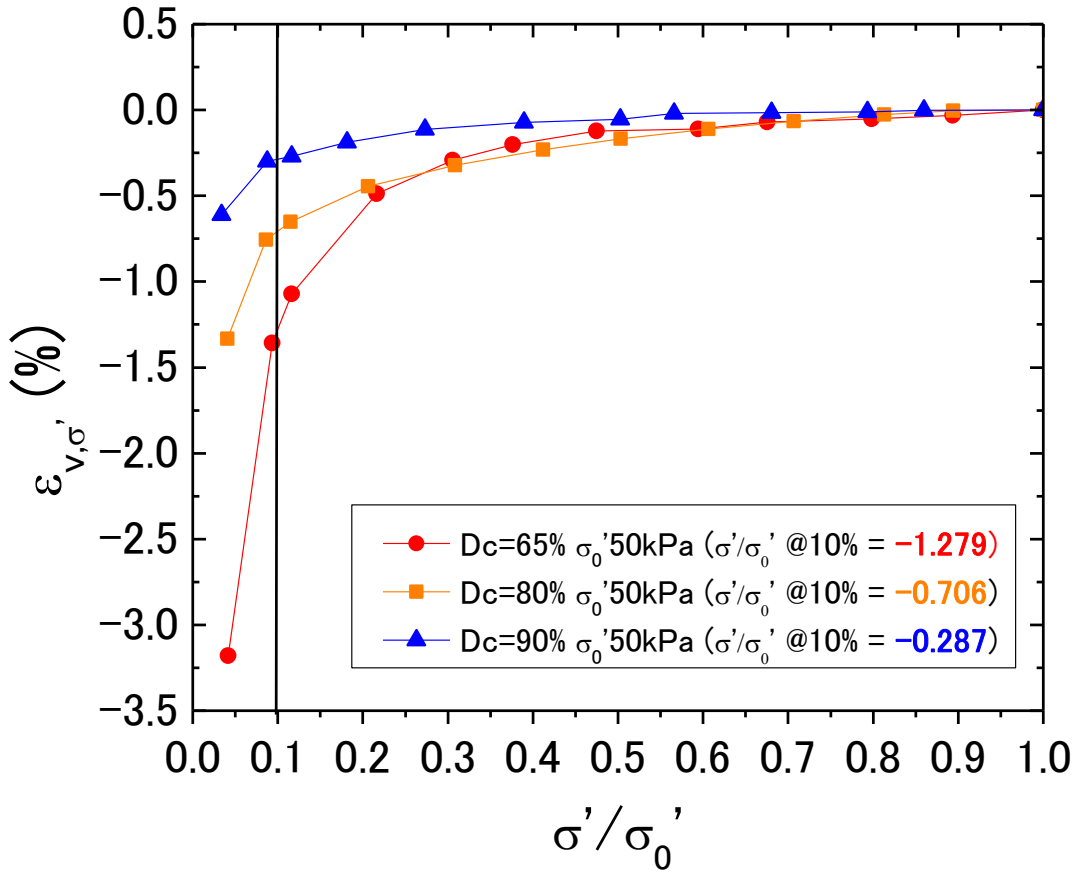

Fig. 3-44. Bauxite Isotropic Consolidation Test (Unloading) relating σ'/σ_0' and $\varepsilon_{v,\sigma'}$

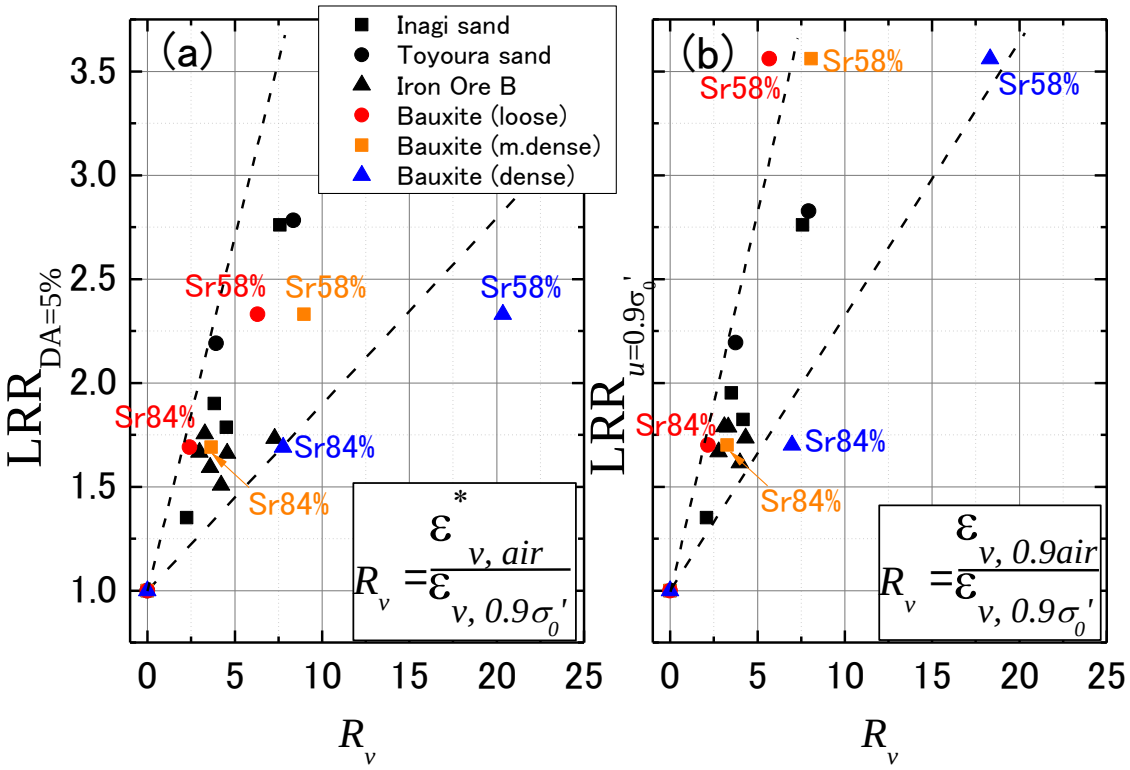

Fig. 3-45. Relationship Relationship between volumetric strain ratio (R_v) and LRR

Chapter 4
Permeability Tests under Different Saturation Conditions and SWRC Tests

Contents

4-1. Introduction

This Chapter describes the Permeability Tests conducted under different saturation conditions and the Soil-Water Retention Curve Tests (SWRC Tests).

Permeability tests were first conducted using the Standard Permeameter Test JIS A 1218, Test Methods for Permeability of Saturated Soils. This test uses a rigid mold in which the specimen is placed to measure the permeability of soils.

In contrast, a flexible wall method using triaxial apparatus was also utilized to measure the permeability to address certain concerns such as the application of confining stress and the minimizing of the effects of the gaps between the mold and specimen (i.e. reduction of interface effects). As for the measurement of the head difference (Δh), a local pin-type sensor was used to measure it directly. In order to establish the validity of the local pin-type sensors, it was investigated in several aspects such as the (1) effect of the pin length in measurement, (2) effect of the confining pressure, (3) effect of the hydraulic gradient, and (4) effect of void ratio.

The local pin-type sensors were further implemented in the unsaturated case, wrapping the pins with membrane filters to measure suction. Inflow rate was measured by Mariotte's bottle and a weighing scale, while outflow rate was measured by burettes and differential pressure transducer. Tests were conducted for bauxite in different degrees of compaction (D_c), while tests were also performed for iron ore and Inagi sand for comparisons. The results were also compared to a well-known indirect method of obtaining coefficient of permeability (k) using Van-Genuchten Model (1980). In order to obtain that, SWRC tests were necessary.

The main purpose of this chapter is to develop new testing procedures in measuring k of a specimen under different saturation conditions using triaxial apparatus. The results of the tests in this chapter were incorporated in the numerical simulations in Chapter 5: Numerical Analysis: Seepage, and Chapter 6: Numerical Analysis: Dynamic Response.

4.1.1. Permeability

The soil permeability is a measure indicating the capacity of the soil to allow fluids to pass through it. It is often represented by the permeability coefficient (k) through the Darcy's equation:

$$v = ki = k\,(\Delta h/L) \qquad \text{(Eqn. 4-1)}$$

Where: v (cm/sec) is the apparent fluid velocity through the medium; i is the hydraulic gradient, Δh (cm) is the head difference between two points, L (cm) is the length or distance between the two points being measured, and k is the coefficient of permeability (hydraulic conductivity) often expressed in cm/sec

The parameter *k* is essential for analyses of flow in unsaturated soils for applications in the geotechnical and geo-environmental areas. However, caution is necessary since Equation 4-1 applies only to laminar flow of fluids. According to American Society for Testing Materials (ASTM) ASTM D 2434: Constant Head Test, direct proportionality of velocity of flow with hydraulic gradients must be observed, beyond which turbulent flow starts.

Permeability of soils is affected by several factors like particle size, impurities in water, void ratio, and degree of saturation. Hence, the physical properties of the sand being tested must be carefully taken into account due to the sensitivity of the factors affecting its value, as well as the low decimal range of permeability of soils (i.e. around 1×10^{-2} cm/s for clean sands to 1×10^{-5} cm/s for silty sands).

The permeability coefficient can be determined in the laboratory using falling head permeability test, or constant head permeability test. Constant head permeability test was implemented in all of the tests conducted.

4-2. Permeameter Tests using Rigid Mold

4.2.1. Standard Permeameter Apparatus

The constant head test was performed using Japanese Industrial Standards (JIS) A 1218: Test Methods for Permeability of Saturated Soils. The constant head permeability test is a common laboratory testing method used to determine the permeability of granular soils like sands and gravels containing little or no silt.

It involves flow of water through a column of cylindrical soil sample under the constant pressure difference. The test is carried out in the permeability cell, or permeameter, which can vary in size depending on the grain size of the tested material. The soil sample has a cylindrical form with its diameter being large enough in order to be representative of the tested soil. The testing apparatus is equipped with a constant head reservoir and an outlet reservoir which allows maintaining a constant head during the test. Before starting the flow measurements, however, the soil sample is saturated. During the test, the amount of water flowing through the soil column is measured for given time intervals.

Fig. 4–1 shows the Constant Head Apparatus used for testing the permeability. Specimen is prepared into the mold either by air pluviation (for Toyoura) or compaction (for bauxite and Inagi sand).

For Toyoura sand, the bottom porous stone, bottom wire mesh, and bottom filter were placed in the mold. After which, water is filled up to the brim of the mold. The outlet reservoir is also filled with water so that once the specimen is placed in the mold, the overflow can easily occur. The collar is also placed on top of the mold. The Toyoura sand was prepared by air pluviation, such that pre-determined weight (i.e. D_r = 78%) was placed in the mold. After all the sand fitted into the mold, the top filter and top porous stone was placed, before sealing completely the collar to the mold. Currently, the apparatus in the laboratory

has only one wire mesh. Hence, it was placed only at the bottom. The test was performed with three different heads: 3 cm, 6 cm, and 12 cm. These heads correspond to hydraulic gradients (*i*) of 0.25, 0.50, and 1.0, respectively.

For bauxite and Inagi sand, the specimen was prepared by compacting pre-determined mass (i.e. D_c=80% for bauxite, D_c=72% for Inagi sand) into the mold into five (5) layers. After which, it was placed in a special contained that was vacuumed over night at -100 kPa as shown in Fig. 4–2. This was done because bauxite and Inagi sand contained silts, which is quite difficult to saturate by implementing the same procedure as Toyoura sand. In the same manner, the test was performed with three different heads: 3 cm, 6 cm, and 12 cm, to obtain the permeability of the sand.

In all materials, and for each head implemented for water to flow, five (5) trials were conducted for three (3) time intervals: 30 sec time interval, 60 sec time interval, and 90 sec time interval. This was to observe and investigate if the permeability changed with respect to time interval and head applied. Fig. 4–3 shows some photos of the actual set-up of the experiment while Table 4-1 summarizes the test conditions implemented.

Table 4-1. Test Conditions of Permeability Tests using JIS A 1218 (Saturated)

Material	Relative Density/ Degree of Compaction	Total head (cm) [hydraulic gradient, *i*]	Time Intervals (sec)	Trials per total head per time interval
Bauxite	D_c = 80.2 %	3, 6, 12 [0.25, 0.50, 1.00]	30, 60, 90	5
Inagi	D_c = 72.1 %			
Toyoura	D_r = 75.1 %			

Knowing the height of the soil sample column *L*, the sample cross section *A*, and the constant head difference *Δh*, the volume of passing water *Q*, and the time interval *ΔT*, one can calculate the permeability of the sample as:

$$k = QL / (A*\Delta h*\Delta t) \quad \text{(Eqn. 4-2)}$$

4.2.2. Modified Permeameter Apparatus

The standard permeability test prescribed by JIS A 1218 was modified to investigate the effects of the interface where the water is expected to flow faster on the gaps between the mold and the specimen than in the specimen itself, causing some discrepancy in the measured values.

In Fig. 4-4 (a), a sketch of the cross section of mold is shown. The flow of water through the rigid mold and soil interface is different from soil to soil interface. For this reason, a modified permeameter test was implemented sketched in Fig. 4-4 (b). The figure presents cylindrical rings, placed on the rigid mold with different diameters while the height was made same as the standard permemeter test (i.e. 12 cm).

1. Test Implementation in Modified Permeameter Apparatus

After conducting the standard permeameter test, cylindrical ring *a* of Fig. 4-4 (b) was placed and the same procedure iterated in the standard permeater test was performed (i.e. five trials, three different heads, three different time intervals). Subsequently, cylindrical ring *b* was also placed in the rigid mold while keeping cylindrical ring *a*. And then permeamter test was again performed with the same iterations. Lastly, cylindrical ring *c* was placed and just the same, permeameter tests were performed. Actual set-up of cylindrical rings placed in the rigid mold with bauxite is shown in Fig. 4-5.

The reason why these tests were implemented was to evaluate the effect of increased side walls by the number of rings being placed and how the corresponding *k* of the specimen would change. In order to quantify this, the total surface area of the apparatus including the cylindrical rings in contact to the specimen was calculated in each step, as well as the total volume of the specimen. Table 4-2 shows the dimensions of the cylindrical rings used and other geometrical properties.

Table 4-2. Dimension of cylindrical rings and other geometrical properties

Set up	Diameter, φ (cm)	Thickness of ring, t (cm)	[A] Total surface area of the interface (cm^2)	[B] Volume of specimen (cm^3)	[A] / [B] (1/cm)
Standard	10	-	377.0	942.5	0.40
with cylinder *a*	*a* = 7.63	*a* = 0.2	944.7	914.1	1.03
with cylinder *a, b*	*b* = 5.08	*b* = 0.2	1320.2	895.3	1.47
with cylinder *a, b, c*	*c* = 2.50	*c* = 0.1	1504.9	890.7	1.69

The parameter [A]/[B] is a normalizing expression of a geometrical property of the cylindrical rings placed on the rigid mold. It is the total surface area of interface with respect to the volume of the specimen. It has a dimension of 1/L. The implication of this parameter is that the higher the number, the more “gaps” or the interface being wider such that water flowing through the interface is supposed to be faster.

2. Test Results in Modified Permeameter Apparatus

Fig. 4-6 plots the results of the specimen tested using the standard permeameter test and the modified permeameter tests. From this plot, it can be seen that the interface affected the *k* of the specimen being tested. The *y*-intercept of each function represents the inferred *k* of the specimen (i.e. soil-to-soil) if the soil-to-interface would not affect the results. In practical terms, the gaps may be deemed negligible but in principle, this test still supports the hypothesis that there is an effect due to the interface and soil interaction during *k* tests. For Toyoura sand at D_r=75.1%, k = 1.53 x 10^{-2} cm/sec, bauxite at D_c=80.2%, resulted to k = 3.91 x 10^{-3} cm/sec, while Inagi sand at D_c=72.1% was k = 4.77 x 10^{-4} cm/sec.

One of the things that can be observed from Fig.4-6 is the steeper slope *m* of bauxite in this plot. It seemed that bauxite (i.e. m = 0.172) was the one most sensitive to the interface effects as compared to Toyoura sand (i.e. m = 0.055) and Inagi sand (i.e. m = 0.089). In

order to understand why this is so, Fig. 4-7 was plotted showing the slope *m* of each material to the different particle size diameter, namely sizes passing 30% (D_{30}), 50% (D_{50}), 60% (D_{60}), and 90% (D_{90}) of a material by weight. While Toyoura sand and Inagi sand had a more narrow range of particle size diameter between 30% passing and 90% passing (i.e. 0.076 mm to 0.29 mm), bauxite comparatively ranged wider (i.e. 0.054 mm to 1.4 mm). This suggests that the particle sizes on the interface for bauxite could have wider variability in particle size, hence resulting to increased effects due to interface.

In view of this test, for the traditional test of permeability, a rigid mold is usually used to confine the specimen to be tested, while one of the drawbacks of using the rigid mold is the interface effect between the soil specimen and the mold, where permeability was shown to be different from that of the tested specimen.

4-3. Permeameter Tests using Flexible Wall (Saturated Case)

In addition to rigid wall permeameters, flexible wall permeameters are also used in geotechnical engineering laboratories for determining *k*. There are several advantages of using flexible wall permeameters. The confining pressure can be applied, hence side wall leakage can be prevented, which commonly occurs in rigid wall permeameters. Another advantage of a flexible wall is that the stress-state variables of a soil specimen can be controlled during the experiment, making it possible to relate the permeability of soils to their stress states (Agus et al., 2003).

Hence, aside from the previous permeability tests in rigid mold, tests were also performed in triaxial apparatus.

4.3.1. Test Apparatus

The apparatus used for the permeability test undertaken on saturated specimens is shown in Fig. 4-8. The main body of the apparatus is the same as the one used for undrained cyclic loading test as described in Chapter 3 Fig. 3-2, with some new additions for permeability test, namely:

1. The water supply part (I). It consists of two water tanks and a water cell. If the valve V1 is kept open, water in tank 1 will flow into the water cell and the overflowed water will be collected by tank 2. On the other hand, water in the water cell will flow through the system, as shown by the arrows.
2. The water used for the permeability test was first distilled from tap water, then filtered by a membrane filter (Supor 450), then de-aired before being injected into water tank 1 and finally filtered again by a coarse membrane filter (Versapor 1200, Pall Corp.) glued at the bottom of tank 1.
3. The water receiver part (III). It bears two main functions in this system, keeping a constant water head and measuring the volume change during consolidation of the specimen. It consists of two water containing pipes, P1 and P2. a) In P1, another smaller pipe B1 is installed. The water initially from the water cell in water supply part (I) is

collected by B1 first and stored in P1 by overflow from B1. In this way, the water head on the receiver side is also constant. b) The volume change of the saturated specimen during consolidation can be measured by a calibrated burette B2, which is installed in P2.

4. The total head applied to the system is measured by connecting a high capacity differential pressure transducer (HC DPT) to the water cell in the water supply part (I) at one side and to the inside of B1 at the other side. The tubes connected to the water cell and burette B1 are inserted into the containers to avoid disturbance from joints.
5. The accumulated volume of water flowed into P1 during seepage is measured by connecting another low capacity differential pressure transducer (LC DPT) to the bottom of P1 at one side and to a reference water level, for instance P2 at the other side. The volume change of the specimen during consolidation is also measured by the same LC DPT by turning the valve V2 to the side of calibrated burette B2.
6. The tubes with a diameter of 1.5 mm are used inside the apparatus (length 0.6 m in total approximately) and the tubes with diameter of 4.5 mm are used outside the apparatus with length of 1.5 m in total approximately.

To directly measure the real head passing through the specimen, the set-up in part (II) of the triaxial apparatus shows the specimen with local pin-type sensors. The local pin-type sensor is made of a hollow stainless steel with 0.15 cm outer diameter and 0.12 cm inner diameter initially. It is then modified by cutting it on the side and crafting its edges to have a pointed side for piercing. The long pins are 2.0 cm long pin while the short pins are 0.5 cm. Fig. 4-9 shows the local pin-type sensors. Both sets of pins are inserted 1 cm below the top cap, and another one is 1 cm above the bottom pedestal as shown in the figure in Fig.4-10 (a), and schematically in Fig 4-10 (b). The sensors are connected independently to their respective low capacity differential pressure transducers (LC DPT), which has a capacity ranging from 0-6 kPa.

As the water flows through the specimen, it was expected that the corresponding measurements could obtain directly the real head.

4.3.2. Test Methodology

The following section describes the detailed methodology in conducting a Permeability Test under saturated case using the Triaxial Apparatus with local pin-type sensors.

1. Preparation of Triaxial Apparatus
   a. Make sure to clean the parts of the triaxial apparatus. There should be no gel and no dust as these may interfere in the results of the tests.
   b. First, measure the dummy specimen height for reference. This is essential so that when an actual specimen is placed, the difference of the dummy specimen height and the actual specimen.
   c. Apply grease on O-ring. Apply grease as well on both the bottom pedestal and top cap to stick with the rubber membrane.

d. Before placing the rubber membrane cut it into 15 cm or longer (recommended) to provide for 10 cm soil specimen, plus 2.5 cm extra length on each ends to secure to the bottom pedestal and top cap, respectively.
e. Mark the location of top pin and bottom pin, each 1 cm away from the top cap and bottom pedestal, respectively.
f. Create a hole on the position where the pin is intended to be inserted so that when an actual specimen is placed, the pin can easily go through. Another reason for this is to alleviate the rubber membrane from unnecessary pressure due to puncture through the surface.

2. Preparation of Specimen

For bauxite and Inagi sand

a. Depending on desired degree of compaction, pre-weigh sample that will fit in the 10 cm height, and 5 cm diameter mold.
b. Introduce bauxite or Inagi sand by 1-dimension consolidation in the mold.
c. Place the porous stone and the filter paper on the bottom pedestal.
d. Transfer the prepared specimen from the mold on top of the porous stone and filter paper on the bottom pedestal.
e. Add filter paper at top cap as well.
f. Connect the load cell cable to the amplitudes to indicate voltage (which was correlated to indicate force). Calibrate the amplitude to have minimal contact force as possible so that when the top cap reaches contact to the specimen, the value would more or less be zero.
g. Gradually touch top cap to specimen. After which, secure the rubber membrane to the top cap.
h. Measure the diameter and height of the specimen. The values obtained are the initial condition of the test.

For Toyoura sand

a. Tighten O-ring and rubber bands to secure rubber membrane to the bottom pedestal and top cap.
b. Insert porous stone and filter paper into the rubber membrane.
c. Secure the mold and tighten screw.
d. Introduce 20 kPa back pressure.
e. Introduce Toyoura sand by Air Pluviation Method.
f. Balance top pedestal using counterweights such that it can freely move.
g. Proceed in preparation of specimen similar to bauxite and Inagi sand from items e to h.

3. Insertion of Pins

a. After properly placing the specimen on the triaxial apparatus, carefully insert the pins by using a quick-hardening glue to create the bond between the pin and the rubber membrane.
b. Wait for about 1 minute once the pin is inserted to allow the connection to take place. As much as possible, avoid disturbing the specimen.

4. Saturation of Specimen

For bauxite and Inagi sand

a. Instead of introducing CO_2, use Double Vacuuming Method (Ampadu and Tatsuoka, 1993) to saturate the specimen. This is more effective since bauxite and Inagi sand have silt contents, which may be difficult to saturate the voids in case of CO_2 flushed by water.
b. Vacuum specimen for at least 8 hours before saturating the specimen.
c. The saturation of the specimen takes about 2 hours at least.
d. After saturation, convert 20 kPa back pressure to 20 kPa cell pressure before proceeding to verify if the specimen has indeed saturated or not.

For Toyoura sand

a. Place the outer cell in the triaxial apparatus.
b. Convert 20 kPa back pressure to 20 kPa cell pressure. This is done by decreasing every 5 kPa from back pressure and increasing 5 kPa to cell pressure until a 20 kPa cell pressure is achieved (and zero back pressure).
c. After converting to positive pressure, introduce CO_2.
d. Wait for another 1 hour for CO_2 to fill the specimen voids. CO_2 is easily dissolved in water once it is introduced.
e. Introduce de-aired, distilled water to the system to saturate. Twice the volume of the specimen dissipated is suggested to be considered saturated condition. In this case, it is 400ml of water.

5. Saturation Check (B-Value)

a. Connect the (+) side of HCDPT to cell pressure. On the other hand, connect the (-) side of HCDPT to the back pressure (i.e. pressure of specimen. The pressure of the specimen must be connected to the reference tube so that excess pore water pressure can migrate through and from.
b. Make sure to saturate all tubes connected to the specimen.
c. Using the pressure regulator, simultaneously increase the cell pressure to 220 kPa, while the back pressure will also be increased to 200 kPa. The effective confining pressure is maintained at 20 kPa. Make sure to maintain isotropic condition by counter-balance.
d. Measure the corresponding voltage values:

$$B = \frac{\Delta u_w}{\Delta \sigma_o} \qquad \text{(Eqn. 4-3)}$$

where B = B-value; Δu_w = excess pore water pressure; and $\Delta\sigma_O$ = increment of total principal stress

$B = \Delta u/\Delta\sigma_o = [(V_2 - V_1)/ (V_2 - V_o)] \geq 0.95$

- V_o = record the voltage value corresponding the 220 kPa
- V_1 = increase to 230 kPa (do not allow water to flow to reference tube so that pressure could be measured if there is air). Record the voltage equivalent to 230 kPa

- V_2 = allow once again for water to flow to reference tube. Record again the voltage equivalent of 230 kPa

e. Consolidate again for 1 hour for bauxite and Inagi sand, and 30 mins for Toyoura sand,.
f. Measure again the height of the specimen before conducting the permeability test. This is the height of the specimen after consolidation.
g. Measure as well the volume change from the reference tube. This accounts for the volume change.

6. Permeability Test
   a. Make sure to collect data by pressing the "Start Saving" button before allowing water to flow through the specimen
   b. Tests are incremented in seven (7) different total heads namely: 5 cm, 10 cm, 15 cm, 20 cm, 35 cm, 50 cm, and 65 cm. For each step, a total of 14.5 ml is collected before proceeding to the next.
   c. Aside from the increments, confining pressures are also adjusted, initially at 30 kPa, and then 60 kPa, and then 100 kPa for isotropic loading, and then 60 kPa, 30 kPa, 25 kPa, 20 kPa, 15 kPa, 10 kPa, and 5 kPa for isotropic unloading.

4.3.3. Tests Conducted

This section presents the tests conducted to determine the saturated permeability of bauxite, Inagi sand, and Toyoura sand.

1. Bauxite

Table 4-3 summarizes the test conditions for bauxite.

Table 4-3. Test Conditions of Permeability Tests using Triaxial Apparatus (bauxite-saturated)

Test No.	D_c (%)	B-value	Total Head supplied, H_{tot} (cm)	σ_c (kPa)	Test Conditions
1	77.8	0.971	5, 10, 15, 20, 35, 50, 65	Loading: 30, 60, 100 Unloading: 60, 30, 25, 20, 15, 10, 5	Permeability test using local pin-type sensor (long and short)
2	78.0	0.959			*k* test using local pin-type sensor (long only) with Image analysis performed
3	78.0	0.974			(1) same as test 2 (2) rubber membrane stretched
4	79.1	0.980			(1) same as test 2 (2) rubber membrane was loose

Four tests were performed for bauxite. The target D_C was a medium dense case at 80%. In addition to permeability tests, image analysis technique was also utilized for Tests 2 to 4 to capture the development of creases on the rubber membrane in every consolidation step increase or decrease.

Test 2 was a normally stretched rubber membrane when specimen was prepared in the triaxial apparatus. Test 3 consists of stretching the rubber membrane when the specimen was being secured on the top cap. In contrast to test 3, test 4 had a loose rubber membrane. From the image analysis, the effect of the confining pressure can be better understood.

2. Inagi Sand

Table 4-4 summarizes the test conditions for Inagi sand.

Table 4-4. Test Conditions of Permeability Tests using Triaxial Apparatus (Inagi-saturated)

Test No.	D_c (%)	B-value	Total Head supplied, H_{tot} (cm)	σ_c (kPa)	Test Conditions
1	72.5	0.969	5, 20, 35, 50, 65	Unloading: 100, 60, 30, 15	Local pin-type sensor (long only)
2	72.6	0.968			
3	69.2	0.946	5, 10, 15, 20, 35, 50, 65	Loading: 30, 60, 100 Unloading: 60, 30, 25, 20, 15, 10, 5	Local pin-type sensor (long and short)
4	70.6	0.986			

The target degree of compaction for Inagi sand was D_c = 72%. This case can be classified as loose case. While the bauxite case is medium dense with D_c = 80%, the tests performed for Inagi sand were loose since the liquefaction tests performed for Inagi sand were also under this condition. While currently the two type of materials may not be directly compared, the loose case of Inagi sand will be compared to the loose case of bauxite under unsaturated permeability tests in Section 4-4 of this chapter.

From Table 4-4, tests 1 and 2 can be seen to have fewer iterations of the experiment and were only conducted using the long pin-type sensors compared to tests 3 and 4. One noticeable adjustment was the loading condition from tests 1 and 2 as compared to tests 3 and 4. Tests 1 and 2 were immediately performed by isotropic unloading, while tests 3 and 4 started with isotropic loading before the isotropic unloading.

While only four (4) tests are presented here, six (6) other tests were performed for Inagi sand in the thesis entitled “Liquefaction Tests using Modified Triaxial Apparatus on Sands under Different Saturation Conditions and Their Permeability Evaluation using Local Measurement” by Tan Tian (2016). Other method was presented there such as the

Calibration Method which can obtain the global permeability of the specimen as compared to this local measurement. Preliminary tests were also performed in the previous work using the local pin-type sensors, which led to the current testing method using local pin-type sensors.

3. Toyoura Sand

Table 4-5 summarizes the test conditions for Toyoura sand.

Table 4-5. Test Conditions of Permeability Tests using Triaxial Apparatus (Toyoura-saturated)

Test No.	D_r (%)	B-value	Total Head supplied, H_{tot} (cm)	σ_c (kPa)	Test Conditions
1	78.9	0.971	5, 20, 35, 50, 65	100	Local pin-type sensor (long only)
2	79.3	0.971			
3	74.4	0.953			
4	69.6	0.950	5, 10, 15, 20, 35, 50, 65	Loading: 30, 60, 100 Unloading: 60, 30, 25, 20, 15, 10, 5	Local pin-type sensor (long and short)
5	78.6	0.946			
6	65.2	0.954			

The target relative density for Toyoura sand was D_r = 75%. The reason this was selected is because existing data from other researchers can be compared at dry density of 1.50 to 1.55 g/cm^3 (i.e. ρ_{dry} = 1.50 to 1.55 g/cm^3) (Unno et al, 1990). For Toyoura sand batch J, a relative density of 75% would correspond to 1.55 g/cm^3.

From Table 4-5, tests 1 to 3 can be seen to have been conducted only at 100 kPa confining pressure while using the long pin-type sensors only. Tests 3 to 6 on the other hand, were performed at isotropic loading and isotropic unloading cases, as well as long and short local pin-type sensors.

Similar to Inagi sand, previous tests were also performed for Toyoura sand. Five (5) other tests were performed, discussed on the "Liquefaction Tests using Modified Triaxial Apparatus on Sands under Different Saturation Conditions and Their Permeability Evaluation using Local Measurement" by Tan Tian (2016).

4.3.4. Tests Analysis (Establishing local pin-type sensors)

The tests are evaluated on four different aspects, namely the (1) effect of pin length, (2) effect of confining pressure (σ_C), (3) effect of hydraulic gradient (i), and (4) effect of void ratio, e, to establish the validity or applicability of the local pin-type sensors.

A. Effect of Pin Length

The two sets of pins were fabricated in such a way that the long pin would measure the heads around the centerline of the cross section of the specimen. This was intended to compare to the short pin, which was only 0.5 cm and closer to the sealing junction at the membrane filter. It was hypothesized that the membrane penetration and the effect of low confining pressure that would cause wrinkle on the rubber membrane, would affect the flow of water, hence resulting to higher flow rate than the long pin. One of the drawbacks of long pin on the other hand is that it disturbs the specimen more when it is being inserted into the specimen. This section describes the results of the tests conducted for each type of material.

1. Bauxite

For bauxite, only test 1 had two sets of pins inserted. Tests 2 and 4 did not permit the insertion of two sets of pins because of image analysis being performed as well (i.e. half of the specimen was exposed to the camera while the pins were inserted on the reverse side.

Fig. 4-11 shows the *k* values obtained from the different total head supplied to the specimen, as well as different confining pressure for the long pin and short pin. From this plot, it can be seen that the *k* values during isotropic loading (i.e. from 30 kPa to 100 kPa) decreased, and then became relatively stable during isotropic unloading from 100 kPa to 30 kPa, before the *k* values increased once again from 30 kPa to 5 kPa. At lower confining pressures, membrane wrinkles begin to develop which affect the results of the *k* values (see Fig. 4-12). The effect of the confining pressure shall be discussed in the next section. Another observation that can be made is that the results generally biased on the short pin, especially during isotropic unloading from 30 kPa to 5 kPa, and total head supplied of 5 cm for all confining pressures. There are several exceptions such as the total head supplied of 5 cm at 5 kPa (indicated by dark green, square figure) which biased on the long pin, indicating higher *k* values. The reason for this cannot be explained at this point but shall be expounded on the Effect of Hydraulic Gradient (*i*).

As for the effect of pin length on bauxite, it can be said that the *k* values biased on the short pin, especially during isotropic unloading from 30 kPa to 5 kPa, as well as total head supplied at 5 cm.

2. Inagi sand

Fig. 4-13 shows the *k* values plot for long pin and short pin for test 3 of Inagi sand. Similar trend with bauxite can be observed. The *k* values during isotropic loading from 30 kPa to 100 kPa decreased, and then the *k* values became relatively stable during isotropic loading from 100 kPa to 20 kPa this time. At confining pressures lower than 20 kPa, the results can be seen to be scattered. The points obtained at total head supplied of 5 cm were erratic in terms of results, primarily affected by the hydraulic gradient (i.e. effect of hydraulic gradient) which shall be explained in the following sections. Similar to bauxite, the points biased on the short pin having higher *k* values, especially at confining pressures lower than

20 kPa. One thing worth pointing out is the behavior of short pin at isotropic unloading confining pressures of 10 kPa and 20 kPa. While the *k* values for the long pin were consistent, the corresponding *k* values for the short pin were varied with a wide range (i.e. 2 x 10^{-3} cm/sec to 2 x 10^{-2} cm/sec), hence the vertical line. This shows that the membrane wrinkle affecting the short pin more significantly than the long pin and suggests that long pin may be better to be used, despite its own drawback. Fig. 4-14 shows the snapshots of the specimen tested at 20 kPa and 10 kPa, while this condition shall be explained further in the Effect of Confining Pressure (σ_C).

3. Toyoura sand

Fig. 4-15 plots the *k* values plot for long pin and short pin for test 5 of Toyoura sand. Compared to bauxite and Inagi sand, the values for long pins and short pins are practically equal, except for those tested at total head supplied of 5 cm. One of the explanation for this is the development of membrane wrinkle at 5 kPa confining pressure, shown in Fig. 4-16. The confining pressures also had minimal effect on the *k* values obtained for Toyoura sand, although it can still be said that the confining pressures had effect on the specimen (i.e. values ranging from from 1 x 10^{-2} cm/sec to 3 x 10^{-2} cm/sec).

Since Toyoura sand is clean sand with little to no fines, volumetric strain during consolidation is minimal compared to bauxite and Inagi sand, where both materials have fines. The presence of fines causing larger volumetric strains affect the isotropic loading and isotropic unloading of the specimen, incurring more membrane wrinkles.

B. Effect of Confining Pressure (σ_C) and Image Analysis

The behavior of the specimen during permeability test can further be explained in this section, where a more detailed plots shall be shown due to the effect of confining pressure, accompanied by image analysis for bauxite.

1. Bauxite

Fig. 4-17 shows the set up employed for tests 2 to 4 conducting both permeability test and image analysis. The front view shows the dots where snapshots are taken by the camera at a certain time interval while at the back, the local pin-type sensors were inserted.

Fig. 4-18 to Fig. 4-20 show the plots of the *k* vs the confining pressure at different hydraulic gradients *i* for tests 2 to 4, respectively. The *i* values were calculated from the head measured between the two points divided by 8 cm (i.e. distance between the two local pin-type sensors).

The figures have three general behaviors: the isotropic loading, the isotropic unloading, and the overestimating of isotropic unloading.

For the isotropic loading part, it was consistent for all tests that the *k* values changed with the confining pressure applied to it. This change shall be better explained by the Effect of Void Ratio (*e*) later. Upon the application of isotropic loading, the specimen also contracts as water is being dissipated from the specimen to the burette, hence decreasing the void ratio of the specimen (i.e. increase in density).

In the isotropic unloading region, the specimen practically resulted to the same *k* values from 100 kPa to 30 kPa before the *k* values started to change by increasing again. At lower than 30 kPa to 10 kPa, it is still assessed to have natural isotropic unloading but at lower than 10 kPa it is assessed to overestimation of the isotropic unloading.

The behavior of tests 2, 3, and 4 were different during the overestimating region. This can be attributed to the initial tension applied to the rubber membrane during preparation. The initial tension for test 3 was that it was stretched, and it showed that the overestimating region was less affected at low confining pressure. Test 4 on the other hand, had initial tension applied to be loose at the rubber membrane, resulting to more dramatic overestimating. Test 2 was prepared without stretching nor intentionally making the rubber membrane loose, hence the behavior of overestimating region somewhere between test 3 and test 4.

Another common trend that can be observed from all three tests is the behavior at the lowest *i* values applied (i.e. black line), the *k* values were also different from the rest. This will be dealt with at the Effect of Hydraulic Gradient (*i*).

To explain the behavior of the specimen especially at overestimating of isotropic unloading, image analysis technique was employed for tests 2, 3, and 4.

Image Analysis Technique

The image analysis employed in this study is based on the technique of Particle Image Velocimetry (PIV). It allows the displacements of an object to be measured through series of digital images taken during moving. The photos were taken at time interval of 30 minutes, since the objective of the test was to observe the development of membrane wrinkles, which does not require small time interval.

The photos were first converted to a gray level of a black-and-white photograph. The gray level is an important parameter used to track the movement of target points. Pixel is viewed as a unit which can be used to measure the distance (pixels) between two points. The images are loaded into the software Move-Tr2D. Prior to analyzing the digital images, the origin and scale from pixel to real distance between two dots placed on the membrane are set in the initial image without deformation. A reference is then set, where all calculations shall be referred to (see Fig. 4-21). All the pixel information will be converted into coordinate by distance. The origin is fixed by the pixels of digital image and is not related to the specimen in the image. Thus, the origin is fixed without considering the deformed specimen during test.

The dots on the rubber membrane were pasted by 5 mm on vertical and horizontal directions. The digital image before test was performed is shown in Fig. 4-22 in which the target dots have been numbered. All the marked dots were selected manually before analyzing.

The target dots are tracked by the gray pattern of dot (Zhao, 2017). The pattern of dot is recorded and compared with the dot in the succeeding images. The tracking squares shown in Fig. 4-23 are indicated. These two squares are set in advance before testing. The pattern of gray inside of the red square is recorded and then same pattern is searched inside the yellow square in the next image. Thus, the suitable tracking squares of images are of importance to obtain image analysis.

The results of the image analysis were processed using MATLAB R2015b version, with the program for the analysis of the images coded by Tsutsumi (2007) of the Institute of Industrial Science, The University of Tokyo.

Implementation of the Image Analysis Technique

For each confining pressure applied, the image was taken and the image was processed (a) relative to the initial condition and (b) relative to previous confining pressure. Fig. 4-24 shows the snapshot for test 2, however the contour maps are also applicable for test 3 and test 4 since the initial condition had σ_c = 30 kPa. The initial condition is the reference point so it has no strain and the succeeding σ_c which the specimen was subjected to was based on this.

Fig. 4-25 to Fig. 4-27 are images from isotropic loading at σ_c = 100 kPa for test 2, test 3, and test 4, respectively. The negative sign (–) in the legend indicates tension, while the positive sign (+) indicates compression. The numbers indicated in the legend are vertical strains in percent. Basing it on the contour map with respect to the initial confining pressure (i.e. σ_c = 30 kPa), the specimen generally underwent compression indicated by yellow contour colors. Test 4 which has loose rubber membrane as the initial tension, specifically had higher magnitudes of strains as shown in darker yellow contour colors. The images showing relative to previous σ_c suggest that the strains were not as large as the one based from the initial condition, which is logically consistent since the confining pressure was also applied at 60 kPa.

From σ_c = 100 kPa to σ_c = 30 kPa through isotropic unloading, Fig. 4-28 to Fig 4-30 show the changes in the strains of the rubber membrane. Relative to the initial σ_c, the images have already formed regions where compression and tension were more emphasized. For example in test 4, the lower half of the specimen shows that the specimen did not rebound or recover to its initial confining pressure condition but the specimen had already consolidated. On the other hand, the images showing relative to the previous confining pressure show regions where it has stretched or compressed since these images were based on the previous loading condition which is 60 kPa. Compared also the strain magnitudes of

isotropic loading shown in Fig. 4-25 to Fig. 4-27 at the images relative to the previous confining pressure, the results at isotropic unloading in Fig. 4-28 to Fig. 4-30 seem to have lower strain magnitudes. This result supports the isotropic unloading region shown in the plots in Fig. 4-18 to Fig. 4-20 when the specimen undergoing isotropic unloading from σ_c = 60 kPa to σ_c = 30 kPa practically had the same *k* values, as compared to the one during isotropic loading from σ_c = 30 kPa to σ_c = 60 kPa, where the *k* values were significantly affected by the change in void ratio.

Proceeding to σ_c = 10 kPa, Fig. 4-31 to Fig. 4-33 show the images at overestimation on isotropic unloading of the specimen. While for test 2 and test 3, the membrane wrinkles have not been evident yet, test 4, which has loose as the initial tension applied to the rubber membrane, already started developing on the lower right hand side of the specimen. The rubber membrane began to show creases on different spots as evident through the images on both the relative to the initial σ_c and the one relative to the previous σ_c.

Finally at σ_c = 5 kPa, Fig. 4-34 to Fig 4-36 show evidence of wrinkles formed for all tests on the rubber membrane. Test 4 being the extreme case where initially the rubber membrane was loose shows regions of compression and tension interchanging across the profile. On the other hand, test 3, which is the test with initial tension stretched on the rubber membrane, shows regions of concentrated red contour map color, indicating tensile strains. Test 2, which was just a typically prepared specimen with no initial tension applied to the rubber membrane, shows regions of tensile strains.

From the images obtained using the image analysis technique, the wrinkles formed could be mapped out by contour maps with color symbols.

2. Inagi Sand

As for Inagi sand, no image analysis was performed but the *k* values were also plotted against the confining pressure at different hydraulic gradients. Fig. 4-37 presents the plot of Inagi sand test 3. Similar to bauxite, the *k* values decreased significantly during the isotropic loading. During the isotropic unloading from 100 kPa to 20 kPa, the *k* values were practically the same, before the overestimation of *k* values at confining pressure less than 20 kPa.

While no image analysis had been performed, Fig. 4-38 shows the snapshots of the progression of the membrane wrinkle. Similar trend of development of membrane wrinkle was observed in Inagi sand test 4.

3. Toyoura sand

In contrast to the results of bauxite and Inagi sand, Toyoura sand was not significantly affected by the change in confining pressure. Fig. 4-39 shows the plot for different hydraulic gradient and for both isotropic loading and isotropic unloading, the *k* values for Toyoura sand test 5 was practically the same. At lower than 30 kPa during isotropic unloading, the *k*

values seemed to be affected a bit by the confining pressure but were assessed to be the effect of natural isotropic unloading only.

C. Effect of Hydraulic Gradient (*i*)

At low hydraulic gradient (*i*), the *k* values seem to be inconsistent with the *k* values obtained at higher *i* values. This observation has been similar for the three types of materials being tested.

One of the conditions of laminar flow is the direct proportionality of velocity flow with hydraulic gradients below certain values. In ASTM standards, it states that "Direct proportionality of velocity of flow with hydraulic gradients below certain values, at which turbulent flow starts" (ASTM D 2434 Section 3.1.4). This indicates that the relationship is proportional if the flow is laminar. Hence, it is essential to verify the relationship between the velocity flow with respect to the hydraulic gradient.

The other thing that needs to be checked is the Reynolds Number. The Reynolds number (Re) is an important dimensionless quantity in fluid mechanics used to help predict flow patterns in different fluid flow situations (Hughes, 1997). The ratio between the inertial forces and the viscous forces driving the flow is computed by the Reynolds number, which is used as a criterion to distinguish between the laminar flow, the turbulent flow and the transition zone. Mathematically, it is generally expressed as:

$$\mathrm{Re} = {}^{sL}/_{\nu} \qquad \text{(Eqn. 4-4)}$$

Where:
s = maximum speed of the object, relative to the fluid (unit: length per unit of time)
L = characteristic linear dimension (travelled length of the fluid; unit: length)
v = kinematic viscosity (dynamic viscosity/density) = (μ/ρ) (unit: length^2 per unit of time)

For porous media, the Reynolds number is defined as:

$$\mathrm{Re} = {}^{QD_{50}}/_{A\nu} \qquad \text{(Eqn. 4-5)}$$

Where:
Q = fluid discharge (unit: length^3 per unit of time)
D_{50} = mean grain diameter or the mean pore dimension (unit: length)
A = cross sectional area of specimen (unit: length^2)
v = kinematic viscosity (dynamic viscosity/density) = (μ/ρ) (unit: length^2 per unit of time)

For water, *v* at 25°C is 0.8926 mm^2/sec. This value was adopted in all calculations.

Figure 4-40 shows the validity of Darcy's Law for porous media. Not only does Re have a threshold before it transitions and becomes turbulent, but also at low hydraulic gradient *i*, fluids can behave in a non-linear flow. It is the case of materials of low permeability. Under a

certain threshold of the gradient, there is no flow due to the action of the adsorption forces, which make the fluid quite rigid.

For porous media, Re ≤ 1 is generally acceptable as laminar flow (Bear, 1972; Khalifa et al., 2002). The lower limit where Re is assessed to be non-linear flow is not established, since many factors are cited for the behavior of non-linear flow at low hydraulic gradients such as (1) non-Newtonian water flow properties, (2) particle migrations that cause blocking and unblocking of flow passages, and (3) local consolidation that is inevitable when hydraulic gradients are applied across a compressible soil (Mitchell J.K. and Soga, K., 2005). Experiments show that it is unlikely that unusual water properties are responsible for the non-linear flow behavior but the other two factors can cause deviations from Darcy's Law, especially in clays.

As for this work, the *k* values at low hydraulic gradient *i* exhibited different behavior (see Fig. 4-11, Fig. 4-13, and Fig. 4-15) when a total head supplied of 10 cm or less was applied to the specimen. Although the total head supplied was 10 cm, the corresponding real head measured for bauxite, Inagi sand, and Toyoura sand were in the average rounded values of 2.0 cm, 4.0 cm, and 0.4 cm, respectively. This is due to several factors such as natural head loss before the water seeps through the specimen or filter clogging effect (Wang, 2014). Since the distance of the two local-pin type sensors inserted to the specimen is 8 cm, the corresponding *i* of bauxite, Inagi sand, and Toyoura sand are 0.25, 0.50, and 0.05, respectively. Hence, the Reynold Numbers at this range is of interest.

1. Bauxite

Fig. 4-41 shows the flow rate (*Q*) vs hydraulic gradient (*i*) plot of bauxite, test 4. From this plot, it can be observed that the flow rate is indicative of the *k* values since at isotropic loading condition, the flow rate decreased from σ_c = 30 kPa to σ_c = 100 kPa. During isotropic unloading however, the flow rates were comparably the same with respect to each other until it reached σ_c = 10 kPa. The *Q* vs *i* plot did not exhibit linear relationship at $\sigma_c \leq$ 10 kPa, as well as the evidence of development of membrane wrinkles from image analysis (Fig. 4-35 and Fig 4-36), hence they were assessed as non-reliable test data.

Fig. 4-42 presents the plot of *k* values vs. *i* values. In this plot, $\sigma_c \leq$ 10 KPa were not included and also the isotropic loading points (i.e. 30 kPa and 60 kPa). The behavior of *Q* vs. *i* plot for isotropic loading will be explained more in the Effect of Void Ratio (*e*). In this figure, it can be noticed that at low hydraulic gradients, the *k* values were not consistent with the other obtained plots at *i* > 0.25. There was an underestimate and overestimate region before funneling into a stable value range of 3 x 10^{-3} to 4 x 10^{-3} cm/sec. By plotting the Reynolds number and hydraulic gradient (see Fig. 4-43), the trend of the plot can be seen to be hyperbolic initially, before it started to become gradually linear at *i* > 0.25. Researchers do not indicate a lower limit threshold for non-linearity of laminar flow but this plot is indicative of the non-linearity since Reynolds Number is not dependent on the measured head of the specimen. Although this does not fully explain the behavior at low hydraulic gradients, this could be one of the explanations for such behavior for underestimate values. As for the

overestimate values, this can be attributed to the inevitable fluctuation of transducers during measurement and at low hydraulic gradient, the mathematical effect is quite significant, hence resulting to some overestimate values.

2. Inagi Sand

Fig. 4-44 shows the *Q* vs *i* plot of Inagi sand at test 3. Similar trend to bauxite, the isotropic loading exhibited decrease in flow rate as σ_c increased. At isotropic unloading, only σ_c = 5 kPa exhibited non-linear relationship but the data at $\sigma_c \leq$ 20 kPa were not accepted because membrane wrinkles started to manifest from this confining pressure (see Fig. 4-38).

Fig. 4-45 shows the *k* values plotted against *i* values without the isotropic loading data points and those $\sigma_c \leq$ 20 kPa. For Inagi sand, only underestimate values were observed. Fig. 4-46 presents the relationship of the Reynolds Number to the hydraulic gradient. At i > 0.5, the relationship between Re and *i* began to exhibit linear relationship although they are not directly related to one another.

3. Toyoura Sand

Fig. 4-47 shows the relationship of *Q* vs *i*. The flow rate seemed to be consistent at any confining pressure applied to it. Only the σ_c = 5 kPa showed non-linear relationship in this plot, and marks of membrane wrinkle can be seen in Fig. 4-16 at σ_c = 5 kPa.

Fig. 4-48 presents the *k* values plotted against *i* values. In this plot, there were also points of overestimate and underestimate *k* values. The *k* values seemed to start to become stable at *i* > 0.05. The Reynolds Number plotted against *i* in Fig. 4-49 also shows the same trend that linear relationship started at *i* > 0.05.

D. Effect of Void Ratio (*e*)

The permeability is affected by a lot of factors and one of which is void ratio. For a given soil, the greater the void ratio, the higher the value of the coefficient of permeability (Anand et al., 2004). Lambe and Whitman (1969) suggests that the effect of one of the characteristics is hard to isolate since these characteristics are closely interrelated (e.g. fabric usually depends on particle size, void ratio, and composition).

One of the early pioneers to give an empirical relationship with particle size was Allen Hazen, where he described *k* of a soil is directly proportional to the square of the particle size at 10% passing (Hazen, 1911). It is known as the Hazen's formula and is useful to estimate the permeability of in situ soil although his proposal was directly applicable only to loose, clean sands with a coefficient of uniformity (D_{60}/D_{10}) less than 2 (Terzaghi and Peck, 1964).

While the Hazen's formula considers only D_{10} of the particle size distribution, Kozeny-Carman (1956) developed a semi-empirical, semi-theoretical formula for predicting the permeability of porous media. Kozeny-Carman Formula is written as:

$$\mathrm{k} = \frac{\gamma}{\mu}\left(\frac{1}{k_o S_o^2}\right)\frac{e^3}{1+e} \qquad \text{(Eqn. 4-6)}$$

Where:
γ = unit weight of permeant (unit: mass/(length^2*time^2))
μ = viscosity of permeant (unit: mass/ (length*time))
k_o = Kozeny-Carman empirical coefficient
S_o = specific surface area per unit volume of particles (unit: 1/length)
e = void ratio

Kozeny-Carman Formula takes into account the particle size and void ratio, together with fluid properties such as the unit weight and the viscosity (Carrier, 2003).

In the tests conducted, the experimental results obtained were compared against the Kozeny-Carman Formula.

1. Bauxite

The *k* values were plotted against *e* values in Fig. 4-50. The plot shows the trend of *k* estimation by Kozeny-Carman Method indicated in violet line. The plot also shows the *k* test results from the standard permeameter test performed where the average *k* values of each of *i* =0.25, *i* =0.50, and *i* =1.00 indicated in dashed circle. Observing the line in isotropic loading, the corresponding *e* value at initial σ_C has the highest value, which means the least "compacted" (i.e. lower degree of compaction (D_C)). The fluid will flow naturally faster since it has more voids. By the increment of σ_C to 60 kPa, *e* changed, hence also affecting the *k* values. Finally at σ_C = 100 kPa, the *k* values were practically the same even during isotropic unloading, and even with the natural isotropic unloading effect (i.e. increase of void ratio), the *k* values also slightly increased. It must be noted however, that the confining pressure less than 10 kPa (i.e. $\sigma_C \leq 10$ kPa) data were omitted because of the previous discussions on the development of membrane wrinkle.

In other words, the isotropic loading *k* values behavior can be explained by the effect of the void ratio change, and the standard permeameter tests coincide with the plot of the triaxial permeameter test, indicating that the discrepancy of *k* values was due to void ratio.

2. Inagi Sand

Similar to bauxite, Fig. 4-51 presents the *k* values were plotted against *e* values for Inagi sand. The *k* estimation by Kozeny-Carman was plotted likewise, and the standard permeameter test results were plotted. For the triaxial permeameter test (i.e. local pin-type sensor to measure head), it can be noticed that the data for *i* = 0.25 was omitted because the *k* values lower than 0.50 were assessed to be unreliable from the previous section, Effect of Hydraulic Gradient (*i*). The resuls of the standard permeameter test was a bit underestimate to the results of the triaxial permeameter test but it nonetheless followed the observation in

bauxite that the change in *e* affects the *k* significantly. One of the thing that can be said though is that the estimate of Kozany-Carman is not exactly similar since the semi-empirical method had several assumptions such as the spherical shape of particles and the perfect isotropy among others (Carrier, 2003).

3. Toyoura Sand

As for Toyoura sand, the *k* values were practically the same, thus one test would have more or less the same *e* values. By looking at Fig. 4-52, it can be seen that tests 5 and 6 were lumped on two different void ratio regions. Test 5, which was tested denser (i.e. lower *e* values) had lower *k* values while test 6, which was tested at looser case (i.e. higher *e* values) resulted to higher *k* values. The result of the standard permeameter test also at $i = 0.25$ is explicitly indicated by a label and it falls between tests 5 and 6. This result follows the assumption of the effect of *e*. Finally, it can be said that the Kozeny-Carman estimate was higher than the ones obtained from the experimental results, nonetheless, the order of *k* values were the same and the slope is comparable.

By establishing the limitations and behavior of the local pin-type sensor with respect to different aspects, the discussion on unsaturated case can now be explored.

In summary, the limitations of local pin-type sensor where the values cannot be accepted include:

- Confining Pressure (σ_c): bauxite ($\sigma_c \leq 10$ kPa), Inagi sand ($\sigma_c \leq 20$ kPa), and Toyoura sand ($\sigma_c \leq 5$ kPa)
- Hydraulic Gradient (*i*): bauxite ($i \leq 0.25$), Inagi sand ($i \leq 0.50$), and Toyoura sand ($i \leq 0.05$)

4-4. Permeameter Tests using Flexible Wall (Unsaturated Case)

Reliable measurements and predictions of soil water retention and unsaturated hydraulic conductivity functions are essential for solving unsaturated flow problems. When dealing with the permeability of unsaturated soils however, the primary consideration would be the distinction between flow of the gas phase (pore air) and flow of the liquid phase (pore water). To measure solely the permeability of pore water, filters preventing air drainage have to be installed. Klute (1972), Dirksen (1991) and Masrouri et al. (2008) summarized permeability testing techniques for unsaturated soils.

In general, there are two ways to determine *k* of an unsaturated soil: direct and indirect techniques (Huang et al., 1998). For direct techniques, it can be further classified according to the flow mode as steady or unsteady state. In the steady state methods (also known as constant head method or constant flow method), a constant flow rate, *Q* or hydraulic gradient, *i* is applied under specific average water pressure head. Masrouri et al. (2008) concluded that constant head steady state flow would be the most accurate way to reveal the permeability of unsaturated soils because of its simplicity and the possibility of controlling the stress state of the soil, though it is relatively expensive. Steady state is supposed to occur when flow rate of the soil specimen is equal upstream and downstream

and if a constant *i* is observed through the tested soil specimen (Masrouri et al., 2008). All methods assume the validity of Darcy's Law, as it also applies for the flow of water through unsaturated soils (Childs et al., 1950; Fredlund et al., 1993). In steady state condition, Darcy's Law (expounded from Equation 4-1) for laminar flow can be expressed as:

$$k = {}^{v}/_{i} = {}^{Q}/_{Ai} = {}^{Q}/_{A(\frac{\Delta h}{L})} \qquad \text{(Eqn. 4-7)}$$

Where:
k = coefficient of permeability (unit: length/time)
Q = flow rate (unit: length^3/time)
A = cross sectional area of the specimen (unit: length^2)
Δh = head difference or head loss between two points in the specimen (unit: length)
L = length of the specimen between the points (unit: length)

While *A* and *L* are geometrical properties of the specimen, *Q* and *Δh* are parameters induced by the fluid flow. Achieving steady state in testing on unsaturated soils is reported to be time consuming because equilibrium attainment may require several hours or days at each saturation level (Goh et al., 2015). Typically, a saturated high air entry ceramic disk is placed sandwiching the specimen, and this porous, ceramic disk allows the passage of water, but prevents the flow of free air (Fredlund et al., 1993). Continuity between the water in the soil and the water in the ceramic disk is necessary in order to correctly establish the matric suction.

Instead of ceramic disk, microporous membrane technology (referred as membrane filter in this paper) has been found out to have slightly higher hydraulic conductivity and can achieve much faster equilibrium time required than ceramic disk, hence, result in improved performance for the measurement or control of matric suctions at low range (~25 kPa) to avoid air diffusion (Nishimura et al., 2012; Wang et al., 2018).

As for the head difference measurement, it is common to use tensiometers to measure the suction. Tensiometer is a measuring instrument used to determine the matric water potential (Richards and Gardner, 1938). In terms of unsaturated soil testing, tensiometers have been used on rigid mold permeameter in measuring capillary conductivity under steady state condition (Nielsen et al., 1961) or measuring hydraulic conductivity by the suction profiles obtained from the tensiometers under unsteady state condition (Daniel, 1983).

In addition to rigid wall, flexible walls have been used in measuring the unsaturated coefficient of permeability (k_{unsat}) (Goh 2015, Moncada 2010, Agus 2003, Huang and Fredlund, 1998). By establishing the reliability of the local pin-type sensors with the tests conducted under saturated case, a newly developed local pin-type sensor was extended in application for unsaturated case. The pins act like a tensiometer, which can be used on flexible wall.

In view of the above, a new system to measure permeability of unsaturated soils by measuring and expediting *Q*, and by directly measuring *Δh* is presented in this section.

4.4.1 Test Apparatus

A triaxial apparatus similar to the saturated case but with modifications was utilized. A schematic figure is shown in Fig. 4-53, divided into three (3) sections: *I*, *II*, *III*.

1. Section *I* Components

This section has two main components: (1) Mariotte's bottle and the (2) weighing scale.

Mariotte's bottle is a device that delivers a constant pressure from closed bottles or tanks. As shown in the schematic diagram in Fig. 4-53 in section *I*, a reservoir is supplied with an air inlet. The pressure at the bottom of the air inlet is always the same as the pressure outside the reservoir, i.e. the atmospheric pressure (P_{atm}). The Mariotte's bottle used in the experiment was designed to supply a total volume of approximately 80 ml to the specimen.

The weighing scale is a commercial scale which has sensitivity up to the hundredth decimal. It is accompanied with USB port which can be connected to the computer (RS-232C interface) and the data can be collected.

2. Section *II* Components

This section is composed of the (1) top cap and bottom pedestal, (2) membrane filter, and (3) local pin-type sensors (connected to pressure transducers (PT)).

The specimen is mounted at the bottom pedestal and connected to the top cap, which is connected to load cell (LC). Fig.4-54 shows the detail of the bottom pedestal and the top cap. The top cap has a pore air path (PAP) so that the specimen is connected to the atmospheric pressure in the duration of the test. Instead of ceramic disk, membrane filter was implemented in this set-up. Membrane filters were secured on both bottom pedestal and top cap by stainless covers.

The membrane filters used in this study were manufactured by Pall Corporation. Membrane type 450 has pore size of 0.45 µm, thickness of 140 µm, air entry value (AEV) of 250 kPa. Further details of the membrane filter can be read in Nishimura et al., (2012) and Wang et al., (2018).

In order to measure Δh directly, local pin-type sensors were used. Similar to the saturated case, the local pin-type sensor is made of a hollow stainless steel with 0.15 cm outer diameter; 0.12 cm inner diameter initially. It is then modified by cutting it on the side and crafting its edges to have a pointed side for piercing. The end product is a 3.5 cm long pin wrapped with membrane filter (same membrane type as the one used in bottom pedestal and top cap). The sensors are connected independently to their respective pressure transducers (PT). Fig. 4-55 shows the local pin-type sensor.

3. Section *III* Components

This section is composed of two pipes, P1 and P2. P1 contains burette B1, which is the downstream of the constant head supplied to the specimen. The overflow of B1 is the outflow of the fluid from the specimen and measurement of flow rate is determined by a differential pressure transducer (DPT).

4.4.2 Test Methodology

A. General Flow of Methodology

Referring to the schematic diagram in Fig. 4-53 the seepage flow can be explained in three sections. In section *I*, valve V1 allows the water to enter through the specimen. Once V1 is turned open, Mariotte's bottle will always supply the water at atmospheric pressure at the bottom of the air inlet and will deliver a flow under constant head height, regardless of the changing water level within the reservoir. The change in mass of the Mariotte's bottle due to volume change was obtained by the weighing scale. One can specify the interval of data collection with a minimum of 1 sec. Inflow rate can then be obtained by the change in volume (change in mass) per time interval.

The fluid flow direction was from top to bottom of the specimen as it flows through section *II*. Pore air path (PAP) was exposed to atmospheric pressure (P_{atm}), hence pore air pressure (u_a) was kept zero throughout the experiment. The fluid flowing through the specimen caused some change to the pressures measured by the pressure transducers (PT) on the local pin-type sensors. The pressure difference was converted to head difference to acquire the head difference of the local pin-type sensors with respect to time.

In section *III*, the overflow from B1 would naturally accumulate water in the outer burette of P1. The change in volume was measured by the DPT between the accumulation of water with respect to the reference level at B2. From the volume change, the outflow rate can be obtained with respect to its time interval.

Seepage was stopped once the inflow rate was assessed to be the same as outflow rate and the measured head difference of the local pin-type sensors was reasonably stable.

After the seepage was stopped, the recording of head difference of the local pin-type sensors was continued. The real head difference was assessed to be the decrease of the head difference when fluid was no longer flowing through the specimen

B. Detailed Methodology

The following section describes the detailed methodology in conducting a Permeability Test under unsaturated case using the Triaxial Apparatus with local pin-type sensors.

1. Preparation of Triaxial Apparatus

a. Saturate the local pin-type sensors overnight in a tank by applying -100 kPa (see Fig. 4-56).
b. Saturate the membrane filters as well in a container for overnight (see Fig. 4-57).
c. Make sure to clean the parts of the triaxial apparatus. There should be no gel and no dust as these may interfere in the results of the tests.
d. First, measure the dummy specimen height for reference. This is essential so that when an actual specimen is placed, the difference of the dummy specimen height and the actual specimen.
e. Saturate the bottom and pedestal and top cap by acylic tube de-aired with vacuum for 30 mins (see Fig. 4-58)
f. Apply grease as well on both the bottom pedestal and top cap to stick with the rubber membrane.
g. Before placing the rubber membrane cut it into 15 cm or longer (recommended) to provide for 10 cm soil specimen, plus 2.5 cm extra length on each ends to secure to the bottom pedestal and top cap, respectively.
h. Mark the location of top pin and bottom pin, each 1 cm away from the top cap and bottom pedestal, respectively.
i. Create a hole on the position where the pin is intended to be inserted so that when an actual specimen is placed, the pin can easily go through. Another reason for this is to alleviate the rubber membrane from unnecessary pressure due to puncture through the surface.

2. Preparation of Specimen
   a. Depending on desired degree of compaction, pre-weigh sample that will fit in the 10 cm height, and 5 cm diameter mold.
   b. Introduce specimen by 1-dimension consolidation in the mold.
   c. Place the membrane filter on the bottom pedestal and top cap and secure by screws.
   d. Transfer the prepared specimen from the mold and mount it at the bottom pedestal.
   e. Connect the load cell cable to the amplitudes to indicate voltage (which was correlated to indicate force). Calibrate the amplitude to have minimal contact force as possible so that when the top cap reaches contact to the specimen, the value would more or less be zero.
   f. Gradually touch top cap to specimen. After which, secure the rubber membrane to the top cap.
   g. Measure the diameter and height of the specimen. The values obtained are the initial condition of the test.
   h. Introduce 5 kPa back pressure.

3. Insertion of Pins
   a. After properly placing the specimen on the triaxial apparatus, carefully insert the local pin-type sensors by using quick-hardening glue to create the bond between the pin and the rubber membrane.
   b. Carefully insert the pins and make sure that no air can diffuse through the rubber membrane (i.e. properly bonded). Wait for about 1 minute once the pin is inserted to allow the connection to take place. As much as possible, avoid disturbing the

specimen. Fig. 4-59 shows the mounted specimen on the pedestal with the local pin-type sensors.

4. Consolidation of Specimen
   a. Place the outer cell in the triaxial apparatus.
   b. Convert 5 kPa back pressure to 5 kPa cell pressure. This is done by decreasing every 1 kPa from back pressure and increasing 1 kPa to cell pressure until a 5 kPa cell pressure is achieved (and zero back pressure).
   c. After converting to positive pressure, increase gradually to the target confining pressure. In this case, 50 kPa.
   d. Consolidate for 2 hours.

5. Seepage
   a. Apply the negative pressure at the burette in section *III* corresponding to the suction measured at the membrane filter from the bottom pedestal and top cap. Otherwise, the fluid cannot flow from the specimen to pipe P1.
   b. Set up the weighing scale to collect the data of inflow rate. Place the Mariotte's bottle on the weighting scale.
   c. Open the tap at Mariotte's bottle to flow to the specimen (section *I* valve V1).
   d. Collect data for both inflow and outflow with the same time interval.
   e. Stop seepage once the inflow rate was assessed to be the same as outflow rate and the measured head difference of the local pin-type sensors was reasonably stable.

6. Post-Seepage
   a. After the seepage was stopped, continue to record the head difference. The real head difference was assessed to be the decrease of the head difference when fluid was no longer flowing through the specimen

4.4.3 Tests Conducted

This section presents the tests conducted to determine the unsaturated permeability of bauxite, iron ore, and Inagi sand.

Five (5) tests were performed for Toyoura sand but the local pin-type sensors were unable to measure reasonable head difference data. The reason is that the suction obtained were not significant enough to develop head difference. In other words, the local pin-type sensor is not applicable to Toyoura sand (i.e. clean sand).

For bauxite, tests were performed under loose (D_c = 65%), medium dense (D_c = 80%), and dense case (D_c = 90%).

For iron ore, tests were only conducted at dense case (D_c = 91.3%).

For Inagi sand, tests were only conducted at loose case (D_c = 72.0%).

1. Bauxite

Table 4-6 summarizes the test conditions for bauxite.

Table 4-6. Test Conditions of *k* Tests using Triaxial Apparatus (bauxite-unsaturated)

Test	D_c (%)	Case	Initial degree of saturation Sr_{init} (%)	Final degree of saturation Sr_{final} (%)	Suction measured by membrane filter (kPa)	Total head (cm) supplied to the specimen	Total accumulated volume (ml) (approximate)
1	80.0	Medium Dense	80	-	-	-	-
2	80.1		75	-	-	-	-
3	80.1		75	-	-	-	-
4	81.1		65	64.2	2.5	55	50
5	80.2			66.2	1.0	60	75
6	80.3			68.2	1.7	52	50
7	80.2			68.1	2.0	53	50
8	79.8		50	57.8	13.4	82	50
9	79.9		52	58.2	10.2	77	50
			70	59.5	-	77	40
			90	59.8	-	77	35
10	79.8		50	85	-	80	25
11	79.7		-	100	-	60	50
12	80.0		43	51.1	34.7	402	75
13	79.8		72	77.9	0.3	35	55
14	67.7	Loose	45	48.8	2.1	62	35
15	71.6		52	52.3	0.8	60	35
16	70.4		-	100	-	35	25
17	88.8	Dense	58	64.5	13.8	85	45
18	88.8		75	74.1	2.4	64	45
19	89.1		-	100	-	35	25
20	88.7		52	57.1	15.1	85	25

Tests 1 -3 are all unsuccessful that did not even proceed to the seepage of water to the specimen as the method was being improved and established. Procedural errors such as error in insertion of pins among others prevented from furthering with the test.

Test 4 is conducted using the set up in Fig. 4-8 (i.e. triaxial permeameter for the saturated condition). Mariotte's bottle and inflow measurements started at test 5.

Test 9 is a special case where the specimen was initially prepared at Sr_{init} = 52%. After collecting data, the same specimen was used by injecting water to the specimen to theoretically achieve Sr_{init} = 70%. After this conducing another test, water was further injected to the specimen to theoretically achieve Sr_{init} = 90%.

Test 10 is another special case because using the membrane filter, the specimen was de-aired overnight by double vacuum method, and was attempted to be saturated from its initial saturation condition of 50% (Sr_{init} = 50%). However, the membrane filter is a special type of filter paper and the method cannot be implemented to the specimen to saturate it

after implementing the double vacuum method. This test was not successful and couldn't be used as data.

Tests 11, 16, and 19 are tests conducted under saturated condition using the triaxial permeameter set up in Fig. 4-53. The results were compared with the results obtained at the saturated condition using the set up of the triaxial permeameter in Fig. 4-8.

2. Iron Ore

Table 4-7 summarizes the test conditions for iron ore.

Table 4-7. Test Conditions of *k* Tests using Triaxial Apparatus (iron ore-unsaturated)

Test	D_c (%)	Case	Initial degree of saturation Sr_{init} (%)	Final degree of saturation Sr_{final} (%)	Suction measured by membrane filter (kPa)	Total head (cm) supplied to the specimen	Total accumulated volume (ml) (approximate)
1	91.5	Dense	-	100	-	32	25
2	92.3		72	74.1	2.4	64	25
3	91.6		60	66.8	4.4	75	25

Test 1 was conducted under saturated condition using the triaxial permeameter set up in Fig. 4-53.

The degree of compaction performed in this test was set to match with the degree of compaction used by Wang (2014) for numerical simulation. The tests performed in Wang, 2014 was D_c = 91.3%. This is also comparable to the dense case of bauxite set at $D_c \approx$ 91.3%.

3. Inagi Sand

Table 4-8 summarizes the test conditions for Inagi sand.

Table 4-8. Test Conditions of *k* Tests using Triaxial Apparatus (Inagi sand-unsaturated)

Test	D_c (%)	Case	Initial degree of saturation Sr_{init} (%)	Final degree of saturation Sr_{final} (%)	Suction measured by membrane filter (kPa)	Total head (cm) supplied to the specimen	Total accumulated volume (ml) (approximate)
0	69.2	Loose	-	100	-	varies	15
1	70.7		65	74.2	1.6	62	25
2	71.0		55	62.2	3.2	72	40

Test 0 was set as zero because this test was not performed using the triaxial permeameter set up in Fig. 4-53. This was just adopted from the saturated case of Inagi sand, test 3 shown in Table 4-4.

The target degree of compaction here was loose case, to be compared to the loose case of bauxite.

4.4.4 Tests Analysis

1. Bauxite (Test 4 to Test 13, Medium Dense, D_c = 80%)

Typical test result is represented by a specimen prepared at initial saturation degree of 65% (Sr_{init}=65%) represented by test 6. In Fig. 4-60, the water inflow and outflow were continuously monitored until a steady-state condition was established when the inflow rate was approximately equal to the outflow rate.

It can be observed that the flow of water seeped through the specimen at a relatively short elapsed time from inflow to outflow. At approximately 1500 sec, the difference of the inflow rate and outflow rate started to exhibit equivalent values, although it cannot be said to have achieved steady state yet since the flows were still decreasing. The steady state of the typical plot shown was achieved at about 10500 sec (marked by a vertical solid line), when the flow difference was approximately zero and the inflow rate and outflow rate were both approaching horizontal (marked by a horizontal solid line).

The head difference (Δh) is measured by the difference of the pressures of the top and bottom local pin-type sensors converted to pressure heads. It can be said from Fig. 4-61 that the head difference measured was reasonably stable from about 1500 sec mark. This is consistent with the information that can be drawn from Fig. 4-60 since initially, when inflow of water surged to a comparatively higher flow rate, the top local pin-type sensor became more saturated first (due to flow direction from top to bottom). Hence, the pore water pressure (u_w) increased, resulting to lower suction values. This implied lower equivalent head value for the top local pin-type sensor, but resulted to an increased Δh. As the water seeping through the specimen affected both the top and bottom local pin-type sensors with respect to time, it achieved a relatively stable Δh at a certain time when the water seeping through the specimen had found its path. Although the head was reasonably stable from approximately 1500 sec, the data obtained from 10500 sec and beyond were treated as the Δh at steady-state condition.

From the flow rate time history and head difference time history, the coefficient of permeability can be obtained from Equation 4-7. Fig. 4-62 shows the corresponding k vs time history from the typical test. Consequently from Fig. 4-60, the k values at steady state condition was also obtained from the 10500 sec mark. The k value for this test was taken to be the simple average of those values (indicated by an ellipse in Fig.4-62), which is equal to kavg=2.47 x 10-4 cm/sec.

Fig. 4-60 to Fig. 4-62 are plots that could be obtained under seepage condition in the specimen. The head difference was continually measured even after the seepage was stopped. Fig. 4-63 shows the typical behavior of the head difference at the post-seepage process.

The head difference was expected to be zero once seepage had been stopped. Depending on the duration of the test, the inevitable fluctuation of the transducers and the

imperfections of fully-saturating the local pin-type sensors caused the pins to respond differently after a long period of time. For this particular example, there was no need to correct Fig.4-61 since the post seepage data suggested that the head difference was zero once the seepage was stopped.

Bauxite special case: Test 9

As previously mentioned, test 9 is a special case where the specimen was initially prepared at Sr_{init} = 52%. After collecting data, the same specimen was used by injecting water to the specimen to theoretically achieve Sr_{init} = 70%, and then subsequently, for Sr_{init} = 90% as well. This test was conducted to hopefully simulate the wetting process of soil (or drying for the case of higher *Sr* values going to lower *Sr* values).

Fig. 4-64 shows the plots at different Sr_{init} of test 9. The *x*-axis of this plot was indicated in accumulated volume in outflow since the time it took for each initial *Sr* was different. Hence, it was more sensible to take the *k* values for a set volume accumulated, in this case, every 0.5 ml. It can be seen from this figure that only the initial testing condition of Sr_{init} = 52% resulted to reasonable Δh values. It seems that the injected water to the specimen does not integrate with the soil water skeleton.

This is supported by the *Q* vs time plots. In Fig. 4-65, it was observed that the inflow rate and outflow rate gradually achieved a steady condition. However in Fig. 4-66, which is the *Q* vs. time after injecting water to achieve target initial condition (using the same specimen) of Sr_{init} = 70%, the inflow rate of water barely moved while outflow was drastic. Similar behavior can be observed at Sr_{init} = 90% in Fig. 4-67, the water injected flowed out of the specimen while there was no inflow. Referring to Table 4-6 where the bauxite tests are summarized, it can be seen that the Sr_{final} reverted back to 59.5% and 59.8% for the Sr_{init} = 70% and Sr_{init} = 90%, respectively.

Fig. 4-68 shows the *k* values. From this figure, the *k* values obtained at Sr_{init} = 70% and Sr_{init} = 90% are unsteady conditions throughout the test. Hence, only the initial condition of Sr_{init} = 52% was accepted as reliable data and the other two were not. This test also suggests that conducting *k* tests with this proposed system is not applicable in conducting further test with the same specimen.

2. Bauxite (Test 14 to Test 16, Loose, D_c = 65%)

The loose case was similar in trend as elaborated in the medium dense case. Referring to Table 4-6, test 14 and test 15 were conducted at almost same test condition. The reason is that the preparation of specimen requires mixing the dry soil to an amount of water to achieve the desired S_r. For loose case at D_c = 65%, the presence of voids does not permit high S_r in preparation. Trials were conducted but the preparation at 52% (i.e. test 15) was the upper limit such that the specimen will hold on its own.

Test 16 is used here to present the comparison between results obtained from the triaxial permeameter apparatus used in saturated case (Fig. 4-8) and the triaxial permeameter apparatus used here in unsaturated case (Fig. 4-53). Since this is S_r=100%, the membrane filters on the local pin-type sensors were removed because it will not be able to measure anything due to the absence of suction at S_r=100%.

Fig. 4-69 shows that the *k* values at of tests 14-16. S_r=100% are practically the same in using both apparatuses. The average *k* values using the apparatus in Fig. 4-8 is 1.54 x 10^{-2} cm/sec while that of apparatus in Fig. 4-53 resulted to 1.46 x 10^{-2} cm/sec. This is only about 5% difference with respect to one another. As for test 14 and test 15, it can be seen that the *k* values are comparatively close to one another, which is reasonable since their final *Sr* values are close to one another (i.e. *Sr* = 48.8% for test 14, and *Sr* = 52.3% for test 15).

3. Bauxite (Test 17 to Test 20, Loose, D_c = 90%)

Fig. 4-70 summarizes the *k* values of tests 17-20. Instead of time, the *k* values were plotted against accumulated volume in outflow because the duration of time conducted for each test was different so this plot would show a better comparison of test results. Similar to the observation made in loose case, the *k* values obtained at S_r=100% were practically the same using the triaxial permeameter apparatus in Fig. 4-8 and the one in Fig. 4-53.

The *k* values seemed to coincide for test 17 and test 20 up to accumulated volume of 20 ml in the outflow but the *k* values decreased for test 20 eventually before stabilizing. Verifying the plot from the inflow rate and outflow rate plot in Fig. 4-71, it can be seen that the steady state condition was achieved at about the 20000 sec mark, which shows that acceptable *k* values were achieved at the later end of the experiment. The erratic data in Fig. 4-71 was accounted by the accidental movements incurred on the inflow system, affecting the collected data.

To summarize all the collected data for bauxite for all cases, Fig. 4-72 presents the *k* vs *i* plot for all tests of bauxite. Test 12 had a high total head supplied to it (402 cm), hence resulting to a high *i* value. Fig. 4-73 summarizes the obtained *k* values in Fig. 4-72 by taking the simple average of the points on each test. The trend in Fig. 4-73 shows that the *k* values drop four (4) orders of exponent from fully saturated case (S_r=100%) to about 50% saturation (S_r=50%). Fig. 4-73 also supports the conclusion made due to the effect of void ratio, where the denser the test condition (i.e. lower void ratio), the lower the *k* values.

4. Iron Ore

Fig. 4-74 summarizes the *k* values plotted against accumulated volume in the outflow for dense case, iron ore. Applying the same technique as that of bauxite, it can be observed that test 1, which is the S_r=100% resulted to practically the same *k* values by using the triaxial permeameter test in Fig. 4-8 and Fig. 4-53. Test 3 was quite unusual since the data started to show at around 9 ml mark. Fig. 4-75 shows that the head difference Δh for test 3 was still not positive until it reached 9 ml.

Fig. 4-76 compares the *k* vs. *i* plot of dense case of bauxite and iron ore. At saturated cases (i.e. test 19 of bauxite and test 1 of iron ore), the *k* values were almost the same with average values of 2.68 x 10^{-3} cm/sec and 2.84 x 10^{-3} cm/sec, respectively. At lower S_r values, the trend began to differ as evidenced by test 18 of bauxite and test 2 of iron ore. While both have the same S_r when tested, the *k* values of iron ore was an order lower. Referring to Table 4-6 test 18 and Table 4-7 test 2, the tests had the same initial suction measured by the membrane filter. So the effect that the *k* was lower for iron ore was not due to the higher suction of iron ore but can be attributed to other factors such as the fabric and composition of iron ore.

Fig. 4-77 compares the results of bauxite and iron ore in dense case. By taking the average values of *k* from Fig. 4-76 for each test, the representative *k* value for each test was plotted in Fig. 4-77 can it can be seen that the iron ore have lower *k* values than bauxite at dense case.

5. Inagi Sand

The test 0 condition was labeled as such because the test was simply adopted from Table 4-4, test 3. Tests 1 and 2 were performed at loose condition. Fig. 4-78 shows the *k* values obtained from the tests.

Fig. 4-79 shows the *k* vs *i* plot of both bauxite and Inagi sand. One noticeable thing is the difference of order of the *k* values at S_r=100%. Bauxite at loose sand has an order of -2 while Inagi sand was -4. The other S_r values cannot be compared directly, however in Fig. 4-80, it can be seen that the behavior of *k* values were similar.

From the *k* values obtained, another important parameter shall be discussed. It is the soil-water retention curve (SWRC) which relates the suction to the volumetric water content or degree of saturation of the soil.

4-5. Soil-Water Characteristic Curve (SWRC)

Suction or matric suction is often defined as the subtraction of pore water pressure (u_w) from pore air pressure (u_a) i.e. $u_a - u_w$, and SWRC describes the relationship between suction and the equilibrium water content. One of the usages of SWRC in this study is to evaluate the water distribution in the heap of bauxite since if the suction distribution is properly estimated it becomes possible to analyze the equilibrium water content distribution in the heap. Fig. 4-81 schematically shows a typical SWRC. A SWRC usually includes two curves: a drying curve, which shows that soil water content reduces as suction increases, and a wetting curve, which shows that water content increases as suction decreases. There is hysteresis between drying and wetting curves induced by reasons such as the non-uniform pore size distribution in the voids, and a difference in the contact angle at the advancing interface during the drying process and wetting process etc. (Fredlund and Rahardjo, 1993). For a single drying curve or wetting curve, an opposite “S” shape of SWRC is rather typical,

while the shape may change depending on the density of the soil element, soil type, particle structure etc. (Standing, 2011).

It is possible to estimate the final water distribution in the heap of bauxite by utilizing the SWRC, while time-dependent water distribution also needs to be evaluated to find the critical water distribution in the heap of bauxite. That is taken care of by the permeability property of bauxite under both saturated and unsaturated condition.

In the low suction range (0.1-100 kPa), the SWRC of bauxite, as well as iron ore and Inagi sand were obtained by membrane filter technique (Nishimura, 2012) and ceramic disk technique. The data obtained from the membrane filter in the triaxial apparatus shall be plotted on the SWRC.

The data from SWRC here shall also be used to estimate *k* values by indirect method. The values will be compared to the experimental data obtained in *k* tests.

4.5.1. Test Apparatus

A traditional pressure plate apparatus, in which a ceramic disk with thickness of 2 mm was employed to conduct the SWRC test in the suction range of 0.1-100 kPa. Another specially manufactured apparatus (membrane filter apparatus), in which the membrane filter technique was introduced instead of the ceramic disk, was also employed to apply suction up to 20 kPa.

A commercial membrane filter, Supor 450 was used in this test. This is similar to the membrane filter used in the triaxial permeameter apparatus used for unsaturated case in Fig. 4-53 and the ones used to wrap the local pin-type sensors to measure suction. A burette and a differential pressure transducer were connected to the water compartment of each apparatus to monitor the volume of water drainage (schematic illustrations of the used apparatuses are shown in Fig. 4-82 and Fig. 4-83).

4.5.2. Test Methodology

The method for applying suction with these two types of apparatus is different. For the ceramic disk apparatus, in the suction range of 0.1 to 20 kPa, suction was applied by the hanging column method. It is a method in which the tested specimen is placed at a higher position than the water surface elevation in the burette connected to the apparatus. By doing so, a negative pore water pressure was applied to the specimens. Fig. 4-84 shows the set-up of the hanging column method. It is basically a simple frame with a pulley system to elevate the apparatus whenever the equilibrium condition is reached. In the suction range of 20-100 kPa, the axis-translation technique was used, in which positive air pressure was applied to the air phase of the tested specimens.

For the membrane filter apparatus, suction was applied by the hanging column method solely (the maximum elevation difference is about 2 m or about 20 kPa).

All the specimens tested in the low suction range were made by static compression. Attention was paid to guarantee good contact between the specimen and the pedestal of the apparatus. The specimens were saturated by soaking them in a vacuum water tank overnight, before conducting the experiment.

4.5.3. Tests Conducted

1. Bauxite

Table 4-9 summarizes the test conditions for bauxite.

Table 4-9. Test Conditions of specimens conducted for SWRC tests (bauxite)

Test	D_c (%)	Case	Initial *Sr* (%)	Void ratio *e*	Dry density ρ_d (g/cm^3)	Apparatus
1	65.3	Loose	91.4	1.380	1.110	Membrane filter
2	80.5	Medium Dense	93.9	0.931	1.368	
3	89.4	Dense	95.4	0.738	1.520	
4	64.9	Loose	94.4	1.396	1.103	Ceramic Disk
5	79.8	Medium Dense	93.2	0.947	1.357	
6	89.0	Dense	91.7	0.747	1.513	

All tests have specimen radius of 2.5 cm and specimen height of 2.0 cm. All tests were also conducted for the drying curve only, except for test 2, which included the wetting curve. Three specimens with different densities were tested by using a pressure plate apparatus where the membrane filter technique (Nishimura et al. 2012) was introduced. Similarly three tests were conducted on a pressure plate apparatus with ceramic disk.

2. Iron Ore

Table 4-10 summarizes the test conditions for iron ore.

Table 4-10. Test Conditions of specimens conducted for SWRC tests (iron ore)

Test	D_c (%)	Case	Initial *Sr* (%)	Void ratio *e*	Dry density ρ_d (g/cm^3)	Apparatus
1	91.6	Dense	94.6	0.740	2.554	Ceramic Disk

SWRC test was necessary for iron ore with the intent to compare the result with the dense case of bauxite.

3. Inagi Sand

Table 4-11 summarizes the test conditions for iron ore.

Table 4-11. Test Conditions of specimens conducted for SWRC tests (Inagi sand)

Test	D_c (%)	Case	Initial *Sr* (%)	Void ratio *e*	Dry density ρ_d (g/cm^3)	Apparatus
1	72.0	Loose	92.5	1.224	1.194	Ceramic Disk

Similar to iron ore, SWRC test was necessary for Inagi sand with the intent to compare the result with the loose case of bauxite.

4.5.4. Tests Analysis

1. Bauxite

Effect of testing technique on SWRC

Water flows out from the membrane filter apparatus faster due to the much thinner membrane filter used (i.e. 0.14 mm for membrane filter compared to 2 mm for ceramic disk). For the membrane filter apparatus, it normally takes several hours for each step of suction to be stabilized. Under similar conditions, it is common to wait for several days for each step of the test conducted on the ceramic disk apparatus. More importantly, it was found that during the test conducted on the ceramic apparatus, sometimes it is very difficult to determine where the equilibrium of each suction step is.

Fig. 4-85, Fig. 4-86, and Fig. 4-87 show the relationship between suction and the degree of saturation (*Sr*) of bauxite at loose case, medium dense case, and dense case, respectively. The intent of these plots is to compare the result obtained from membrane filter and ceramic disk. The test data obtained in Table 4-6 measured by the membrane filter when unsaturated permeability tests were conducted were also plotted in the figures.

Fig. 4-85 compares the SWRCs of test 1 (membrane filter) and test 4 of bauxite (ceramic disk). It shows that for the drying curve, the equivalent *Sr* during test 4 with the ceramic disk apparatus was higher than that of the test using the membrane filter apparatus when suction was less than 2 kPa. These two curves converged when suction exceeded 2 kPa.

Fig. 4-86 compares the SWRCs of test 2 (membrane filter) and test 5 of bauxite (ceramic disk). For the drying curve, the equivalent *Sr* during test 2 with membrane filter apparatus had a different behavior than test 5 with ceramic disk apparatus with test 2 decreasing in *Sr* more than test 5 until 10 kPa. The two curves converged when suction exceeded 10 kPa.

Fig. 4-87 compares the SWRCs of test 3 (membrane filter) and test 6 of bauxite (ceramic disk). For the drying curve, the equivalent *Sr* during test 3 with membrane filter apparatus was higher than that of the test using the ceramic disk apparatus when suction was less than about 3.5 kPa. These two curves converged at 10 kPa and were practically the same at higher suctions.

The test data in Fig. 4-86 also shows that the data obtained from Table 4-6 measured by the filter paper when unsaturated *k* tests were performed agree with the drying curve of test 2 (membrane filter apparatus) at suction greater than 2 kPa. The other plots with suction less than 2 kPa do not coincide with the drying curve but nonetheless, within the hysteresis of the SWRC of test 2. In view of this, it can be said that the plots obtained from Table 4-6 are acceptable. Fig. 4-85 also support the trend since test 14 of Table 4-6 obey the drying curve while test 15 of Table 4-6 underestimates from the results of both test 1 (membrane filter apparatus) and test 4 (ceramic disk apparatus). In Fig. 4-87, the data obtained for test 17 of Table 4-6 obeys the trend obtained from the drying curve at suction greater than 10 kPa. Test 20 of Table 4-6 though deviated from the trend, while test 18 of Table 4-6 was much lower than the ones obtained from the membrane filter apparatus and ceramic disk apparatus.

For bauxite from these experiments, the result of membrane filter apparatus and ceramic disk agree at suctions greater than 10 kPa in general. At loose case (i.e. D_c = 65%), it occurred much earlier at 2 kPa.

Effect of density on SWRC at low level suction

Fig. 4-88 shows tests 1 to 3 with different density conditions that were conducted using the membrane filter apparatus. In Wang (2014), it was observed that the values on the drying or curves converge together when the suction value exceeds 1.5 kPa regardless of specimen void ratio, which implies that the void ratio may not affect *Sr* significantly when suction exceeds certain values. However for bauxite, this trend cannot be observed even at suctions greater than 20 kPa. Similar conclusion can be said by observing Fig. 4-89, which shows the plots of tests 4 to 6 with different density conditions that were conducted using the ceramic disk apparatus. The trends did not converge even at suctions greater than 100 kPa.

One of the possible explanation is that the mechanical and physical properties of iron ore is different than typical soils while bauxite did not show any evidence to be different than typical soils (see Chapter 2: Test Materials, Table 2-1). Furthermore, Wang (2014) reports that similar results were reported on clayey silty sand (Salager et al. 2013) and bentonite (Romero et al. 1999, Lloret et al. 2003) that this phenomenon can be explained by the existence of a large portion of intra-aggregate water, which exists inside the clay particle layer structures and actually becomes a part of the clay minerals. The amount of intra-aggregate water in clay depends mostly on the clay particle itself and, thus, the void ratio has less effect on *Sr* (Bradbury & Baeyens 2002, Jacinto et al. 2012).

For granular materials however, the amount of water is governed by the retention of particle surface due to van der Waals force and by micro-pores in individual soil particles. This is not significantly affected by a change in relatively low suction range. Thus, the amount of water in the specimens was controlled by void ratio. When the granular materials are densified, the volume of relatively large pores is easier to be compressed than that of relatively small pores. The amount of water retained between particles is governed by relatively small pores. For specimens of bauxite with different densities, it is possible that

the volumes of relatively small pores in the specimens with different densities are different. Thus, the relationship between suction and gravimetric water content *Sr* was significantly affected by void ratio. Although bauxite is not purely a granular material, its material properties are similar to silty sand, which could behave like granular material than clayey material.

2. Iron Ore

Fig. 4-90 plots the SWRC of iron ore at dense case using the ceramic disk apparatus, and the data from bauxite at dense case using the ceramic disk apparatus in Fig 4-87 was extracted and plotted as well in Fig. 4-90. At first, glance, it may be perceived that the SWRC results of the two types of materials are the same. However, the data obtained from iron ore shows that the equivalent *Sr* values were higher than that of bauxite when suction was less than about 15 kPa. The trend began to change as the equivalent *Sr* values from about 15 kPa to 25 kPa were higher in bauxite, before shifting back again to the original trend where iron ore had higher equivalent *Sr* values.

As for test 2 and test 3 in Table 4-7, the points obtained from the membrane filter were plotted on Fig. 4-90, and the values are underestimate of the SWRC results even at suction of 5 kPa.

3. Inagi Sand

Fig. 4-91 shows the SWRC of Inagi sand at loose case using the ceramic disk apparatus, and the data from bauxite at loose case using the ceramic disk apparatus in Fig 4-85 was extracted and plotted as well in Fig. 4-91. The air entry value (AEV) of the two tests was different, with bauxite occurring at a lower suction value. The trend of the two lines was parallel at suction values greater than 10 kPa. At suction values lower than 10 kPa, the decrease of the equivalent *Sr* value of bauxite was abrupt compared to Inagi sand, until it decreased almost at the same rate to Inagi sand at greater than 10 kPa.

As for test 1 and test 2 in Table 4-8, the points obtained from the membrane filter were plotted on Fig. 4-91, and the values are underestimate of the SWRC results even at suction of 3 kPa.

4-6. Permeability Tests using Indirect Method

Permeability can also be evaluated by using an empirical model. Mualem (1976) proposed a model for estimating the permeability of unsaturated porous media from the knowledge of SWRC. This proposed model includes a dimensionless water content, Θ:

$$\Theta = \frac{\theta - \theta_r}{\theta_s - \theta_r} \qquad \text{(Eqn. 4-8)}$$

where, θ stands for volumetric water content and, subscripts '*s*' and '*r*' indicate the saturated and residual volumetric water content, respectively. To solve the model proposed by Mualem (1976), Van Genuchten (1980) proposed an equation to correlate Θ with pressure head *h*:

$$\Theta = \begin{cases} \frac{1}{[1+|\alpha h|^n]^{1-1/n}} & h < 0 \\ 1 & h \geqq 0 \end{cases} \quad \text{(Eqn. 4-9)}$$

where, α and n are model parameters, and α is a unit of (m^{-1}) when unit of *h* is (m); *h* is pressure head (m). It is assumed that the suction (kPa)= $\gamma_w \times h$, γ_w is the unit weight of water in this study.

By introducing Eq. 4-9, the model proposed by Mualem (1976) was converted to:

$$k = k_s \Theta^{1/2} \left[1 - \left(1 - \Theta^{n/(n-1)}\right)^{1-1/n}\right]^2 \quad \text{(Eqn. 4-10)}$$

where, *k* is permeability of unsaturated soil; k_s is permeability of saturated soil; and *n* is the parameter in Eqn. 4-9.

Eqn. 4-10 involves 5 parameters: (1) θ_s, which is known when the density of soil is given; (2) θ_r, which has to be evaluated from SWRC result; (3) α and (4) *n*, which are determined by fitting SWRC using Eqn. 4-9; and (5) k_s, which is determined by the permeability test of the saturated specimen.

The data from SWRC were used to come up with the parameters, using the results from ceramic disk apparatus since the results provide even at higher suction values (i.e. membrane filter apparatus can only measure up to 20 kPa).

By applying Eqn. 4-10 to compare with experimental data under unsaturated permeability, Fig. 4-73, Fig. 4-77, and Fig. 4-80 were re-plotted to Fig. 4-92, Fig. 4-93, and Fig. 4-94, respectively.

Fig. 4-92 shows the results for bauxite for all tests. At loose case, the experimental data and results of Van Genuchten estimate (VG estimate) agree. As the specimen becomes denser, such as the medium dense and dense cases, the results of VG estimate do not agree with the experimental data, with VG being underestimate. For simulations however, the experimental data shall be adopted since they represent the obtained data from tests, while VG estimate rely on model parameters, which have some assumptions. The results obtained also suggest that VG estimate may represent slower accumulation of water into the heap, which experimental data suggest otherwise.

Fig. 4-93 compares the results from experimental data and VG estimate for bauxite and iron ore at dense case. The result for iron ore suggests that the experimental data were underestimate, which is the opposite of what can be observed from bauxite. However, the curvature of VG estimate dip steeper than the experimental data line by observing *Sr* = 74%,

having a larger difference between the *k* value of experimental data and VG estimate, while *Sr* = 67% shows that the difference of *k* values being much less. At lower *Sr* values, the VG estimate is expected to underestimate the experimental data, assuming the same trend will happen.

Fig. 4-94 compares the results from experimental data and VG estimate for bauxite and Inagi sand at loose case. For the loose case, the experimental data and VG estimate agree well for both bauxite and Inagi sand.

4-7. Chapter Summary

In this Chapter, the following points can be stated.

1. Standard Permeameter Tests prescribed by JIS A 1218 is the standard method for testing permeability of soils. In order to investigate the side wall effects (i.e. gap between the mold-specimen interface), a Modified Permeameter Apparatus was performed (Fig. 4-4 and Fig 4-5) and it was found out that in a rigid mold, the coefficient of permeability *k*, resulted to higher values due to side wall leakage effects.

2. To address the concern of side wall effects, flexible wall permeameter is commonly implemented since side wall leakage can be addressed, confining stress can be applied, and stress-state condition of the specimen can be controlled. For saturated case, a triaxial permeameter apparatus with the newly developed local pin-type sensors (Fig. 4-8 and Fig 4-9) to measure head difference directly was presented as a new technique for obtaining *k* values.

3. In order to establish the limits and applicability of the local pin-type sensors, it was investigated on four different aspects, namely the (1) effect of pin length, (2) effect of confining pressure (σ_C), (3) effect of hydraulic gradient (*i*), and (4) effect of void ratio, *e.* The local pin-type sensors can be said to have following limitations and applicability:
   - (1) effect of pin length: It was found out that the long pin, with pin length of 2 cm (pin length/specimen diameter = L/D = 0.4) was generally more reliable than short pin with 0.5 cm length (L/D = 0.1), which results are significantly affected by membrane wrinkles formed at lower σ_C.
   - (2) effect of confining pressure (σ_C): bauxite ($\sigma_c \leq$ 10 kPa), Inagi sand ($\sigma_c \leq$ 20 kPa), and Toyoura sand ($\sigma_c \leq$ 5 kPa) are not reliable data. Data are supported with image analysis.
   - (3) effect of hydraulic gradient (*i*): bauxite ($i \leq 0.25$), Inagi sand ($i \leq 0.50$), and Toyoura sand ($i \leq 0.05$) are not reliable data
   - (4) effect of void ratio, *e*: The isotropic loading *k* values behavior can be explained by the effect of the void ratio change with *k* values decreasing with decreasing *e*.

4. The *k* values obtained using the rigid mold modified permeameter tests coincide with the plot of the triaxial permeameter test showing *k* vs *e* (Fig. 4-50 to Fig. 4-52).

5. The local pin-type sensors were used also in unsaturated permeability tests. A new triaxial permeameter apparatus was presented in Fig. 4-53, with the following features of the system:
   - Inflow rate was measured by Mariotte's bottle and a weighing scale, while outflow rate was measured by burettes and differential pressure transducer. Steady state flow condition can be achieved by using membrane filters to facilitate flow of water but prevent flow of free air.
   - Unsaturated permeability could be evaluated using the newly developed local pin-type sensors to measure the head difference directly. Permeability values were obtained by simple average at steady state flow condition and measured head is reasonably stable.
   - Currently tests done show the applicability range of the local pin-type sensor on bauxite ($1x10^{-5}$ to $1x10^{-3}$ cm/sec), iron ore ($1x10^{-5}$ to $1x10^{-4}$ cm/sec), and Inagi sand ($1x10^{-5}$ to $1x10^{-4}$ cm/sec). The local pin-type sensor was found out to be ineffective for Toyoura sand.

6. Experiments and results from the triaxial permeameter apparatus for unsaturated soils show that:
   - conducting *k* tests with this proposed system is not applicable in conducting multiple test with the same specimen
   - Under saturated case, the triaxial permeameter apparatus used for saturated case (Fig. 4-8) and the triaxial permeameter apparatus used for unsaturated case have practically the same *k* values.
   - For different densities of bauxite, the local pin-type sensors could be a way to measure *k* of unsaturated materials. Results show that *k* values drop four (4) orders of exponent from fully saturated case (S_r=100%) to about 50% saturation (S_r=50%) (Fig. 4-73). It also supports the conclusion made due to the effect of void ratio, where the denser the test condition (i.e. lower void ratio), the lower the *k* values.
   - Iron ore have lower *k* values than their bauxite counterpart at dense case (Fig. 4-77) despite having practically the same *k* saturated (2.68×10^{-3} cm/sec for bauxite, 2.84×10^{-3} cm/sec for iron ore). Inagi sand, on the other hand, was less permeable than bauxite at loose case but their trends were the same

7. Two kinds of apparatuses were used for the measurement of soil-water retention curve (SWRC): the membrane filter apparatus and the ceramic disk apparatus. It was found out that for bauxite at different densities, the result of membrane filter apparatus and ceramic disk agree at suctions greater than 10 kPa in general (Fig 4-85 to Fig. 4-87). It was also found out that for bauxite, the void ratio does affect the SWRC results for both membrane filter apparatus and ceramic disk apparatus (Fig. 4-88 and Fig. 4-89). Results also show in general that the suction values obtained with their corresponding *Sr* values using membrane filter at unsaturated permeability tests (Table 4-6 to Table 4-8 with data points plotted on Fig. 4-85 to Fig. 4-87 and Fig 4-90 to Fig 4-91) were underestimate of the ones obtained at the drying curve of SWRC.

8. Permeability results using the data obtained from SWRC drying curve (i.e. indirect method), Van Genuchten estimate (VG estimate) was calculated and compared with the experimental data (Fig. 4-92 to Fig. 4-94). For bauxite, it shows that as the specimen becomes denser, the results of VG estimate do not agree with the experimental data, with VG being underestimate. The result for iron ore compared to bauxite at dense case suggest the opposite, being the experimental data as underestimate, while trend suggests that the VG estimate will underestimate experimental data eventually due to steeper curvature. For Inagi sand compared to bauxite at loose case, the experimental data and VG estimate agree well.

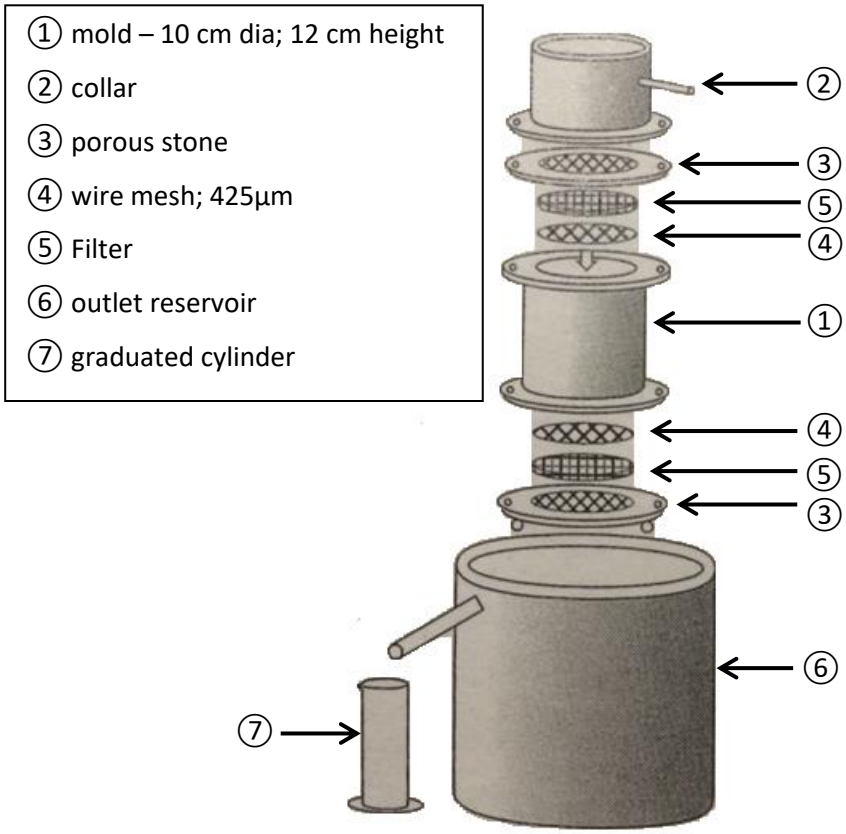

Fig. 4-1. Constant Head Apparatus (JIS A 1218)

Fig. 4-2. Specimen preparation of bauxite and Inagi sand for Standard Permeameter Test

Fig. 4-3. (Left) Front view of Permeameter test set-up at 12 cm head; (Right): Top view

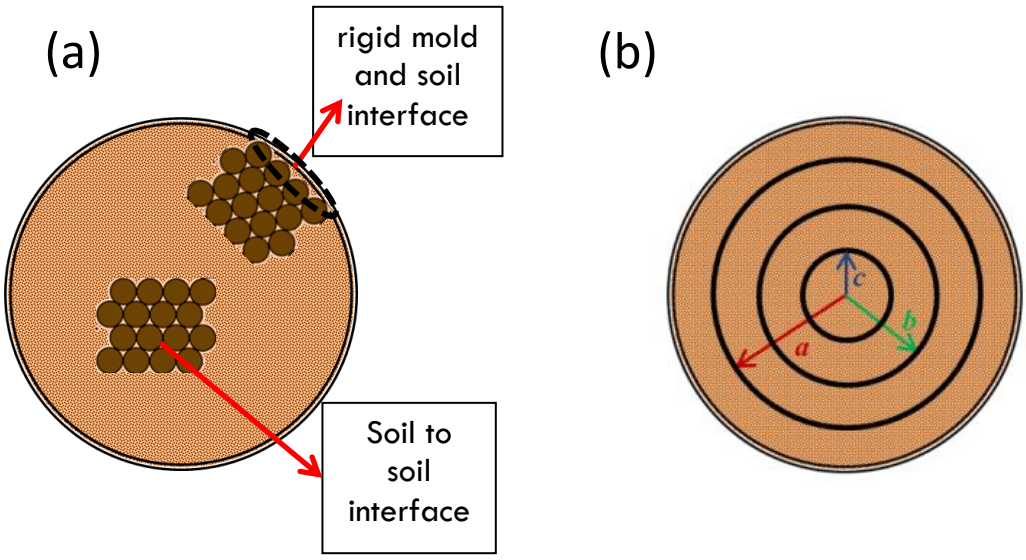

Fig. 4-4. (a) Cross Section Sketch of Mold with Specimen for Permeability Test;
(b) Cross section of Modified Permeameter Tests with cylindrical rings

Fig. 4-5. Modified Permeameter Apparatus with cylindrical rings

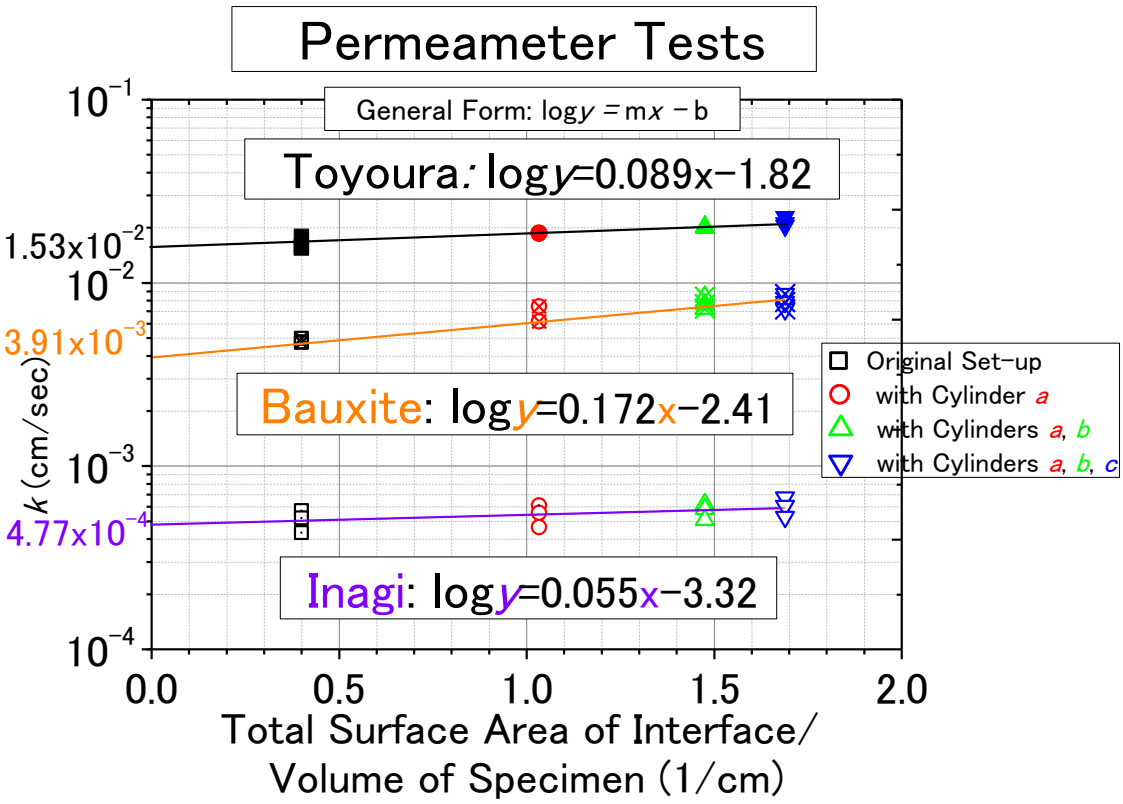

Fig. 4-6. *k* vs. interface effect of rigid mold and cylindrical rings parameter

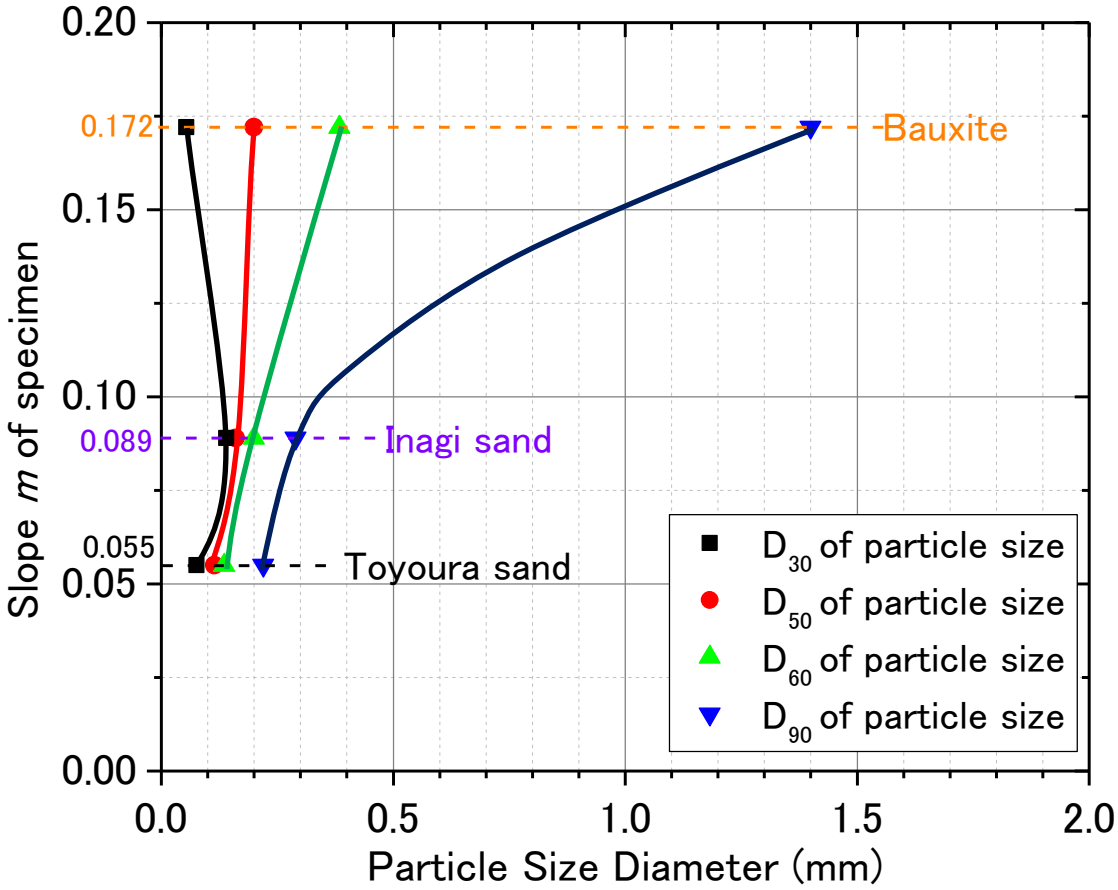

Fig. 4-7. Slope of *m* of specimen vs. Particle Size Diameter

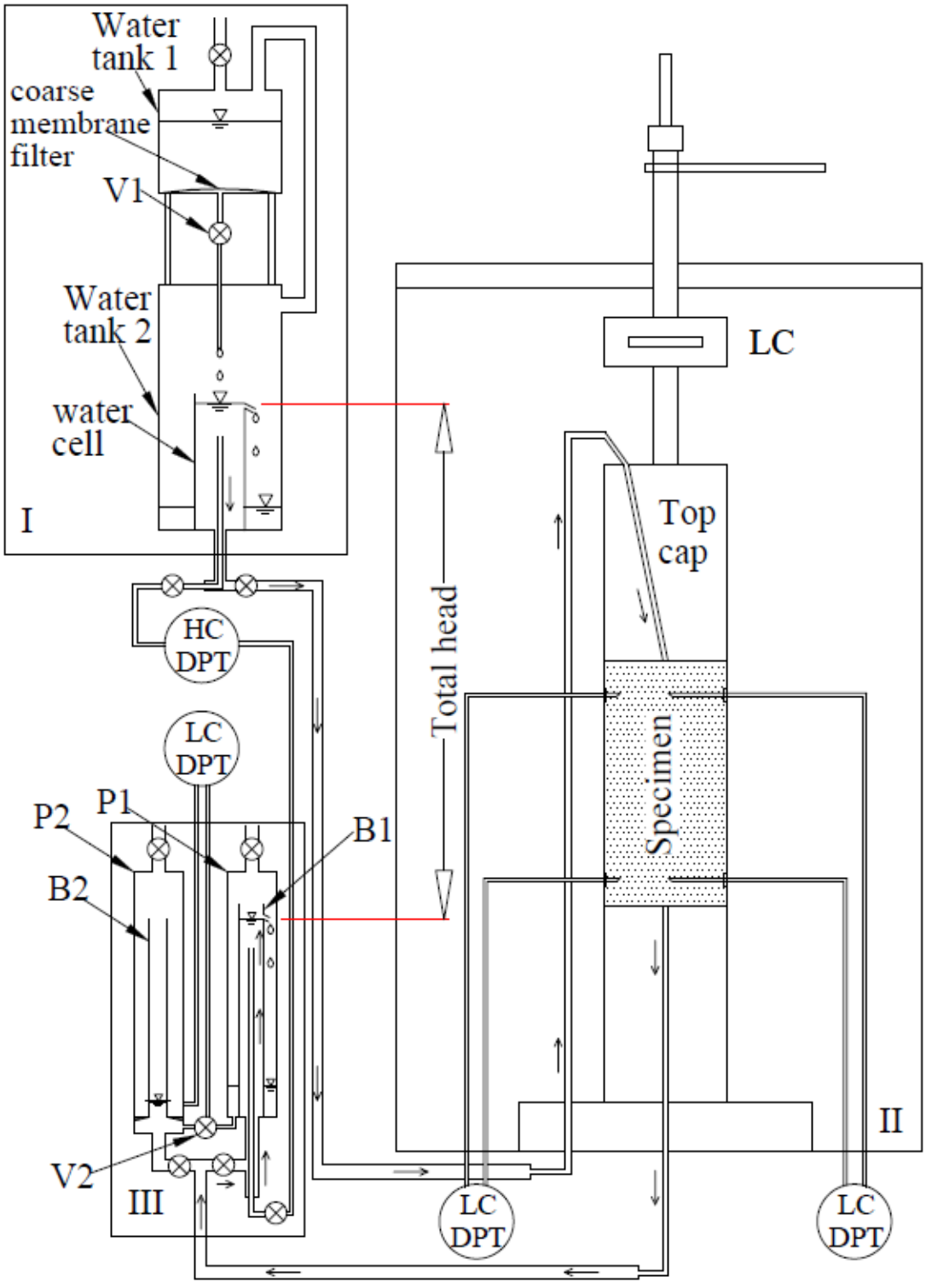

Fig. 4-8. Apparatus for Permeability Test with Local Pin-Type Sensors
(Modified from Wang, 2014)

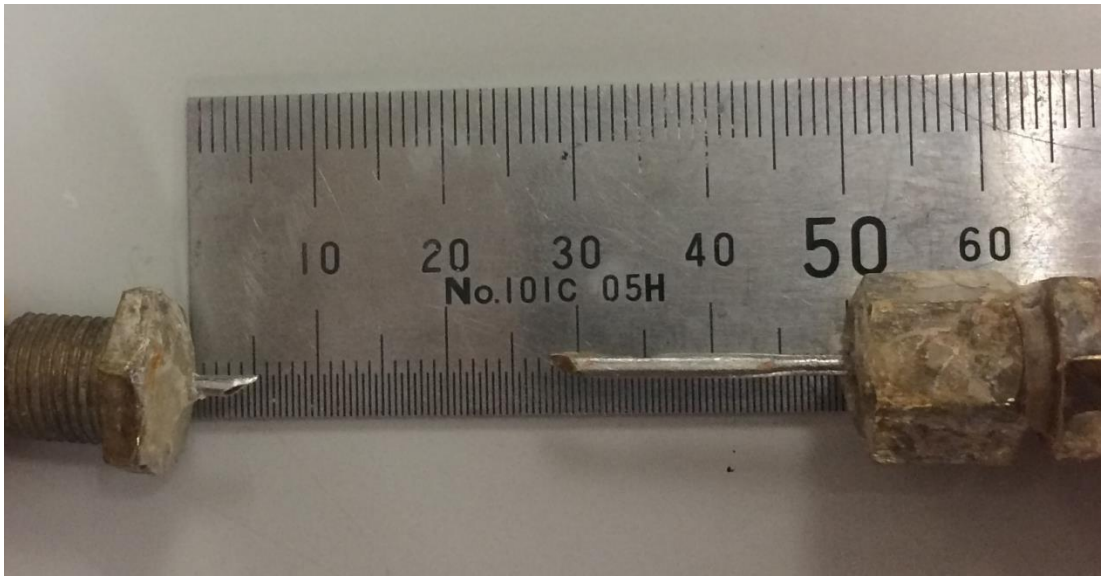

Fig. 4-9. Local Pin-Type Sensors pin lengths indicated in mm. Short pins (pin shown on the left) are 0.5 cm while long pins (pin shown on the right) are 2.0 cm.

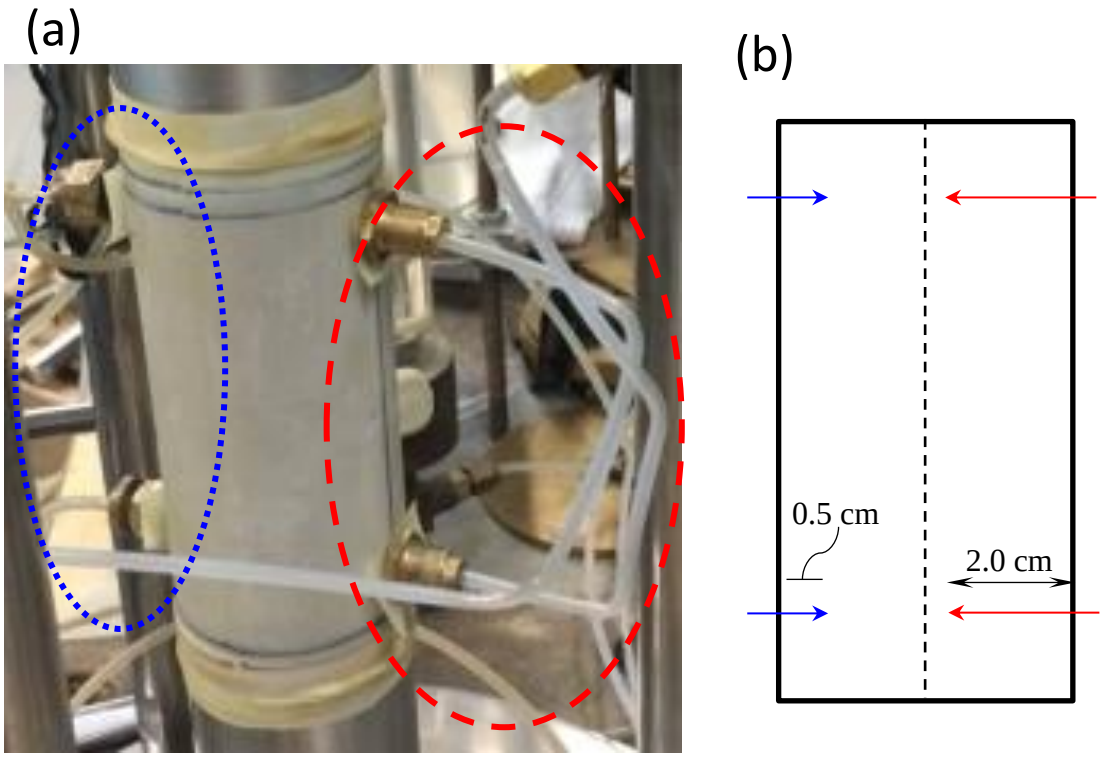

Fig. 4-10. Specimen placed on triaxial apparatus with two sets of local pin-type sensors (i.e. long and short) located on top and bottom of the specimen.

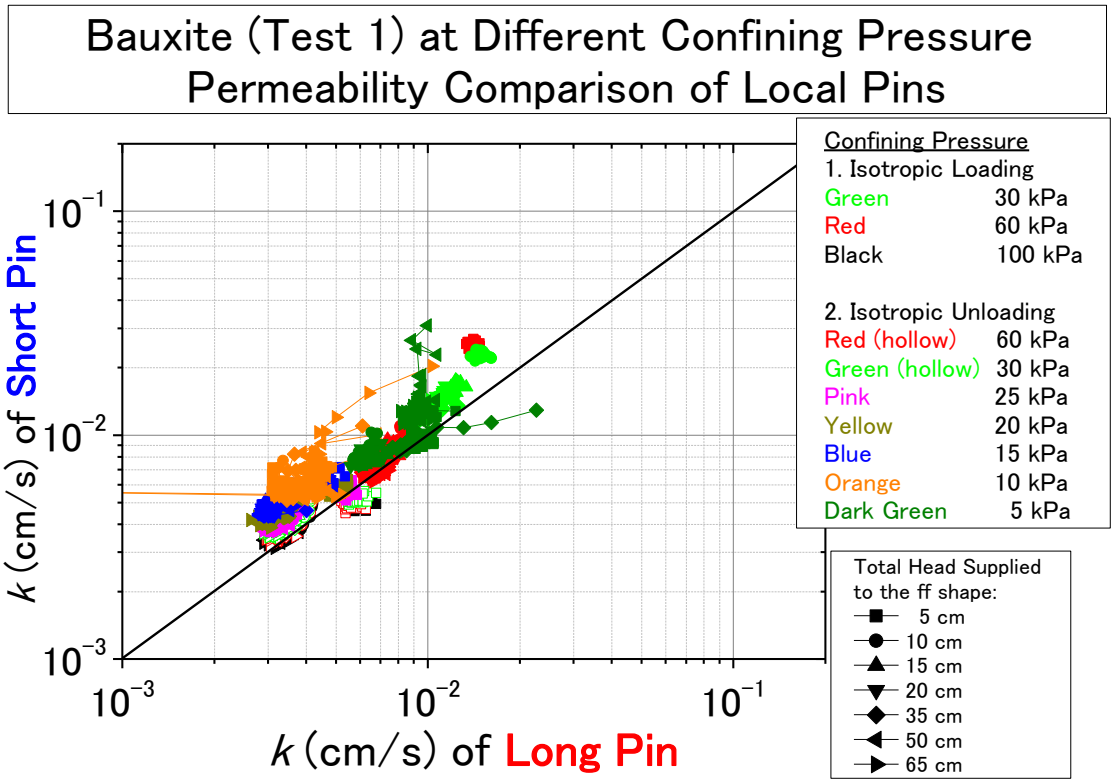

Fig. 4-11. Comparison of *k* values of long pins and short pins (bauxite)

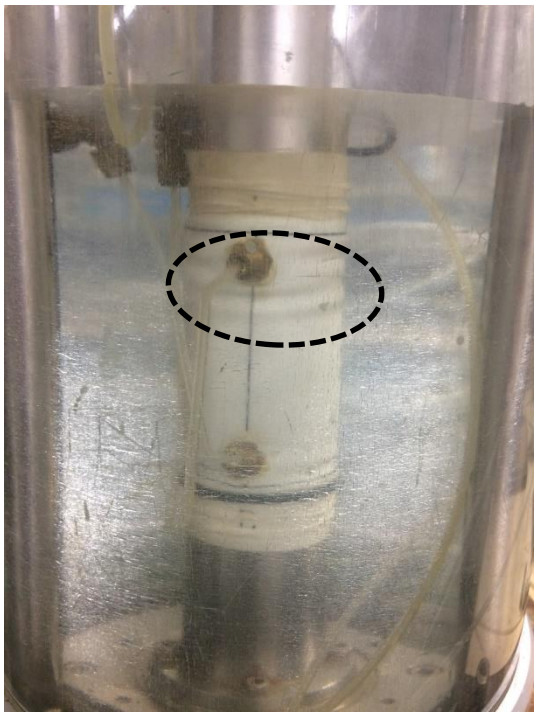

Fig. 4-12. Snapshot of specimen at 5 kPa showing membrane wrinkle (bauxite test 1 – saturated)

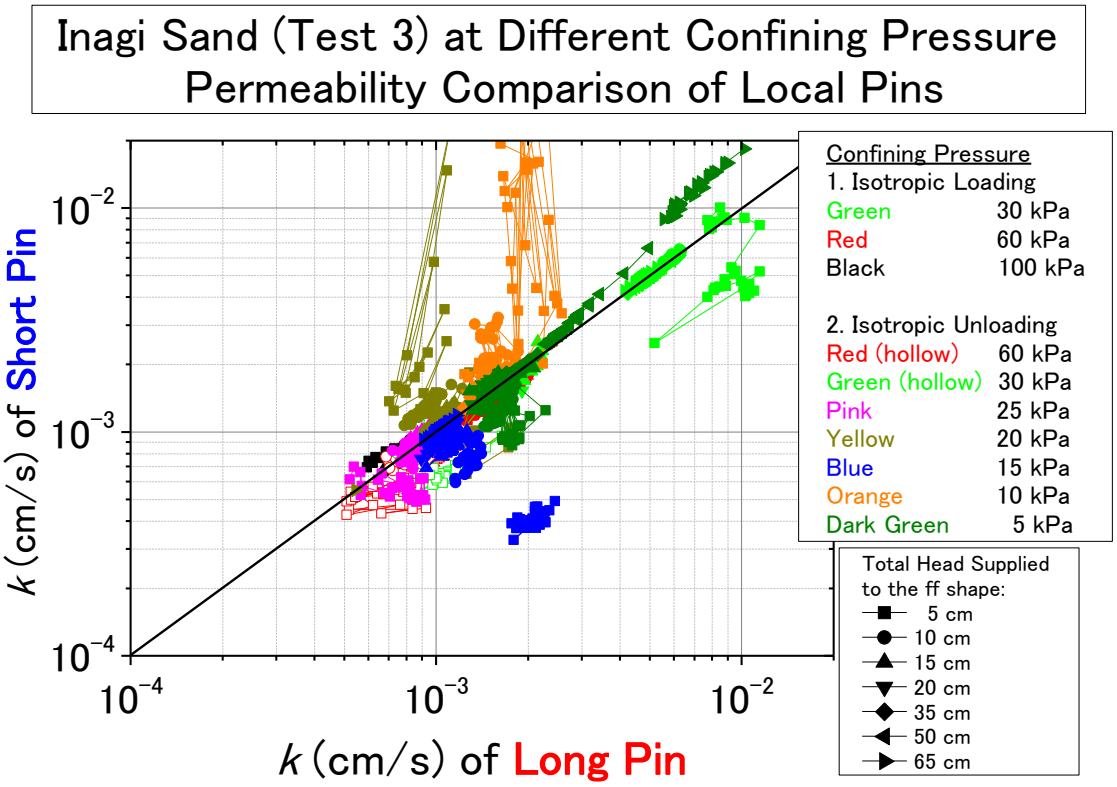

Fig. 4-13. Comparison of *k* values of long pins and short pins (Inagi sand)

Fig. 4-14. Snapshots of specimen at 20 kPa (left figure) and 10 kPa (right figure) showing membrane wrinkle (Inagi sand test 3 – saturated)

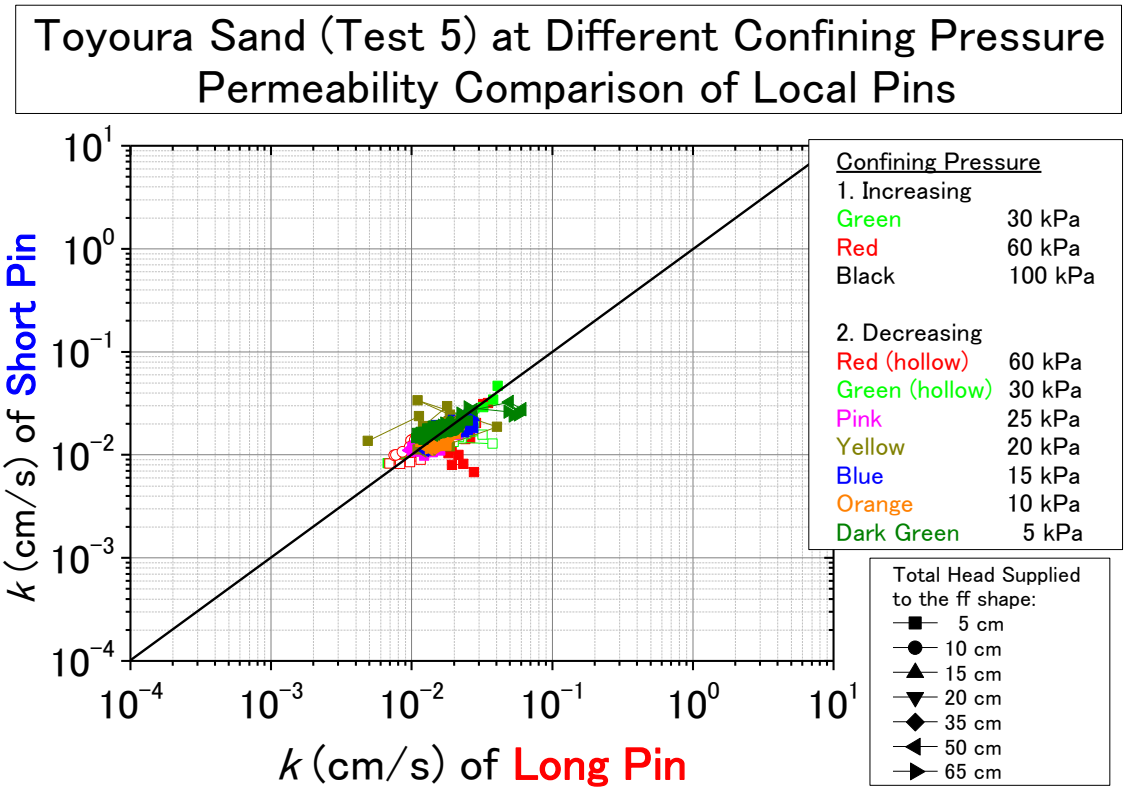

Fig. 4-15. Comparison of *k* values of long pins and short pins (Toyoura sand)

Fig. 4-16. Snapshot of specimen at 5 kPa showing membrane wrinkle
(Toyoura sand test 5 – saturated)

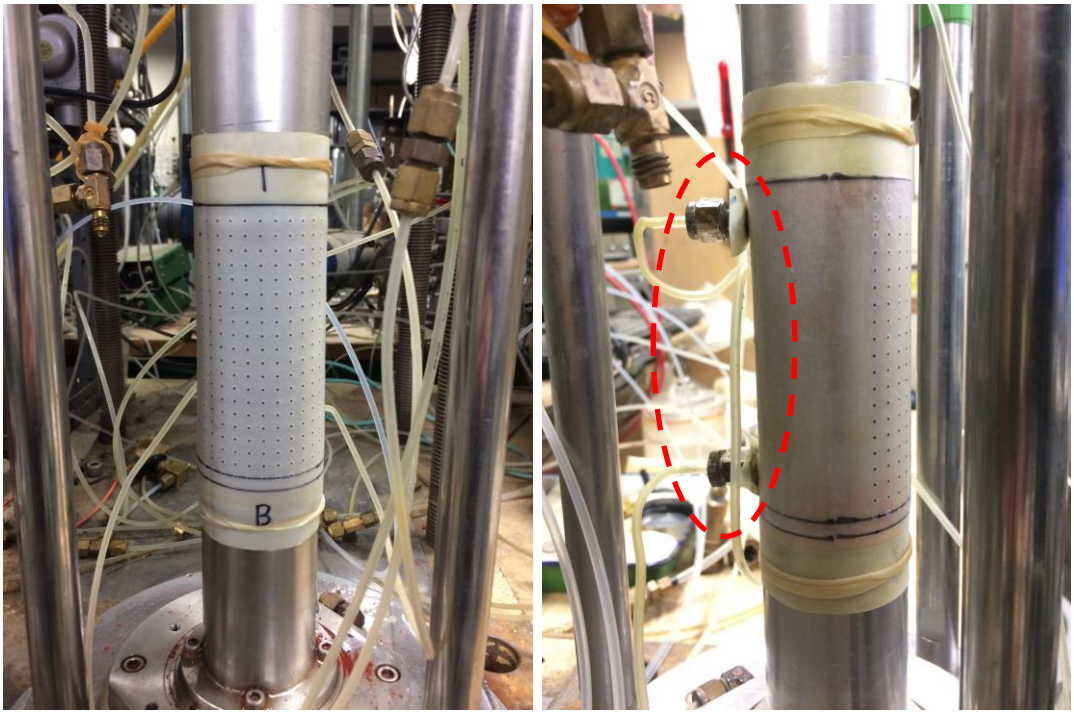

Fig. 4-17. Snapshots of bauxite tests with image analysis; front view (left figure), and side view (right figure) with local pin-type sensors (long pins)

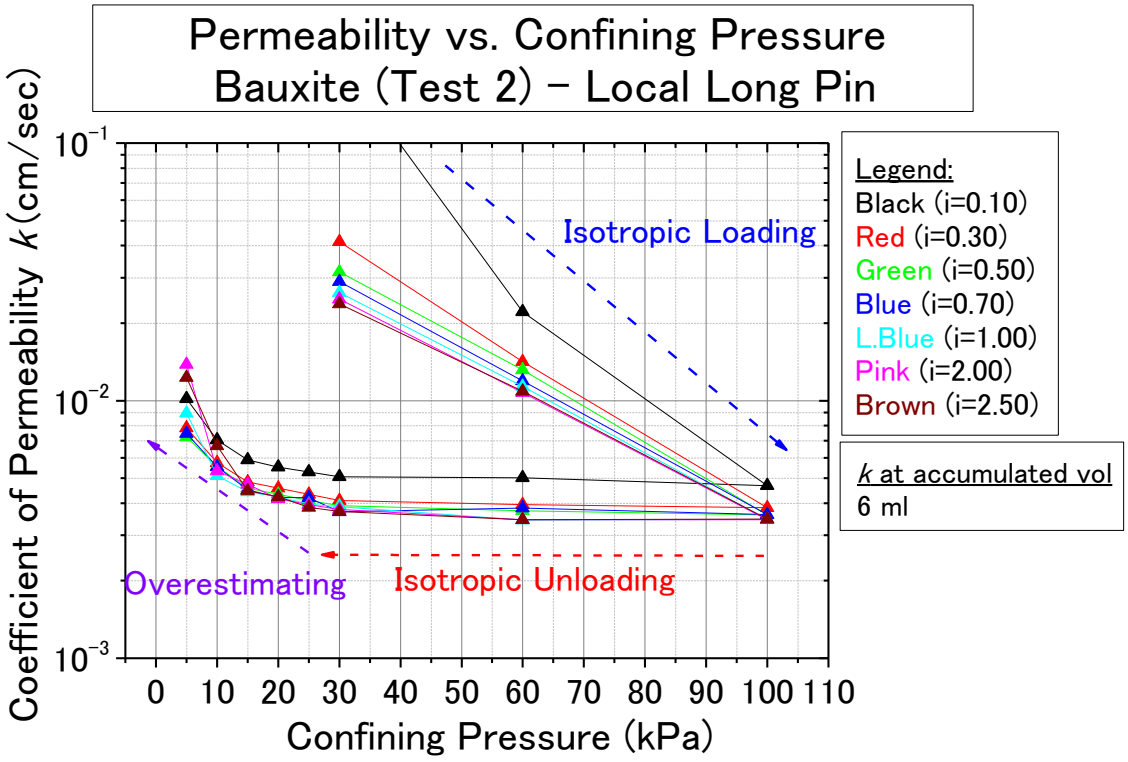

Fig. 4-18. *k* vs. Confining Pressure at different *i* (bauxite-test 2, long pin, saturated)

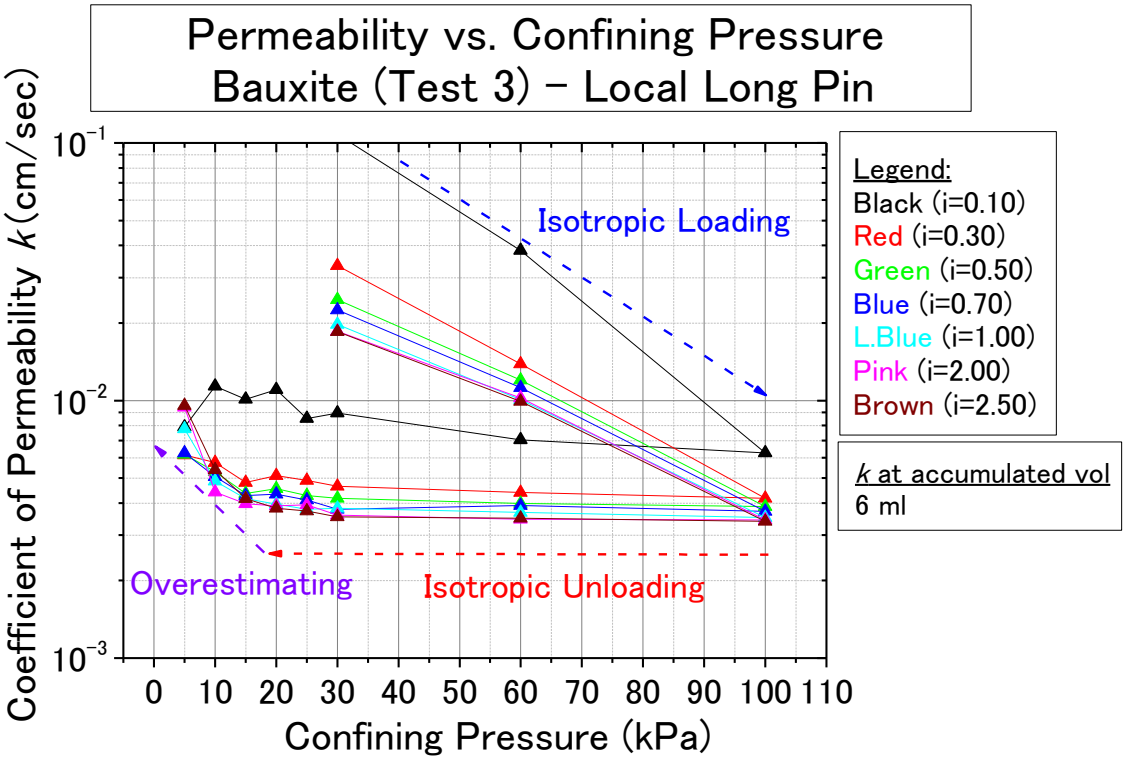

Fig. 4-19. *k* vs. Confining Pressure at different *i* (bauxite-test 3, long pin, saturated)

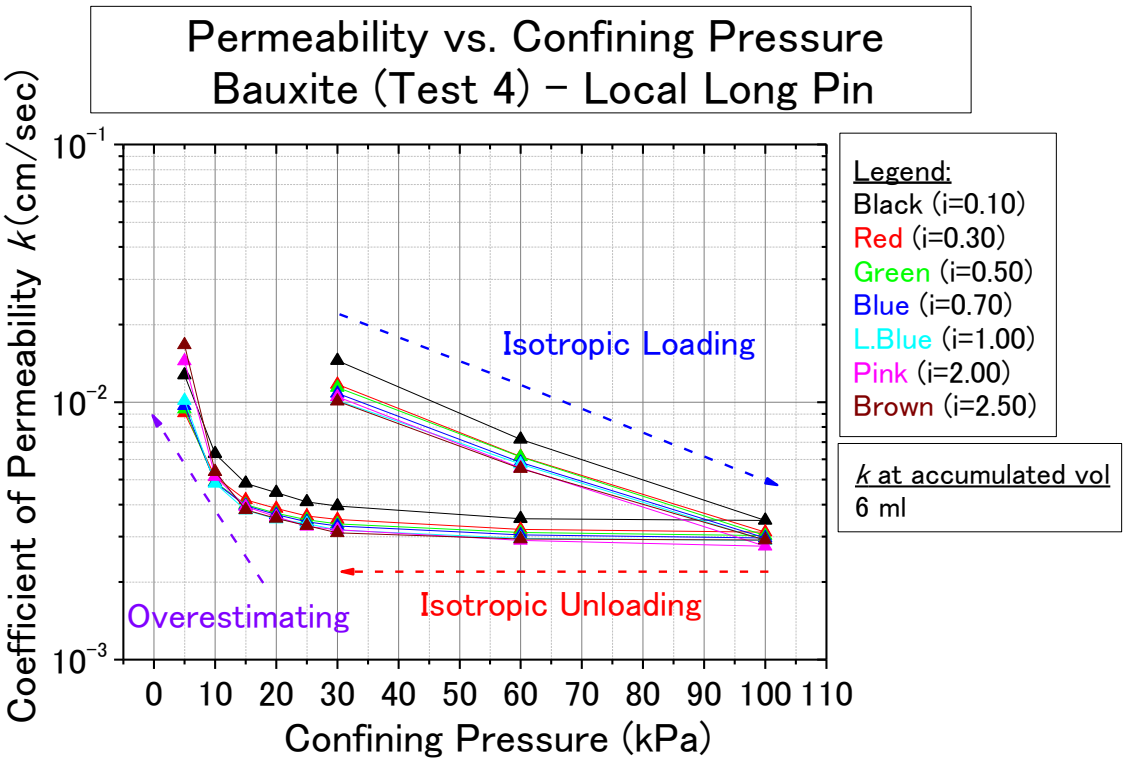

Fig. 4-20. *k* vs. Confining Pressure at different *i* (bauxite-test 4, long pin, saturated)

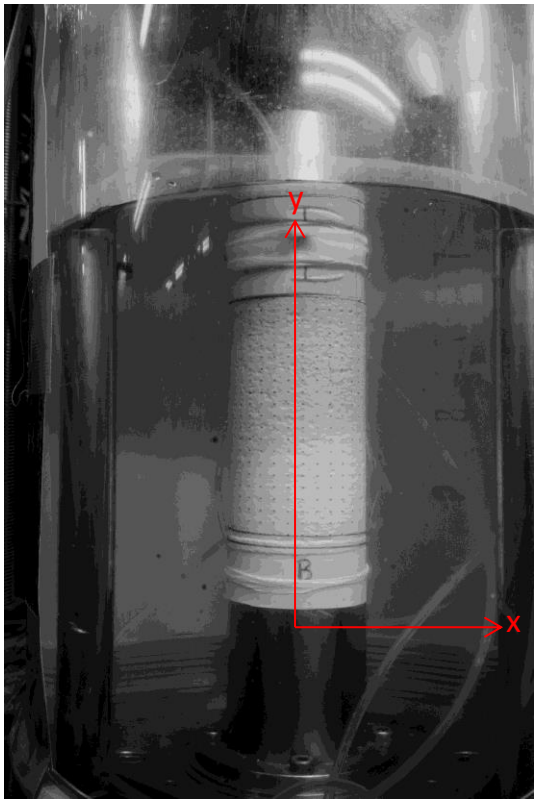

Fig. 4-21. Origin of coordinate axis

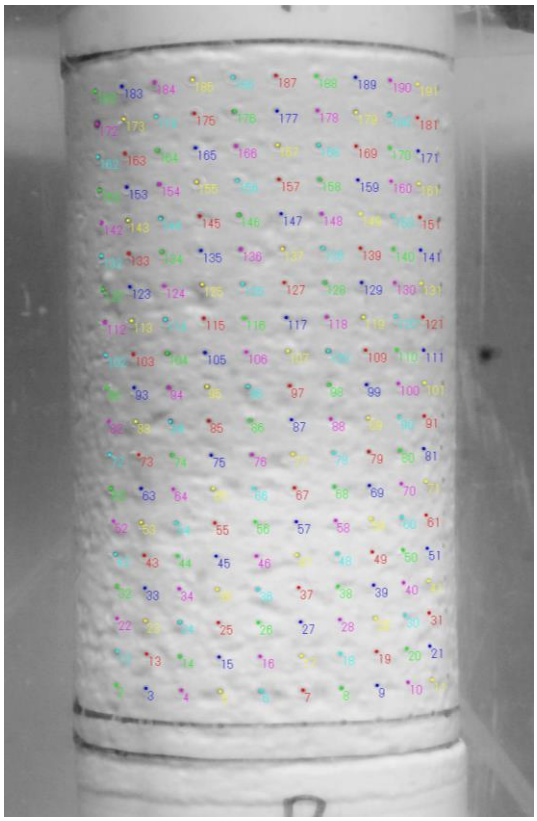

Fig. 4-22. Target dots marked manually and numbered before analyzing

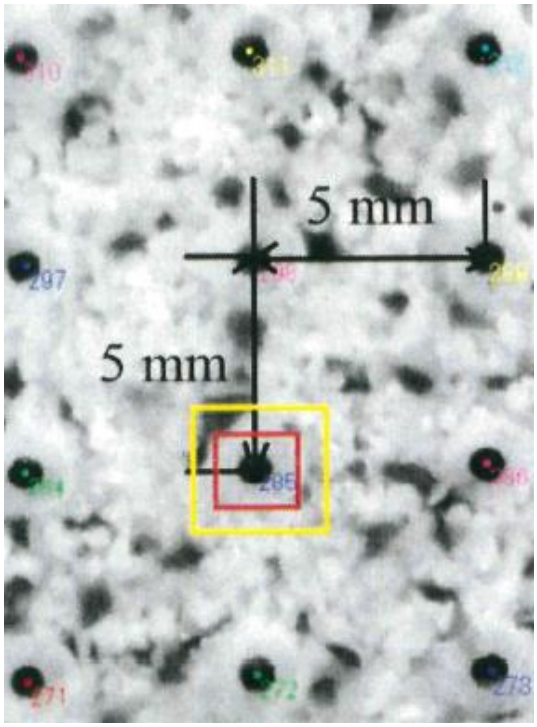

Fig. 4-23. Target dot enclosed by tracking squares (Zhao, 2017)

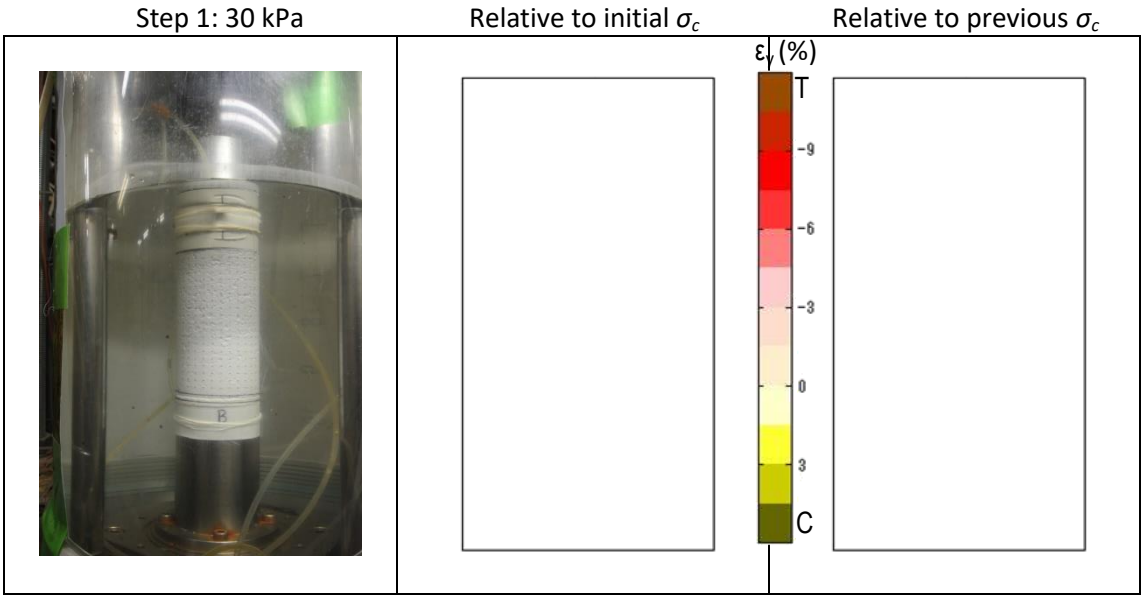

Fig. 4-24. Image Analysis of specimen at isotropic loading σ_c = 30 kPa (bauxite–test 2, saturated)

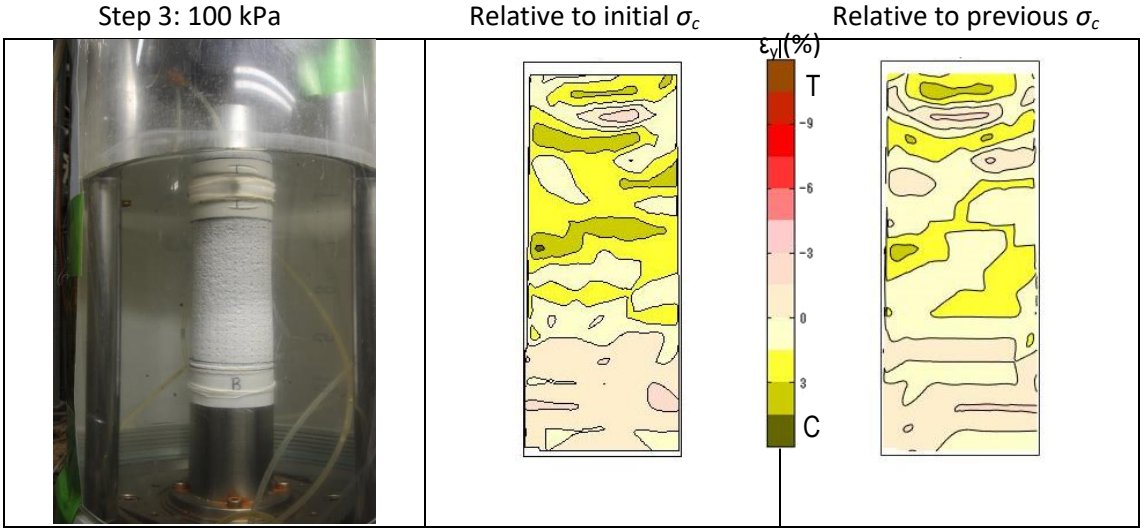

Fig. 4-25. Images of specimen at isotropic loading σ_c = 100 kPa (bauxite–test 2, saturated)

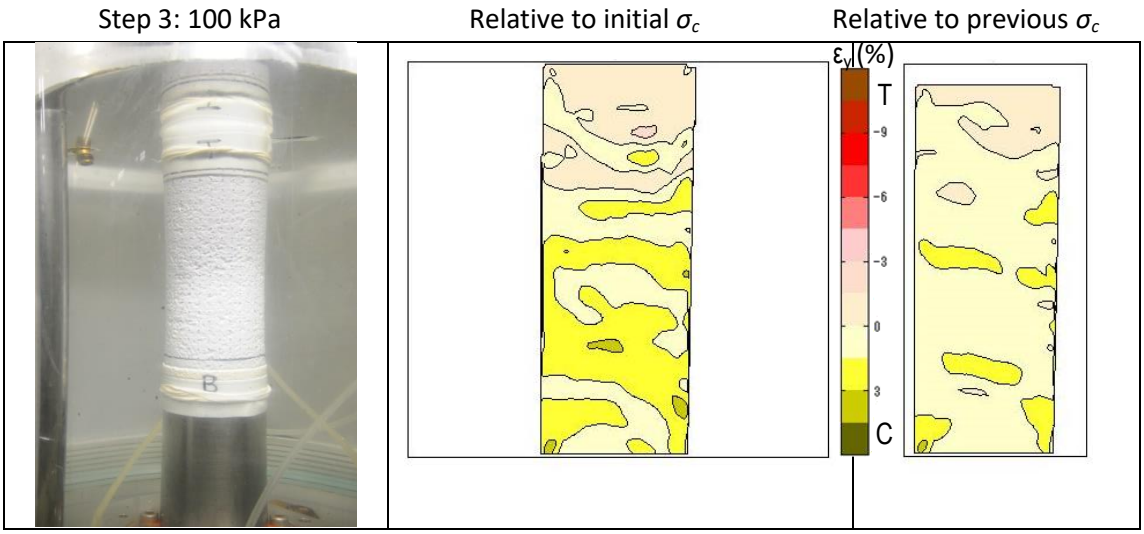

Fig. 4-26. Images of specimen at isotropic loading σ_c = 100 kPa (bauxite–test 3, saturated)

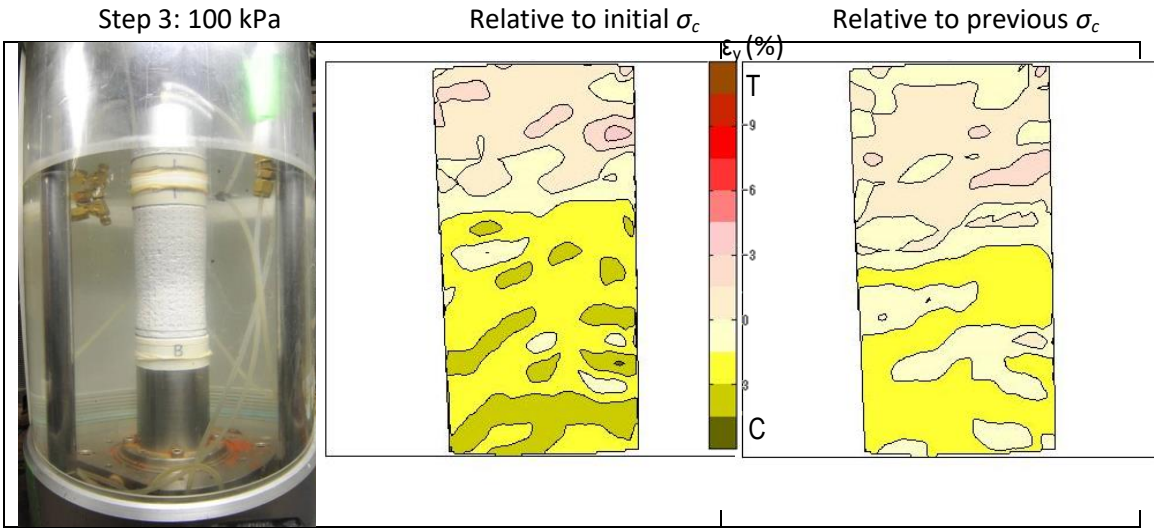

Fig. 4-27. Images of specimen at isotropic loading σ_c = 100 kPa (bauxite–test 4, saturated)

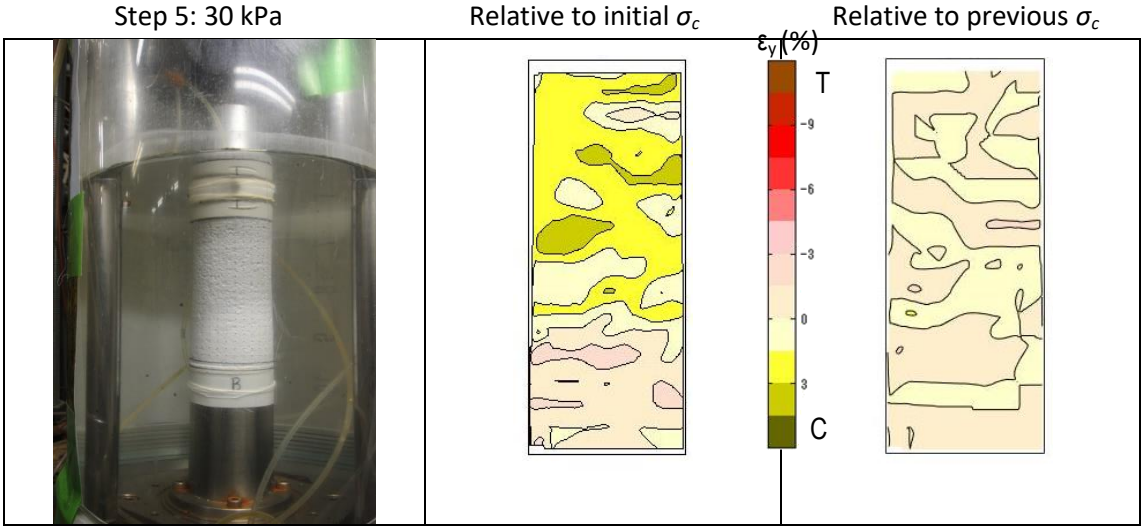

Fig. 4-28. Images of specimen at isotropic unloading σ_c = 30 kPa (bauxite–test 2, saturated)

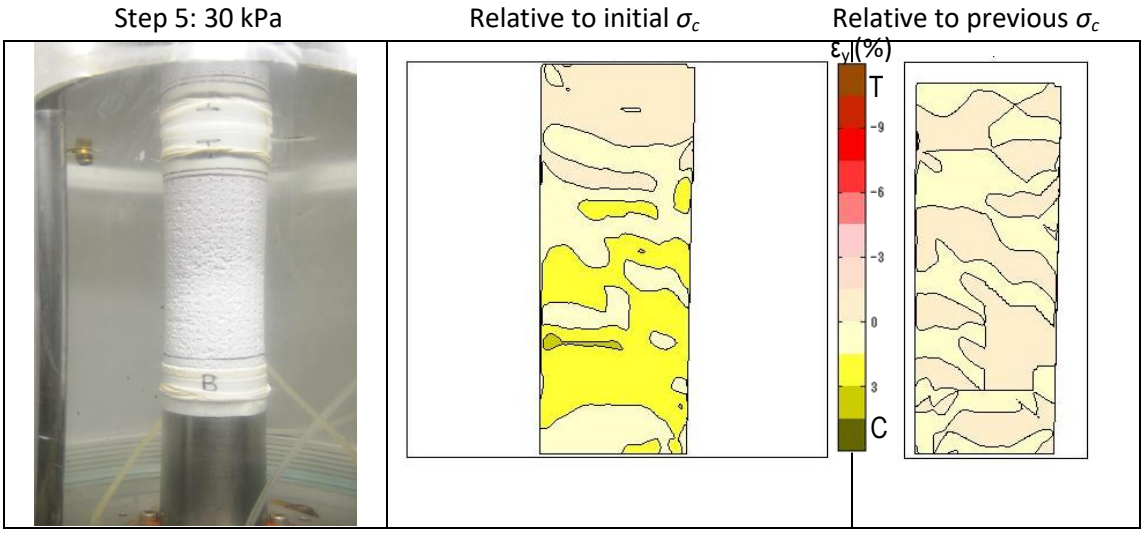

Fig. 4-29. Images of specimen at isotropic unloading σ_c = 30 kPa (bauxite–test 3, saturated)

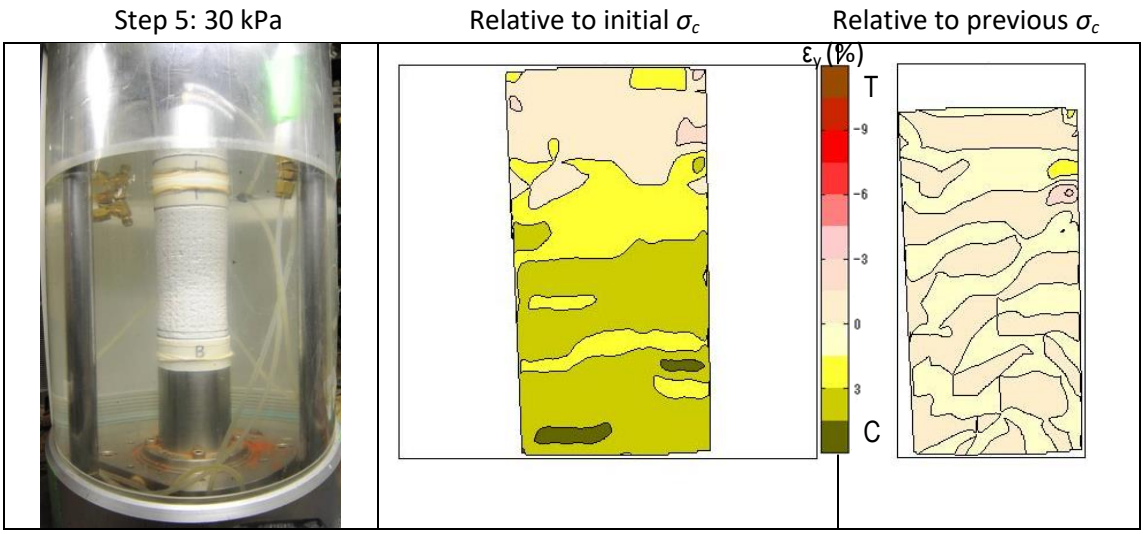

Fig. 4-30. Images of specimen at isotropic unloading σ_c = 30 kPa (bauxite–test 4, saturated)

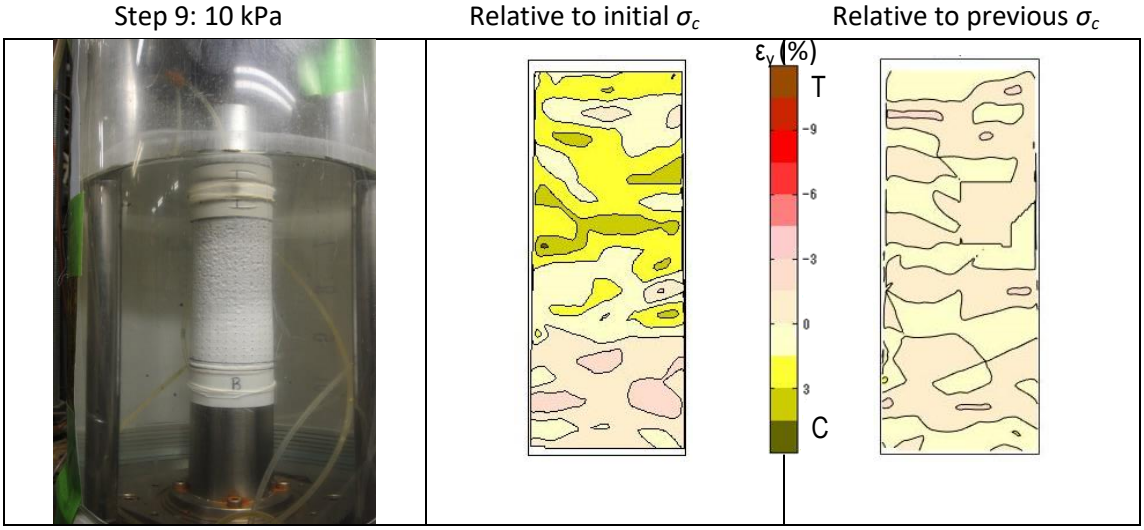

Fig. 4-31. Images of specimen at isotropic unloading σ_c = 10 kPa (bauxite–test 2, saturated)

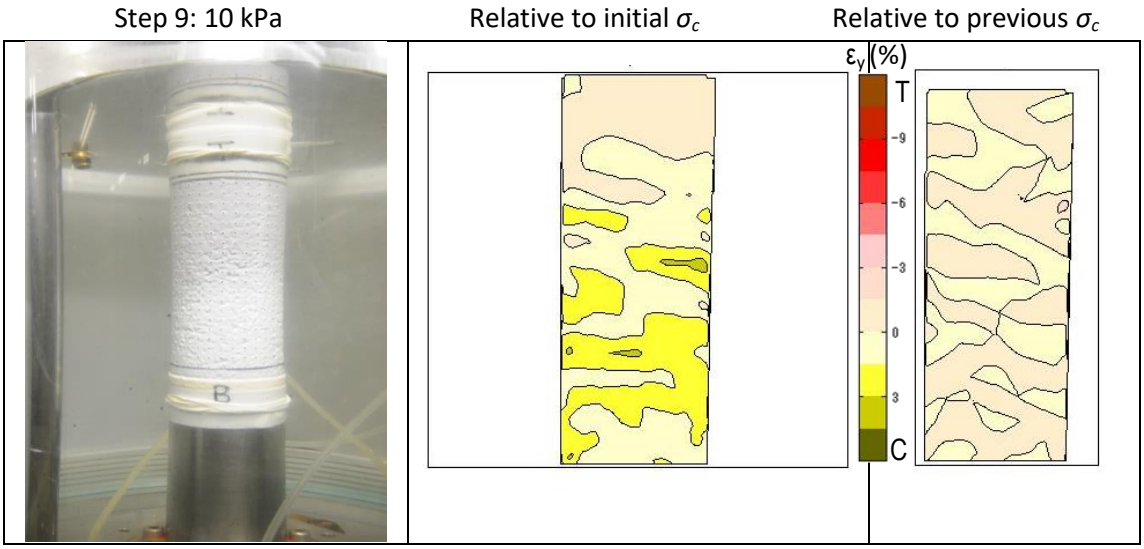

Fig. 4-32. Images of specimen at isotropic unloading σ_c = 10 kPa (bauxite–test 3, saturated)

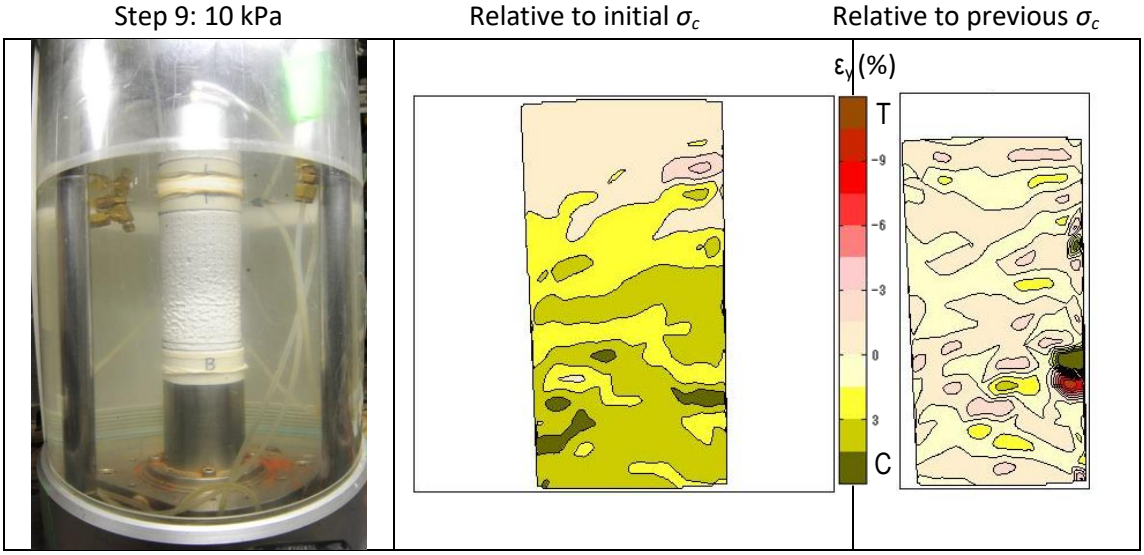

Fig. 4-33. Images of specimen at isotropic unloading σ_c = 10 kPa (bauxite–test 4, saturated)

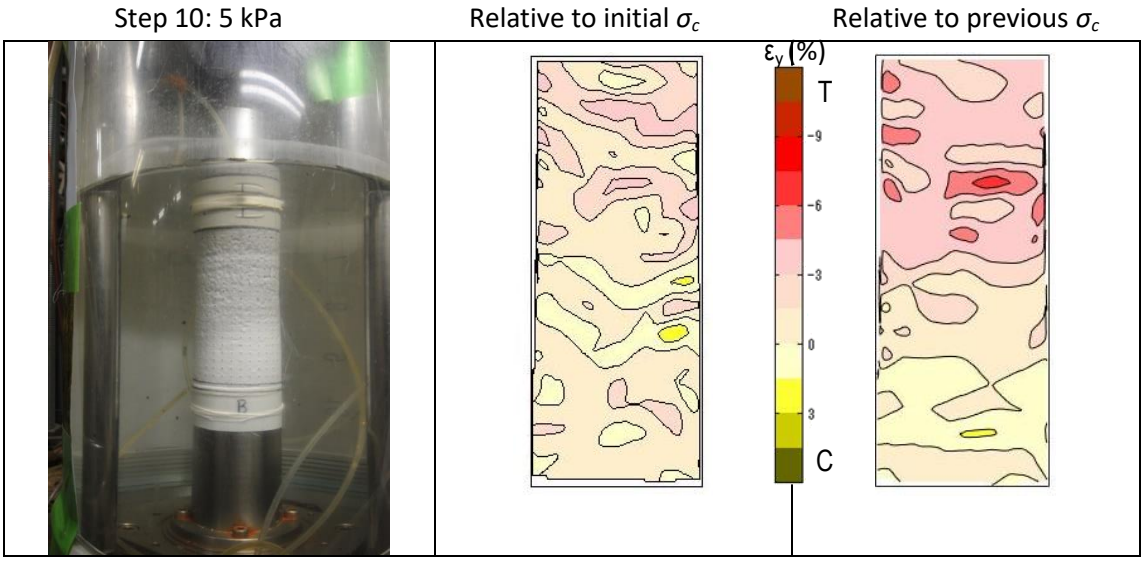

Fig. 4-34. Images of specimen at isotropic unloading σ_c = 5 kPa (bauxite–test 2, saturated)

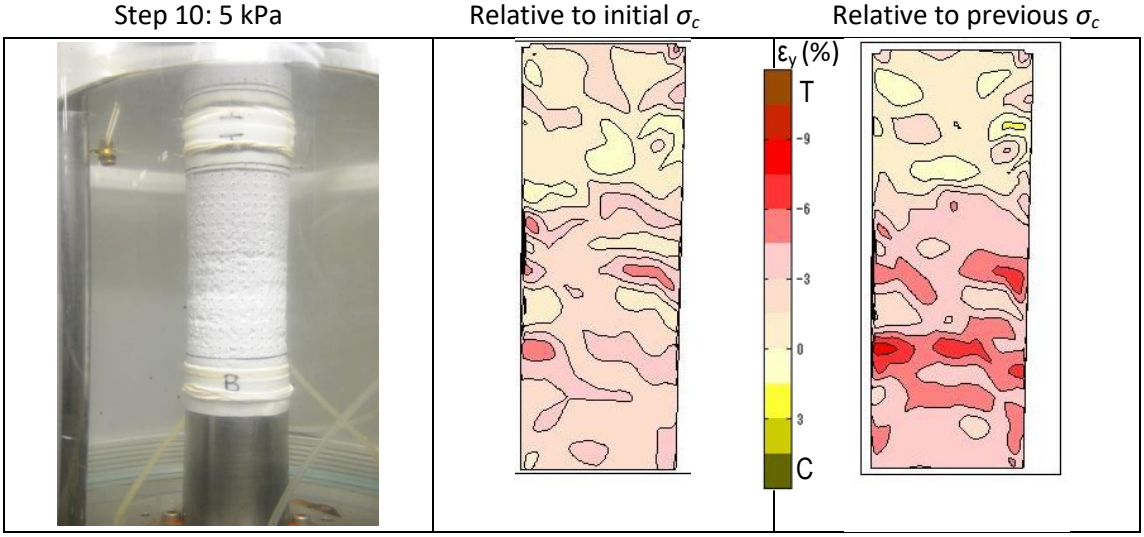

Fig. 4-35. Images of specimen at isotropic unloading σ_c = 5 kPa (bauxite–test 3, saturated)

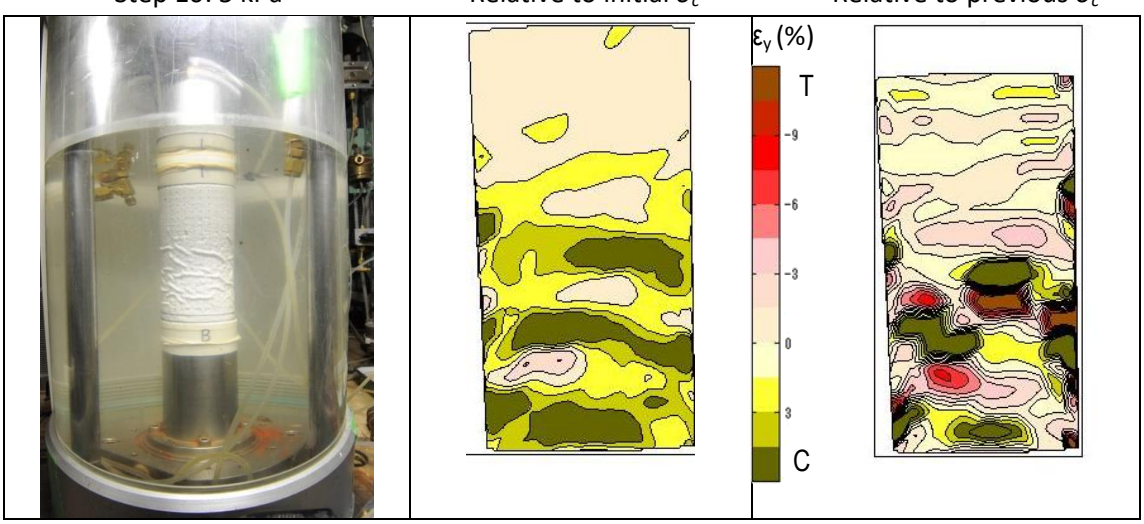

Fig. 4-36. Images of specimen at isotropic unloading σ_c = 5 kPa (bauxite–test 4, saturated)

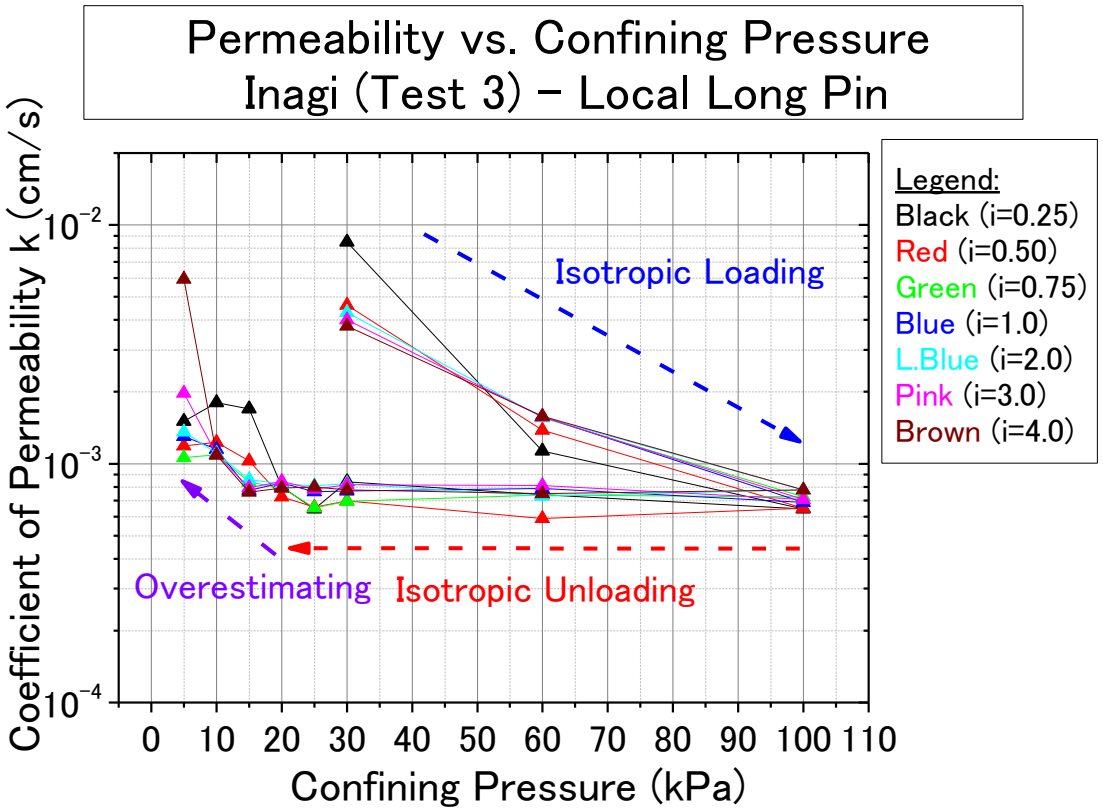

Fig. 4-37. *k* vs. Confining Pressure at different *i* (Inagi sand-test 3, long pin, saturated)

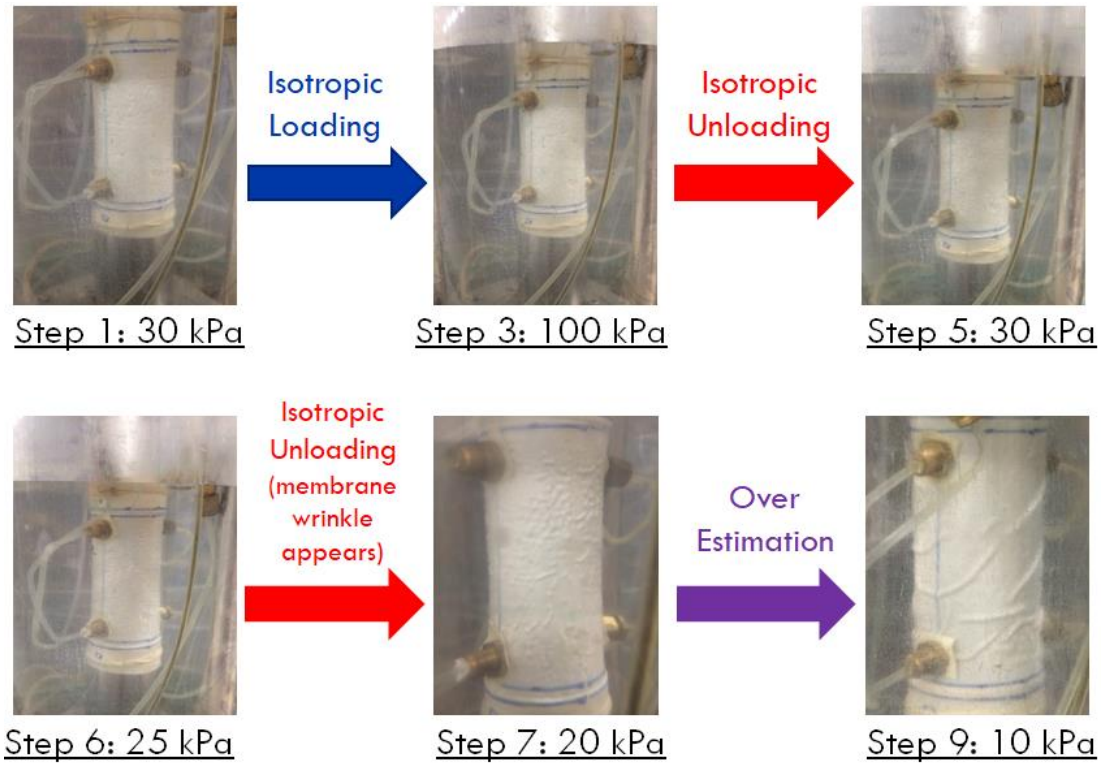

Fig. 4-38. Snapshots of rubber membrane showing the development of membrane wrinkle (Inagi sand-test 3, long pin, saturated)

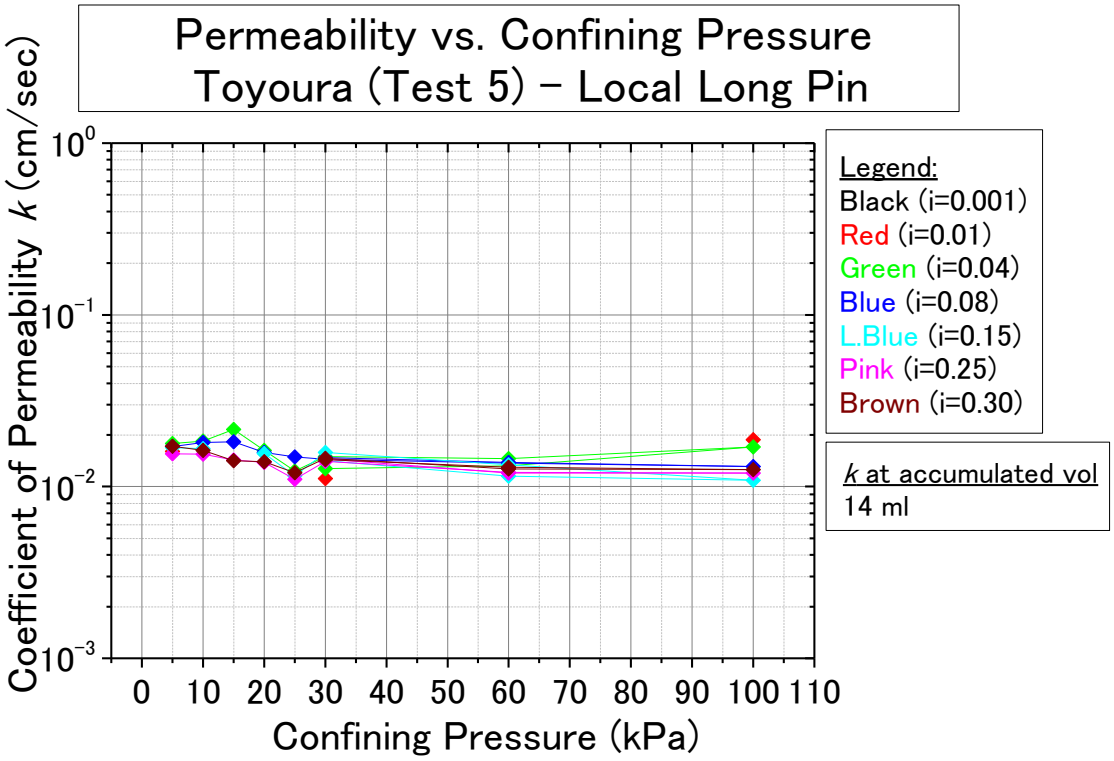

Fig. 4-39. *k* vs. Confining Pressure at different *i* (Toyoura sand-test 5, long pin, saturated)

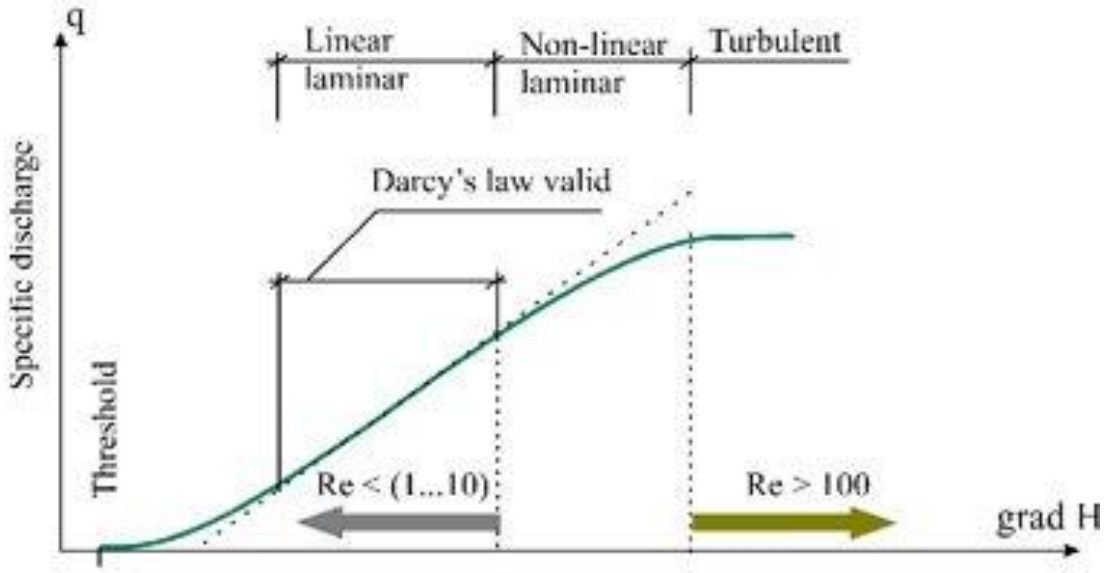

Fig. 4-40. Range of Validity of Darcy's Law (Bear, 1972)

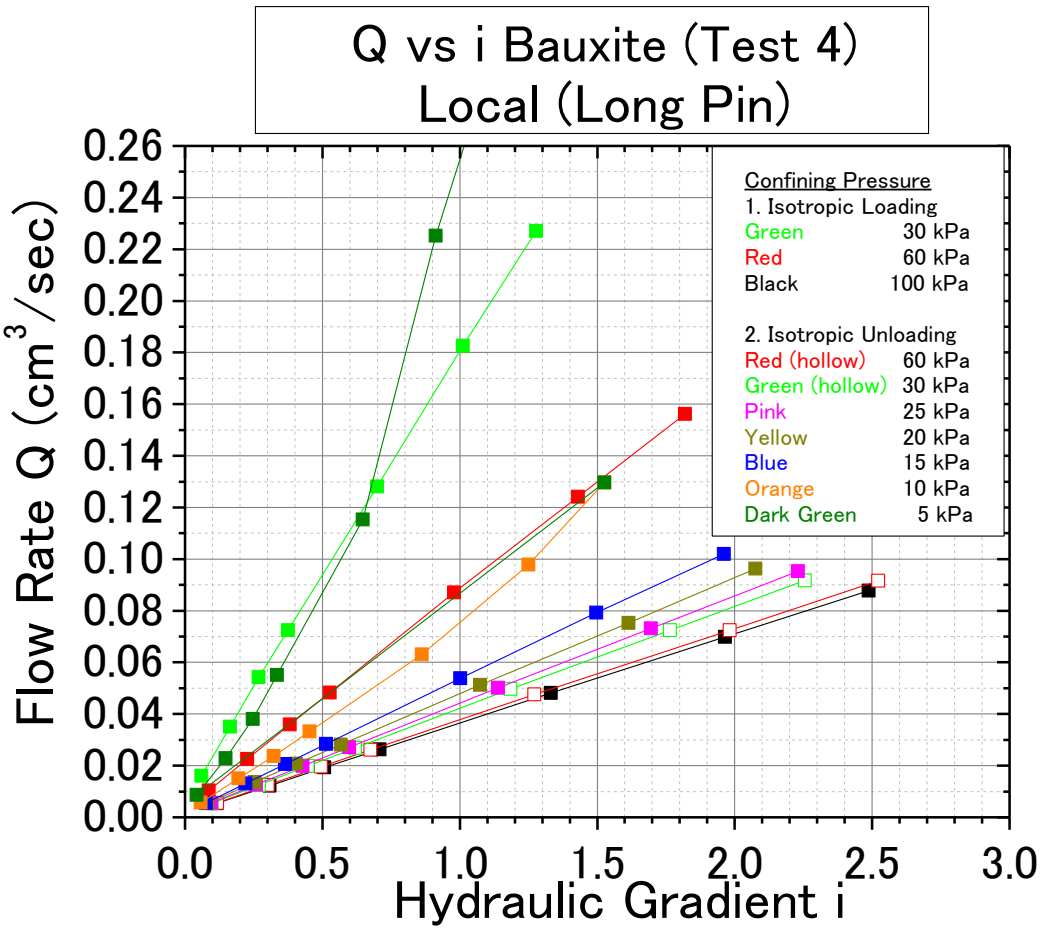

Fig. 4-41. *Q* vs *i* (bauxite- test 4, long pin, saturated)

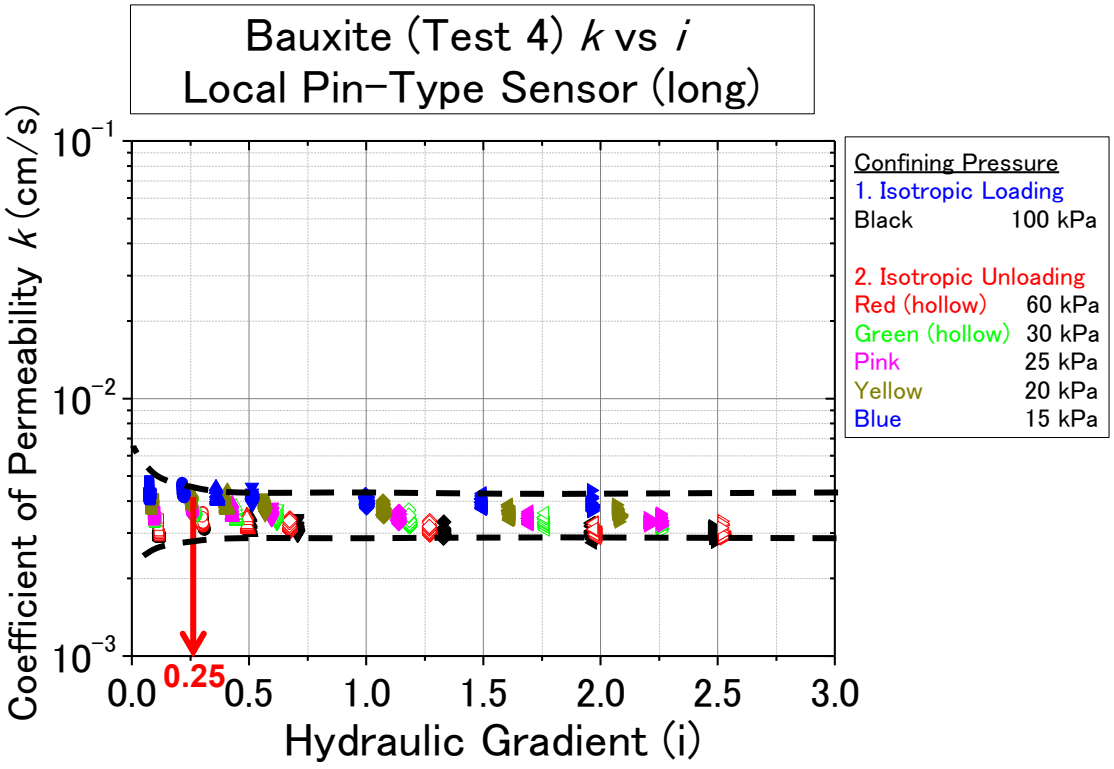

Fig. 4-42. *k* vs *i* (bauxite-test 4, long pin, saturated)

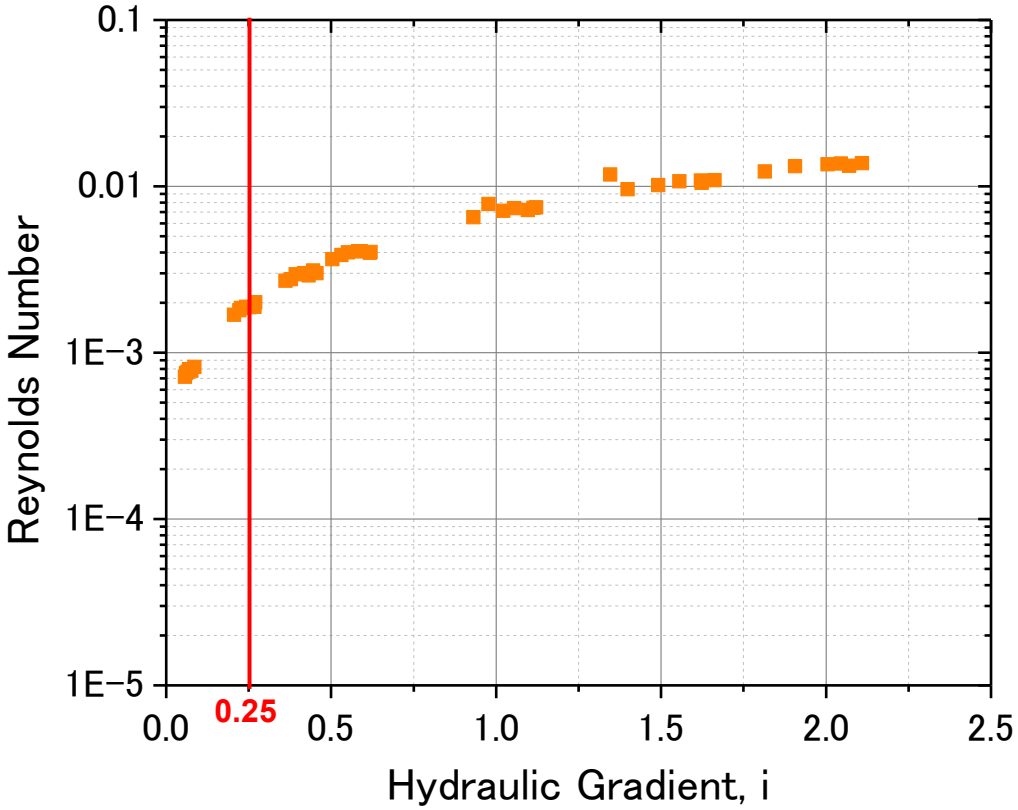

Fig. 4-43. Re vs *i* (bauxite-test 4, long pin, saturated)

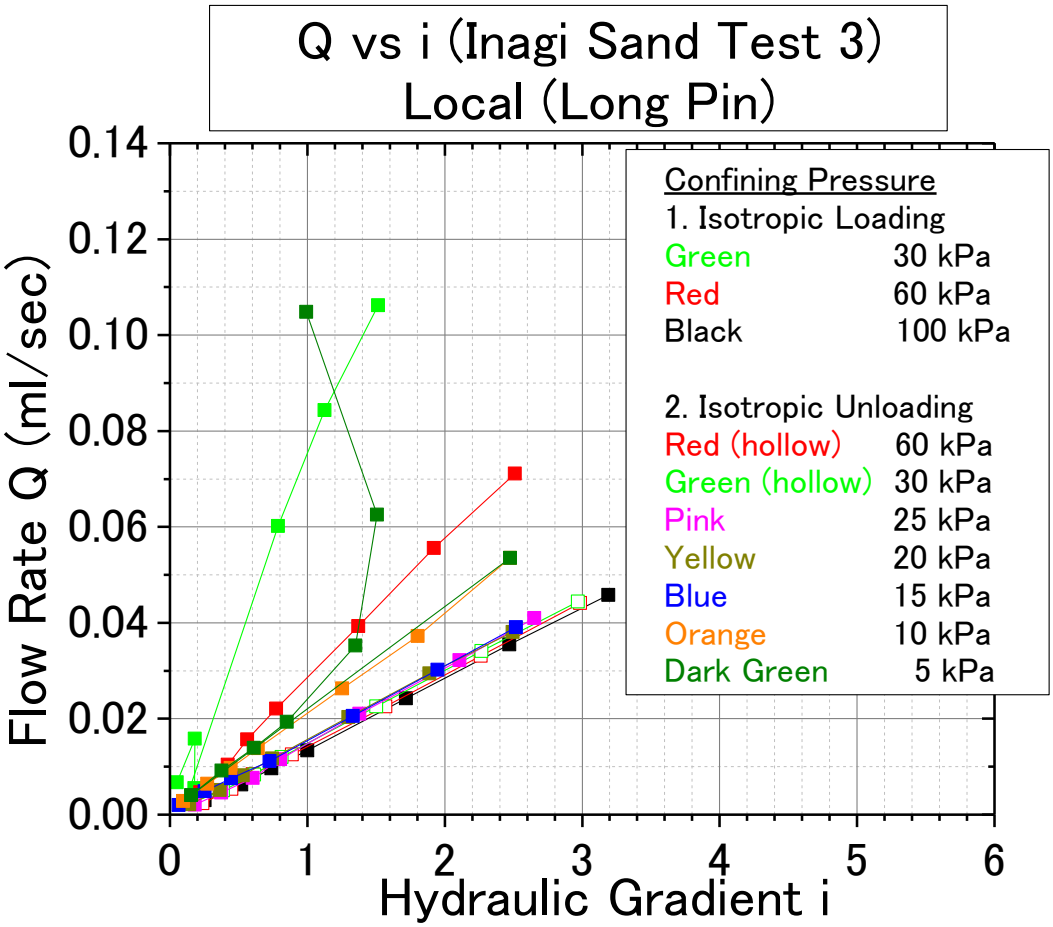

Fig. 4-44. *Q* vs *i* (Inagi sand- test 3, long pin, saturated)

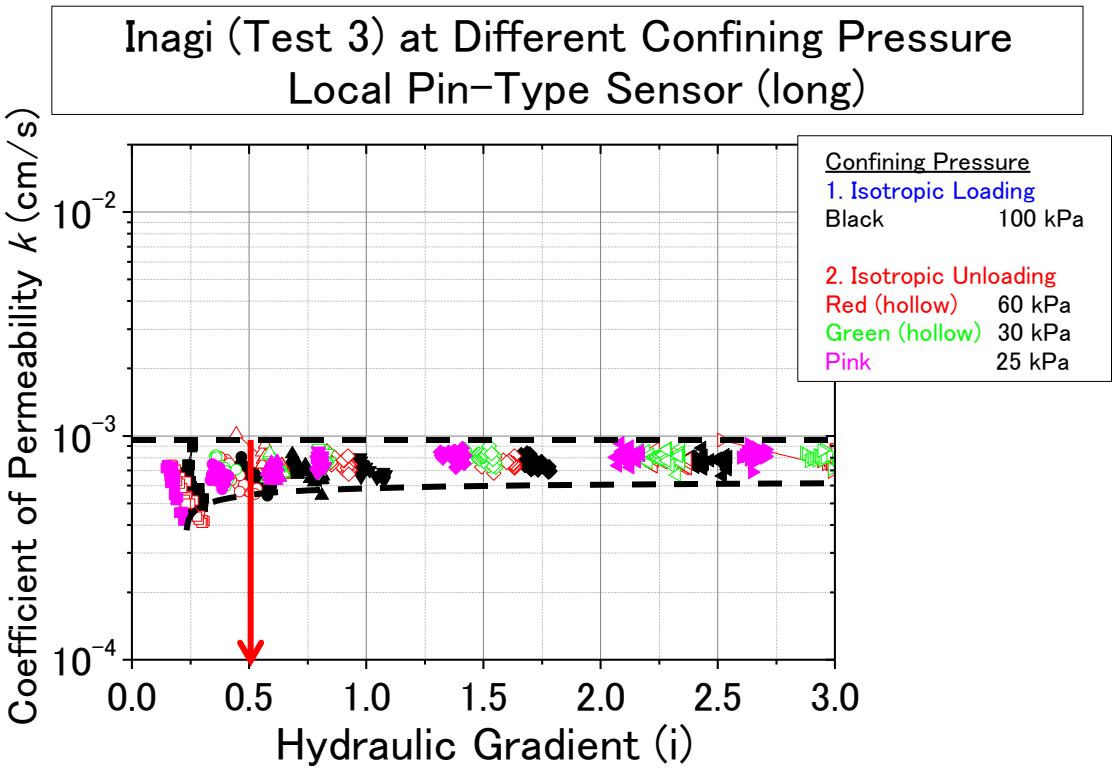

Fig. 4-45. *k* vs *i* (Inagi sand-test 3, long pin, saturated)

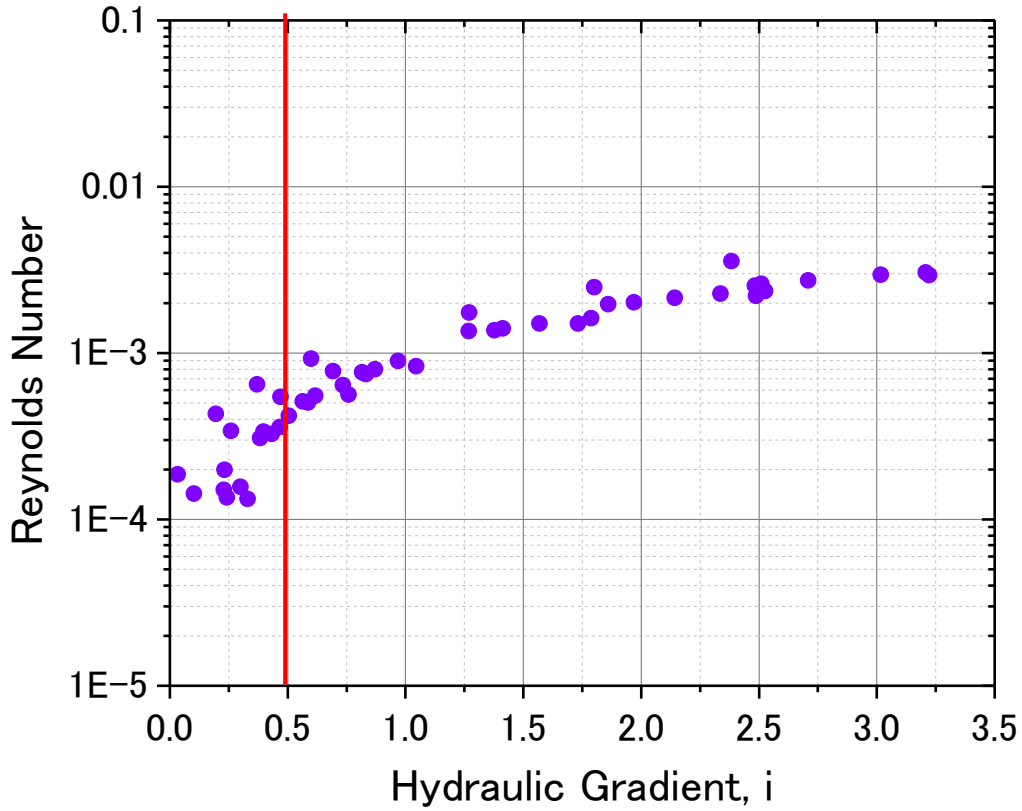

Fig. 4-46. Re vs *i* (Inagi sand-test 3, long pin, saturated)

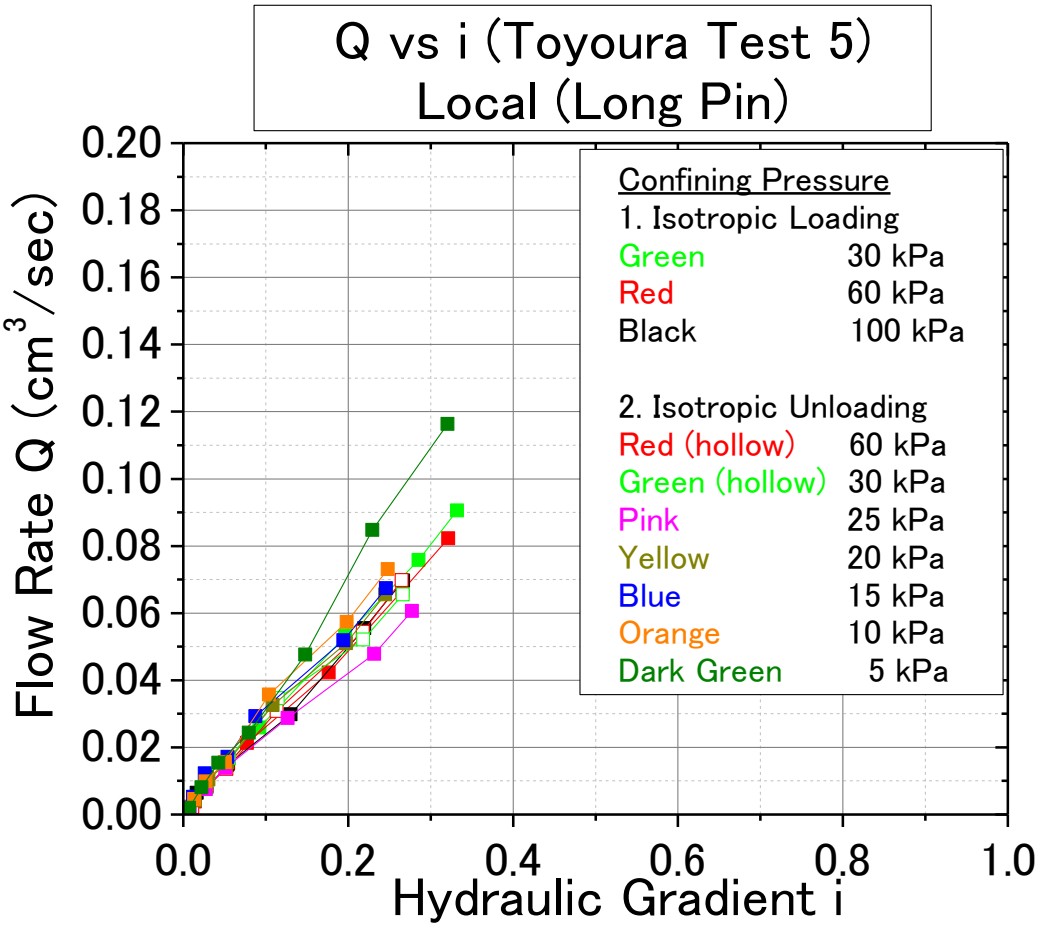

Fig. 4-47. *Q* vs *i* (Toyoura sand- test 5, long pin, saturated)

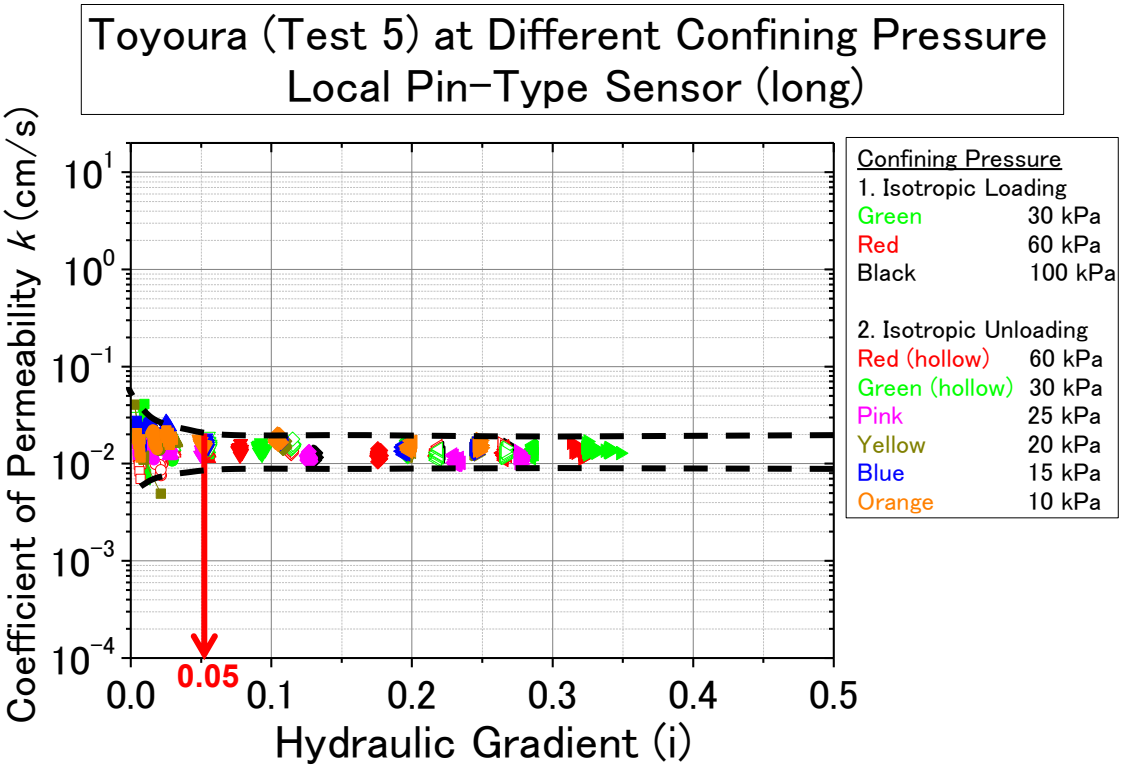

Fig. 4-48. *k* vs *i* (Toyoura sand-test 5, long pin, saturated)

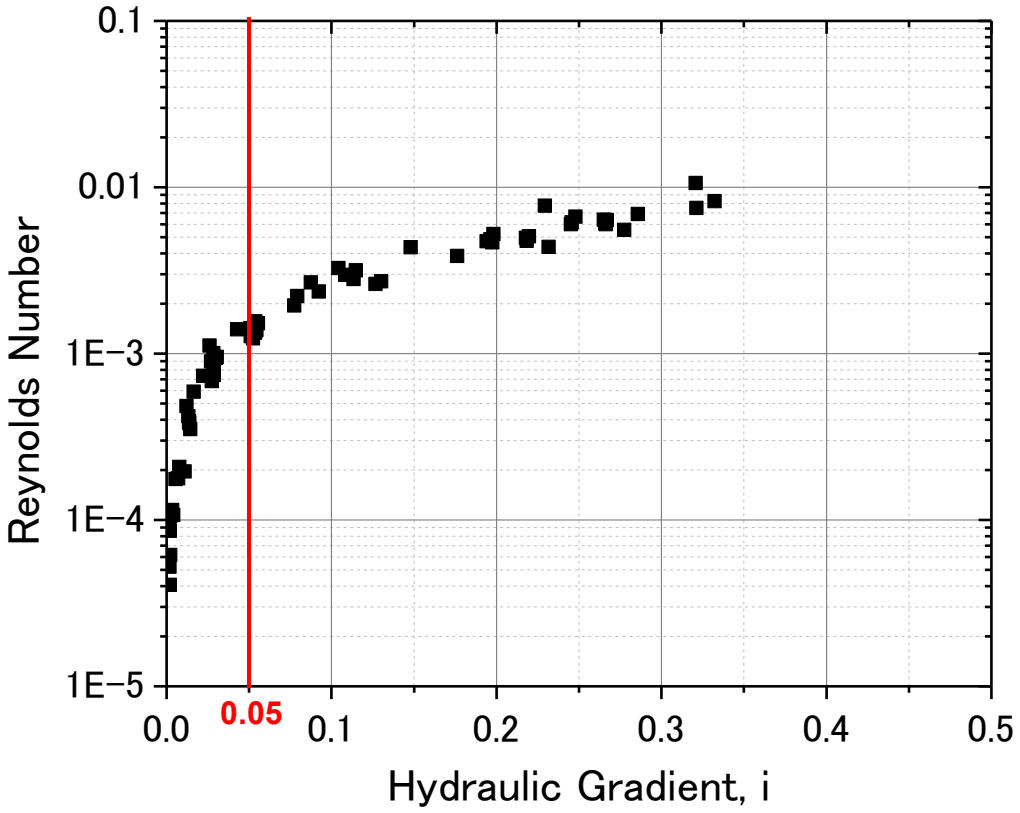

Fig. 4-49. Re vs *i* (Toyoura sand-test 5, long pin, saturated)

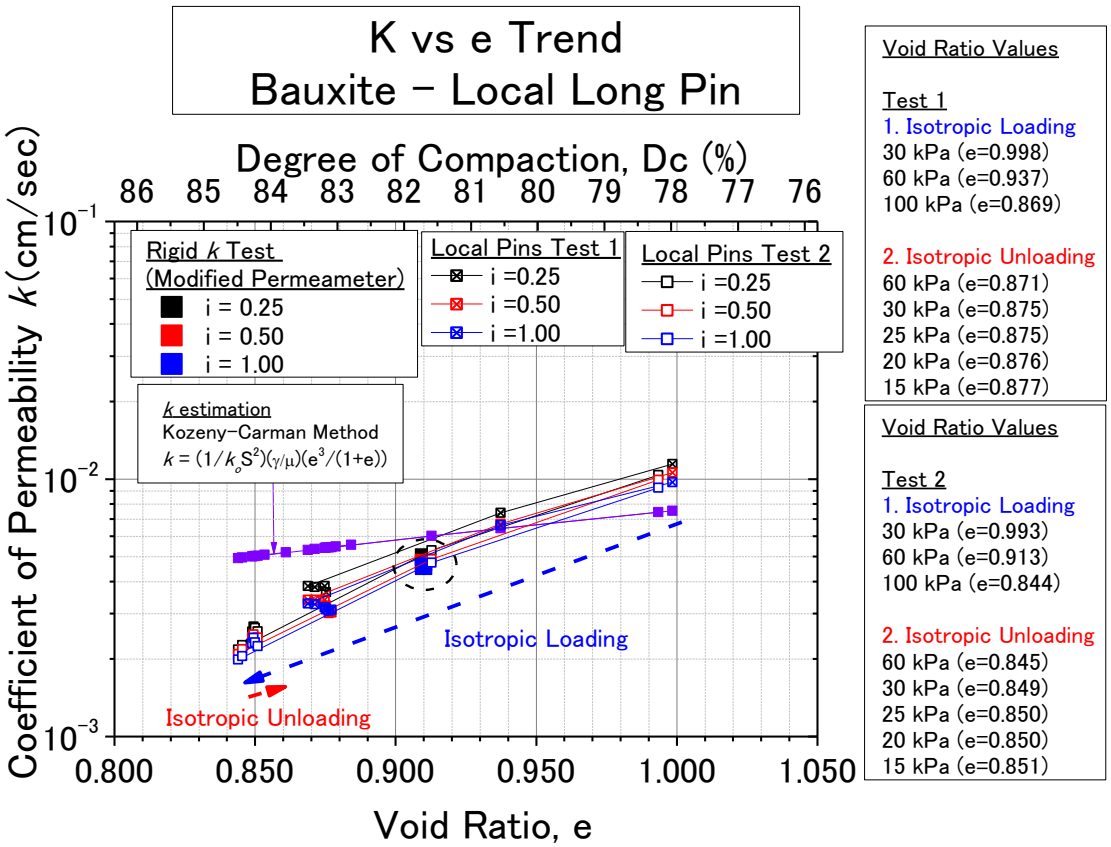

Fig. 4-50. *k* vs *e* (bauxite, long pin, saturated)

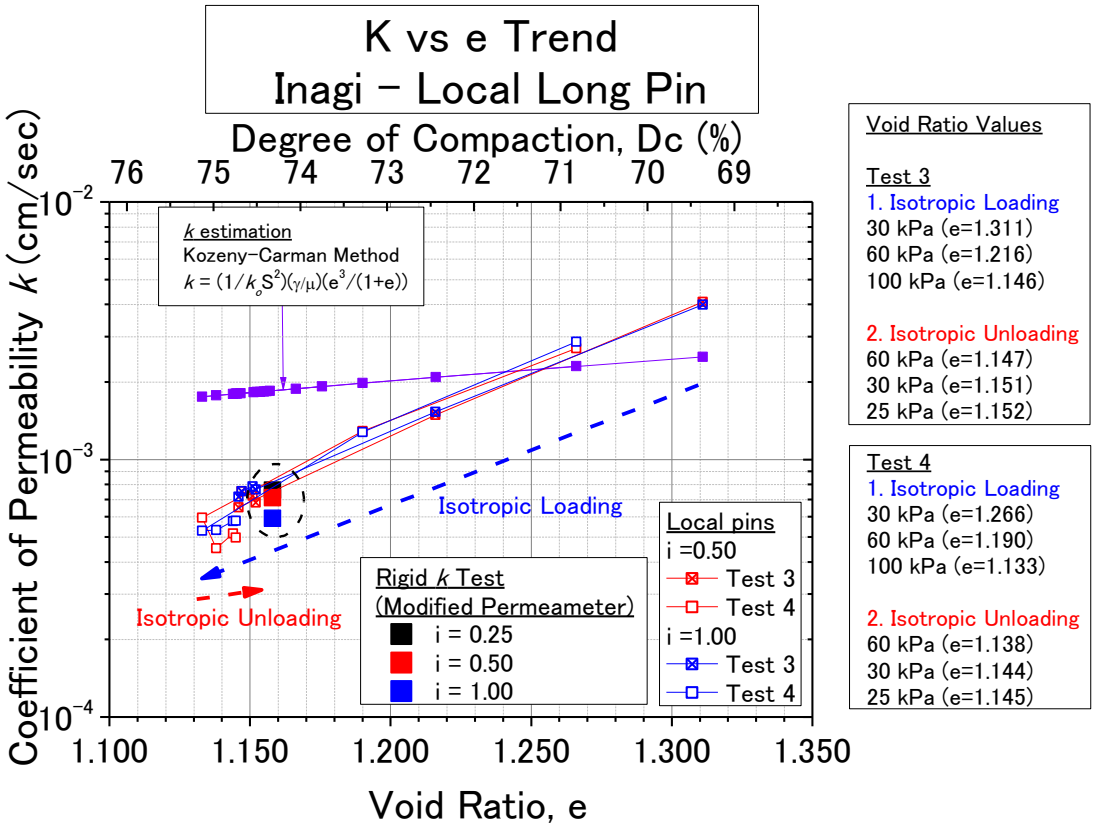

Fig. 4-51. *k* vs *e* (Inagi sand, long pin, saturated)

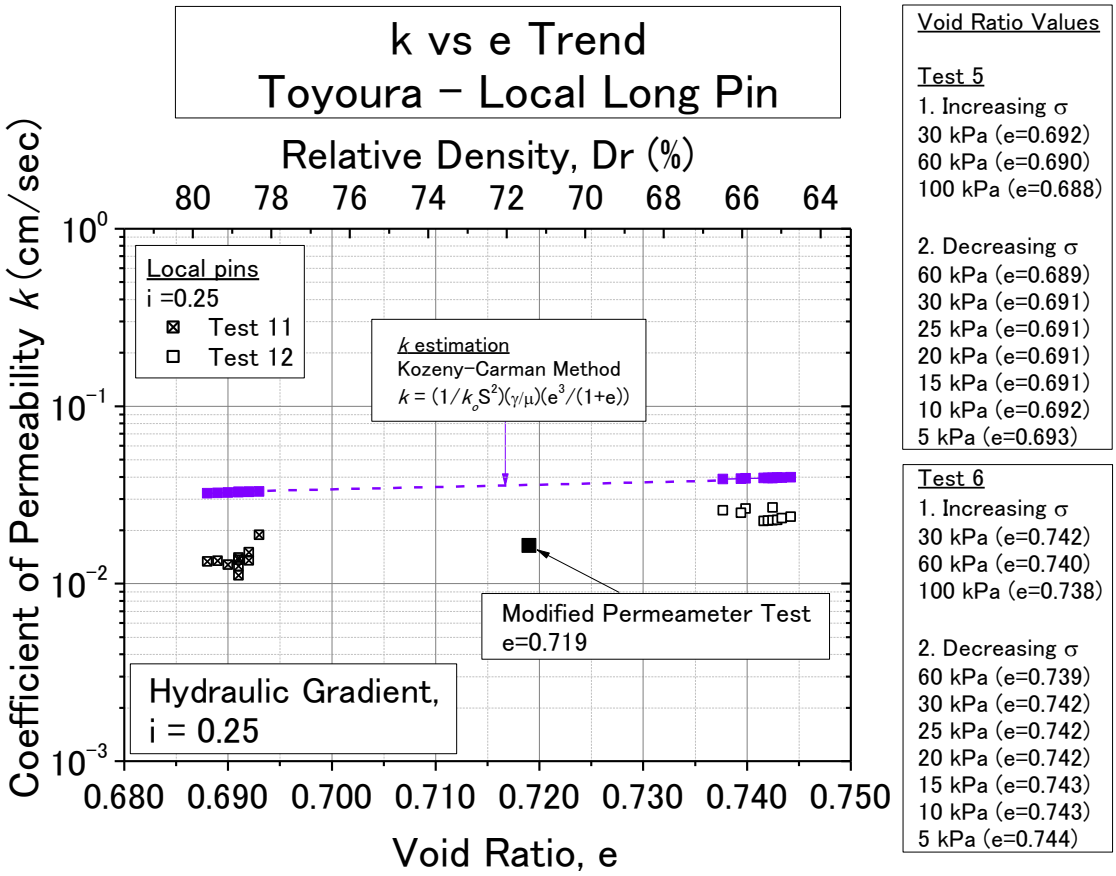

Fig. 4-52. *k* vs *e* (Toyoura sand, long pin, saturated)

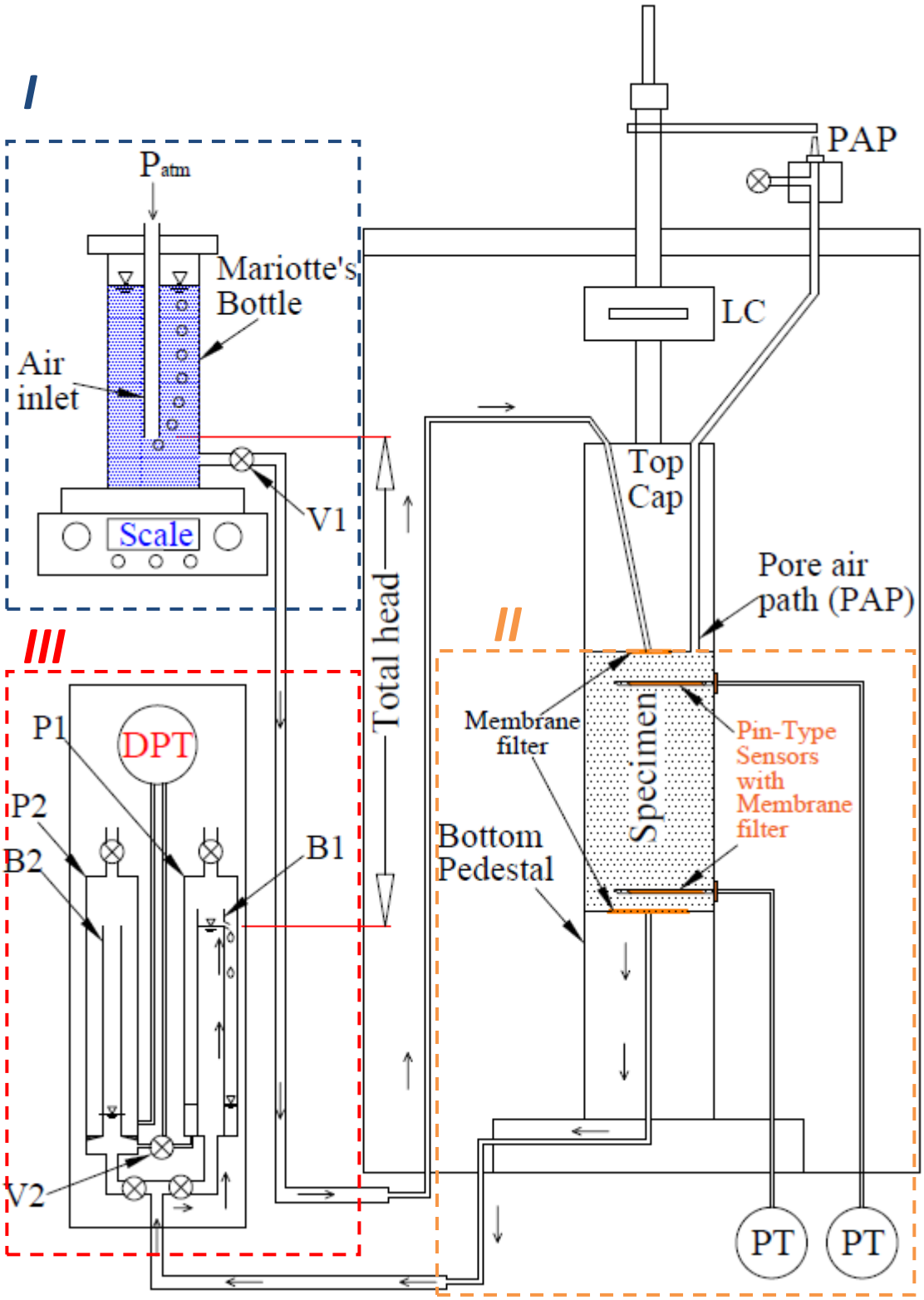

Fig. 4-53. Triaxial Permeameter System for Unsaturated Case

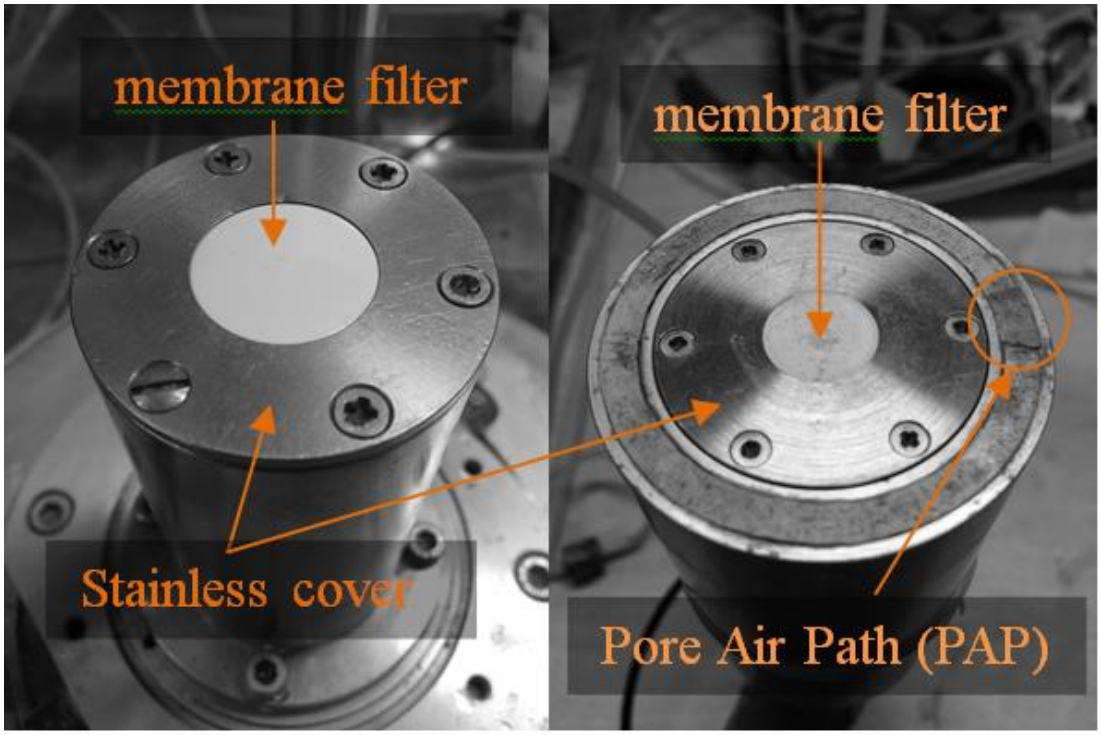

Fig. 4-54. bottom pedestal (left figure) and top cap inverted (right figure)

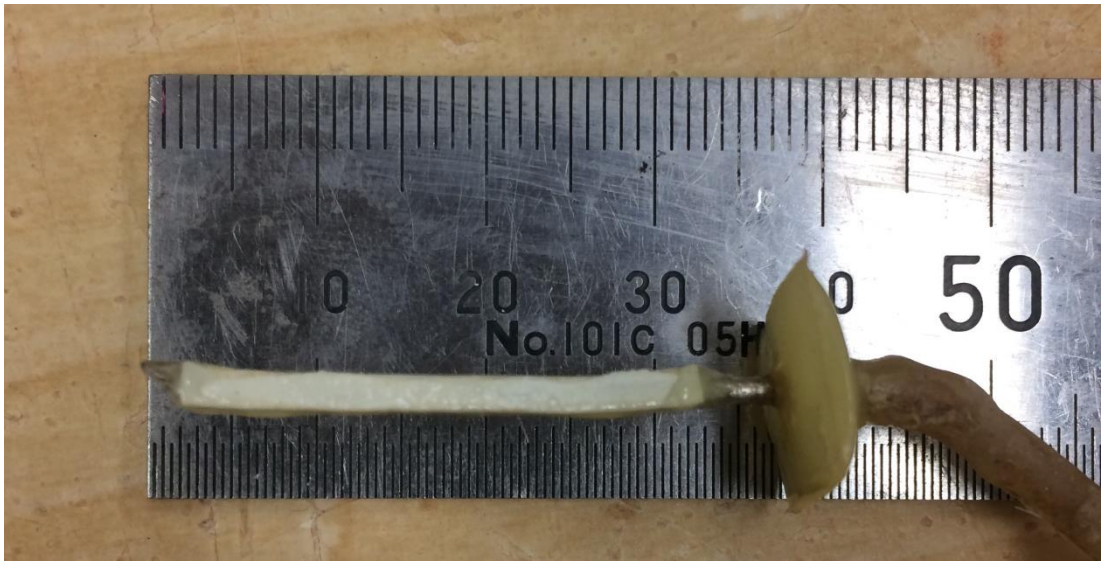

Fig. 4-55. Local pin-type sensor wrapped with membrane filter (3.5 cm long)

Fig. 4-56. Local pin-type sensors submerged in a tank with pressure of -100 kPa

Fig. 4-57. Membrane filters being saturated in a container with pressure of -100 kPa

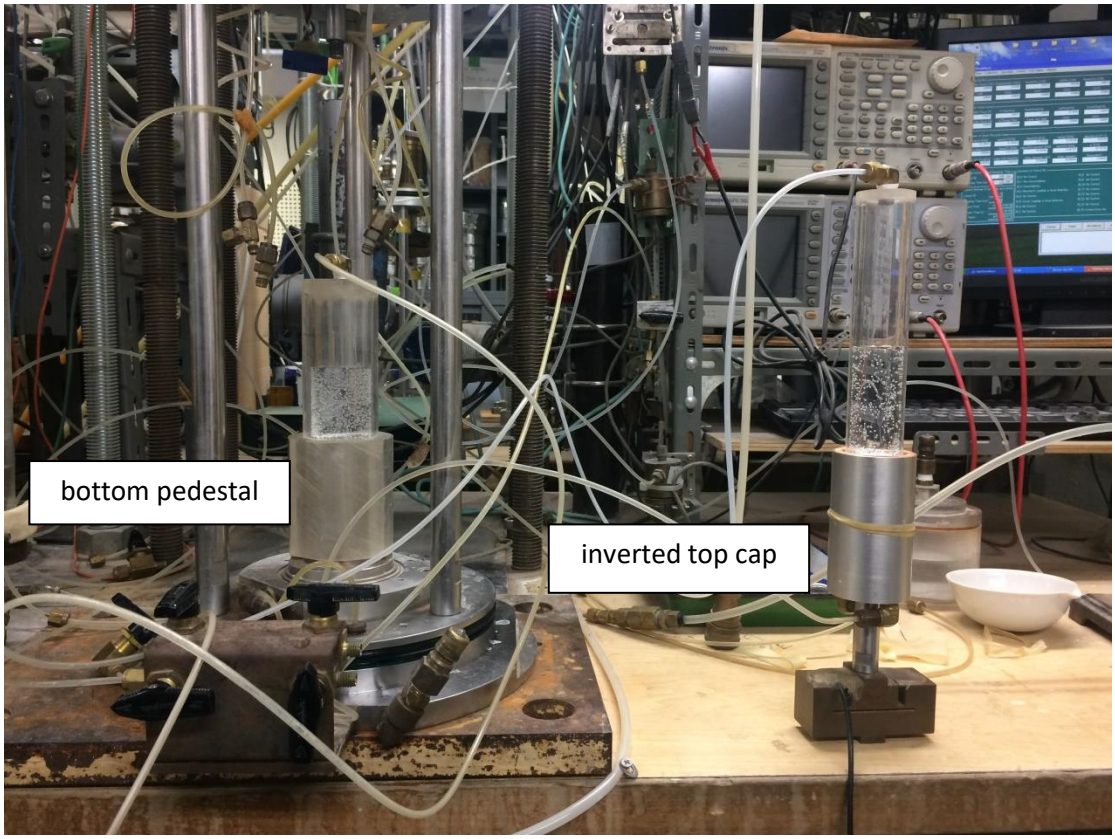

Fig. 4-58. Bottom pedestal and top cap and the tubes being saturated

Fig. 4-59. Mounted specimen on the pedestal with inserted local pin-type sensors

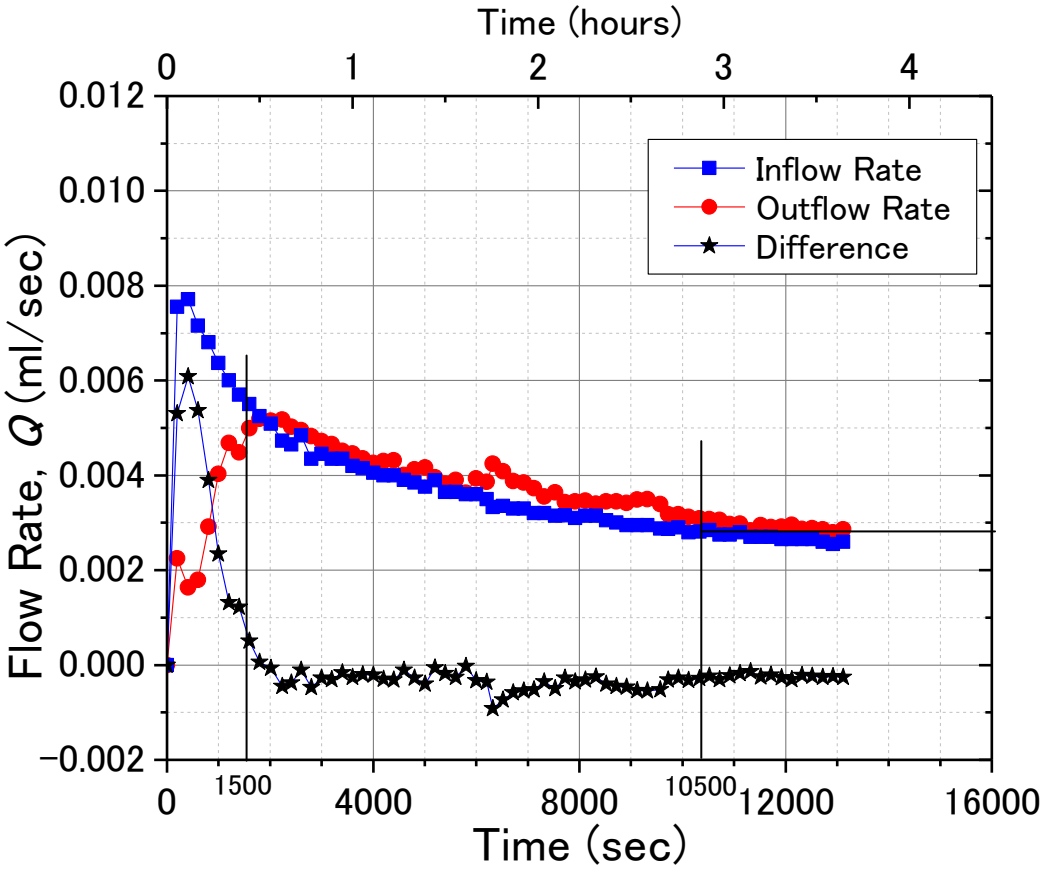

Fig. 4-60. Typical plot of the steady flow condition (bauxite, test 6, unsaturated)

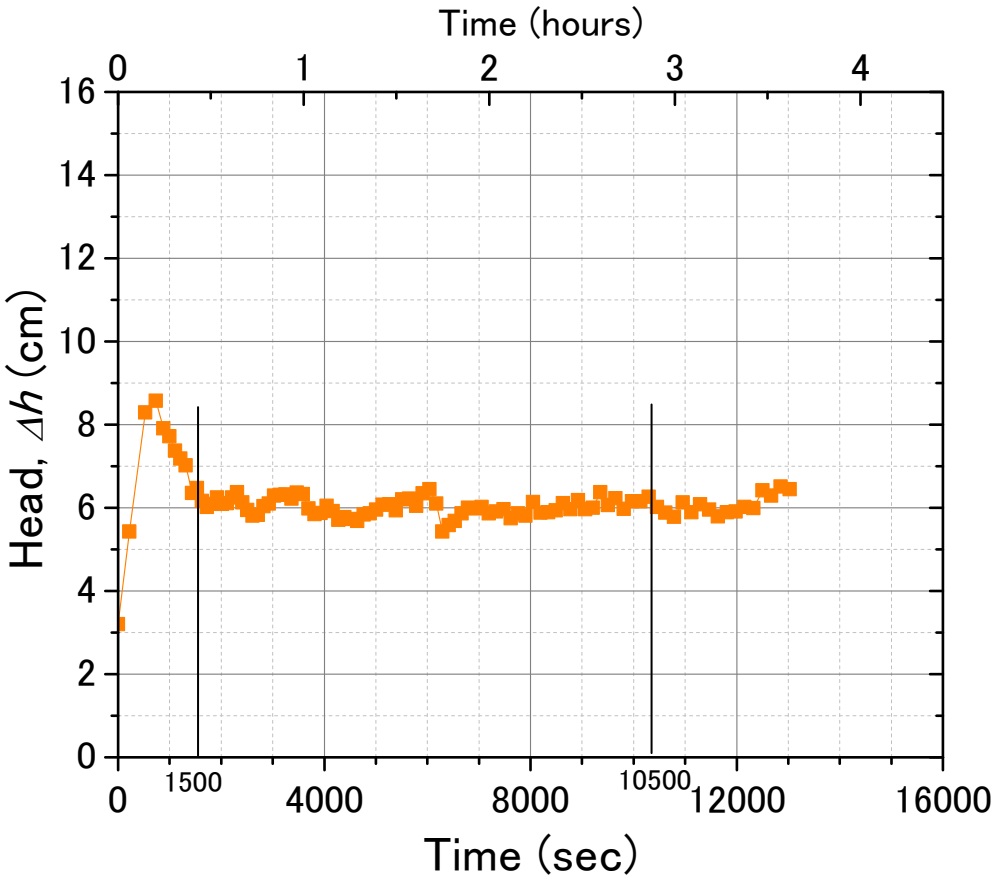

Fig. 4-61. Typical plot of the head difference measured by the local pin-type sensors (bauxite, test 6, unsaturated)

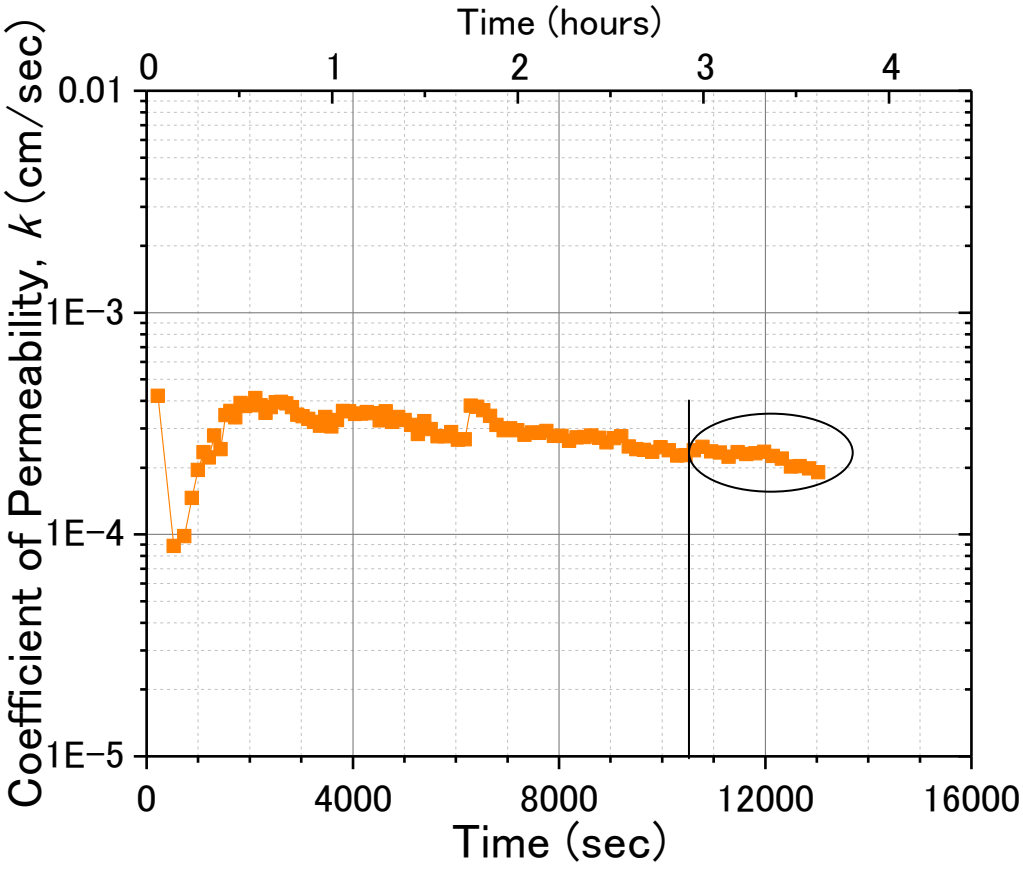

Fig. 4-62. Corresponding *k* vs time plot (bauxite, test 6, unsaturated)

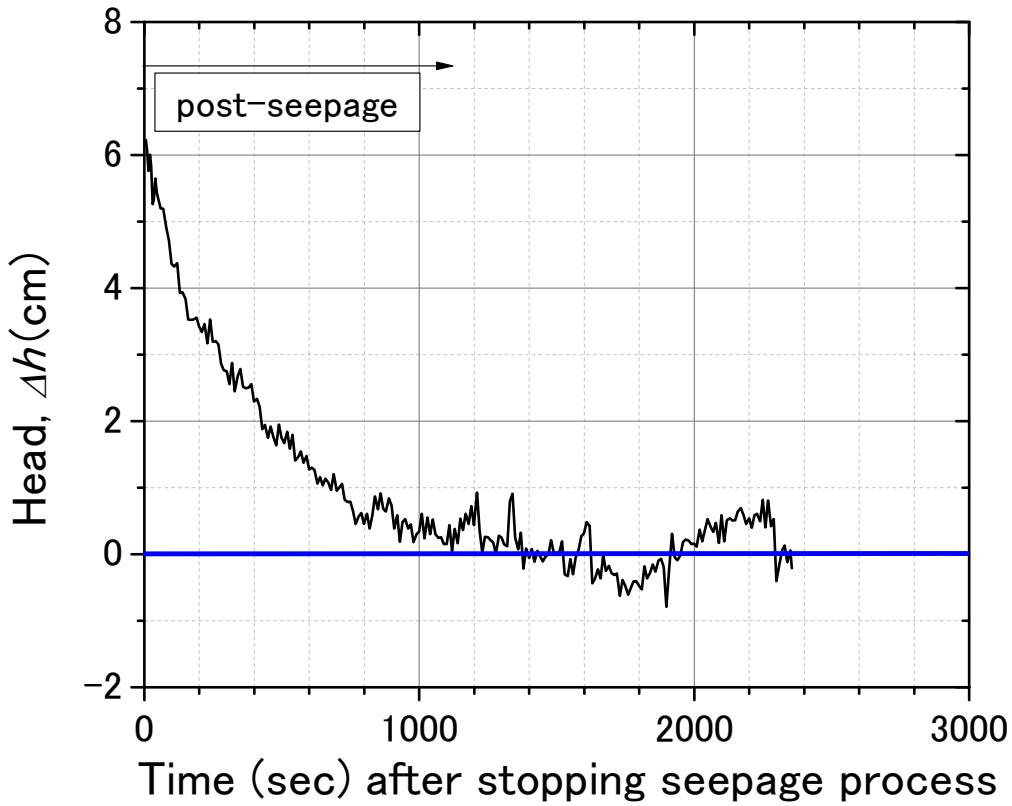

Fig. 4-63. Typical plot of the head difference measured by the local pin-type sensors at post-seepage (bauxite, test 6, unsaturated)

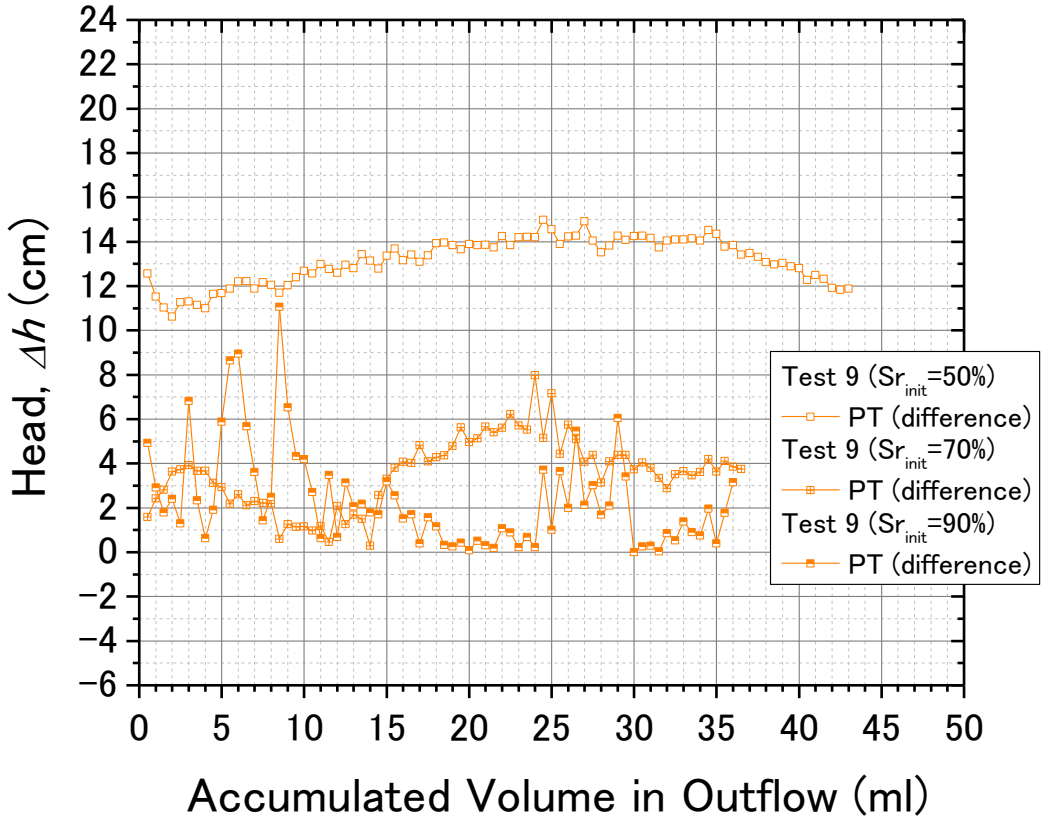

Fig. 4-64. Δh measured by the local pin-type sensors vs. Accumulated volume in outflow (bauxite, test 9, unsaturated)

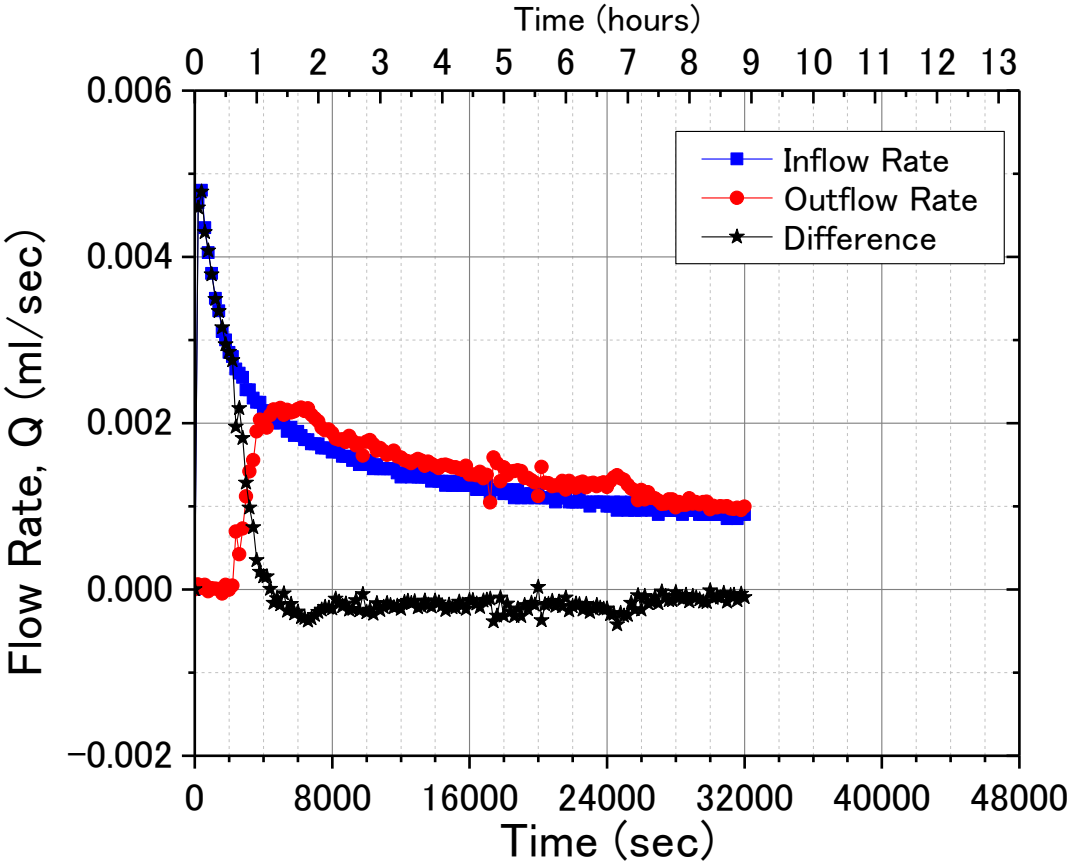

Fig. 4-65. Q vs. time plot (bauxite, test 9 at Sr_{init}=52%, unsaturated)

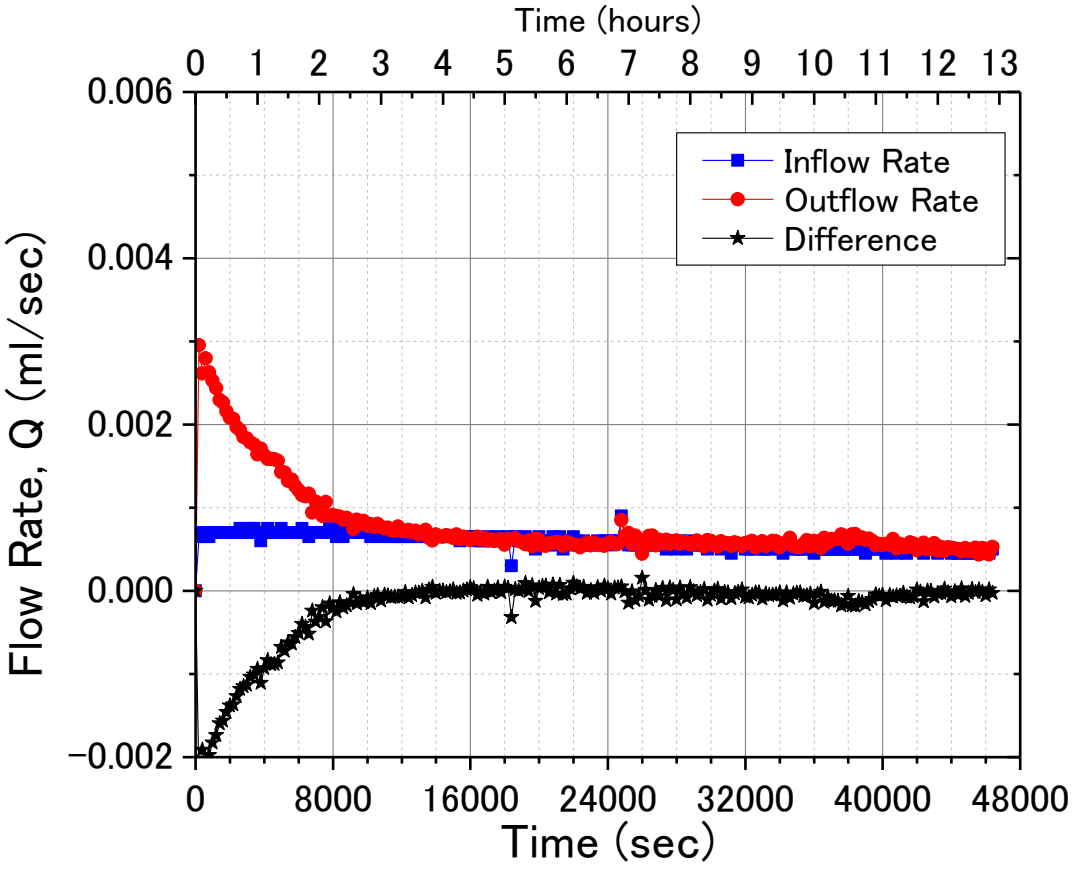

Fig. 4-66. *Q* vs. time plot (bauxite, test 9 at Sr_{init}=70%, unsaturated)

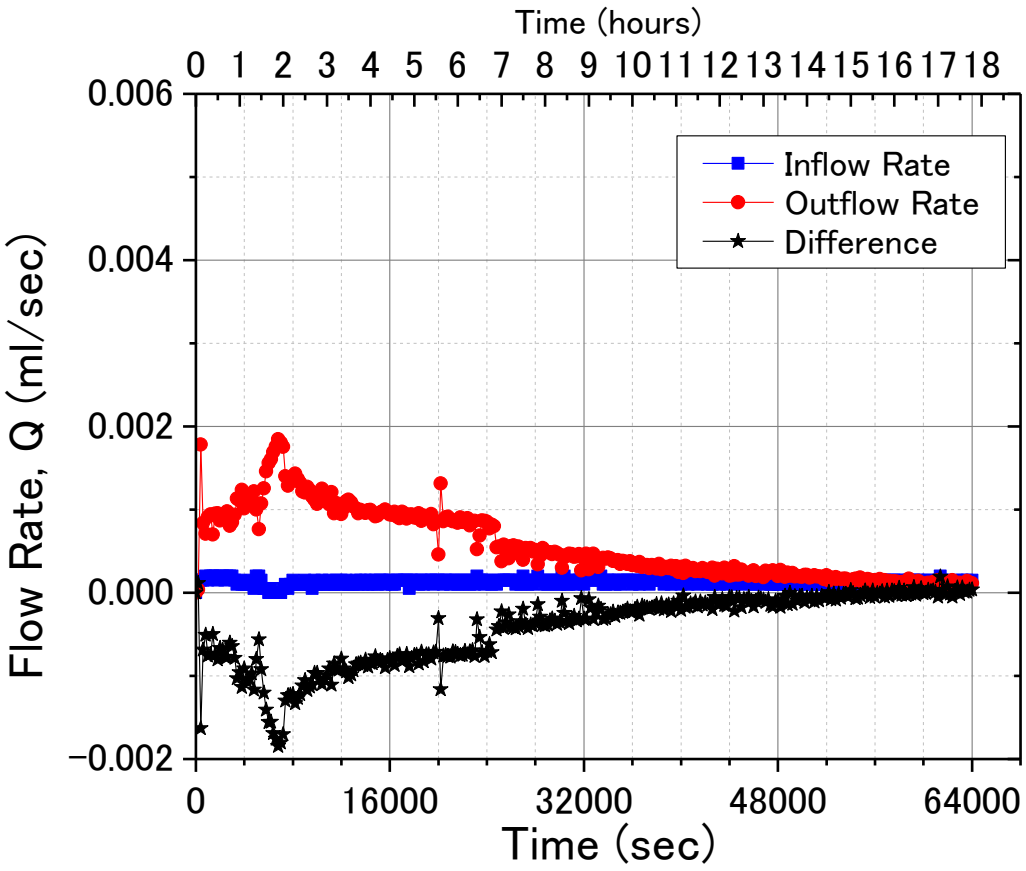

Fig. 4-67. *Q* vs. time plot (bauxite, test 9 at Sr_{init}=90%, unsaturated)

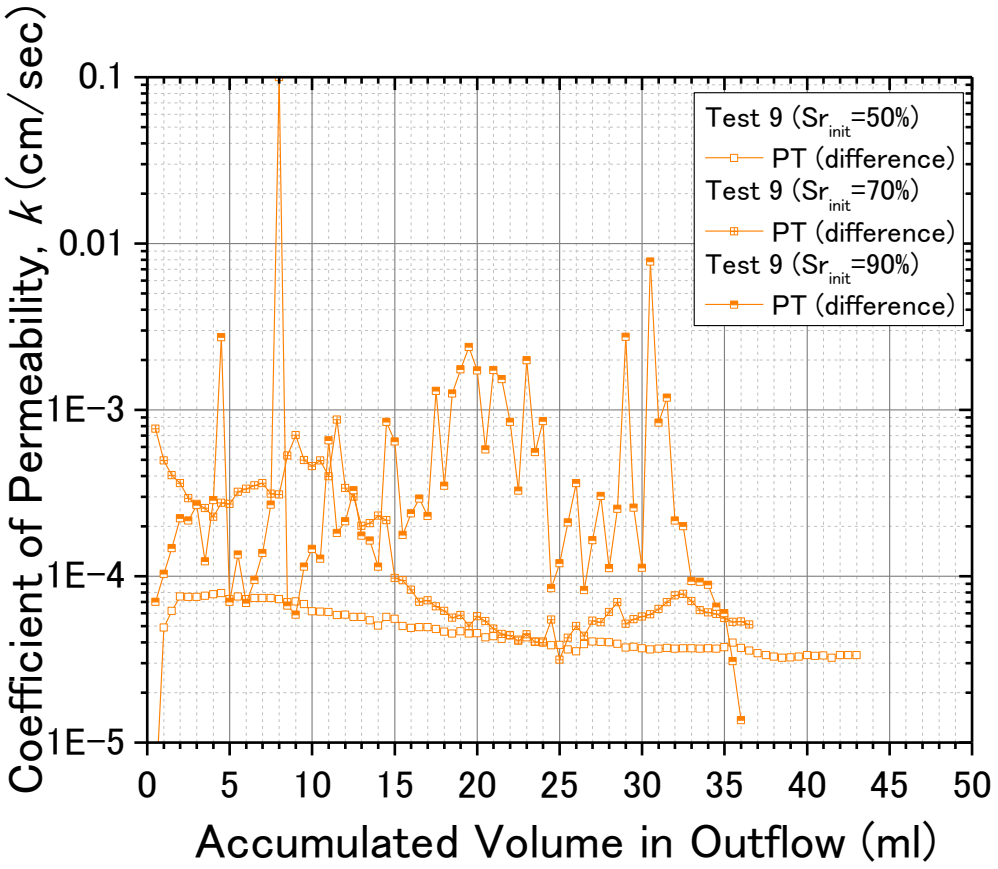

Fig. 4-68. Corresponding *k* vs accumulated volume in outflow (bauxite, test 9, unsaturated)

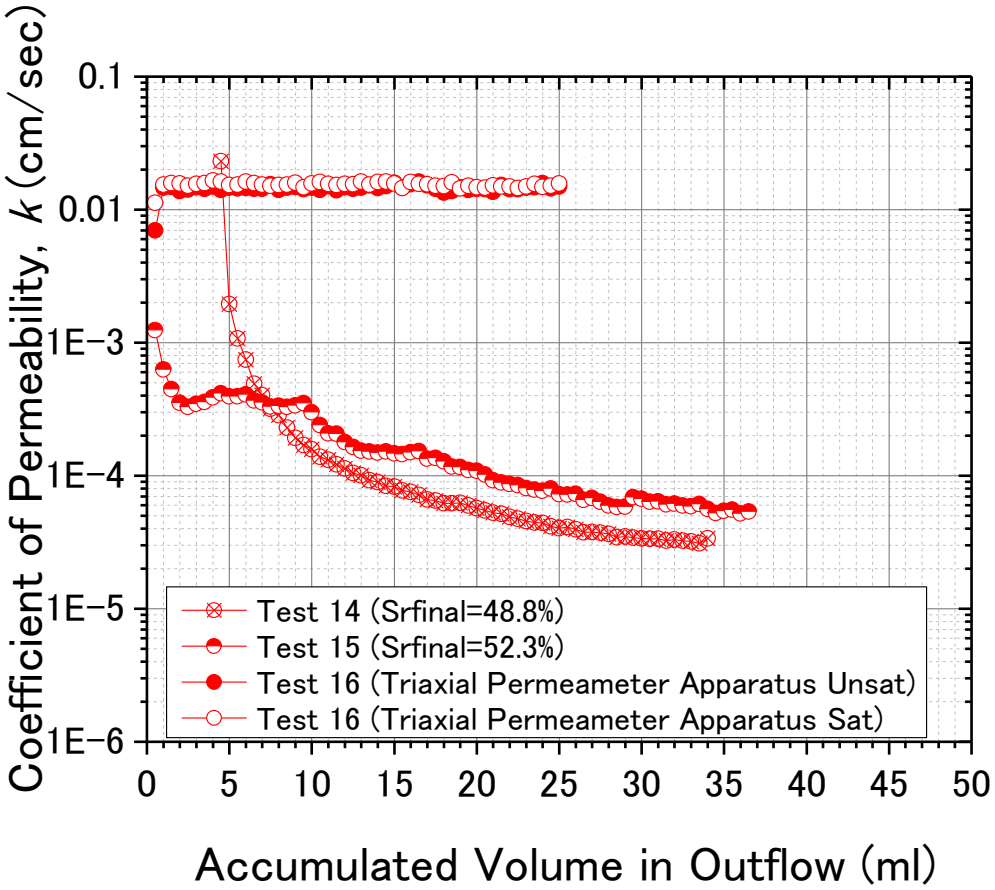

Fig. 4-69. *k* vs accumulated volume in outflow (bauxite, loose case, unsaturated)

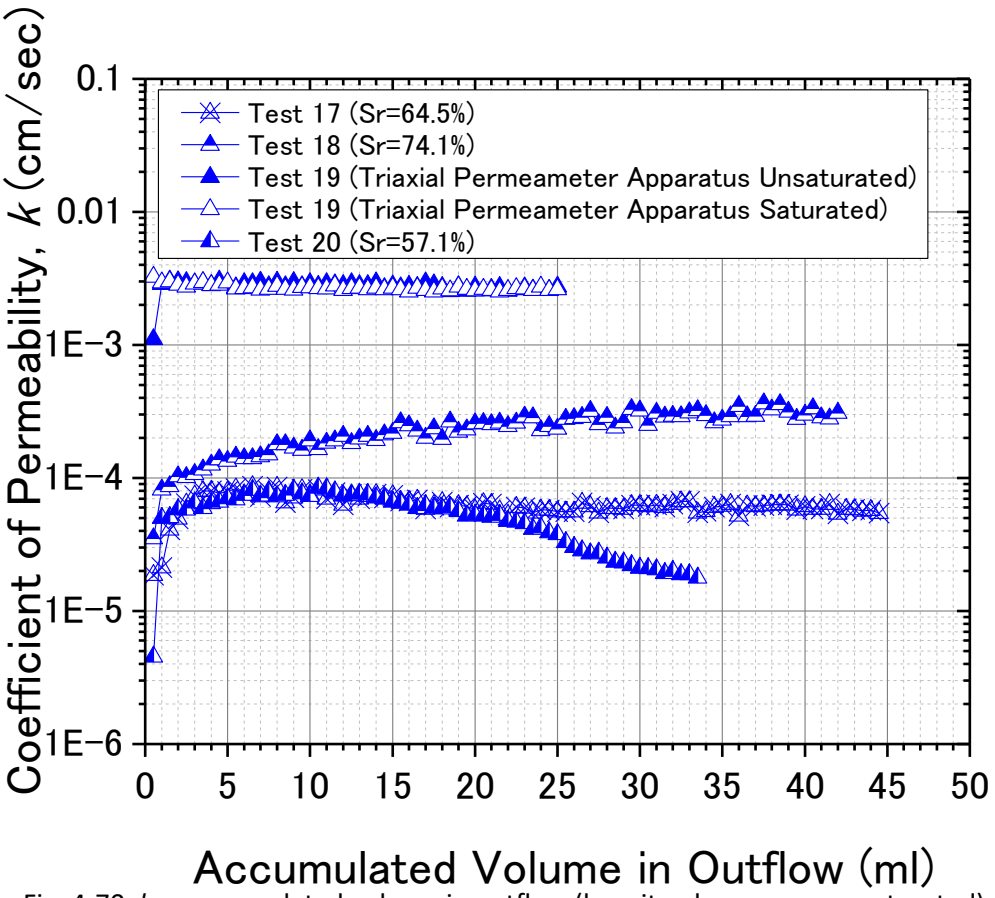

Fig. 4-70. *k* vs accumulated volume in outflow (bauxite, dense case, unsaturated)

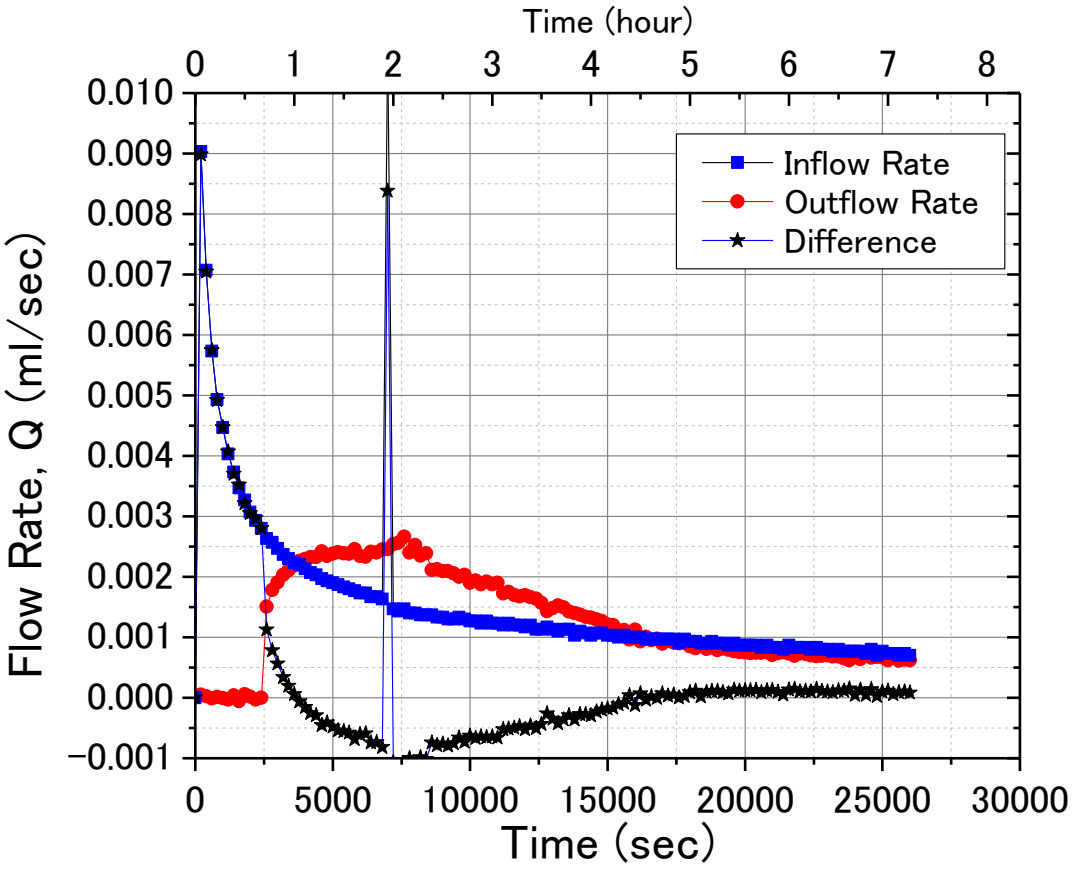

Fig. 4-71. *Q* vs. time plot (bauxite, test 20 at Sr_{init}=52%, unsaturated)

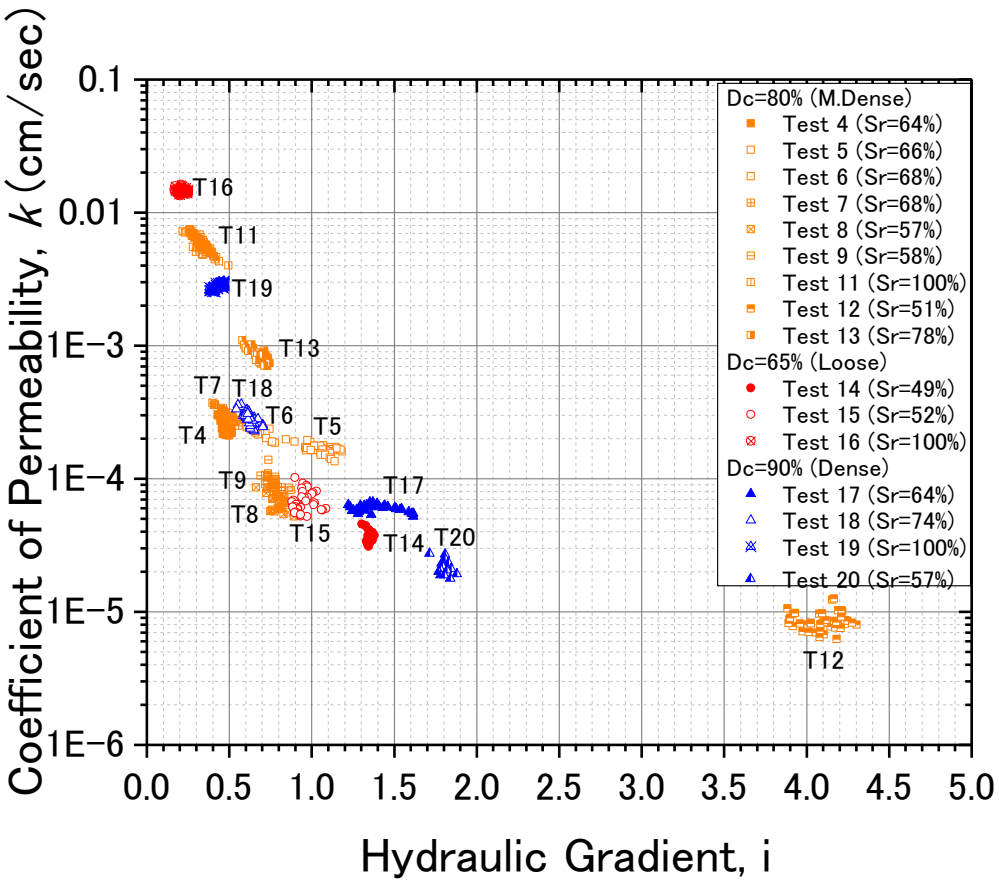

Fig. 4-72. *k* vs. *i* plot (bauxite, all tests, unsaturated)

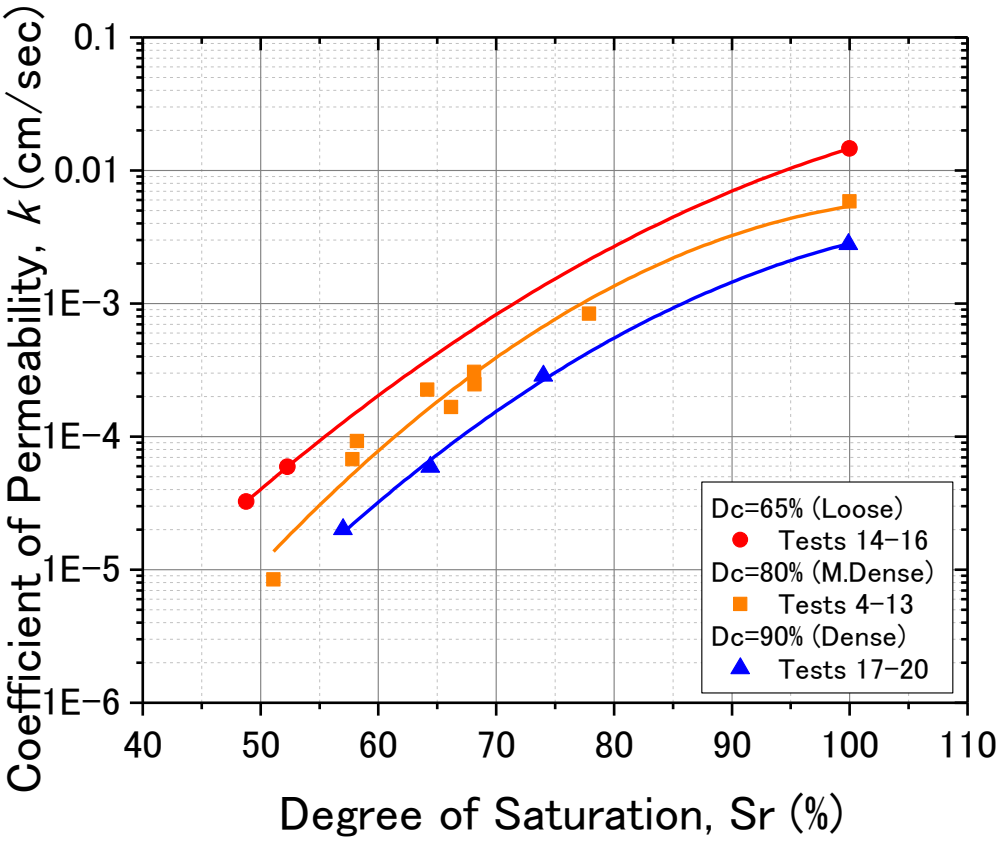

Fig. 4-73. *k* vs. *Sr* plot (bauxite, all tests, unsaturated)

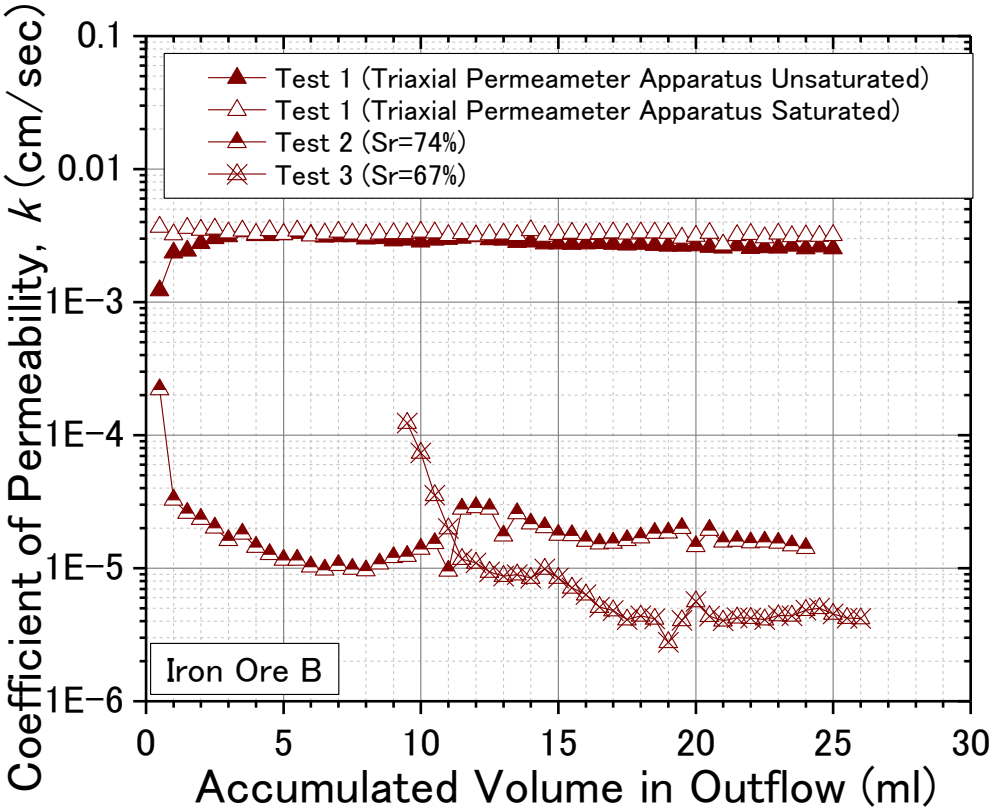

Fig. 4-74. *k* vs accumulated volume in outflow (Iron Ore, dense case, unsaturated)

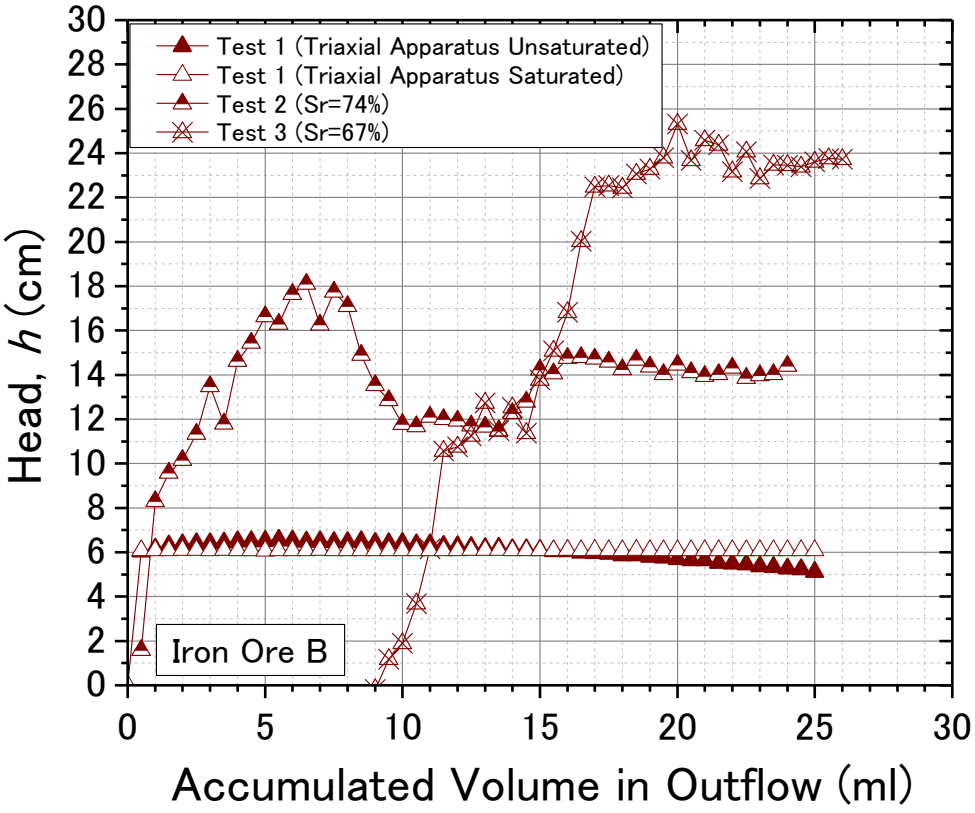

Fig. 4-75. *Δh* measured by the local pin-type sensors vs. Accumulated volume in outflow (iron ore, dense, unsaturated)

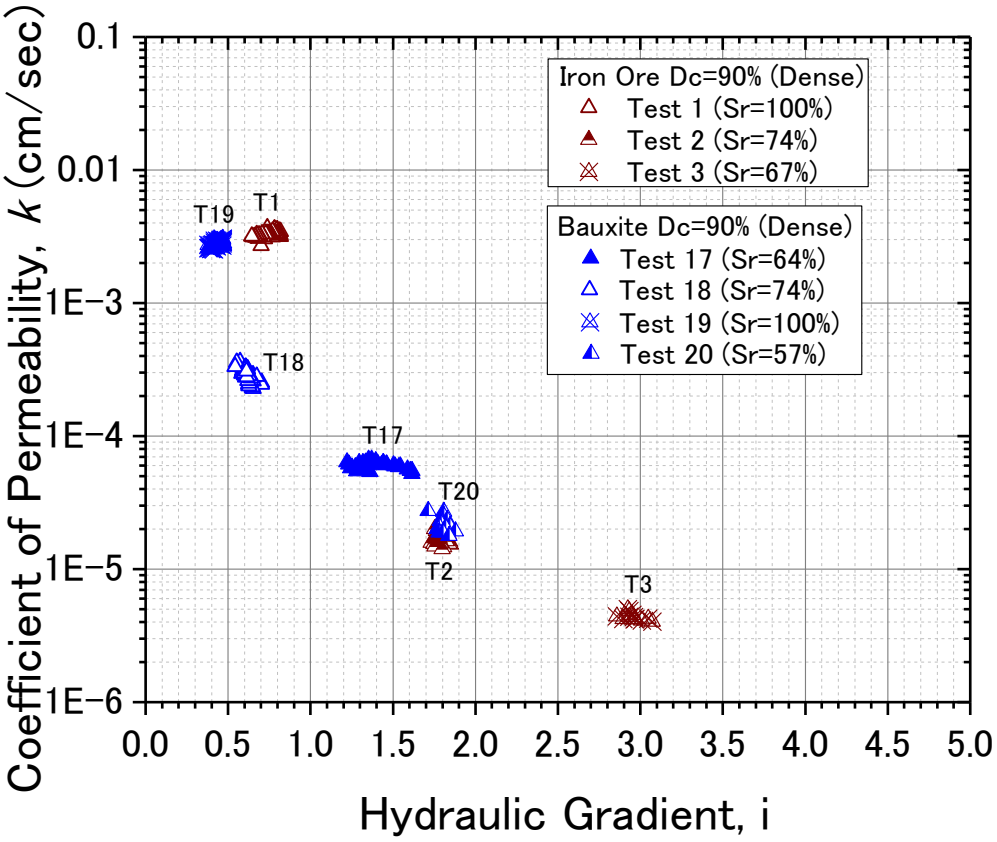

Fig. 4-76. *k* vs. *i* plot (comparison of bauxite and iron ore, dense, unsaturated)

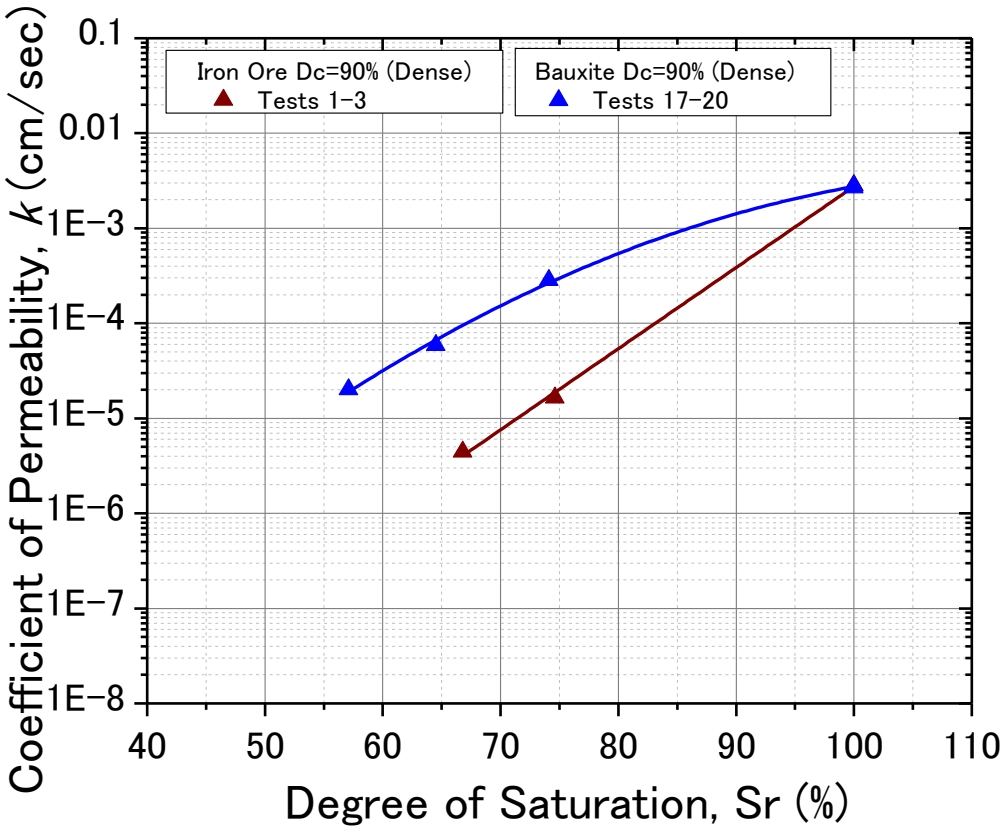

Fig. 4-77. *k* vs. *Sr* plot (comparison of bauxite and iron ore, dense, unsaturated)

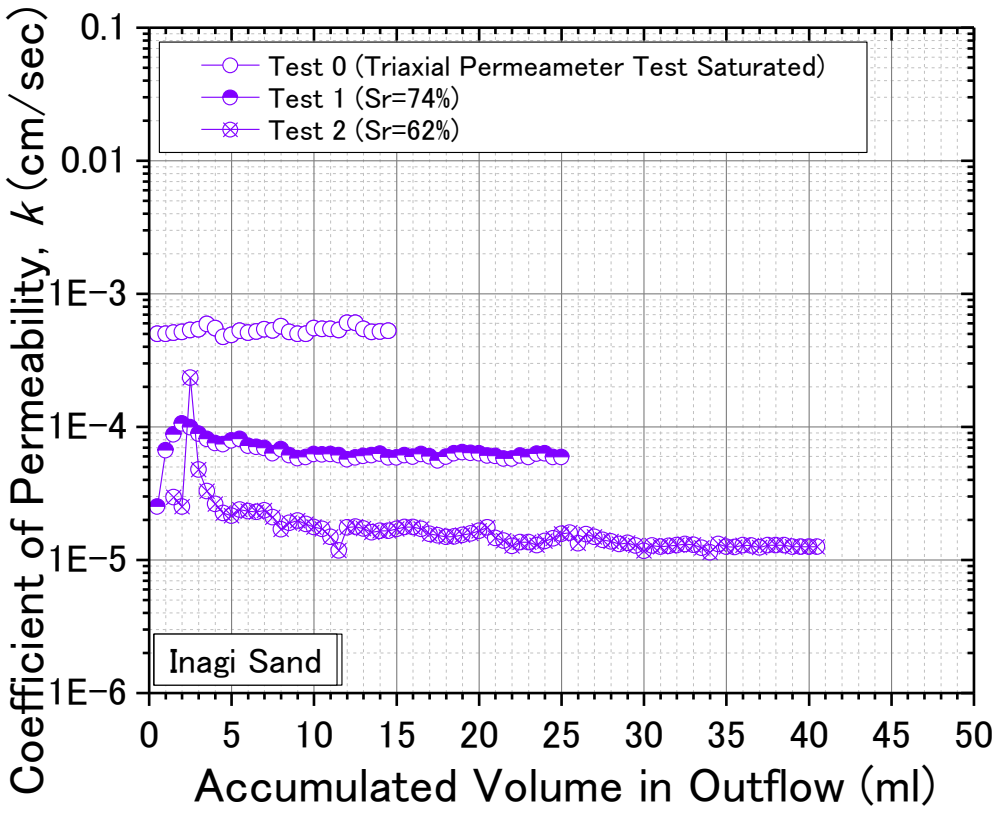

Fig. 4-78. *k* vs accumulated volume in outflow (Inagi sand, loose, unsaturated)

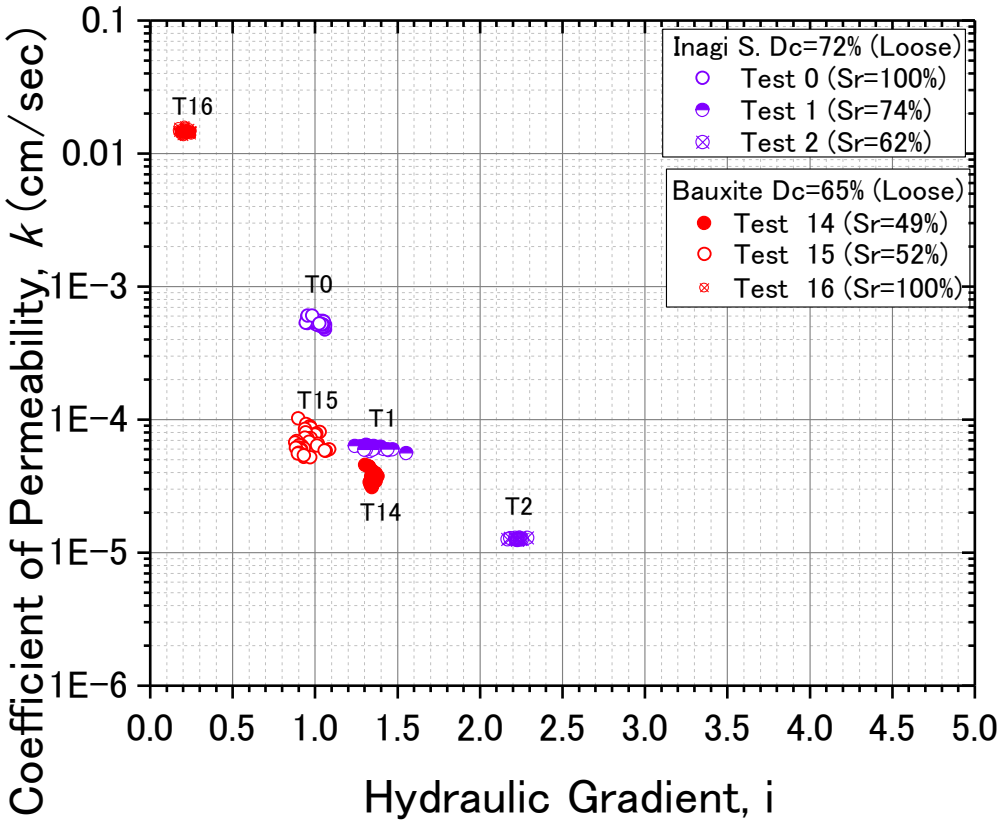

Fig. 4-79. *k* vs. *i* plot (comparison of bauxite and Inagi sand, loose, unsaturated)

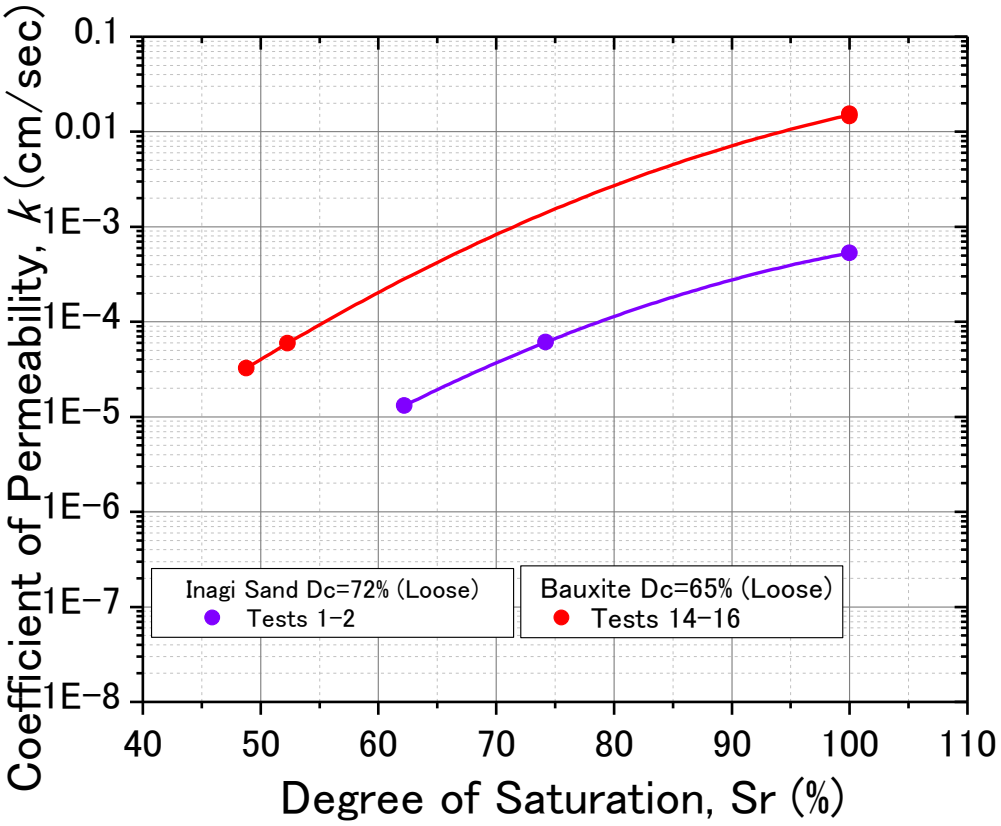

Fig. 4-80. *k* vs. *Sr* plot (comparison of bauxite and Inagi sand, loose, unsaturated)

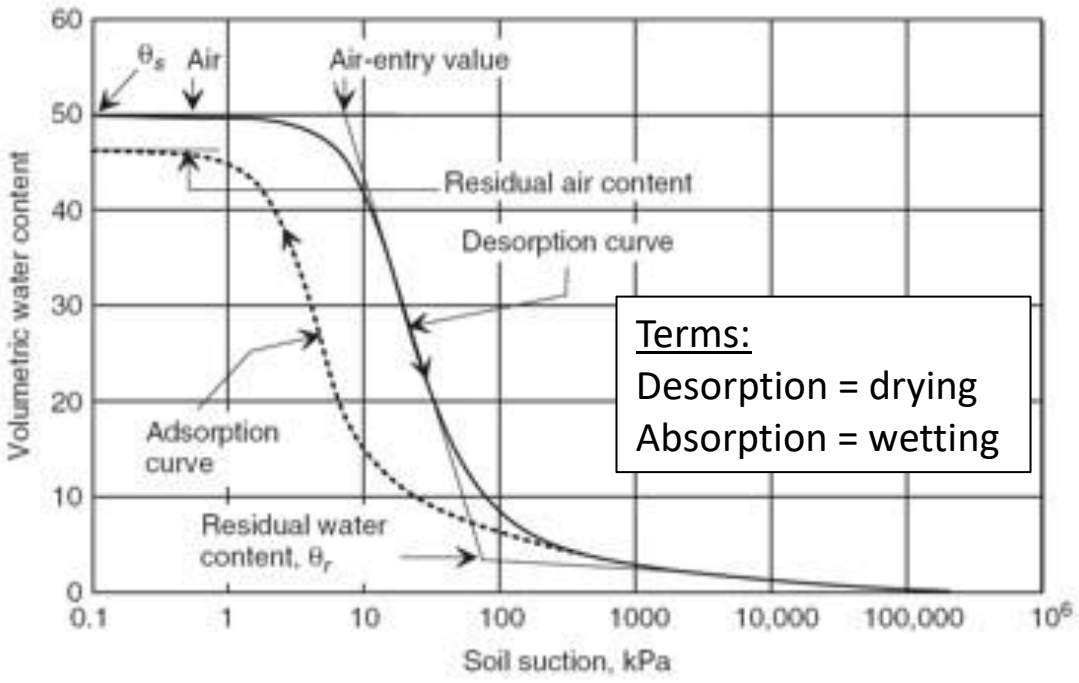

Fig. 4-81. Typical SWRC Plot (Fredlund and Rahardjo, 1993)

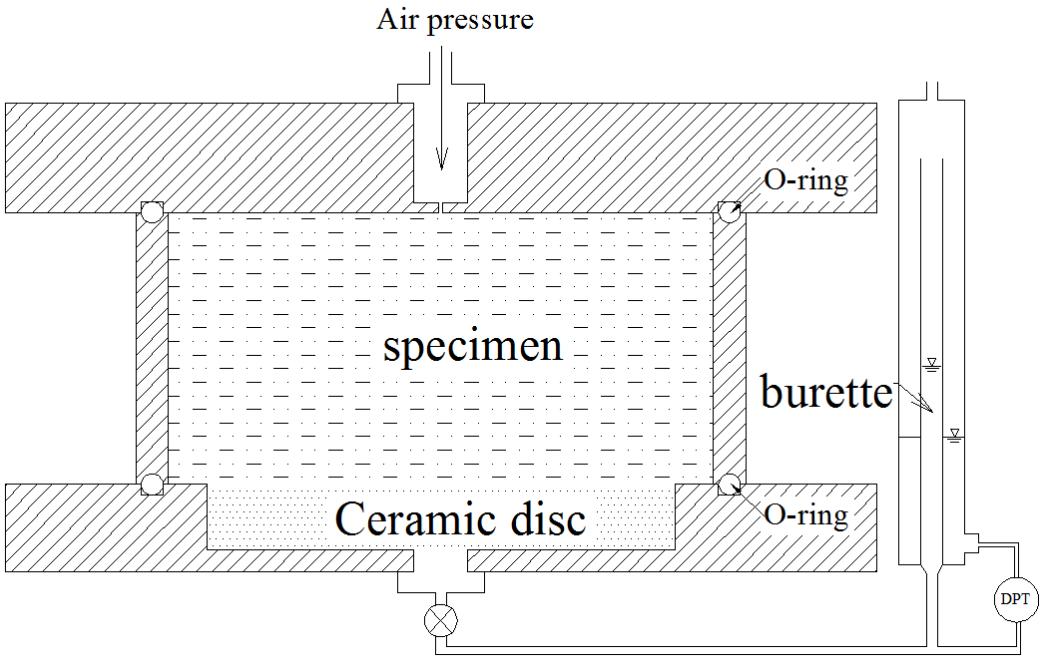

Fig. 4-82. Pressure plate apparatus equipped with ceramic disk (Wang, 2014)

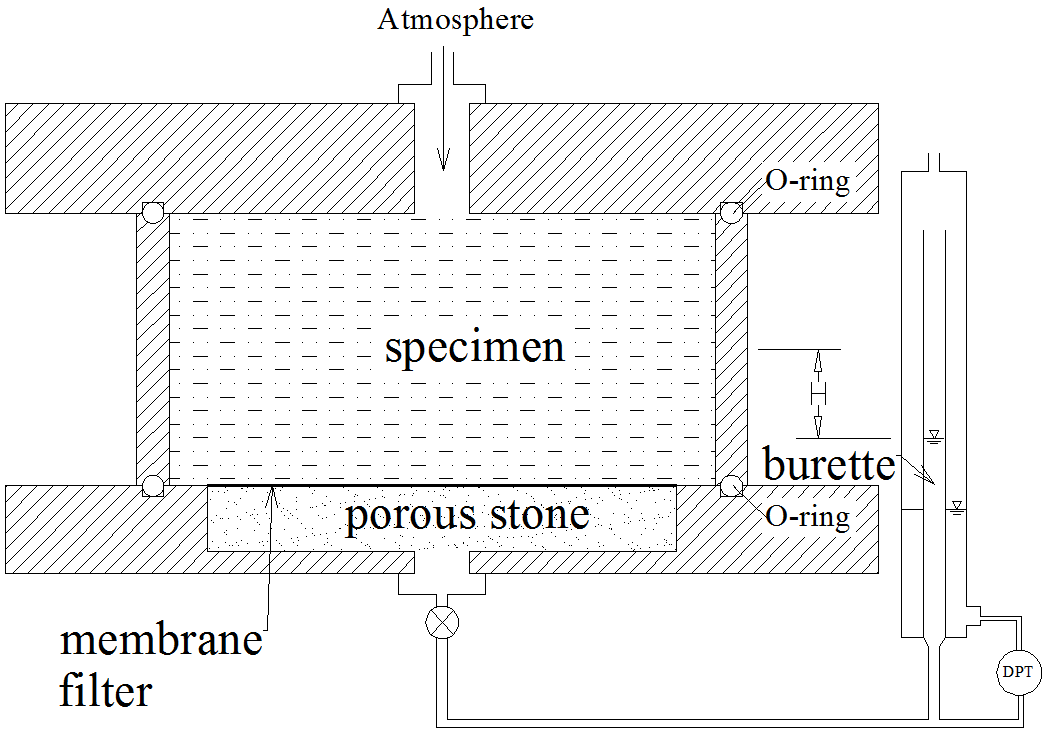

Fig. 4-83. Pressure plate apparatus equipped with membrane filter (Wang, 2014)

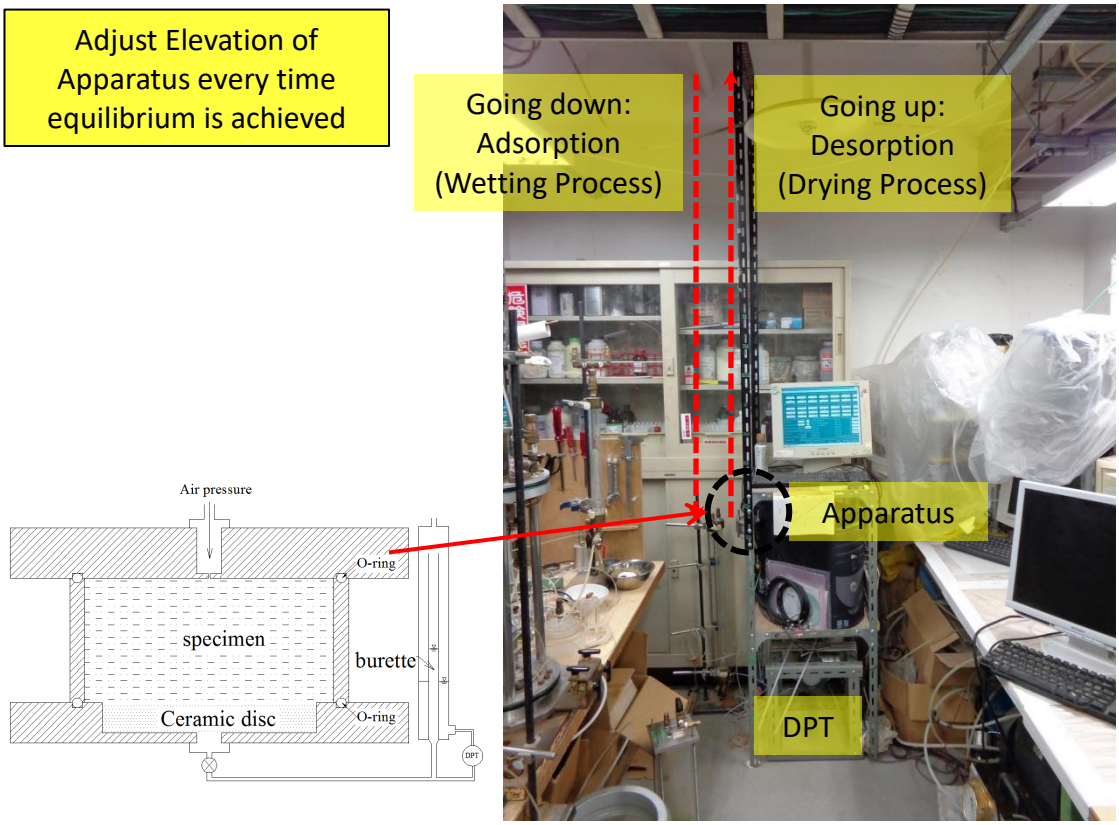

Fig. 4-84. Hanging Column Method set-up

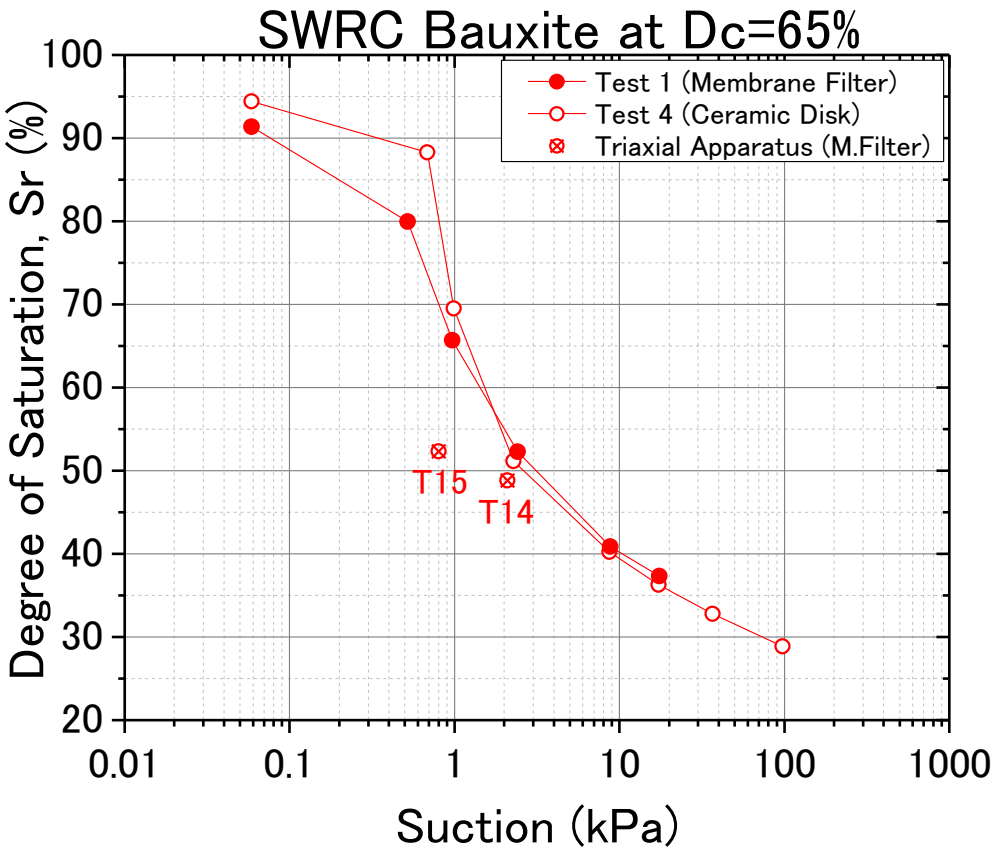

Fig. 4-85. SWRC of bauxite (loose)

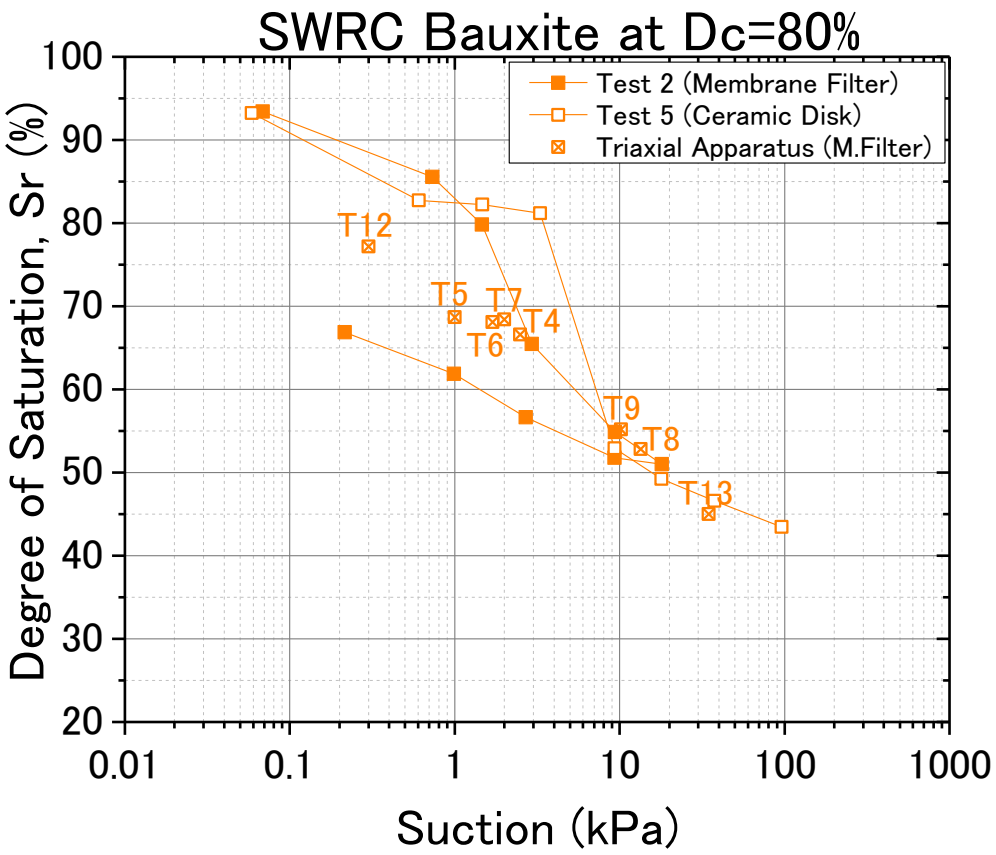

Fig. 4-86. SWRC of bauxite (medium dense)

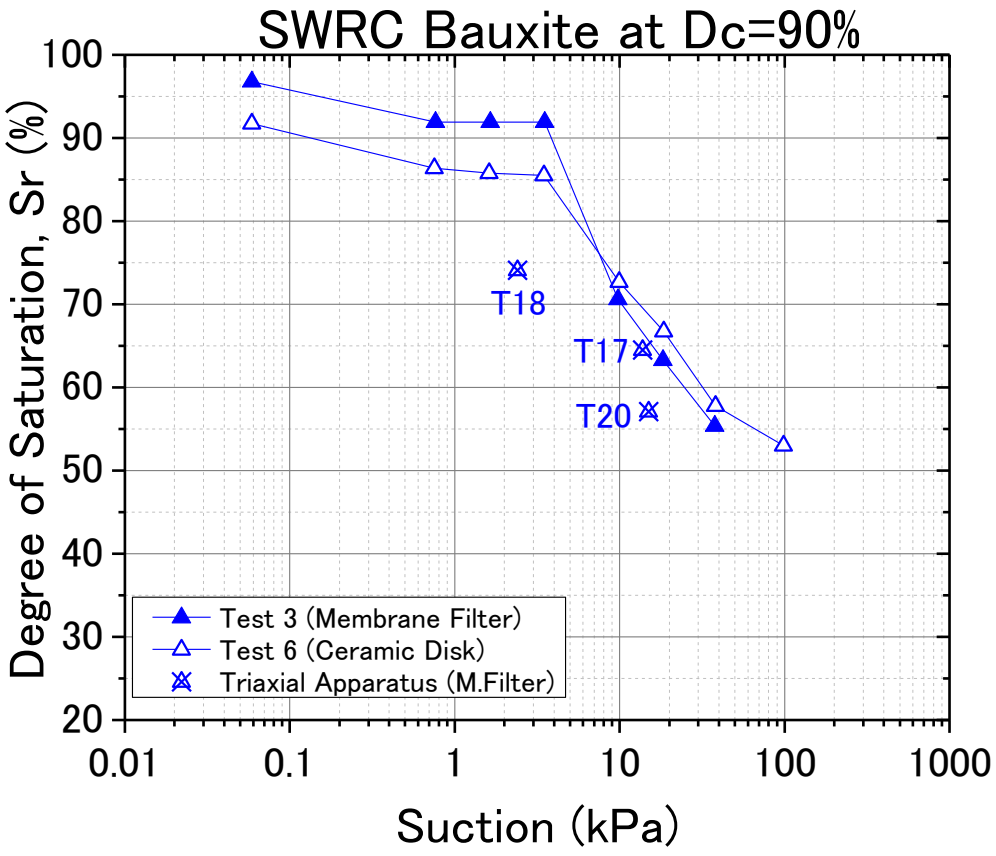

Fig. 4-87. SWRC of bauxite (dense)

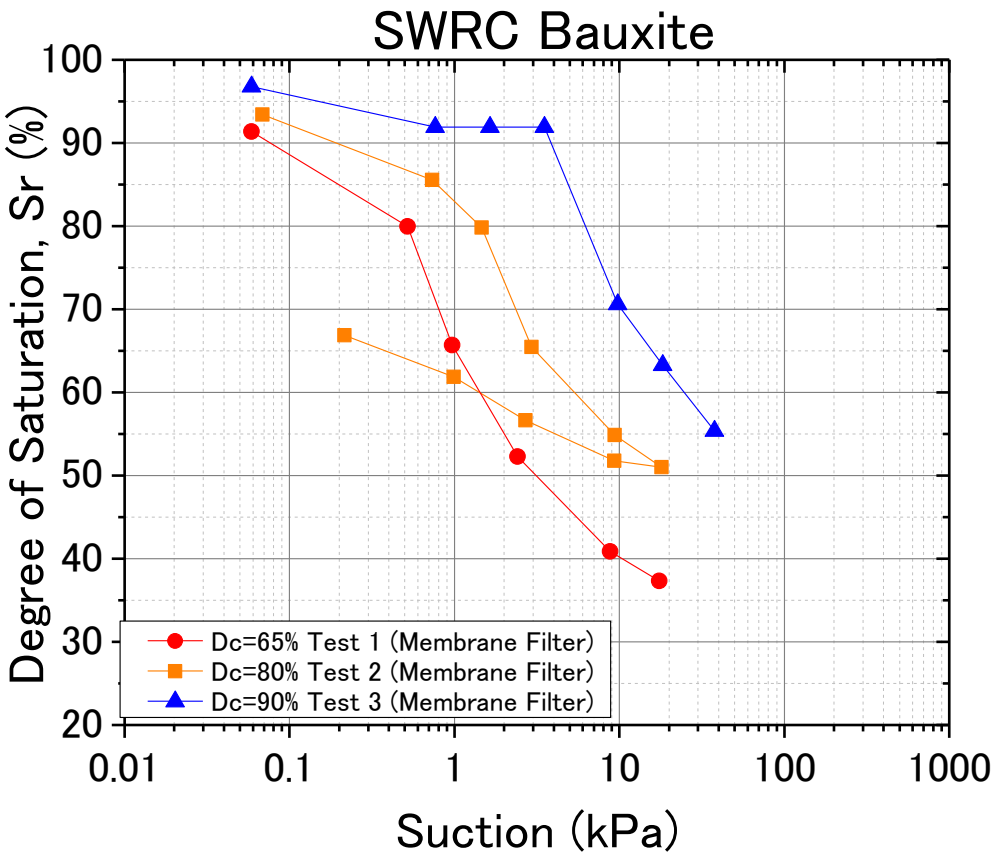

Fig. 4-88. SWRC of bauxite (membrane filter)

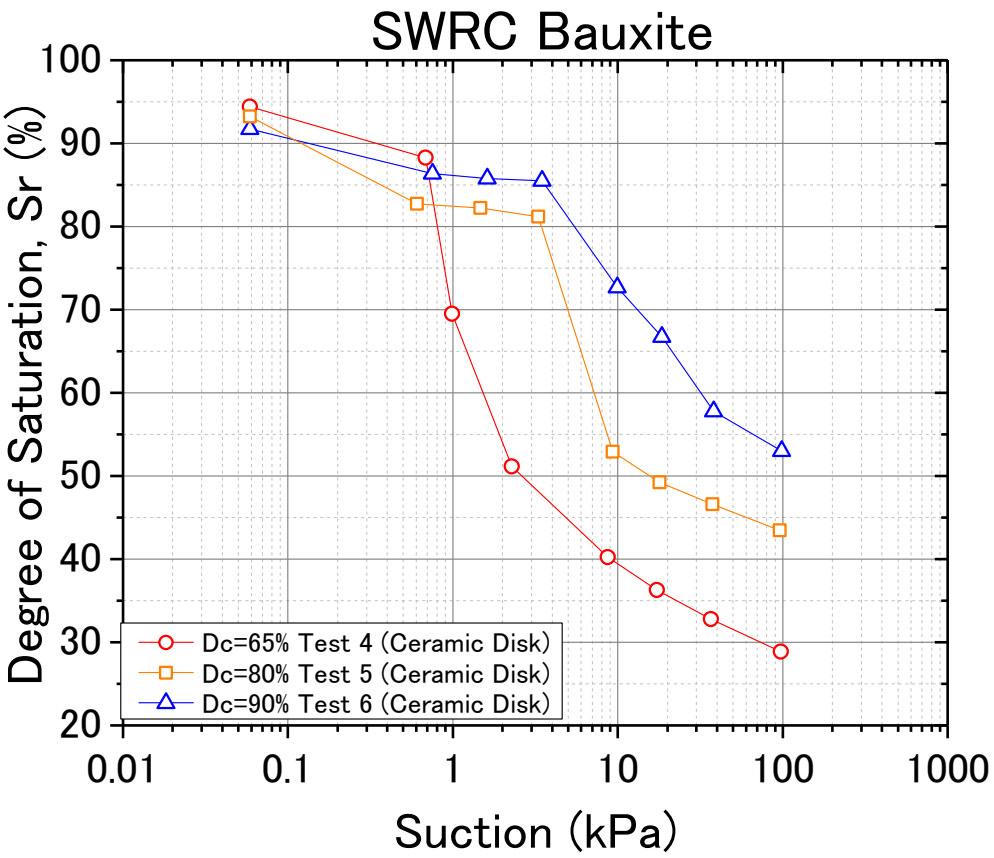

Fig. 4-89. SWRC of bauxite (ceramic disk)

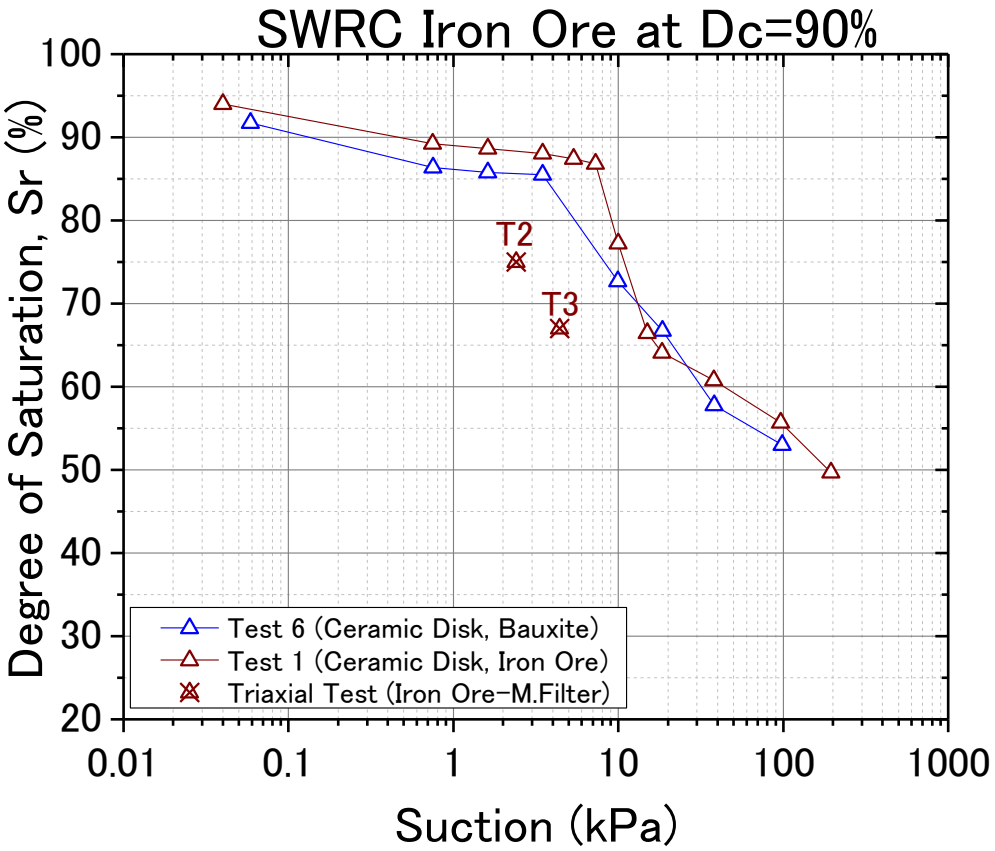

Fig. 4-90. SWRC of iron ore and bauxite (dense)

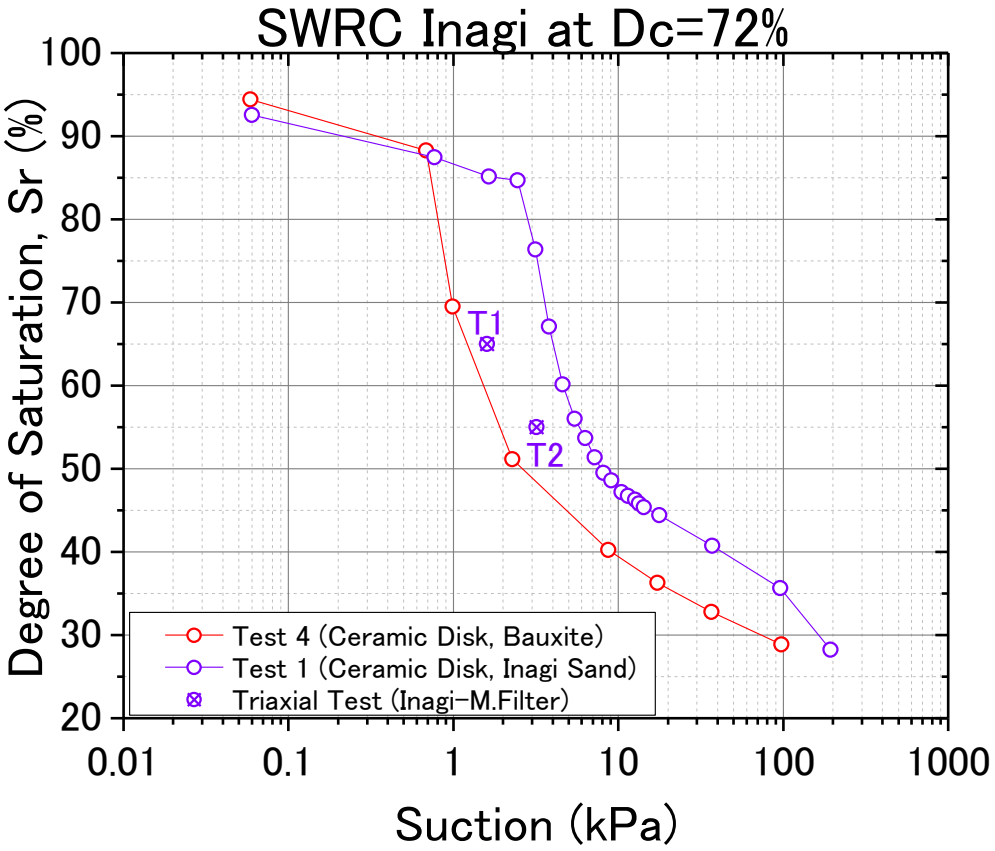

Fig. 4-91. SWRC of Inagi sand and bauxite (loose)

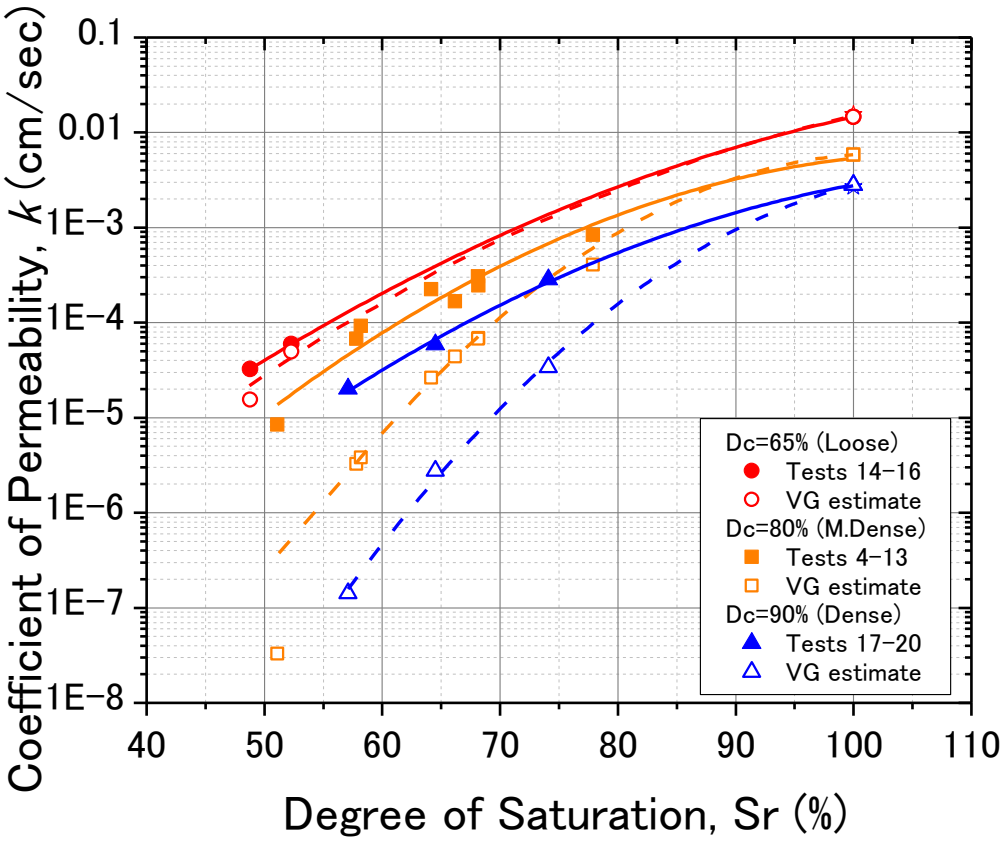

Fig. 4-92. *k* vs. *Sr* plot experimental and VG estimate (bauxite, all tests, unsaturated)

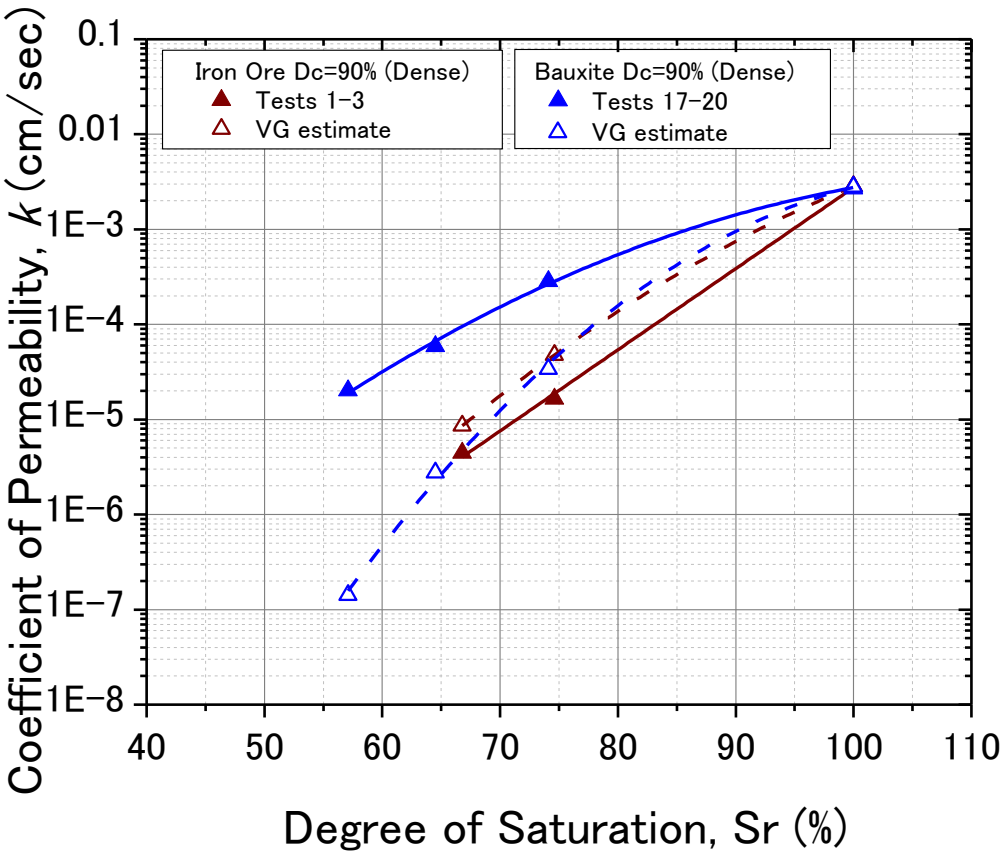

Fig. 4-93. *k* vs. *Sr* plot experimental and VG estimate
(comparison of bauxite and iron ore, dense, unsaturated)

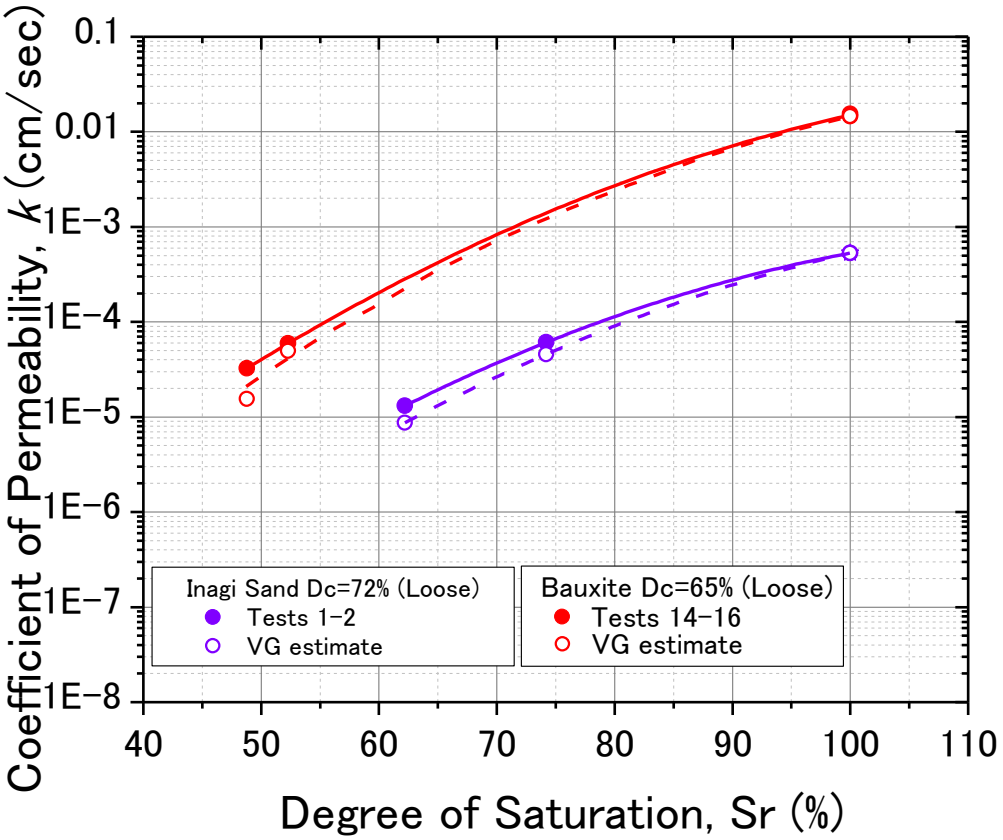

Fig. 4-94. *k* vs. *Sr* plot experimental and VG estimate
(comparison of bauxite and Inagi sand, loose, unsaturated)

Chapter 5
Numerical Analysis: Seepage

Contents

5-1. Introduction

In Chapter 3, it was found out that the liquefaction resistance of bauxite is closely related to its degree of saturation (*Sr*). The heap with a large saturated zone may be easier to liquefy than that with a small saturated zone; on the other hand, analysis considering the effect of the liquefaction potential of the unsaturated zone on the overall resistance of the heap against liquefaction should be more realistic than that without considering it. Hence, identifying or providing a rational way of stratifying the heap with respect to its water distribution is necessary.

In this Chapter, distribution of *Sr* in the heap of bauxite is evaluated through seepage analysis. The seepage analysis was performed based on the permeability of bauxite and the knowledge of water retention ability which were evaluated from the permeability test and SWRC as discussed in Chapter 4.

Seepage analyses were performed for bauxite under different degrees of compaction (*Dc*), as well as iron ore and Inagi sand.

The main goal of this chapter is to find the extent of the saturated zones and the distribution of *Sr* in the unsaturated zone of the heap under a given initial condition. From the distribution, the model of heap can be established for dynamic response analysis in Chapter 6.

5-2. Program and Model

A finite element method (FEM) program, Guslope, coded by Geotechnical Lab, Gunma Univ., Japan, is employed for the seepage analysis. This program is capable of analyzing two dimensional movement of water of the unsaturated material and giving a result of water head distribution.

5.2.1 Geometry of Bauxite Heap

As introduced in Chapter 1, the MV Bulk Jupiter is a Handymax type of vessel carrying 46.4 kDWT of bauxite from Malaysia to China (see Fig. 1-1 of Chapter 1). A typical voyage from Malaysia to China takes 9 to 14 days (Global Bauxite Working Group, 2017). MV Bulk Jupiter has overall length of 190 m, breadth of 32.26 m, and depth of 17.90 m (The Commonwealth of the Bahamas: Report on MV Bulk Jupiter, 2015). A typical cross section of a handymax type vessel is shown in Fig. 5-1. This design is consistent with the design code with the International Association of Classification Societies (IACS) (Common Structural Rules of Bulk Carriers, 2006). Due to the absence of actual cross section of MV Bulk Jupiter, the cross section of heap in one hold was extracted from the Global Bauxite Working Group (2017) typical for Malaysia to China voyage, with the geometry sketched (Fig. 5-2). This sketch was adopted as the model for all simulations, both for seepage analysis, as well as in Chapter 6.

5.2.2 Initial Conditions and Boundary Conditions

From the sketched geometry in Fig. 5-2, the dimensions of the heap to be simulated are shown in Fig. 5-3, which is very typical for the heaps of bauxite loaded on the Handymax type bulk carriers (typically 45 kDWT or more). The initial volumetric water content in the heap of bauxite after being loaded to a ship is thought to be rather uniform generally. To simulate this condition in the seepage analysis, as shown in Fig. 5-4, the initial water table is set at the bottom boundary of the heap, a transition phase with thickness of 0.1 m is set above the water table and the rest part of the heap (from the height of 0.1 m to the height of 10.5 m) is set to be of the same initial degree of saturation (Sr_{init}).

The density of bauxite is assumed to be uniform everywhere in the heap. Possible change of the density caused by the seepage, the rolling motion, etc. is not considered in the simulation. The effect of rolling motion on the seepage in the heap is not taken into account due to the limitation of the software.

There are 4 boundaries for this heap, B1-B4 as shown in Fig. 5-4. B3 (top surface) and B4 (bottom surface indicated by black lines) are always set to be impervious in all simulation conditions. B1 and B2 are set to be either impervious or pervious depending on the simulation conditions. The condition with fully impervious boundaries is expected to produce a result with the highest level of water table for a given Sr_{init}, which may be the most critical condition. However, the condition with pervious boundaries B1 and B2 corresponds to the real condition of the heap during transportation.

The model also takes into account the bilge of the hold. The bilge is the lowest part of a ship where the bottom curves up to meet the sides. The water that collects there is called bilge water. It is 0.3 m wide on both ends of the base. The bilge serves as drainage for the water to be dissipated from the heap during transport to prevent excessive development of wet base.

5.2.3 Experimental Representation of Densities of Bauxite

Fig. 5-5 shows the compaction curves with the density preparation for loose, medium dense, and dense cases. As elaborated in Chapter 2, two (2) types of compaction methods were performed, namely: type A method and type E method. Table 2-2 of Chapter 2 shows the details of each type of compaction methods, including the compaction energy information. As discussed in Chapter 2, type A method was performed only on particles less than 2 mm since the standard testing code for preparation of soil specimen used for triaxial tests do not permit the largest particle size of bauxite which is greater than 19 mm. Type E method was performed as the higher compaction energy that can be exerted on the specimen for maximum particle size greater than 19 mm.

Table 5-1 shows the summary of representation of the densities in the laboratory, assuming that the actual heap's maximum dry density (MDD) is that of the MDD obtained from type E compaction in this test which was 1.947 g/cm^3.

Table 5-1. Experimental Representation of Densities of Bauxite

Condition	Type E Method (entire gradation) (assumed actual density)			Type A Method (<2 mm particles) (equivalent laboratory preparation)		
	Dry Density, ρ_d (g/cm^3)	Max. Dry Density, $\rho_{d,max}$ (g/cm^3)	Degree of Compaction, D_c (%)	Dry Density, ρ_d (g/cm^3)	Max. Dry Density, $\rho_{d,max}$ (g/cm^3)	Degree of Compaction, D_c (%)
Loose	1.311	1.947	67.3	1.105	1.702	65
M.Dense	1.549		79.6	1.360		80
Dense	1.800		92.4	1.530		90

For loose case, the dry density of 1.311 g/cm^3 was obtained from the published density value in the official report of MV Bulk Jupiter (The Commonwealth of the Bahamas: Report on MV Bulk Jupiter, 2015).

For medium dense case, the dry density of 1.549 g/cm^3 was obtained from the bulk density of a trip from Malaysia to China which is 1.88 g/cm^3 as reported from the Global Bauxite Working Group (2017) and a moisture content of 21.3% (The Commonwealth of the Bahamas: Report on MV Bulk Jupiter, 2015). The resulting dry density of the bulk density of 1.88 g/cm^3 and a moisture content of 21.3% is 1.549 g/cm^3.

For dense case, the dry density of 1.800 g/cm^3 was a suggested value to represent dense case by a practitioner/expert on bauxite in Australia.

From these values, they were converted accordingly to the laboratory tests to represent each type of D_c as shown in Table 5-1.

5.2.4 Simulation Duration and Results Conversion

The duration of seepage is set to be 350 hours (about 14 days) which corresponds to a voyage from Malaysia to China. Aside from the maximum duration, a duration of 57.5 hours was also taken into account since the MV Bulk Jupiter capsized at this duration from the start of its voyage (The Commonwealth of the Bahamas: Report on MV Bulk Jupiter, 2015).

The water head of the point A at the bottom center of the heap as shown in Fig. 5-3 is traced to show the time history of water head at the point A. The output result of the program is water head with unit of meter. A point with the positive water head in the heap is considered to be saturated and that with the negative value is thought to be unsaturated. The water table is assumed to be the contour line with water head of zero and it can be located through the water head at the bottom boundary. Since the *Sr* of the unsaturated zone is not directly given, it was determined with the help of SWRC curve which can be expressed as a relationship between suction and *Sr* (assuming suction=9.81 kN/m^3 * water head).

5-3. Simulation Conditions

The availability of permeability tests results under different saturation conditions and SWRC tests permit the input for the seepage analysis. The experimental data are simply implemented by input to the software. For comparison purposes, the built-in Van Genuchten model (VG Model) (Van Genuchten, 1980) is used also to predict the permeability of the unsaturated bauxite. The Van Genuchten model was already introduced in detail in Section 4-6 of Chapter 4. Basically the permeability of the unsaturated soils is proposed to be a function of water head (*h*) with 5 parameters:

k_{unsat} = f (k_s, θ_s, θ_r, α, n, h) (Eqn. 5-1)

where,
k_s = coefficient of permeability of the soil in saturated condition
θ_s = saturated volumetric water content
θ_r = residual water content
α and n = model parameters
h: water head

5.3.1 SWRC Simulation and *k* ratio simulation (k_r)

The parameter, k_s, is obtained from permeability tests as discussed in Chapter 4. Parameters, θ_s and θ_r, are determined by the density and SWRC of bauxite. Parameters, α and n, can be determined by fitting SWRC of bauxite. Utilizing an online tool developed by Seki, K. (2007), the curves of VG model estimate was plotted against the experimental data obtained from the ceramic disk apparatus in SWRC in Chapter 4.

Fig. 5-6 to Fig. 5-8 show the fitting curves for bauxite under loose, medium dense, and dense cases, respectively.

Table 5-2 lists the conditions of SWRC tests and obtained parameters.

Table 5-2. SWRC tests and Van Genuchten model fitting (bauxite)

Test name	*Dc (%)*	Case	*e*	ρ_d *(g/cm^3)*	θ_s	θ_r	*a (/m)*	*n*
Test 4 of Table 4-9	64.9	Loose	1.396	1.103	0.507	0.172	11.140	2.220
Test 5 of Table 4-9	79.8	M.Dense	0.947	1.357	0.332	0.170	2.009	2.185
Test 6 of Table 4-9	89.0	Dense	0.747	1.513	0.252	0.127	1.624	1.635

Since the built-in VG model could not consider the hysteresis effect in the simulation, only drying curve parameter settings were examined.

The results obtained for iron ore and Inagi sand were also compared to VG model estimate.

Fig. 5-9 shows the fitting curve for iron ore at dense case, while Fig. 5-10 shows the fitting curve for Inagi sand at loose case.

Table 5-3 and Table 5-4 present the condition of SWRC test and obtained parameter for iron ore and Inagi sand, respectively.

Table 5-3. SWRC tests and Van Genuchten model fitting (iron ore)

Test name	*Dc (%)*	Case	*e*	ρ_d *(g/cm^3)*	θ_s	θ_r	*a (/m)*	*n*
Test 1 of Table 4-10	91.6	Dense	0.740	2.554	0.153	0.0882	1.010	2.643

Table 5-4. SWRC tests and Van Genuchten model fitting (Inagi sand)

Test name	*Dc (%)*	Case	*e*	ρ_d *(g/cm^3)*	θ_s	θ_r	*a (/m)*	*n*
Test 1 of Table 4-11	72.0	Loose	1.224	1.194	0.424	0.159	3.218	2.215

As for the experimental data, the ratio of permeability of the unsaturated case with respect to the saturated case is necessary. This is known as *k* ratio or k_r. Mathematically, it is:

$$k_r = {}^{k_{unsat}}/_{k_s} \qquad \text{(Eqn. 5-2)}$$

Table 5-5 summarizes the k_r values for the unsaturated permeability of bauxite for the experimental data and for the VG estimate. The VG model estimate is calculated from equation 4-10 of Chapter 4. The test numbers were all adopted from Table 4-6 where the tests conditions were obtained.

Table 5-5. k_r values for the experimental data and VG estimate (bauxite)

Test	D_c (%)	Case	Final degree of saturation Sr_{final}(%)	Experimental Data		VG Model Estimate	
				k_{unsat} (cm/sec)	k_r	k_{unsat} (cm/sec)	k_r
4	81.1	M.Dense	64.2	2.25×10^{-4}	3.85×10^{-2}	2.63×10^{-5}	4.50×10^{-3}
5	80.2		66.2	1.67×10^{-4}	2.86×10^{-2}	4.38×10^{-5}	7.50×10^{-3}
6	80.3		68.2	2.47×10^{-4}	4.23×10^{-2}	6.88×10^{-5}	1.18×10^{-2}
7	80.2		68.1	3.06×10^{-4}	5.24×10^{-2}	6.79×10^{-5}	1.16×10^{-2}
8	79.8		57.8	6.77×10^{-5}	1.16×10^{-2}	3.25×10^{-6}	5.57×10^{-4}
9	79.9		58.2	9.24×10^{-5}	1.58×10^{-2}	3.83×10^{-6}	6.56×10^{-4}
11	79.7		100	5.84×10^{-3}	1	5.84×10^{-3}	1
12	80.0		51.1	8.45×10^{-6}	1.45×10^{-2}	3.28×10^{-8}	5.62×10^{-6}
13	79.8		77.9	8.40×10^{-4}	1.44×10^{-1}	4.06×10^{-4}	6.95×10^{-2}
14	67.7	Loose	48.8	3.25×10^{-5}	2.23×10^{-3}	1.55×10^{-5}	1.06×10^{-3}
15	71.6		52.3	5.94×10^{-5}	4.07×10^{-3}	4.96×10^{-5}	3.40×10^{-3}

16	70.4		100	1.46×10^{-2}	1	1.46×10^{-2}	1
17	88.8	Dense	64.5	5.91×10^{-5}	2.11×10^{-2}	2.76×10^{-6}	9.86×10^{-4}
18	88.8		74.1	2.86×10^{-4}	1.02×10^{-1}	3.09×10^{-5}	1.21×10^{-2}
19	89.1		100	2.80×10^{-3}	1	2.80×10^{-3}	1
20	88.7		57.1	2.01×10^{-5}	7.18×10^{-3}	1.43×10^{-7}	5.11×10^{-5}

Fig. 5-11 shows the plot of the k_r values vs. *Sr* for experimental data and VG model estimate of bauxite. The plot shows that the k_r vs *Sr* formed a unique line regardless of the density of the material while VG estimate shows that as the specimen becomes denser, such as the medium dense and dense cases, the results of VG estimate do not agree with the experimental data, with VG being underestimate. This behavior can be seen already from Fig. 4-92 of Chapter 4 which is basically the same plot to Fig. 5-11 when Fig. 4-92 is normalized with respect to its *k* at saturated condition. For simulations however, the experimental data shall be adopted since they represent the obtained data from tests, while VG estimate rely on model parameters, which have some assumptions. The results obtained also suggest that VG estimate may represent slower accumulation of water into the heap, which experimental data suggest otherwise.

Table 5-6 and Table 5-7 summarize the k_r values for the unsaturated permeability of iron ore and Inagi sand for the experimental data and for the VG estimate. The test numbers were all adopted from Table 4-7 and Table 4-8 for iron ore and Inagi sand, respectively.

Table 5-6. k_r values for the experimental data and VG estimate (iron ore)

Test	D_c (%)	Case	Final degree of saturation Sr_{final} (%)	Experimental Data		VG Model Estimate	
				k_{unsat} (cm/sec)	k_r	k_{unsat} (cm/sec)	k_r
1	91.5	Dense	100	2.84×10^{-3}	1	2.84×10^{-3}	1
2	92.3		74.1	1.65×10^{-5}	5.81×10^{-3}	4.77×10^{-5}	1.68×10^{-2}
3	91.6		66.8	4.44×10^{-6}	1.56×10^{-3}	8.60×10^{-6}	3.03×10^{-3}

Table 5-7. k_r values for the experimental data and VG estimate (Inagi sand)

Test	D_c (%)	Case	Final degree of saturation Sr_{final} (%)	Experimental Data		VG Model Estimate	
				k_{unsat} (cm/sec)	k_r	k_{unsat} (cm/sec)	k_r
0	69.2	Loose	100	5.31×10^{-4}	1	5.31×10^{-4}	1
1	70.7		74.2	6.10×10^{-5}	1.15×10^{-1}	4.56×10^{-5}	8.59×10^{-2}
2	71.0		62.2	1.31×10^{-5}	2.47×10^{-2}	8.71×10^{-6}	1.64×10^{-2}

Fig. 5-12 shows the plot of the k_r values vs. *Sr* for experimental data and VG model estimate of bauxite and iron ore at dense case. The results of VG estimate do not agree with the experimental data. The trend obtained here is similar in behavior as that of Fig. 4-93 of Chapter 4 which is basically the same plot to Fig. 5-12 when Fig. 4-93 is normalized with respect to its *k* at saturated condition.

Fig. 5-13 shows the plot of the k_r values vs. *Sr* for experimental data and VG model estimate of bauxite and Inagi sand at loose case. For the loose case, the experimental data and VG

estimate agree well for both bauxite and Inagi sand. The trend obtained here is similar in behavior as that of Fig. 4-94.

5.3.2 Test Cases for Simulations

Table 5-8 indicates the conditions of seepage analysis

Table 5-8. Conditions of seepage analysis

Case	k_{unsat} data	Boundary Conditions	Sr_{init} (%)
1	From experimental results	Pervious B1 & B2 (see Fig.5-5)	55, 60, 70, 80, 90
2		Impervious B1 & B2 (see Fig.5-5)	
3	VG model estimate	Pervious B1 & B2 (see Fig.5-5)	
4		Impervious B1 & B2 (see Fig.5-5)	

For bauxite, all cases were conducted for loose, medium dense, and dense cases. Drying curve was used for SWRC for all tests.

As for iron ore and Inagi sand, only cases 1 and 3 were conducted.

5-4. Software Input Methodology

This section describes the general steps in software implementation.

1. Create the geometry of the heap by indicating nodes and lines connecting them. The software only permits clockwise direction of input of nodes and no lines can intersect (Fig. 5-14).
2. For experimental data, input data by indicating volumetric water content and k_r, as well as volumetric water content and suction (Fig. 5-15). For VG model, indicate relevant parameters k_s, θ_s, θ_r, α, and n (Fig. 5-16).
3. Click sides of model and indicate boundary conditions (Fig. 5-17)
4. Indicate distribution of volumetric water content throughout the heap (Fig. 5-18)
5. Indicate time step of runs and time where data is necessary (Fig. 5-19)
6. Create mesh for the model (Fig. 5-20)
7. Indicate nodes which are necessary to extract its time history of suction.
8. Run the analysis.

5-5. Tests Results and Discussions

5.5.1 Time Histories at the Bottom Center at Point A

This section shows the time histories at the bottom center at point A (see Fig. 5-3).

1. Bauxite

Fig. 5-21 shows the water head change of point A at the bottom center of the heap with time for five different Sr_{init}, which indicates the time history of the height of the saturated zone. It is noticed that for conditions with relatively low Sr_{init}, the water head at point A may momentarily become negative (e.g. black and red lines in Fig. 5-21) and it takes longer time for stabilization than those conditions with relatively high Sr_{init}. The longer duration of the stabilization may be attributed to the low permeability in the conditions with low Sr_{init}. Another finding that can be observed in Fig 5-21 is that the VG Model estimate are generally underestimate of the experimental data. This is consistent with the findings in unsaturated permeability (Fig. 5-11) where VG model permeability estimates are generally underestimate of the experimental data. At high $Sr_{init,}$ it can be seen that the water head initially spikes up higher and then gradually decreases and converges at about 1.5 m elevation from point A at t=350 hours for both experimental data and VG model. At Sr_{init} = 55%, the water head at point A is at lower elevation, suggesting that the saturated region could be lower if the heap was loaded at a low Sr_{init}.

Regarding the effect of different boundary conditions, Fig. 5-22 shows the experimental results data of medium dense bauxite, comparing the pervious and impervious boundaries B1 and B2 labeled in Fig. 5-4. It seems that there is no reduction of the water head histories in cases with the impervious boundaries, while the reduction from peak values is observed in cases with pervious boundary. For impermeable side boundary B1 and B2, it can be seen that the water head can get as high as 8 m for Sr_{init} = 90%. This implies that if water is unable to dissipate out of the heap and there's improper drainage, the heap is basically submerged up to 8 m high with water. This scenario is unlikely though and too conservative, hence this scenario is for comparison's sake only.

Fig. 5-23 shows the comparison of the water head at point A with respect to time (duration) for various densities of bauxite. A general trend can be seen that denser the material is, the lower it accumulates water at the heap at the final point of voyage (i.e. t=350 hours). The water head at point A at t=350 hours is around 1.8 m, 1.5 m, and 0.4 m for loose case, medium dense case, and dense case, respectively.

Another point of interest is the 57.5th hour which is indicated by a vertical line in Fig. 5-23 since it is the reported duration when MV Bulk Jupiter capsized (The Commonwealth of the Bahamas: Report on MV Bulk Jupiter, 2015). That point of time is assessed to be more critical since the water head at that instant is higher than the water head at the 350th hour. It can be seen that the water head can be up to 3.5 m high for loose case at Sr_{init} = 90%, 2.5 m high for medium dense case at Sr_{init} = 90%, and 1.0 m high for dense case at Sr_{init} = 90% at t=57.5 hours.

There are cases when the water head do not even accumulate at all. For example at dense case, it is even possible at low initial Sr to not develop positive water head (i.e. suction governs throughout the duration). Take Sr_{init} = 55% for example, the dense case does not indicate any water head value at point A throughout the duration of the voyage. This implies that it takes much longer time for water to permeate at denser materials in addition to its SWRC. However, at high Sr_{init}, it can be said that depending on the density of the material,

the water head at point A varies and can accumulate up to 3.3 m high at *t*=57.5 hours for pervious boundary B1 and B2.

In Fig. 5-24, the water head at point A is summarized with respect to the Sr_{init} for bauxite at various densities for both 57.5th hour of voyage and 350th hour of voyage (whole duration). The water head at point A varies, depending on the density and Sr_{init}. The lower the density, the higher the water head at point A for both 57.5th hour and 350th hour. It seems that at Sr_{init} = 70% or greater, the water head achieved at point A is the same generally.

Hence, by simply investigating the water head at point A, it has given us the information about the possible wet base at which elevation it can accumulate. The water head distribution along the vertical line of heap shall be discussed on section 5.5.2 to fully understand the distribution of water.

2. Iron Ore

Fig. 5-25 compares the water head at point A with respect to time using the experimental data at pervious B1 and B2 side boundary for bauxite and iron ore at dense case. From this plot, it can be seen that the water head at point A for iron ore is lower than bauxite in general. This is supported by the obtained experimental data of bauxite and iron ore in Fig. 5-12. Just like the observation for bauxite, iron ore at dense case has low water head (~0.2 m at *t* = 350 hr) at point A for pervious B1 and B2 side boundary.

Fig. 5-26 is a comparison of bauxite and iron ore of the water head at point A with respect to the Sr_{init} using experimental data and pervious B1 and B2 side boundary. The data for 57.5th hour and 350th hour seem to agree starting from Sr_{init} = 80% at *t* = 350 hr. At *t* = 57.5 hr however, the water head for bauxite is 1.0 m, as discussed earlier already.

3. Inagi Sand

Fig. 5-27 compares the water head at point A with respect to time using the experimental data at pervious B1 and B2 side boundary for bauxite and Inagi sand at loose case. While bauxite shows a uniform trend especially from Sr_{init} = 60% or higher, the result for Inagi sand was dependent on the $Sr_{init.}$ The development of water head varies extensively from the $Sr_{init.}$ One of the possible reasons is that the permeability of Inagi sand is 2 orders lower than that of bauxite. From Fig. 4-94 of Chapter 4, the permeability of Inagi sand is in the order of -4 while bauxite at loose case is -2. This is in addition to the SWRC of both materials in Fig. 4-91 of Chapter 4 where Inagi sand has higher air entry value (AEV) than its bauxite counterpart at loose case. Investigating the trend of Inagi sand in Fig. 5-27 for Sr_{init} = 70% or greater, the water head at point A values seem to be still decreasing even at 350th hour. At longer durations, it is possible that the water head at point A will eventually converge at a specific head.

Fig. 5-28 is a comparison of bauxite and Inagi sand of the water head at point A with respect to the Sr_{init} using experimental data and pervious B1 and B2 side boundary. The data for

57.5th hour and 350th hour do not agree, with Inagi sand even having a negative water head (suction) at Sr_{init} =70% at 57.5th hour.

5.5.2 Contour Figures of Final Water Head Distribution

1. Bauxite

In this section, the contour figures of water head distribution in the heap (Fig. 5-29 to Fig. 5-33) at 57.5 hours of voyage are displayed using experimental data with pervious B1 and B2 boundary for bauxite at medium dense. The legends shown in the figures indicate the magnitude of the water head. It should be noted, however, that because of the limitation of the software, the same color in different contour figures does not always represent the same value of water head, thus the direct comparison of water head between figures is difficult. This issue may not be serious since these contour figures are only used for general observation of simulation results in this section.

Fig. 5-29 to Fig. 5-33 show that the patterns of water head distribution are different depending on the Sr_{init}. For Fig. 5-29 to Fig. 5-31 (i.e. Sr_{init}.=90%, Sr_{init}.=80%, and Sr_{init}.=70%, respectively), the wet base accumulates up to 2.5 m from the base, and then a 2.5 to 3.5 m thick transition zone with a sharp drop from saturated region to low degrees of saturation (i.e. 55% to 60%), and then a residual saturation degree up to the surface of the heap. The distribution is converted from the volumetric water content since the output of the software indicates the water head at the node. The wet base accumulated forms an ellipsoidal shape, with the peak at the centerline of the cross section, tapering to the side boundary. Due to the bilge, the water is able to drain on the extreme points of the base, hence forming the shape of the ellipsoidal wet base.

Fig. 5-32 shows the distribution for Sr_{init} = 60%. Here, the thickness of wet base is only 1.8 m, which the data in Fig. 5-21 (solid red line) supports this trend. A transition zone of 2.5 m follows after that, before the residual saturation degree up to the surface of the heap.

Fig. 5-33 is a special case too, showing the distribution for Sr_{init} = 55%. It did not even form a wet base and then a 1.5 m transition zone before converging to the residual saturation degree up to the heap after that.

Fig. 5-34 shows the pattern of water head distribution at Sr_{init}.=90% at t = 350 hr for medium dense case. It can be seen that compared to Fig. 5-29 (t = 57.5 hr), the wet base is lower. This is supported by the discussion on the water heads at point A in the previous section and also Fig. 5-21. Another thing that can be noticed is that in Fig. 5-34, the equipotential lines became more horizontal than that of Fig. 5-29. At the entire duration of the voyage, the water has already permeated down the heap, exiting the bilge, and the water distribution has minimal change even from hereon.

Investigating the loose case at Sr_{init}.=90% at t = 57.5 hr, Fig. 5-35 shows the water head distribution on the heap. Comparing to Fig. 5-29, which is the equivalent for the medium

dense, the wet base accumulates up to 3.5 m, which is higher. It has a transition zone of 3.5 m, before approaching the residual saturation degree up to the heap. This implies that depending on the density of the heap, the wet base that can accumulate varies, with the looser the heap is, the higher the wet base.

Fig. 5-36 is the equivalent for dense case at Sr_{init}.=90% at t = 57.5 hr. Here, it can be seen that the wet base accumulates only up to 1.0 m. The transition zone is 2.5 m, and then converges to the residual saturation degree.

Fig. 5-37 is the extreme scenario, which is the same state for t = 57.5 hr and t = 350 hr using experimental data with impervious B1 and B2 boundary for bauxite at medium dense. Assuming the water cannot dissipate on its side boundary, or ineffective drainage at the bilge on the hold of the cargo, the wet base can accumulate up to 8 m high from the base at Sr_{init} = 90%. The transition zone follows that and it seems that the residual saturation degree has not been achieved until it reached the surface of the heap.

It can be said that for permeable B1 and B2 side boundary which is the more realistic case, the extreme case at t = 57.5 hr is that of 3.5 m wet base for loose (Fig. 5-35), 2.5 m wet base for medium dense (Fig. 5-29), and 1.0 m wet base for dense (Fig. 5-36). The wet base is followed by a transition zone with varying thickness of 2.5 m to 3.5 m zone at extreme case scenario at t = 57.5 hr, before it decreases to residual saturation degree up to the surface of the heap. As for the impermeable B1 and B2 side boundary, the wet base can accumulate up to 8 m high, before the transition zone up to the surface of the heap.

2. Iron Ore

At Sr_{init} = 90%, Fig. 5-38 shows the contour figures of water head distribution in the heap at the 57.5th hour using experimental data with pervious B1 and B2 boundary for iron ore at dense state. The trend is similar to that of Fig. 5-36 at Sr_{init} = 90% of bauxite at dense state. Wet base accumulates up to 0.5 m high, with 4.0 m transition zone, before the residual saturation degree up to the surface of the heap.

3. Inagi Sand

At Sr_{init} = 90%, Fig. 5-40 shows the contour figures of water head distribution in the heap at the 57.5th hour using experimental data with pervious B1 and B2 boundary for Inagi sand at loose state. Wet base accumulates up to 4.5 m high, with 3.5 m transition zone, before the residual saturation degree up to the surface of the heap.

5-6. Chapter Summary

In this Chapter, the following conclusions can be stated:

1. Seepage analysis using Guslope was performed to study the water content distribution in the heap of bauxite for handymax type vessel. Seepage analysis was also performed on iron ore at dense condition and Inagi sand at loose condition, for comparison's sake. With the availability of experimental data on permeability and SWRC, the software permits the input of actual data for analysis. The experimental data results were compared with VG model and in general, the VG model estimate is an underestimate of the results that can be obtained from the experimental data.

2. Time history at the bottom center of point A (see Fig. 5-3) for bauxite shows that the water head depends on the density of the heap. In general, the water head at point A at t=57.5 hr is greater than at t=350 hr. At extreme condition, the water head at point A for loose bauxite is 3.5 m, medium dense is 2.5 m, and dense is 1.0 m. For iron ore dense case, it is even possible that the water head at point A is a negative value (suction) for the whole duration of 350 hours. The result for Inagi sand on the other hand, was dependent on the Sr_{init}. Inagi sand has two (2) orders lower permeability than its bauxite counterpart at loose condition in addition to its higher air entry value (AEV), causing longer time to increase water head. At longer durations, it is possible that the water head at point A will eventually converge at a specific head for Inagi sand.

3. For permeable B1 and B2 side boundary condition (see Fig. 5-4), the extreme case has S_r profile along the centerline of the heap depending on the density:
   - bauxite, loose: wet base = 3.5 m high, transition zone = 3.5 m thick, residual S_r = 3.5 m thick (Fig. 5-35)
   - bauxite, medium dense: wet base = 2.5 m high, transition zone = 3.5 m thick, residual S_r = 4.5 m thick (Fig. 5-29)
   - bauxite, dense: wet base = 1.0 m high, transition zone = 2.5 m thick, residual S_r = 7.0 m thick (Fig. 5-36)
   - iron ore, dense: wet base = 0.5 m high, transition zone = 4.0 m thick, residual S_r = 6.0 m thick (Fig. 5-38)
   - Inagi sand, loose: wet base = 4.5 m high, transition zone = 3.5 m thick, residual S_r = 2.5 m thick (Fig. 5-39)

   The shape of the wet base accumulated is generally ellipsoidal, with the peak at the centerline of the cross section, tapering to the side boundary.

4. For impermeable B1 and B2 side boundary condition, the extreme case has wet base that can accumulate up to 8 m high, before the transition zone up to the surface of the heap (Fig. 5-37). This condition is assessed to be unrealistic, as it would imply that drainage was not totally working and there is totally no dissipation of water out of the heap.

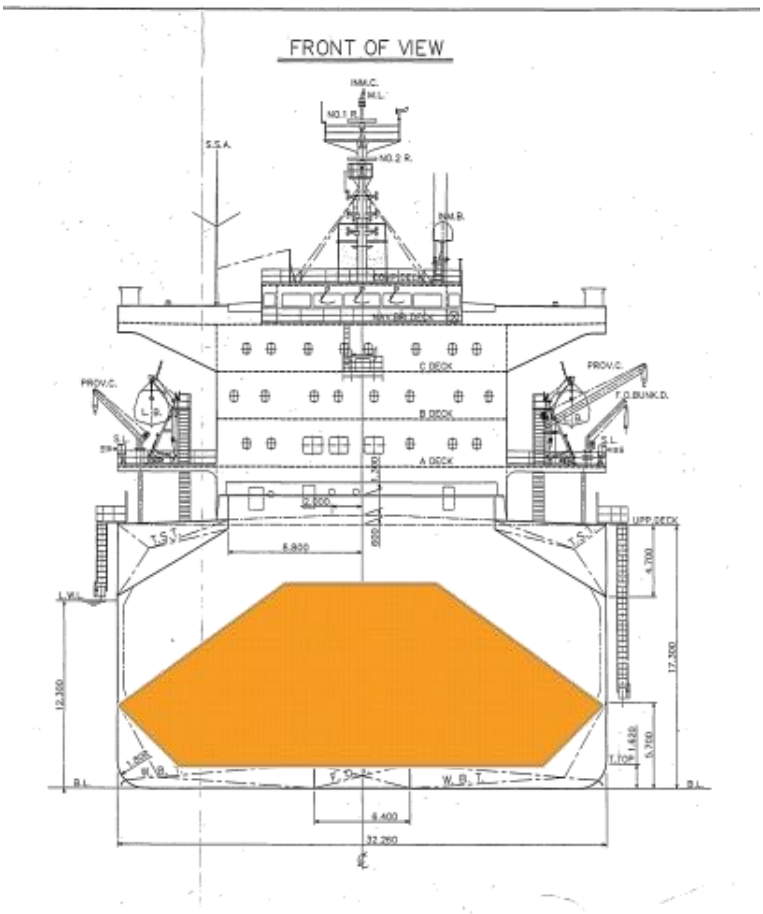

Fig. 5–1. Typical cross sectional area of handymax per hold with heap of bauxite (modified after The Commonwealth of the Bahamas: Report on MV Bulk Jupiter, 2015)

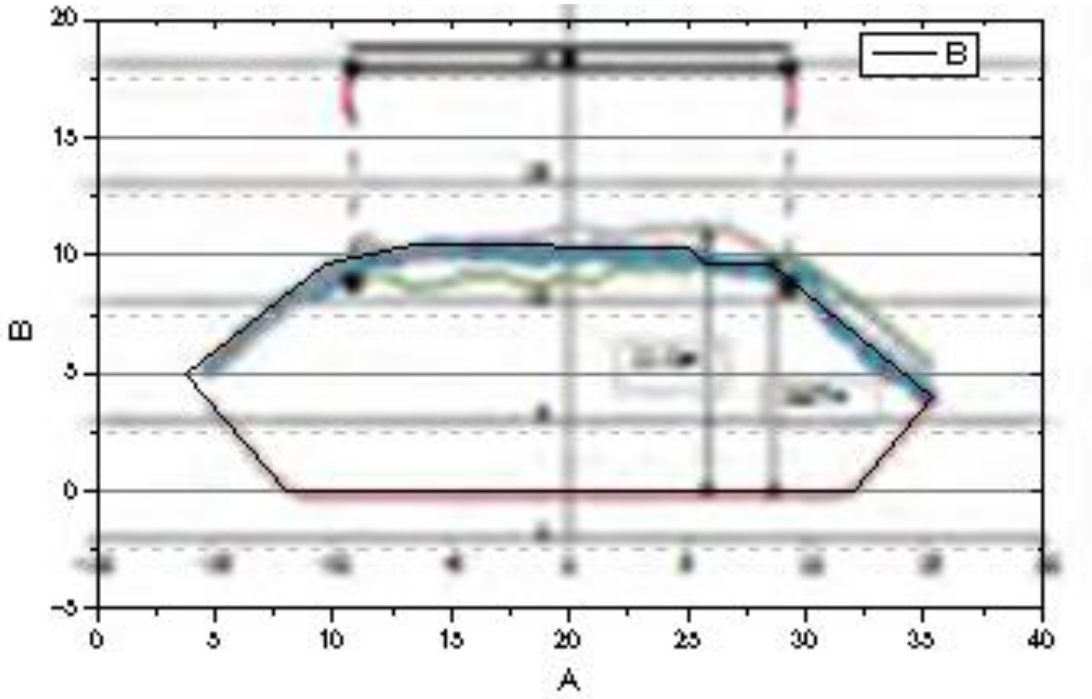

Fig. 5–2. Geometry of heap of bauxite in one hold for Malaysia to China voyage (Global Bauxite Working Group, pp. 46-47)

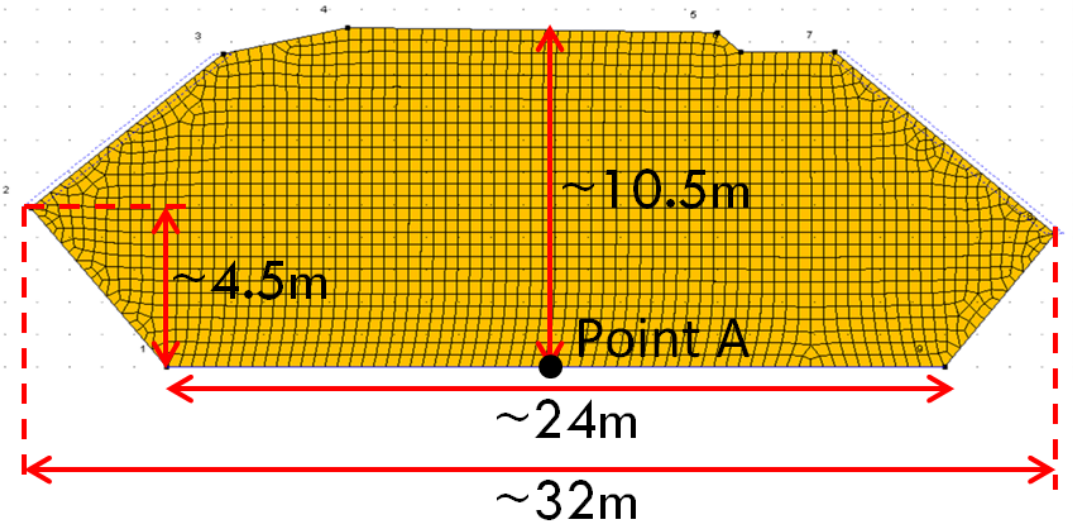

Fig. 5–3. Model of heap of bauxite for seepage analysis

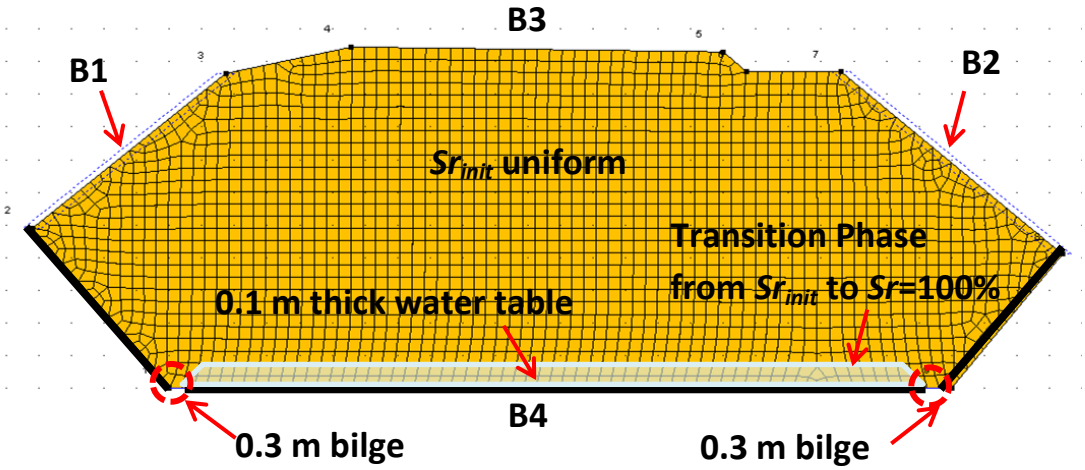

Fig. 5–4. Initial condition and boundary conditions of heap of bauxite for one hold

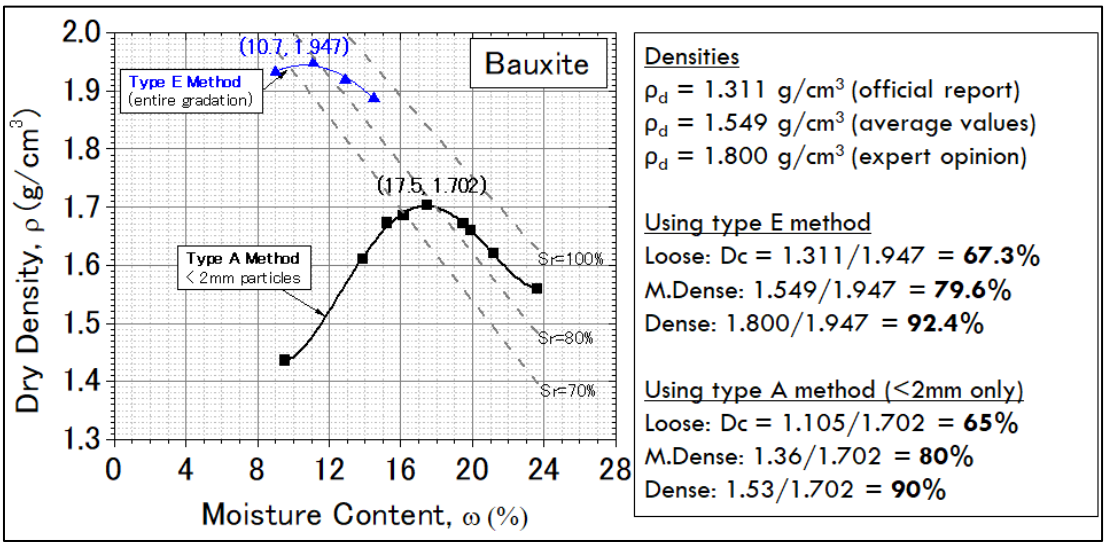

Fig. 5–5. Experimental Representation of Densities of Bauxite (Modified after Fig. 2-4)

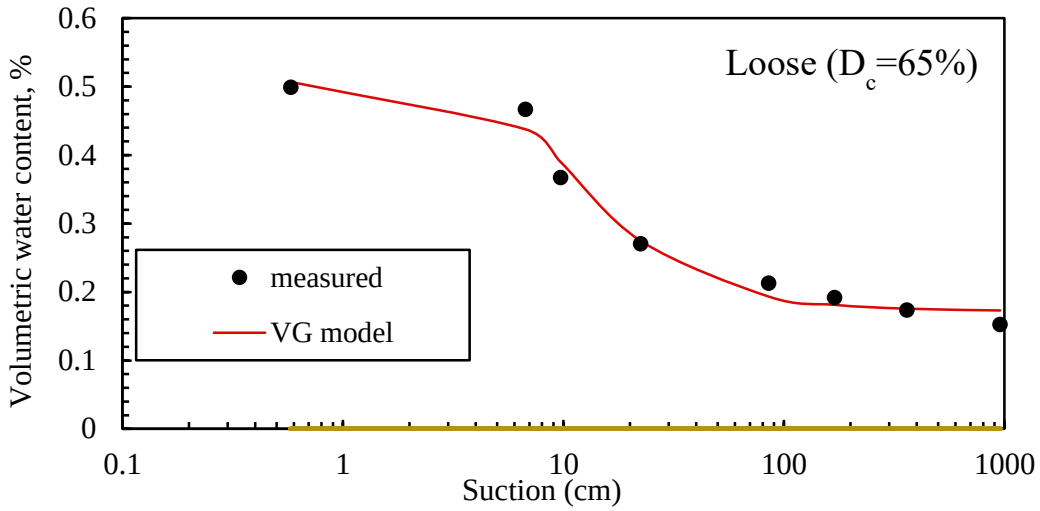

Fig. 5–6.SWRC plots showing measured (experimental) data and VG model estimate (bauxite, loose)

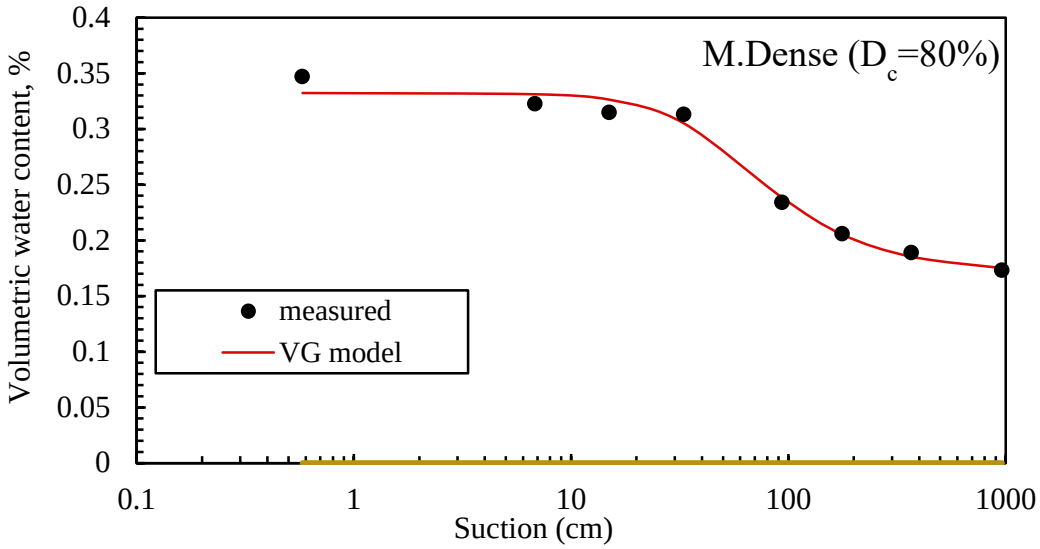

Fig. 5–7.SWRC plots showing measured (experimental) data and VG model estimate (bauxite, medium dense)

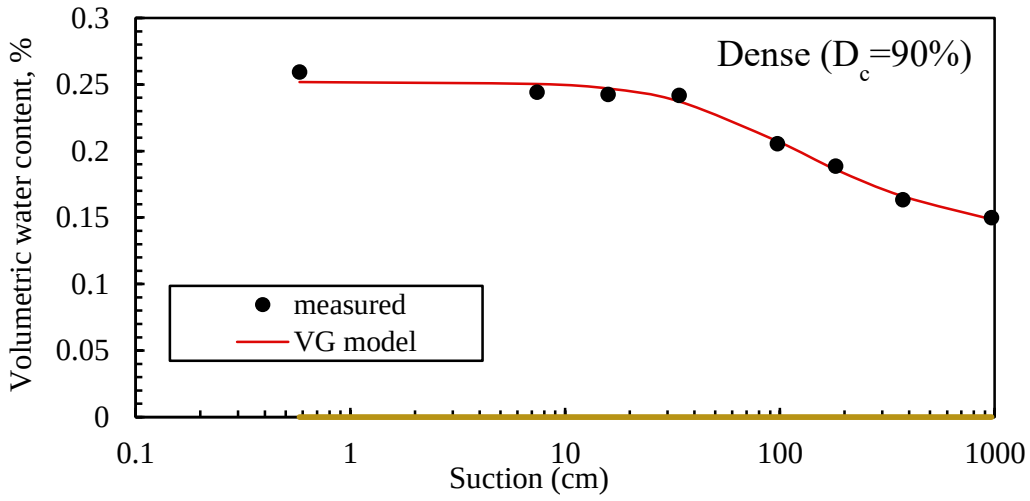

Fig. 5–8.SWRC plots showing measured (experimental) data and VG model estimate (bauxite, dense)

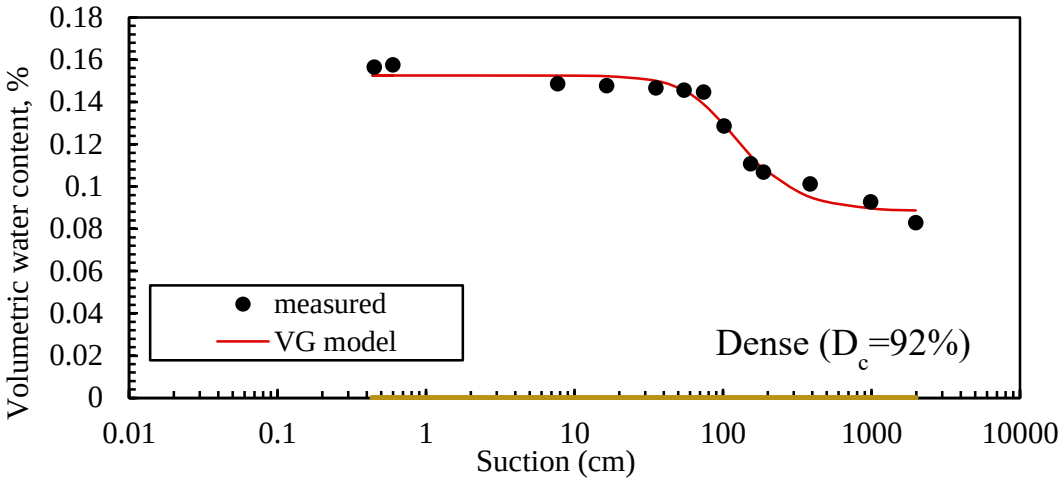

Fig. 5–9.SWRC plots showing measured (experimental) data and VG model estimate (iron ore, dense)

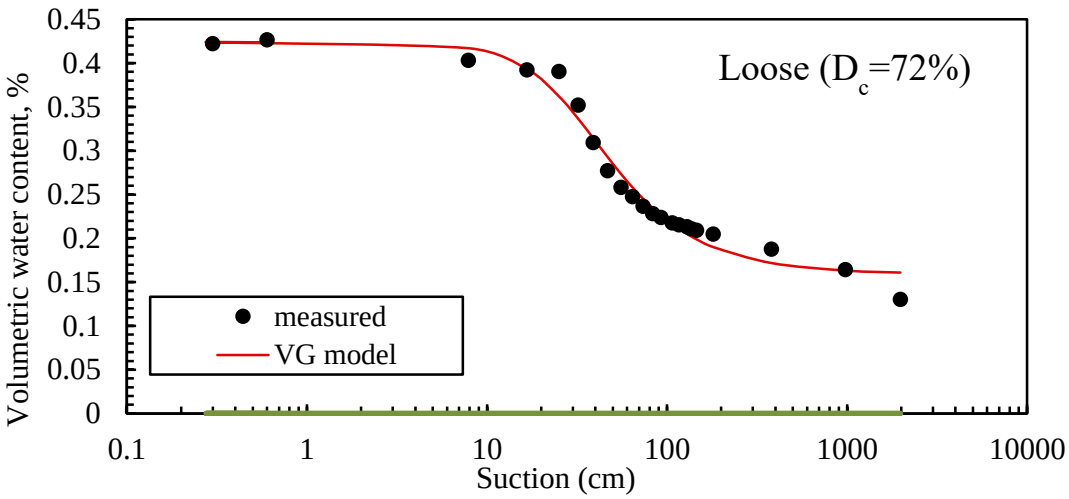

Fig. 5–10.SWRC plots showing measured (experimental) data and VG model estimate (Inagi sand, loose)

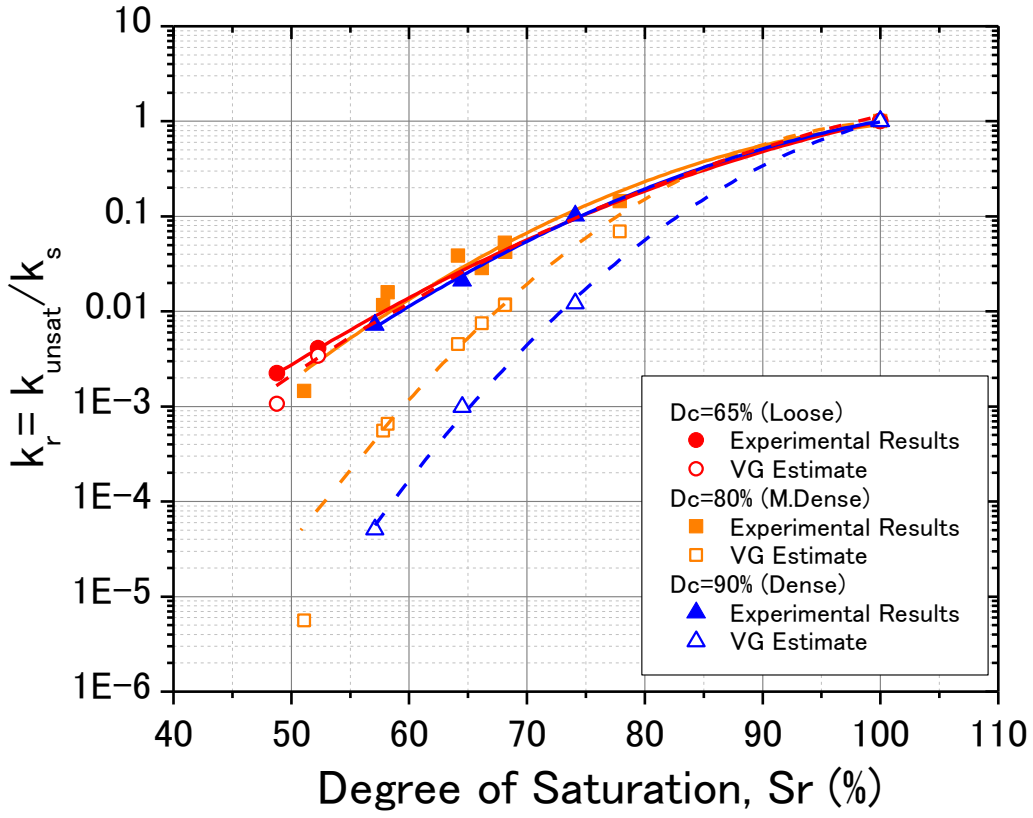

Fig. 5-11. k_r vs. *Sr* plot of experimental data and VG estimate (bauxite, all tests, unsaturated)

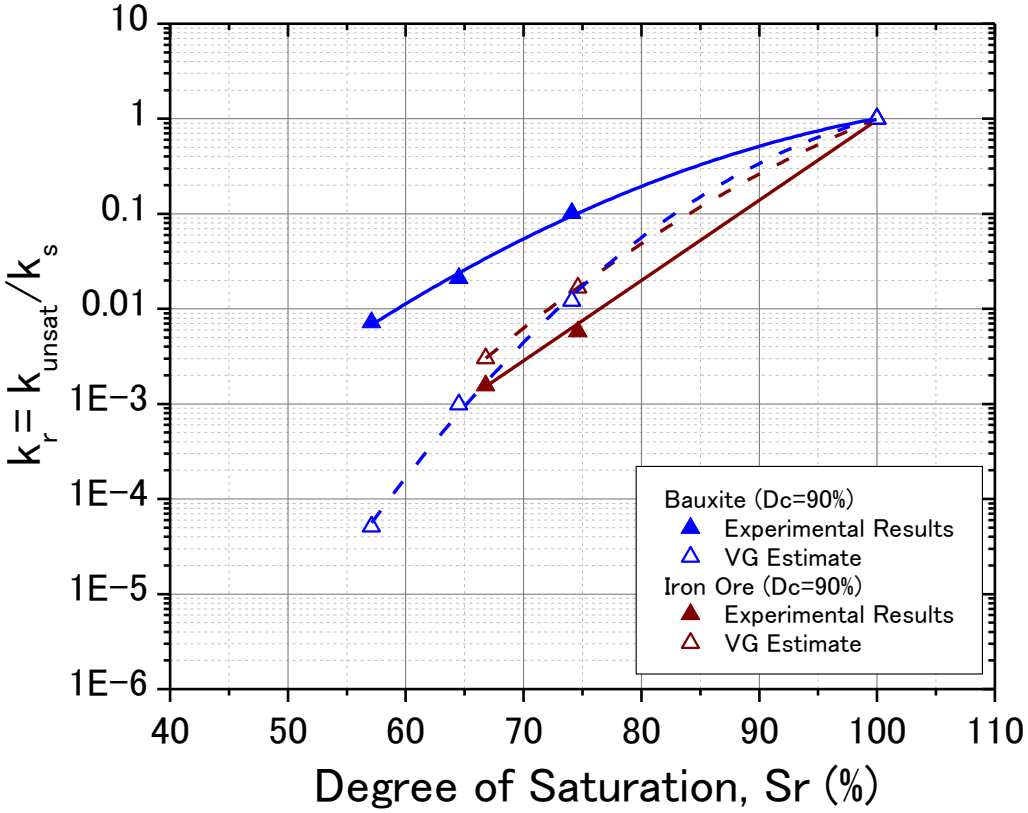

Fig. 5-12. k_r vs. *Sr* plot of experimental data and VG estimate
(bauxite and iron ore, dense, unsaturated)

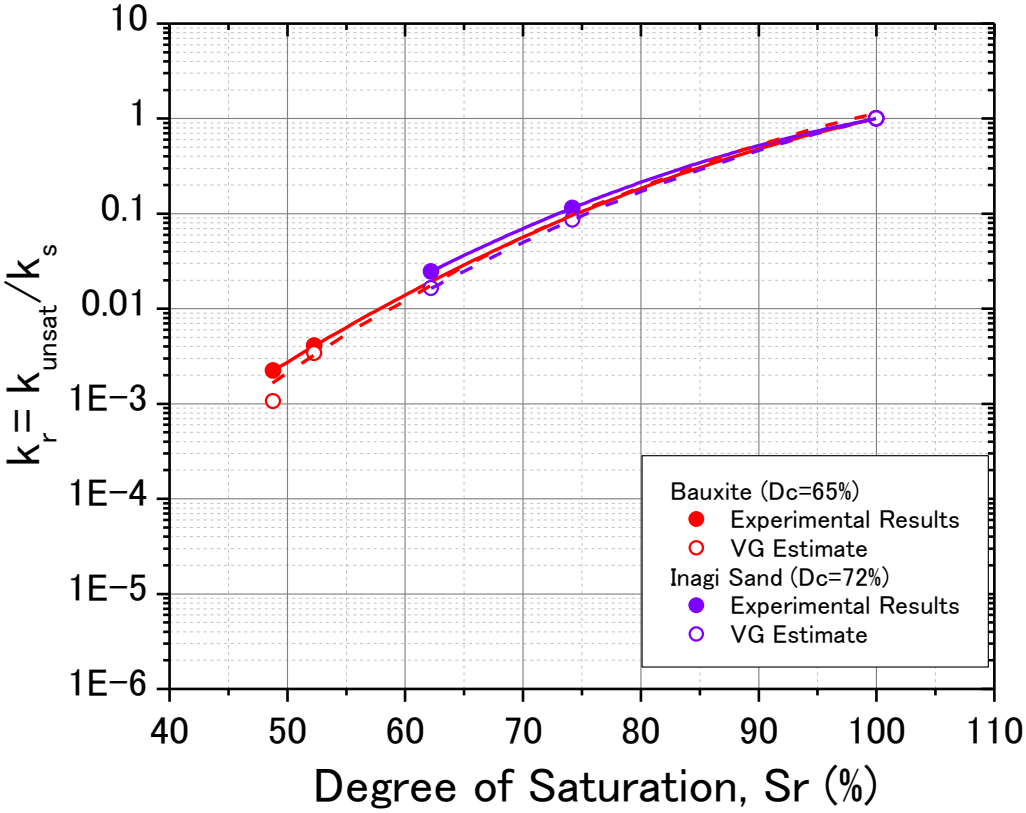

Fig. 5-13. k_r vs. Sr plot of experimental data and VG estimate
(bauxite and Inagi sand, loose, unsaturated)

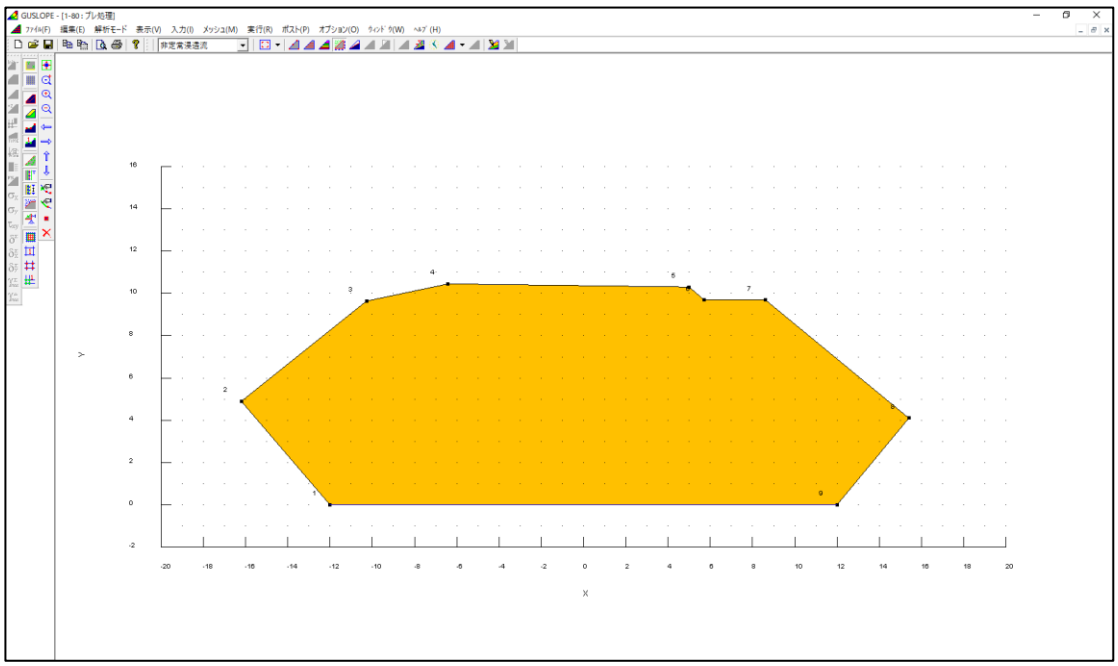

Fig. 5-14. Create the geometry of the heap

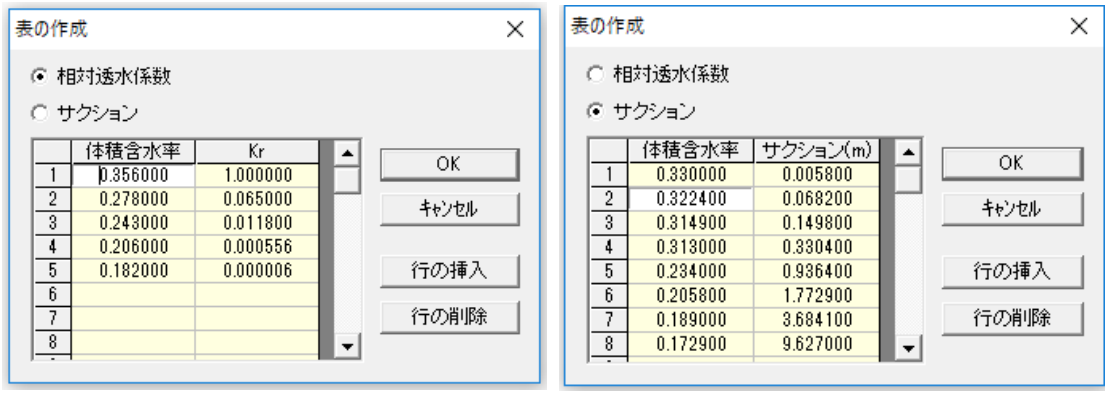

Fig. 5-15. Input parameters for experimental data

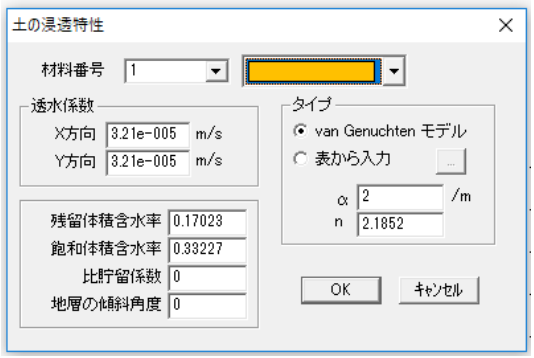

Fig. 5-16. Input parameters for VG model estimate

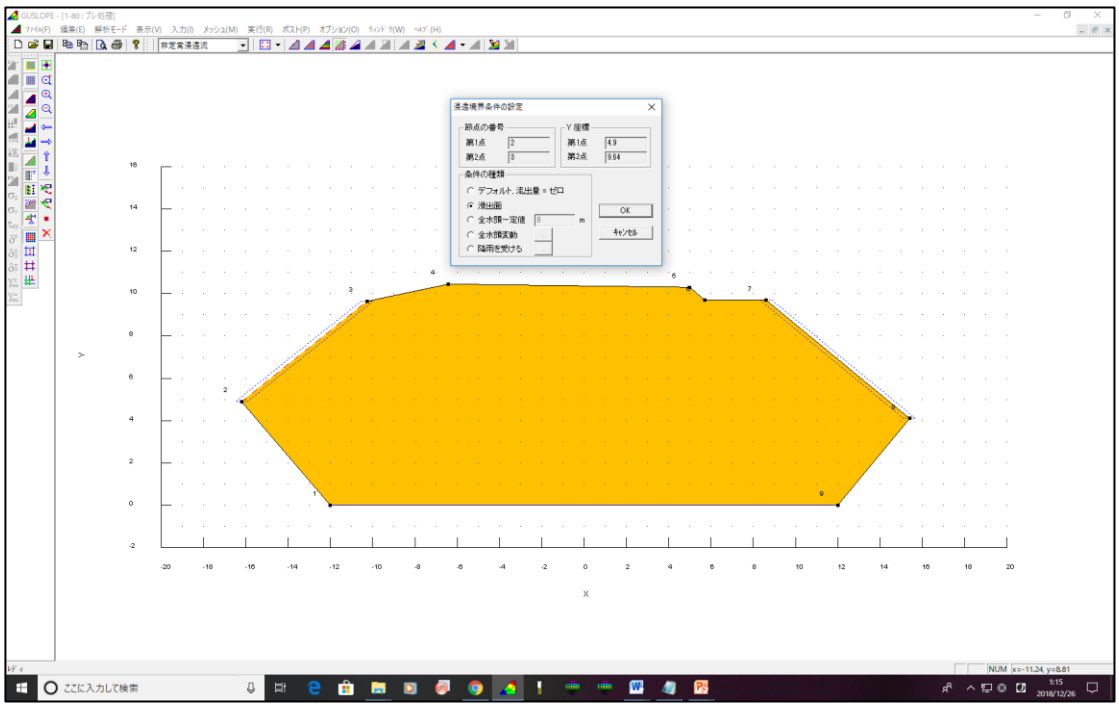

Fig. 5-17. Input water boundary conditions

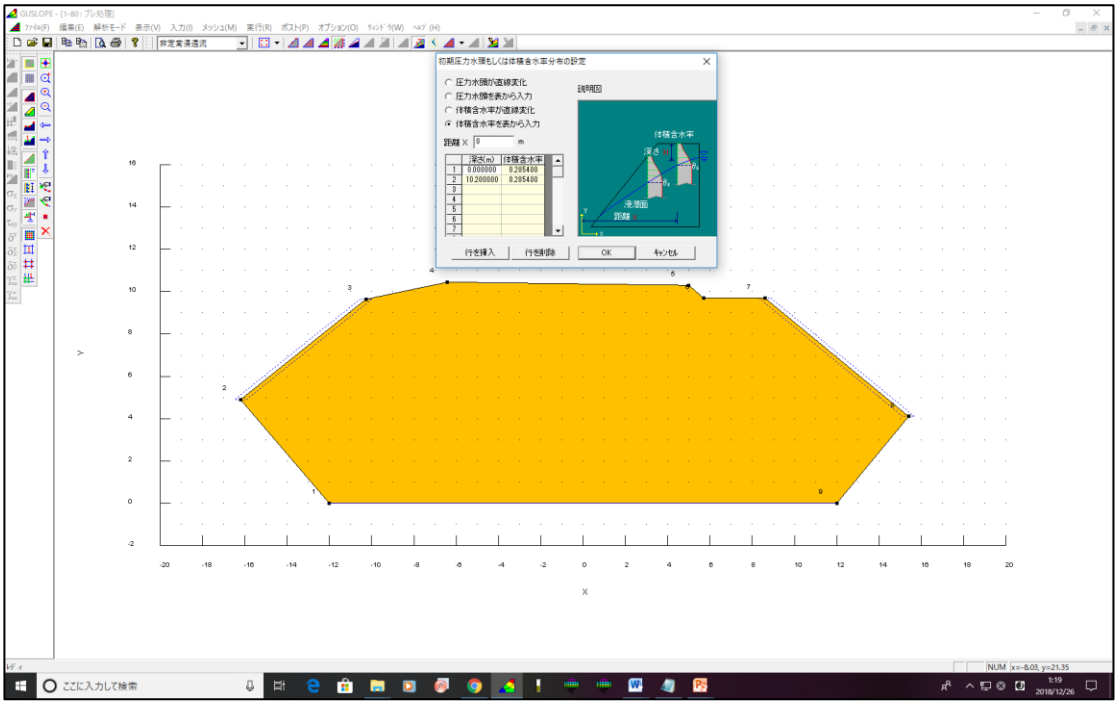

Fig. 5-18. Input water distribution

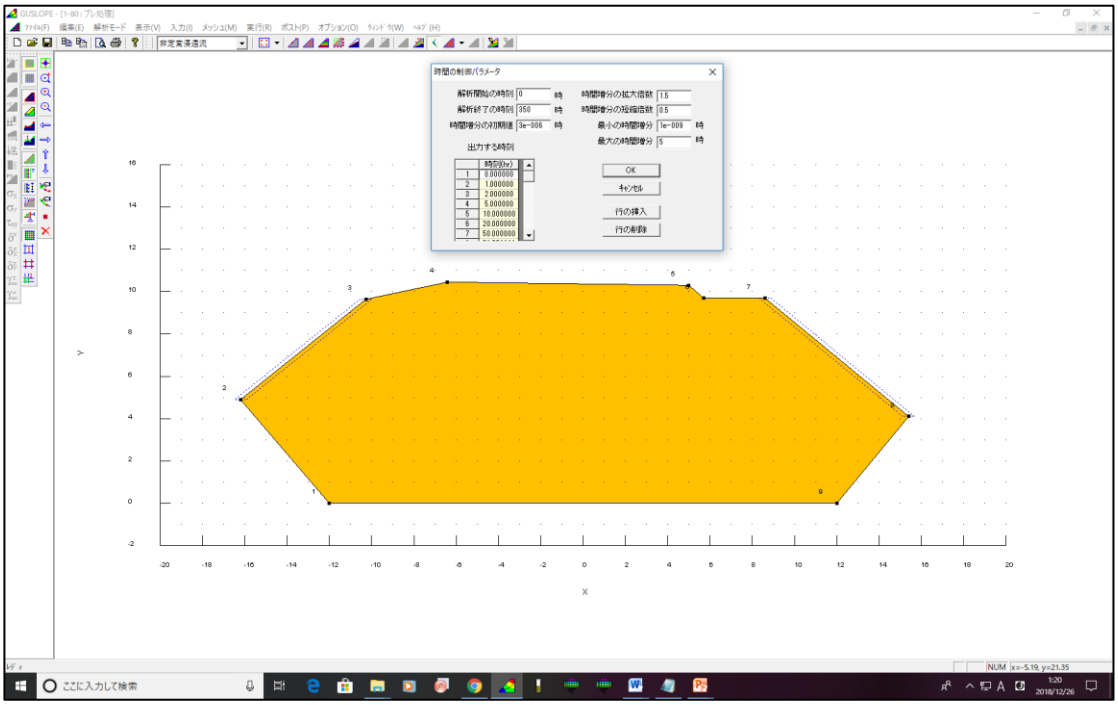

Fig. 5-19. Input time step of runs

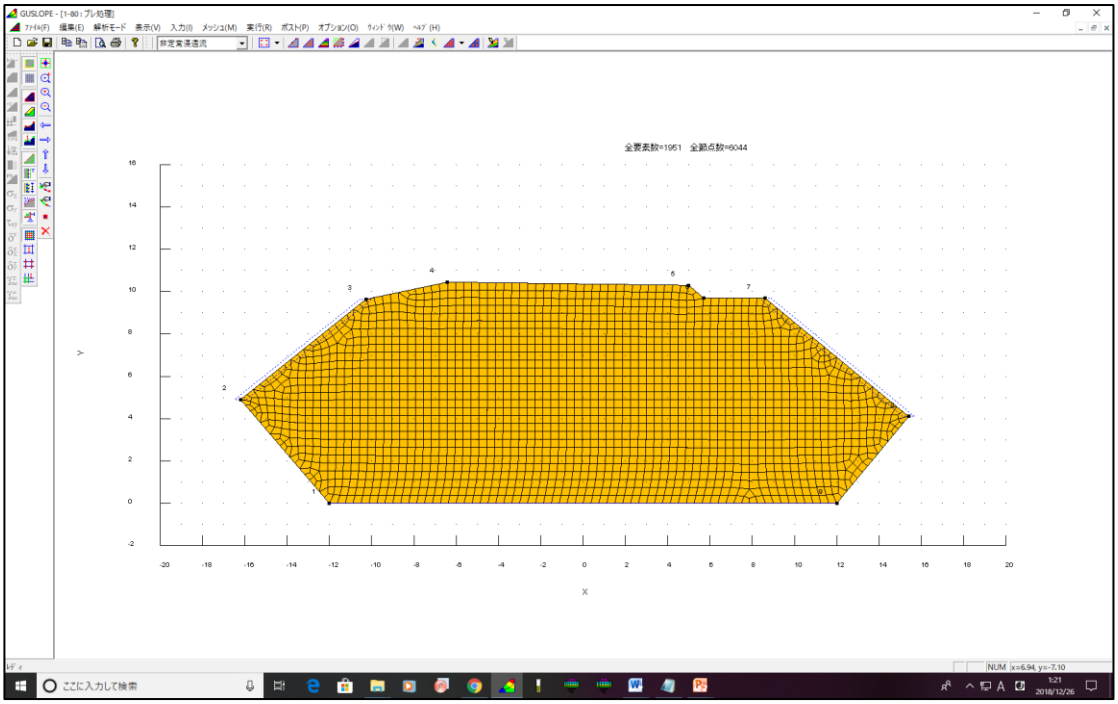

Fig. 5-20. Create mesh of model

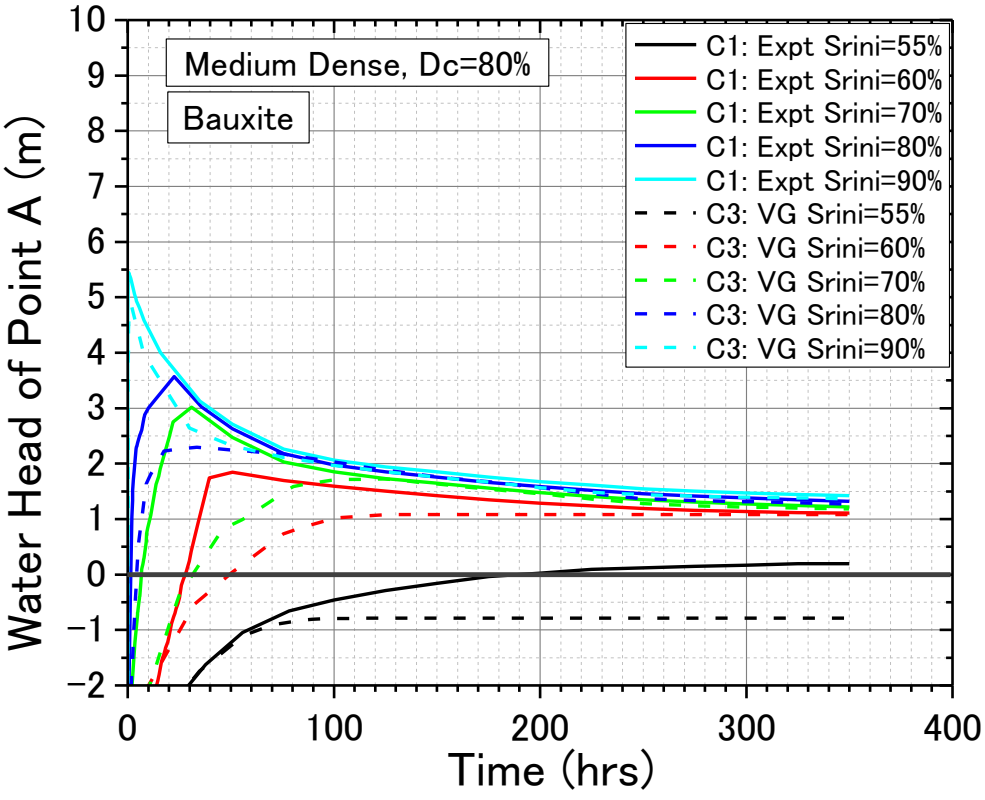

Fig. 5-21. Water head at point A vs time: Pervious B1 and B2 boundary
(Experiment results vs. VG Model for bauxite, medium dense)

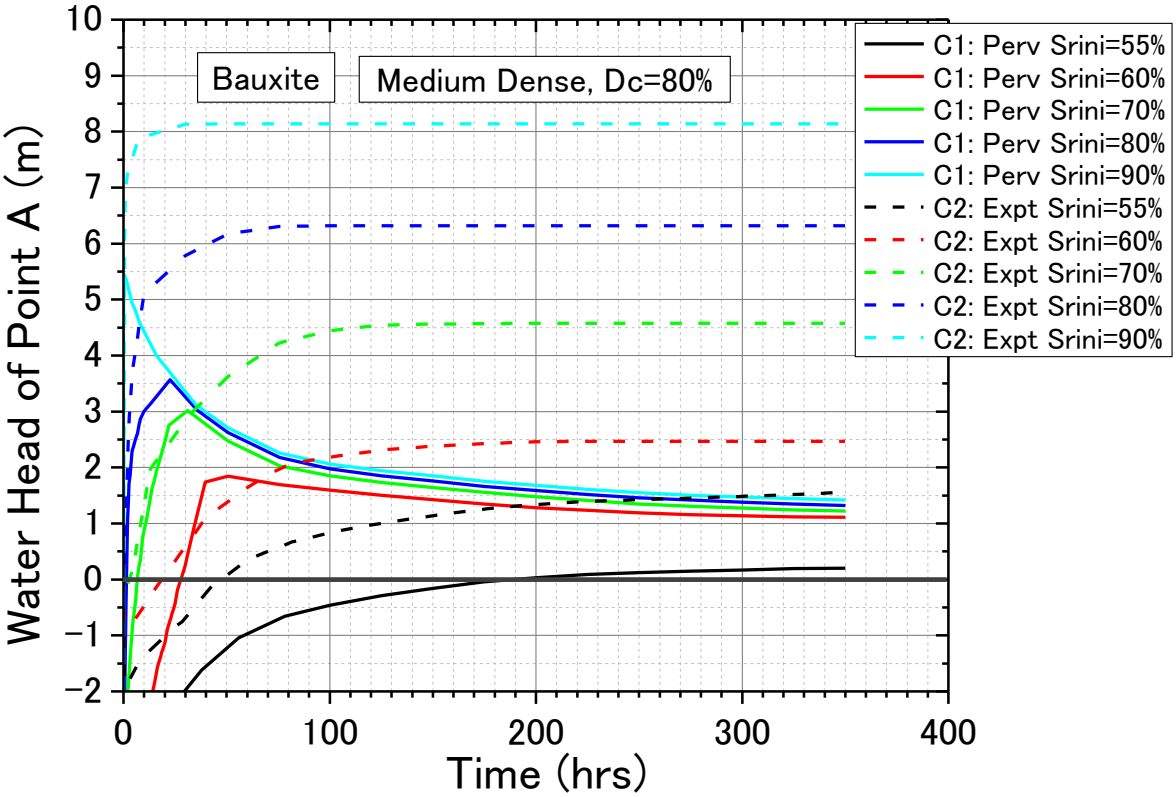

Fig. 5-22. Water head at point A vs time: Experimental Results
(Pervious vs. Impervious B1 and B2 boundary for bauxite, medium dense)

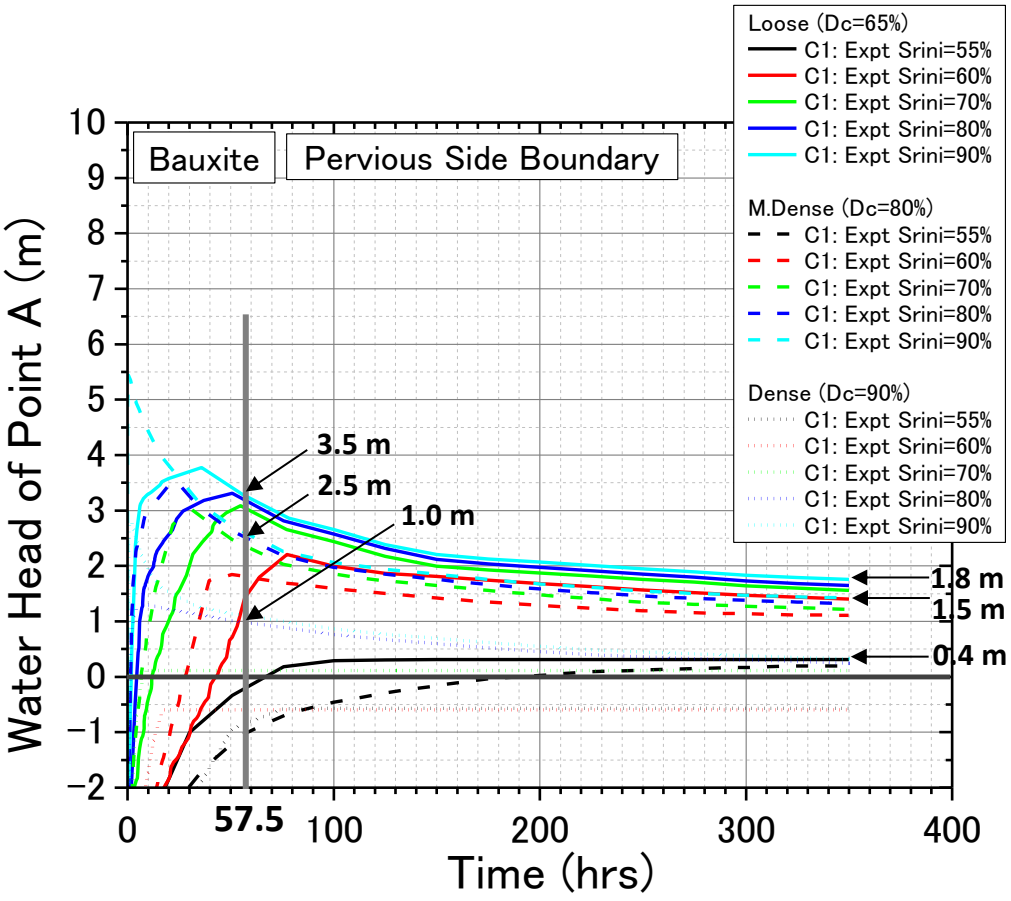

Fig. 5-23. Water head at point A vs time: Experimental Results
(comparison at various densities for bauxite)

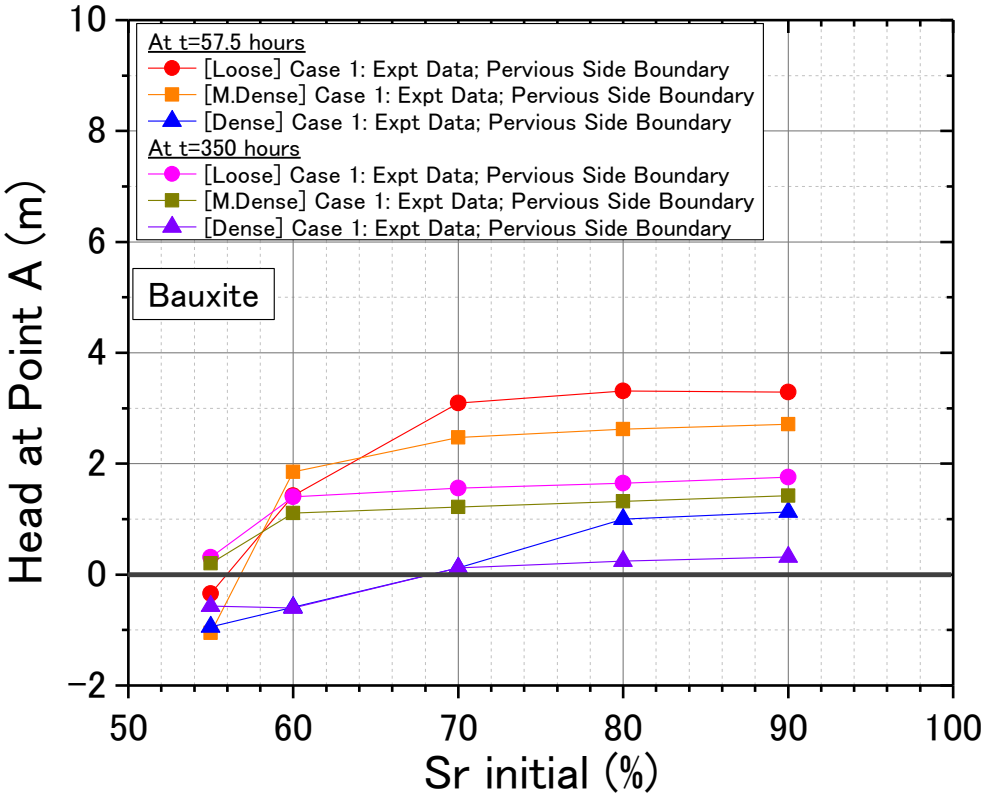

Fig. 5-24. Water head at point A vs Sr_{init}: Experimental Results, Case 1 – pervious B1 and B2 side boundary (bauxite, various densities)

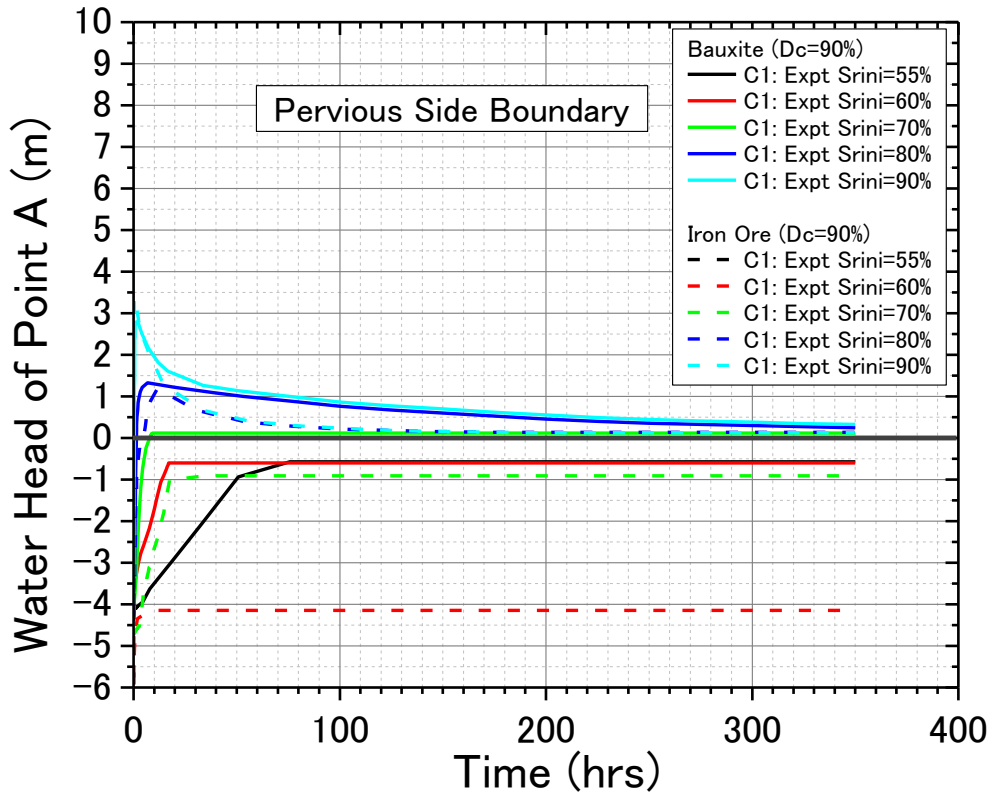

Fig. 5-25. Water head at point A vs time: Experimental Results, Case 1 – pervious B1 and B2 side boundary (bauxite vs iron ore, dense)

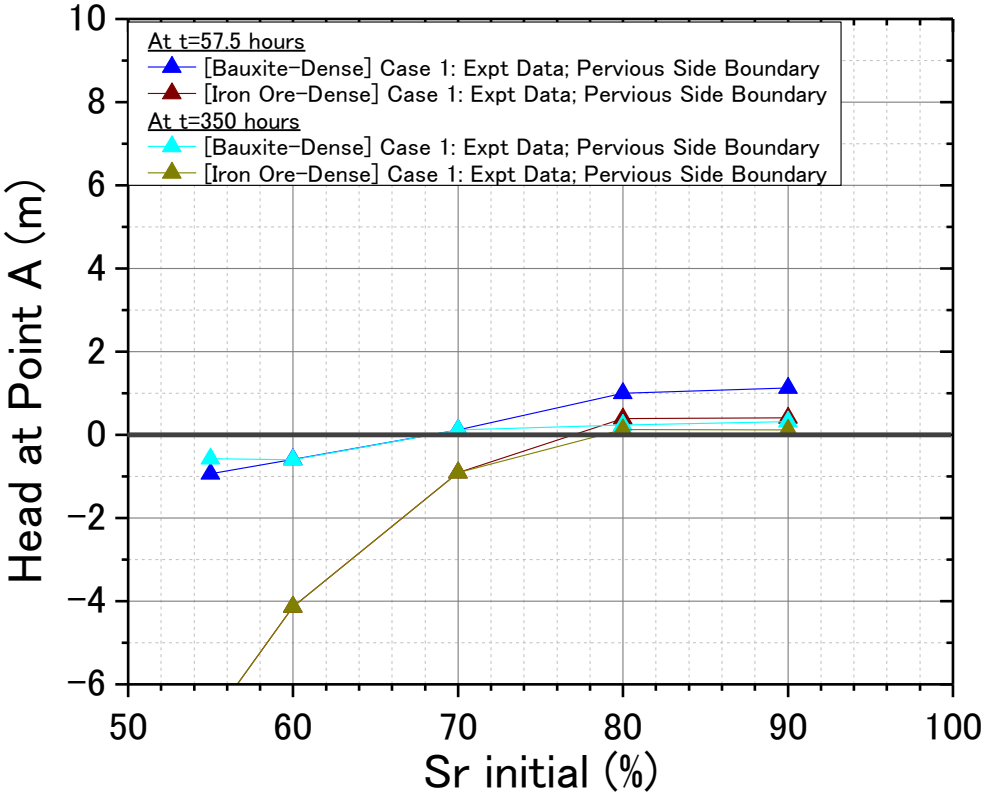

Fig. 5-26. Water head at point A vs Sr_{init}: Experimental Results, Case 1 – pervious B1 and B2 side boundary (bauxite vs. iron ore, dense)

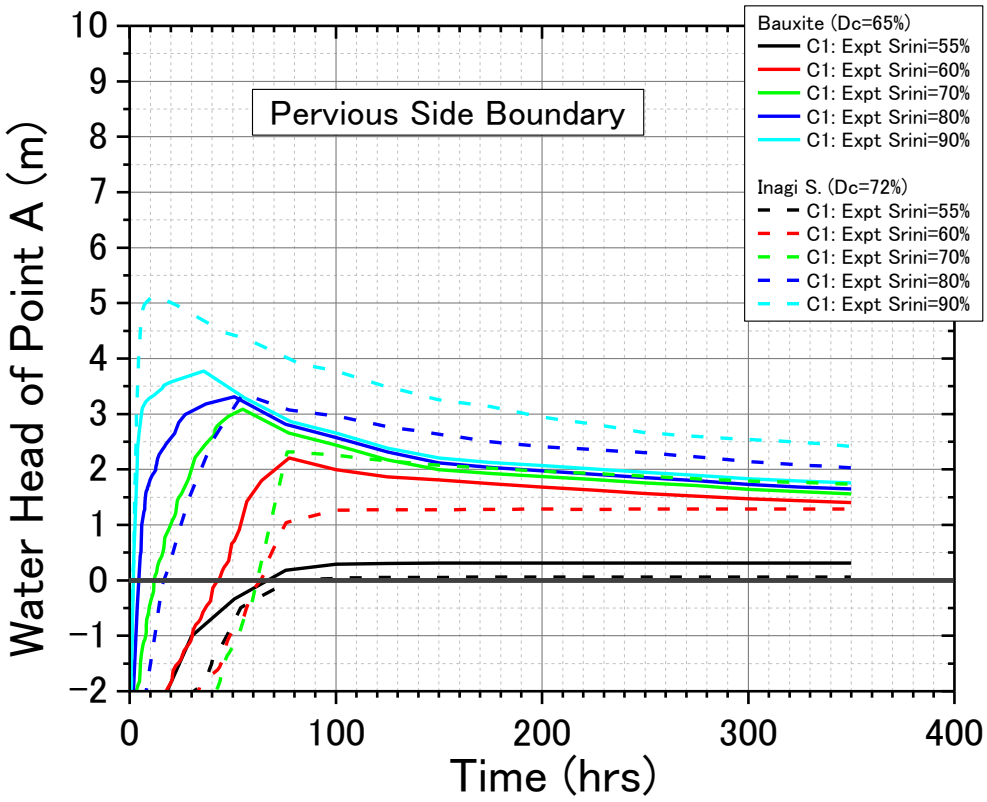

Fig. 5-27. Water head at point A vs time: Experimental Results, Case 1 – pervious B1 and B2 side boundary (bauxite vs Inagi sand, loose)

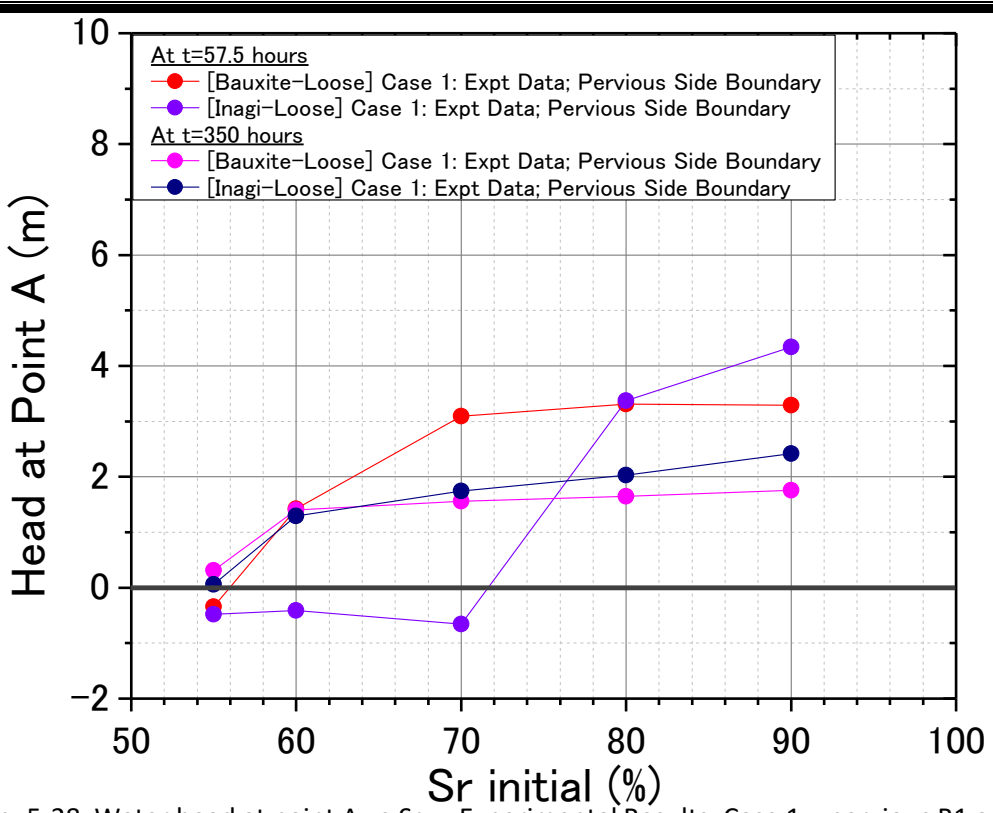

Fig. 5-28. Water head at point A vs Sr_{init}: Experimental Results, Case 1 – pervious B1 and B2 side boundary (bauxite vs. Inagi sand, loose)

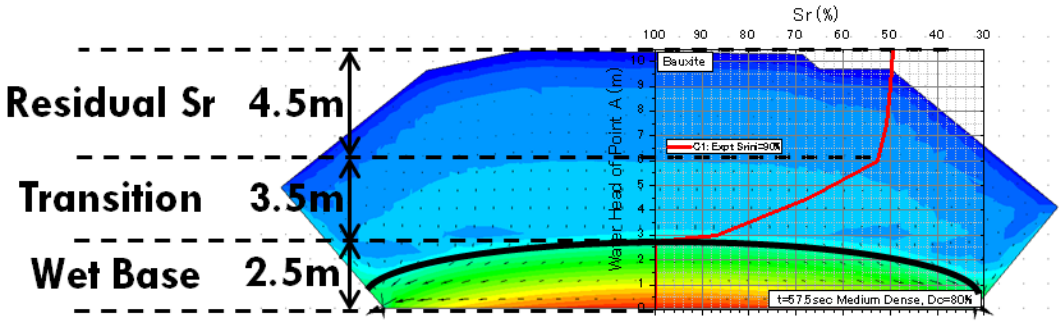

Fig. 5-29. Water head distribution at t=57.5 hr along the vertical direction of heap at Sr_{init}=90%: Experimental Data, Case 1 – pervious B1 and B2 boundary (bauxite, m. dense)

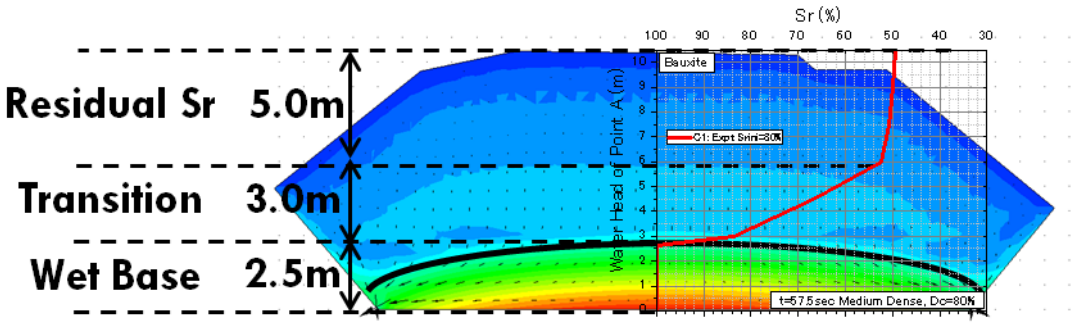

Fig. 5-30. Water head distribution at t=57.5 hr along the vertical direction of heap at Sr_{init}=80%: Experimental Data, Case 1 – pervious B1 and B2 boundary (bauxite, m. dense)

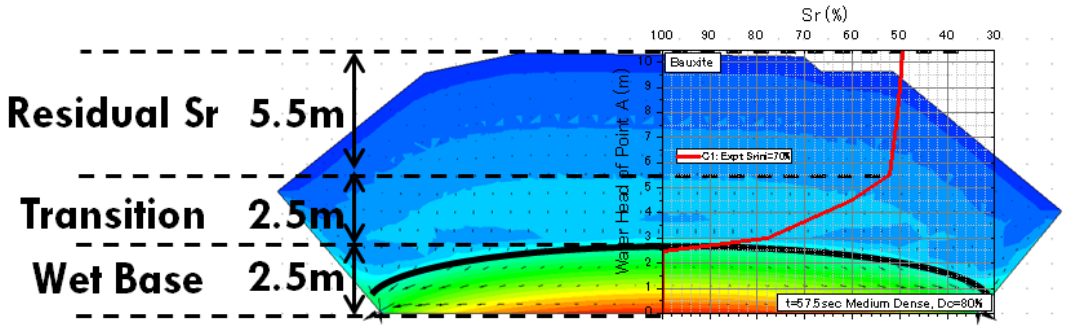

Fig. 5-31. Water head distribution at t=57.5 hr along the vertical direction of heap at Sr_{init}=70%: Experimental Data, Case 1 – pervious B1 and B2 boundary (bauxite, m. dense)

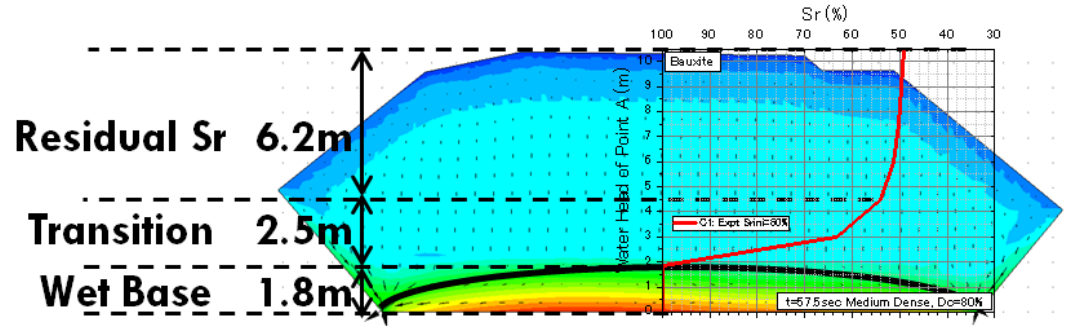

Fig. 5-32. Water head distribution at t=57.5 hr along the vertical direction of heap at Sr_{init}=60%: Experimental Data, Case 1 – pervious B1 and B2 boundary (bauxite, m. dense)

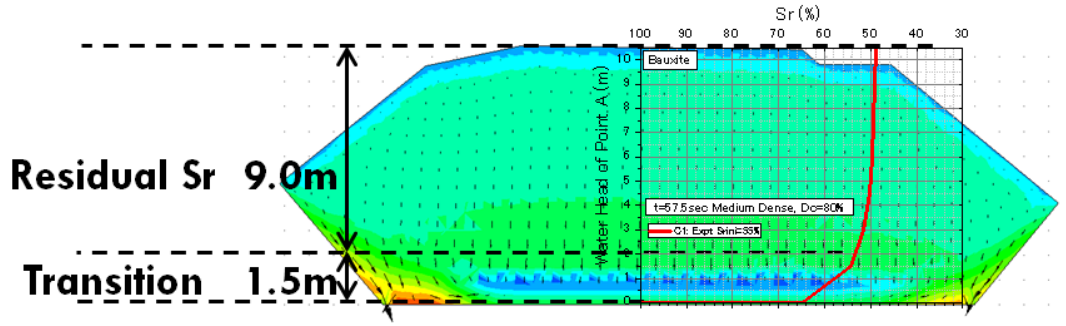

Fig. 5-33. Water head distribution at t=57.5 hr along the vertical direction of heap at Sr_{init}=55%: Experimental Data, Case 1 – pervious B1 and B2 boundary (bauxite, m. dense)

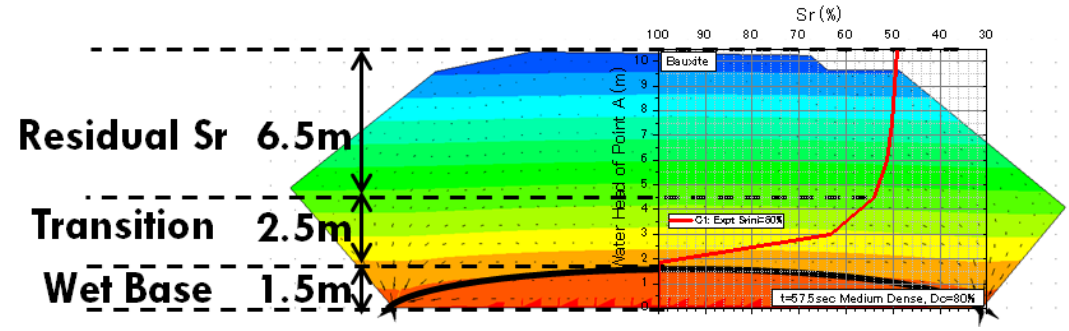

Fig. 5-34. Water head distribution at t=350 hr along the vertical direction of heap at Sr_{init}=90%: Experimental Data, Case 1 – pervious B1 and B2 boundary (bauxite, m. dense)

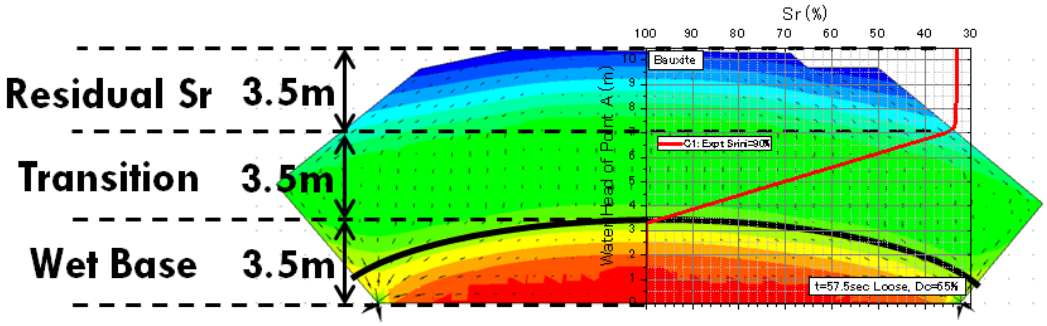

Fig. 5-35. Water head distribution at t=57.5 hr along the vertical direction of heap at Sr_{init}=90%: Experimental Data, Case 1 – pervious B1 and B2 boundary (bauxite, loose)

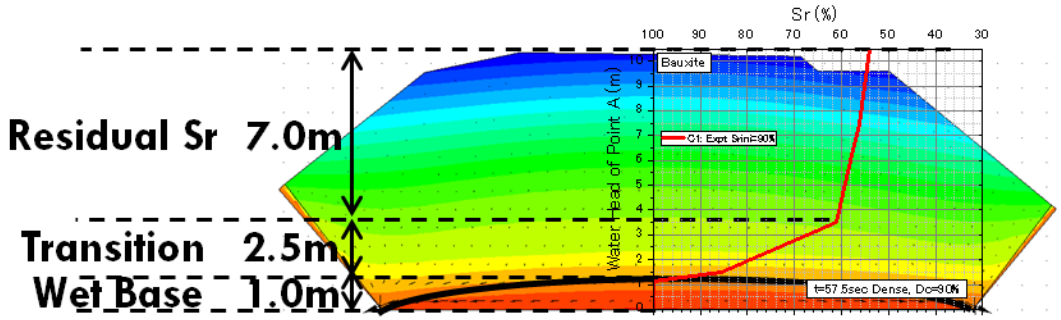

Fig. 5-36. Water head distribution at t=57.5 hr along the vertical direction of heap at Sr_{init}=90%: Experimental Data, Case 1 – pervious B1 and B2 boundary (bauxite, dense)

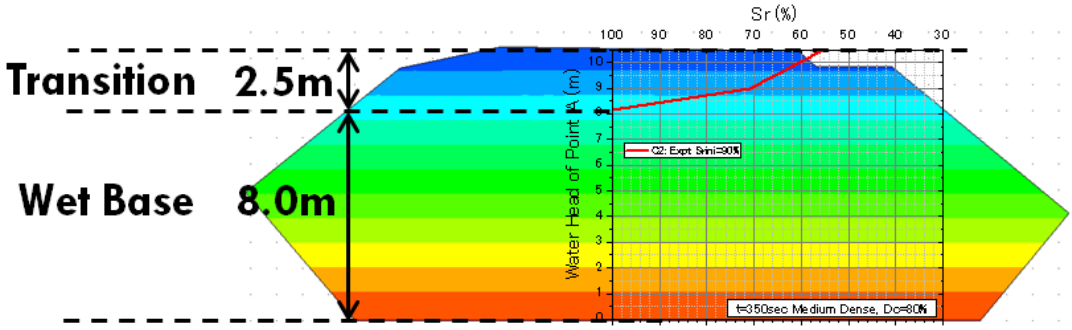

Fig. 5-37. Water head distribution along the vertical direction of heap at Sr_{init}=90%: Experimental Data, Case 2 – impervious B1 and B2 boundary (bauxite, m. dense)

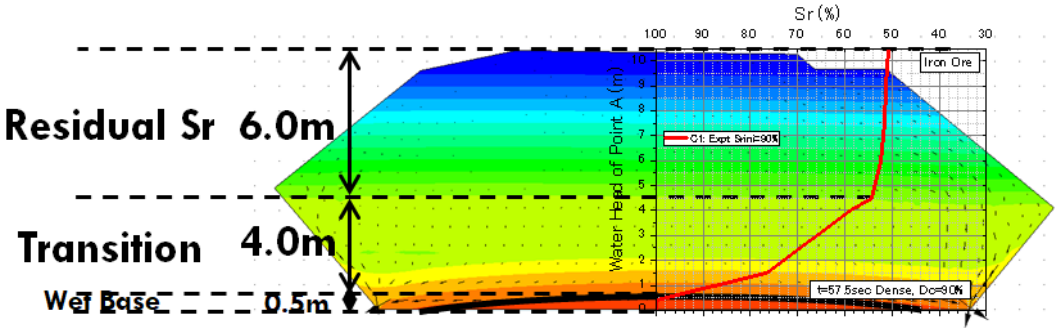

Fig. 5-38. Water head distribution at t=57.5 hr along the vertical direction of heap at Sr_{init}=90%: Experimental Data, Case 1 – pervious B1 and B2 boundary (iron ore, dense)

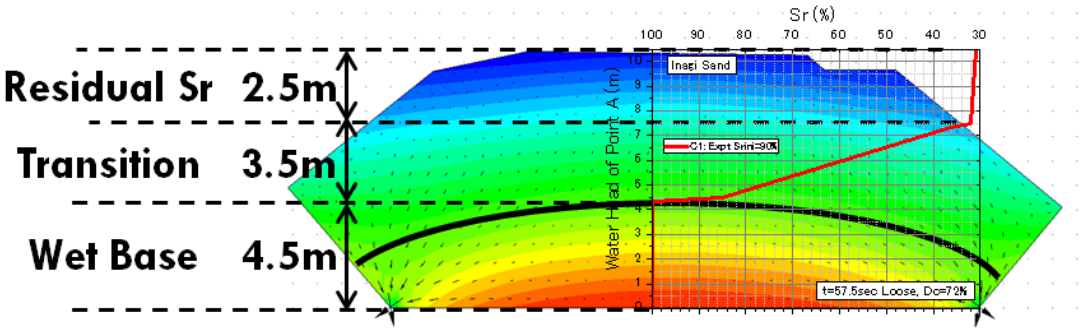

Fig. 5-39. Water head distribution at t=57.5 hr along the vertical direction of heap at Sr_{init}=90%: Experimental Data, Case 1 – pervious B1 and B2 boundary (Inagi sand, loose)

Chapter 6
Numerical Analysis: Dynamic Response

Contents

6-1. Introduction

In Chapter 5, the seepage in the heap of bauxite was analyzed numerically based on the experimental data obtained from permeability tests under different saturation conditions and SWRC. The results in Chapter 5 provide reference data, such as the height of the water table and the distribution of degree of saturation (*Sr*) in the heap for the dynamic response analysis. Together with the results of cyclic loading tests of bauxite addressed in Chapter 4, and the undrained monotonic loading tests of bauxite extracted from Cabrera (2018), the liquefaction potential of the partially saturated heap of bauxite is evaluated for a given initial and boundary conditions.

The motion a ship may experience depends on various factors such as voyage route, weather conditions, or height and mode of ocean waves, but the problem was simplified from the view point of geotechnical engineering as described in Chapter 1 section 1.3.1. The assumptions made in Chapter 1 are repeated here to provide the general conditions of the simulation described in this Chapter:

1. Only consider the effect of predominant motion, the rolling motion (six motion components of a ship, Surge, Sway, Heave, Roll, Pitch and Yaw are shown in Fig. 1-2 in Chapter 1);

2. Only consider the shear stress induced by rolling motion, effect of acceleration is not considered;

3. Assuming the period of rolling motion is 10 second (0.1 Hz) (Global Bauxite Working Group, 2017);

4. A ship/a heap is assumed to experience a certain number of cycles of roll in a voyage;

5. Only analyze response of one heap in a ship (there are 5 holds in a ship for hanydmax type bulk carrier; one heap in each hold).

As for the fourth (4^{th}) assumption pertaining the number of cycles of roll, maximum of 400 cycles of sinusoidal rolling motion with constant amplitude were applied to the model. This number of cycles was assumed based on the narrative of events of MV Bulk Jupiter in which the duration of the ship when it started to roll more heavily until the Japanese Coast Guard received a stress signal was 60 minutes (The Commonwealth of the Bahamas: Report on MV Bulk Jupiter, Section 3: Narrative of Events, 2015). The duration 60 minutes, by assuming the period of rolling motion of 10 seconds (3^{rd} assumption) is 360 cycles. Hence, 400 cycles was set to provide allowance or buffer to evaluate if the ship can sustain 360 cycles.

6-2. Program and Model

The commercial software, UWLC Ver. 2 was used for the determination of the parameters used in the constitutive models, the initialization of the static stress distribution and the post

process. The rolling motion was applied by a separate program provided by Associate Professor F. Cai from Gunma University, Japan. Both the software and the program used to simulate the rolling motion were for two dimensional analysis.

6.2.1. Geometry of Bauxite Heap

Fig. 6-1 to Fig. 6-3 show the model of the heap used for simulation for bauxite at loose, medium dense, and dense cases, respectively. The zonings are different since the distribution of water along the heap was found out to be different as discussed in Chapter 5 and reiterated as follow:

- bauxite, loose: wet base = 3.5 m high, transition zone = 3.5 m thick, residual S_r = 3.5 m thick (referred from Fig. 5-35)
- bauxite, medium dense: wet base = 2.5 m high, transition zone = 3.5 m thick, residual S_r = 4.5 m thick (referred from Fig. 5-29)
- bauxite, dense: wet base = 1.0 m high, transition zone = 2.5 m thick, residual S_r = 7.0 m thick (referred from Fig. 5-36)

The dimensions of the model are the same as those used in the seepage analysis introduced in Chapter 5 (see Fig. 5-3), which are typical for heaps in handymax type of bulk carriers (typically 50 kDWT).

For iron ore at dense case, Fig. 6-3 was also used as the model of heap to compare directly the results with bauxite at dense case.

The model is divided into four (4) zones, which are assigned to different properties. Zone 1 is the elastic zone. This was deliberately set to be a non-liquefiable region to prevent numerical instability by slope failure among others, which is not the intended simulation in this study. Zone 2 is the residual degree of saturation (*Sr*) (converted from residual volumetric water content). Zone 3 is the unsaturated transition zone, as concluded from Chapter 5 which is 2.5 to 3.5 m thick, depending on the density of the heap. Finally, Zone 4 is the wet base of the heap.

Four (4) points were also labeled in the model. All points were along the centerline of the heap, with point A being at the bottom most part of the wet base in Zone 4, point B at the transition region in Zone 3, and point C at the residual *Sr* region in Zone 2. Points A, B, and C were evaluated for a liquefaction criterion that shall be discussed later. Point D is the top most part of the centerline of the heap, which was evaluated for displacements.

Fig. 6-2 (model for the medium dense condition) shall be used for discussion purposes in the subsequent sections of this chapter, unless explicitly mentioned otherwise.

6.2.2. Simulation Conditions and Boundary Conditions

Referring once again to Fig. 6-2, the side boundaries which were fixed were labelled with "Fixed Support". Fixed support implies disallowing any movement on those sides. The rest of the boundaries are set free.

As for cases run and zonings, Table 6-1 shows the general conditions considered in the simulation.

Table 6-1. Cases and Zone Conditions for Fig. 6-2 (medium dense condition)

Zone	Case 1			Case 2			Case 3		
	Model	Elevation from pt. A (m)	*Sr* (%)	Model	Elevation from pt. A	*Sr* (%)	Model	Elevation from pt. A	*Sr* (%)
1	NL	9.0~10.5	Sr_{res}	NL	9.0~10.5	Sr_{res}	NL	10~10.5	80
2	L	6.0~9.0	Sr_{res}	NL	6.0~9.0	Sr_{res}			
3	L	2.5~6.0	80	NL	2.5~6.0	80	L	8.0~10.0	80
4	L	0~2.5	100	L	0~2.5	100	L	0~8.0	100

Notes:

1. L = liquefiable, NL = non-liquefiable;
2. Sr_{res} = residual saturation degree. Value depends on the degree of compaction
3. Zone 4 for loose is 0~3.5 while dense is 0~1.0;
4. Zone 3 for loose is 3.5~7.0 while dense is 1.0~3.5;
5. Zone 2 for loose is 7.0~9.0 while dense is 3.5~9.0.

In Case 1, Zone 4 was assumed to be liquefiable since it is the wet base, and Zones 2 and 3 were also assumed to be liquefiable, which is more realistic since the potential of liquefaction of unsaturated bauxite was observed, as discussed in Chapter 3. Zone 1 was kept non-liquefiable to avoid numerical instability. The elevation from point A is a reference of the height of the zonings with respect to point A (see Fig. 6-2 for point A label). Sr_{res} is the residual degree of saturation. Since this value depends on the degree of compaction, specific value cannot be written on this box.

In Case 2, Zones 2 and 3 were assumed to be non-liquefiable (i.e. unsaturated regions). Other zones were kept with the same conditions as Case 1.

In Case 3, the extreme condition was assumed in which improper drainage exists and the wet base accumulates up to 8 m high as discussed in Chapter 5 (see Fig. 5-37). Fig. 6-4 shows the model for Case 3, in which the wet base is up to 8 m high, and transition zone up to the surface of the heap. Zone 2 in this case is non-existent since residual saturation degree cannot be achieved due to the assumed impermeable side boundaries of the heap, and the improper drainage of the bilge at the base. Point C was consequently removed for Case 3.

Table 6-2 presents the simulations conducted and conditions for each case.

Table 6-2. Simulations for each case

Case	Bauxite Simulations	Iron Ore Simulations	Roll Angle (°)	Cycles, N
1	Loose (D_c=65%), M.Dense (D_c=80%), Dense (D_c=90%)	Dense only (D_c=92%)	5, 10, 15, 20, 25, 30	400
2				
3	Dense only (D_c=90%)			

For all cases, the experimental data obtained were utilized, both for liquefaction resistance properties of the heap and the water flow properties (i.e. permeability and SWRC). For iron ore, undrained monotonic and undrained cyclic properties were extracted from Wang (2014).

6-3. Constitutive Model, Element Test Simulations, and Parameters Assignment

The built-in constitutive model, PZ-sand model, is used for the liquefiable zones. PZ-sand model is a generalized model developed by Pastor et al. (1990). The main advantage of this model is that no plastic potential or yield surfaces need to be explicitly defined, and consistency rules need not be applied (Pastor et al., 1990). It has 15 parameters as shown in Table 6-3 in which all parameters are dimensionless. The first 12 parameters were determined according to the undrained monotonic loading tests of saturated bauxite and the last 3 parameters were determined based on the undrained cyclic loading tests. PZ-sand model is essentially used for the saturated soils, while in order to consider the unsaturated condition of bauxite, the parameters were adjusted to match the liquefaction resistance curve of unsaturated bauxite.

Table 6-3. Parameters of PZ-sand model

Obtained From	Symbol	Parameter Definition
Undrained Monotonic Loading Tests and Consolida-tion Tests	M_f	Slope of failure line in p'-q plane
	M_g	Slope of the critical state line in p'-q plane
	C	Ratio of M_g in extension side of triaxial test to the compression side
	α_f	Parameter related to yield
	α_g	Parameter related to plastic flow
	K_{evo}	Coefficient of bulk modulus
	G_{eso}	Coefficient of shear modulus
	m_v	Exponent of bulk modulus
	m_s	Exponent of shear modulus
	β_o	Parameter related to soil softening
	β_1	Parameter related to soil softening
	H_o	Coefficient of loading plastic modulus
Undrained Cyclic Loading Tests	H_{uo}	Unloading plastic modulus
	γ	Parameter related to reloading plastic deformation
	γ_u	Parameter related to unloading plastic modulus

6.3.1. Undrained Monotonic Tests and Consolidation Tests

The parameters in Table 6-3 were assigned based on undrained monotonic tests conducted by Cabrera (2018), and consolidation tests from the tests conducted on this thesis for bauxite. In the absence of data, the values were assigned based on representative or suggested values from the UWLC Element Test Simulation Manual. As for iron ore, the parameters were all extracted from Wang (2014).

1. Coefficient of loading plastic modulus (H_o)

The parameter H_o is given by:

$$H_o = {(1 + e_o)}/{(\lambda - \kappa)} \quad \text{(Eqn. 6-1)}$$

where: λ = slope of virgin loading in consolidation test; κ = slope of elastic unloading in consolidation test; and e_o = initial void ratio.

In consolidation tests, the virgin loading is commonly plotted in a void ratio (e) vs mean effective stress ($\ln p'$) plane as:

$$e = e_L - \lambda \ln p' \quad \text{(Eqn. 6-2)}$$

where: e_L = initial void ratio of the virgin loading (normally consolidated); λ = slope of virgin loading in consolidation test; and p' = mean effective stress.

On the other hand, the elastic unloading is commonly plotted in a void ratio (e) vs mean effective stress ($\ln p'$) plane as:

$$e = e_U - \kappa \ln p' \quad \text{(Eqn. 6-3)}$$

where: e_U = initial void ratio of the unloading-reloading line; κ = slope of elastic unloading in consolidation test; and p' = mean effective stress.

Fig. 6-5 shows the e vs. $\ln p'$ plot of bauxite at medium dense. From the plot, the value of λ is 0.0995 and the value of κ is 0.0074. The value of H_o can then be obtained and it is equivalent to 20.78 for medium dense. For the H_o values of the other D_c of bauxite, the plots are shown in Appendix D.

2. Coefficient of bulk modulus (K_{evo}) and Exponent of bulk modulus (m_v)

The parameters K_{evo} and m_v are related by:

$$K_{ev} = K_{evo} P_a ({p'}/{P_a})^{m_v} \quad \text{(Eqn. 6-4)}$$

where: K_{ev} = bulk modulus; K_{evo} = coefficient of bulk modulus; P_a = confining pressure; and *p'* = mean effective stress; and m_v = exponent of bulk modulus.

Fig. 6-6 shows the K_{ev} vs. *p'/Pa* plot of bauxite at medium dense. From the plot, the value of $K_{evo}P_a$ is taken to be 12881. Since P_a is 100 kPa, the value of K_{evo} of bauxite at medium dense is 128.81 ≈ 130. The value of m_V is 1.0.

3. Coefficient of shear modulus (G_{eso}) and Exponent of shear modulus (m_s)

The parameters G_{eso} and m_s are related by:

$$G_{eso} = {3E}\Big/{[2(1+0.5)P_a(\frac{p'}{P_a})^{m_s}]} \qquad \text{(Eqn. 6-5)}$$

where: G_{eso} = coefficient of shear modulus; *E* = modulus of elasticity; P_a = confining pressure; and *p'* = mean effective stress; and m_s = exponent of shear modulus.

In order to calculate G_{eso}, it was necessary to first obtain the value of *E* from small strains. Hence, the deviatoric stress (*q*) was plotted against axial strain (ε_a) at strains less than 0.01% (Goto et al, 1991) for bauxite at loose, medium dense, and dense in Fig. 6-7. There was one (1) datum available for loose case, two (2) data available for medium dense case, and two (2) data available for dense case.

From the *E* values obtained in Fig. 6-7, the shear modulus (*G*) can be calculated by the following equation:

$$G = {E}\Big/{(1+\nu)} \qquad \text{(Eqn. 6-6)}$$

where: *G* = shear modulus; *E* = modulus of elasticity; ν = Poisson's ratio.

For undrained condition, the value of *v* can be assumed to be 0.5. Hence, Fig. 6-8 shows the log *G* vs log *p'* plot. The intent of this graph is to obtain the m_s values of bauxite at loose, medium dense, and dense. The value of m_s is the slope of the log *G* vs log *p'* plot. Since loose case has only one (1) point, a line cannot be created, hence the m_s value for loose case was assumed to be 1.0. The dense exceeded the maximum permissible value (i.e. 1.0) to input in the software, hence it had to be assumed as 1.0 as well.

Once the values of m_s were obtained, Eqn. 6-5 was utilized to calculate G_{eso} and the resulting values were G_{eso} = 469 for loose case, G_{eso} = 1073~1154 for medium dense case, and G_{eso} = 1236~1645 for dense case. The more conservative (i.e. lower value) was adopted for medium dense and dense cases for G_{eso}.

4. Slope of failure line in p'-q plane (M_f), Parameter related to yield (α_f), Slope of the critical state line in p'-q plane (M_g), Parameter related to plastic flow (α_g), and Ratio of M_g in extension side of triaxial test to the compression side (C)

These set of parameters can be obtained from the undrained monotonic loading tests. Fig. 6-9 shows the *p'-q* plot of undrained monotonic loading tests with experimental data extracted from Cabrera (2018) to obtain M_f and M_g for bauxite at medium dense. Simulations were also performed indicated in dashed lines. The data for *p'* = 100 kPa and *p'* = 200 kPa were mainly used to obtain the desired parameters. The data for *p'* = 400 kPa was used for comparison only. Cabrera (2018) reports that particle crushing starts to occur at *p'* = 400 kPa, hence one of the reasons why the experimental results for *p'* = 400 kPa do not fall in the obtained M_f line. For this test, M_f for bauxite at medium dense is 0.96, and M_g is 1.45. The effective stress paths for loose case and dense case are shown in Fig. 6-10 and Fig. 6-11, respectively for reference.

The values for α_f and α_g for bauxite at medium dense were both assigned from the range of suggested values in the UWLC Element Test Simulation Manual that provide the best fit simulation curve indicated in dashed lines in Fig. 6-12. These parameters affect the curvature at the region of yielding point. Fig. 6-13 and Fig. 6-14 are *q*-ε_a plots of loose and dense case, respectively.

The value of C was obtained by dividing the M_g of the extension side to the compression side. Mathematically, it is expressed as:

$$C = \frac{M_{ge}}{M_{gc}} = \frac{6sin\phi' / 3+sin\phi'}{6sin\phi' / 3-sin\phi'} \qquad \text{(Eqn. 6-7)}$$

where: M_{ge} = slope of critical state line (CSL) in *p'-q* plane in the extension side; M_{gc} = slope of critical state line (CSL) in *p'-q* plane in the compression side; ϕ' = peak friction angle.

Using Eqn. 6-7, the value of C for bauxite at medium dense is 0.644.

5. Parameters related to soil softening (β_o and β_1)

For β_o and β_1, the values were simply obtained from the UWLC Element Test Simulation Manual range of values.

6.3.2. Undrained Cyclic Tests (Saturated)

The remaining three (3) parameters in PZ-sand model, namely unloading plastic modulus (H_{uo}), parameter related to reloading plastic deformation (γ), and parameter related to unloading plastic modulus (γ_u), were all determined from undrained cyclic tests. While keeping the values of the parameters obtained in undrained monotonic tests and consolidation tests, the experimental data from Chapter 4 were simulated as well.

Fig. 6-15 compares the simulated and test result of test M1 of the undrained behavior of saturated medium dense bauxite under cyclic loading. This test was selected from Table 3-2

in Chapter 3. The simulations of other tests can be found in Appendix D. The simulation result show that the effective stress path (*p'-q* plot) was roughly consistent with the test result, while the stress strain behavior (*q*-ε_a plot) in Fig. 6-16 may not be properly simulated. The test results show that axial strain is progressively developed under the cyclic loading, while the predicted axial strain is very small in the early stage of cyclic loading and it is developed or tends to be developed suddenly when the effective stress approaches zero. It implies that, in the simulation, large deformation could be suddenly trigged either locally or universally when the effective stress reaches zero. Hence, the result after the large deformation had been triggered cannot be used but nonetheless, the simulation and model are still useful because it is indicative of the onset of liquefaction.

The simulations in Fig. 6-15 and Fig. 6-16 were determined by assigning a representative H_{uo}, γ, and γ_u values from UWLC Element Test Simulation that would fit the experimental data the best, while maintaining the obtained parameters from undrained monotonic loading and consolidation test.

6.3.3. Undrained Cyclic Tests (Unsaturated)

Fig. 6-17 shows test a3 of the predicted undrained behavior for unsaturated medium dense bauxite under cyclic loading. The test was selected from Table 3-4 of Chapter 3. Other simulations are shown in Appendix D. Although the PZ-sand model is for saturated soils, it can be observed from Fig. 6-17 that the predicted effective stress path (net normal stress-*q* plot) was reasonably simulated. Test a3 was a test under *Sr*=84%. It can be seen from Table 3-4 that tests under *Sr*=84% generally have minimal discrepancy in the values of the two criteria (i.e. $N_{DA=5\%}$ criteria and $N_{0.9\sigma o'}$ criteria) as discussed and elaborated in Chapter 3.

Similar to the problem encountered in the stress strain relationship (*q*-ε_a plot) shown in Fig. 6-16, Fig. 6-18 shows the sudden development of axial strain for unsaturated bauxite.

Fig. 6-19 shows test b5 of the predicted undrained behavior for unsaturated medium dense bauxite under cyclic loading. The test was selected from Table 3-5 of Chapter 3. Other simulations are shown in Appendix D. Test b5 was a test under *Sr*=58%. It can be seen from Table 3-5 that tests under *Sr*=58% have large discrepancy in the values of the two criteria (i.e. $N_{DA=5\%}$ criteria and $N_{0.9\sigma o'}$ criteria) as discussed and elaborated in Chapter 3. The simulation in Fig. 6-19 shows that the stress path had not yet achieved the 90% reduction of strength. This is supported with the information in Table 3-5 that the $N_{DA=5\%}$ criteria was initially achieved (i.e. $N_{DA=5\%}$ = 12.6 cycles), while the $N_{0.9\sigma o'}$ criteria was achieved after 58 cycles (i.e. $N_{0.9\sigma o'}$ = 58 cycles). Fig. 6-20 shows the *q*-ε_a plot when $N_{DA=5\%}$ criteria was achieved and this is the corresponding *q*-ε_a plot of Fig. 6-19.

By showing the complete test data in Fig. 6-21, it can be seen that the experimental data decreased its net normal stress until about 5 kPa. The simulation, however, cannot proceed once the DA=5% was achieved. Similarly, Fig. 6-22 shows the complete *q*-ε_a plot of the test data.

From these simulations in both the saturated and unsaturated cases, the values of H_{uo}, γ, and γ_u were assigned, which shall be used in the dynamic response analysis.

6.3.4. Liquefaction Resistance Curve

Fig. 6-23 compares the liquefaction resistance curves of the test results and the simulations for both saturated and unsaturated conditions of bauxite. The number of cycles (N) of the saturated and unsaturated tests is the 5% double amplitude of axial strain.

For medium dense case, the liquefaction resistance curves roughly match especially when N is higher than 20. The figure also shows that the predicted resistance against liquefaction under unsaturated conditions is much higher than that under saturated conditions. This is similar to what we have observed in the experimental data.

For loose case, the simulated plot did not seem to match well, though on the conservative side. Similar to loose case, dense case also had a more emphasized difference between the experimental data and the simulated one, although also on the conservative side.

Comparisons between the test and simulation results discussed above show that the parameters used for the PZ-sand model may not be very appropriate to predict the real behavior of bauxite. They may need to be further optimized. However, the simulations in this study focus on the responses of the heap in different densities of bauxite, including with or without considering the liquefaction potential of unsaturated bauxite (i.e. Cases 1 to 3 in Table 6-1), and the effect of permeability (in which experimental data were used) on the response of the heap.

6.3.5. Parameter Values Assigned

Table 6-4 indicates the parameter values assigned for the zones indicated in Fig. 6-1 to 6-4.

The following points are notes pertaining Table 6-4:

1. *Italicized Numbers* are parameters which were assigned based on UWLC Element Test Manual suggested range of values and simulation curve fitting.

2. Iron Ore values were all extracted from Wang (2014). No values are *italicized* on this column since the values are simply extracted.

3. In Zone 2 and Zone 3, only the H_o and H_{uo} values are shown because all the other assigned parameter values are the same as that of Zone 4 (wet base).

4. The symbol E represents Young's modulus, while v represents Poisson's ratio. The description of the other symbols can be referred in Table 6-3.

Table 6-4. Parameter Values Assigned

Zone	Symbol	Bauxite			Iron Ore
		Loose (D_c=65%)	M.Dense (D_c=80%)	Dense (D_c=90%)	Dense (D_c=92%)
1 (*Sr*≈residual) (Elastic model)	E (kPa)	126	1041	1426	16000
	ν	*0.3*	*0.3*	*0.3*	0.3
2 (*Sr*≈residual) (PZ-sand model)	H_o	*300*	*1200*	*2400*	20000
	H_{uo}	*9320*	*13980*	*23300*	3000
3 (*Sr*≈80%) (PZ-sand model)	H_o	*300*	*1200*	*2400*	20000
	H_{uo}	*6760*	*10140*	*16900*	3000
4 (wet base, *Sr*=100%) (PZ-sand model)	M_f	0.63	0.96	1.00	1.80
	M_g	1.45	1.45	1.59	1.88
	C	0.674	0.644	0.653	0.600
	α_f	*0.45*	*0.45*	*0.45*	0.45
	α_g	*0.45*	*0.45*	*0.45*	0.45
	K_{evo}	60	130	310	400
	G_{eso}	469	1073	1236	800
	m_v	*1.0*	*1.0*	*1.0*	0.5
	m_s	*1.0*	0.953	*1.0*	0.5
	β_o	*4.2*	*1.2*	*20*	99
	β_1	*0.15*	*0.1*	*0.005*	0.001
	H_o	17.2	20.8	250	20000
	H_{uo}	*4000*	*6000*	*10000*	3000
	γ	*8*	*12.5*	*17*	9
	γ_u	*6*	*10.5*	*15*	9

6-4. Software Input Methodology

This section describes the general steps in software implementation.

1. Create the geometry of the heap by indicating nodes and lines connecting them. The software only permits regions enclosed by three (3) to four (4) sides (Fig. 6-24). The blue line indicates the water table and at the same time, a boundary.
2. Assign the zones from the created geometry. Input also the parameters and constitutive models for each zones (Fig. 6-25).
3. Create mesh by assigning the number of nodes per mesh (Fig. 6-26). The actual meshing can be verified until the desired mesh is achieved (Fig. 6-27).
4. Assign boundary conditions in both static and dynamic cases (Fig. 6-28).
5. Input the cyclic loading conditions of the analysis (Fig. 6-29).
6. Input the step loading and initial conditions of the test (Fig. 6-30)
7. Run the analysis.
8. From the output, modify the .liq file and use the program developed by Professor Cai of Gunma University.

6-5. Simulation Results and Discussions

6.5.1. Initial Stress Distribution

It is essential to initialize the stress distribution in the heap before applying dynamic motion. Fig. 6-31 to Fig. 6-34 show the initial mean principal stress (p_0') distribution of bauxite at dense condition at Case 1, 2, and 3, and iron ore, respectively. It can be seen that generally the distribution of p_0' is proportional to the gravity force. It seems that for initial condition, the distribution of p_o' are the same for Fig. 6-31 and Fig. 6-32 and is not affected by the assumption of the unsaturated regions (Zone 2 and 3) to be assigned liquefiable (Case 1 condition) or non-liquefiable (Case 2). However, discontinuity of p_0' along the interface between Zone 1 and Zone 2 can be observed for all cases. This irregular distribution may be caused by the Young's modulus assigned to the elastic model in Zone 1, which may be too large and as a result the non-liquefiable zone forms a hard shell bearing overmuch loading. Fig. 6-33 (Case 3) is the extreme condition with wet base up to 8 m high. The p_o' distribution has lower values since effective stresses are lower. For iron ore in Fig. 6-34, the p_o' distribution has higher values since iron ore at dense case (D_c = 92%) has unit weight of 25.07 kN/m^3 while bauxite at dense case (D_c = 90%) is only 19.14 kN/m^3. The high stress concentration in Zone 1 can be attributed to the high Young's modulus assigned to it (see Table 6-4).

Likewise, the normalized initial shear stress ratio τ_0/p_0' (τ_0 is in xy direction) for Cases 1, 2, and 3, and iron are shown in Fig. 6-35 to Fig. 6-38. It can be observed that generally, the τ_0/p_0' is symmetric along the vertical line. The distribution of τ_0/p_0' seems to be affected slightly by the assumed Young's modulus since Zone 1 has inconsistent contours observed for Fig. 6-35 to Fig. 6-38.

6.5.2. Deformation Divergence

For each simulation in the three cases, 400 rolling motion cycles at a frequency of 0.1 Hz were applied to the bauxite heap. However, there are some runs where deformation divergence was observed before the completion of the 400 cycles in the simulations. Fig. 6-39 to Fig. 6-42 show an example of the deformation divergence, of which 400 cycles of rolling motion with rolling angle (θ) of 20° were applied to the model of Case 1 for iron ore, but diverged in its deformation suddenly.

Fig. 6-39 shows the deformed grids (grids with blue color) at the 44.8th cycle. The grids in gray color with dashed lines indicate the initial grid before applying cyclic motion. The deformation of the grid was very small after applying 44.8 cycles of motion. Fig. 6-40 shows the next snapshot, at 44.9th cycle. The portion indicated in red circle shows the deformation of the nodes abruptly developed devastatingly and the divergent deformation spreads to the whole grid in a very short time thereafter, as can be seen in Fig. 6-41 at 45.5th cycle, and Fig. 6-42 at 46.0th cycle. The collapse at the extreme ends of the base is assessed to be due to the strain developments in such regions, which shall be discussed in the next section, and also the stress concentration on those regions.

Fig. 6-43 shows the vertical stress (σ_y) of a Gauss point at point A (see Fig. 6-3). It seems that the program terminated the computation of σ_y at the Gauss point on the 44.8^{th} cycle before the onset of large deformation was observed. The computations of stress and strain on the model were automatically stopped before the deformation divergence, regardless if it started on the point or elsewhere. The large deformation may be triggered sooner or later depending on the input motion, and the treatment after the large deformation may vary depending on the algorithm of the programs.

Deformation divergence does not always occur, however. Fig. 6-44 shows the vertical stress (σ_y) of a Gauss point at point A for a rolling angle of 15° for bauxite at medium dense condition at Case 1. It can be seen that σ_y decreased gradually until 201.6^{th} cycle. The effective stress can then be considered at this point and can be calculated. For these cases, this is the point of termination that the heap was considered "liquefied state".

Hence, for the program used in this study, there are two ways to determine terminal point of analysis. One is when the large deformation or failure that may be indicated by the number of cycles at the terminal ($N_{terminal}$), after which the computation of stress and strain is terminated. And, it can also mean that the values of $N_{terminal}$ have terminated due to the effective stress equal to zero.

This shall be discussed further in the liquefaction potential of the heap. First, the strain distribution in the heap is discussed in the next section.

6.5.3. Strain Distribution in the Heap

1. Bauxite, dense, Case 1 (i.e. unsaturated Zone 2 and Zone 3 – assumed liquefiable)

Fig. 6-45 to 6-50 show the distributions of strains ε_x, ε_y, τ_{xy} (normal strain in the x direction, normal strain in the y direction and shear strain in the xy direction, respectively), which considers the liquefaction potential of both the saturated (Zone 4) and the unsaturated zone (Zone 2 and 3). The interfaces between the zones are indicated by the white lines in each figure. The results show that the magnitude of strain increases with the rolling motion with an angle of 5° to 30°. Regarding the locations where large normal and shear strains are mobilized, very clear failure planes running through both the saturated liquefiable zone and the unsaturated liquefiable zone are observed in Fig. 6-48 to Fig. 6-50 at higher rolling angles (20° to 30°). Though the predicted liquefaction resistance of unsaturated bauxite (Fig. 3-39 in Chapter 3) is about 1.7 times higher than that of the saturated condition for Zone 3 and 2.3 times higher than that of the saturation condition for Zone 2 according to the definition of liquefaction resistance ratio (LRR) defined in section 3.4.5 in Chapter 3, it seems that the mobilized strain in the simulation is not restricted by the higher resistance. Using the PZ-model on unsaturated soils, the liquefaction potential of the heap may become much broader rather than limited to the local areas when they are otherwise assumed non-liquefiable.

Observing the rolling angle at 20° in Fig. 6-48, it can be seen that large ε_x and τ_{xy} strains started to develop at the toes of the base. This could be a contributing factor to the deformation divergence that occurred as shown in Fig. 6-43.

2. Bauxite, dense, Case 2 (i.e. unsaturated Zone 2 and Zone 3 – assumed non-liquefiable)

Fig. 6-51 to 6-56 show the distributions of strains ε_x, ε_y, τ_{xy} at the terminals for Case 2 with different rolling angles, which considers the liquefaction potential of the saturated zone only. Likewise, the interfaces between the zones are indicated by the white lines in each figure. It can be seen that the magnitude of strains are generally smaller and more evenly distributed that their counterparts in Case 1 (Fig. 6-45 to Fig. 6-50), although same pattern development of strains can be observed. For example, the development of large strains at the toe of the heap at the base and side boundaries for ε_x (Fig. 6-48a to Fig. 50a, and Fig. 6-54a to Fig. 56a) and τ_{xy} (Fig. 6-48c to Fig. 50c, and Fig. 6-54c to Fig. 56c). As for ε_y, the development of strains for Case 2 (Fig. 6-48b to Fig. 6-50b) seems to be gearing only in the compressive side (which should be), with larger strains at the saturated region at the base in Zone 4. For Case 1, the development is rather scattered (Fig. 6-48b to Fig. 6-50b).

The comparison of strains of Case 1 and Case 2 suggest that it is worthwhile to consider the liquefaction potential of the unsaturated zone when analyzing the responses of the heap under the rolling motion.

3. Bauxite, dense, Case 3 (i.e. extreme condition)

Fig. 6-57 to Fig. 6-62 show the distributions of strains ε_x, ε_y, τ_{xy} at the terminals in Case 3, which is the extreme condition with wet base up to 8 m high (see Fig. 6-4). Zone 3 in this case is assumed to be liquefiable. The ε_y strain development seems to be progressing from the base to the top. Even at rolling angle of 10°, large strains can already be observed for the extreme condition.

Results in Case 3 imply that if water in the heap cannot seep out through its side boundaries and bilge at the base of the hold, the heap becomes weaker to resist the rolling motion than that predicted in Case 1 and Case 2.

4. Iron ore, dense, Case 1 (i.e. unsaturated Zone 2 and Zone 3 – assumed liquefiable)

Fig. 6-63 to 6-68 show the distributions of strains ε_x, ε_y, τ_{xy} for iron ore, which considers the liquefaction potential of both the saturated (Zone 4) and the unsaturated zone (Zone 2 and 3). The pattern of strain development is similar to that of bauxite (Fig. 6-45 to Fig. 6-50), although ε_y specifically shows higher magnitude of strains. This can be attributed to the much higher unit weight of iron ore.

6.5.4. Liquefaction Potential of the Heap

Four parameters can be considered to represent the liquefaction potential of the heap (Wang, 2014):

1. Maximum pore water pressure ratio (PWP_{max}/p_0'): it is the ratio of maximum value of PWP during cyclic rolling motion to the initial effective mean principle stress (p_0'). This is a widely used term in both laboratory tests and numerical simulations; however, it is difficult to use this parameter for the cases where large deformation was observed before completion of the assigned 400 cycles of rolling motion. Since PWP in the computation unreasonably increases or decreases, in order to use this parameter, a huge amount of data needs to be processed manually to extract PWP_{max} from the data before the development of large deformation. In addition, this parameter may not be a good parameter to be used for this simulation, since PWP may also be generated by the change of total stress, and thus the parameter may become larger than unity.

2. Terminal pore water pressure ratio (PWP_t/p_0'): this is a ratio of PWP at terminal, where the program stops the computation of stress and strain, to p_0'. Since PWP changes sinusoidally with the rolling motion, PWP could not represent the PWP_{max}.

3. Maximum effective stress reduction ratio ($1-p'_{min}/p_0'$): This parameter represents the maximum reduction in effective stress. It equals to unity when the minimum value of p' (p'_{min}) reduces to 0 kPa (liquefaction). Since there is no direct way to obtain p'_{min} by using the current software, processing a huge amount of data limits the use of this ratio.

4. Terminal effective stress reduction ratio ($1-p_t'/p_0'$): This parameter represents the effective stress reduction at the terminal. Since the effective stress usually decreases with an increase in the number of rolling motions, $1-p_t'/p_0'$ may be a good representative value of $1-p'_{min}/p_0'$. This parameter is used in this study to show the liquefaction potential of the heap.

Referring again to the incident of MV Bulk Jupiter, it was reported that the duration of the ship when it started to roll more heavily until the Japanese Coast Guard received a stress signal was 60 minutes (The Commonwealth of the Bahamas: Report on MV Bulk Jupiter, Section 3: Narrative of Events, 2015). The duration 60 minutes, by assuming the period of rolling motion of 10 seconds is equivalent to 360 cycles. Hence, 400 cycles was set to provide allowance or buffer to evaluate if the ship can sustain 360 cycles.

1. Bauxite, different densities, Case 1 (i.e. unsaturated Zone 2 and 3 – assumed liquefiable)

The relationship between rolling angle (θ) and the number of cycles at the terminal point ($N_{terminal}$) is plotted in Fig. 6-69 for bauxite at various densities. $N_{terminal}$ here is defined as runs terminated due to deformation divergence or the point when the effective mean stress approaches zero.

From the plot, it can be seen that the loose case can only exceed 360 cycles with rolling angle of 5° or less, and then at higher rolling angles, the $N_{terminal}$ were below 360 cycles. For medium dense case, it satisfied up to the rolling angle of 10°, while for dense case, at 15°. Another thing that can be observed is that for the same density, point A, which is at Zone 4 (wet base) has lower $N_{terminal}$ values. This makes sense since the liquefaction resistance generally increases with saturation degree (*Sr*). Dense case at rolling angles 20° and 30° are the exceptions. The reason why the $N_{terminal}$ values are the same is because this diverged in its deformation, hence the stress values are not unique for points A, B, and C.

Fig. 6-70 shows the contour map showing $1\text{-}p_t'/p_o'$ of the heap for dense case from rolling angle 5° to 30°. Dense case is shown for ease of comparison to other cases in the subsequent sections. Initially, the $1\text{-}p_t'/p_o'$ is low, and then gradually develops until red marks can be seen at the wet base at Zone 4. Characteristic of the test for dense case is the reduction of effective strength at the toe at the base. The unsaturated regions, likewise developed reduction of effective strength although less intensified than the wet base for all rolling angles.

2. Bauxite, different densities, comparing Case 1 and Case 2

Using the same criteria in Fig. 6-69, Fig. 6-71 presents the rolling angle θ plotted against $N_{terminal}$ to compare Case 1 and Case 2. Since Zone 2 and Zone 3 are both assumed non-liquefiable for Case 2, points B and C were omitted because it would be pointless to compare the results with Case 1 (i.e. all would result to 400 cycles). Hence, only point A (i.e. Zone 4, wet base) was plotted against each other. It can be seen that by assuming Zone 2 and Zone 3 to be either liquefiable or not had an effect on the terminal point of the test. The effects are quite minimal/negligible though for loose and medium dense case, but for dense, assuming Zone 2 and 3 to be non-liquefiable can exceed 360 cycles of 20° rolling (indicated by violet line) as oppose to assuming Zone 2 and 3 to be liquefiable which can only exceed 15° rolling (indicated by blue line). Several reasons why this trend was observed can be associated with the assigned parameters to the heap, and development of wet base (or zonings of the heap).

Fig. 6-72 shows the contour map of $1\text{-}p_t'/p_o'$ for Case 2. The blue portions indicate that it is non-liquefiable. Patterns of development of $1\text{-}p_t'/p_o'$ can only be seen at the wet base, and it seems to be similar to the development of Case 1 in Fig. 6-70.

3. Bauxite, dense, comparing Case 1 and Case 3

Fig. 6-73 shows the comparison between Case 1 (i.e. unsaturated Zone 2 and 3 assumed to be liquefiable) and Case 3 (i.e. extreme condition, wet base up to 8 m). From the plot, $N_{terminal}$ values exceeded the 360 cycles at rolling angle of 5° only.

The contour in Fig. 6-74 shows that even at 5° rolling, the $1\text{-}p_t'/p_o'$ started to develop and became more intensified as the rolling angles increased. This shows that even when heap is dense or densification is applied, improper drainage at the bilge, or accumulation of wet base does affect the overall resistance of the heap.

4. Bauxite and Iron ore, dense, Case 1 (i.e. unsaturated Zone 2 and 3 – assumed liquefiable)

Fig. 6-75 presents the comparison of bauxite and iron ore at dense case at Case 1. With the assumed parameters shown in Table 6-4, the iron ore was able to exceed the 360 cycle mark up to 10° rolling angle. After which, all simulations experience deformation divergence from rolling angles 15° and higher. Bauxite at dense case had deformation divergence at 20° and 30°, on the other hand.

Fig. 6-76 shows the contour of $1\text{-}p_t'/p_o'$ for iron ore at dense case. Similar to Fig. 6-70 for bauxite, the development of $1\text{-}p_t'/p_o'$ can be seen to develop from the wet base, with stronger intensity at the toes of the base.

5. Bauxite, different densities, Case 1 assuming $1\text{-}p_t'/p_o' = 0.90$ criteria (i.e. unsaturated Zone 2 and 3 – assumed liquefiable)

Since bauxite was observed to achieve double amplitude (DA) of 5% axial strain at 90% effective strength reduction of specimen to occur almost simultaneously in the lab test, the criteria $1\text{-}p_t'/p_o' = 0.90$ was also set to observe the sensitivity of the results of the test. Fig. 6-77 shows the result for Case 1 for loose, medium dense, and dense cases. As expected, the occurrence of terminal point (i.e. $1\text{-}p_t'/p_o' = 0.90$ or deformation divergence) was earlier although not significantly earlier.

6.5.5. Vertical Displacement at the Surface of the Heap

Setting a criterion for the vertical displacement at the surface of the heap may prove to be challenging since the runs conducted assumed Zone 1 to be stiff enough to avoid numerical instability (and slope stability problems among others). This can be observed from the normal strain (ε_y) distributions in Fig. 6-45 to Fig. 6-68 that Zone 1 has different ε_y distribution behavior than the heap in general. Hence, the vertical displacement of the heap, although a practical way to physically report unusual behavior in the heap during transportation, may not be directly adoptable in the simulated runs.

In the Global Bauxite Working Group, GBWG (2017) however, it was presented on its section 2.3.2.3 for Malaysian Bauxite Products that the average compaction for 31 observed vessels from Malaysia to China is 0.5% reduction of height of heap. The measurements are considered accurate to ±10cm. From this information, a vertical displacement at the surface exceeding -15 cm was set as another criteria just to infer if the heap at terminal point exceeded the average recorded vertical displacements or not. The information however does not suggest liquefaction if the vertical displacement is exceeded.

1. Bauxite, different densities, Case 1 (i.e. unsaturated Zone 2 and 3 – assumed liquefiable)

The relationship between rolling angle (θ) and the vertical displacement at point D (see Fig. 6-3) at the terminal point is plotted in Fig. 6-78 for bauxite at various densities. In case there is deformation divergence, the vertical displacement of the cycle prior to it was adopted.

From the plot, it can be seen that the loose case all exceeded the average vertical displacement of -15 cm. For medium dense case, it satisfied up to the rolling angle of 5°, and then exceeded the average values for observed vertical displacement. For dense case, the vertical displacement did not exceed the -15 cm criteria for all cases.

As for the trend, decreasing values cannot be observed for all cases since the plot shows the vertical displacement only at the terminal point of each simulation. It is possible that for loose and medium dense condition that due to the presence of voids, prolonged rolling naturally caused the heap to displace more at higher number of cycles at the terminal point ($N_{terminal}$), while at higher rolling angle, the vertical displacement could be less since $N_{terminal}$ (i.e. number of cycles) is also lower.

Same thing can be said that point C (see Fig. 6-3), which is at Zone 2 (unsaturated region), had displaced more compared to point B (Zone 3, unsaturated region) and point A (wet base) for the same density. This may be counterintuitive at first but the $N_{terminal}$ for point C and point B has a larger value than point A. Hence, more cycles of rolling could cause more vertical displacements.

2. Bauxite, different densities, comparing Case 1 and Case 2

Using the same criteria in Fig. 6-78, Fig. 6-79 presents the rolling angle θ plotted against the vertical displacement at point D comparing Case 1 and Case 2. While Case 1 is discussed above, Case 2 shows that for all densities, the vertical displacement values at D did not exceed the -15 cm criteria. In effect, assuming Zone 2 and 3 to be non-liquefiable contributed to the reduction of vertical displacement at point D for loose and medium dense condition. For dense condition, the values are practically the same.

3. Bauxite, dense, comparing Case 1 and Case 3

Fig. 6-80 shows the comparison between Case 1 (i.e. unsaturated Zone 2 and 3 assumed to be liquefiable) and Case 3 (i.e. extreme condition, wet base up to 8 m). From the plot, Case 3 shows that at the terminal point, vertical displacement exceeded the -15 cm average vertical displacement criteria for rolling angles greater than 10°.

4. Bauxite and Iron ore, dense, Case 1 (i.e. unsaturated Zone 2 and 3 – assumed liquefiable)

Fig. 6-81 presents the comparison of bauxite and iron ore at dense case at Case 1. For iron ore, the vertical displacement seems to be within the -15 cm average values however the values were all the same for all rolling angles due to deformation divergence.

In essence, dense materials generally do not exceed the -15 cm vertical displacement, except when wet base was assumed to be extremely high like the one in Case 3.

6-6. Discussion

In the official report published by the Global Bauxite Working Group (GBWG, 2017), bauxites that exhibit potential instabilities have (1) considerable amount of fines particles, (2) high moisture content, and (3) experience sufficient forces due to vessel motions (GBWG, 2017). Hence, a common way to avoid liquefaction is to set a criterion for permissible fines and to set a Transportable Moisture Limit (TML).

In the Global Bauxite Working Group (2017), the criterion proposed to distinguish Group A and Group C bauxites is:

- Group C (no known risk) D_{30}≥1mm OR D_{40}≥2.5mm OR BOTH
- Group A (potential risk) D_{30}<1mm AND D_{40}<2.5mm

where $\underline{D_x}$ is the size corresponding to x% on the cumulative particle size distribution curve.

In the tests conducted in this study with only particles less than 2 mm were utilized, D_{30} = 0.054 mm while D_{40} = 1.65 mm. If the existing code were to be referred to, the tested material falls into the category of Group A of bauxite.

TML, on the other hand, is set to ensure the safe shipping of Group A bauxites. Proctor-Fagerberg test (PFT) is used to determine TML and was proposed and further developed by the GBWG suitable for bauxite. The GBWG recommends that the TML of the tested bauxite is read at 70% or 80% saturation, depending on the saturation degree (*Sr*) of its optimum moisture content (OMC). Although generally composed of similar minerals, bauxites have large differences in particle size distribution depending on the deposit and subsequent processing, thus have wide variation of moisture levels corresponding to its respective *Sr*. As a general, separate study, simulations were performed at *Sr* = 90%, a rather conservative assumption.

The simulations in this study attempted to represent loose condition, which is equivalent to the published information from The Commonwealth of the Bahamas: Report on MV Bulk Jupiter (2015) at 1.311 g/cm^3, medium dense condition to represent the calculated dry density of bauxite from the average bulk densities of bauxite shipped from Malaysia to China (GBWG, 2017) of 1.549 g/cm^3, and dense condition at 1.800 g/cm^3 to adopt the suggestion of an Australian professional working on Bauxite.

With the conservative assumptions and the information on densities, simulations were performed for loose (D_c=65%), medium dense (D_c=80%), and dense conditions (D_c=90%) of bauxite. The dense condition was compared to iron ore (D_c=92%), with the parameters adopted from Wang (2015). The simulations include identifying the number of rolling cycles before the terminal point, the strain distribution on the heap, the liquefaction potential distribution, and the displacement of the surface of the heap at terminal point. Considerations of the effects of the liquefaction potential and permeability (using experimental data) were implemented for the unsaturated zones. The simulations suggest that while the liquefaction resistance of unsaturated bauxite is higher than the saturated

one, the liquefaction potential of the two are not far from each other, due to the large strains developed with the PZ-sand model.

6-7. Chapter Summary

In this Chapter, the following conclusions can be stated:

1. The predictions of the cyclic behaviors of bauxite by using the PZ-sand model qualitatively match the experimental results (Fig. 6-23), while the parameters used in this study may need to be further optimized in order to produce better results. Currently, some parameters were obtained from undrained monotonic tests, isotropic consolidation tests, and undrained cyclic tests.

2. Strain distributions show that the development of strains increases with the rolling motion with an angle of 5° to 30°. Regarding the locations where large normal and shear strains are mobilized, they are developed at the (1) toes of the heap, (2) side boundaries, (3) interfaces of zones of both saturated and unsaturated regions, and (4) wet base/saturated zone.

3. Liquefaction potential of heap was evaluated with the number of cycles at the terminal point ($N_{terminal}$). Terminal point in the simulations was defined as deformation divergence (Fig. 6-43) or reduction of effective stress to zero (Fig. 6-44). The following observations were made from the simulations:
   - Bauxite at loose: ≤5° rolling angle; medium dense: ≤10° rolling angle; dense: ≤15° rolling angle; and Iron ore at dense: ≤10° rolling angle, could withstand a 360 cycle rolling motion (i.e. 60-minute duration) (Fig. 6-69 to Fig. 6-70 and Fig. 6-75 to Fig. 6-76).
   - Assuming the unsaturated region to be liquefiable (i.e. Case 2) decreased the overall resistance of heap of bauxite (Fig. 6-71 and Fig. 6-72). Hence, the considerations of liquefaction potential of the unsaturated zone in the heap of bauxite, the overall liquefaction potential of the heap may become higher than that without considering them.
   - Assuming the extreme case of heap having poor drainage and impermeable side boundaries (i.e. Case 3) caused the heap to liquefy earlier (Fig. 6-73 and Fig. 6-74).

4. Vertical displacements of heap simulations were made to compare with the average compaction for 31 observed vessels from Malaysia to China as shown in GBWG (2017). By investigating the vertical displacements, the following limits can be said:
   - Bauxite at loose: exceeded the average compaction values for all rolling angles; medium dense: did not exceed for rolling angle ≤5°; dense: did not exceed for all rolling angles; and iron ore at dense: did not exceed for all rolling angles simulated (Fig. 6-78 and Fig. 6-81).
   - Assuming the unsaturated region to be liquefiable (i.e. Case 2) increased the vertical displacement of the heap of bauxite at the surface (Fig. 6-79).

- Assuming the extreme case of heap having poor drainage and impermeable side boundaries (i.e. Case 3) caused the heap to exceed the vertical displacement criteria limit (Fig. 6-80).

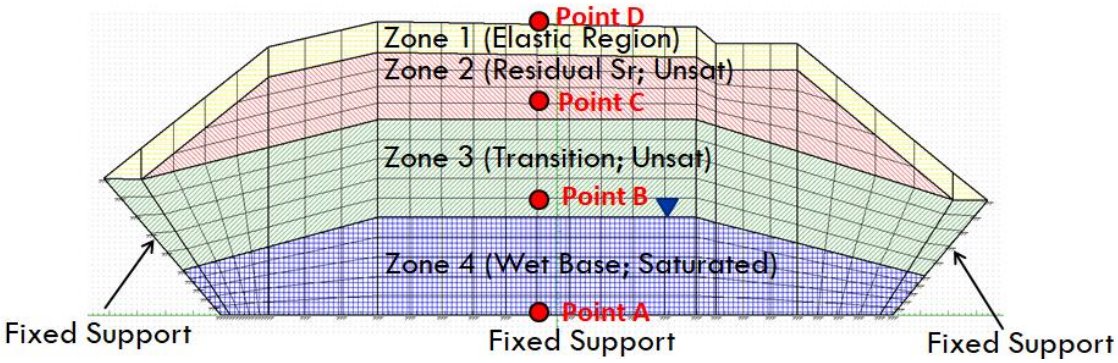

Fig. 6–1. Heap of bauxite for loose condition (Case 1 and Case 2)

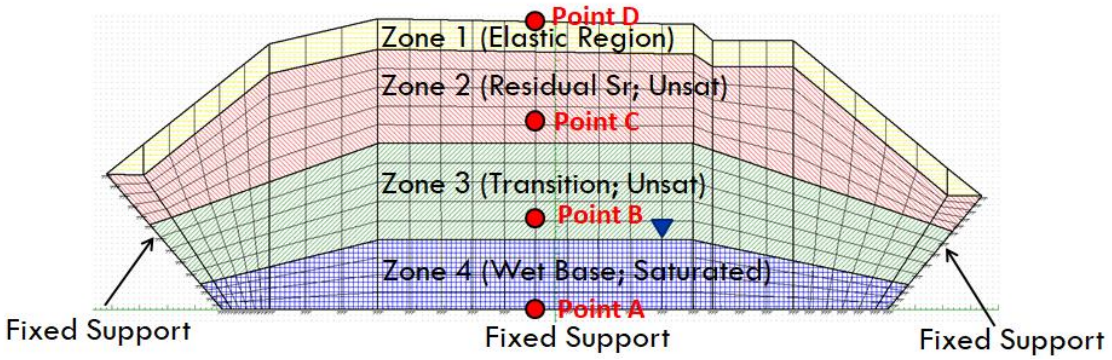

Fig. 6–2. Heap of bauxite for medium dense condition (Case 1 and Case 2)

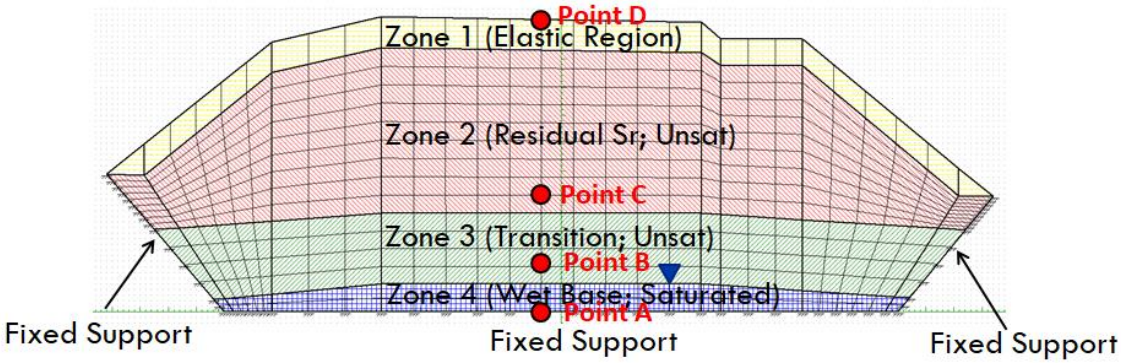

Fig. 6–3. Heap of bauxite and iron ore for dense condition (Case 1 and Case 2)

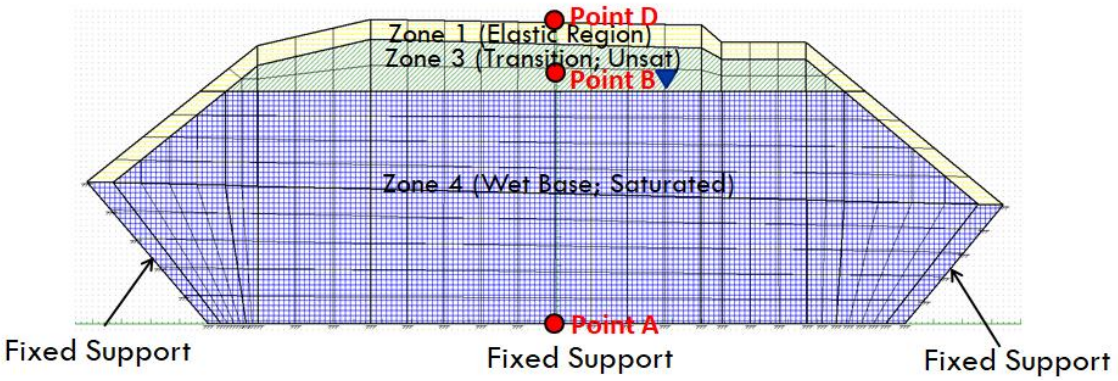

Fig. 6–4. Heap of bauxite for extreme condition (Case 3)

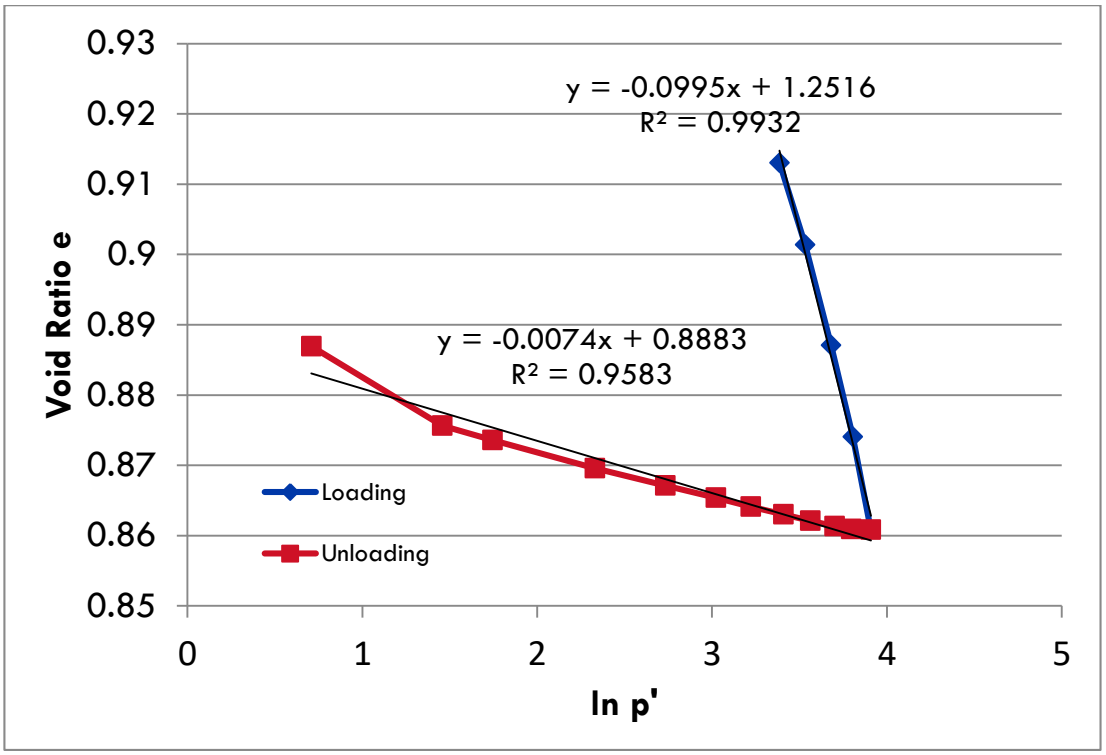

Fig. 6–5. Void ratio *e* vs ln*p'* plot (bauxite, medium dense)

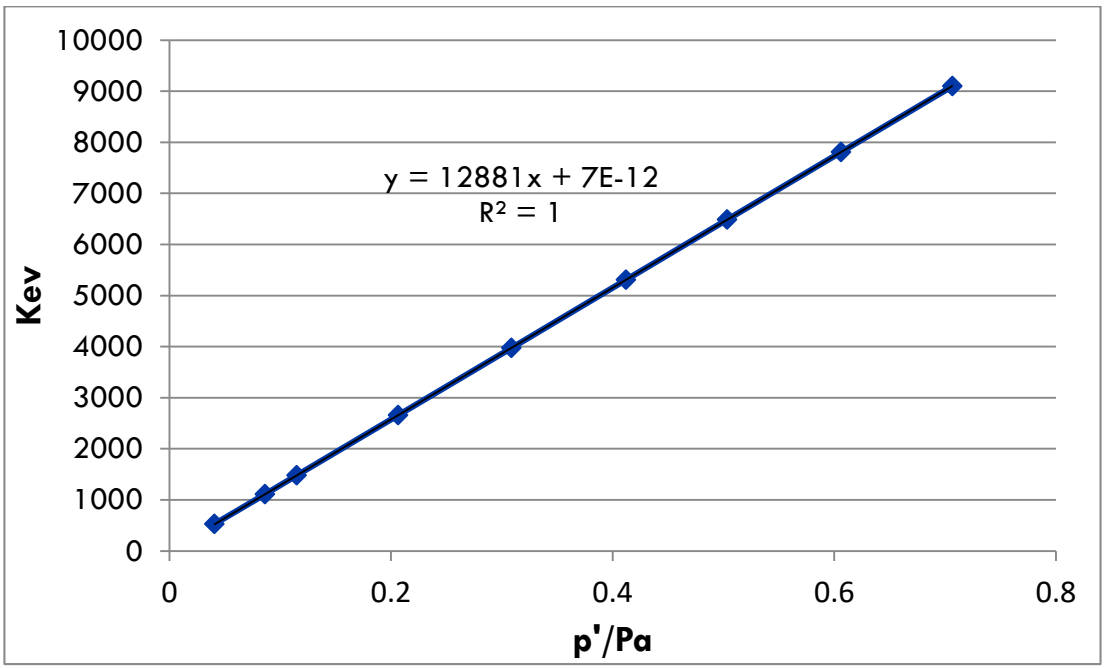

Fig. 6–6. K_{ev} vs. *p'/Pa* plot (bauxite, medium dense)

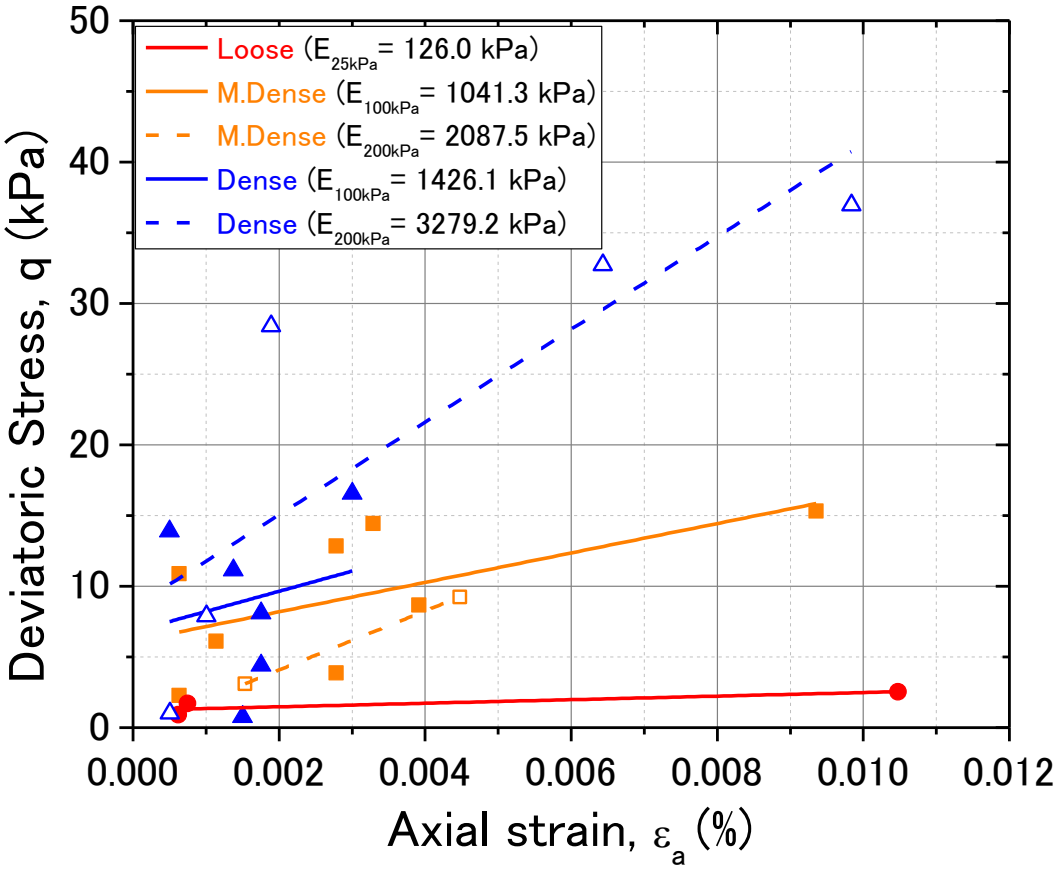

Fig. 6–7. Deviatoric stress *q* vs axial strain ε_a (bauxite tests)

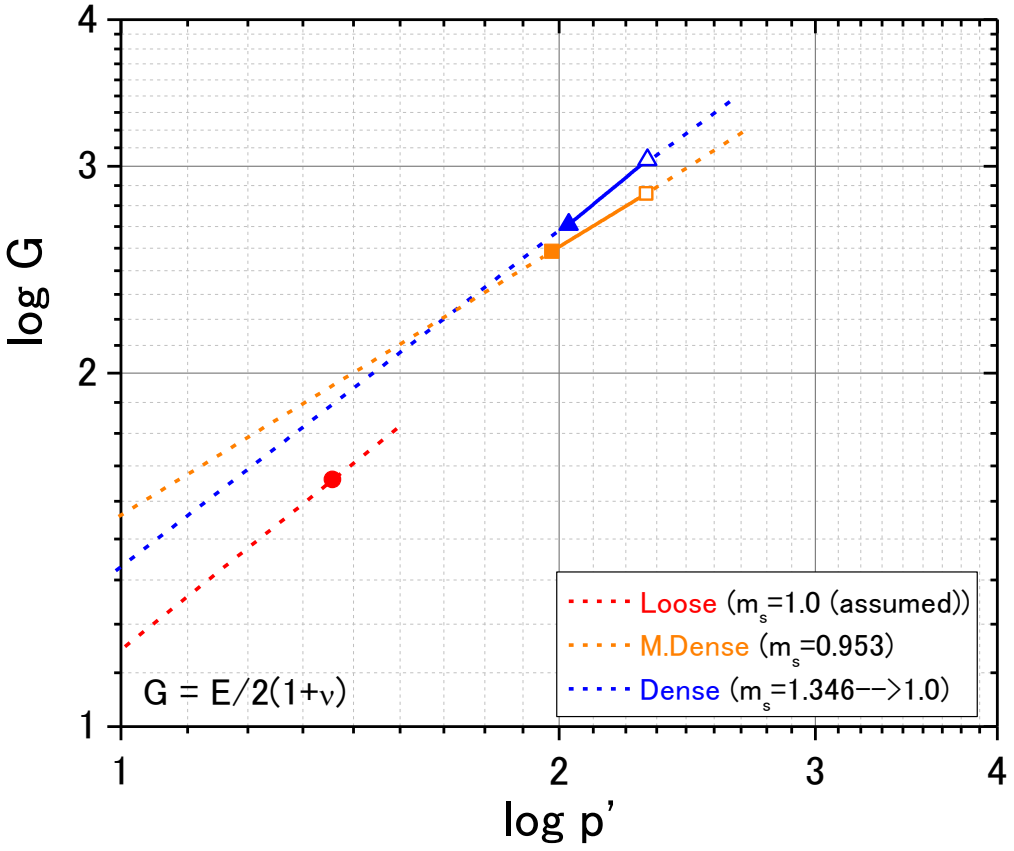

Fig. 6–8. log G vs log p' plot (bauxite tests)

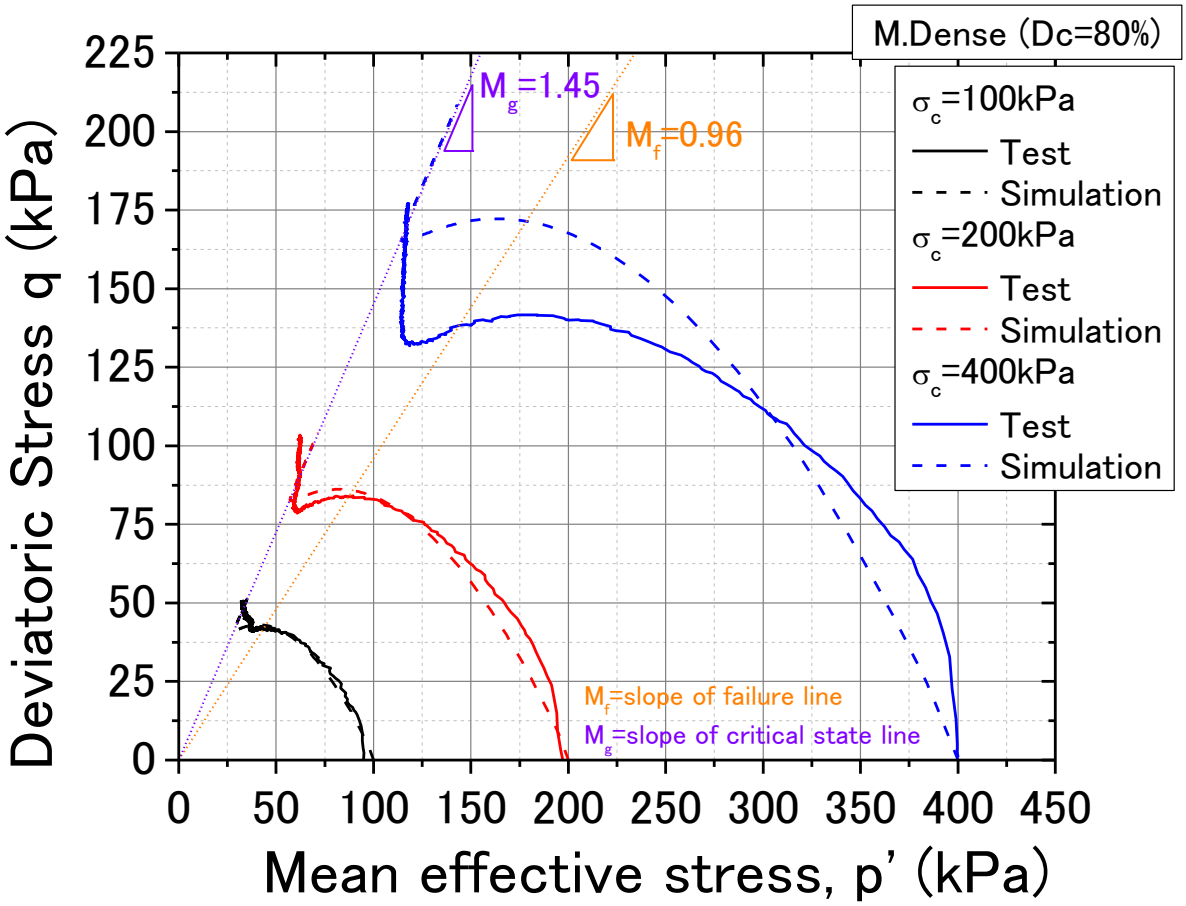

Fig. 6–9. Undrained monotonic tests, p'-q plot (bauxite, medium dense)

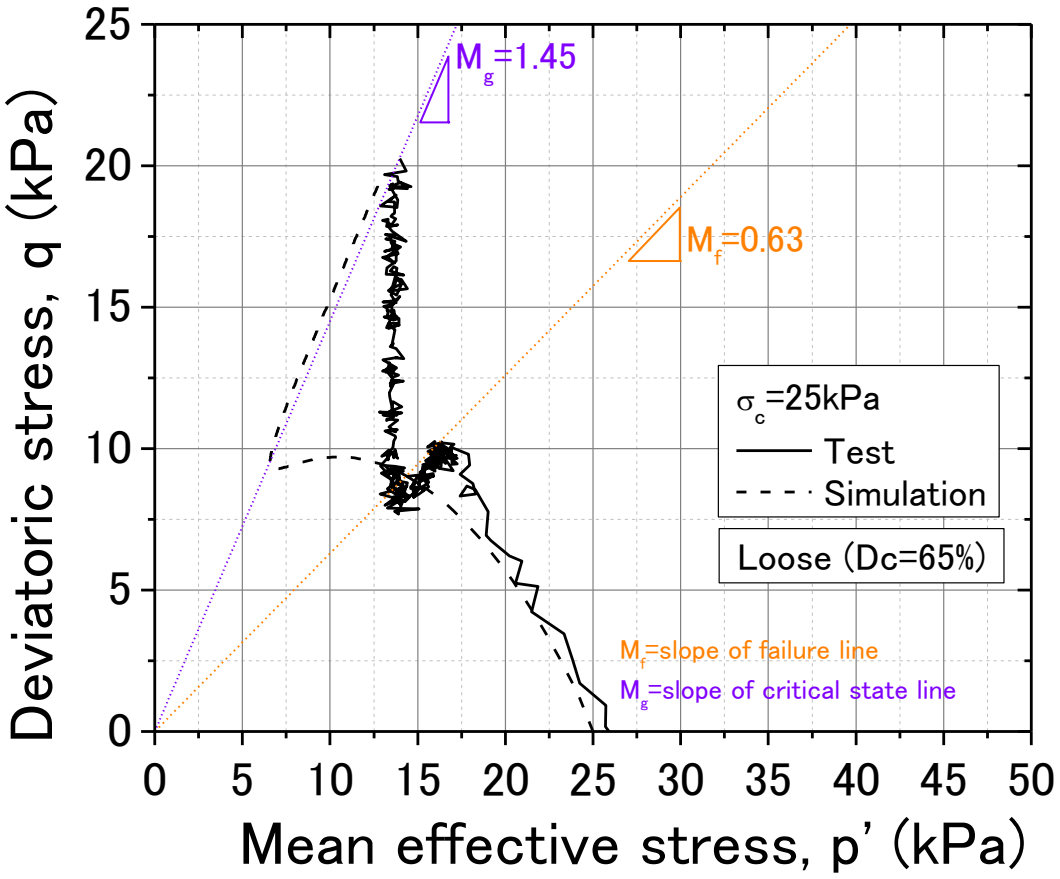

Fig. 6–10. Undrained monotonic tests, p'-q plot (bauxite, loose)

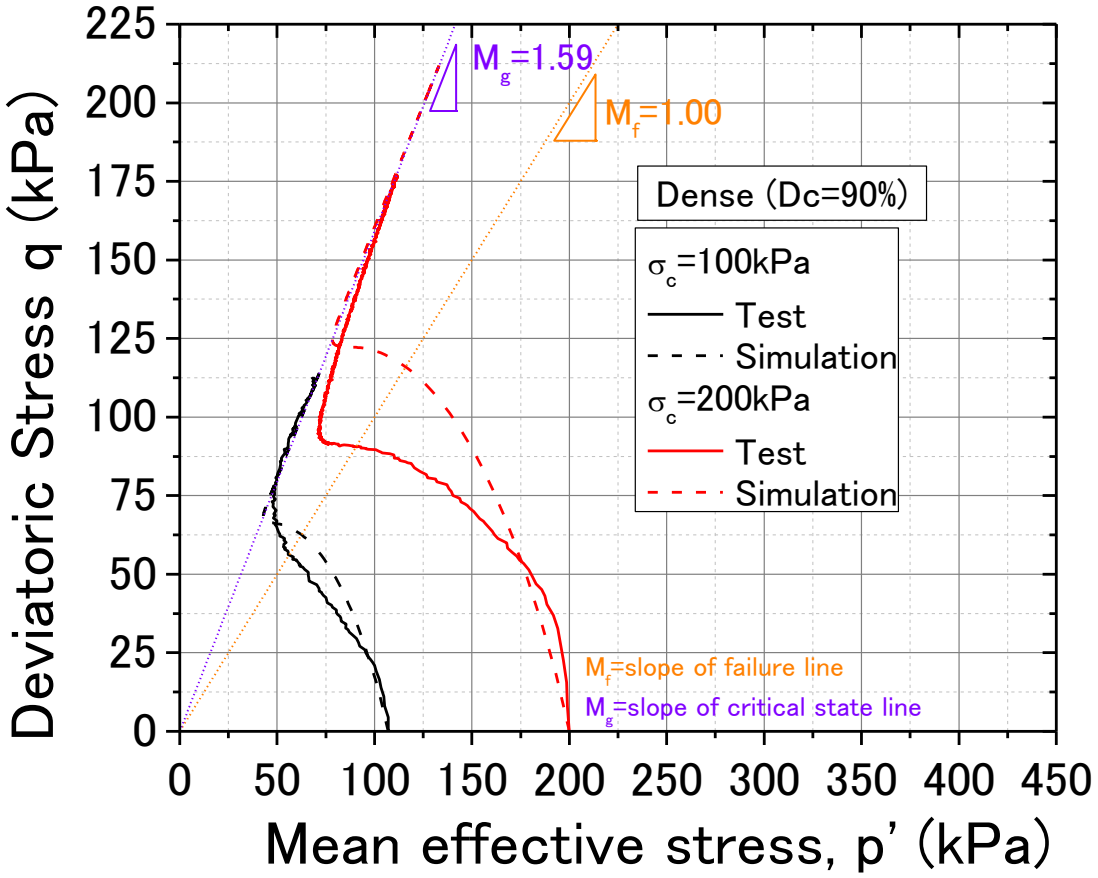

Fig. 6–11. Undrained monotonic tests, p'-q plot (bauxite, medium dense)

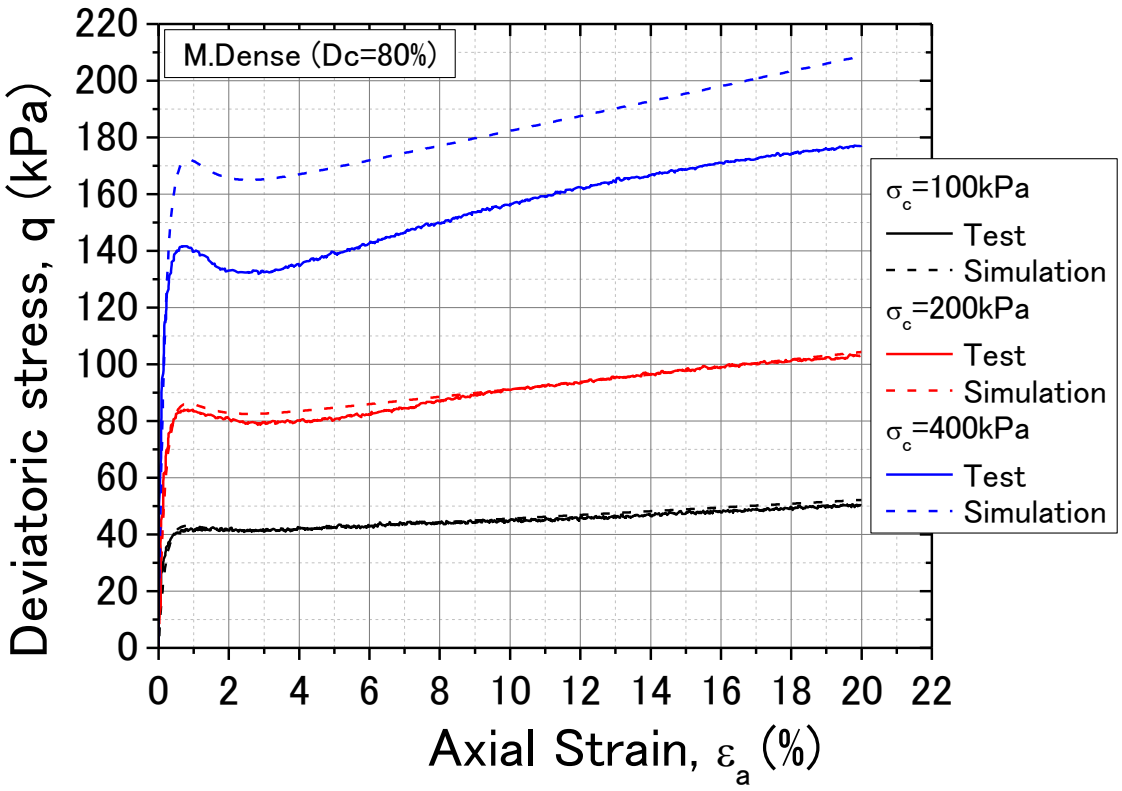

Fig. 6–12. Undriained monotonic tests, *q* vs ε_a plot (bauxite, medium dense)

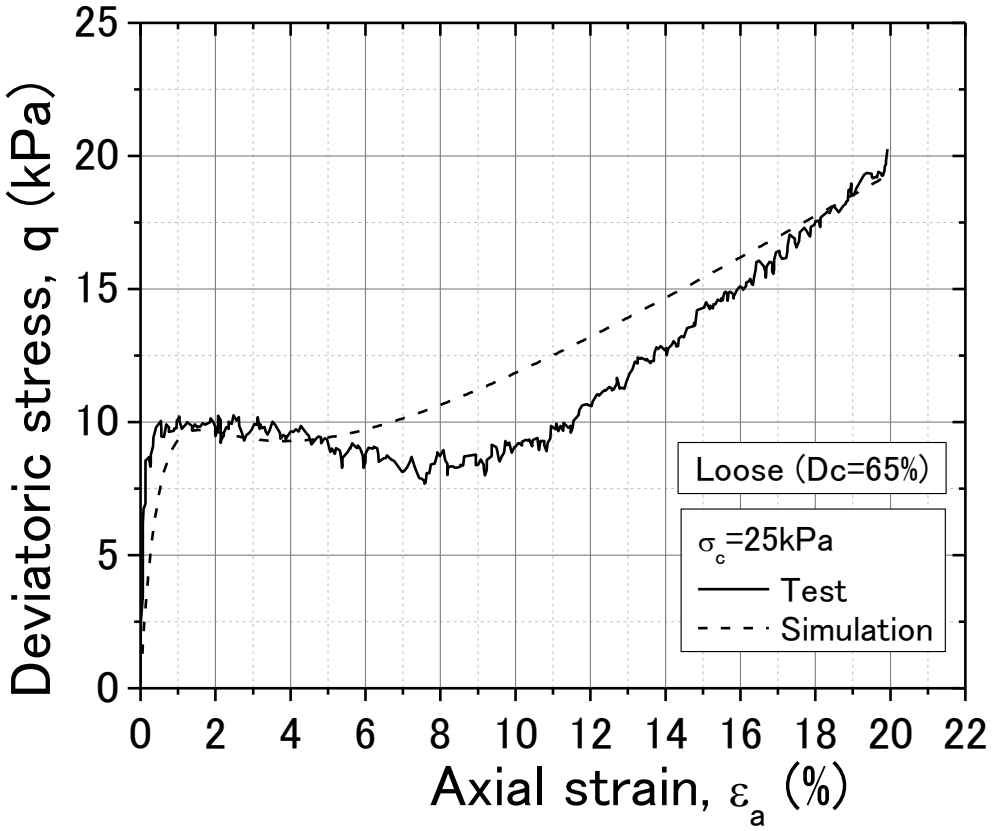

Fig. 6–13. Undriained monotonic tests, *q* vs ε_a plot (bauxite, loose)

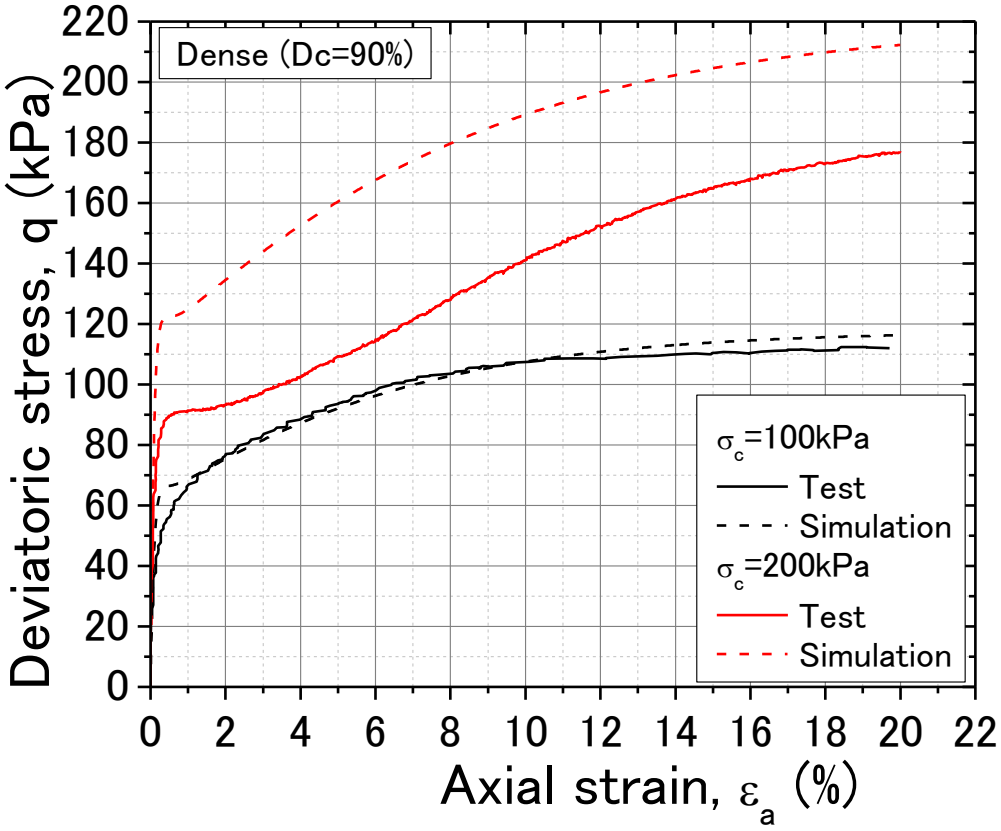

Fig. 6–14. Undriained monotonic tests, *q* vs ε_a plot (bauxite, dense)

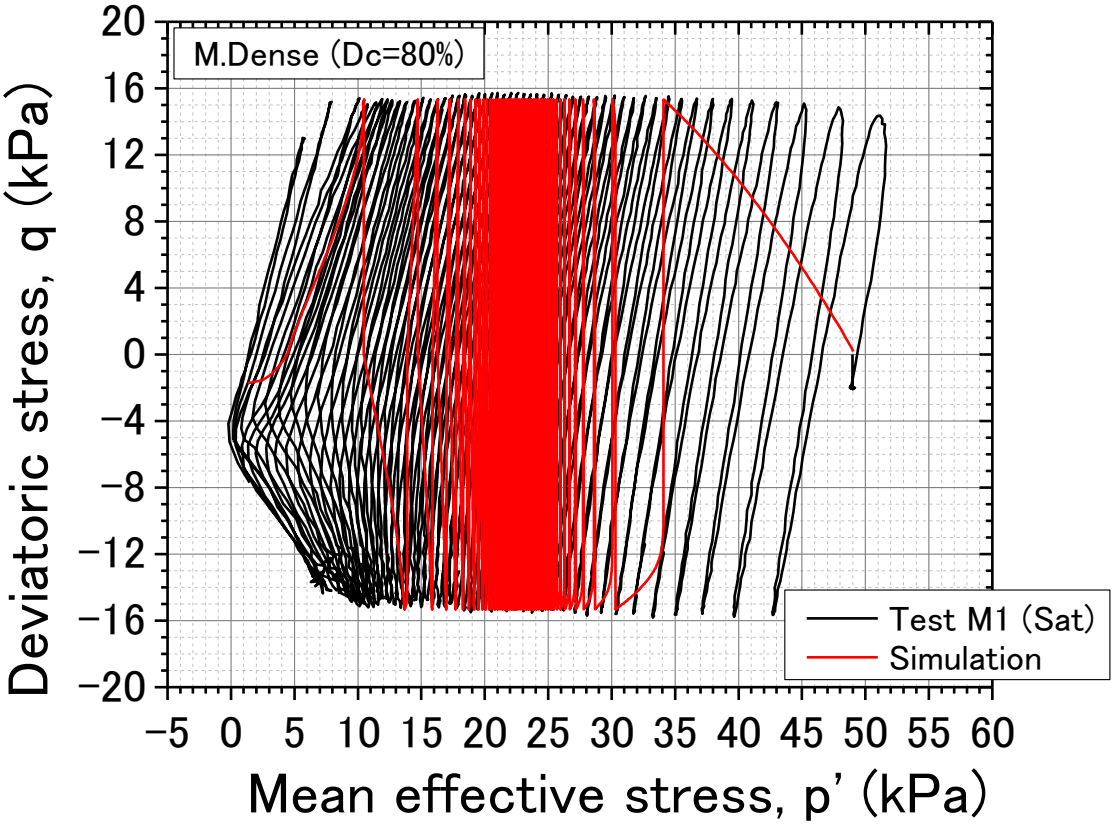

Fig. 6–15. Undrained cyclic test (saturated), p'-q plot (test M1 bauxite, medium dense)

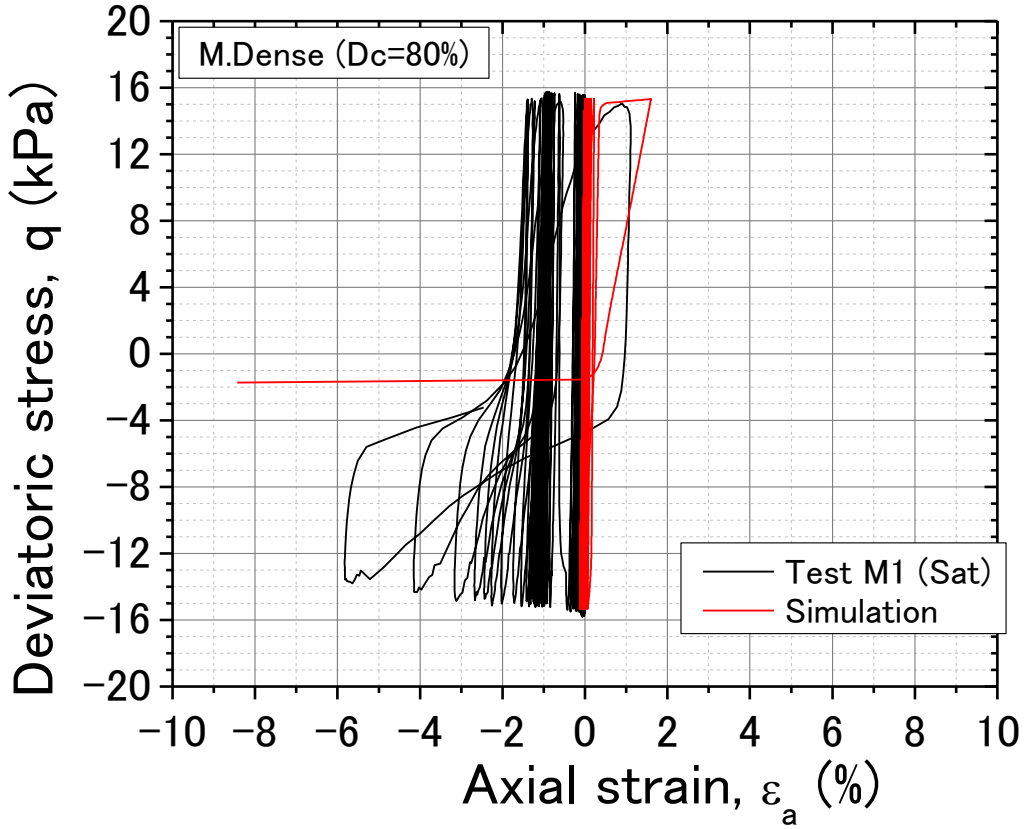

Fig. 6–16. Undrained cyclic test (saturated), *q* vs ε_a plot (test M1 bauxite, medium dense)

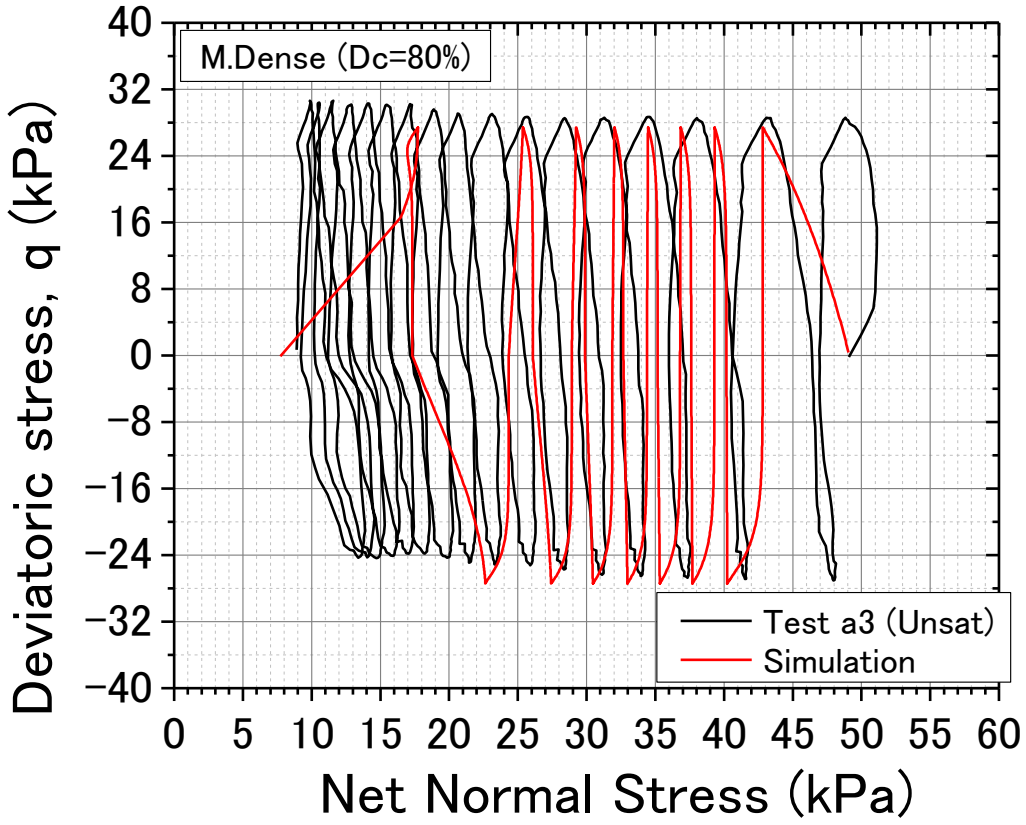

Fig. 6–17. Undrained cyclic test (unsaturated), p'-q plot (test a3 bauxite, medium dense)

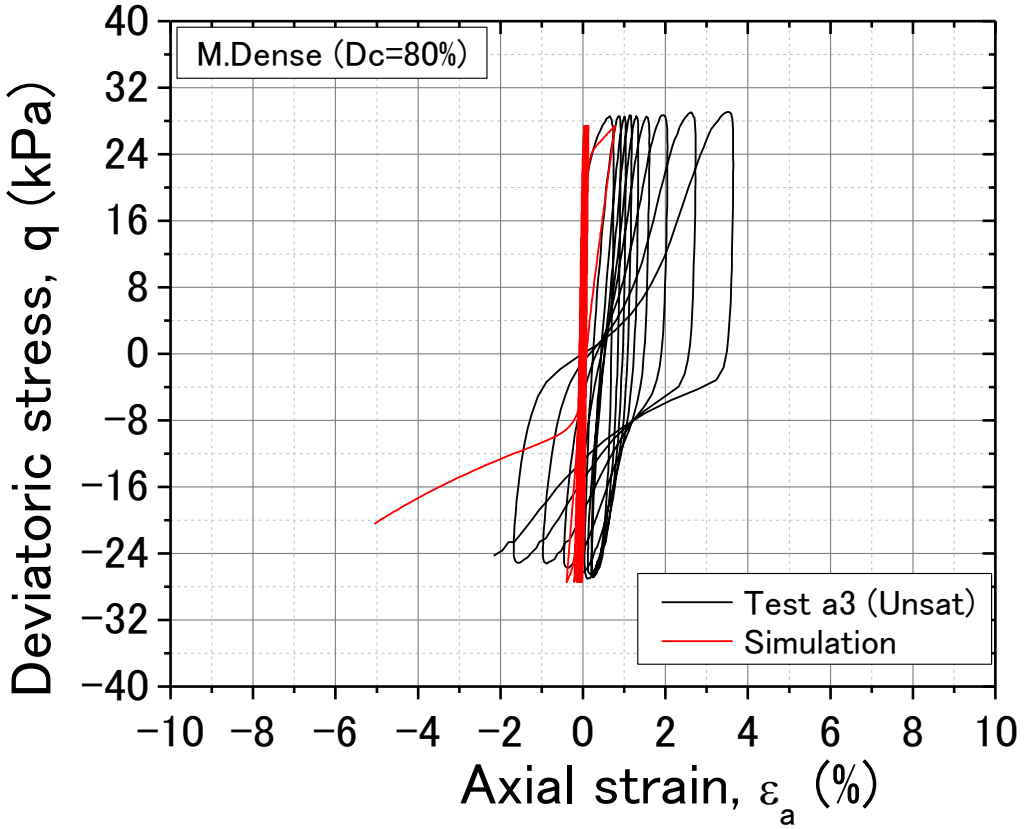

Fig. 6–18. Undrained cyclic test (unsaturated), *q* vs ε_a plot (test a3 bauxite, medium dense)

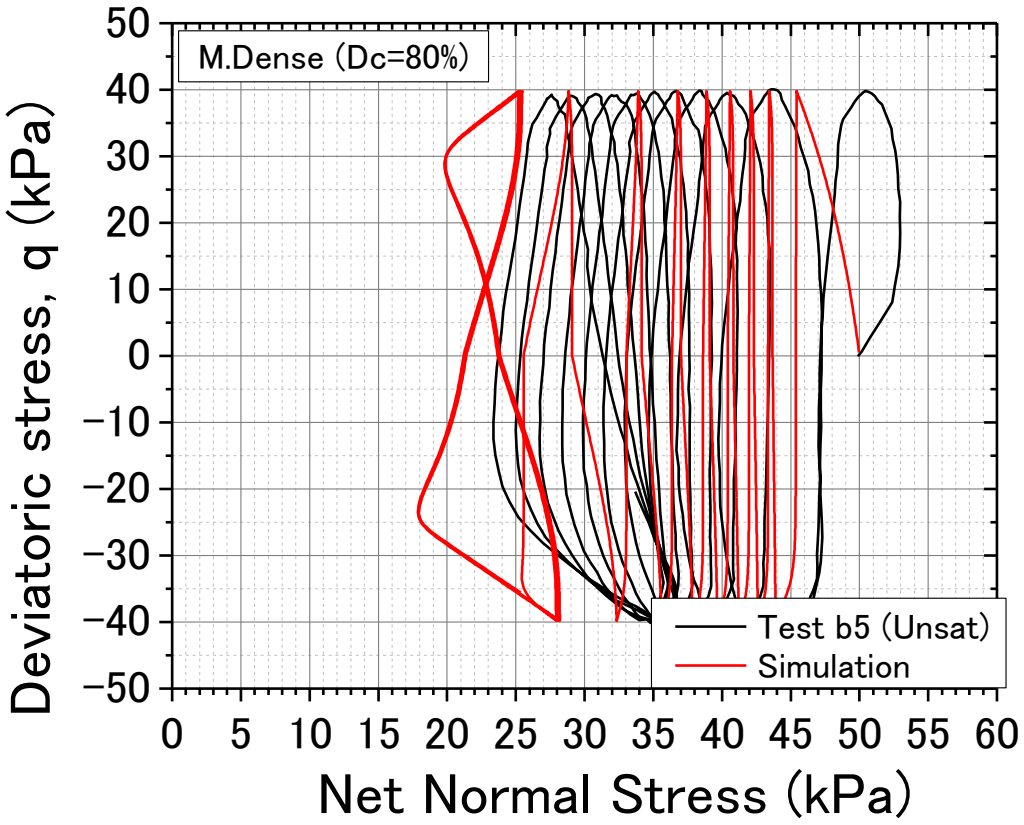

Fig. 6–19. Undrained cyclic test (unsaturated), p'-q plot (test b5 bauxite, medium dense)

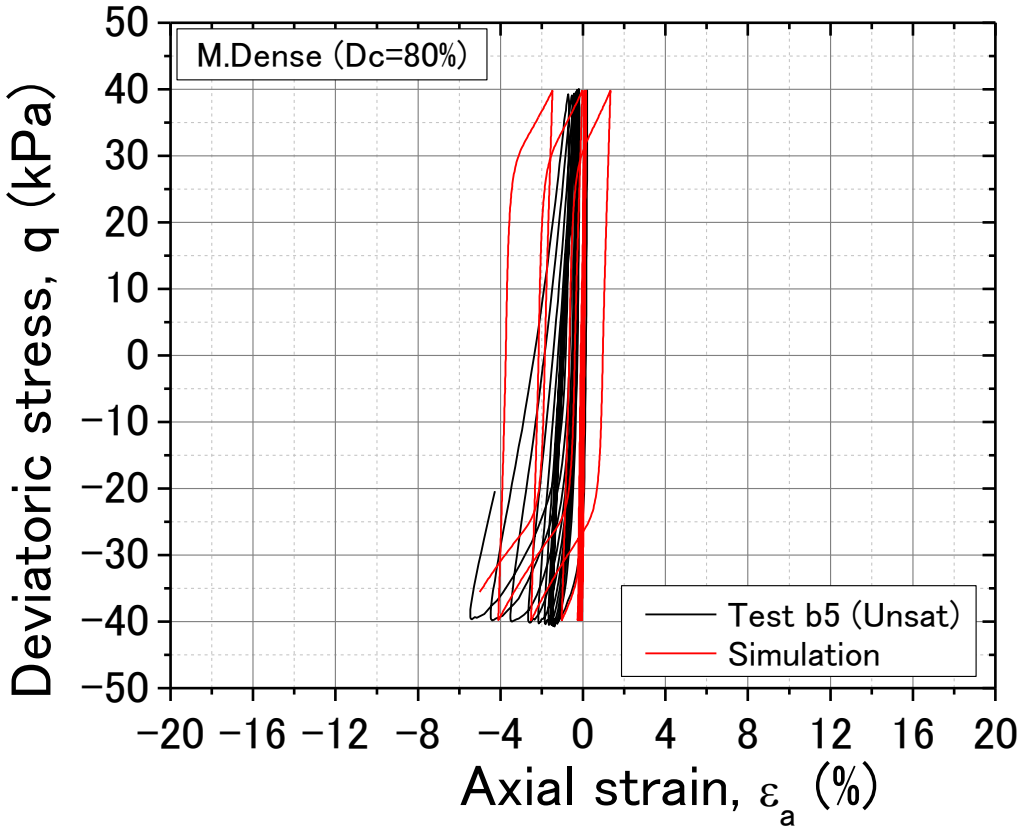

Fig. 6–20. Undrained cyclic test (unsaturated), *q* vs ε_a plot (test b5 bauxite, medium dense)

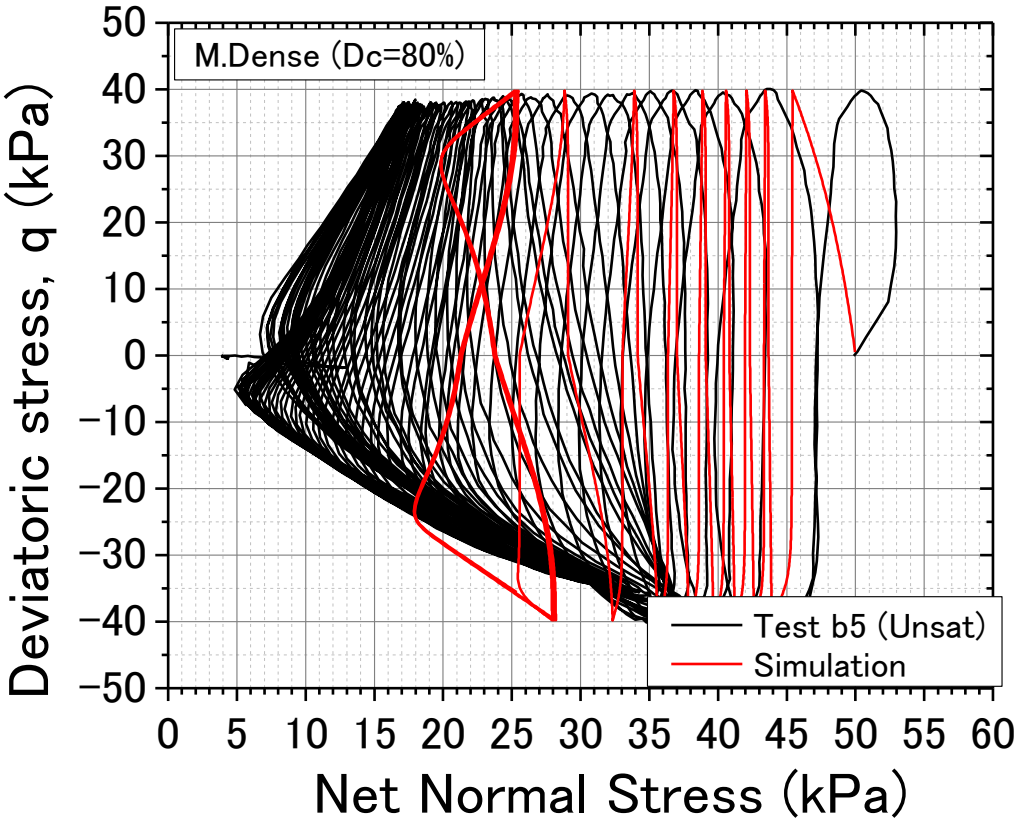

Fig. 6–21. Modified Fig. 6-19 with complete test data (test b5 bauxite, medium dense)

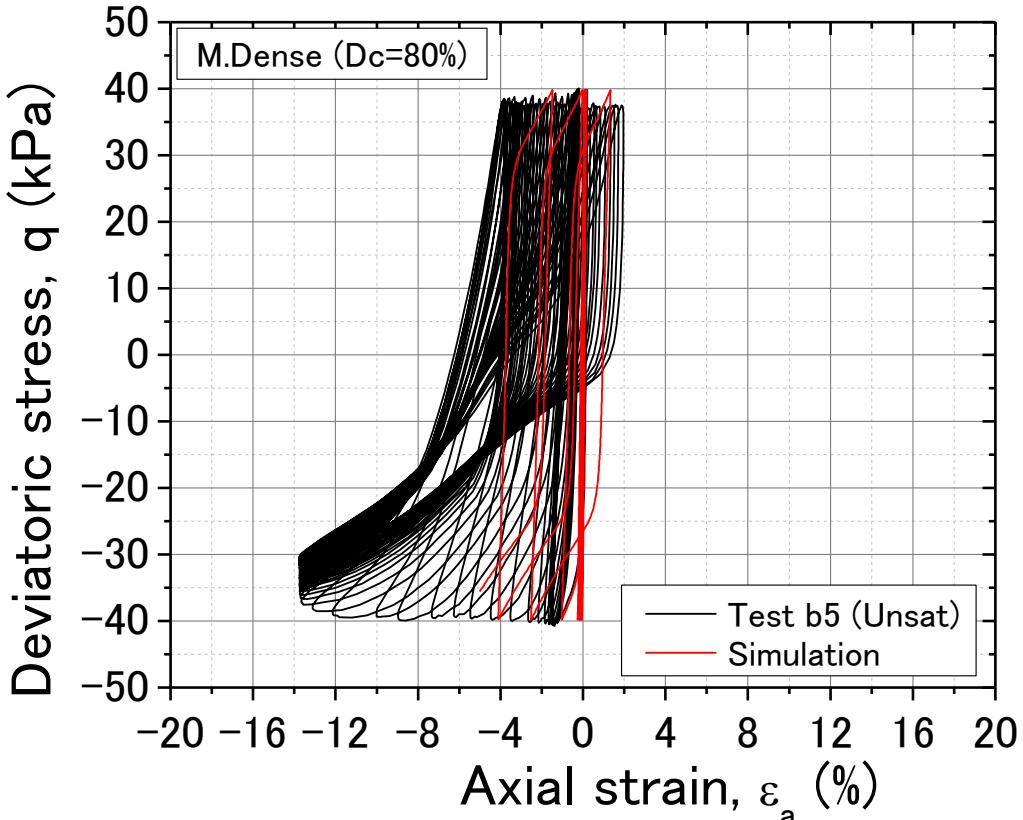

Fig. 6–22. Modified Fig. 6-20 with complete test data (test b5 bauxite, medium dense)

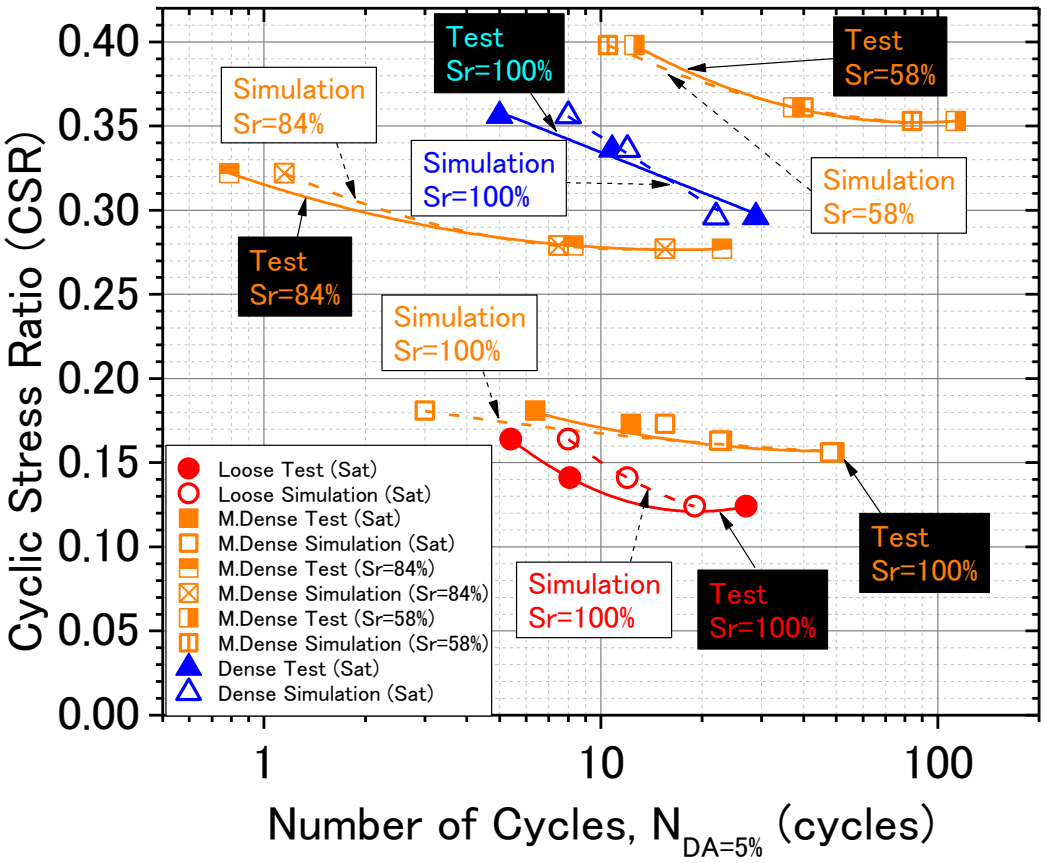

Fig. 6–23. Comparisons of liquefaction resistance curves of bauxite between the test and simulation results

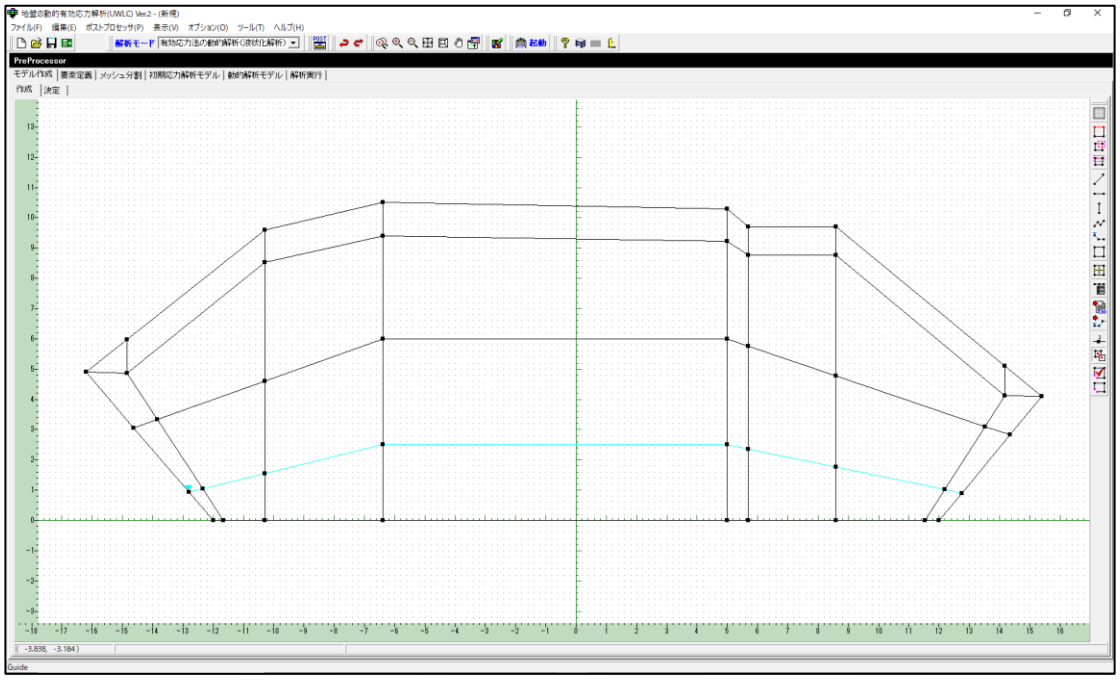

Fig. 6–24. Nodes, water table, and boundary input

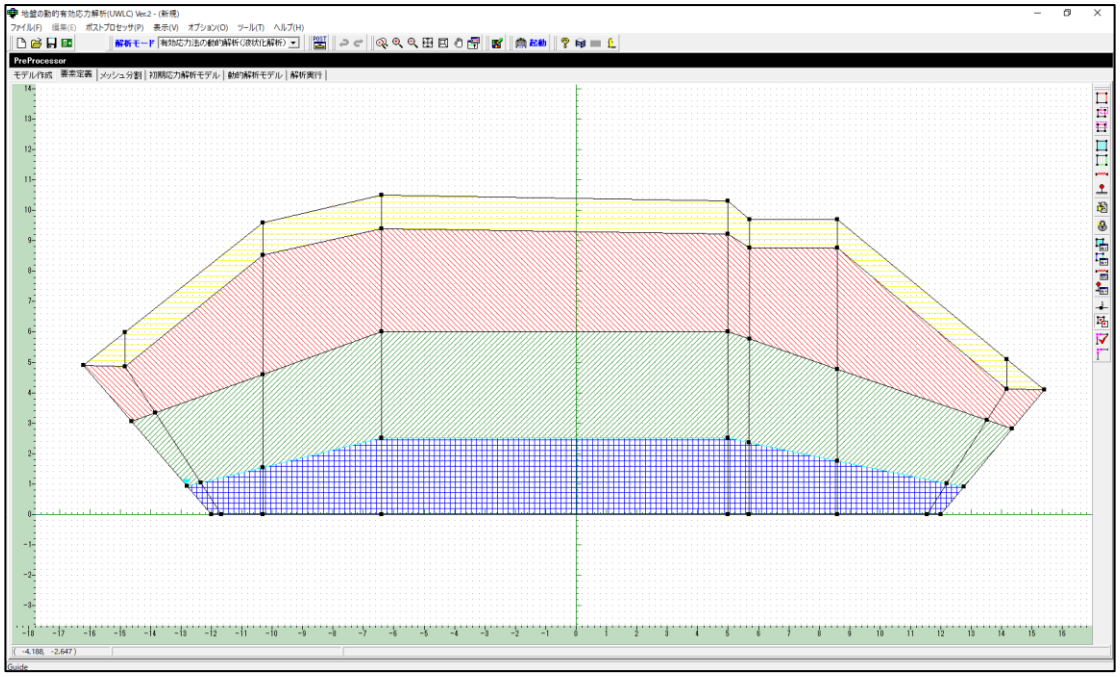

Fig. 6–25. Assignment of zones and parameters

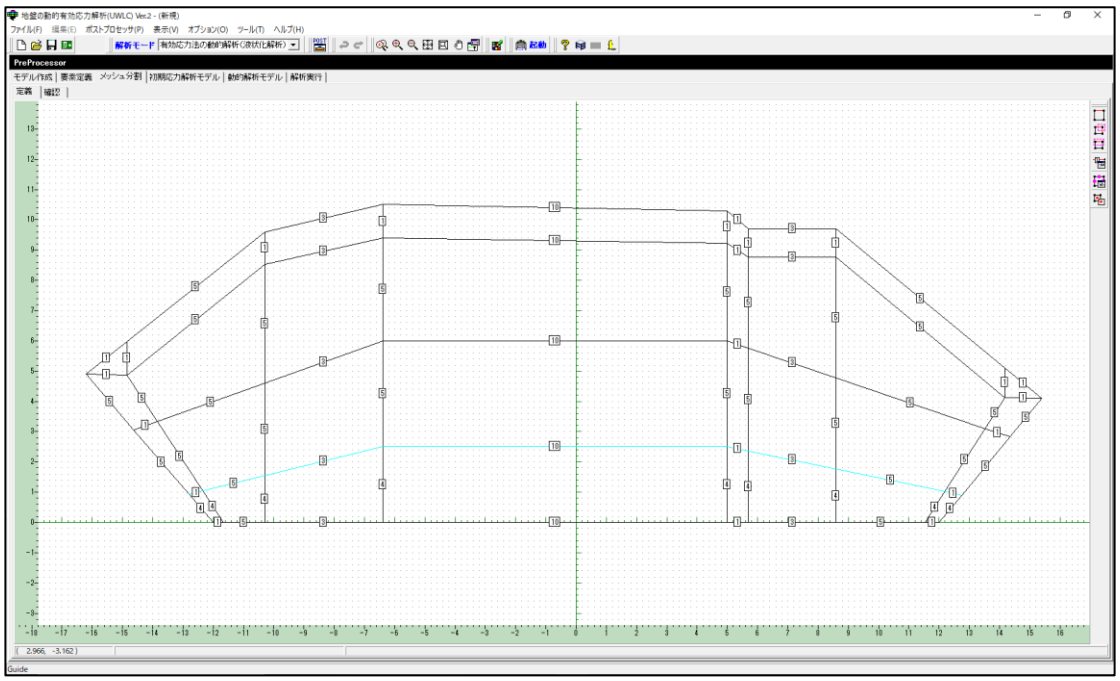

Fig. 6–26. Meshing by assigning the number of nodes per side

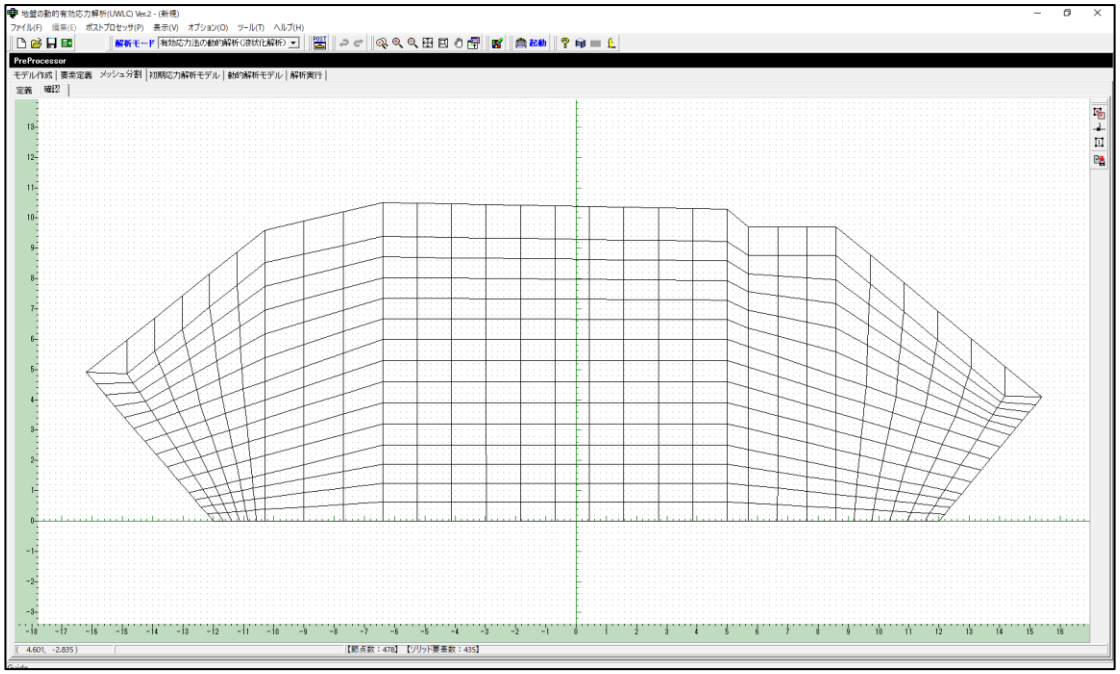

Fig. 6–27. Actual Meshing for verification of appearance after assigning

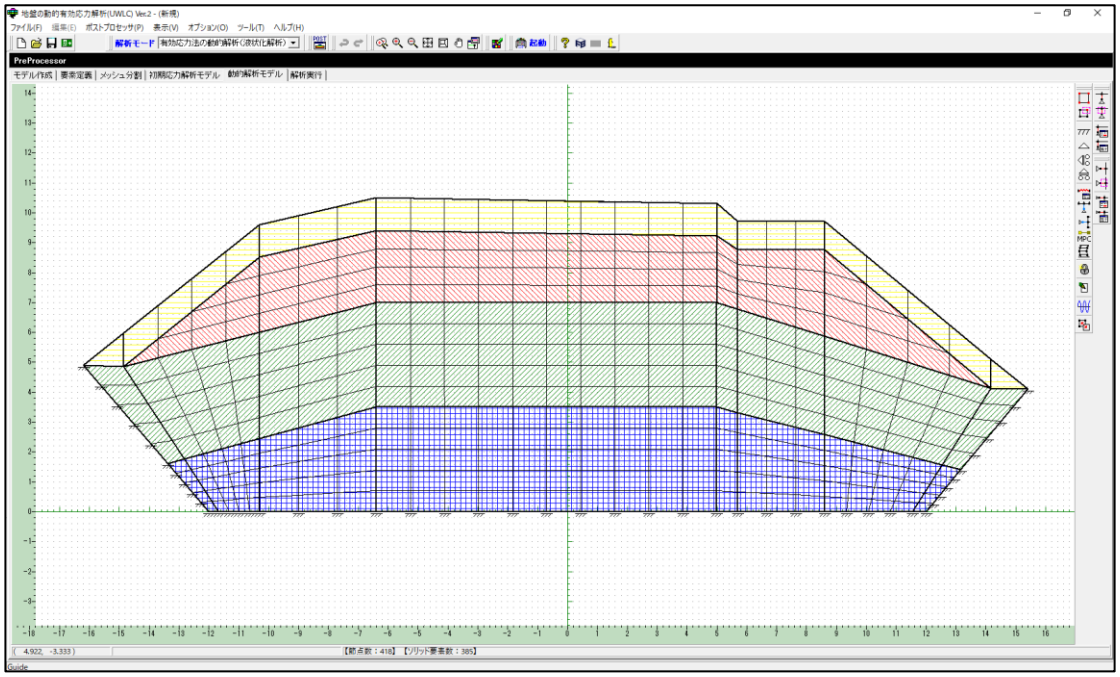

Fig. 6–28. Assign boundary condition in both static and dynamic cases (e.g. fixed)

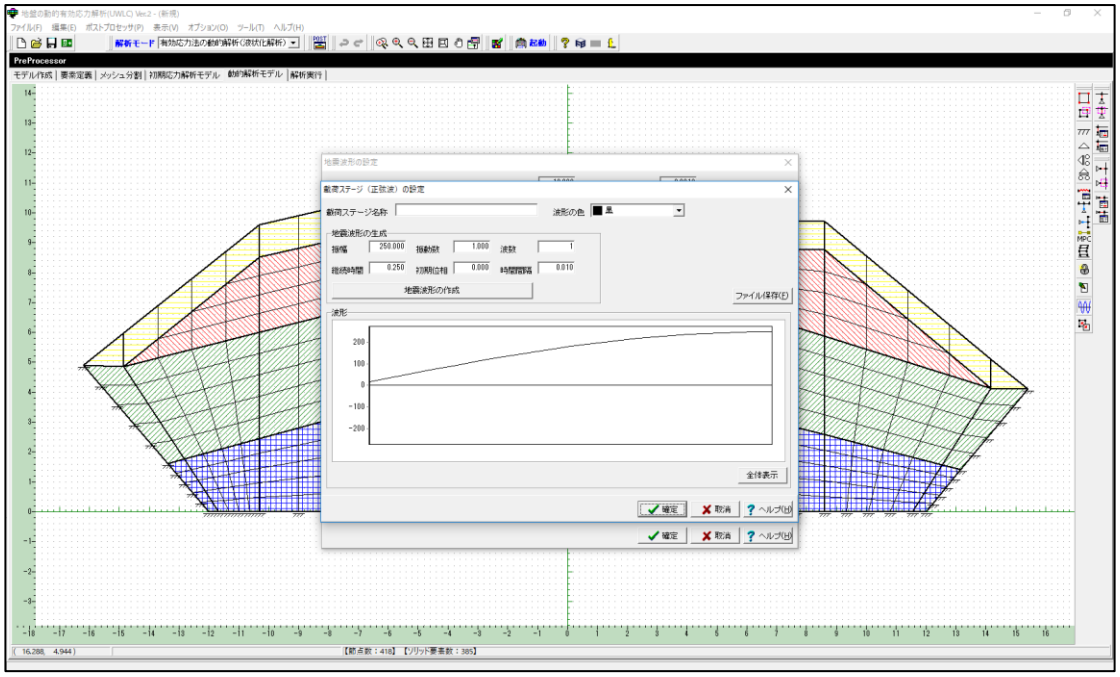

Fig. 6–29. Input the cyclic loading conditions

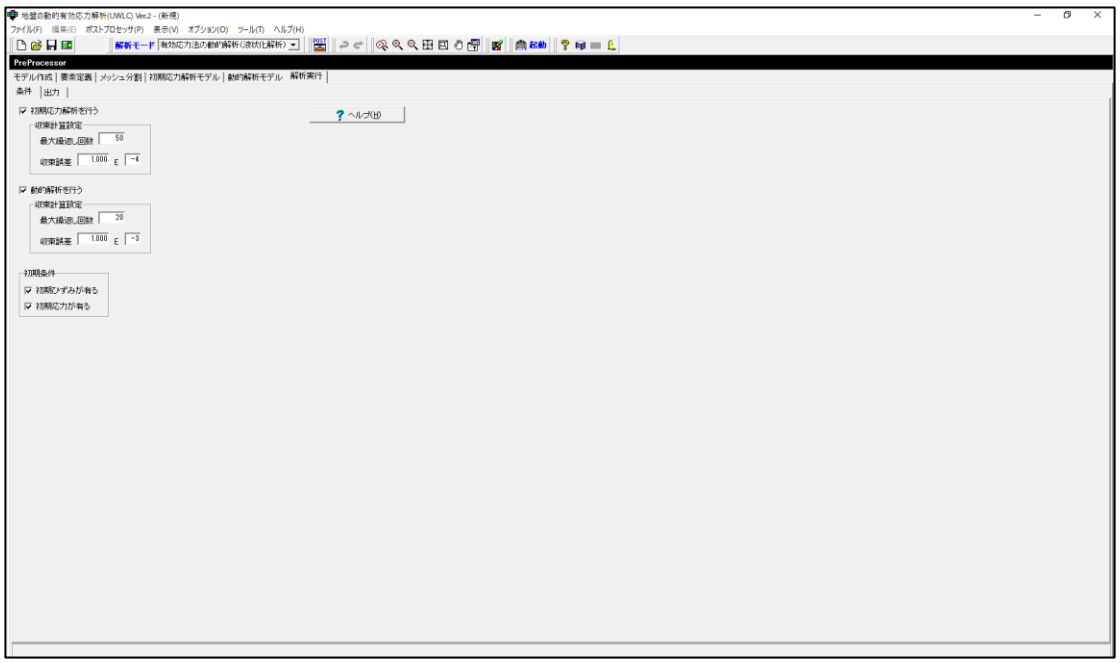

Fig. 6–30. Input step loading and initial conditions

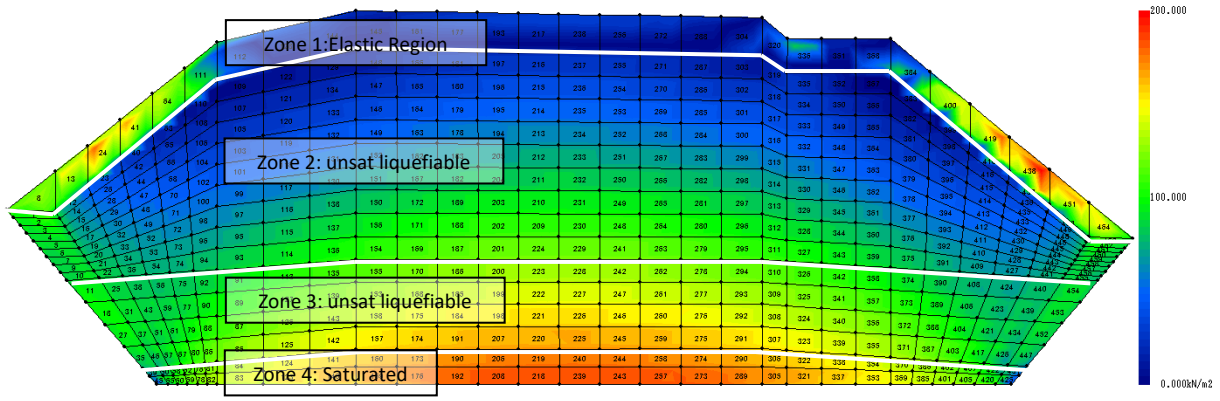

Fig. 6–31. Initial effective stress distribution for bauxite, dense (Case 1)

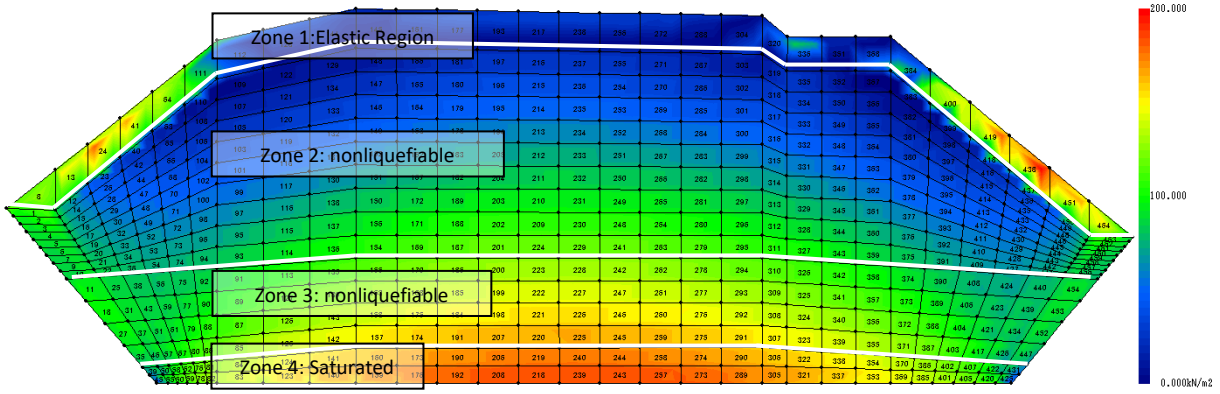

Fig. 6–32. Initial effective stress distribution for bauxite, dense (Case 2)

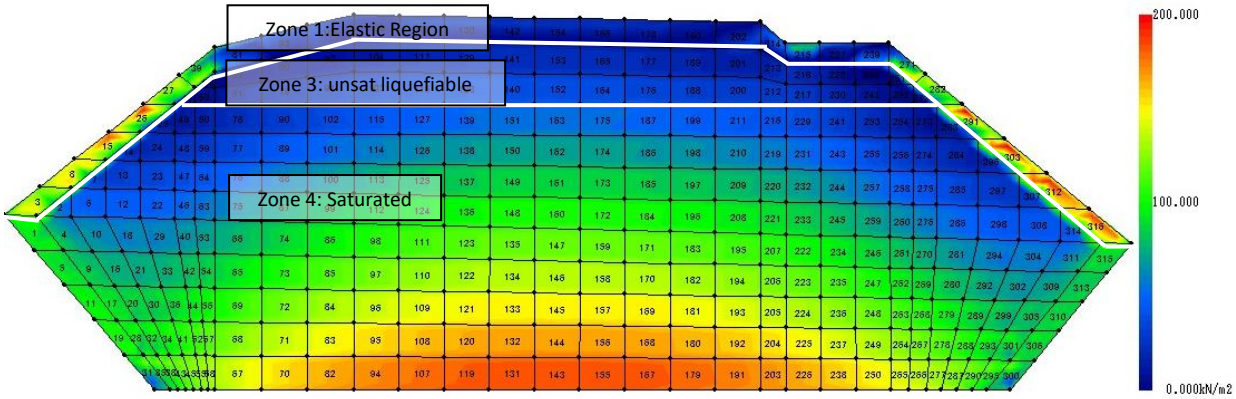

Fig. 6–33. Initial effective stress distribution for bauxite, dense (Case 3)

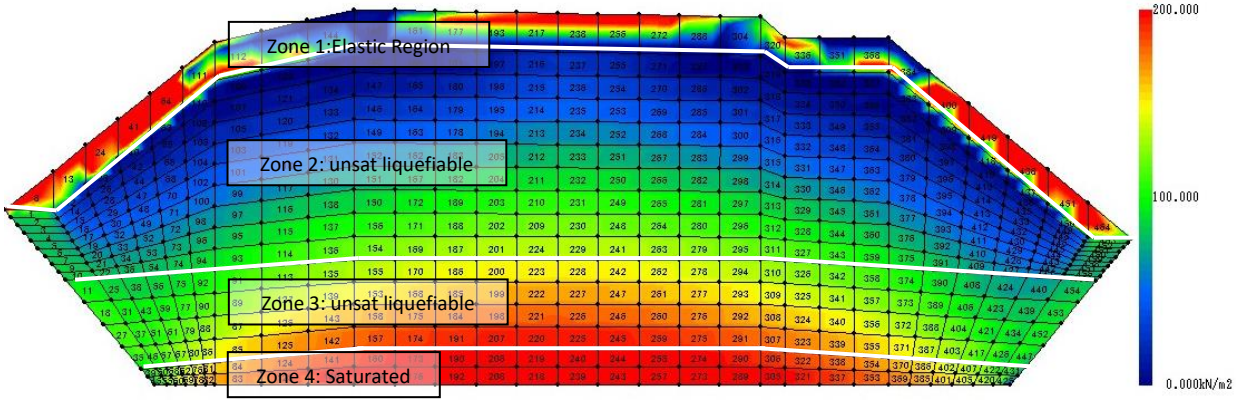

Fig. 6–34. Initial effective stress distribution for iron ore, dense (Case 1)

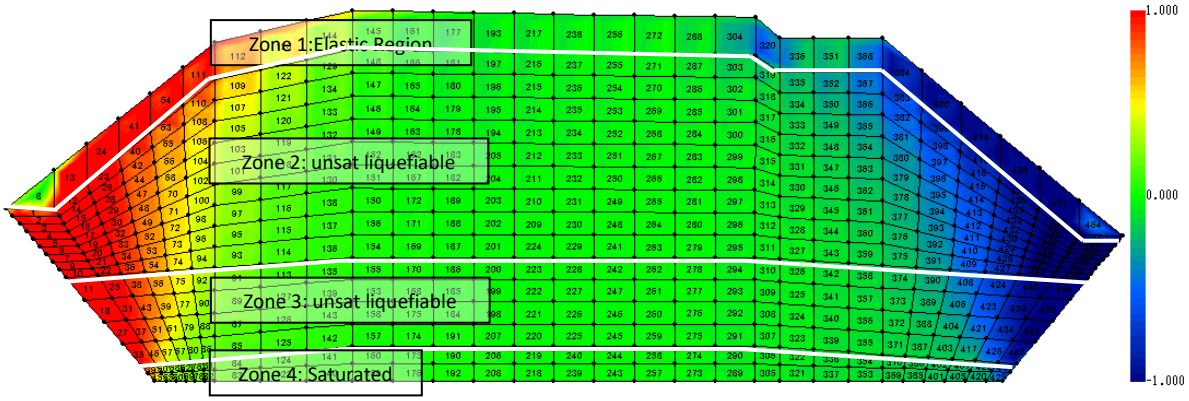

Fig. 6–35. Normalized initial shear stress distribution for bauxite, dense (Case 1)

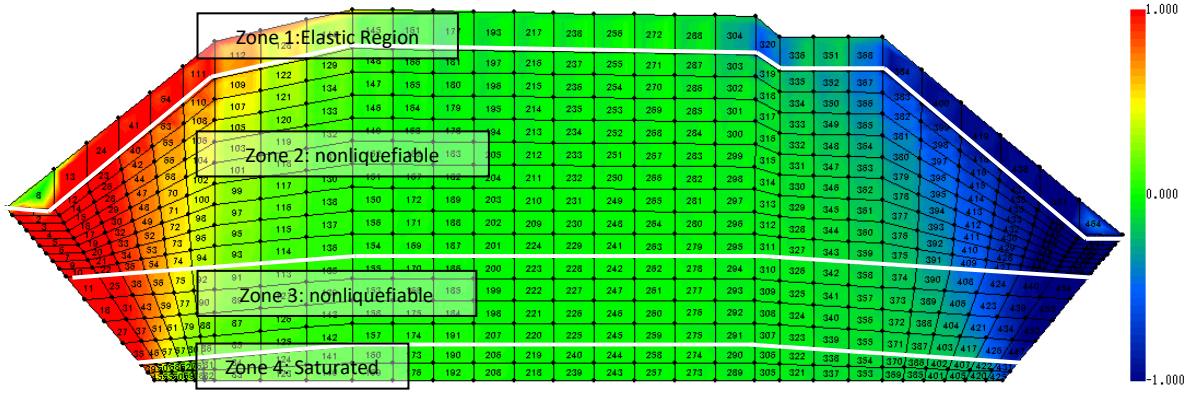

Fig. 6–36. Normalized initial shear stress distribution for bauxite, dense (Case 2)

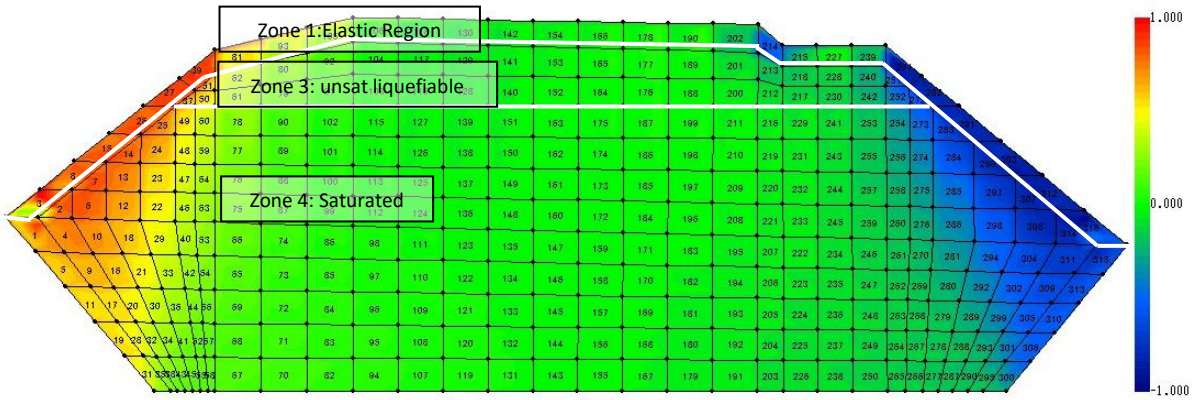

Fig. 6–37. Normalized initial shear stress distribution for bauxite, dense (Case 3)

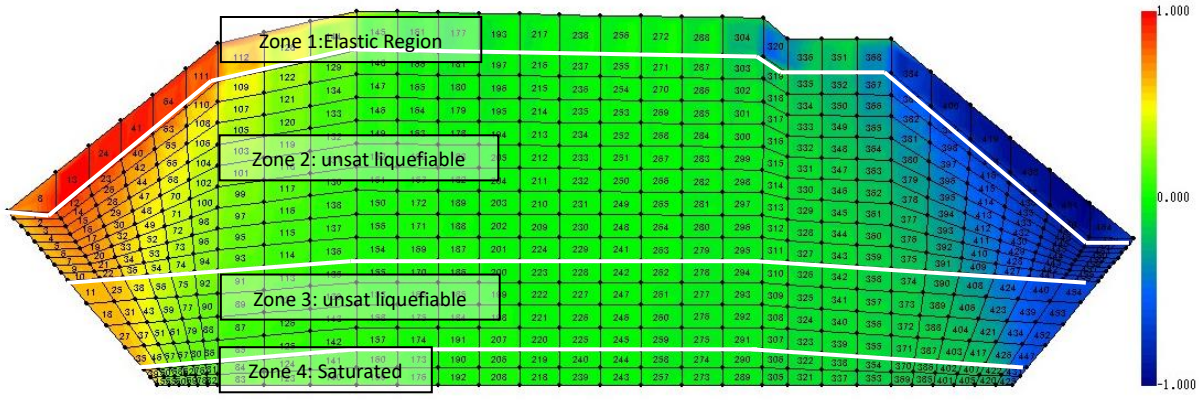

Fig. 6–38. Normalized initial shear stress distribution for iron ore, dense (Case 1)

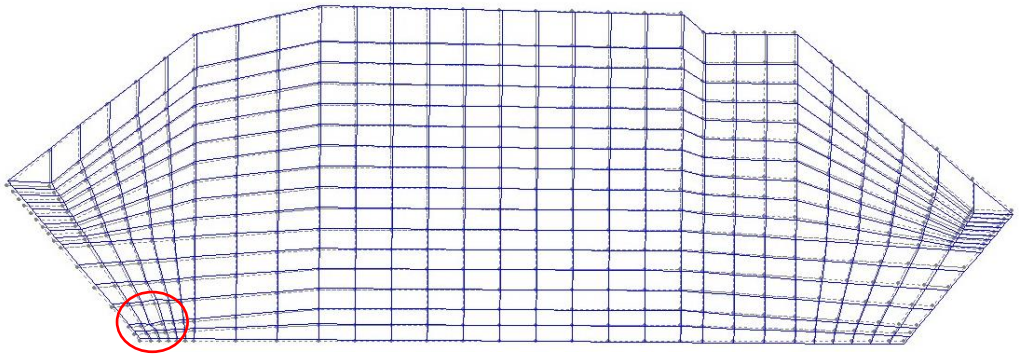

Fig. 6–39. Grid deformation at 20° rolling at 44.8th cycle (iron ore, dense, Case 1)

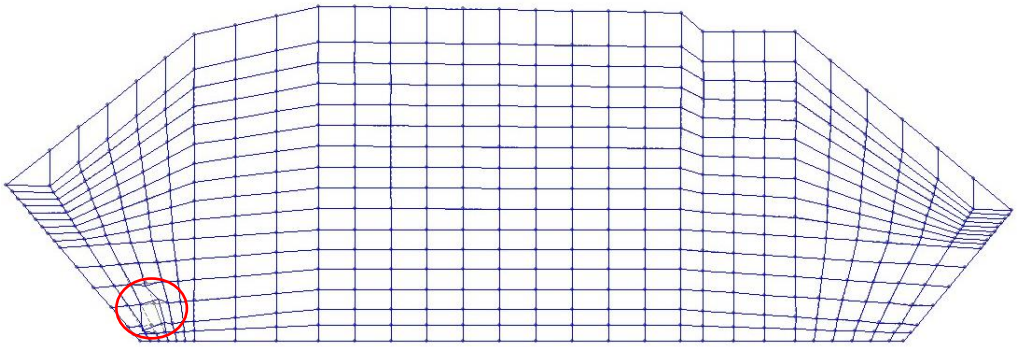

Fig. 6–40. Grid deformation at 20° rolling at 44.9th cycle (iron ore, dense, Case 1)

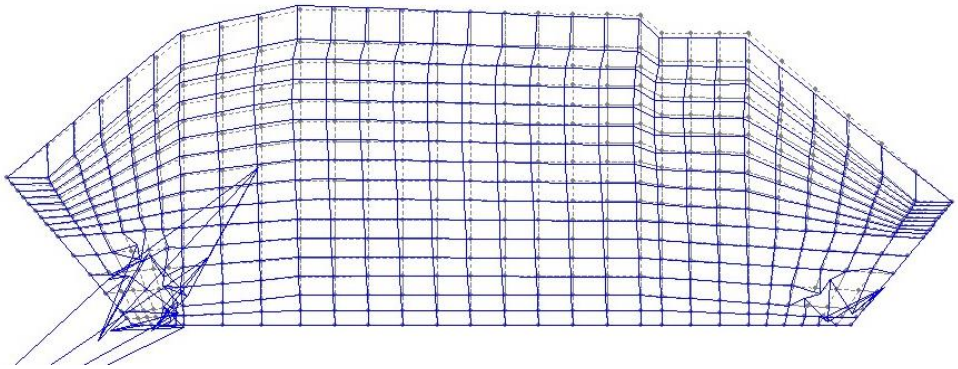

Fig. 6–41. Grid deformation at 20° rolling at 45.5th cycle (iron ore, dense, Case 1)

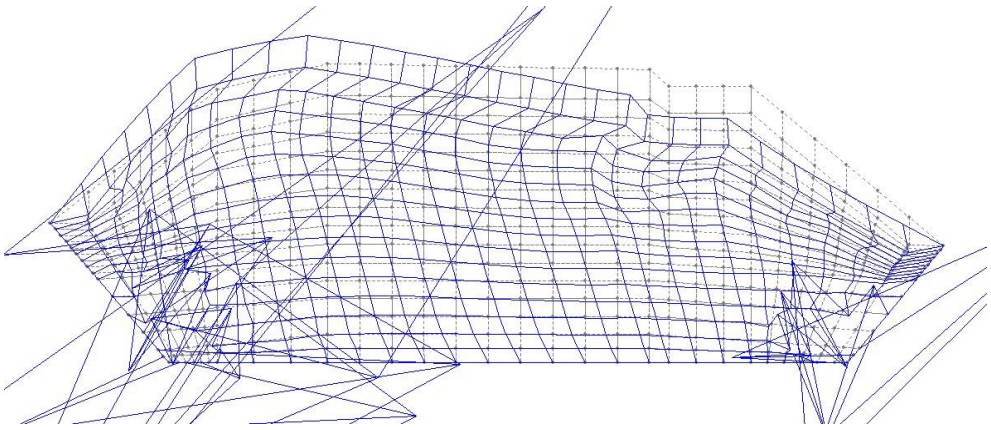

Fig. 6–42. Grid deformation at 20° rolling at 46.0th cycle (iron ore, dense, Case 1)

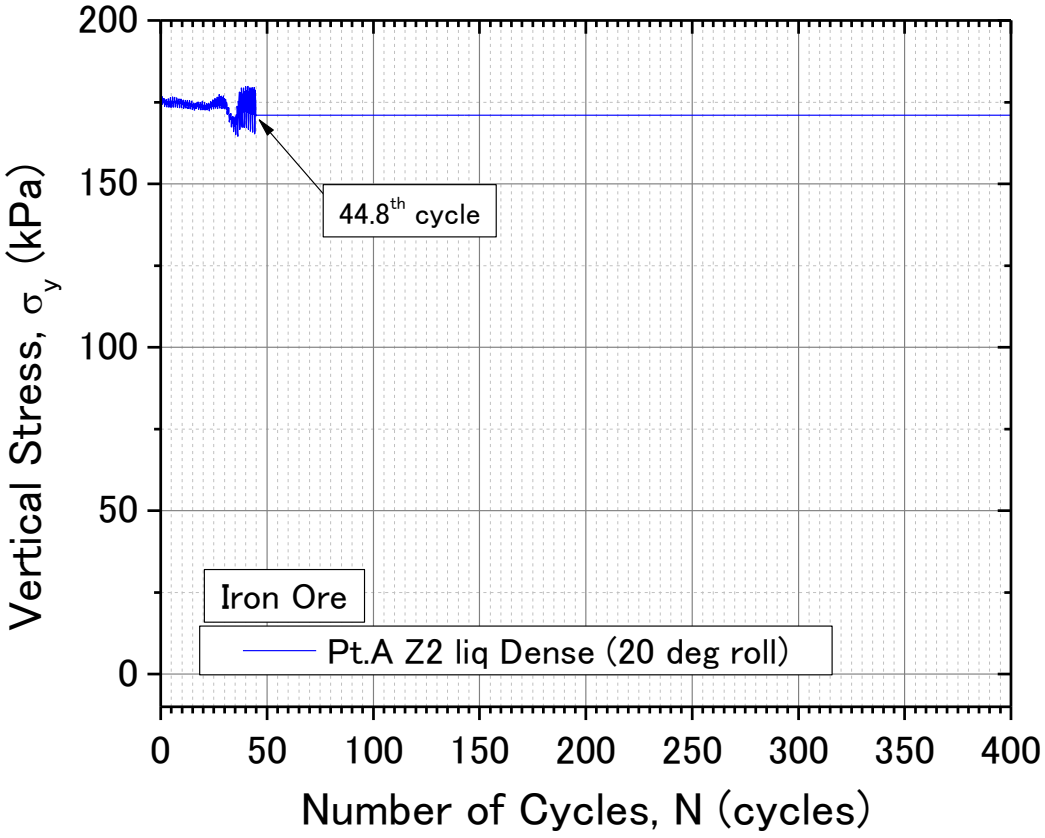

Fig. 6–43. Vertical stress at point A under 20° rolling angle (iron ore, dense, Case 1)

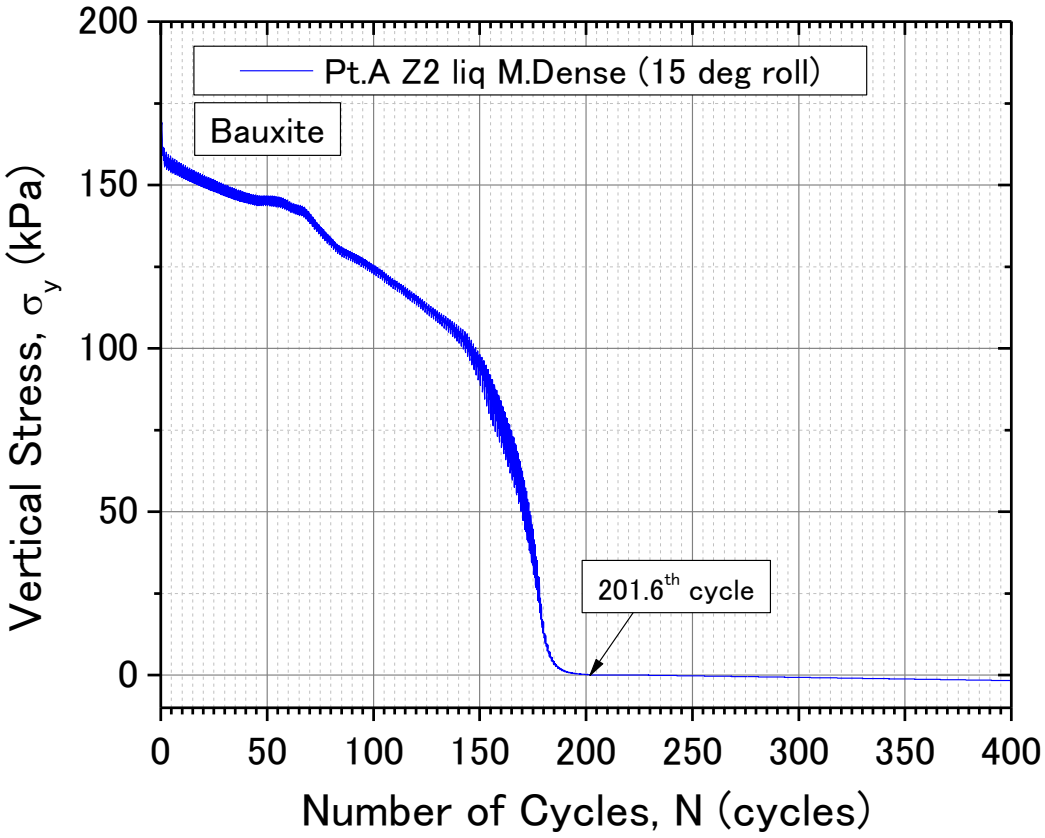

Fig. 6–44. Vertical stress at point A under 15° rolling angle (bauxite, medium dense, Case 1)

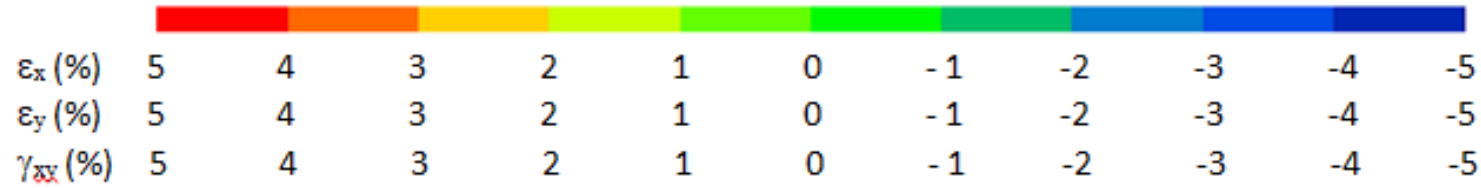

a.) ε_x @5° rolling b.) ε_y @5° rolling c.) γ_{xy} @5° rolling

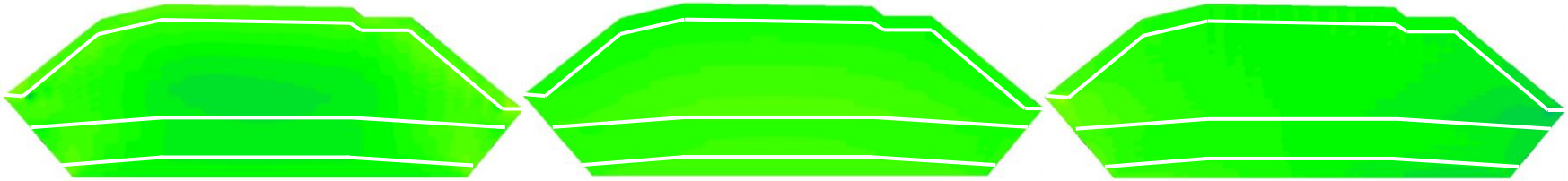

Fig. 6–45. Contour of strains at failure under 5° rolling (bauxite, dense, Case 1)

a.) ε_x @10° rolling b.) ε_y @10° rolling c.) γ_{xy} @10° rolling

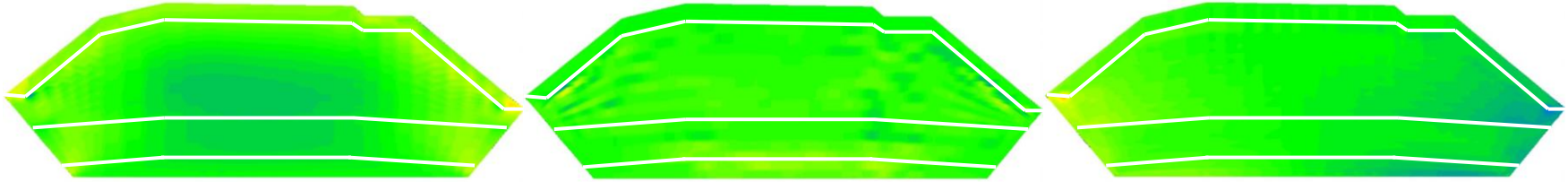

Fig. 6–46. Contour of strains at failure under 10° rolling (bauxite, dense, Case 1)

a.) ε_x @15° rolling b.) ε_y @15° rolling c.) γ_{xy} @15° rolling

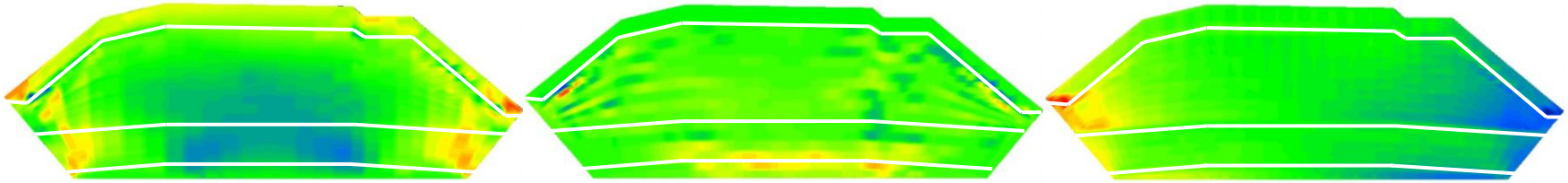

Fig. 6–47. Contour of strains at failure under 15° rolling (bauxite, dense, Case 1)

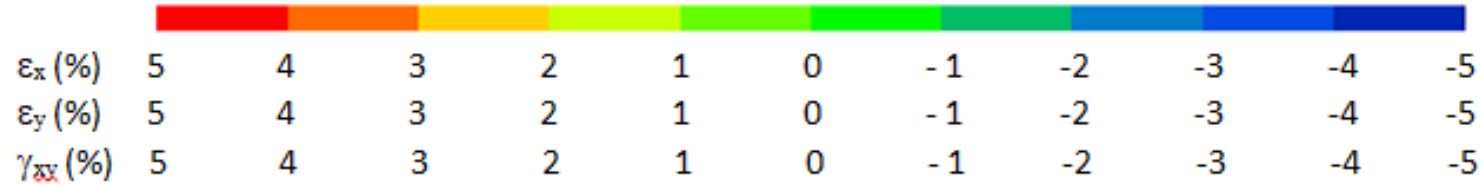

a.) ε_x @20° rolling b.) ε_y @20° rolling c.) γ_{xy} @20° rolling

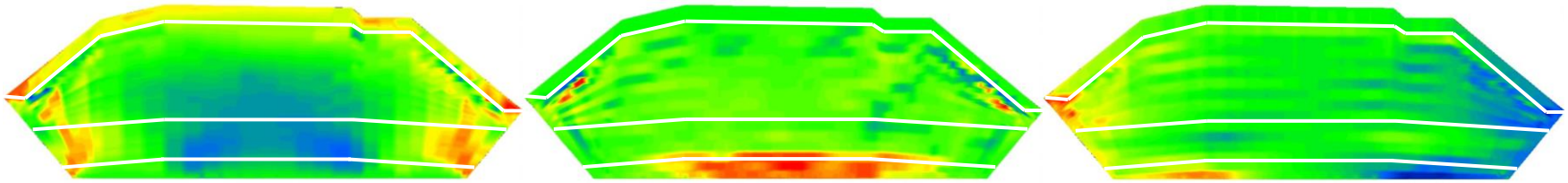

Fig. 6–48. Contour of strains at failure under 20° rolling (bauxite, dense, Case 1)

a.) ε_x @25° rolling b.) ε_y @25° rolling c.) γ_{xy} @25° rolling

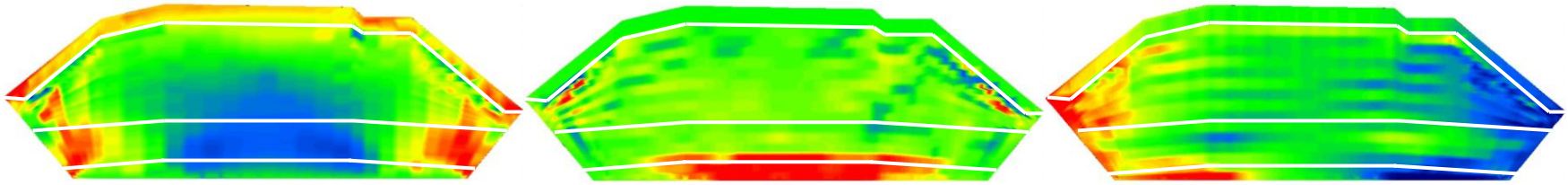

Fig. 6–49. Contour of strains at failure under 25° rolling (bauxite, dense, Case 1)

a.) ε_x @30° rolling b.) ε_y @30° rolling c.) γ_{xy} @30° rolling

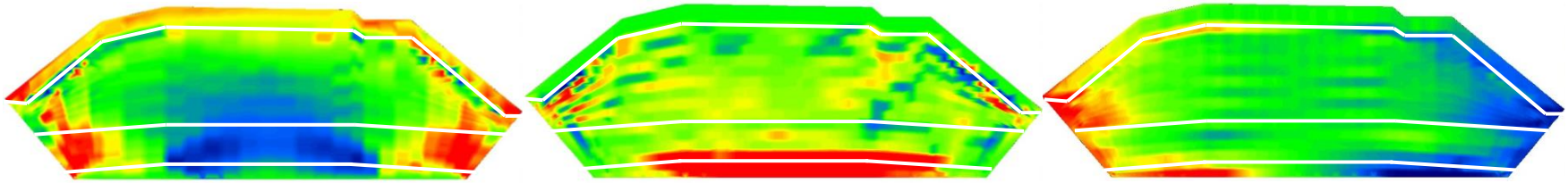

Fig. 6–50. Contour of strains at failure under 30° rolling (bauxite, dense, Case 1)

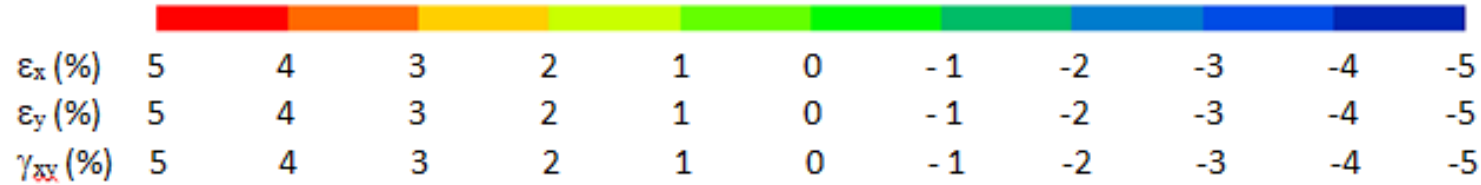

a.) ε_x @5° rolling b.) ε_y @5° rolling c.) γ_{xy} @5° rolling

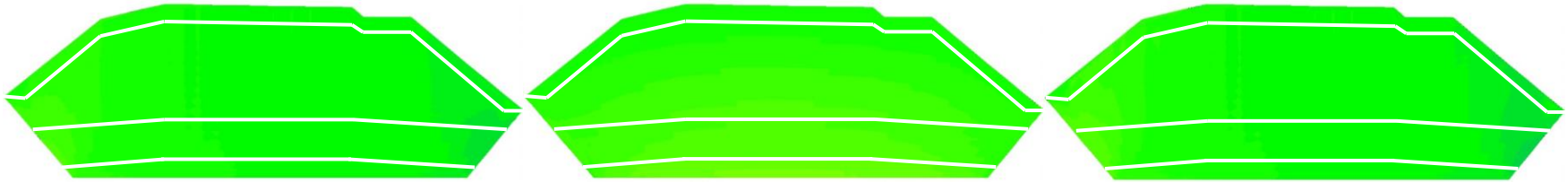

Fig. 6–51. Contour of strains at failure under 5° rolling (bauxite, dense, Case 2)

a.) ε_x @10° rolling b.) ε_y @10° rolling c.) γ_{xy} @10° rolling

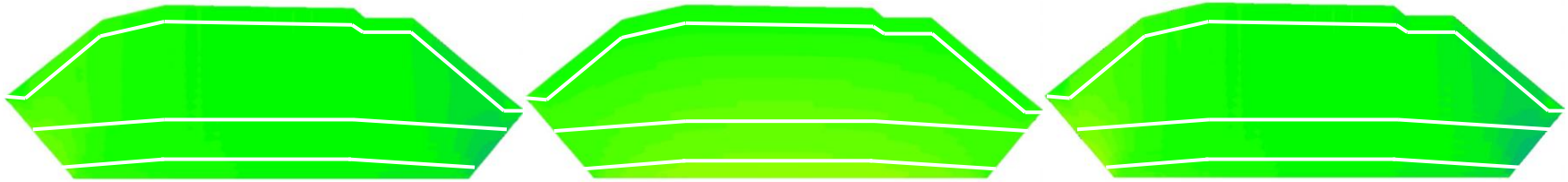

Fig. 6–52. Contour of strains at failure under 10° rolling (bauxite, dense, Case 2)

a.) ε_x @15° rolling b.) ε_y @15° rolling c.) γ_{xy} @15° rolling

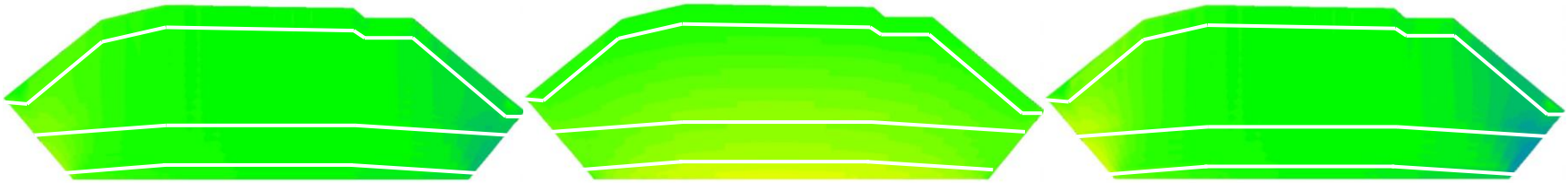

Fig. 6–53. Contour of strains at failure under 15° rolling (bauxite, dense, Case 2)

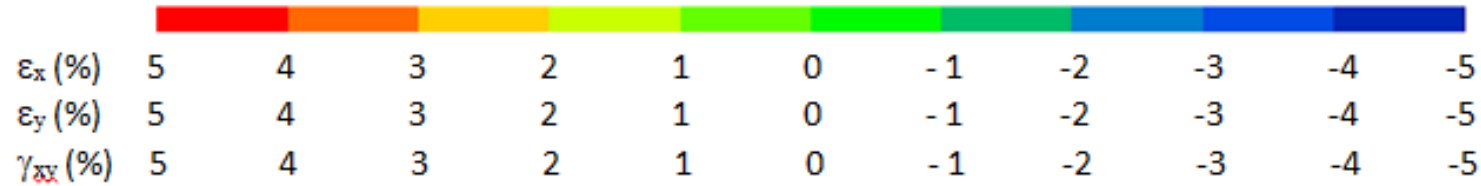

a.) ε_x @20° rolling b.) ε_y @20° rolling c.) γ_{xy} @20° rolling

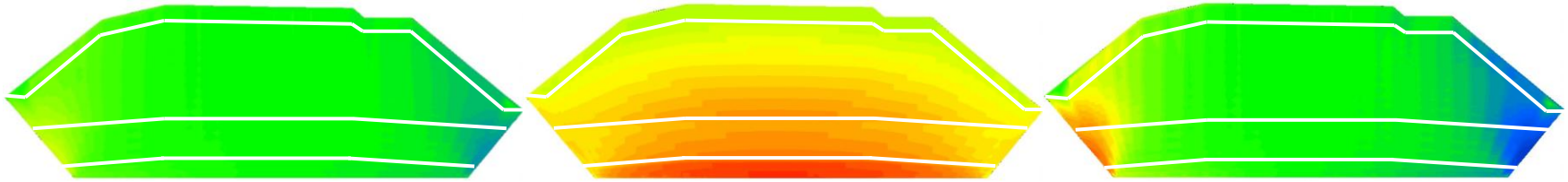

Fig. 6–54. Contour of strains at failure under 20° rolling (bauxite, dense, Case 2)

a.) ε_x @25° rolling b.) ε_y @25° rolling c.) γ_{xy} @25° rolling

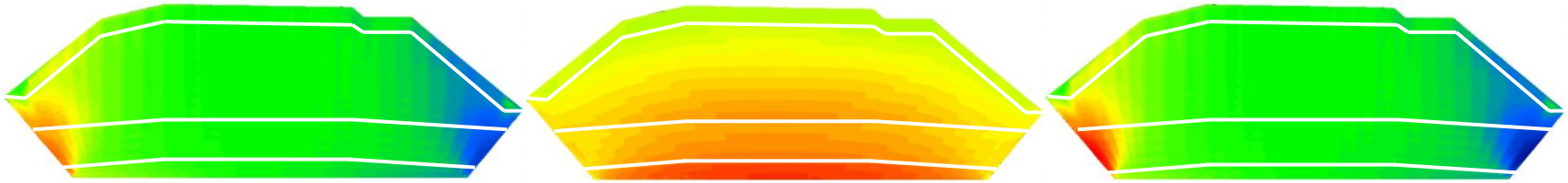

Fig. 6–55. Contour of strains at failure under 25° rolling (bauxite, dense, Case 2)

a.) ε_x @30° rolling b.) ε_y @30° rolling c.) γ_{xy} @30° rolling

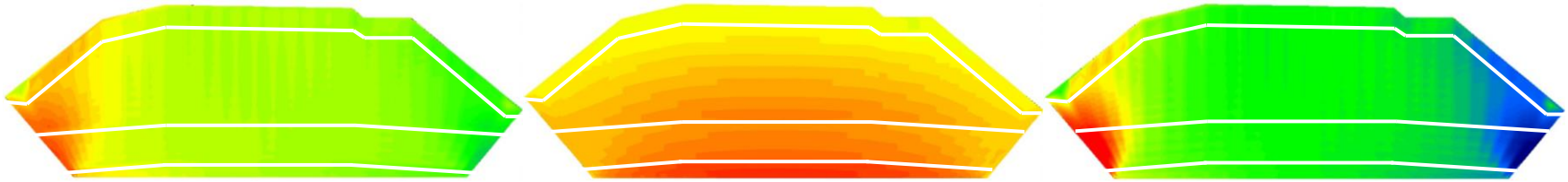

Fig. 6–56. Contour of strains at failure under 30° rolling (bauxite, dense, Case 2)

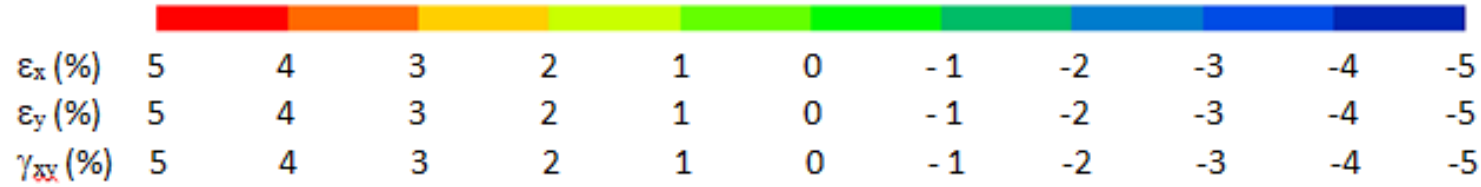

a.) ε_x @5° rolling b.) ε_y @5° rolling c.) γ_{xy} @5° rolling

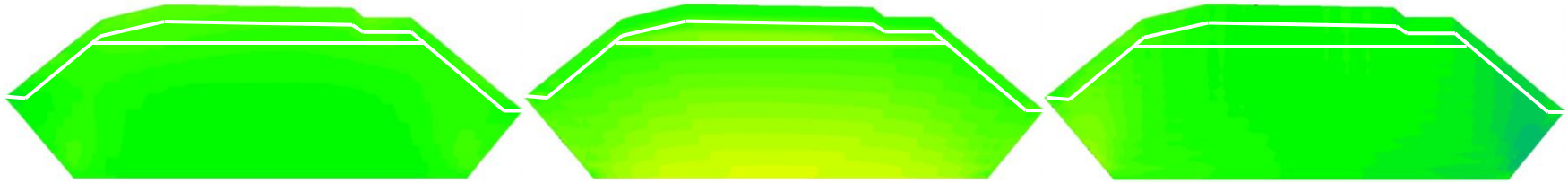

Fig. 6–57. Contour of strains at failure under 5° rolling (bauxite, dense, Case 3)

a.) ε_x @10° rolling b.) ε_y @10° rolling c.) γ_{xy} @10° rolling

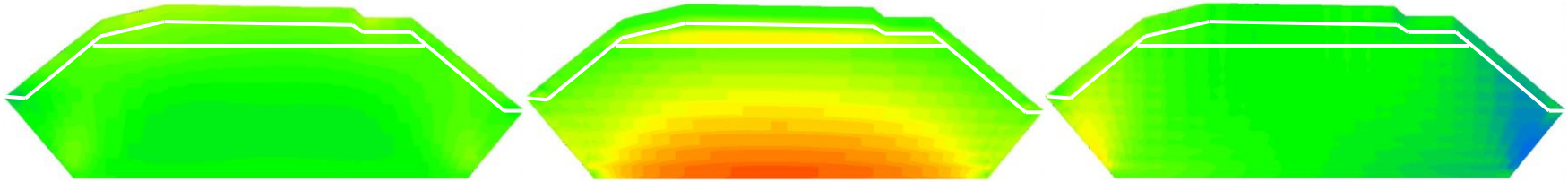

Fig. 6–58. Contour of strains at failure under 10° rolling (bauxite, dense, Case 3)

a.) ε_x @15° rolling b.) ε_y @15° rolling c.) γ_{xy} @15° rolling

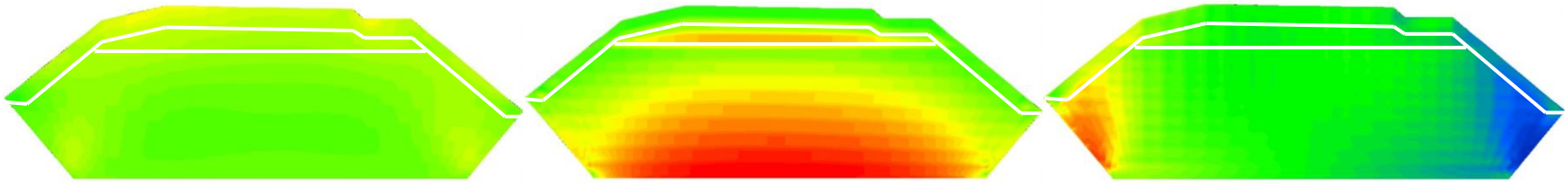

Fig. 6–59. Contour of strains at failure under 15° rolling (bauxite, dense, Case 3)

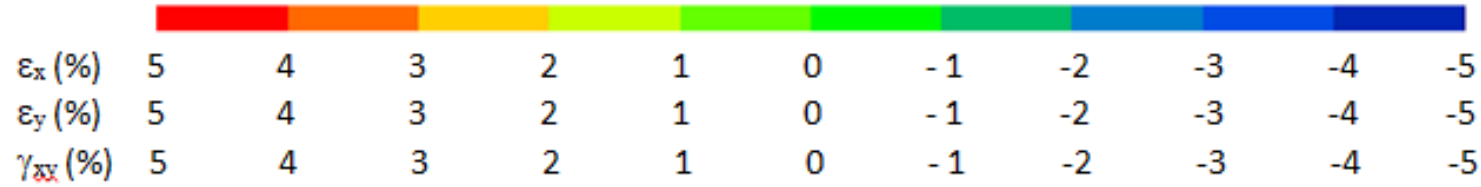

a.) ε_x @20° rolling b.) ε_y @20° rolling c.) γ_{xy} @20° rolling

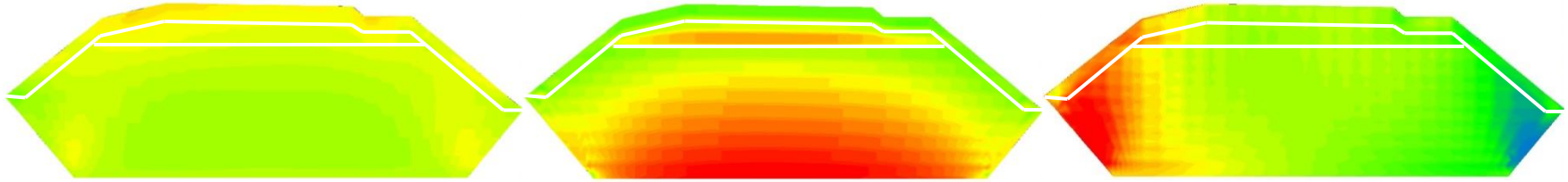

Fig. 6–60. Contour of strains at failure under 20° rolling (bauxite, dense, Case 3)

a.) ε_x @25° rolling b.) ε_y @25° rolling c.) γ_{xy} @25° rolling

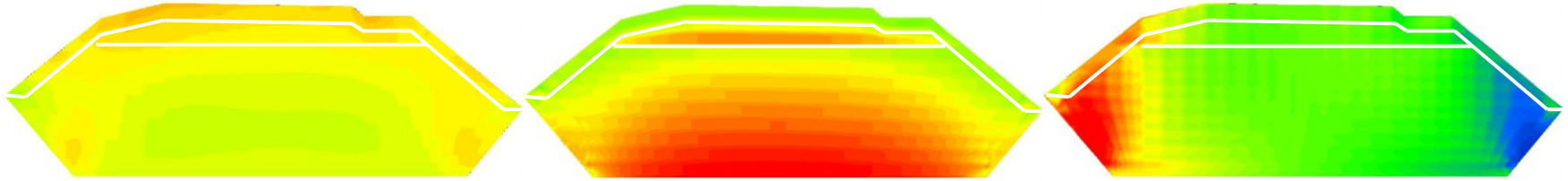

Fig. 6–61. Contour of strains at failure under 25° rolling (bauxite, dense, Case 3)

a.) ε_x @30° rolling b.) ε_y @30° rolling c.) γ_{xy} @30° rolling

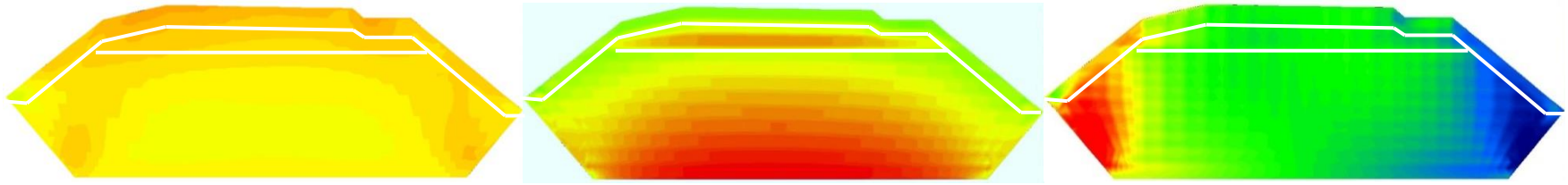

Fig. 6–62. Contour of strains at failure under 30° rolling (bauxite, dense, Case 3)

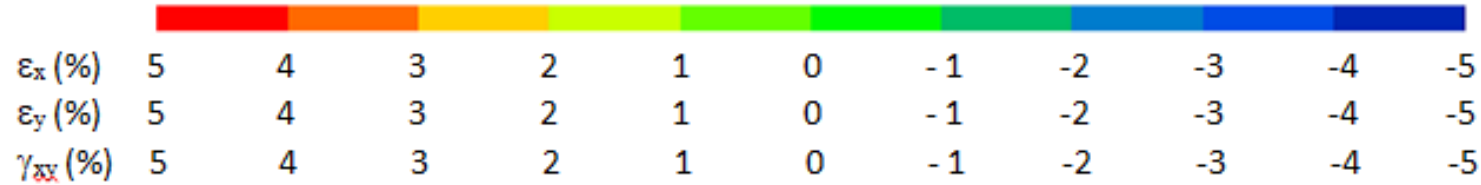

a.) ε_x @5° rolling b.) ε_y @5° rolling c.) γ_{xy} @5° rolling

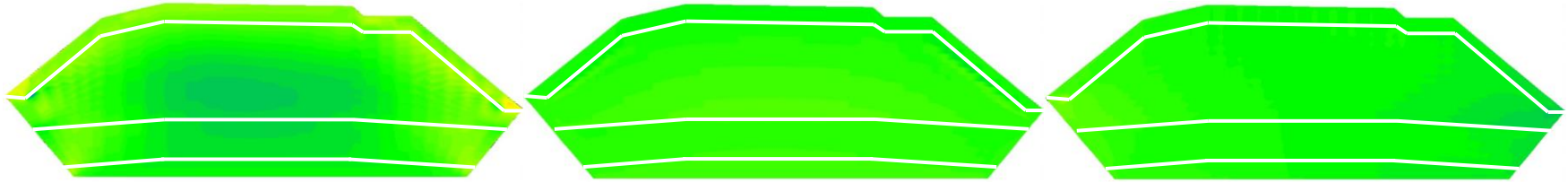

Fig. 6–63. Contour of strains at failure under 5° rolling (iron ore, dense, Case 1)

a.) ε_x @10° rolling b.) ε_y @10° rolling c.) γ_{xy} @10° rolling

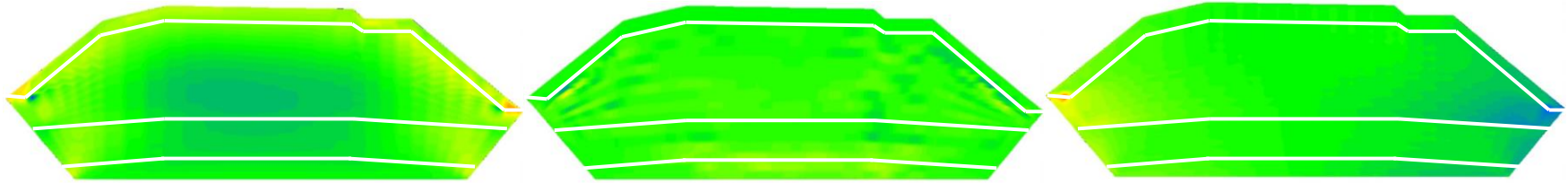

Fig. 6–64. Contour of strains at failure under 10° rolling (iron ore, dense, Case 1)

a.) ε_x @15° rolling b.) ε_y @15° rolling c.) γ_{xy} @15° rolling

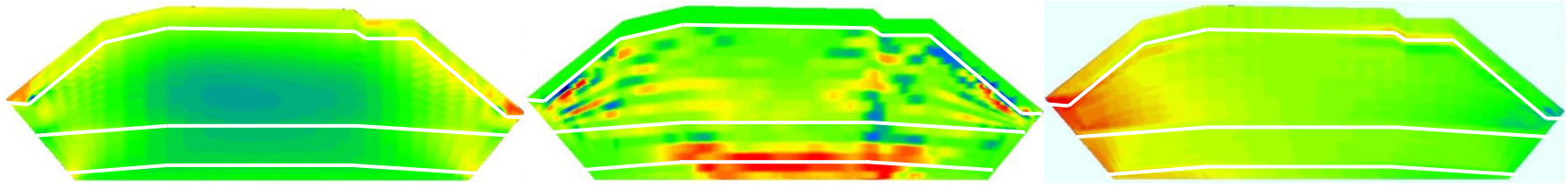

Fig. 6–65. Contour of strains at failure under 15° rolling (iron ore, dense, Case 1)

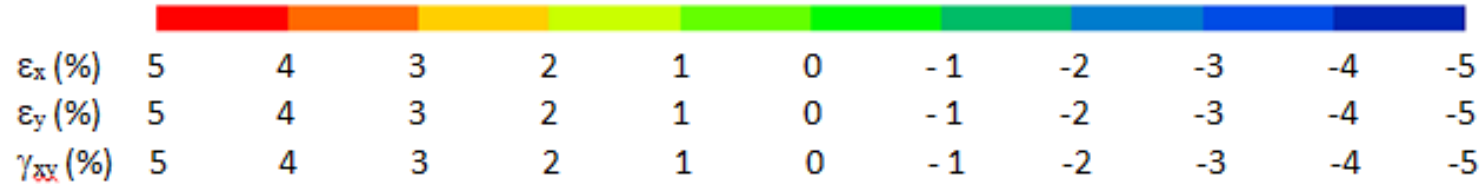

a.) ε_x @20° rolling b.) ε_y @20° rolling c.) γ_{xy} @20° rolling

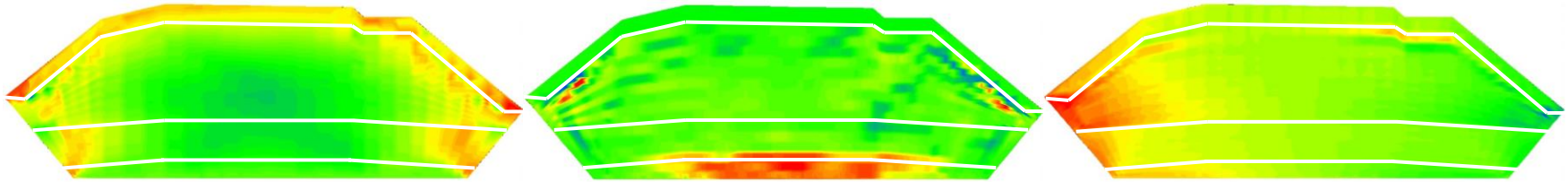

Fig. 6–66. Contour of strains at failure under 20° rolling (iron ore, dense, Case 1)

a.) ε_x @25° rolling b.) ε_y @25° rolling c.) γ_{xy} @25° rolling

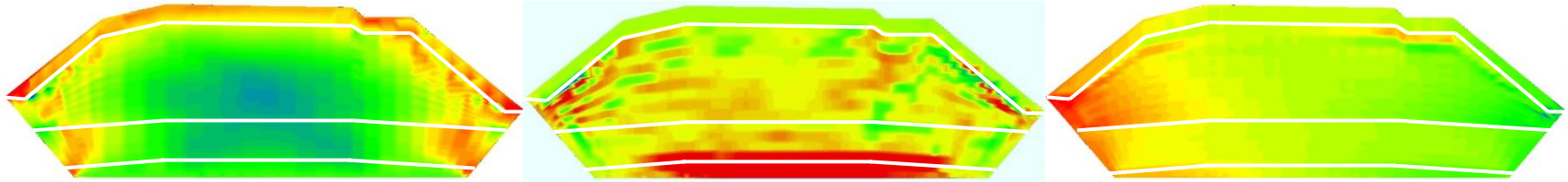

Fig. 6–67. Contour of strains at failure under 25° rolling (iron ore, dense, Case 1)

a.) ε_x @30° rolling b.) ε_y @30° rolling c.) γ_{xy} @30° rolling

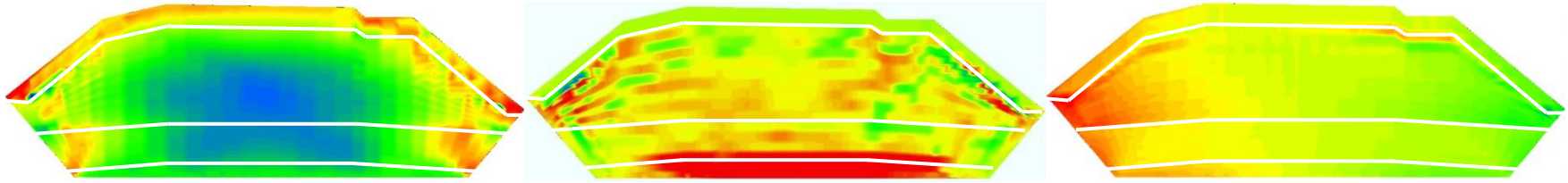

Fig. 6–68. Contour of strains at failure under 30° rolling (iron ore, dense, Case 1)

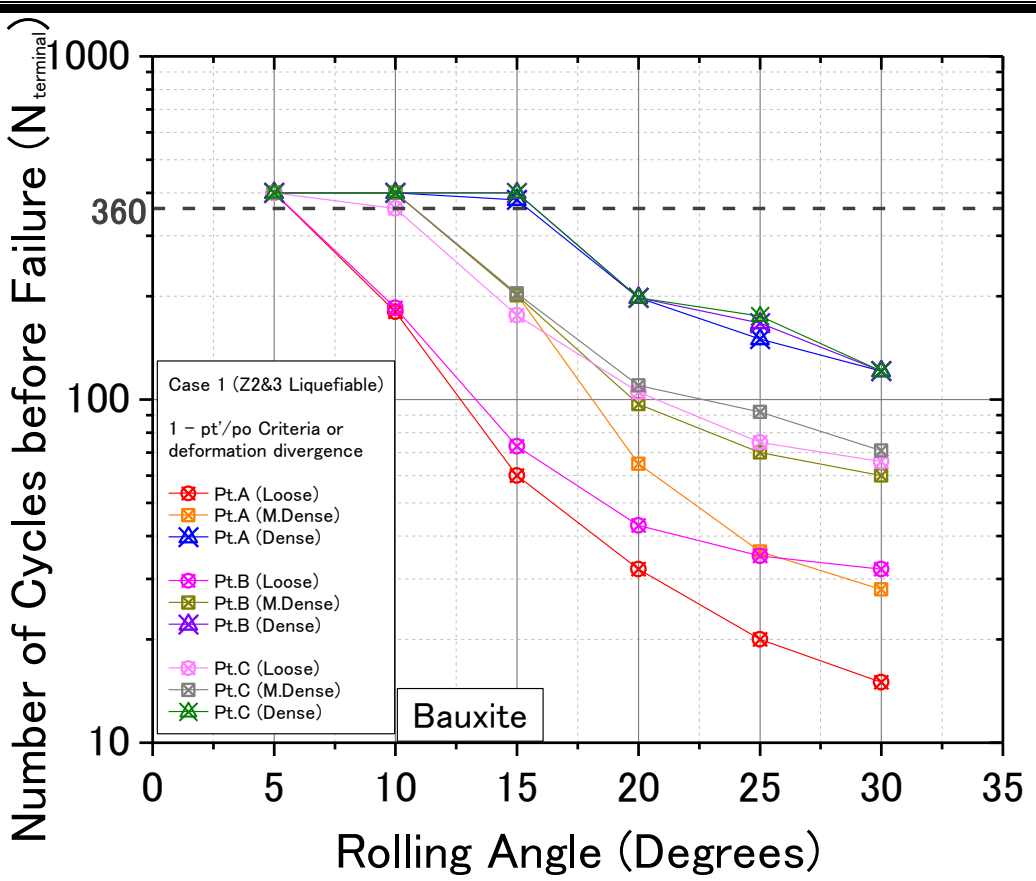

Fig. 6–69. Relationship between rolling angle and number of cycles before failure of heap (bauxite, various densities, points A, B, and C)

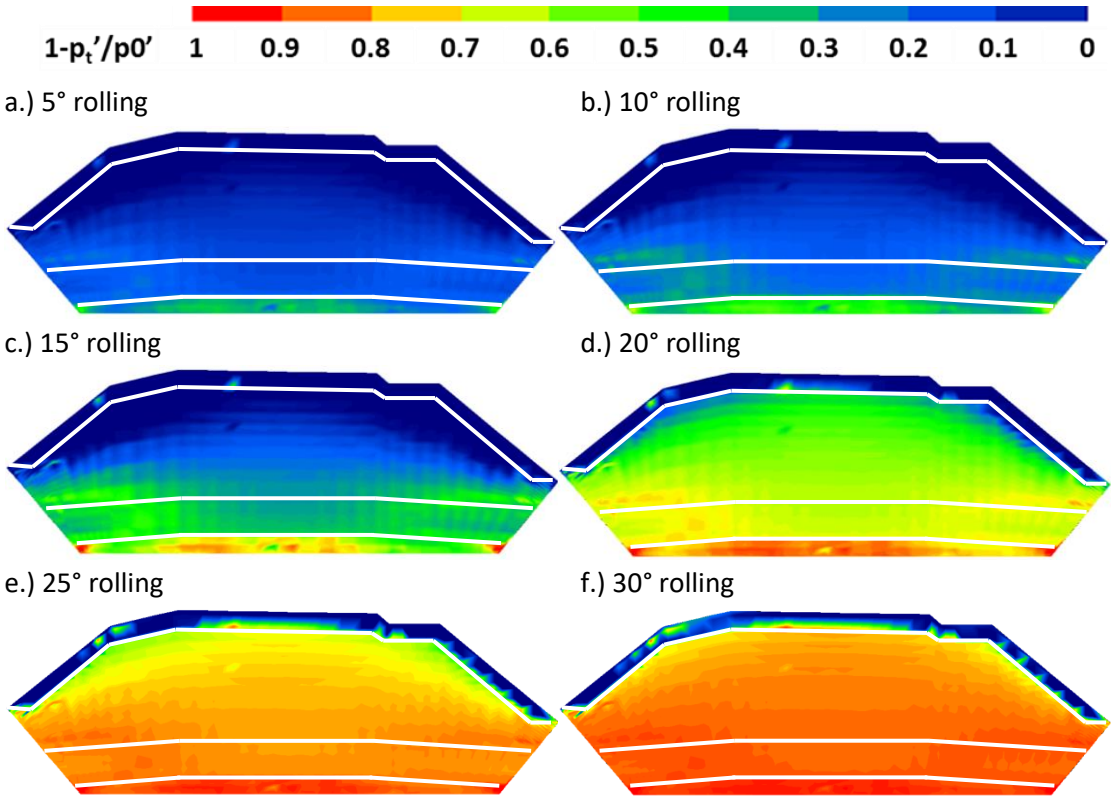

Fig. 6–70. Contour of effective stress reduction ratio failure with rolling angle of a.) 5°; b.) 10°; c.) 15°; d.) 20°; e.) 25°; f.) 30° (bauxite, dense, Case 1)

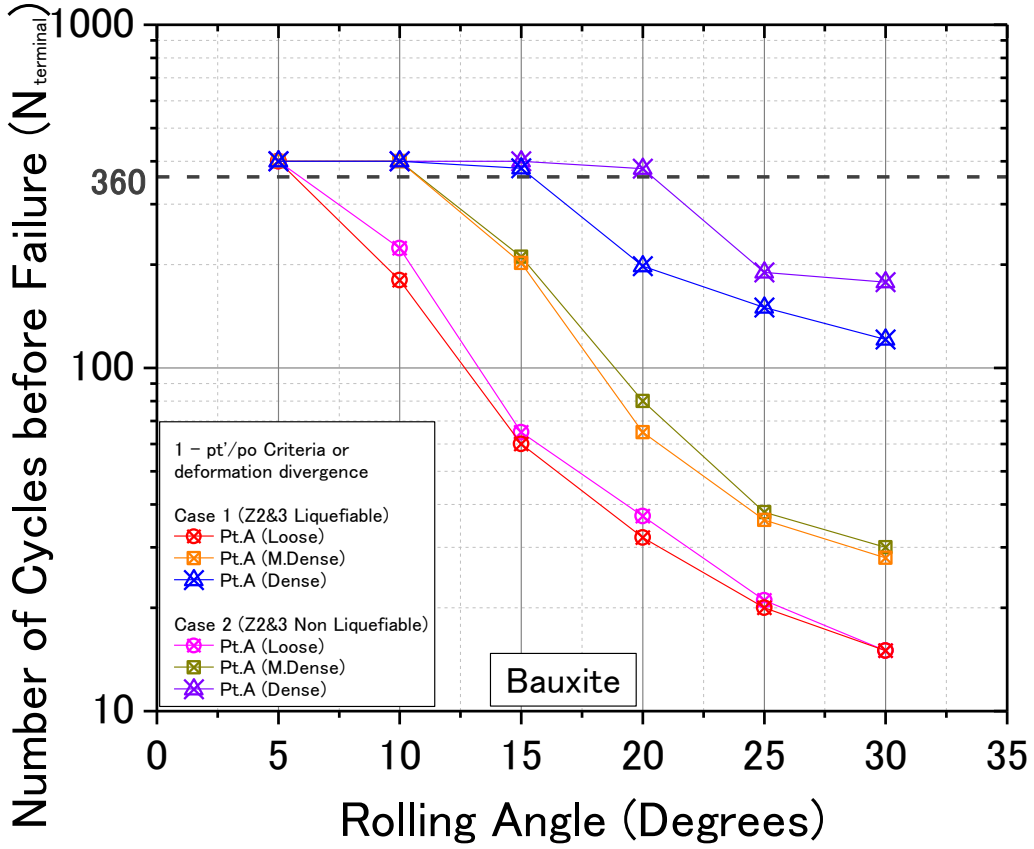

Fig. 6–71. Relationship between rolling angle and number of cycles before failure of heap (bauxite, various densities, Case 1 vs Case 2, point A)

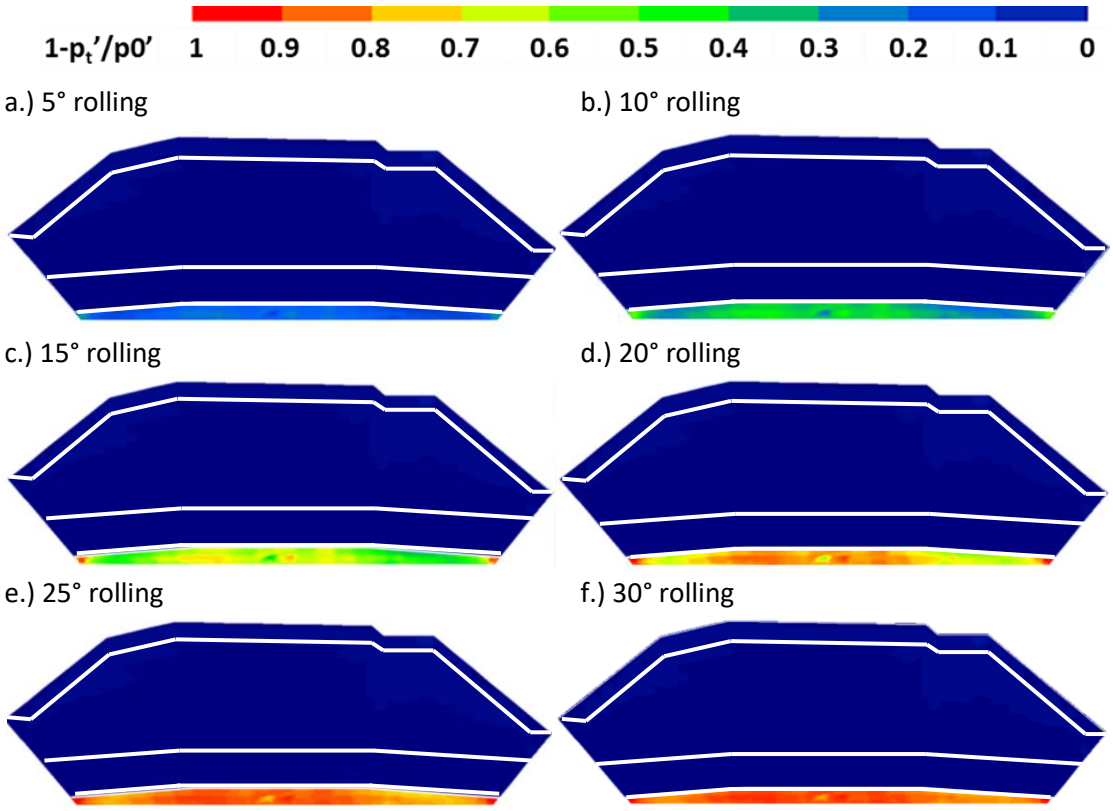

Fig. 6–72. Contour of effective stress reduction ratio failure with rolling angle of a.) 5°; b.) 10°; c.) 15°; d.) 20°; e.) 25°; f.) 30° (bauxite, dense, Case 2)

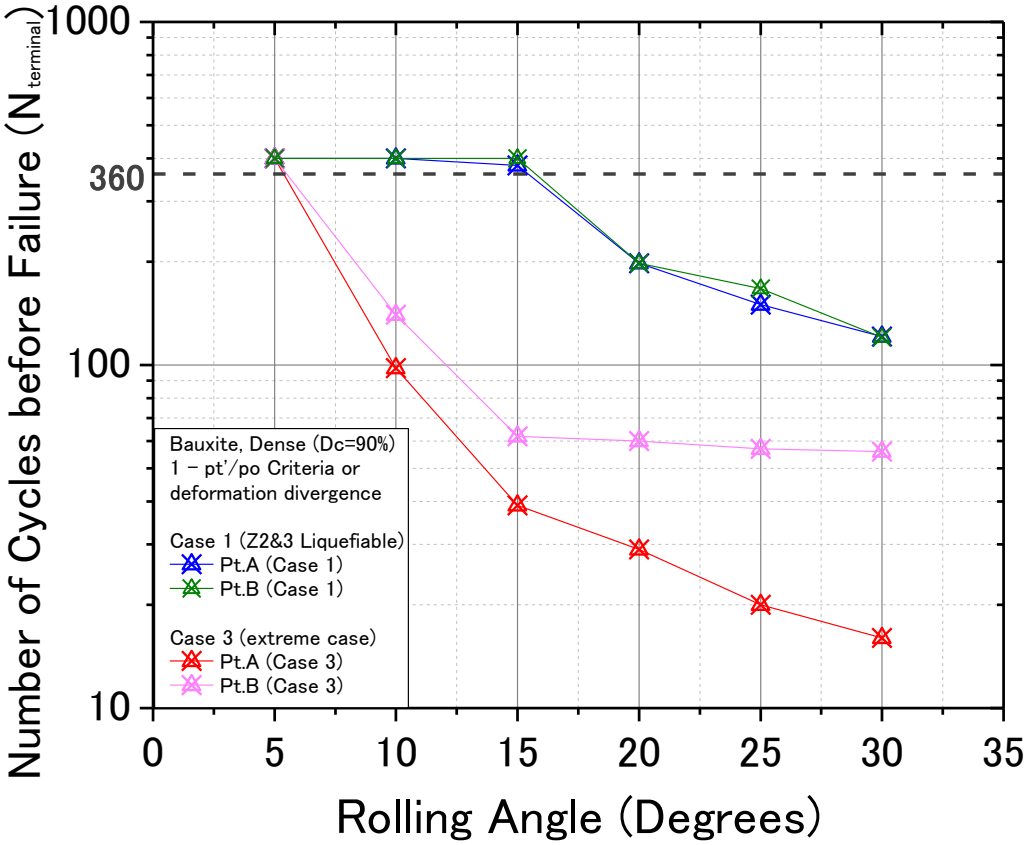

Fig. 6–73. Relationship between rolling angle and number of cycles before failure of heap (bauxite, dense, Case 1 vs Case 3, point A)

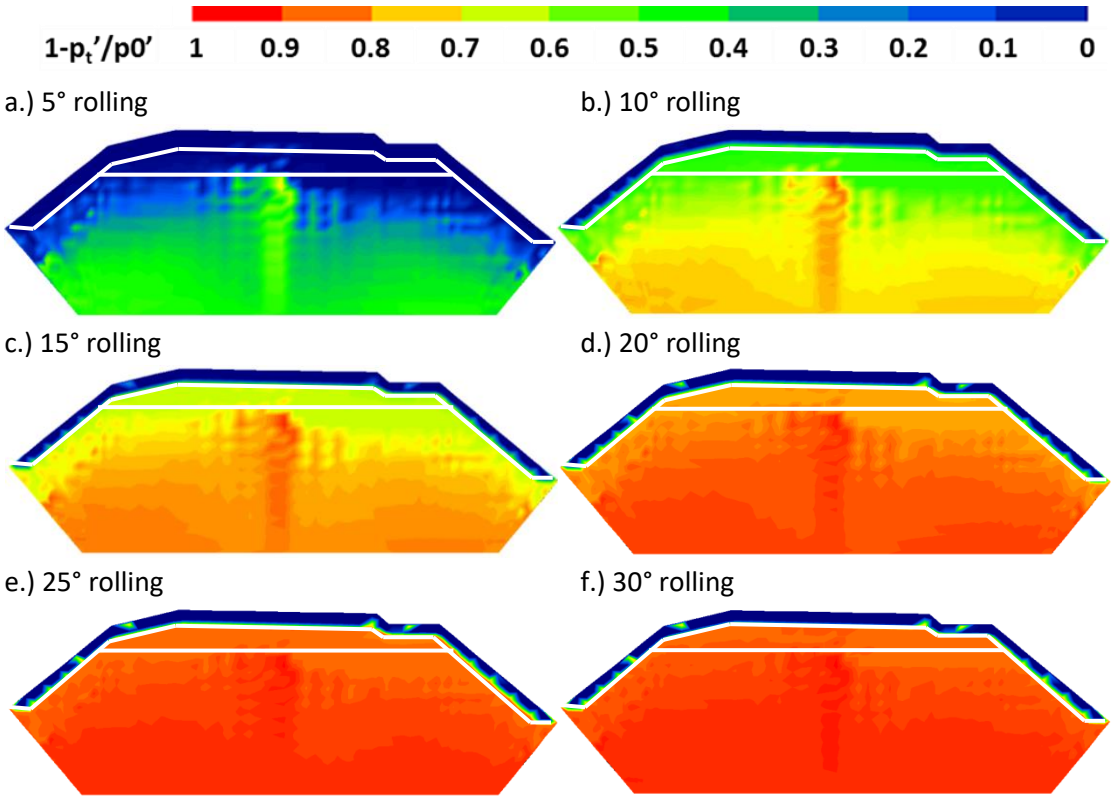

Fig. 6–74. Contour of effective stress reduction ratio failure with rolling angle of a.) 5°; b.) 10°; c.) 15°; d.) 20°; e.) 25°; f.) 30° (bauxite, dense, Case 3)

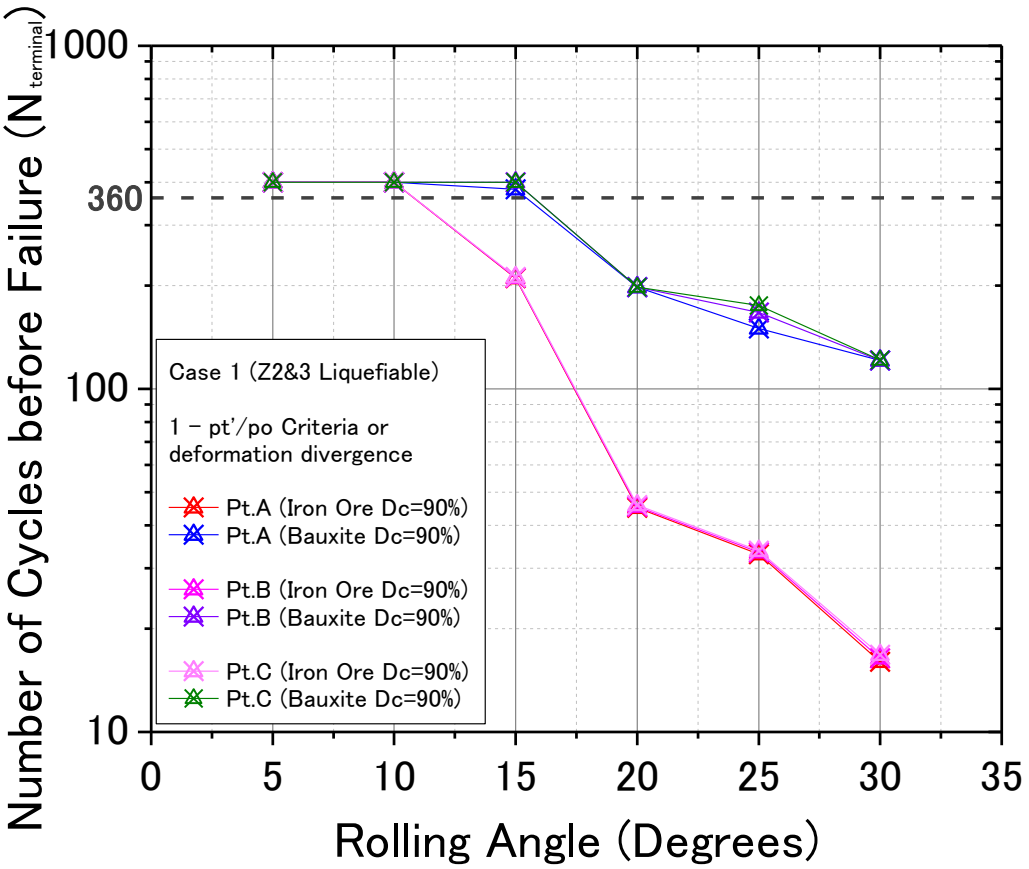

Fig. 6–75. Relationship between rolling angle and number of cycles before failure of heap (bauxite vs iron ore, dense, Case 1, points A, B, and C)

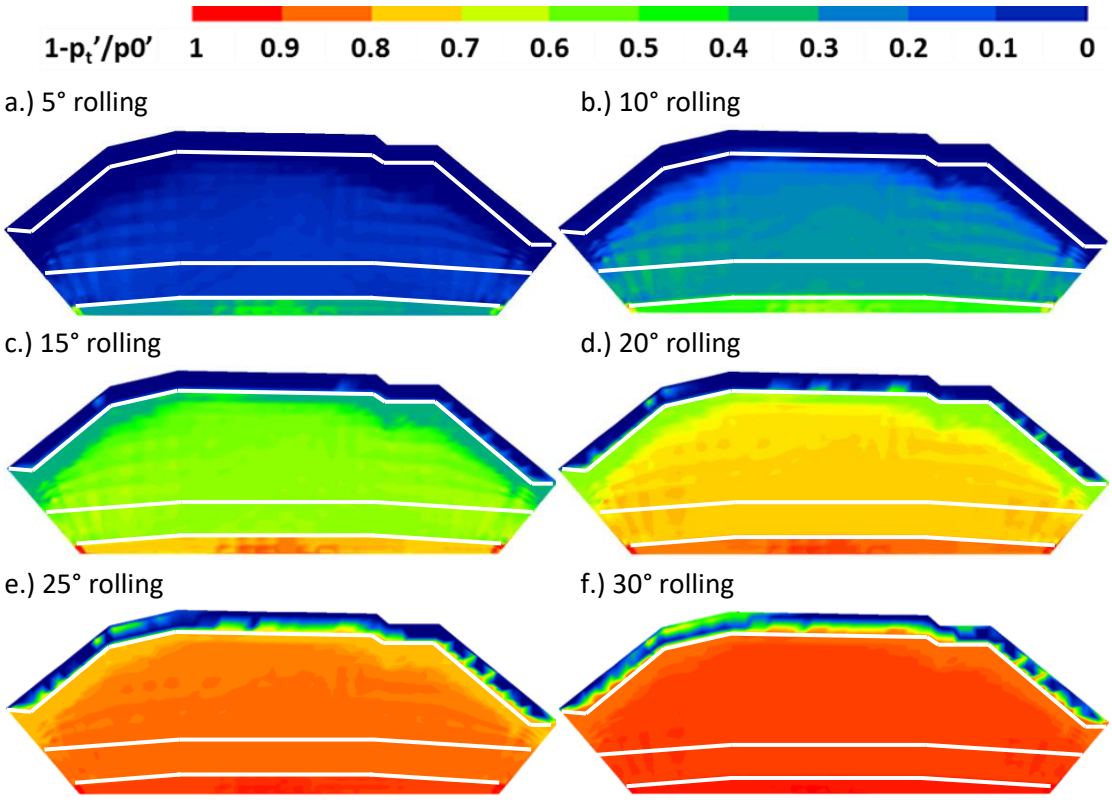

Fig. 6–76. Contour of effective stress reduction ratio failure with rolling angle of a.) 5°; b.) 10°; c.) 15°; d.) 20°; e.) 25°; f.) 30° (iron ore, dense, Case 1)

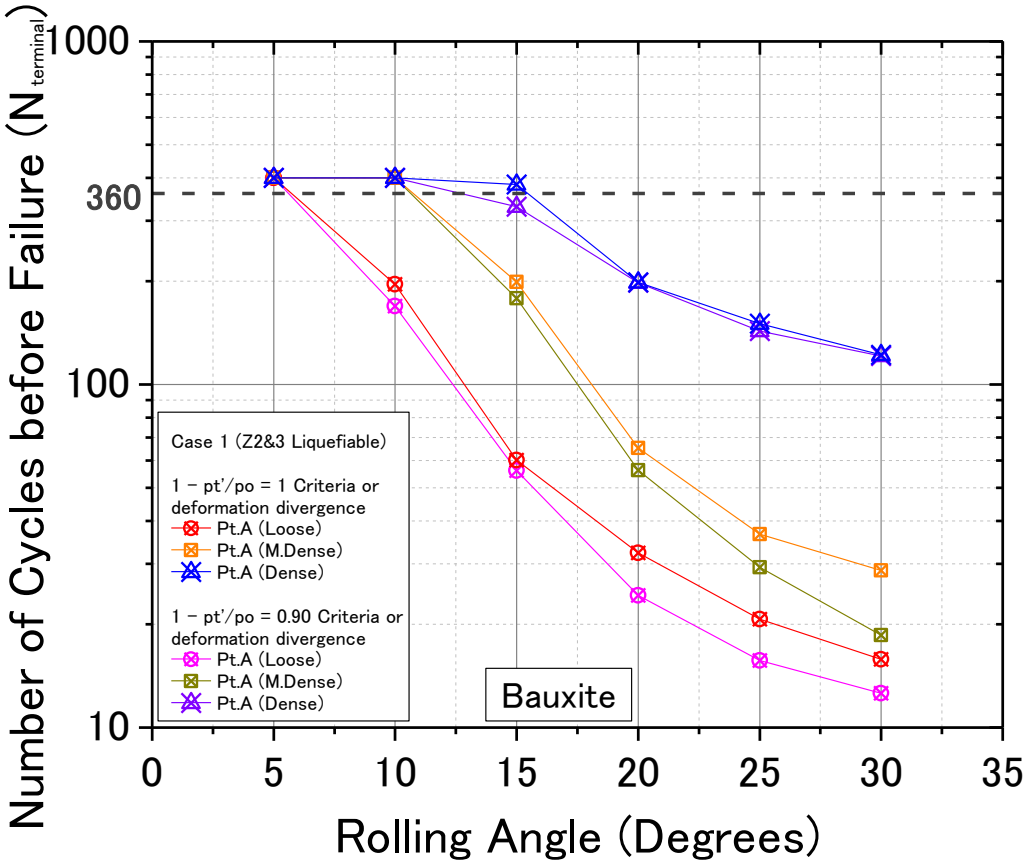

Fig. 6–77. Relationship between rolling angle and number of cycles before failure of heap at 1-p_t/p_o'=0.90 citeria/deformation divergence (bauxite, various densities, points A, B, and C)

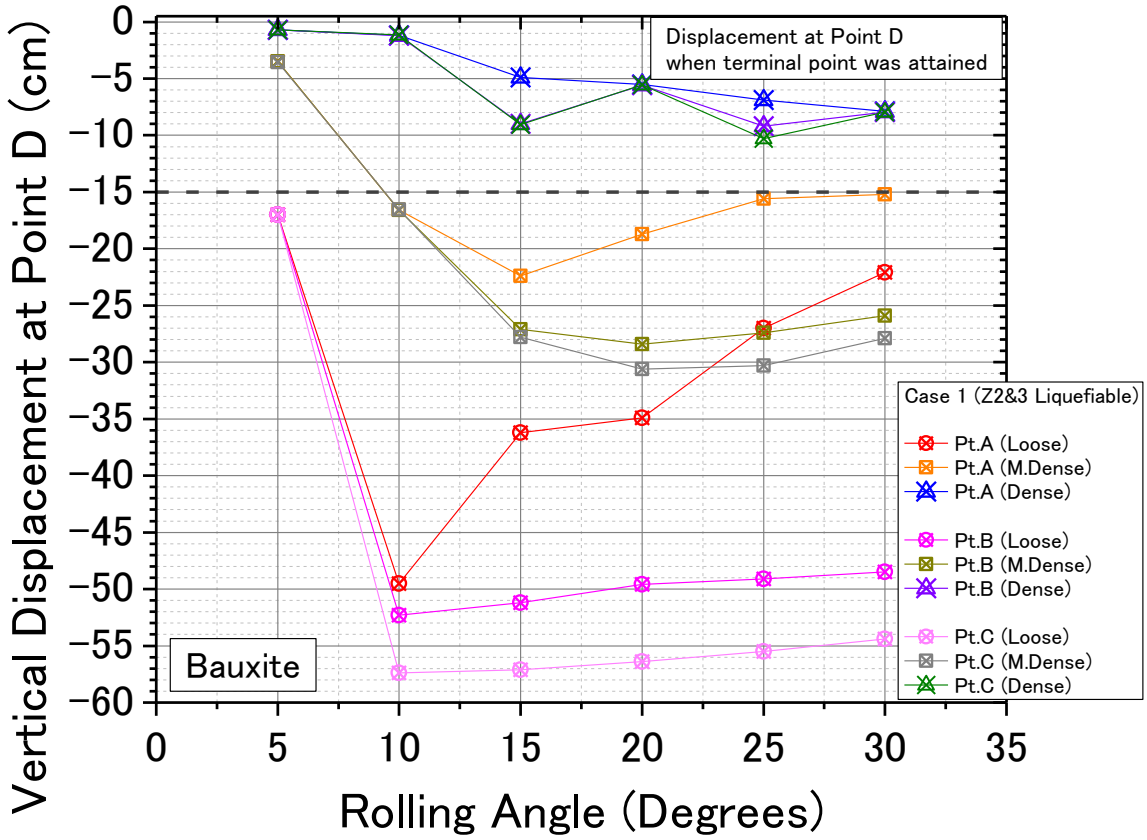

Fig. 6–78. Relationship between rolling angle and vertical displacement at point D when terminal point was attained (bauxite, various densities, points A, B, and C)

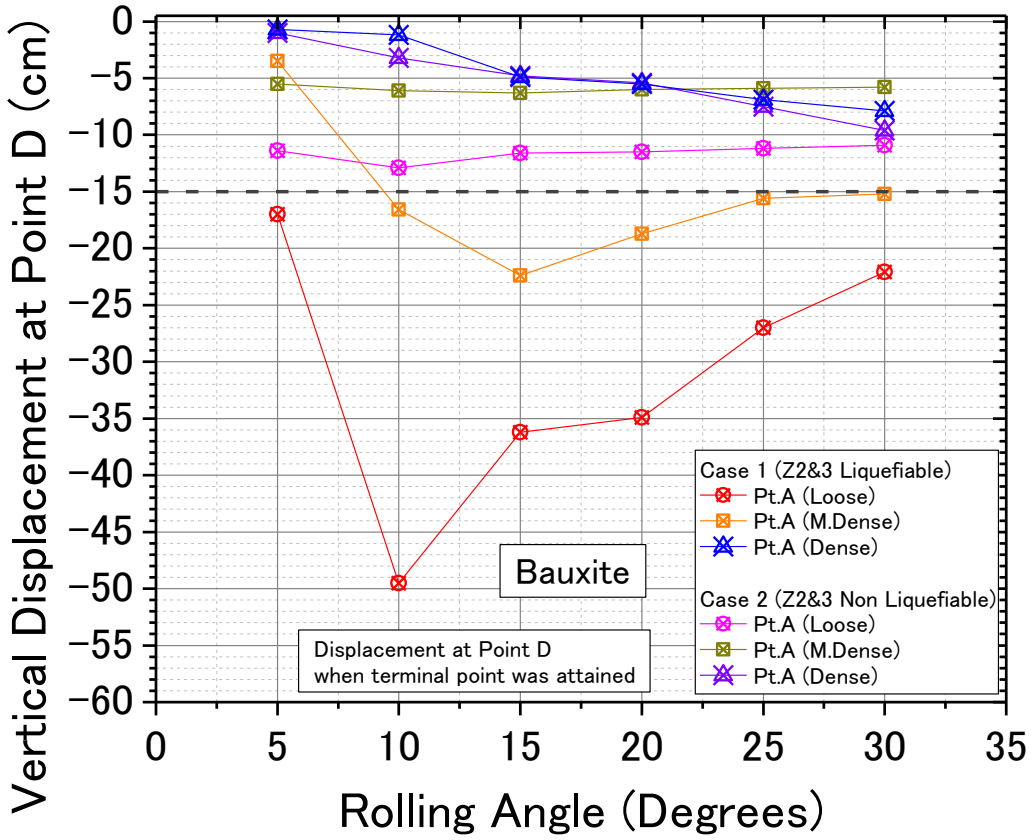

Fig. 6–79. Relationship between rolling angle and vertical displacement at point D when terminal point was attained (bauxite, various densities, Case 1 vs Case 2, point A)

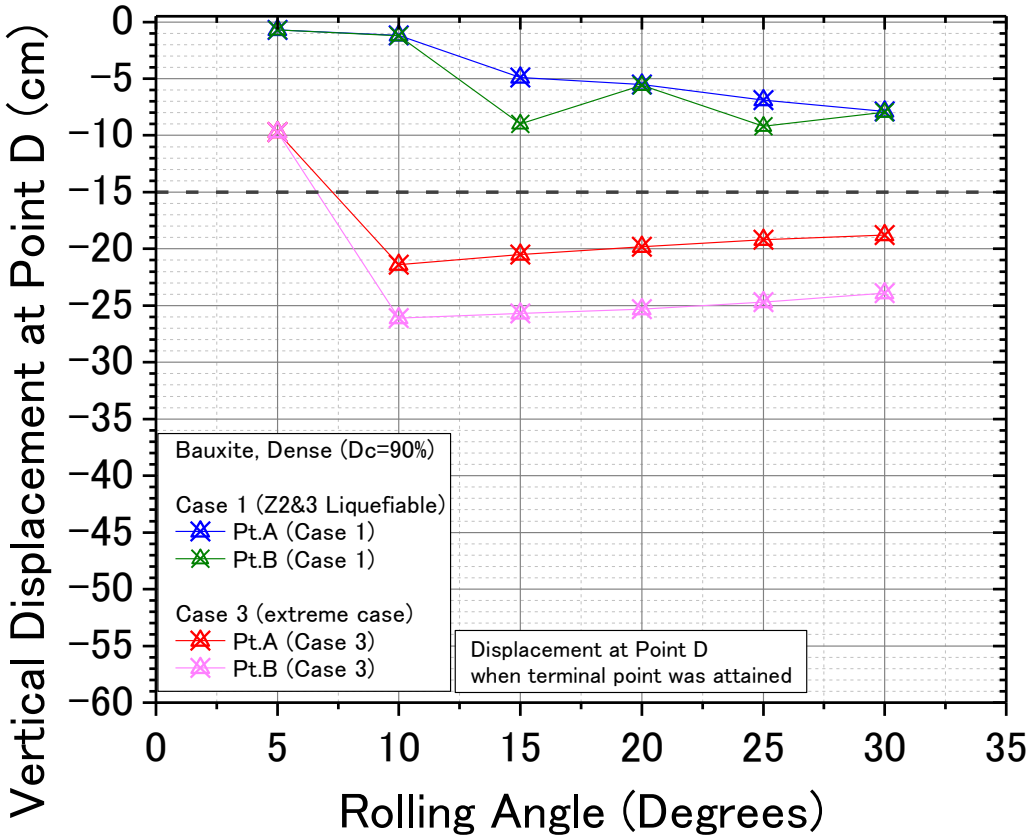

Fig. 6–80. Relationship between rolling angle and vertical displacement at point D when terminal point was attained (bauxite, dense, Case 1 vs Case 3, point A)

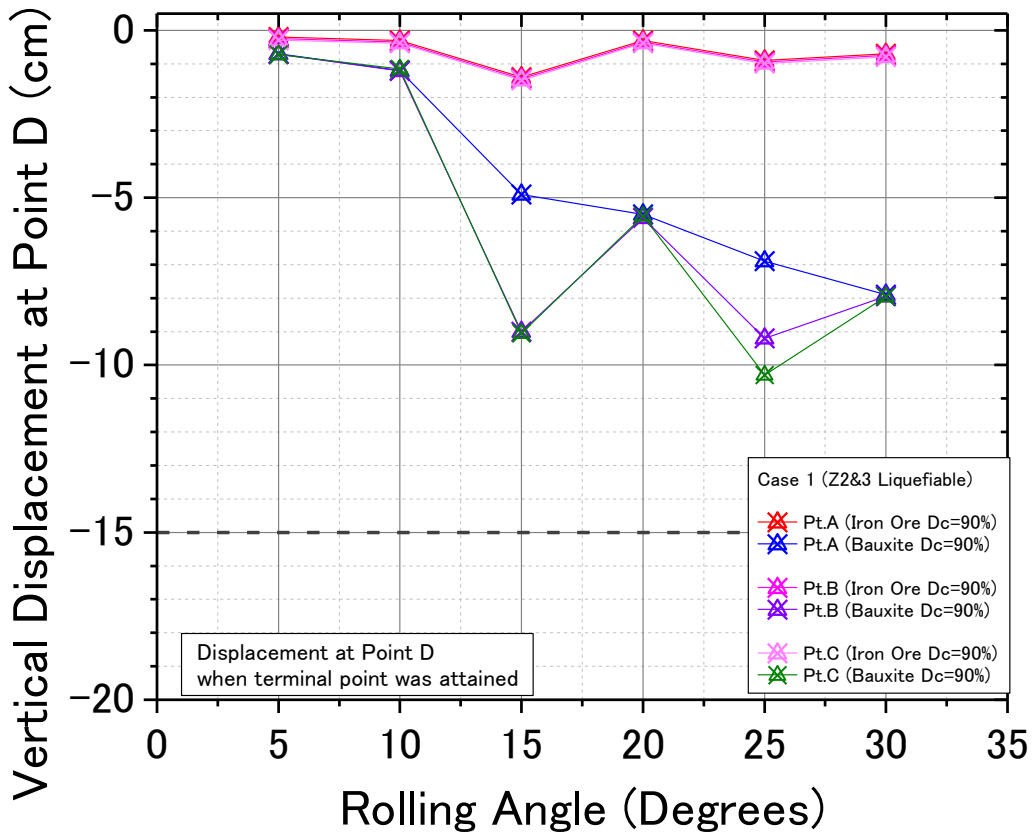

Fig. 6–81. Relationship between rolling angle and vertical displacement at point D when terminal point was attained (bauxite vs iron ore, dense, Case 1, points A, B, and C)

Chapter 7
Conclusions and Recommendations

Contents

7-1. Conclusions

Fig. 1-7 is again shown below to present the flow of study and the main contents involved in this study.

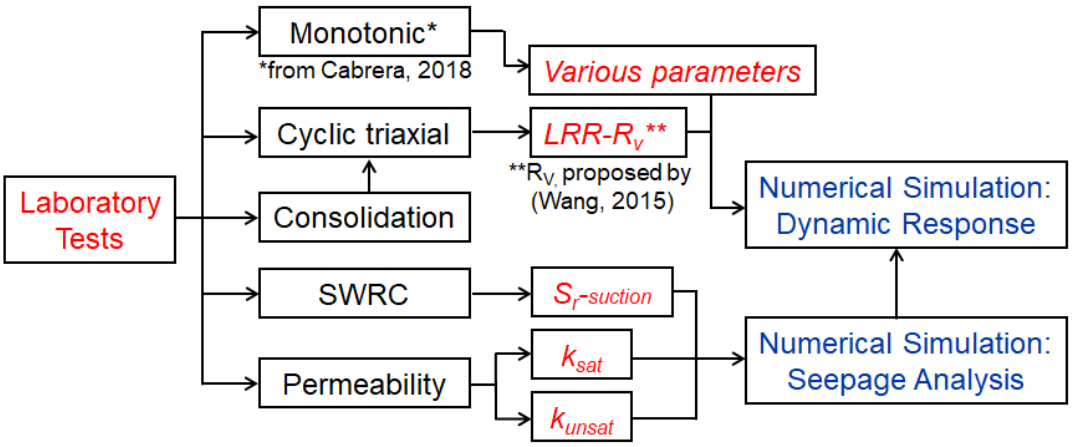

Adopted from Fig. 1–1. Flow of Study

In order to characterize bauxite on its geotechnical properties, experiments were carried out by using existing techniques and attempts were made to develop more advanced techniques. Bauxite was compared to iron ore and other conventional types of soils (Inagi sand and Toyoura sand) to describe its behavior. Finally, with the motivation of evaluating liquefaction potential of the unsaturated heap of bauxite suffering from the dynamic motions at sea, numerical simulations were performed in conjunction with the experimental results obtained in this study, and likewise were compared.

In view of the research objectives, the following conclusions can be made:

7.1.1. Characterization of Bauxite on its Geotechnical Properties and Comparisons with other Geomaterials (Objective 1)

1. Under saturated condition, bauxite's behavior during cyclic loading evidenced gradual increase of pore water pressure (u_w), exhibiting liquefaction condition under 5% double amplitude of axial strain (DA=5%) or 90% of initial confining pressure strength reduction (Δu=0.9 σ_0') simultaneously. In unsaturated condition however, the development of DA=5% takes place earlier than Δu=0.9σ_0' as degree of saturation (S_r) decreases.

2. Comparing bauxite to Toyoura sand at loose condition, it can be said that bauxite's behavior is different than Toyoura sand's behavior. Toyoura sand's behavior is characterized by the sudden increase in excess pore water pressure at the instance of liquefaction, as well as the large increase of axial strains in the extension side with a small increase in deviator stress. On the other hand, bauxite exhibited characteristics closer to Inagi sand (silty sand) and iron ore such as excess pore water pressure building up

gradually, or development of the axial strain generally symmetric to a little bias on the extension side. For bauxite however, 100% development of excess pore pressure couldn't be achieved in some cases, while it was achieved in Inagi sand and iron ore.

3. A new index called volumetric strain ratio (R_v) was proposed to correlated liquefaction resistance ratio (LRR) with various geomaterials (Wang et al., 2015). Like the previously tested materials such as iron ore and Inagi sand, bauxite follows the trend of the proposed LRR plotted against R_v, which exhibits a better correlation than LRR plotted against $\varepsilon^*_{v,air}$.

4. Bauxite behaves closer to Inagi sand in its permeability properties under saturated and unsaturated conditions.

7.1.2. Development of a testing method to measure permeability of Bauxite and other geomaterials under diff. saturation conditions (Objective 2)

1. It was found out that in a rigid mold, the coefficient of permeability *k* resulted to higher values due to side wall leakage effects. Hence, triaxial apparatus was utilized to address that concern, as well as applying confining pressure and maintaining stress state variables. With bauxite as the main geomaterial used in the study, a newly developed local pin-type sensors to measure head difference directly was presented as a new technique for obtaining *k* values.

2. In order to establish the limits, validity, and applicability of the local pin-type sensors, it was investigated and evaluated on different aspects and it was found out that the *k* values are primarily affected by the void ratio (*e*). *k* values decreases with decreasing *e*, hence density of the soil/geomaterial must clearly be regulated/specified.

3. The local pin-type sensors were extended in applicability to unsaturated permeability tests. A new triaxial permeameter apparatus was presented in Fig. 4-53, with the following features of the system:
   - Inflow rate was measured by Mariotte's bottle and a weighing scale, while outflow rate was measured by burettes and differential pressure transducer. Steady state flow condition can be achieved by using membrane filters to facilitate flow of water but prevent flow of free air.
   - Unsaturated permeability could be evaluated using the newly developed local pin-type sensors to measure the head difference directly. Permeability values were obtained by simple average at steady state flow condition and measured head is reasonably stable.
   - Current tests were done on bauxite (range: $1x10^{-5}$ to $1x10^{-3}$ cm/sec), iron ore (range: $1x10^{-5}$ to $1x10^{-4}$ cm/sec), and Inagi sand (range: $1x10^{-5}$ to $1x10^{-4}$ cm/sec). The local pin-type sensor was found out to be ineffective for Toyoura sand.

4. Experiments and results from the triaxial permeameter apparatus for unsaturated soils show that:

- Conducting *k* tests with this proposed system is not applicable in conducting multiple test with the same specimen.
- Under saturated case, the triaxial permeameter apparatus used for saturated case (Fig. 4-8) and the triaxial permeameter apparatus used for unsaturated case have practically the same *k* values.
- For different densities of bauxite, the local pin-type sensors could be a way to measure *k* of unsaturated materials. Results show that *k* values drop four (4) orders of exponent from fully saturated case (S_r=100%) to about 50% saturation (S_r=50%) (Fig. 4-73). It also supports the conclusion made due to the effect of void ratio, where the denser the test condition (i.e. lower void ratio), the lower the *k* values.
- Iron ore have lower *k* values than their bauxite counterpart at dense case (Fig. 4-77) despite having practically the same *k* saturated (2.68 x 10^{-3} cm/sec for bauxite, 2.84 x 10^{-3} cm/sec for iron ore). This is attributed to the void ratio of the specimens tested among others. Inagi sand, on the other hand, was less permeable than bauxite at loose case but their trends were the same.

5. Permeability results using the data obtained from SWRC (i.e. indirect method), Van Genuchten estimate (VG estimate) was calculated and compared with the experimental data (Fig. 4-92 to Fig. 4-94). For bauxite, it shows that as the specimen becomes denser, the results of VG estimate do not agree with the experimental data, with VG being underestimate. The result for iron ore compared to bauxite at dense case suggest the opposite, being the experimental data as underestimate, while trend suggests that the VG estimate will underestimate experimental data eventually due to steeper curvature. For Inagi sand compared to bauxite at loose case, the experimental data and VG estimate agree well.

7.1.3. Seepage and Dynamic Response Analysis on Bauxite and Comparisons with other Geomaterials (Objective 3)

A. Numerical Analysis: Seepage

1. Seepage analysis using Guslope software was performed to study the water content distribution in the heap of bauxite for handymax type vessel. With the availability of experimental data on permeability and SWRC, the software permits the input of actual data for analysis. The experimental data results were compared with VG model and in general, the VG model estimate is an underestimate of the results that can be obtained from the experimental data. This implies that direct measurement of *k* values is necessary.

2. Initial degree of saturation of 90% (Sr_{init}=90%) was considered for seepage analysis for modeling. Results show that the water distribution is a function of the density of the heap with looser materials having higher wet base in general. The shape of the wet base accumulated is generally ellipsoidal, with the peak at the centerline of the cross section, tapering to the side boundary.

3. For iron ore dense case, it is even possible that the water head at point A is a negative value (suction) for the whole duration of 350 hours. The result for Inagi sand on the other hand, was dependent on the Sr_{init}. Inagi sand has two (2) orders lower permeability than its bauxite counterpart at loose condition in addition to its higher air entry value (AEV), causing longer time to increase water head.

B. Numerical Analysis: Dynamic Response

1. The predictions of the cyclic behaviors of bauxite by using the PZ-sand model qualitatively match the experimental results (Fig. 6-23), while the parameters used in this study may need to be further optimized in order to produce better results. Currently, some parameters were obtained from undrained monotonic tests, isotropic consolidation tests, and undrained cyclic tests.

2. Strain distributions show that the development of strains increases with the rolling motion with an angle of 5° to 30°. Regarding the locations where large normal and shear strains are mobilized, they are developed at the (1) toes of the heap, (2) side boundaries, (3) interfaces of zones of both saturated and unsaturated regions, and (4) wet base/saturated zone.

3. Liquefaction potential of heap was evaluated with the number of cycles at the terminal point ($N_{terminal}$). Terminal point in the simulations was defined as deformation divergence (Fig. 6-43) or reduction of effective stress to zero (Fig. 6-44). The following observations were made from the simulations:
   - Bauxite at loose: ≤5° rolling angle; medium dense: ≤10° rolling angle; dense: ≤15° rolling angle; and Iron ore at dense: ≤10° rolling angle, could withstand a 360 cycle rolling motion (i.e. 60-minute duration) (Fig. 6-69 to Fig. 6-70 and Fig. 6-75 to Fig. 6-76).
   - Assuming the unsaturated region to be liquefiable decreased the overall resistance of heap of bauxite (Fig. 6-71 and Fig. 6-72). Hence, consideration of liquefaction potential of the unsaturated zone in the heap of bauxite is necessary to evaluate the overall liquefaction potential of the heap.
   - Assuming the extreme case of heap having poor drainage and impermeable side boundaries caused the heap to liquefy earlier (Fig. 6-73 and Fig. 6-74).

7.1.4. General Remarks

This study provides a qualitative understanding of the behavior of heap of bauxite during maritime transport. While simple assumptions were adopted to describe the kind of motions a ship may experience in a typical voyage, the results suggest thresholds and extents for different heap densities and wet base, which can affect the safety of the carrier.

Although bauxites have large differences in particle size distribution depending on the deposit and subsequent processing, the results in this study can be helpful for other gradations by following similar methodology and approach.

7-2. Recommendations

For future work, the following items are recommended to be considered in conducting the experiments and numerical simulations.

7.2.1. Experiments

1. Characterize Hematite, a type of iron ore on its liquefaction resistance, permeability, and SWRC, and compare them with existing results on iron ore fines type B (IOF-B), bauxite, and other conventional soils.

2. Consider the effect of suction in addition to the net normal stress in calculations to complete the stress state of the unsaturated soils subjected to undrained cyclic loading.

3. Perform more tests using the local pin-type sensors at higher degrees of saturation (*Sr*) and also extend the range of applicability by investigating on finer particles.

4. For the study presented here, the triaxial permeameter system to measure unsaturated permeability (k_{unsat}) did not measure the change in volume during testing. It is necessary to measure the volume change to improve the accuracy of the determined values and to confirm if the stress state of the specimen is maintained.

5. Conduct k_{unsat} measurement by water flow from bottom to top (instead of the current top to bottom). Several existing literatures conduct the tests by water flow from bottom to top (Goh, 2015; Moncada 2010, Agus 2003). Incorporate temperature measurements as well since density of water changes with temperature.

6. Membrane filter technique applied in this study performed very well on measuring negative pore water pressure. However, the application is limited to suction values less than 25 kPa in this study. Further development of the application of membrane filter technique is recommended.

7.2.2. Numerical Simulations

1. For a more comprehensive study, model the heap in 3D to better understand its behavior when subjected to different rolling angles or vessel motions.

2. Improve assignment of parameters by conducting necessary tests to obtain the parameters needed in the model. Validate PZ-sand model with field measurements and actual tests.

3. In the seepage analysis, consider wetting curve as the SWRC values to run the simulation.

4. Aside from liquefaction potential, consider the slope stability problem of the heap subjected to rolling motions.

References

Agus,S.S., Leong,E.C., Rahardjo,H. (2003). A flexible wall permeability for measurements of water and air coefficient of permeability of residual soil. Canadian Geotechnical Journal. 40, 559–574.

Aitchison, G.D., 1973."Problems of Soil Mechanics and construction on structurally unstable soils (Collapsible, Expansive and Others)." Proceedings. 8th Int . Conf. on Soil Mechanics and Foundation Engineering, Moscow, U.S.S.R., Toi. 3, pp.161-198

Alonso E. E., Gens A. & Hight D. W. (1987). "Special problems soils". General report. Proc. 9th Eur. Conf. Soil Mech., Dublin, p.p. 1087-1146.

American Society for Testing Materials (ASTM) D 2434. 2000. Standard Test Method for Permeability of Granular Soils (Constant Head).

Ampadu, S.K. & Tatstuoka, F. 1993. Effects of setting method on the behavior of clays in triaxial compression from saturation to undrained shear, Soils and Foundations, 33(2): 14-34.

Anand, S. and Arora RC. 2004. ASME 2004 Heat Transfer/Fluids Engineering Summer Conference Volume Charlotte, North Carolina, USA, July 11–15, 2004

Bear, J. (1972) Dynamics of Fluids in Porous Media. American Elsevier Publishing Company, New York, 764 p

Bishop and Blight (1963)Japanese Geotechnical Society (JGS) test method for particle size distribution of soils (JGS 0131-2009)

Bishop, A.W. (1959). The principle of effective stress. Lecture delivered in Oslo, Norway, in 1955; published in Teknisk Ukeblad, Vol. 106, No. 39, pp: 859-863.

Bradbury, M.H. & Baeyens, B. 2003. Porewater chemistry in compacted re-saturated MX-80 bentonite. J. Contam. Hydrol.,61: 329-338.

Cabrera, B. (2018). Flow Failure of Saturated Bauxite Under Undrained Monotonic Loading. MS thesis, Dep. of Civil Engineering, The University of Tokyo

Carrier, D. W., III. 2003. "Goodbye, Hazen; Hello, KozenyCarman." Journal of Geotechnical & Geoenvironmental Engineering 129(11): 1054–1056

Castro, G. & Poulos, S.J. (1977). Factors affecting liquefaction and cyclic mobility. Journal of the Geotechnical Engineering Division, ASCE, Vol. 103, No. GT6, 502-516.

Castro, G., 1975. Liquefaction and cyclic mobility of saturated sands. In: Proceeding of ASCE, vol. 101, GT6, pp. 551-569.

Childs EC, Collis-George N (1950). The permeability of porous materials. Proceedings of the Royal Society 201A:392-405

Common Structural Rules of Bulk Carriers, 2006.
Website: http://www.iacs.org.uk/publications/common-structural-rules/previous-csr/01-csr-for-bulk-carriers-full-text/

Daniel DE (1983) Permeability test for unsaturated soil. Geotech Test J 6(2):81–86

Dirksen C (1991) Unsaturated hydraulic conductivity. In: Smith KA, Mullins CE (eds) Soil analysis. Physical methods. Marcel Dekker, New York, pp 209–270

Fredlund D.G. & Morgenstern N. R. (1976) "Constitutive relation for volume change in unsaturated soils." Canadian Geotechnical Journal. 13(3), pp. 261-276.

Fredlund D.G.. & Morgenstern, N. R. (1977). "Stress state variables for unsaturated soils." J. Geotech. Eng. Div., ASCE 103, GT5, pp. 447-466.

Fredlund, D.G. and Morgenstern, N.R. (1977). Stress state variables for unsaturated soil. ASCE J. Geotech. Eng. Div. GT5, Vol 103, pp: 447-466.

Fredlund, D.G. and Rahardjo, H. (1993). "Soil Mechanics for unsaturated soils", John Wiley & Sons Inc., Toronto, Canada.

Fredlund, D.G. Soil Mechanics for Unsaturated Soils. 2007. John Wiley and Sons Publishing.
Global Bauxite Working Group. (2017). Report on Research into the Behaviour of. Bauxite during Shipping

Goh, S.G. & Rahardjo, H & Leong, E. (2015). Modification of triaxial apparatus for permeability measurement of unsaturated soils. Soils and Foundations. 55(1), 63-73

Hazen, A (1911). "Discussion of Dams on sand foundations by A.C. Koenig" Trans. Am. Soc. Civ. Eng. 73, 199-203.

Huang, S., Fredlund, D. G., and Barbour, S. L., 1998, "Measurement of the Coefficient of Permeability for a Deformable Unsaturated Soil Using a Triaxial Permeameter" Can. Geo. J., Vol. 35, No. 3, pp. 426‑432.

Huang,S., Fredlund, D.G., Barbour, S.L. (1998). Measurement of the coefficient of permeability for a deformable unsaturated soil using a triaxial permeameter. Canadian Geotechnical Journal. 35, 426–432.

Hughes, S.S., Casper, J.L., and Geist, Dennis, 1997, Potential influence of volcanic constructs on hydrogeology beneath Test Area North, Idaho National Engineering Laboratory, Idaho:

Symposium on engineering geology and geotechnical engineering, 32d, Boise, Idaho, March 26-28, 1997, Proceedings, p. 59-74.

Ishihara, K., Tsuchiya, H., H., Huang, Y., Kamada, K., 2001. Recent studies on liquefaction resistance of sand- effect of saturation, In: Proc. 4th Int. Conf. Recent Advance in Geotech. Earthquake Engineering and Soil Dynamics, pp. 1-7.

Jacinto, A.C., Villar, M.V., Ledesma, A. 2012. Influence of water density on the water-retention curve of expansive clays. Geotechnique 62 (8): 657-667.

Japanese Geotechnical Society. 2009. JGS 0111: Test method for density of soil particles

Japanese Geotechnical Society. 2009. JGS 0520: Preparation of Soil Specimens for Triaxial Tests

Japanese Geotechnical Society. 2009. JGS 0711: Test method for soil compaction using a rammer

Japanese Industrial Standards. 2009. JIS A 1218: Test Methods for Permeability of Saturated Soils.

Khalifa, M.-A.O.A., Wahyudi, I., Thomas, P. 2002. New extension of Darcy's Law to unsteady flows. Soils and Foundation. 42 (6), 53-63.

Klute A (1972) The determination of the hydraulic conductivity and diffusivity of unsaturated soils. Soil Sci 113(4):264–276

Kozeny, J. and P.C. Carman, (1956) "Flow of gases through porous media." Butterworths, London

Lambe, T. W. and Whitman, R. V., 1969, Soil Mechanics, Wiley, New York, p. 553.

Lloret, A., Villar, M.V., Sanchez, M., Gens, A., Pintado, X., Alonso, E.E. (2003). Mechanical behaviour of heavily compacted bentonite under high suction changes. Geotechnique 53 (1): 27-40.

Masrouri, F., Bicalho K.V., Kawai, Katsuyuki (2008). Laboratory Testing in Unsaturated Soils. Geotechnical and Geological Engineering. 26, 691-704.

Matyas, E.L., and Radhakrishna, H.S. (1968). "Volume change characteristics of partially saturated soils," Geotechnique, Vol. 18,pp. 432-448

Mitchell, J.K. and Soga, K. (2005) Fundamentals of Soil Behavior. 3rd Edition, John Wiley & Sons, Hoboken.

Moncada, M.P.H.,Campos,T.M.P.,2010. A new permeameter for the determination of the unsaturated coefficient of permeability. In: Proceedings of the Firth International Conference of Unsaturated Soil, UNSAT 2010, Barcelona,Spain,6–8 September,pp.701–706.

Mualem Y (1976) A new model for predicting the hydraulic conductivity of unsaturated porous media. Water Resour Res 12(3):513–522

Munro, Michael C. and Mohajerani, Abbas. "Liquefaction Incidents of Mineral Cargoes on Board Bulk Carriers," Advances in Materials Science and Engineering, vol. 2016, Article ID 5219474, 20 pages, 2016.

Ng, C.W.W. and Menzies, B., (2007). "Advanced unsaturated soil mechanics and engineering,"Taylor and Francis2Park square, Milton park, Abingdon, Oxon OX14 4RN.

Ng, C.W.W., Zhan, L.T., and Cui, Y.J. 2002. A New Simple System for Measuring Volume Changes in Unsaturated Soils. Canadian Geotechnical Journal, Vol. 39, pp. 757-764.

Ngo Tuan Anh, (2009)."Undrained cyclic triaxial tests on partially saturated Inagi sand under controlled cell pressure."Master thesis, Dep. of Civil Engineering, The University of Tokyo

Nielsen, D.R. and Biggar, J.W. (1961) "Measuring Capillary Conductivity." Soil Science. Vol 92, pp.192-193.

Nishimura, T., Koseki, J., Fredlund, D.G. and Rahardjo, H. (2012). Microporous membrane technology for measurement of soil-water characteristic curve. Geotechnical Testing Journal, Vol.35, 201-208.

Nishimura, T., Toyota, H. and Koseki, J., (2009)."Evaluation of apparent cohesion of an unsaturated soil", Proceedings of the 4thAsia Pacific Conference on Unsaturated Soils.New Castle, Australia.

Okamura, M., Soga, Y., 2006. Effects of pore fluid compressibility on liquefaction resistance of partially saturated sand, Soils Found. 46 (5), 695-700

Parker, J. C., J. B. Kool, and M. Th. van Genuchten. (1985) Determining soil properties from one-step outflow experiments by parameter estimation, II. Experimental studies, Soil Sci. Soc. Am. J., 49, 1354-1359.

Pastor, M., Zienkiewicz, O.C. and Chan, A.H.C. (1990) Generalized plasticity and the modelling of soil behaviour. Int. J. Numer. Anal. Meth. Geomech. 14 (3): 151–190

Richards LA, Gardner W (1938) Tensiometers for measuring the capillary tension of soil water. J Am Soc Agron 28:352–358

Richards, B.G., Peter, P. and Martin, R. (1984). “The determination of volume change properties in expansive soils.” Proc. 5th Int. Conf. Expansive Soils, Adelaide: pp. 179-186.

Romero, E., Gens, A., Lloret, A. (1999). Water permeability, water retention and microstructure of unsaturated compacted Boom clay. Engineering Geology 52: 117-127

Salager, S., Nuth, M., Ferrari, A., Laloui, L. (2013). Investigation into water retention behavior of deformable soils. Can. Geotech. J. 50: 200-208.

Schofield R. K., (1935). “The pF of the water in soil.” Trans. Int. Congr. Soil Sci., 3rd, H, 38-48.

Seed, H.B., 1979. Soil liquefaction and cyclic mobility evaluation for level ground during earthquakes. In: Proceeding of ASCE, vol. 105, GT2, pp. 201-255.

Seed, H.B., Idriss, M., 1971. Simplified procedure for evaluating soil liquefaction potential. In: Proceeding of ASCE, vol. 97, SM9, pp. 1249-1273.

Seki, K. (2007) SWRC fit - a nonlinear fitting program with a water retention curve for soils having unimodal and bimodal pore structure. Hydrol. Earth Syst. Sci. Discuss., 4: 407-437. doi:10.5194/hessd-4-407-2007

Standing, J.R. (2011). The development of unsaturated soil mechanics at Imperial College, London. Unsaturated soils: Theory and practice 2011, pp: 119-138.

Tan Tian, J., Koseki, J., Wang, H., Sato, T. (2016). Local Measurement of the Permeability of Sands using Pin-Type Sensors in the Triaxial Apparatus. The 18th International Symposium, CS2-029. JSCE Conference. Sendai, Sept 08 2016

Tan Tian, J.U. 2016. Liquefaction Tests using Modified Triaxial Apparatus on Sands under Different Saturation Conditions and Their Permeability Evaluation using Local Measurement. MS thesis, Dep. of Civil Engineering, The University of Tokyo

Terzaghi (1943), “Theoretical Soil Mechanics”, John Wiley, New York.

Terzaghi, K. and Peck, R.B. (1964). Soil mechanics in engineering practice, Wiley, New York

The Commonwealth of the Bahamas. 2015. “MV Bulk Jupiter”. IMO Number 9339947, Official Number 8001956. Bahamas Maritime Authority, London, UK

Towhata, Ikuo. 2008. Geotechnical Earthquake Engineering. Scientific Publishing Services Pvt. Ltd. pp.344-345

Unno, T., Kazama, M., Uzuoka, R. and Sento, N. (2008). Liquefaction of unsaturated sand considering the pore air pressure and volume compressibility of the soil particle skeleton. Soils and Foundations, Vol. 48, No. 1, 87-99.

Van Genuchten, M. Th. (1980) A closed-form equation for predicting the hydraulic conductivity of unsaturated soils, Soil Sci. Soc. Am. J., 892-898.

Wang, H. 2014. Evaluation of Liquefaction Potential of Partially Saturated Heap of Iron Ore Fines during Maritime Transportation. PhD thesis, Dep. of Civil Engineering, The University of Tokyo

Wang, H., Koseki, J., and Sato, T. 2017. p-constant condition applied to undrained cyclic triaxial test of unsaturated soils. Geotechnical Testing Journal, 40(4). doi: 10.1520/GTJ20160115.

Wang, H., Koseki, J., Cai, F., Nishimura, T. (2018). Membrane filter properties and application of the filter to undrained cyclic triaxial test of unsaturated materials. Canadian Geotechnical Journal, 55 (9): 1349-1357. https://doi.org/10.1139/cgj-2017-0480

Wang, H., Koseki, J., Sato, T., Chiaro, G., and Tan Tian, J. 2016a. Effect of saturation on liquefaction resistance of iron ore fines and two sandy soils. Soils and Foundations, 56(4): 732–744. doi:10.1016/j.sandf.2016.07.013.

Wang, H., Sato, T., Koseki, J., Chiaro, G., and Tan Tian, J. 2016b. A system to measure volume change of unsaturated soils in undrained cyclic triaxial tests. Geotechnical Testing Journal, 39(4): 532–542. doi:10.1520/GTJ20150125.

Wulfsohn, D., Adams, B.A. and Fredlund, D.G. (1996). “Application of unsaturated soil mechanics for agricultural conditions. “ Can. Agric. Eng. 38:173-181.

Yasuda, S., Kobayashi, T., Fukushima, Y., Kohari, M. and Simazaki, T. (1999). Effect of degree of saturation on the liquefaction strength of Masa (in Japanese). Proc., 34th Jpn. Nat. Conf. Geotech. Eng., 2071-2072.

Yoshimi, Y., Tanaka, K. and Tokimatsu, K. (1989). Liquefaction resistance of a partially saturated sand. Soils and Foundations, Vol. 29, No. 3, 157-162.

Yuk Gehling, W.Y. (1994). “Suelos expansivos: estudio experimental y aplicación de un modelo teórico.” Tesis Doctoral, Universidad Politécnica de Catalunya.

Appendix A: Liquefaction Tests

Contents

A-1 Liquefaction on Bauxite (Saturated)

Table A-1. Saturated Test Conditions of Liquefaction Tests for bauxite, D_c = 67% (Loose)

Test No.	Initial Confining Pressure σ_o' (kPa)	Void ratio, e at σ_o'	Degree of Compaction, D_c (%)	B-value	Liquefaction	
					CSR	$N_{DA=5\%}$
L1	48.7	1.074	68.3	0.997	0.164	5.4
L2	48.7	1.107	67.6	0.989	0.141	8.1
L3	47.7	1.150	66.1	0.995	0.124	48.5
L4	48.2	1.155	66.3	0.992	0.124	27.0

Test L1

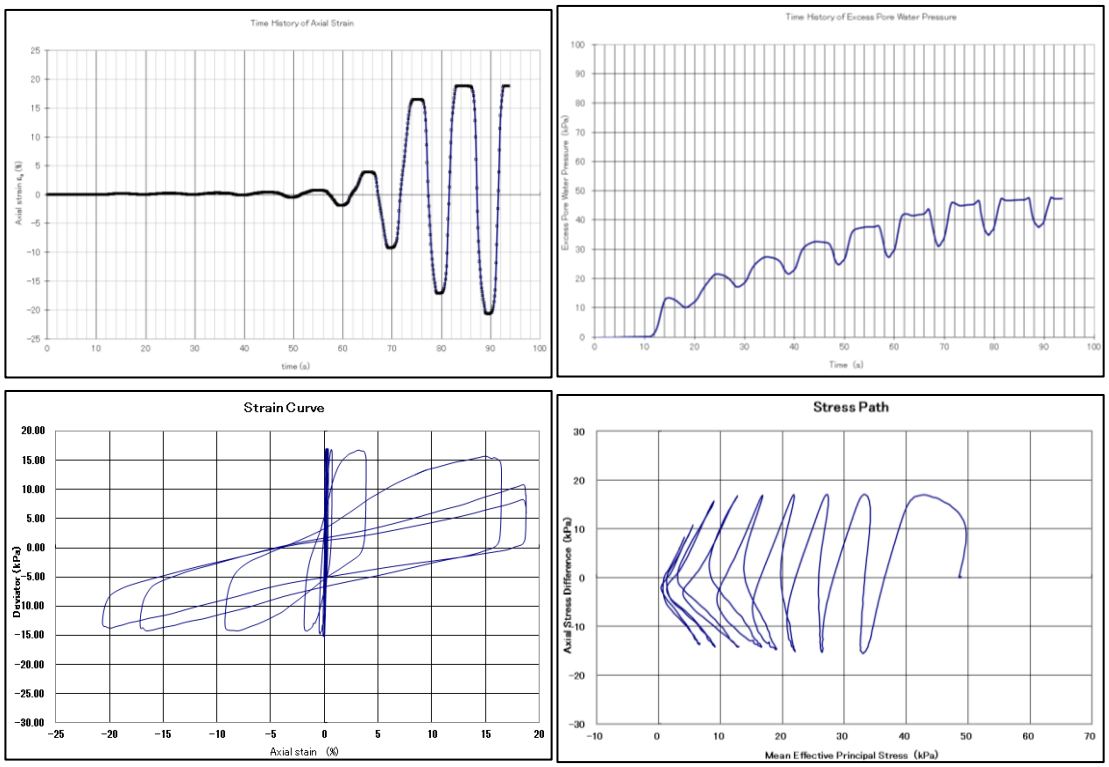

Figure A - 1. Liquefaction Test (Test L1-bauxite; saturated)

Test L2

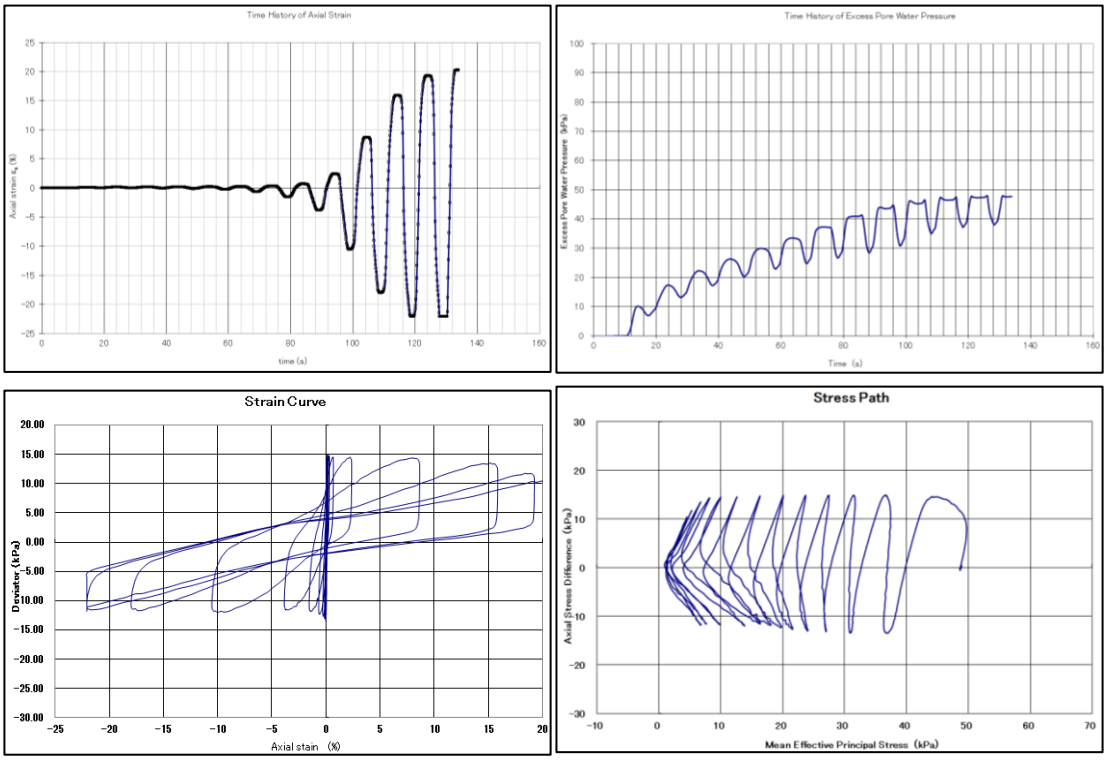

Figure A - 2. Liquefaction Test (Test L2-bauxite; saturated)

Test L3

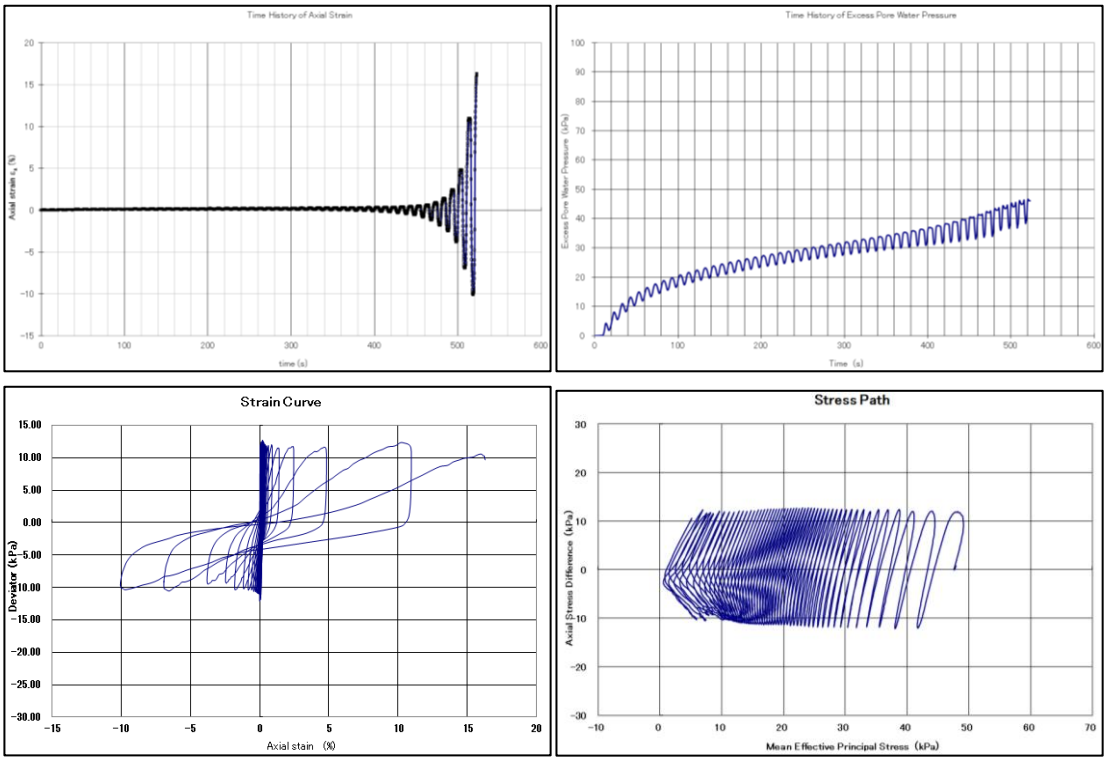

Figure A - 3. Liquefaction Test (Test L3-bauxite; saturated)

Test L4

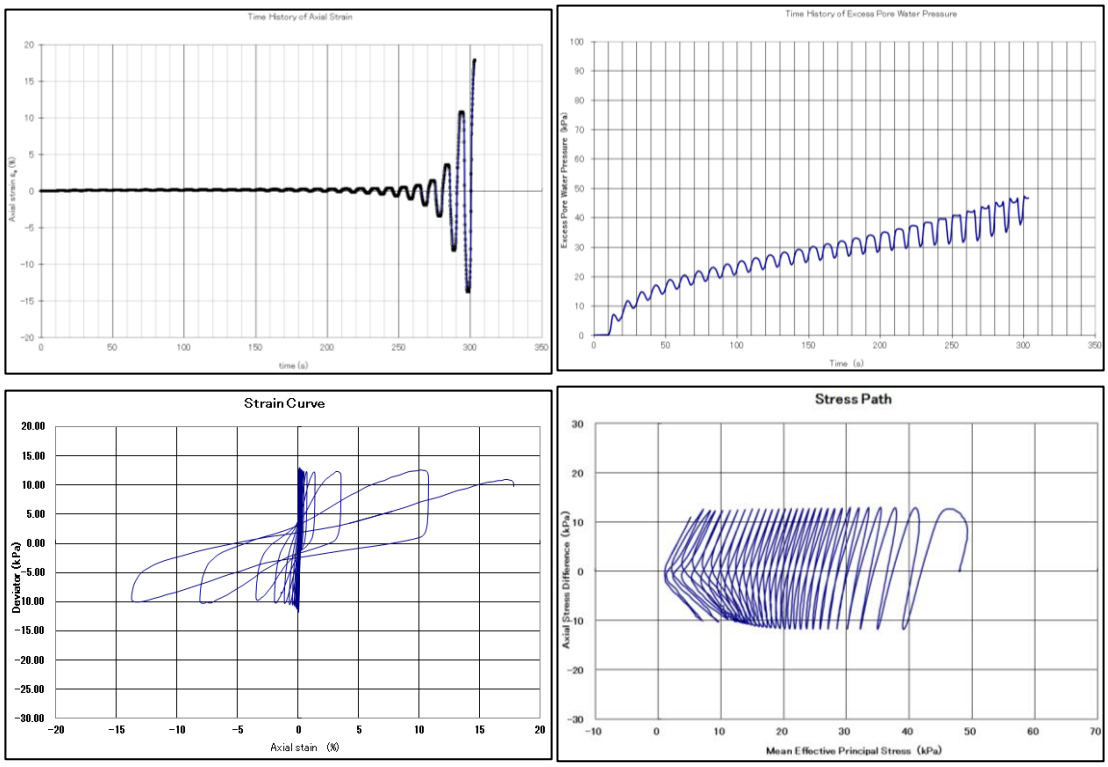

Figure A - 4. Liquefaction Test (Test L4-bauxite; saturated)

Table A-2. Saturated Test Conditions of Liquefaction Tests for bauxite, D_c = 82% (M.Dense)

Test No.	Initial Confining Pressure σ_o' (kPa)	Void ratio, e at σ_o'	Degree of Compaction, D_c (%)	B-value	Liquefaction	
					CSR	$N_{DA=5\%}$
M1	49.1	0.932	80.4	0.972	0.156	49.4
M2	48.6	0.857	83.7	0.983	0.181	6.4
M3	49.0	0.839	84.5	0.987	0.173	12.3
M4	48.9	0.891	82.2	0.987	0.163	22.9
M5	48.2	0.865	83.3	0.985	0.191	1.7
M6	50.2	0.911	81.3	0.988	0.165	11.6

Test M1

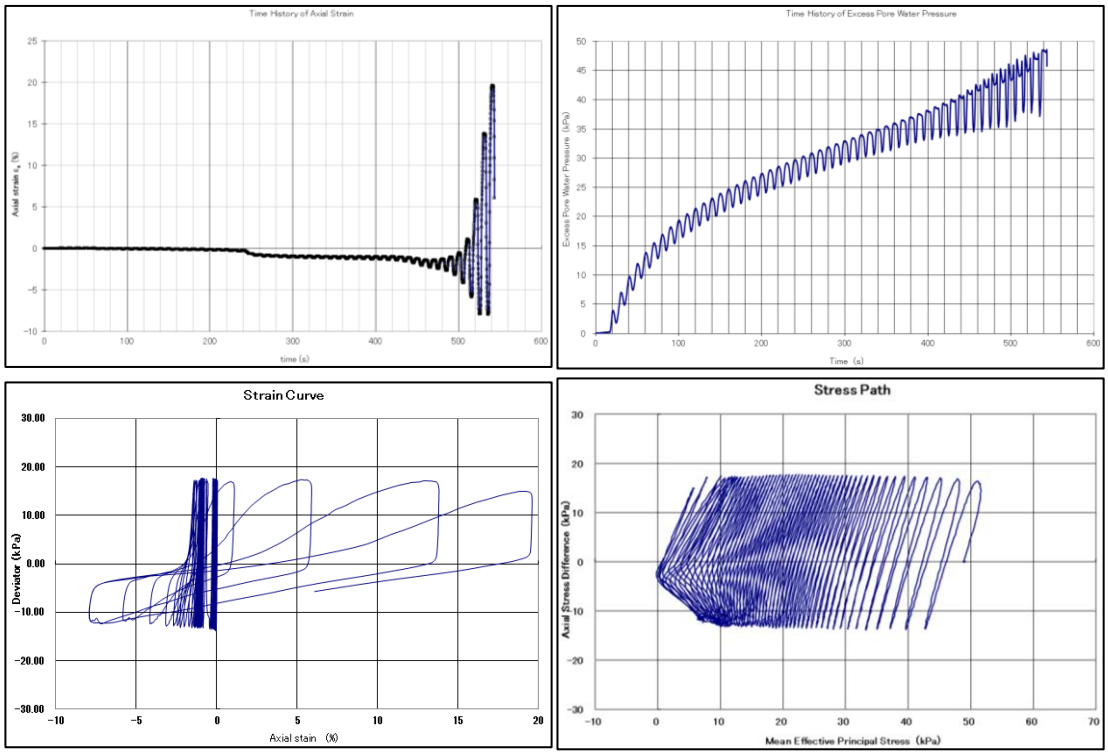

Figure A - 5. Liquefaction Test (Test M1-bauxite; saturated)

Test M2

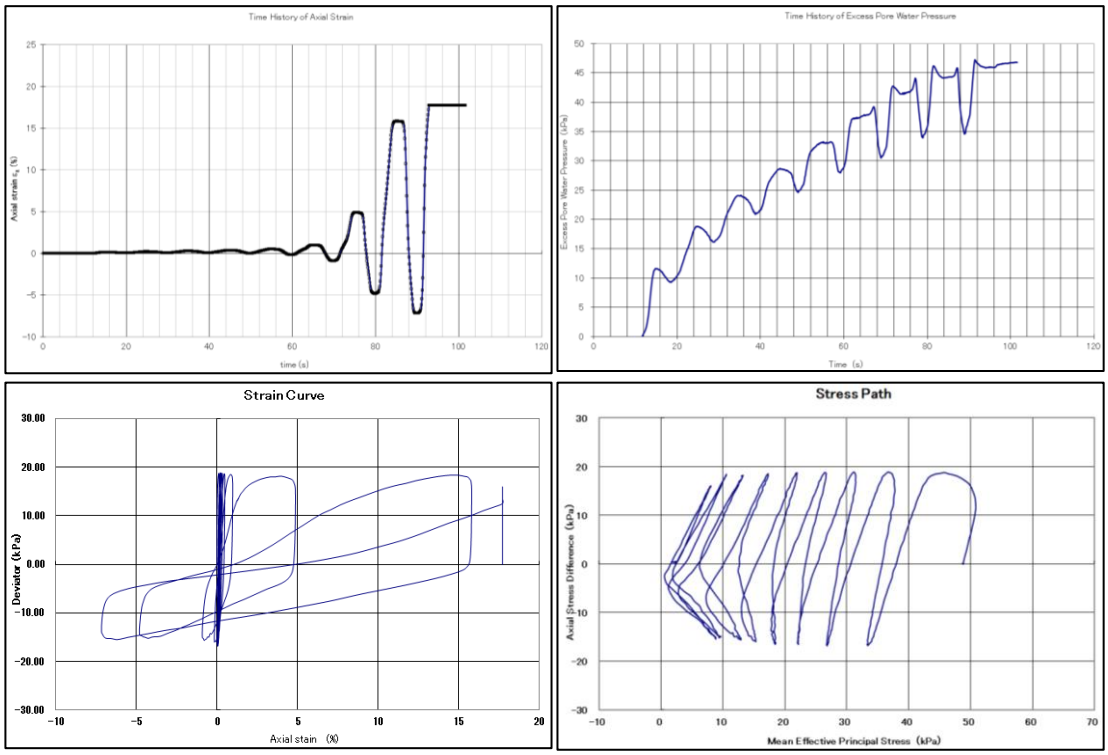

Figure A - 6. Liquefaction Test (Test M2-bauxite; saturated)

Test M3

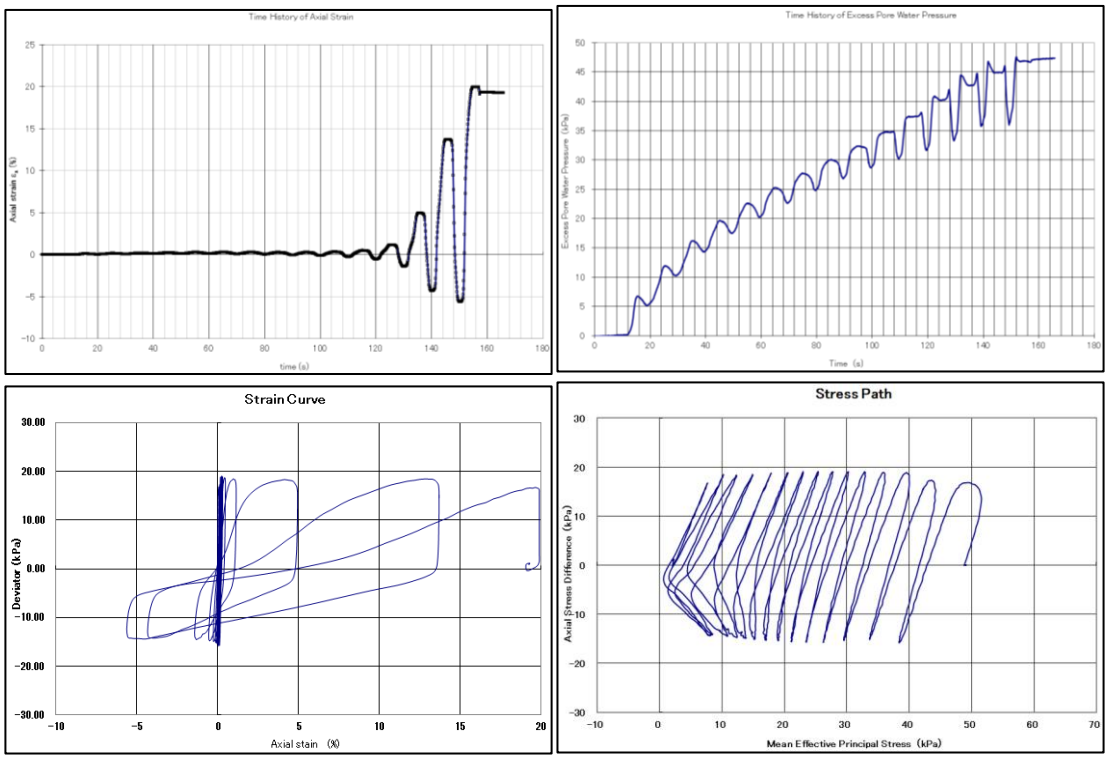

Figure A - 7. Liquefaction Test (Test M3-bauxite; saturated)

Test M4

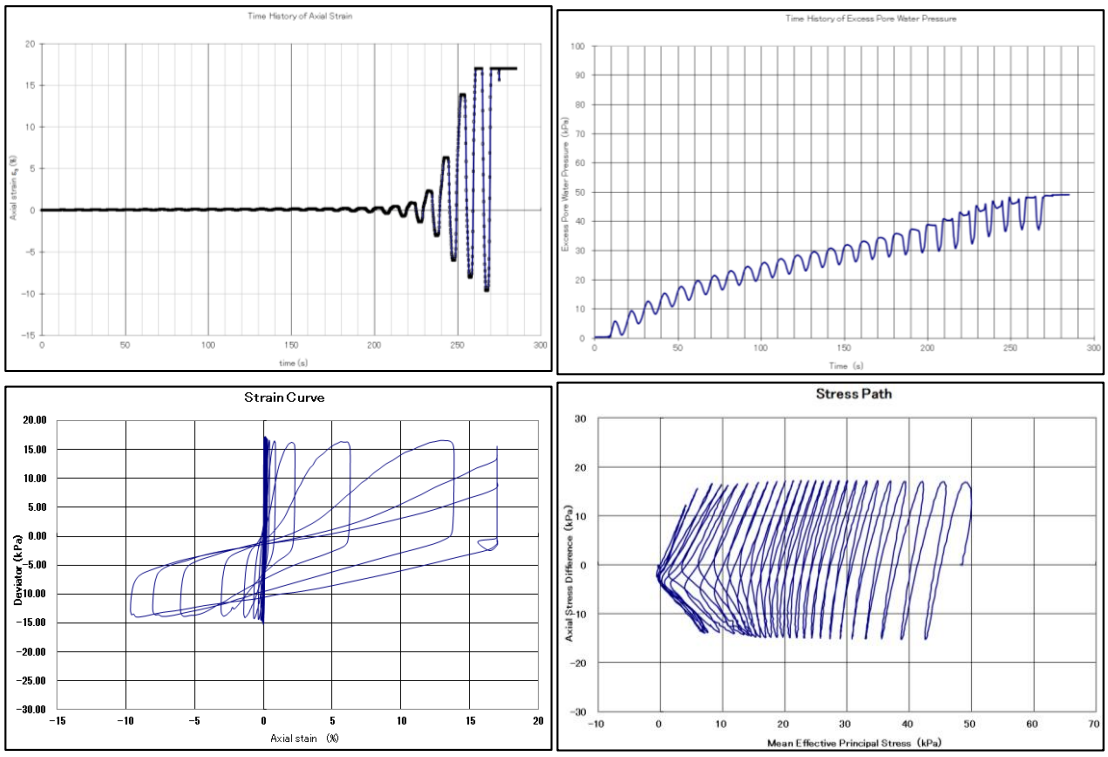

Figure A - 8. Liquefaction Test (Test M4-bauxite; saturated)

Test M5

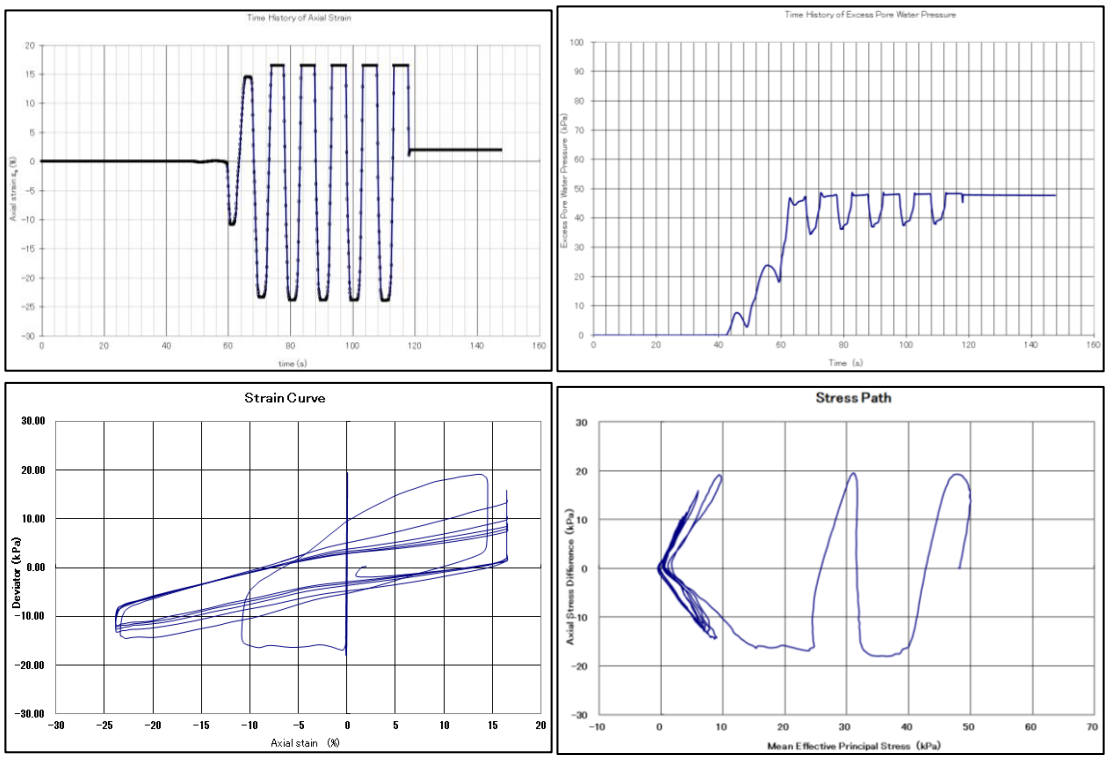

Figure A - 9. Liquefaction Test (Test M5-bauxite; saturated)

Test M6

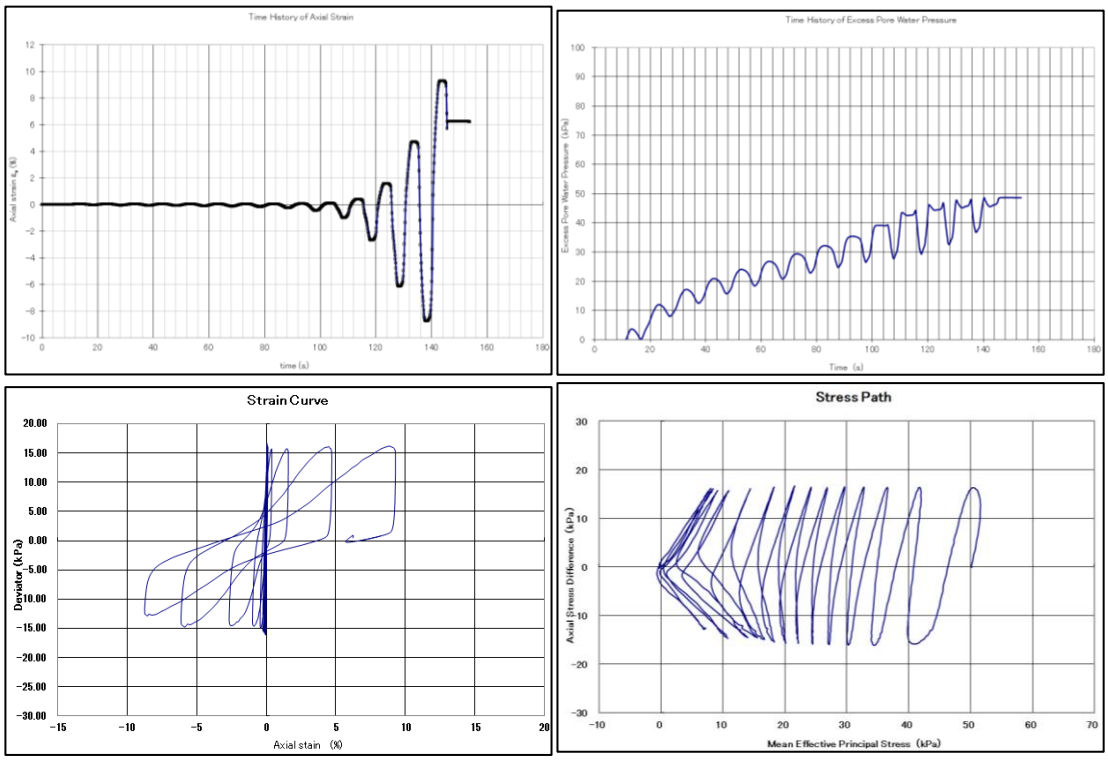

Figure A - 10. Liquefaction Test (Test M6-bauxite; saturated)

Table A-3. Saturated Test Conditions of Liquefaction Tests for bauxite, D_c = 88% (Dense)

Test No.	Initial Confining Pressure σ_o' (kPa)	Void ratio, e at σ_o'	Degree of Compaction, D_c (%)	B-value	Liquefaction	
					CSR	$N_{DA=5\%}$
D1	49.7	0.746	88.4	0.979	0.266	315.3
D2	48.8	0.749	88.4	0.980	0.356	5.0
D3	49.2	0.757	88.2	0.974	0.336	10.8
D4	49.6	0.760	88.1	0.975	0.297	28.9

Test D1

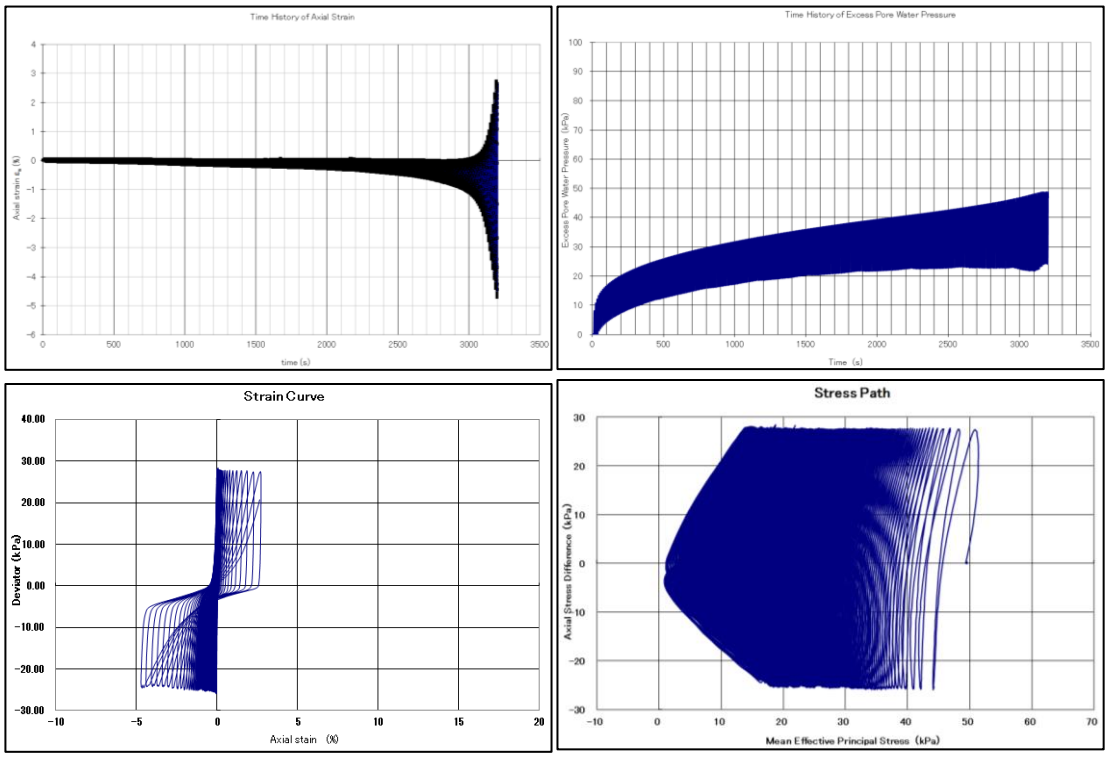

Figure A - 11. Liquefaction Test (Test D1-bauxite; saturated)

Test D2

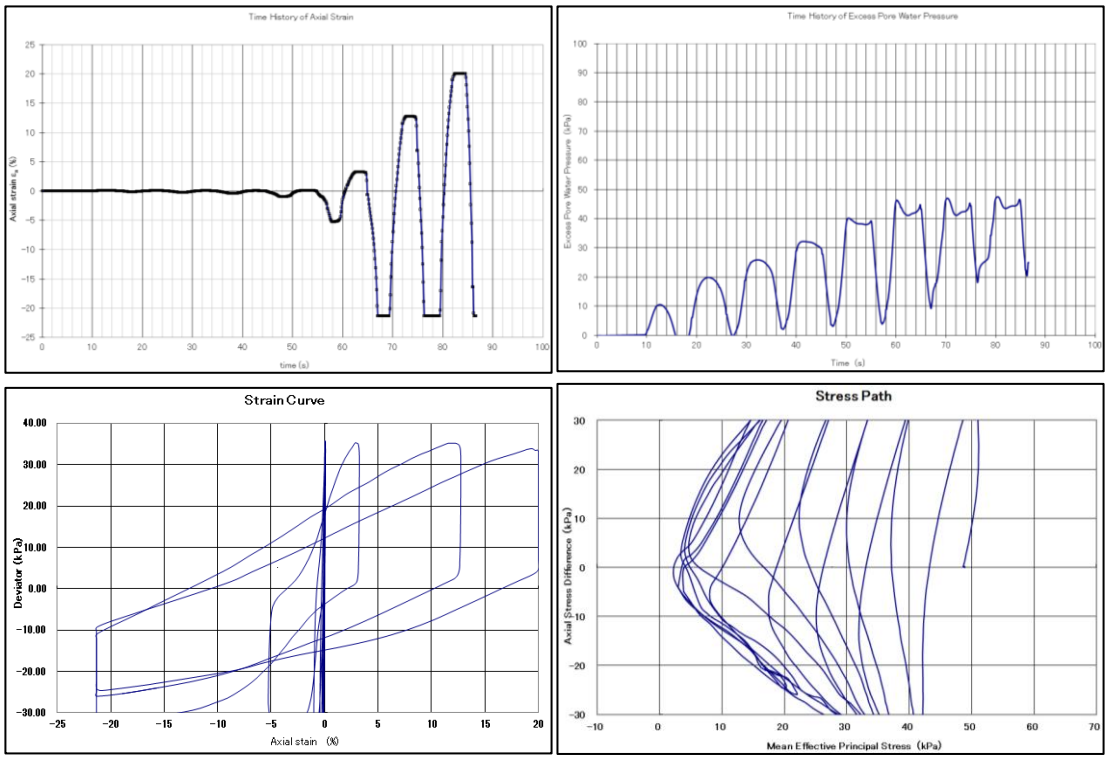

Figure A - 12. Liquefaction Test (Test D2-bauxite; saturated)

Test D3

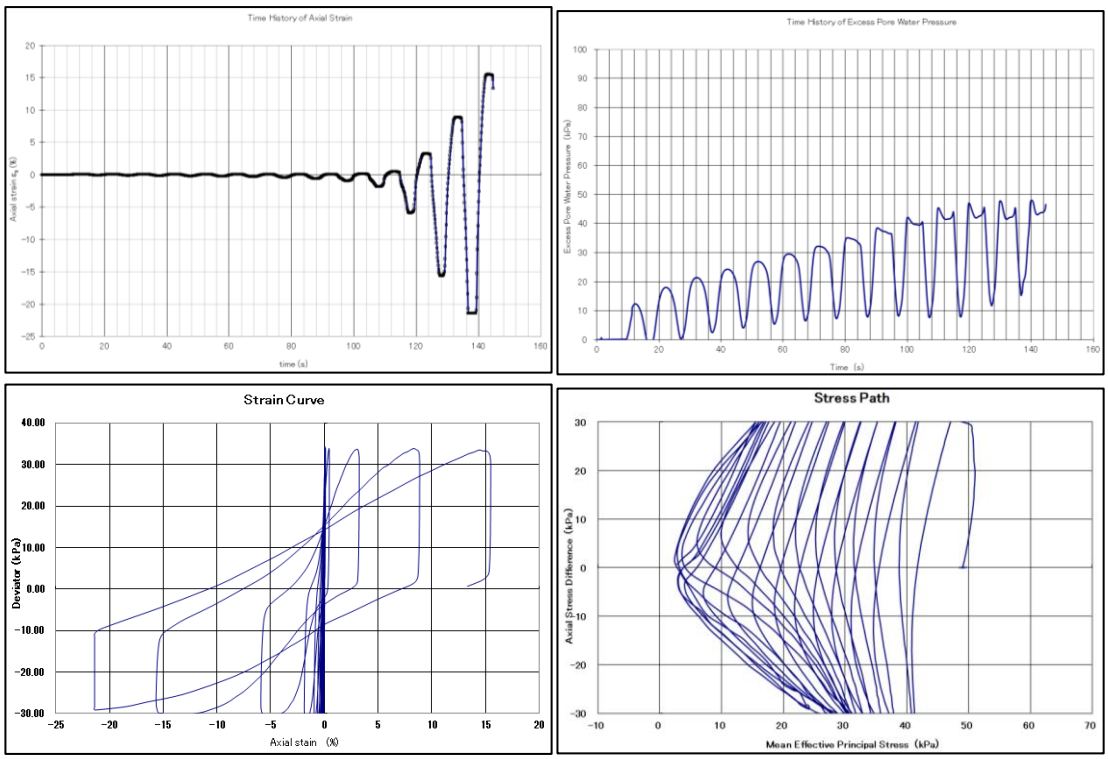

Figure A - 13. Liquefaction Test (Test D3-bauxite; saturated)

Test D4

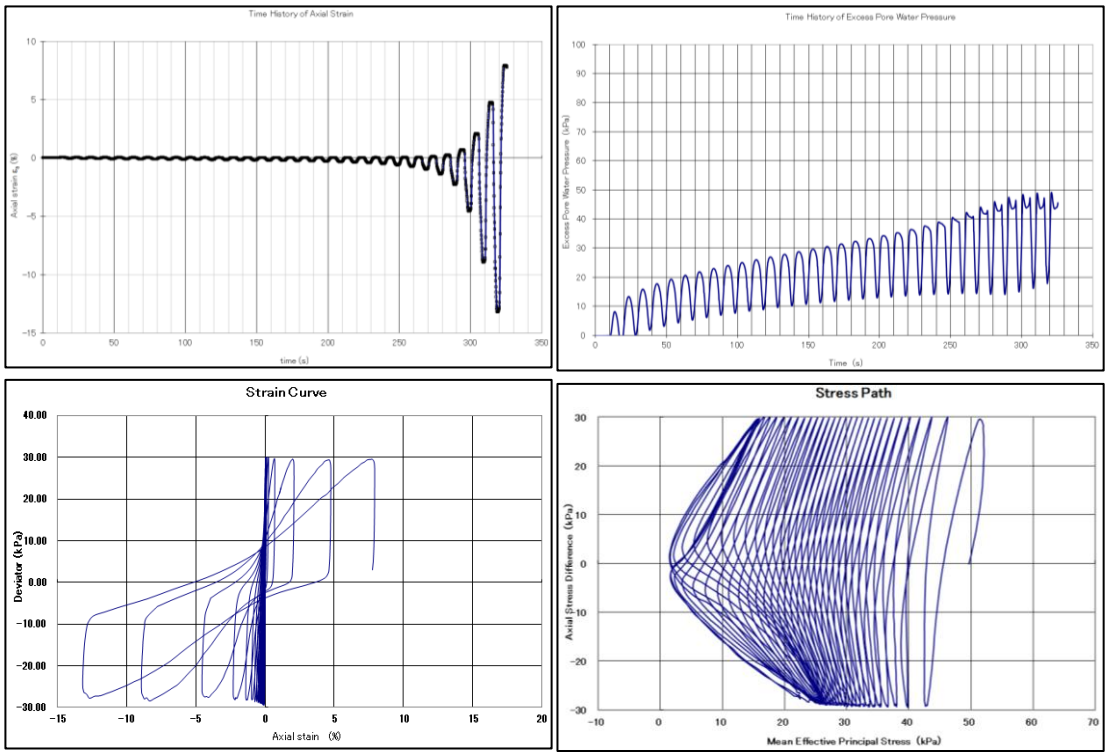

Figure A - 14. Liquefaction Test (Test D4-bauxite; saturated)

A-2 Liquefaction on Bauxite (Unsaturated)

Table A-4. Unsaturated Test Conditions of Liquefaction Tests for bauxite, S_r=84%

Test No.	Initial Confining Pressure σ_o' (kPa)	Degree of Saturation, S_r (%)	Degree of Compaction, D_c (%)	Liquefaction		
				CSR	$N_{DA=5\%}$	$N_{0.9\sigma o'}$
a1	49.1	80.7	78.5	0.284*	78.8	103.2
a2	50.0	84.3	78.5	0.322	0.8	3.0
a3	49.1	84.6	78.6	0.279	8.3	8.6
a4	51.1	75.5	78.5	0.277	22.9	27.0
a5	50.0	85.8	77.9	0.259	42.8	42.9
a6	49.8	84.4	78.9	0.268	17.8	18.4

*Initial CSR was 0.230. At 400 cycles, specimen has not yet liquefied. Air was diffused and test was continued using the same specimen

Test a1

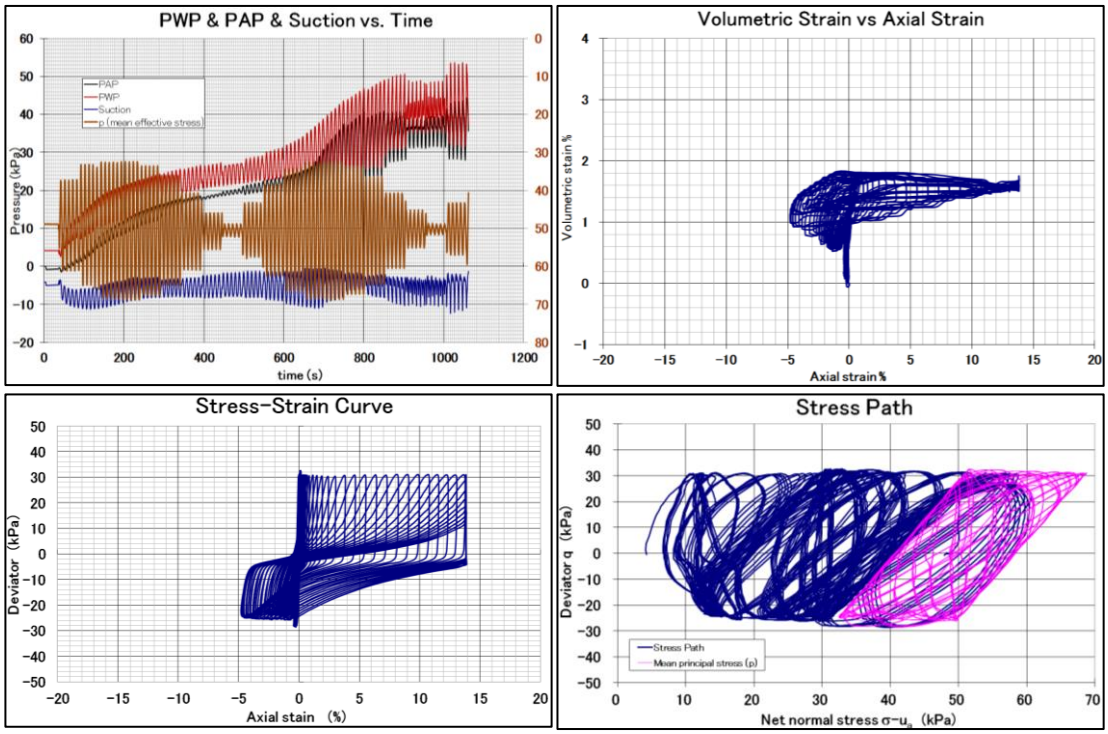

Figure A - 15. Liquefaction Test (Test a1-bauxite; unsaturated)

Test a2

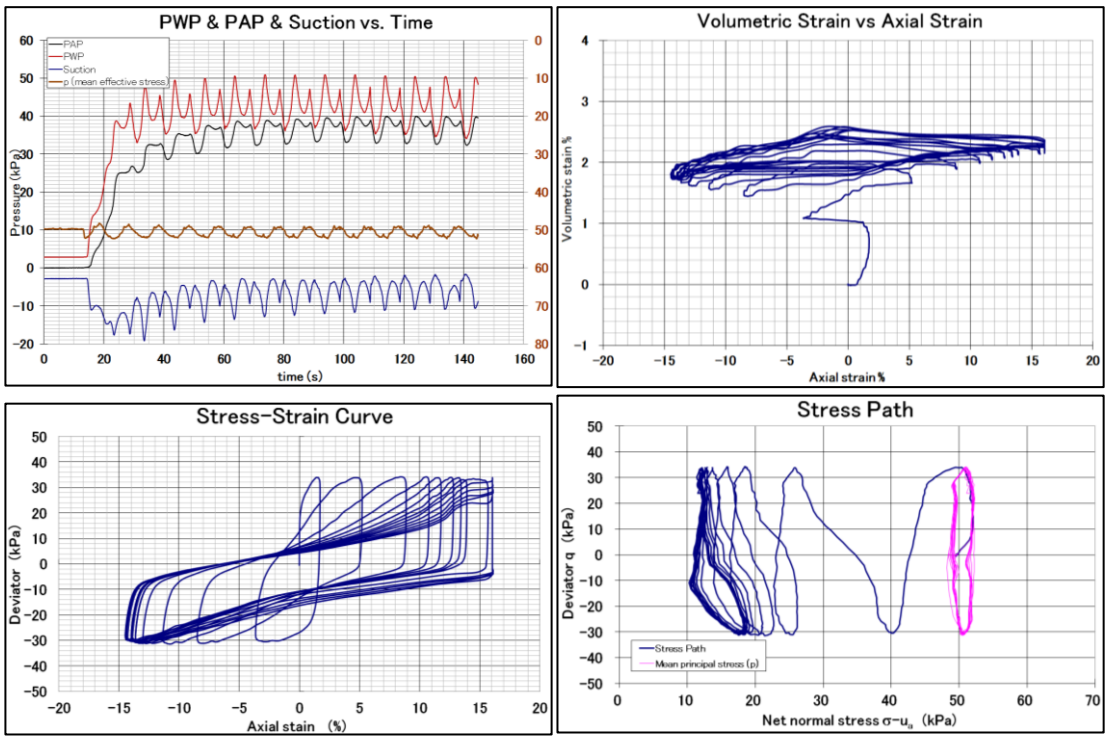

Figure A - 16. Liquefaction Test (Test a2-bauxite; unsaturated)

Test a3

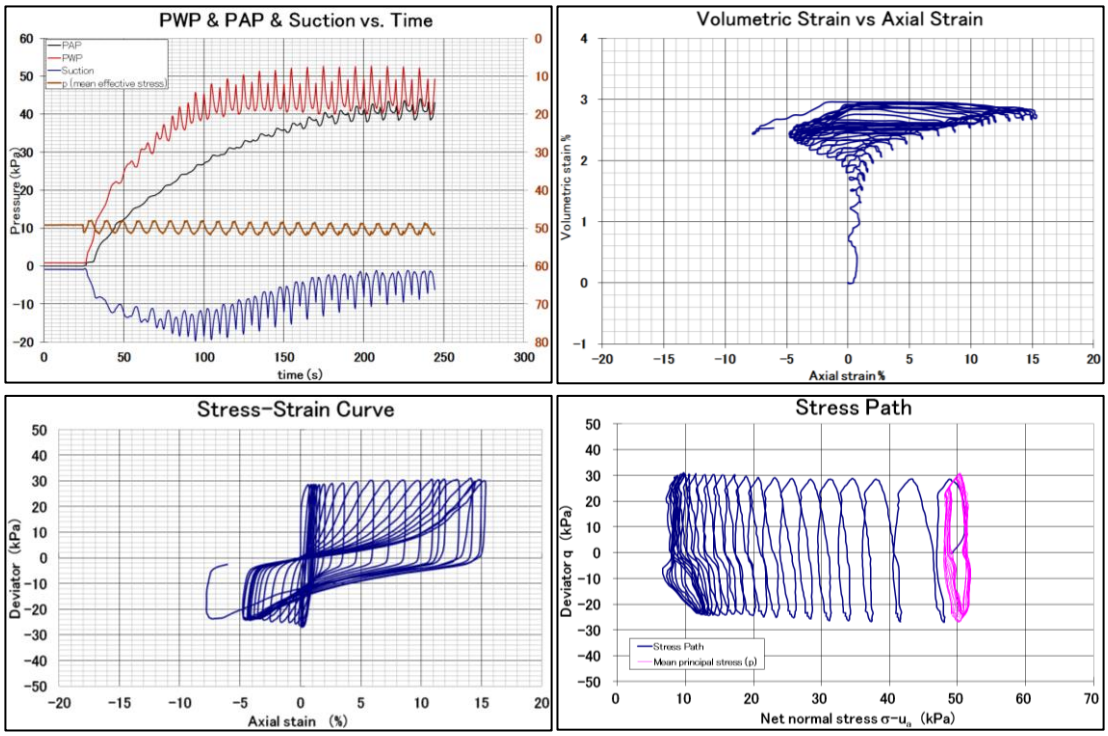

Figure A - 17. Liquefaction Test (Test a3-bauxite; unsaturated)

Test a4

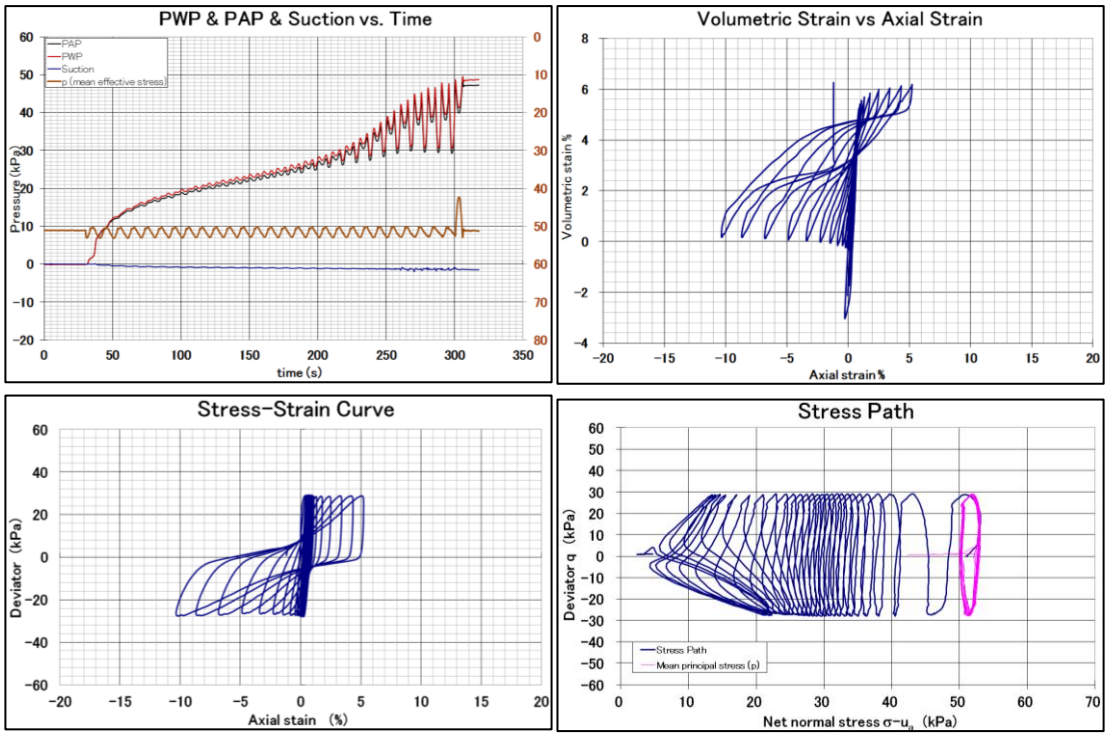

Figure A - 18. Liquefaction Test (Test a4-bauxite; unsaturated)

Test a5

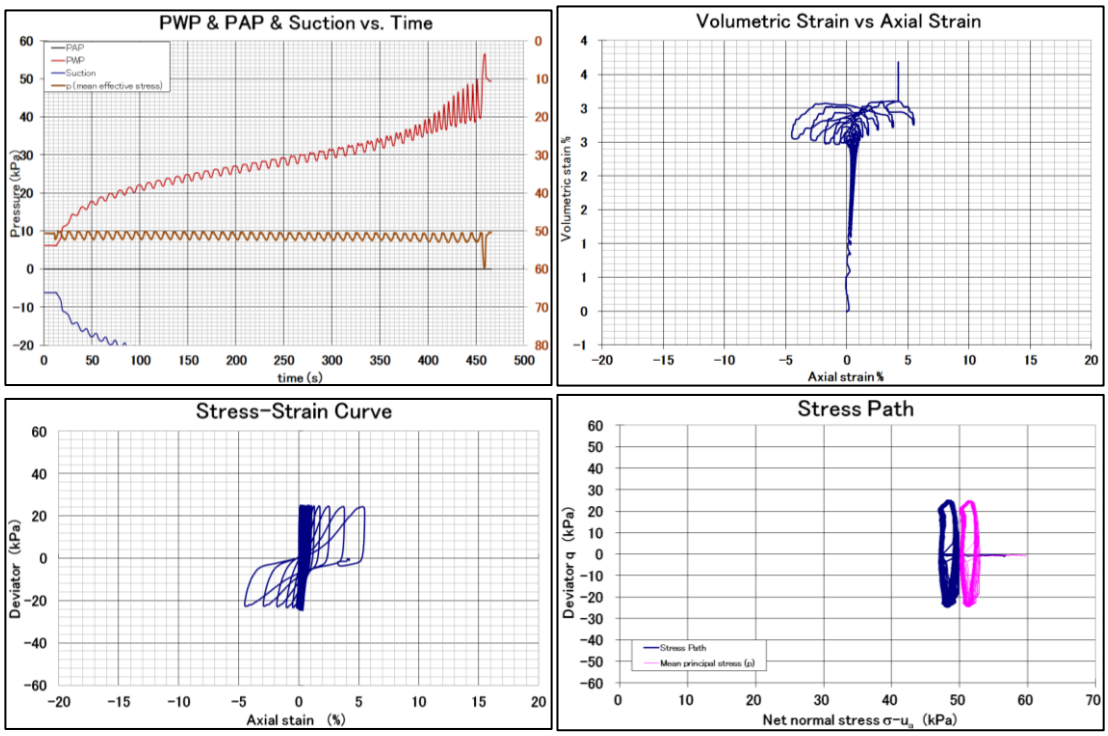

Figure A - 19. Liquefaction Test (Test a5-bauxite; unsaturated)

Test a6

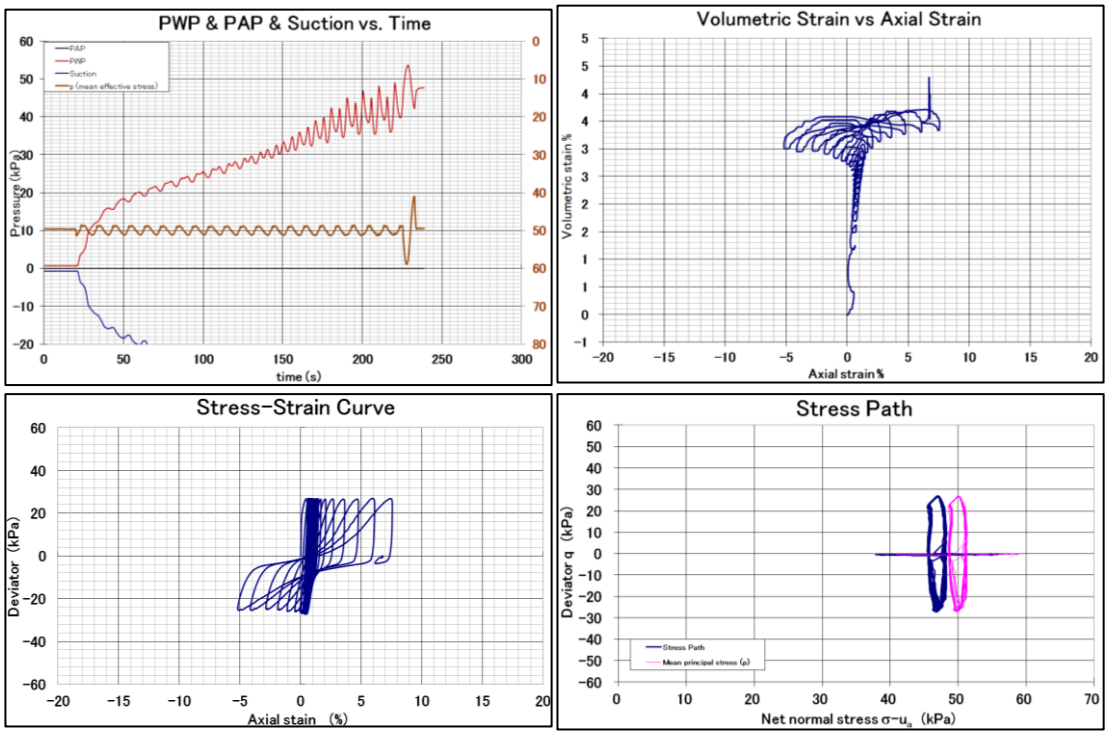

Figure A - 20. Liquefaction Test (Test a6-bauxite; unsaturated)

Table A-5. Unsaturated Test Conditions of Liquefaction Tests for bauxite, S_r=58%

Test No.	Initial Confining Pressure σ_o' (kPa)	Degree of Saturation, S_r (%)	Degree of Compaction, D_c (%)	Liquefaction		
				CSR	$N_{DA=5\%}$	$N_{0.9\sigma o'}$
b1	49.9	56.9	81.0	0.368	5.8	21.0
b2	50.8	61.5	80.8	0.358	5.1	12.0
b3	49.7	57.9	81.4	0.353	113.2	149.0
b4	51.3	56.1	81.0	0.361	37.3	78.4
b5	50.0	56.2	80.1	0.398	12.6	58.0

Test b1

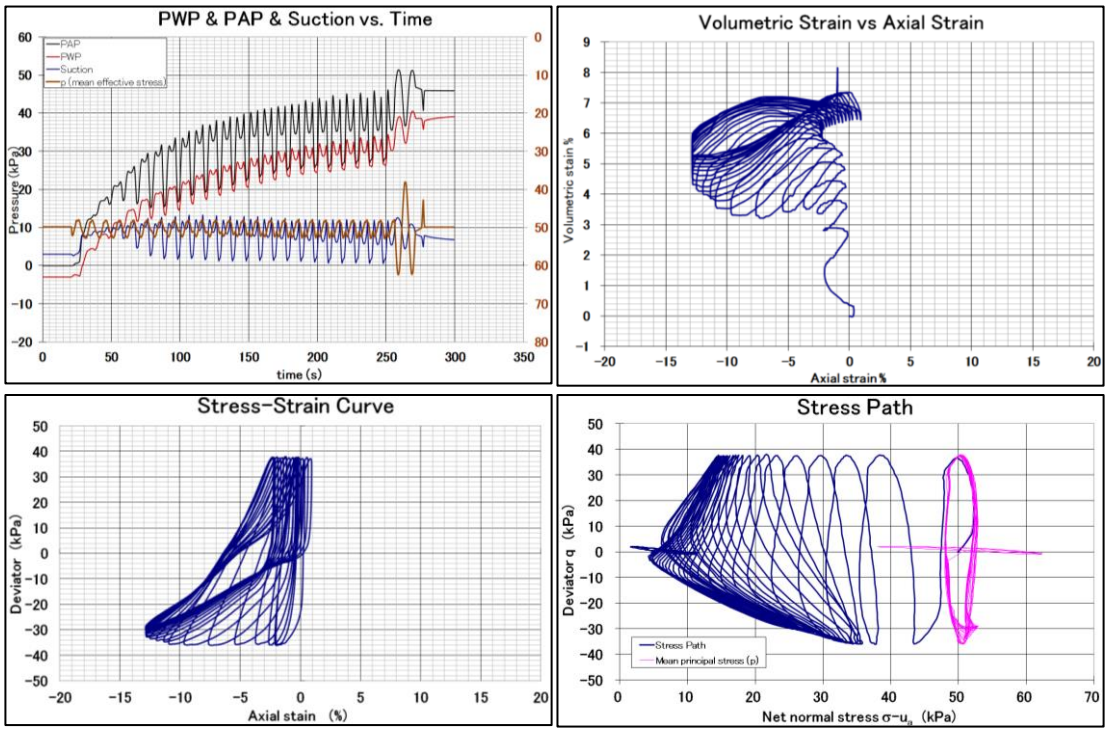

Figure A - 21. Liquefaction Test (Test b1-bauxite; unsaturated)

Test b2

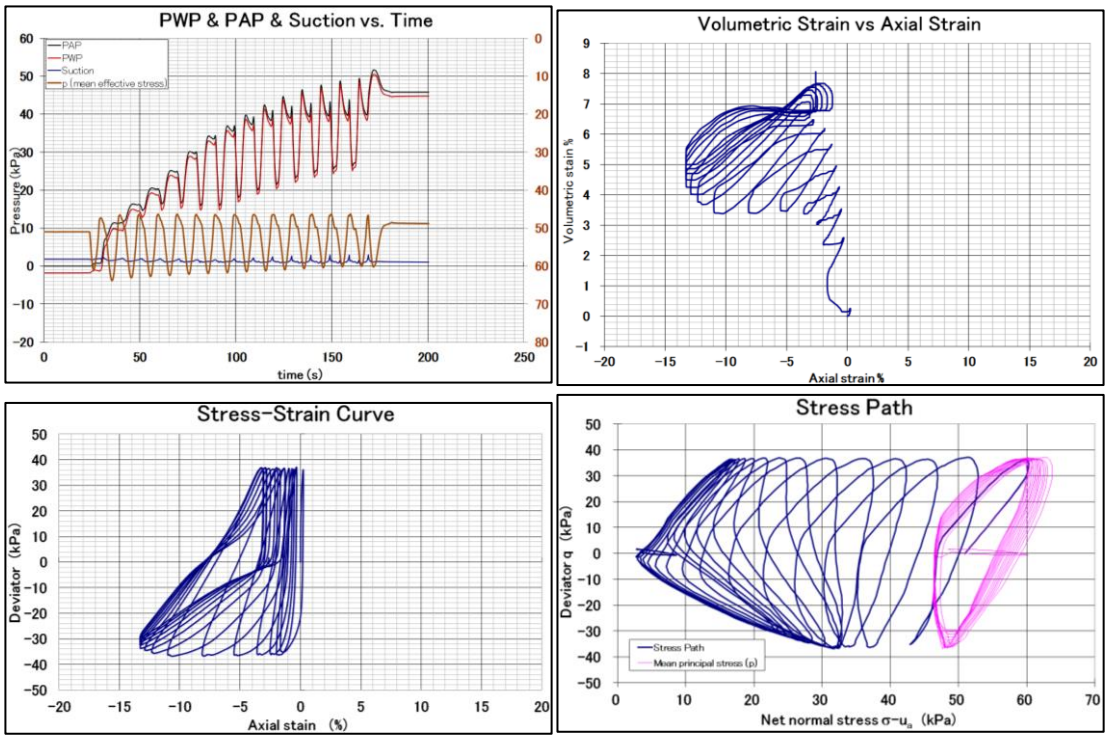

Figure A - 22. Liquefaction Test (Test b2-bauxite; unsaturated)

Test b3

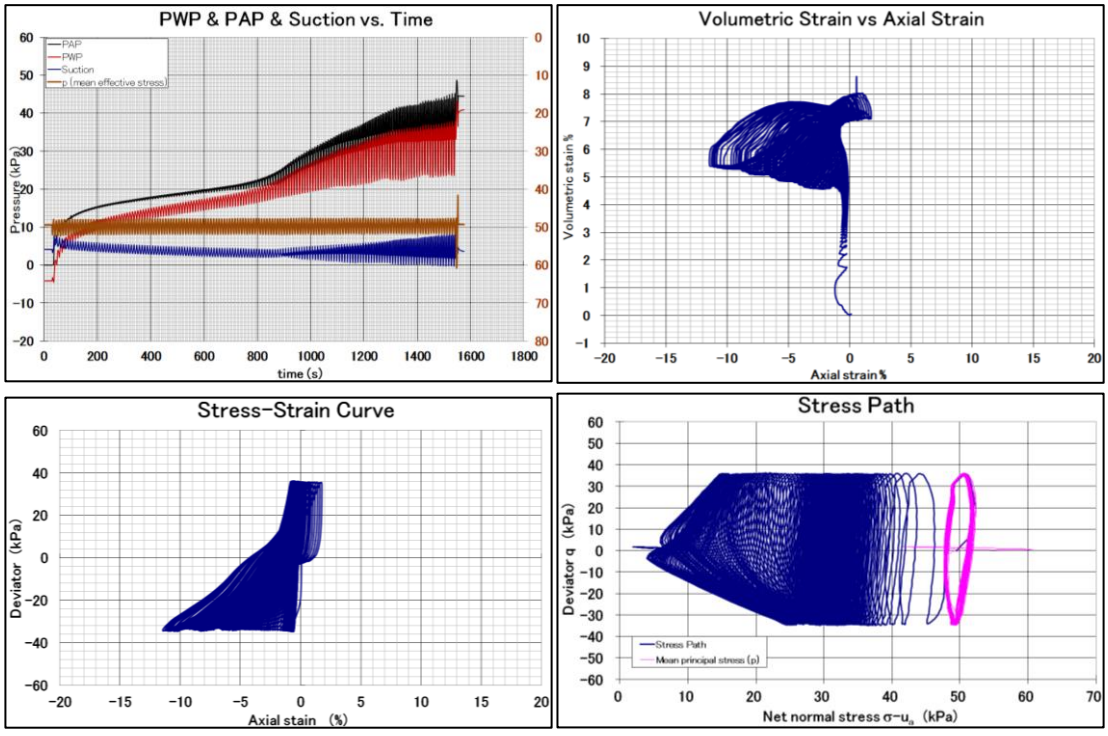

Figure A - 23. Liquefaction Test (Test b3-bauxite; unsaturated)

Test b4

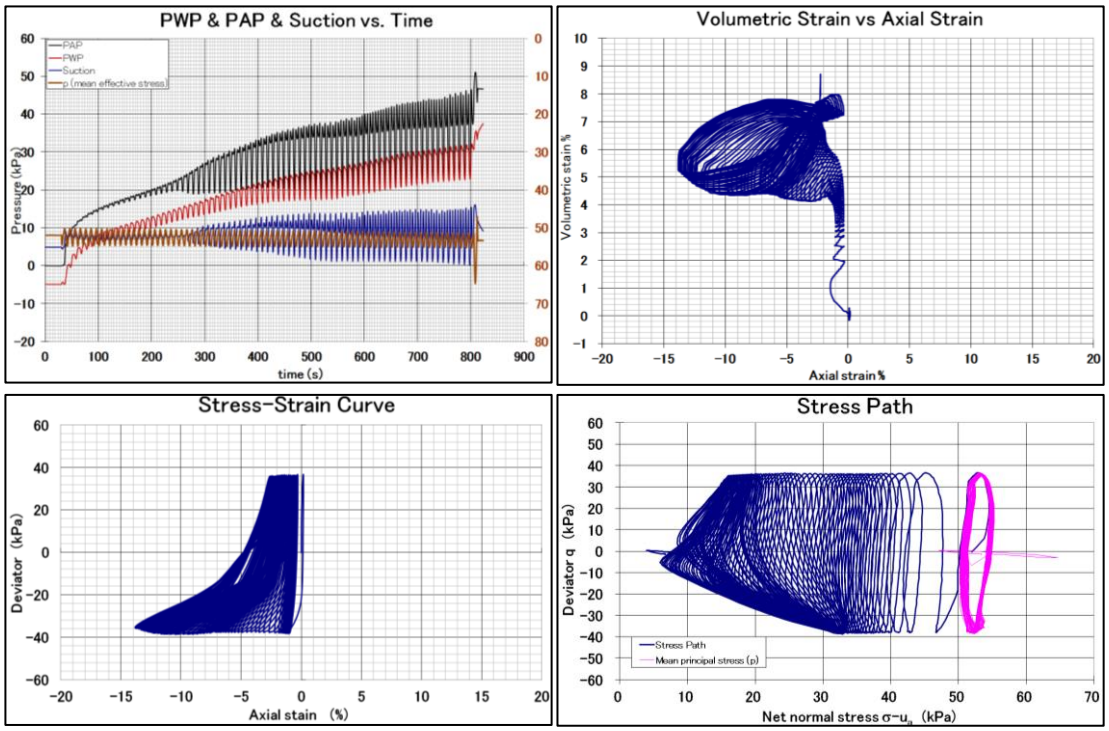

Figure A - 24. Liquefaction Test (Test b4-bauxite; unsaturated)

Test b5

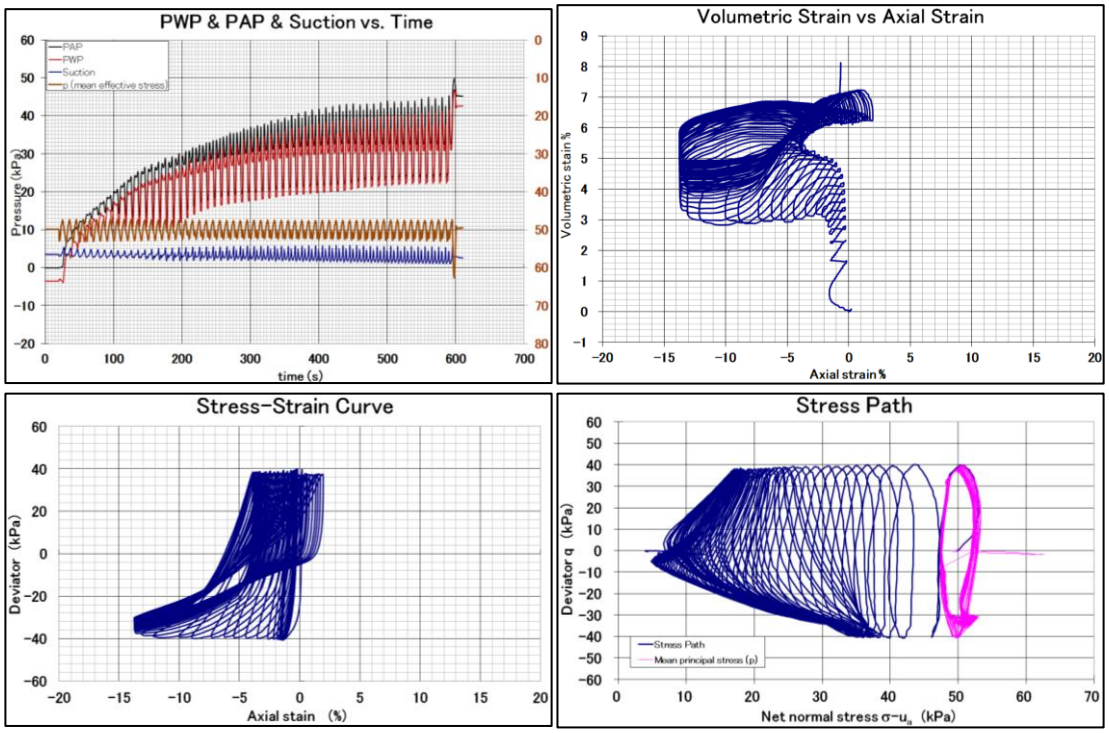

Figure A - 25. Liquefaction Test (Test b5-bauxite; unsaturated)

Appendix B: Permeability Tests and SWRC Tests

Contents

B-1. Permeability Tests on Bauxite (Saturated)

Table B-1. Test Conditions of Permeability Tests using Triaxial Apparatus (bauxite-saturated)

Test No.	D_c (%)	B-value	Total Head supplied, H_{tot} (cm)	σ_c (kPa)	Test Conditions
1	77.8	0.971	5, 10, 15, 20, 35, 50, 65	Loading: 30, 60, 100 Unloading: 60, 30, 25, 20, 15, 10, 5	Permeability test using local pin-type sensor (long and short)
2	78.0	0.959			*k* test using local pin-type sensor (long only) with Image analysis performed
3	78.0	0.974			(1) same as test 2 (2) rubber membrane stretched
4	79.1	0.980			(1) same as test 2 (2) rubber membrane was loose

Test 1

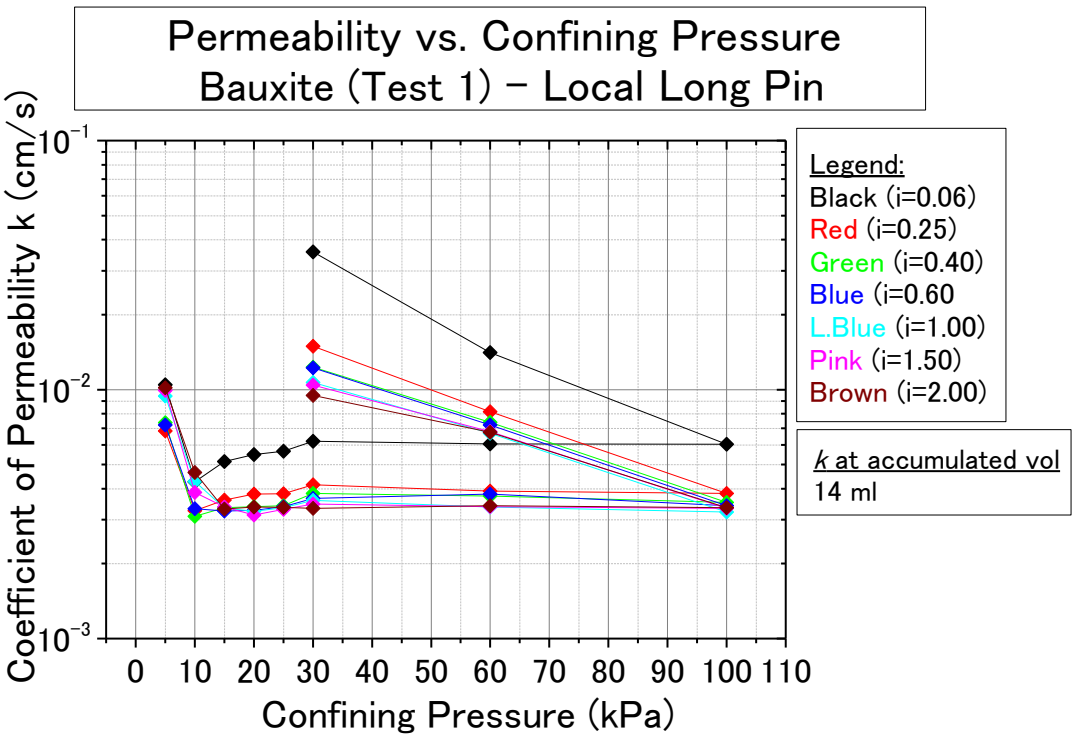

Figure B - 1. Permeability Test (Test 1-bauxite; Saturated)

Test 2

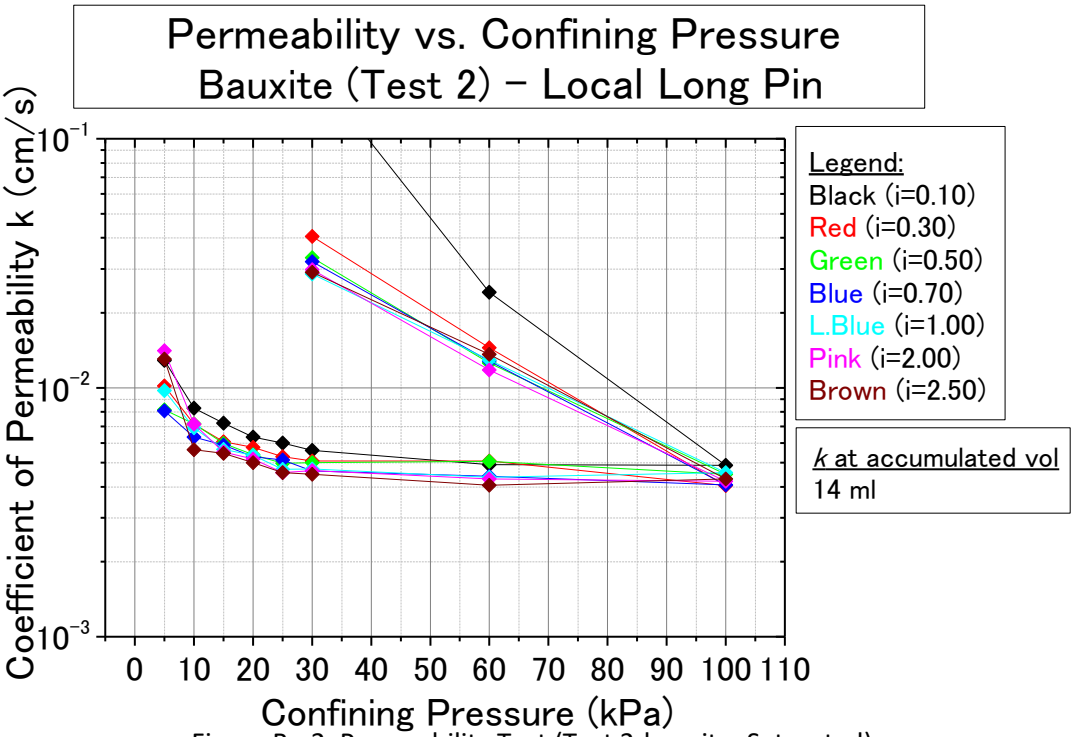

Figure B - 2. Permeability Test (Test 2-bauxite; Saturated)

Test 3

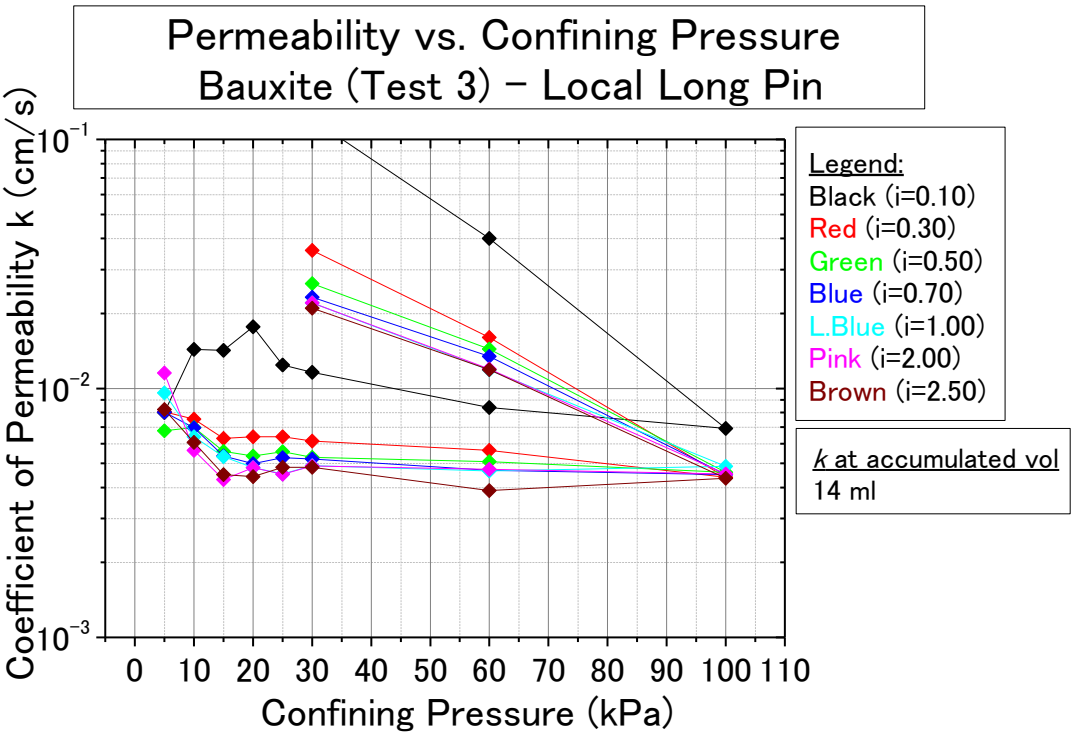

Figure B - 3. Permeability Test (Test 3-bauxite; Saturated)

Test 4

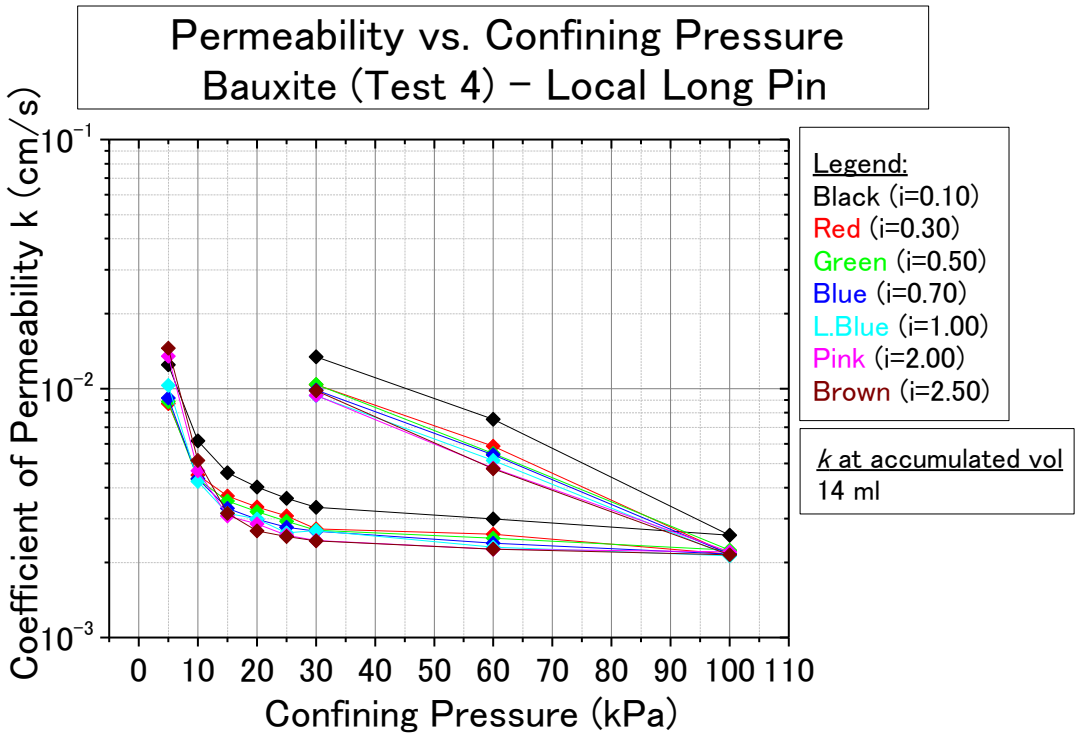

Figure B - 4. Permeability Test (Test 4-bauxite; Saturated)

Tests 1-4

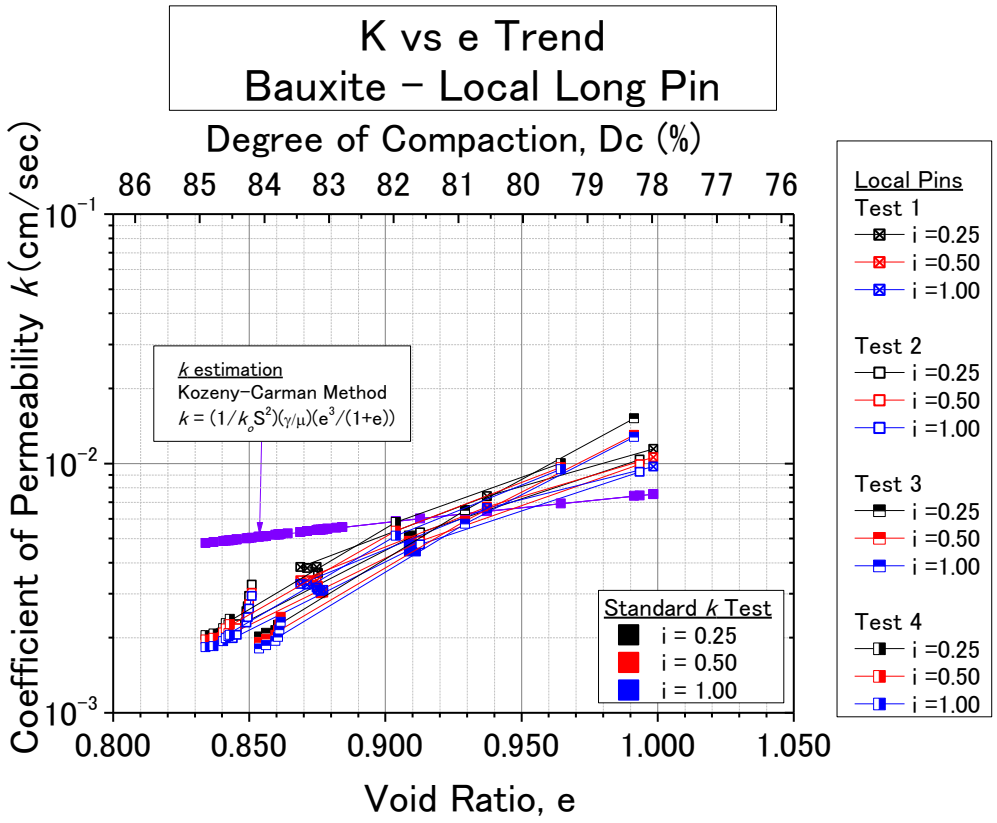

Figure B - 5. Permeability Test (Test 1 to 4-bauxite; Saturated)

B-2. Permeability Tests on Inagi Sand (Saturated)

Table B-2. Test Conditions of Permeability Tests using Triaxial Apparatus (Inagi-saturated)

Test No.	D_c (%)	B-value	Total Head supplied, H_{tot} (cm)	σ_c (kPa)	Test Conditions
1	72.5	0.969	5, 20, 35, 50, 65	Unloading: 100, 60, 30, 15	Local pin-type sensor (long only)
2	72.6	0.968			
3	69.2	0.946	5, 10, 15, 20, 35, 50, 65	Loading: 30, 60, 100 Unloading: 60, 30, 25, 20, 15, 10, 5	Local pin-type sensor (long and short)
4	70.6	0.986			

Test 1

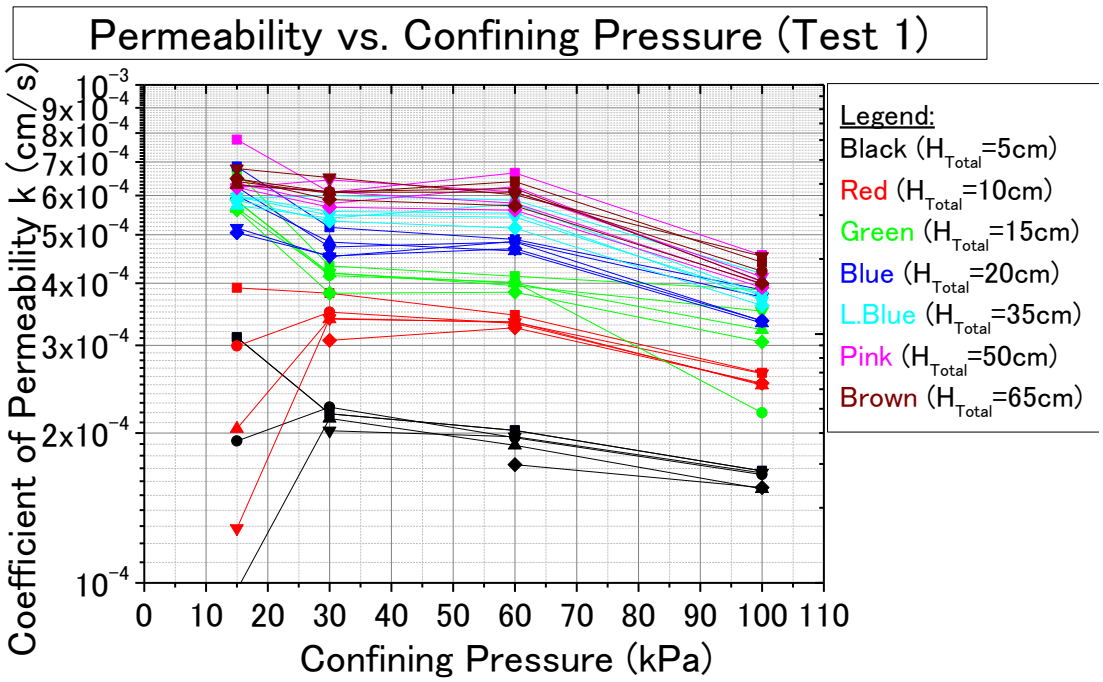

Figure B - 6. Permeability Test (Test 1-Inagi sand; Saturated)

Test 2

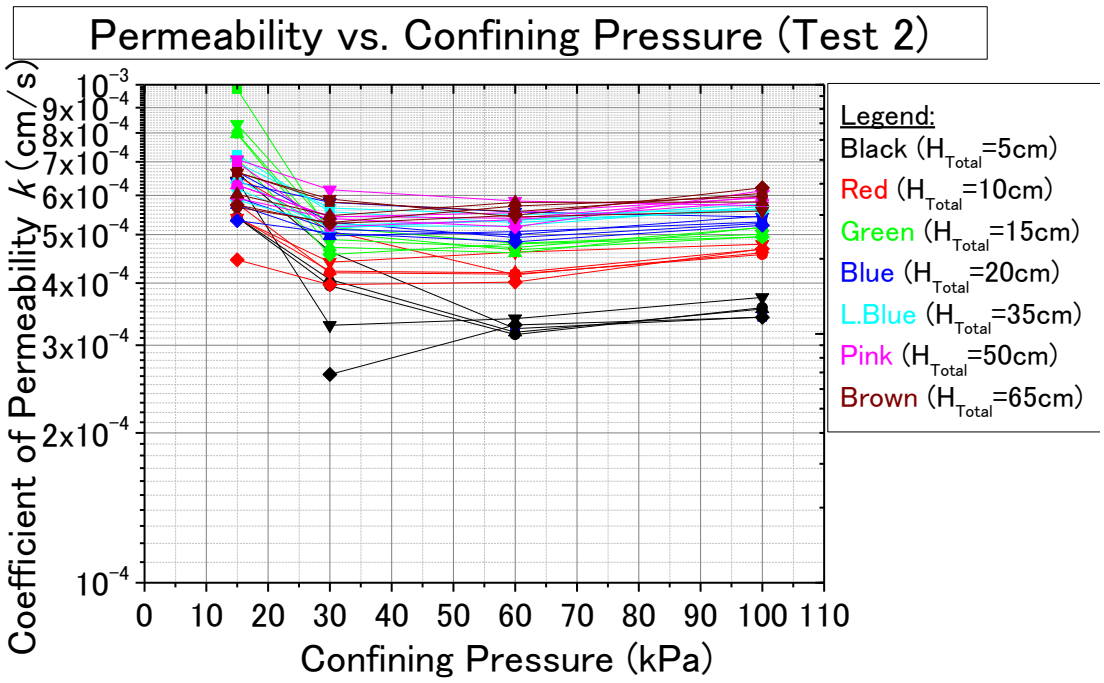

Figure B - 7. Permeability Test (Test 2-Inagi sand; Saturated)

Test 3

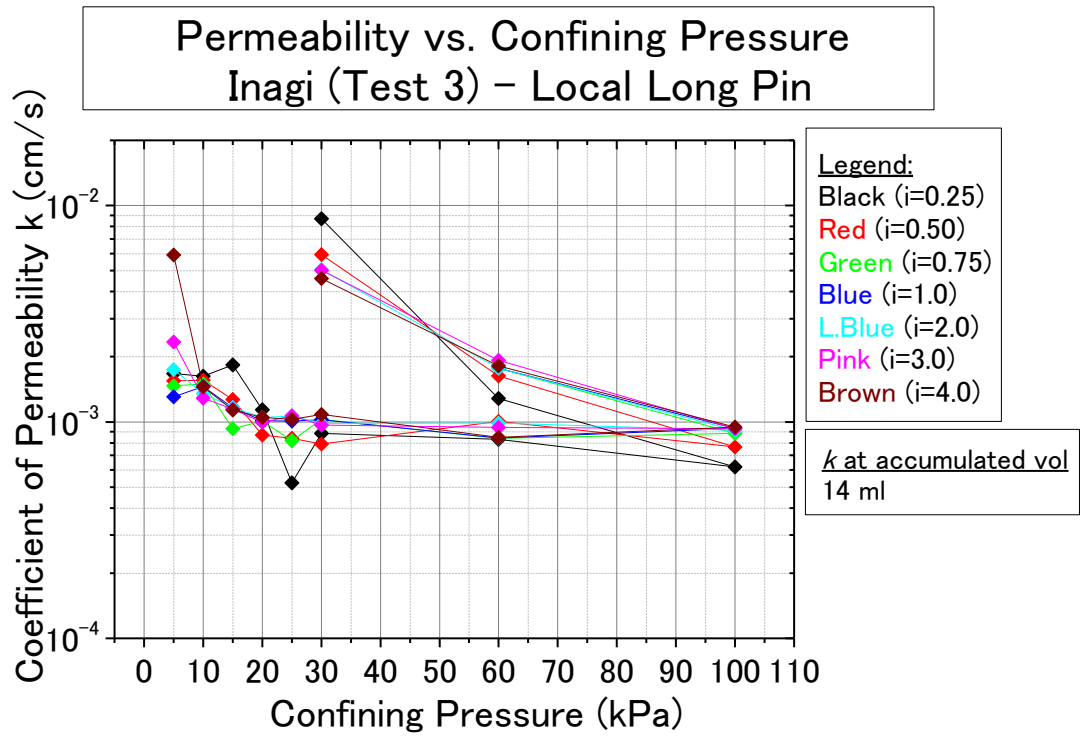

Figure B - 8. Permeability Test (Test 3-Inagi sand; Saturated)

Test 4

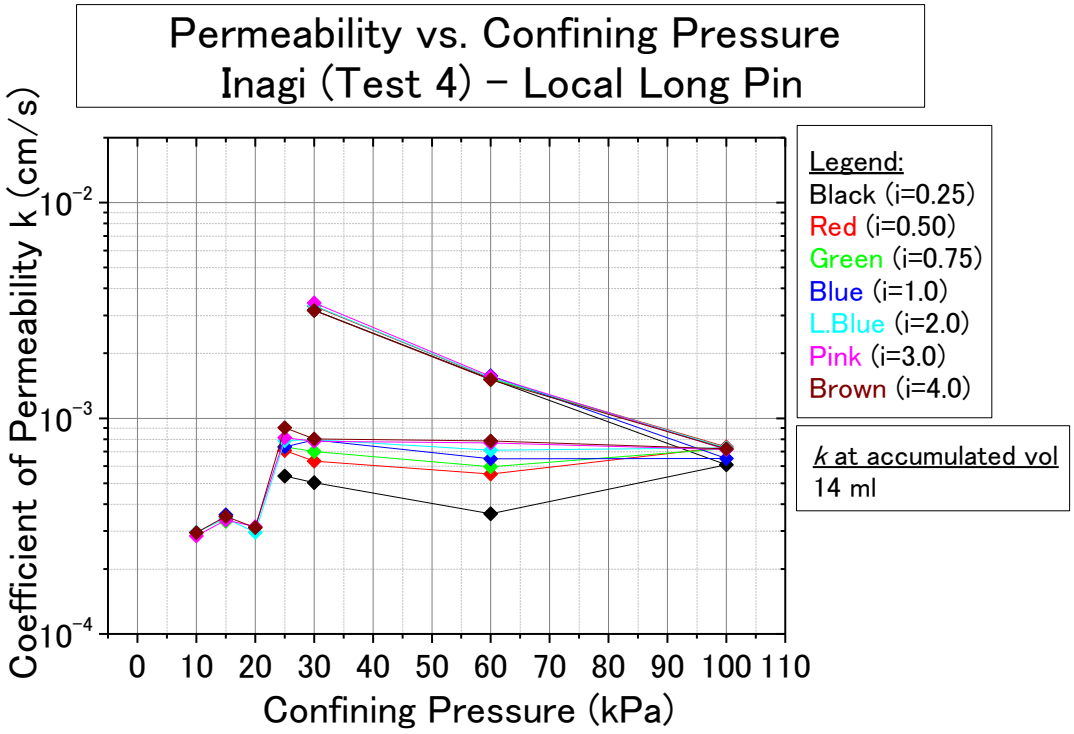

Figure B - 9. Permeability Test (Test 4-Inagi sand; Saturated)

Test 3-4

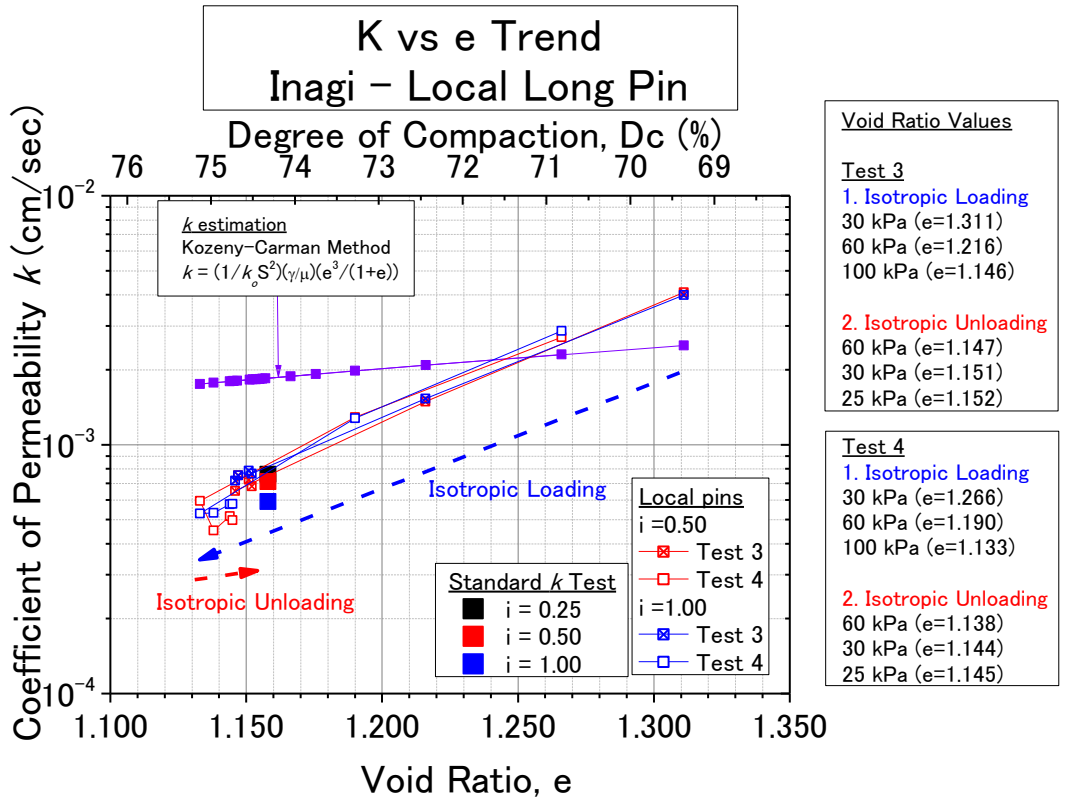

Figure B - 10. Permeability Test (Test 3 to 4-Inagi sand; Saturated)

B-3. Permeability Tests on Toyoura Sand (Saturated)

Table B-3. Test Conditions of Permeability Tests using Triaxial Apparatus (Toyoura-saturated)

Test No.	D_r (%)	B-value	Total Head supplied, H_{tot} (cm)	σ_c (kPa)	Test Conditions
1	78.9	0.971	5, 20, 35, 50, 65	100	Local pin-type sensor (long only)
2	79.3	0.971			
3	74.4	0.953			
4	69.6	0.950	5, 10, 15, 20, 35, 50, 65	Loading: 30, 60, 100 Unloading: 60, 30, 25, 20, 15, 10, 5	Local pin-type sensor (long and short)
5	78.6	0.946			
6	65.2	0.954			

Test 1 and 2

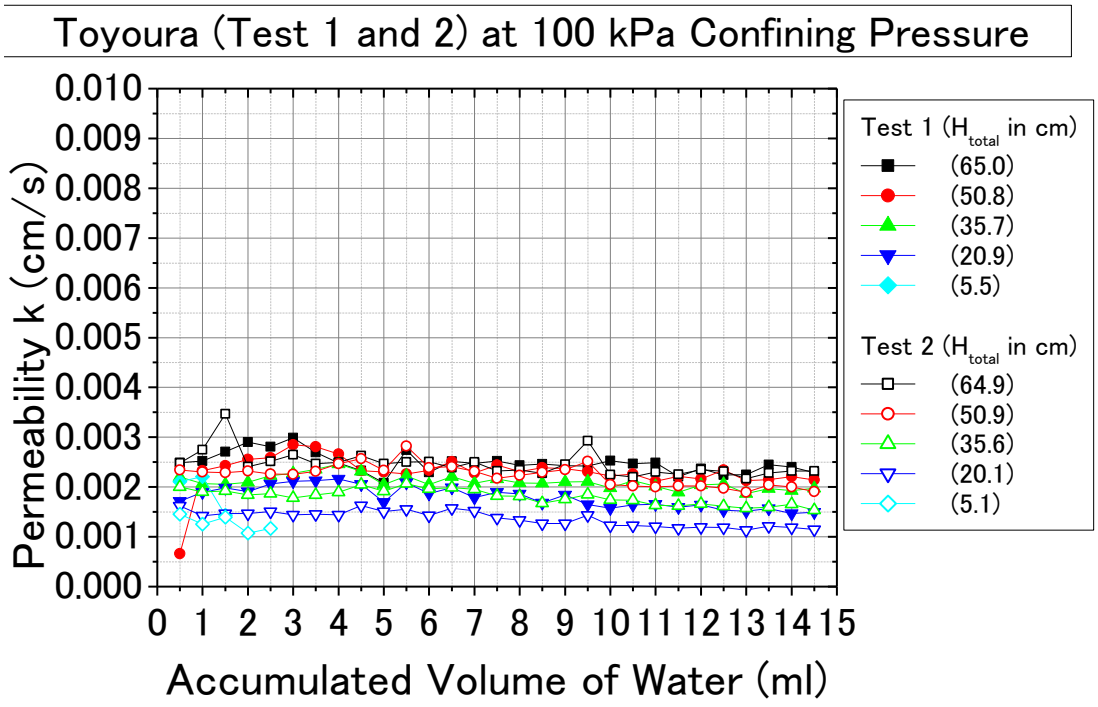

Figure B - 11. Permeability Test (Test 1 to 2-Toyoura sand; Saturated)

Test 3

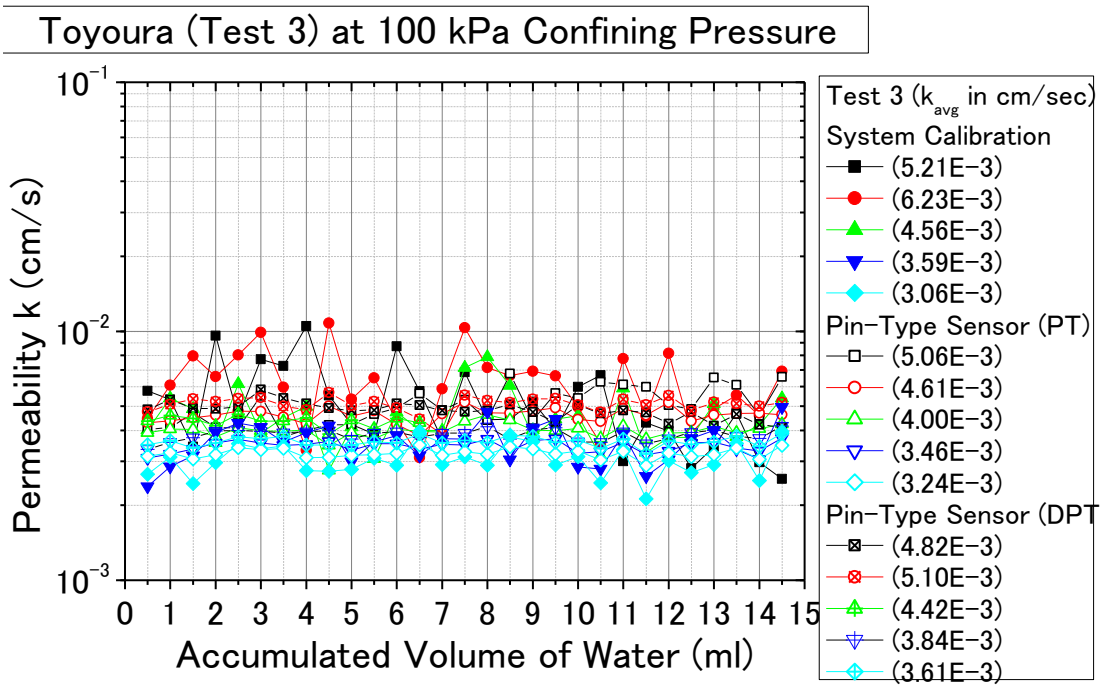

Figure B - 12. Permeability Test (Test 3-Toyoura sand; Saturated)

Test 4

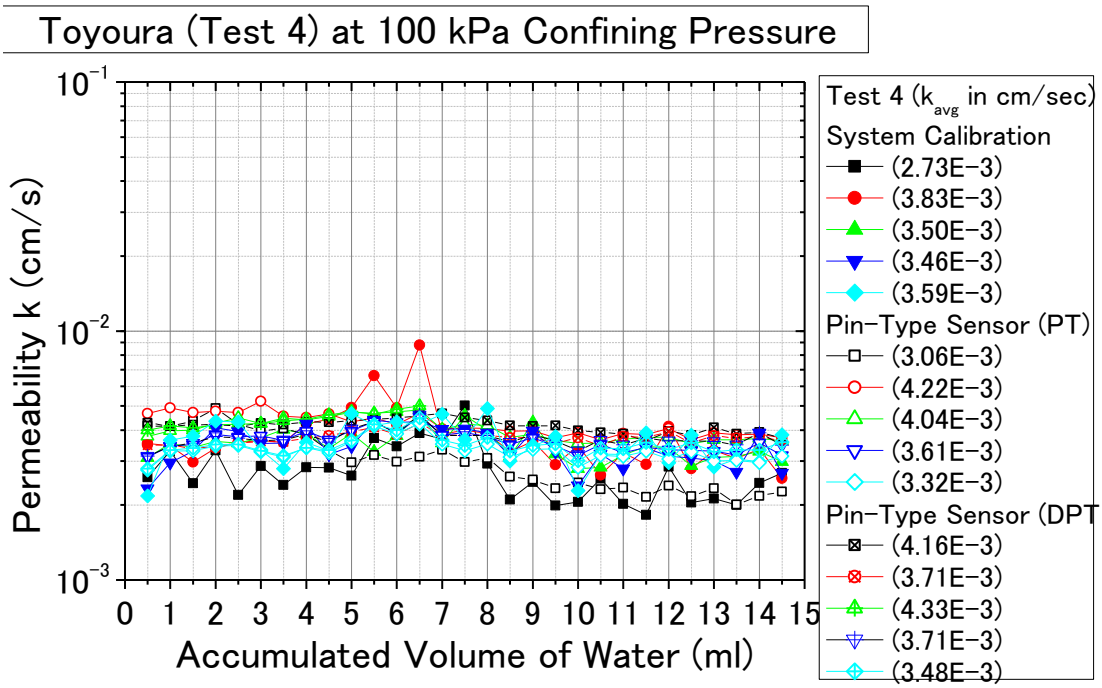

Figure B - 13. Permeability Test (Test 4-Toyoura sand; Saturated)

Test 5

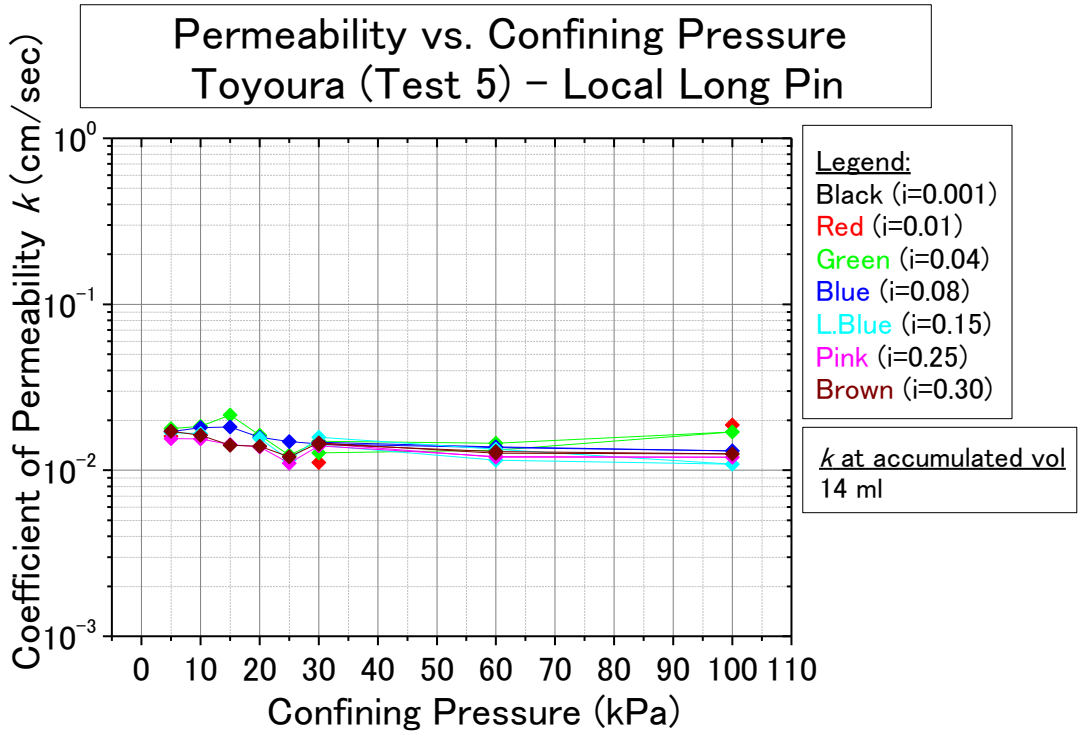

Figure B - 14. Permeability Test (Test 5-Toyoura sand; Saturated)

Test 6

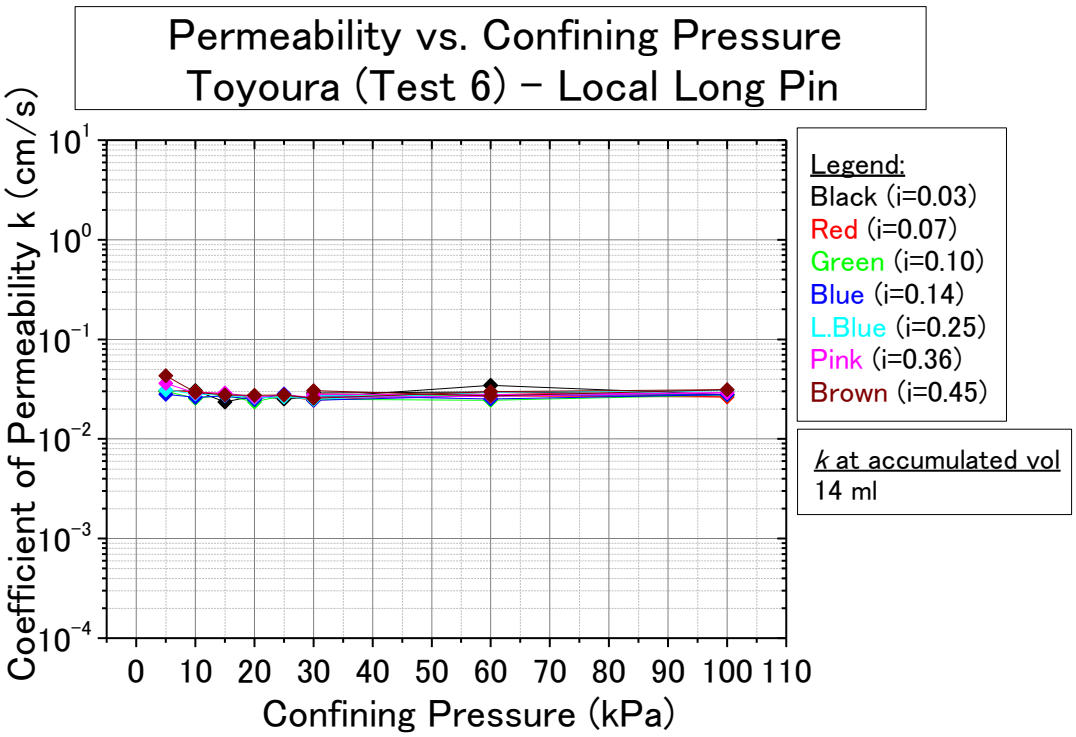

Figure B - 15. Permeability Test (Test 6-Toyoura sand; Saturated)

Test 5 and 6

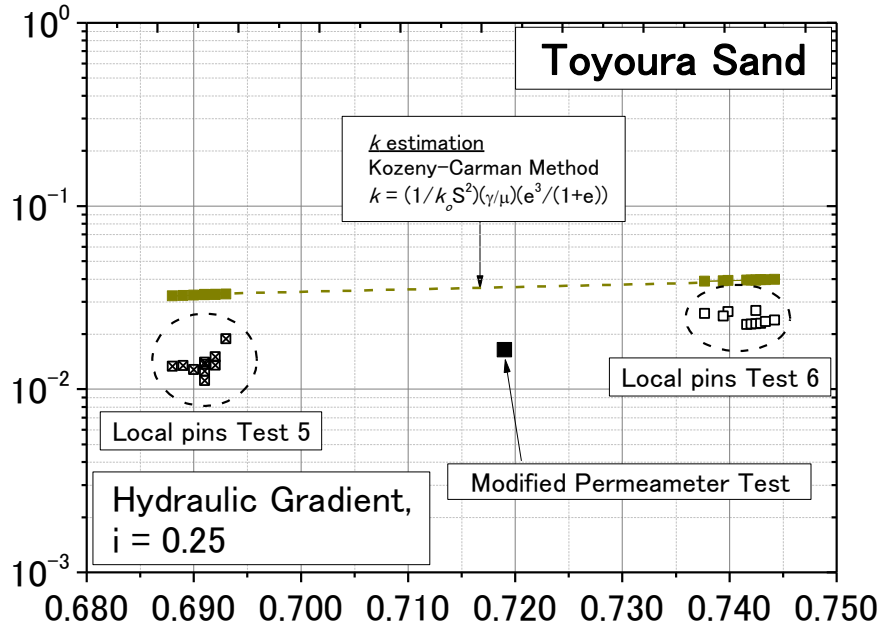

Figure B - 16. Permeability Test (Test 5 and 6-Toyoura sand; Saturated)

B-4. Permeability Test on Bauxite (Unsaturated)

Table B-4. Test Conditions of *k* Tests using Triaxial Apparatus (bauxite-unsaturated)

Test	D_c (%)	Case	Initial degree of saturation Sr_{init} (%)	Final degree of saturation Sr_{final} (%)	Suction measured by membrane filter (kPa)	Total head (cm) supplied to the specimen	Total accumulated volume (ml) (approximate)
1	80.0	Medium Dense	80	-	-	-	-
2	80.1		75	-	-	-	-
3	80.1		75	-	-	-	-
4	81.1		65	64.2	2.5	55	50
5	80.2			66.2	1.0	60	75
6	80.3			68.2	1.7	52	50
7	80.2			68.1	2.0	53	50
8	79.8		50	57.8	13.4	82	50
9	79.9		52	58.2	10.2	77	50
			70	59.5	-	77	40
			90	59.8	-	77	35
10	79.8		50	85	-	80	25
11	79.7		-	100	-	60	50
12	80.0		43	51.1	34.7	402	75
13	79.8		72	77.9	0.3	35	55
14	67.7	Loose	45	48.8	2.1	62	35
15	71.6		52	52.3	0.8	60	35
16	70.4		-	100	-	35	25
17	88.8	Dense	58	64.5	13.8	85	45
18	88.8		75	74.1	2.4	64	45
19	89.1		-	100	-	35	25
20	88.7		52	57.1	15.1	85	25

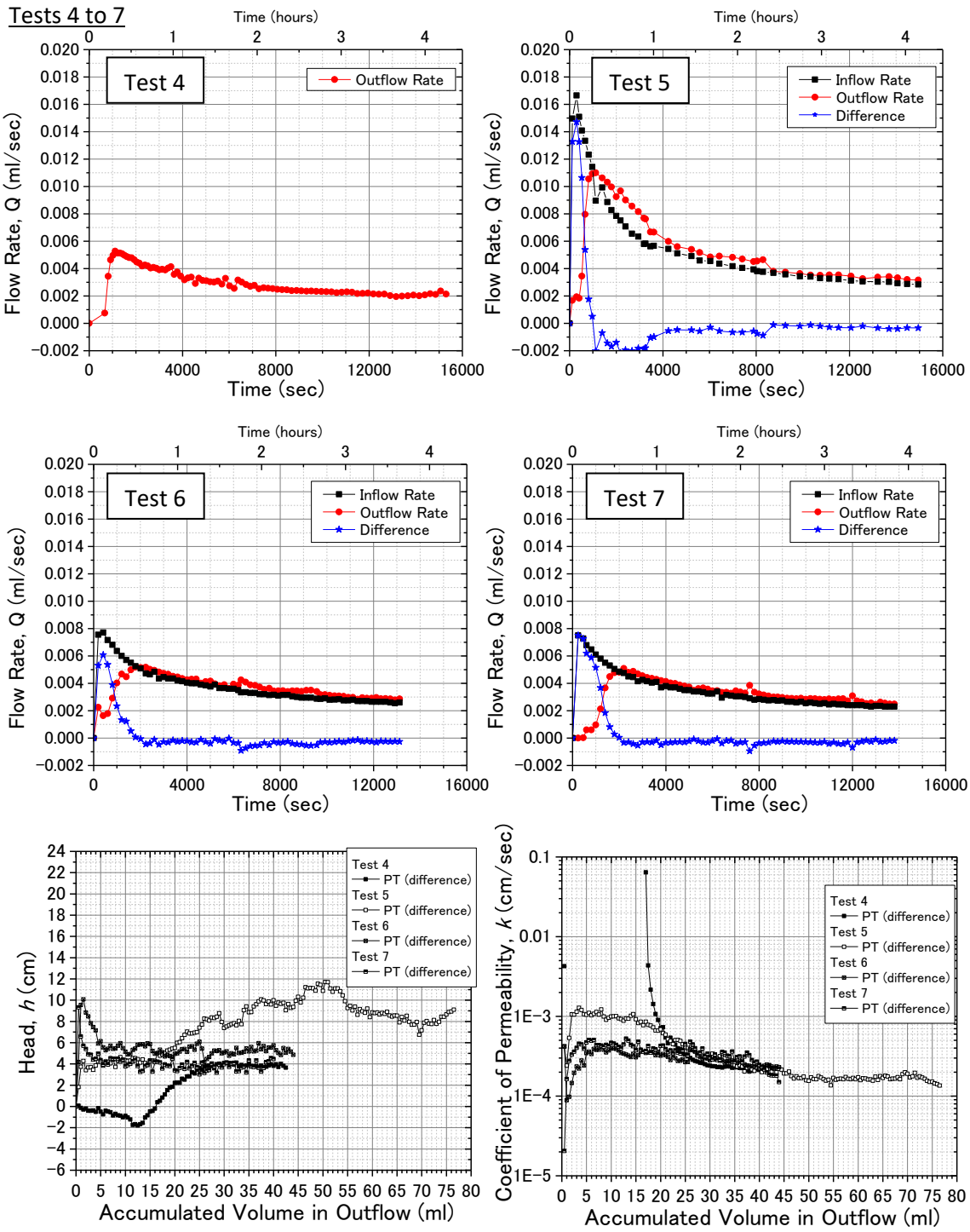

Figure B - 17. Permeability Test (Test 4 to 7-bauxite; unsaturated)

Tests 8 to 9

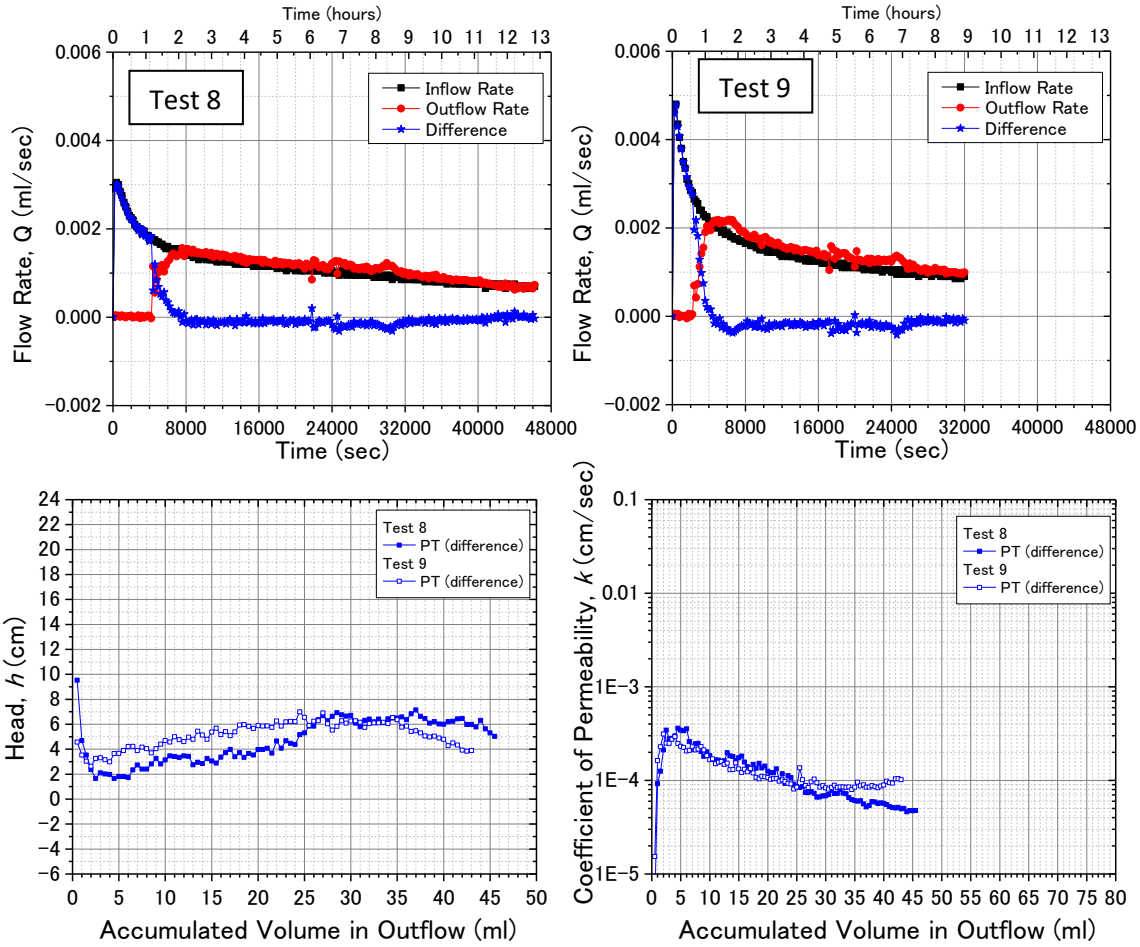

Figure B - 18. Permeability Test (Test 8 to 9-bauxite; unsaturated)

Tests 10 to 11

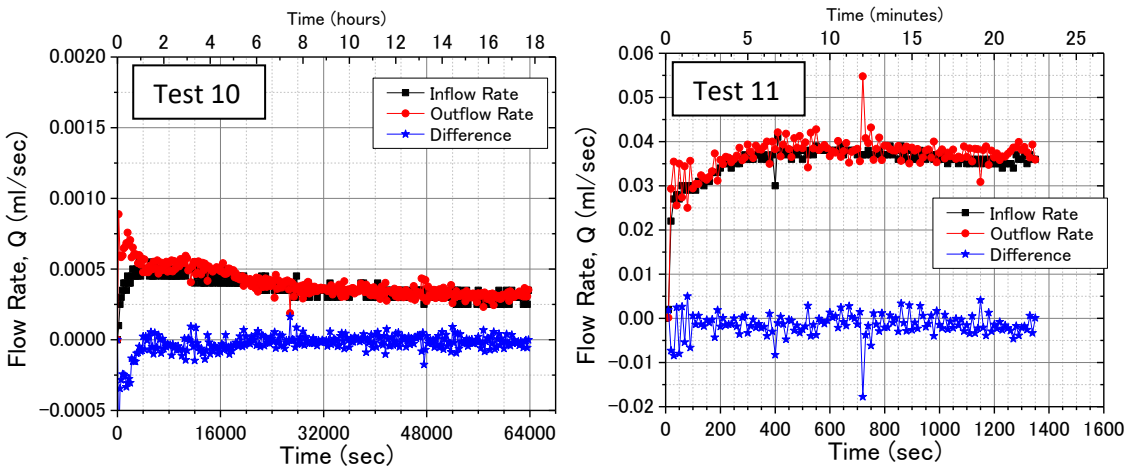

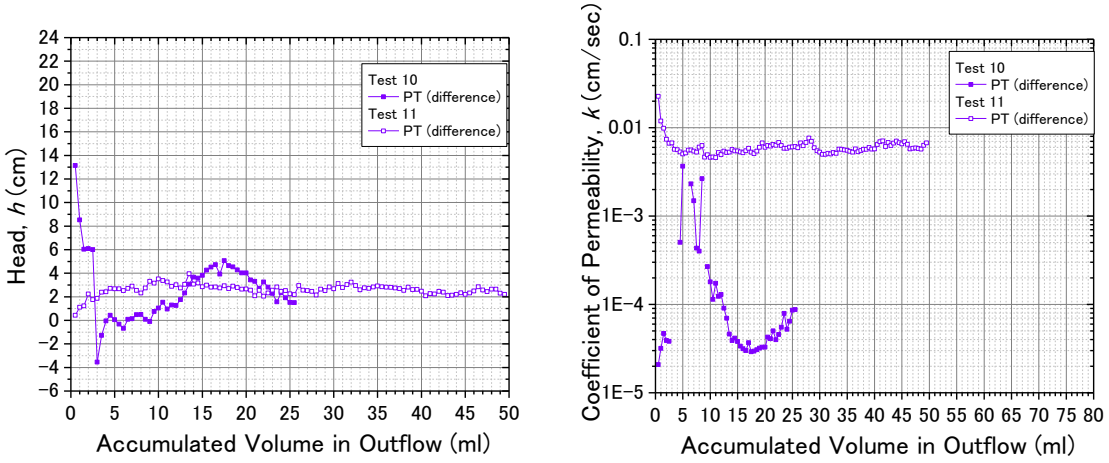

Figure B - 19. Permeability Test (Test 10 to 11-bauxite; unsaturated)

Tests 12

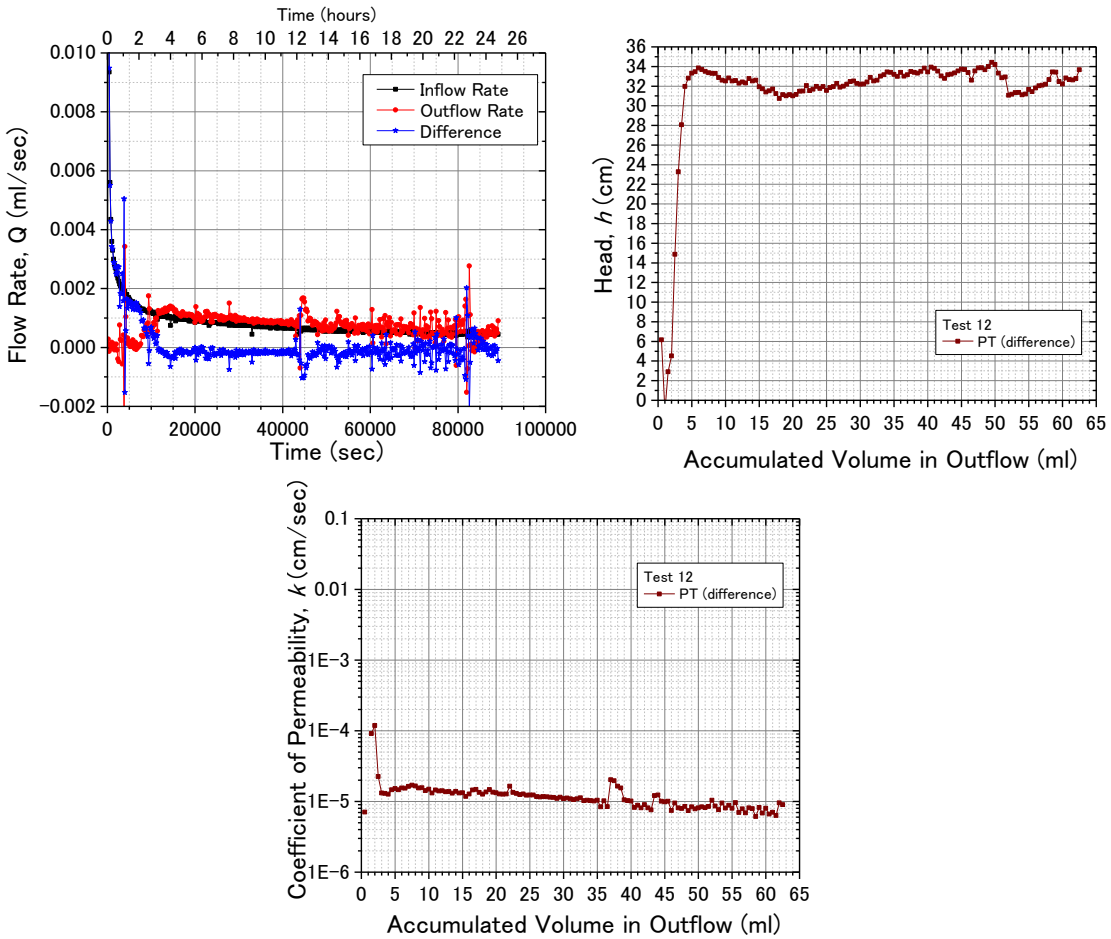

Figure B - 20. Permeability Test (Test 12-bauxite; unsaturated)

Tests 13

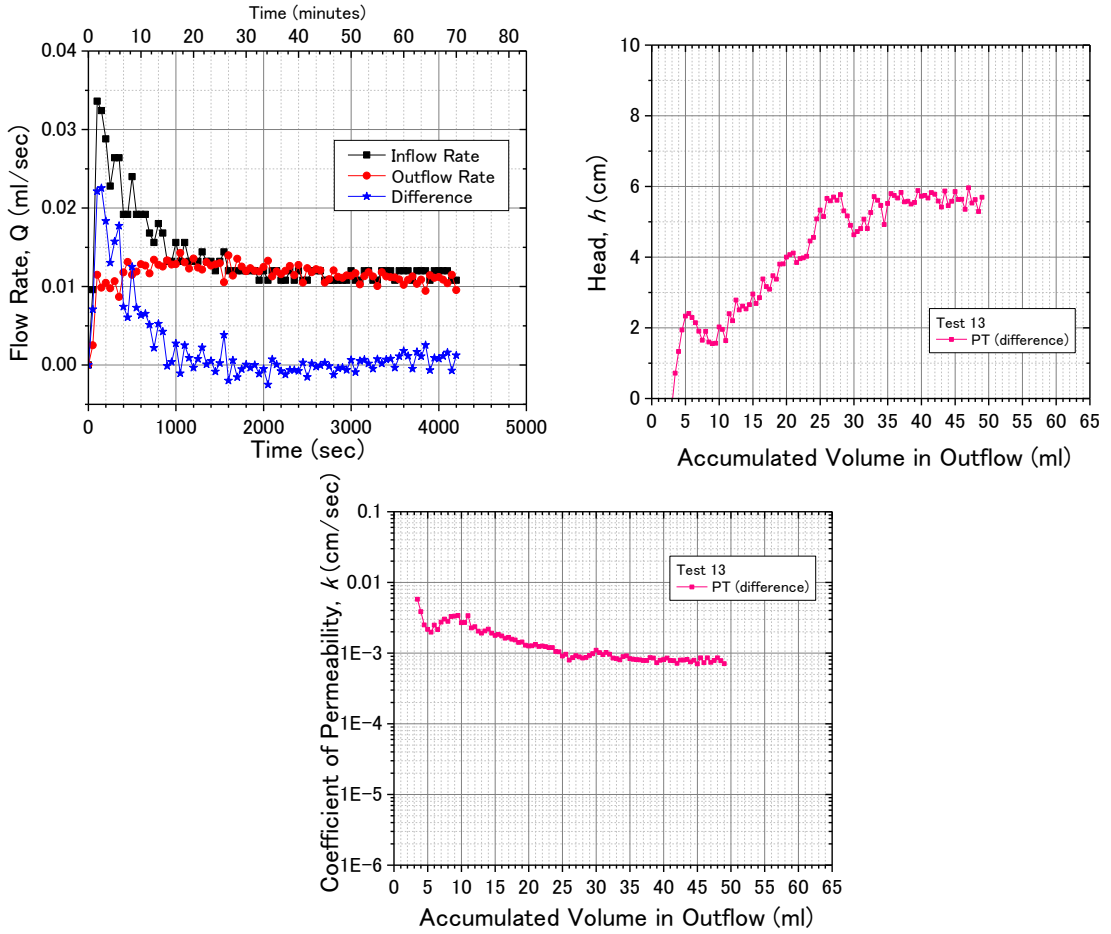

Figure B - 21. Permeability Test (Test 13-bauxite; unsaturated)

Test 14 to 16

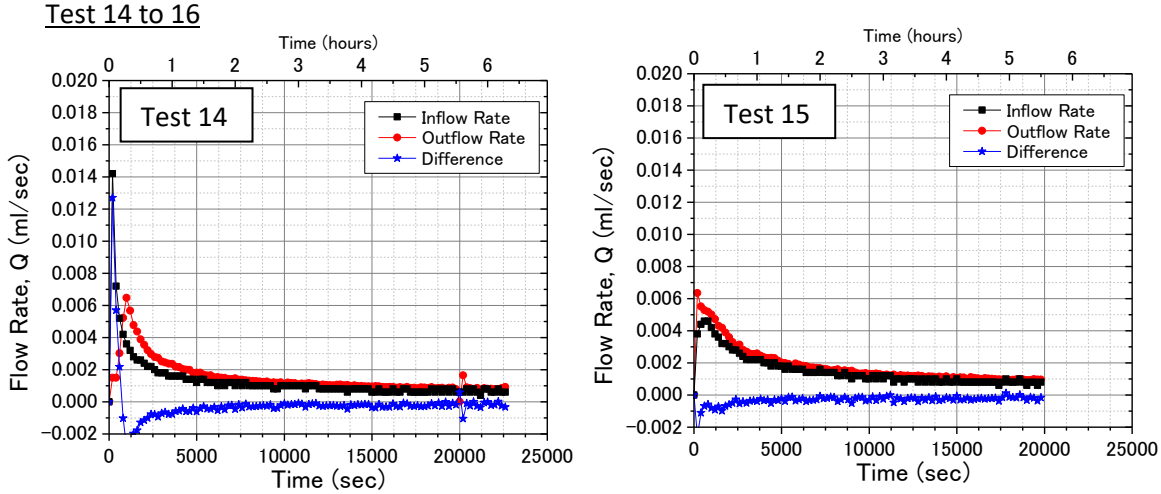

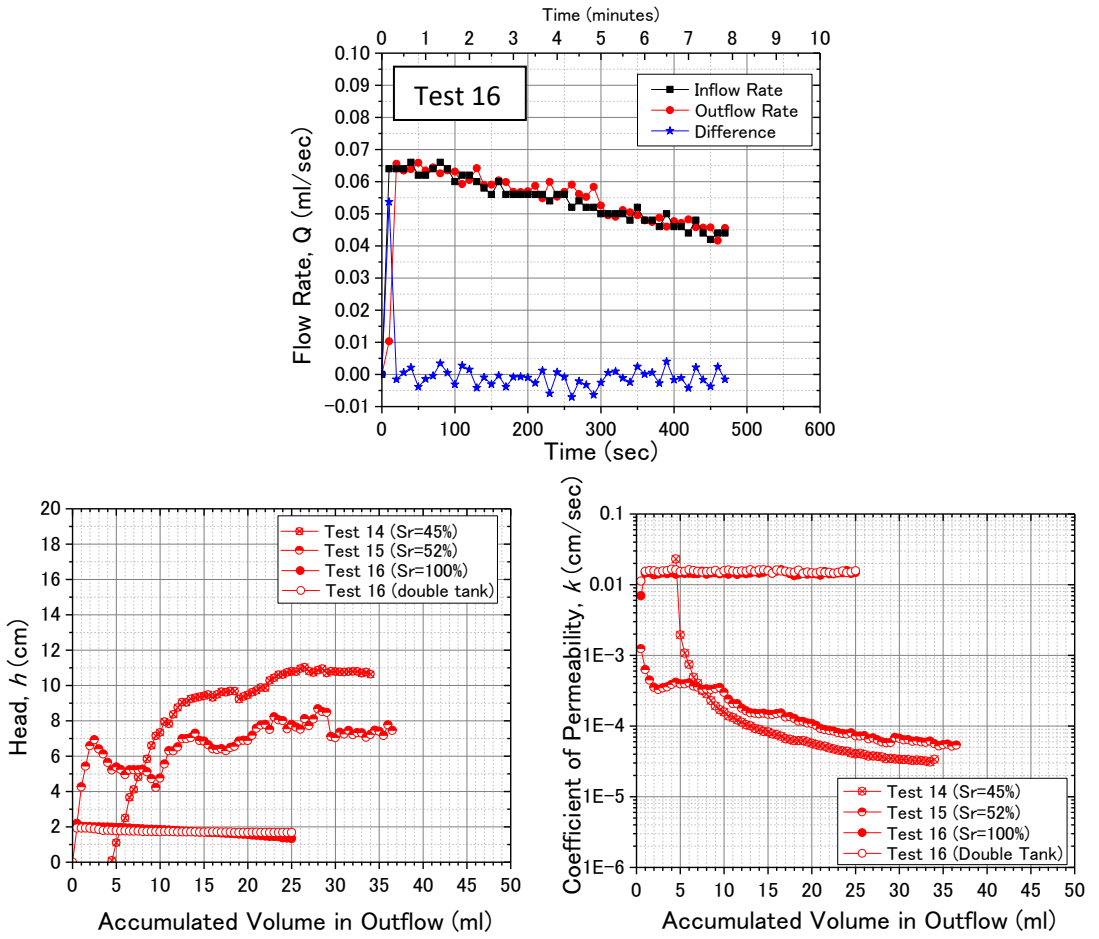

Figure B - 22. Permeability Test (Test 14 to 16-bauxite; unsaturated)

Test 17-20

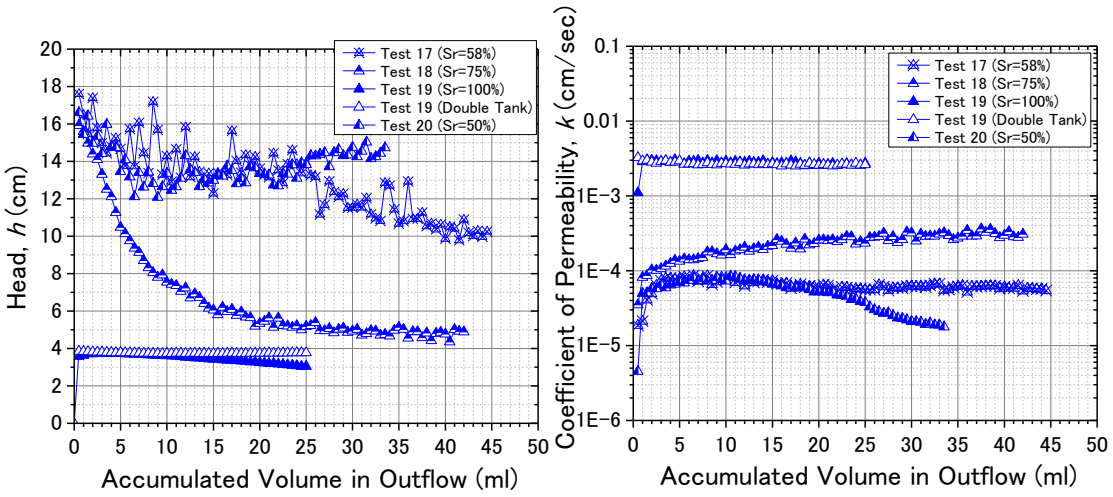

Figure B - 23. Permeability Test (Test 14 to 16-bauxite; unsaturated)

Summary of Tests

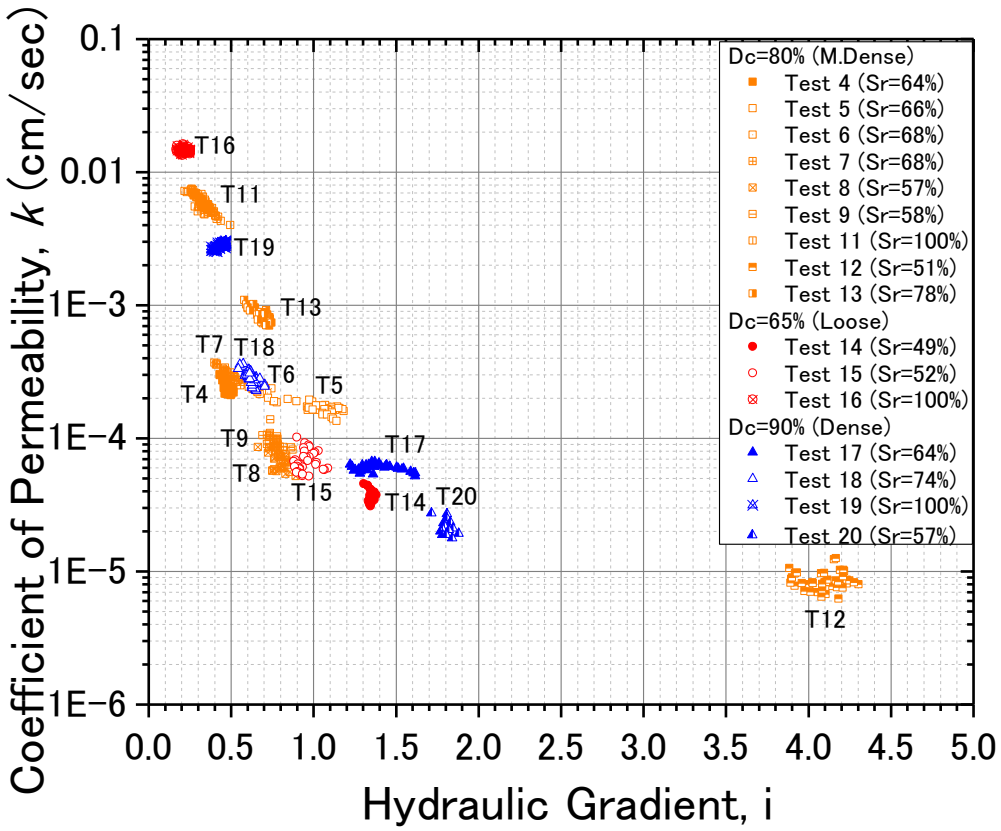

Figure B - 24. Permeability Test (all tests-bauxite; unsaturated)

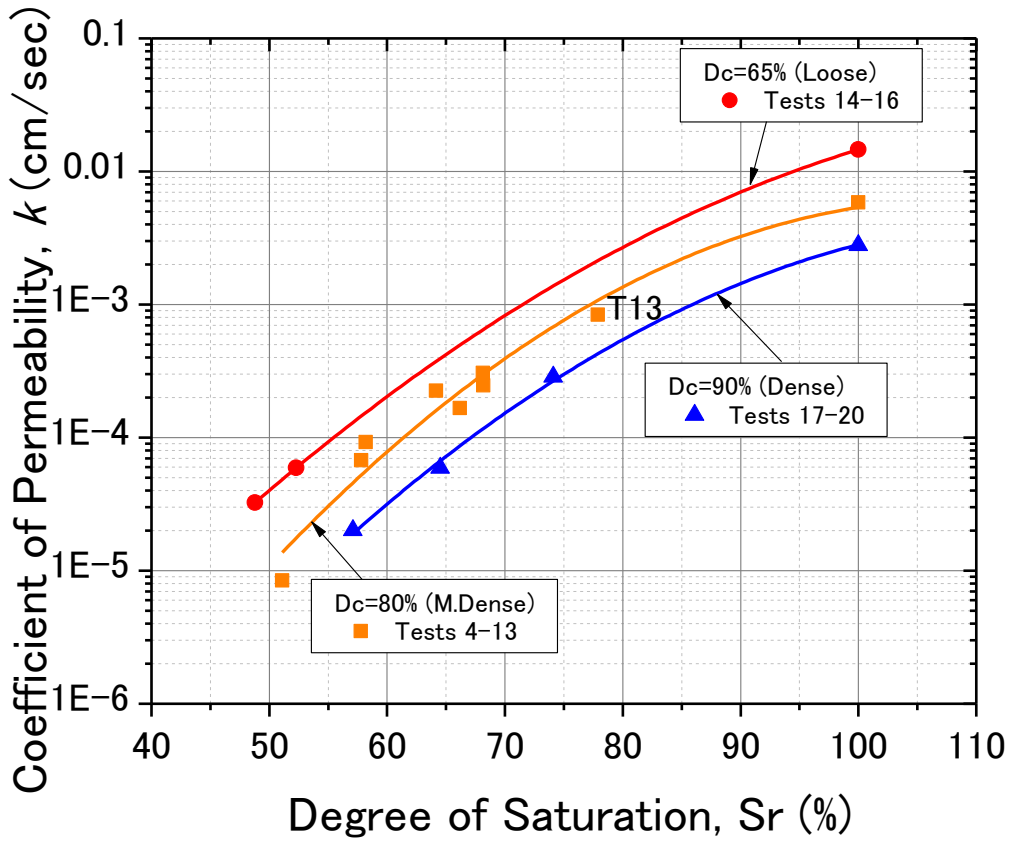

Figure B - 25. Permeability Test (all tests-bauxite; unsaturated)

B-5. Permeability Test on Iron Ore (Unsaturated)

Table B-5. Test Conditions of *k* Tests using Triaxial Apparatus (iron ore-unsaturated)

Test	D_c (%)	Case	Initial degree of saturation Sr_{init} (%)	Final degree of saturation Sr_{final} (%)	Suction measured by membrane filter (kPa)	Total head (cm) supplied to the specimen	Total accumulated volume (ml) (approximate)
1	91.5	Dense	-	100	-	32	25
2	92.3		72	74.1	2.4	64	25
3	91.6		60	66.8	4.4	75	25

Tests 1 to 3

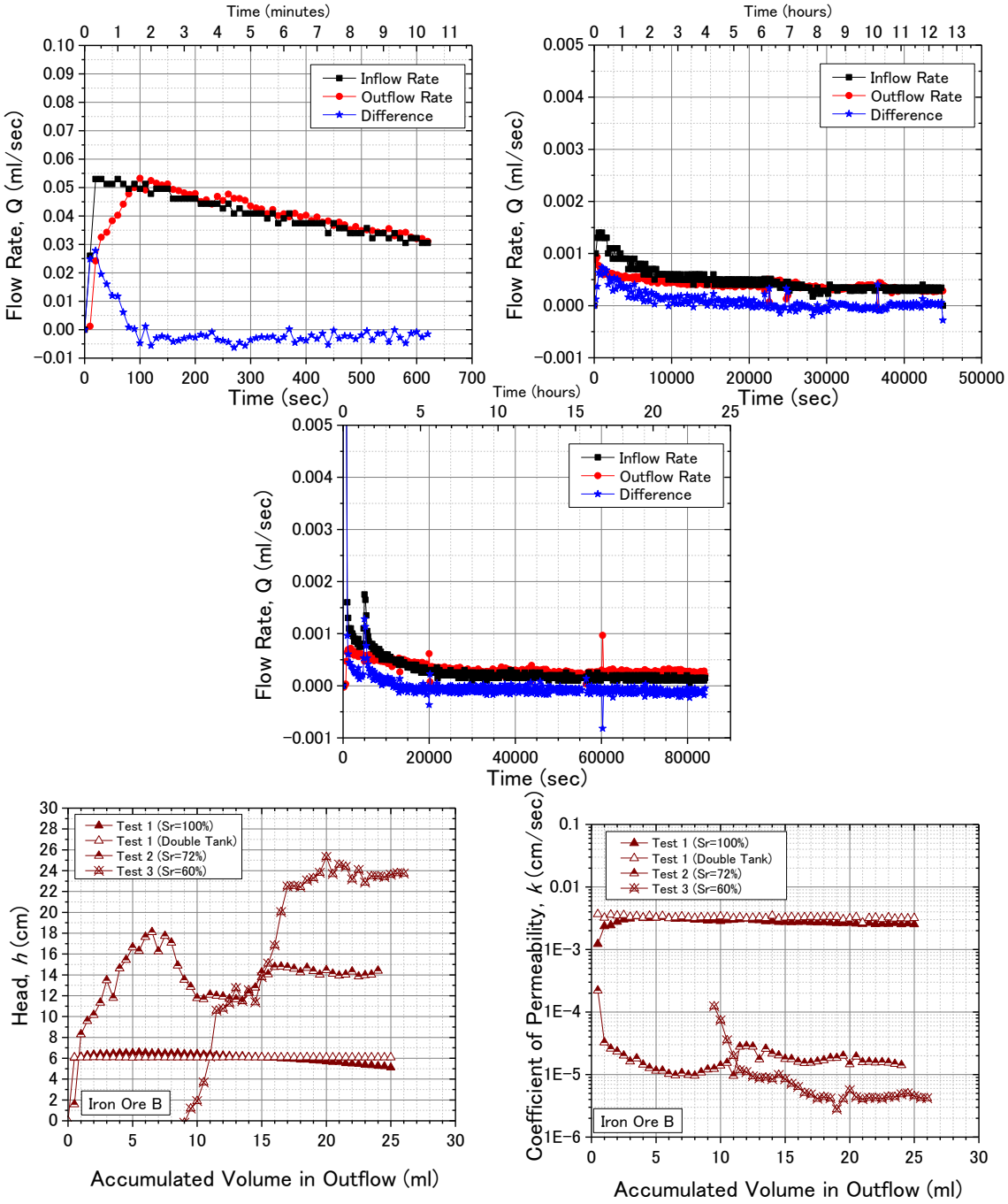

Figure B - 26. Permeability Test (all tests-iron ore; unsaturated)

B-6. Permeability Test on Inagi Sand (Unsaturated)

Table B-6. Test Conditions of *k* Tests using Triaxial Apparatus (Inagi sand-unsaturated)

Test	D_c (%)	Case	Initial degree of saturation Sr_{init} (%)	Final degree of saturation Sr_{final} (%)	Suction measured by membrane filter (kPa)	Total head (cm) supplied to the specimen	Total accumulated volume (ml) (approximate)
0	69.2	Loose	-	100	-	varies	15
1	70.7		65	74.2	1.6	62	25
2	71.0		55	62.2	3.2	72	40

Tests 1 to 2

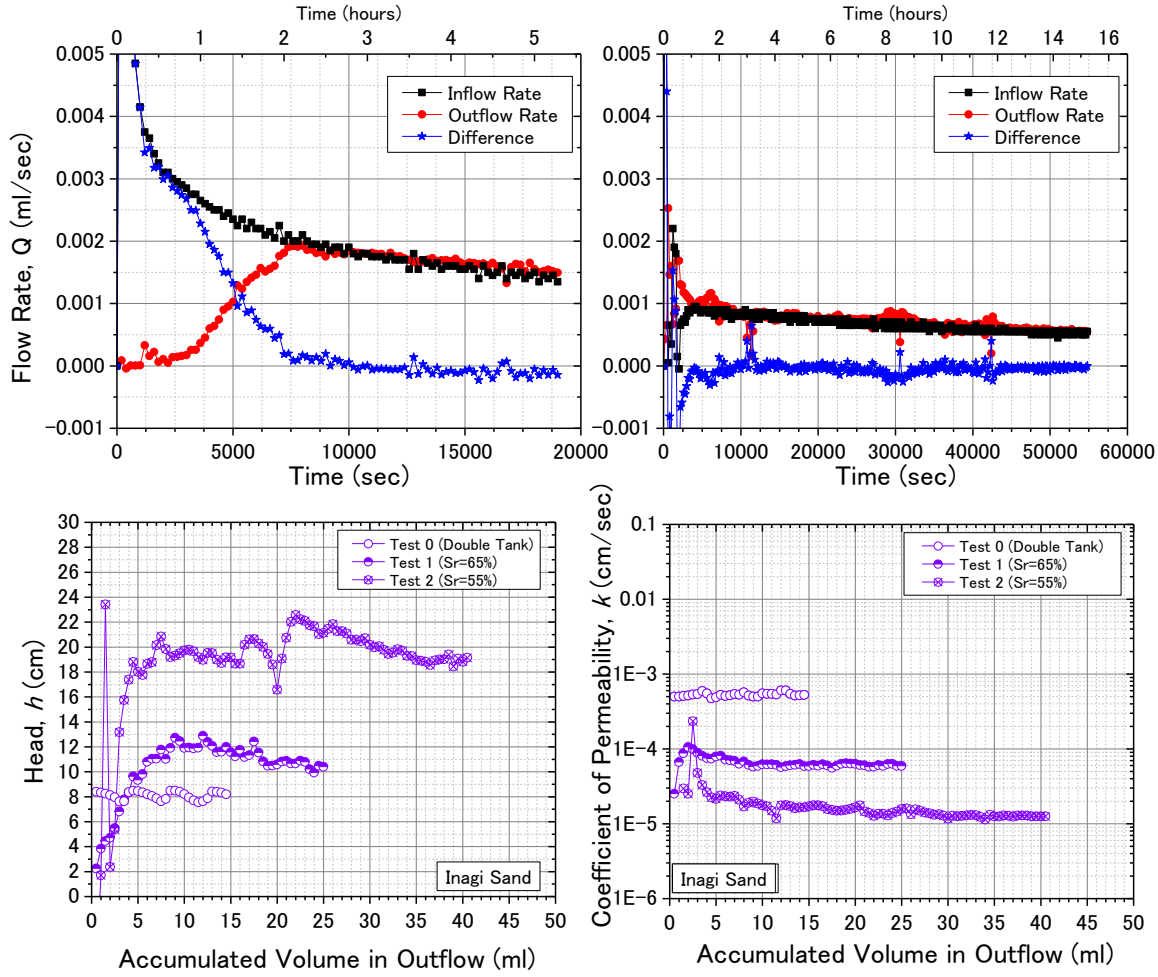

Figure B - 27. Permeability Test (all tests-Inagi sand; unsaturated)

Appendix C: Seepage Analysis

Contents

C-1. Seepage Analysis Runs Bauxite (Loose; Dc=65%) at t=57.5 hrs

Case 1: Experimental Results; Pervious Side Boundary

Sr_{init} = 55%

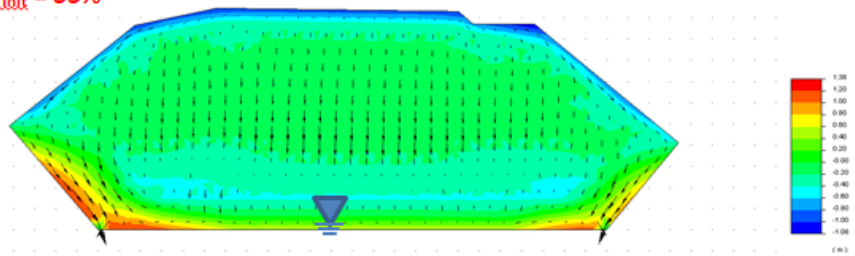

Sr_{init} = 60%

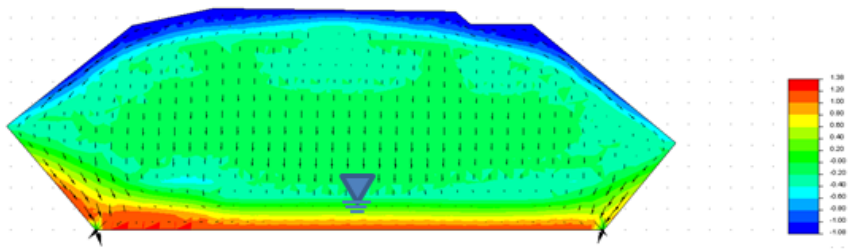

Sr_{init} = 70%

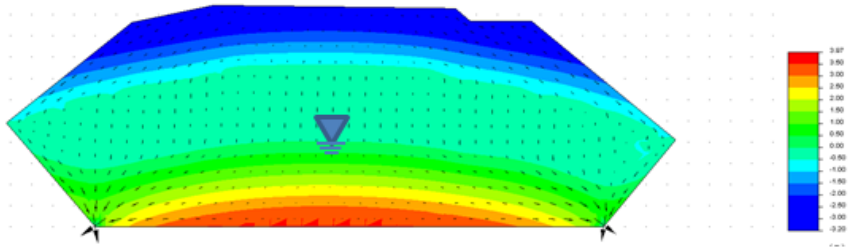

Sr_{init} = 80%

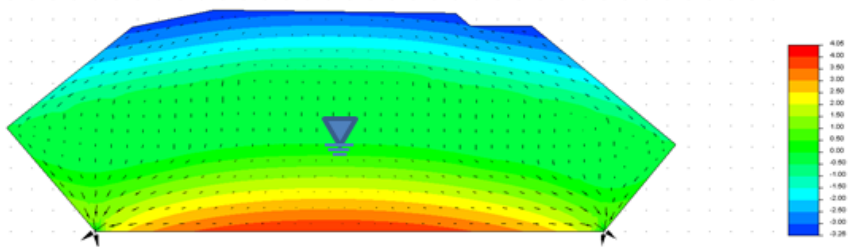

Sr_{init} = 90%

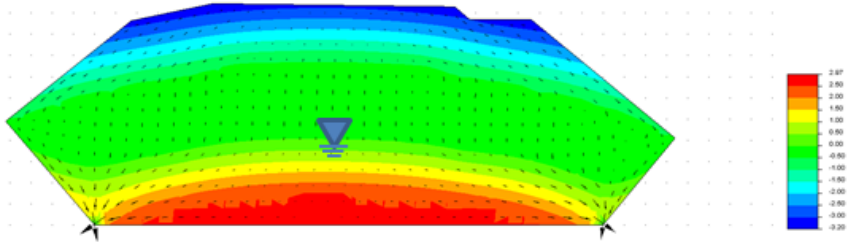

Case 2: Experimental Results; Impervious Side Boundary

Sr_{init} = 55%

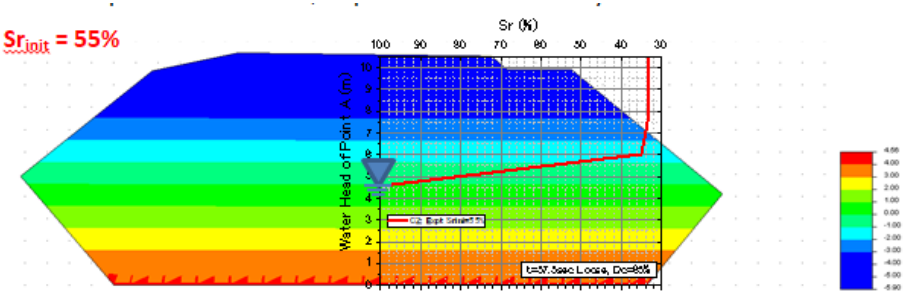

Sr_{init} = 60%

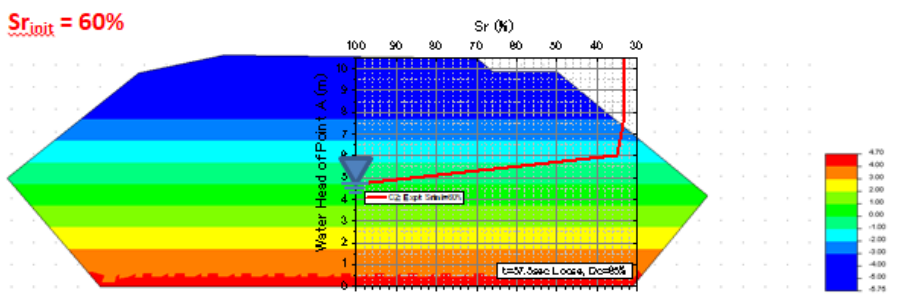

Sr_{init} = 70%

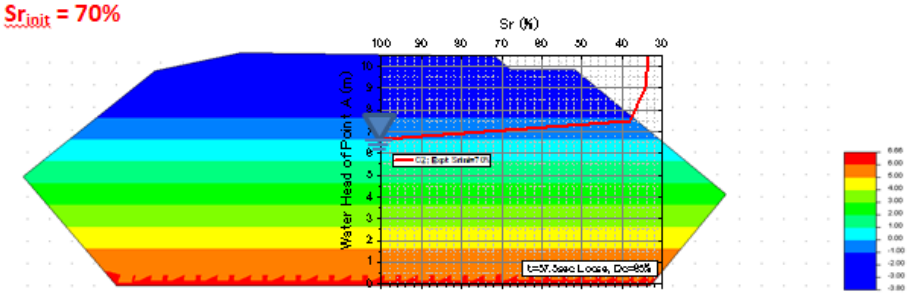

Sr_{init} = 80%

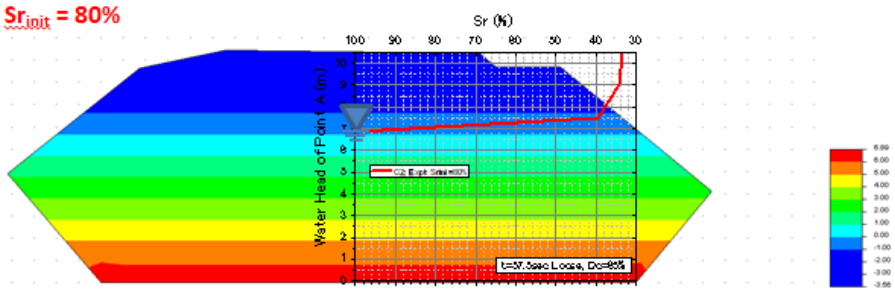

Sr_{init} = 90%

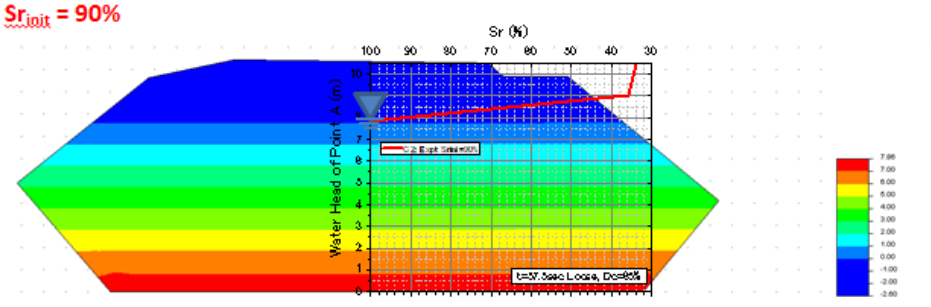

C-2. Seepage Analysis Runs Bauxite (Loose; Dc=65%) at t=350 hrs

Case 1: Experimental Results; Pervious Side Boundary

Sr_{init} = 55%

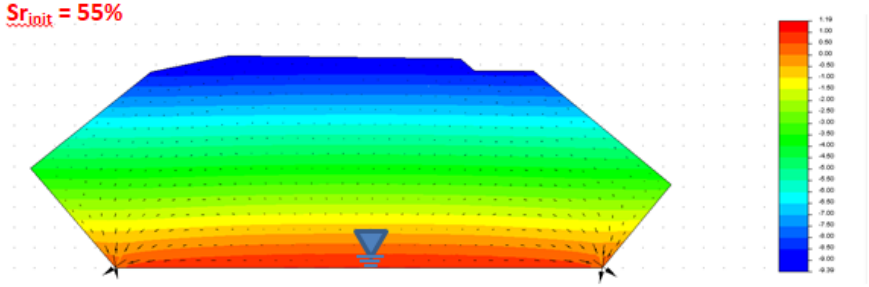

Sr_{init} = 60%

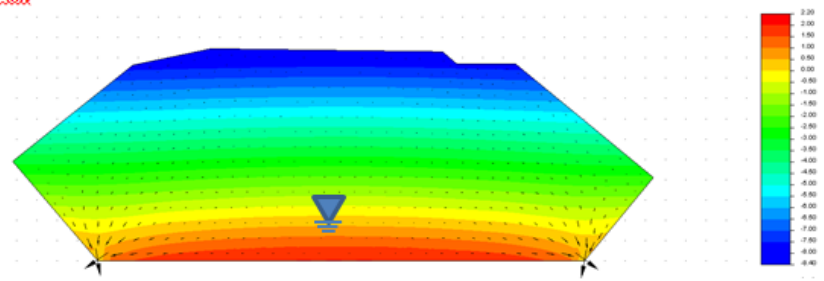

Sr_{init} = 70%

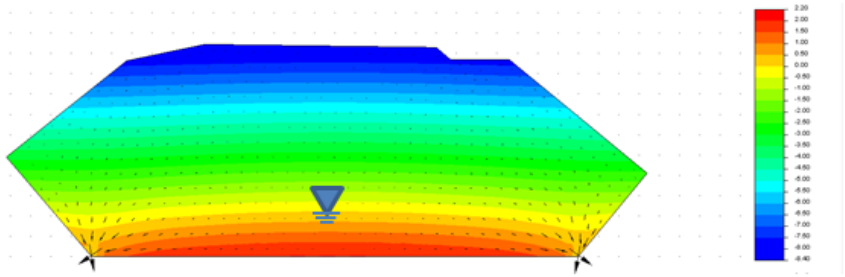

Sr_{init} = 80%

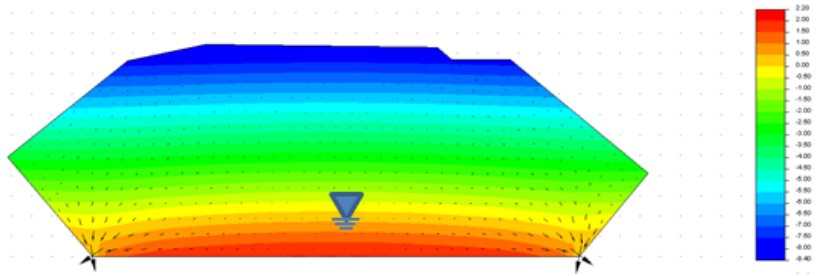

Sr_{init} = 90%

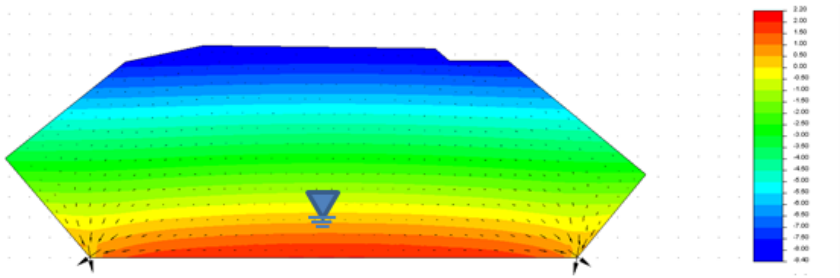

Case 2: Experimental Results; Impervious Side Boundary

Sr_{init} = 55%

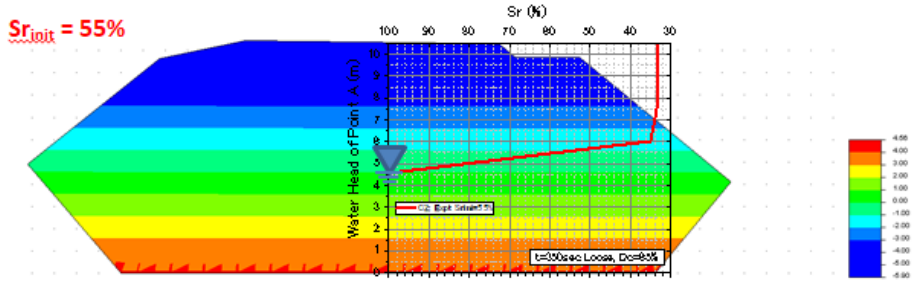

Sr_{init} = 60%

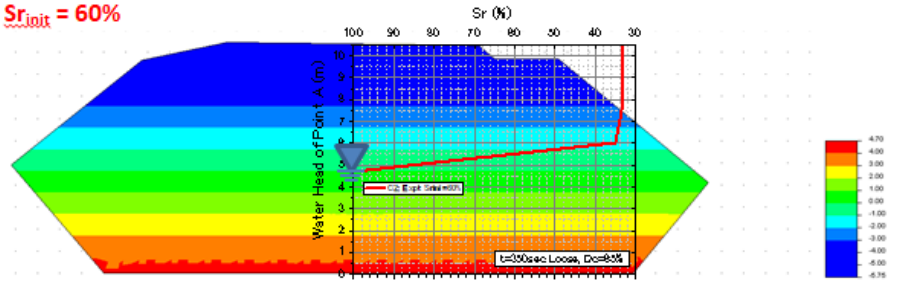

Sr_{init} = 70%

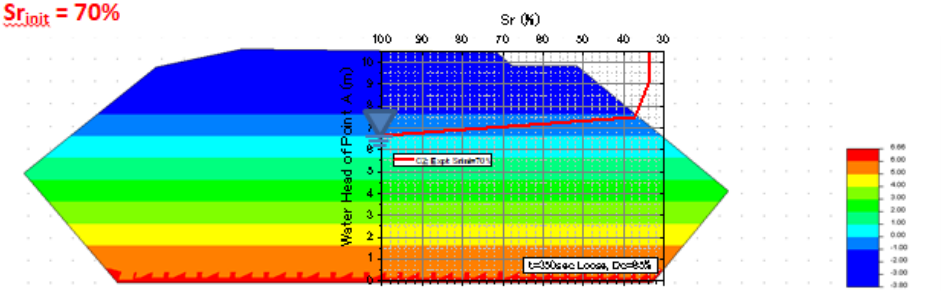

Sr_{init} = 80%

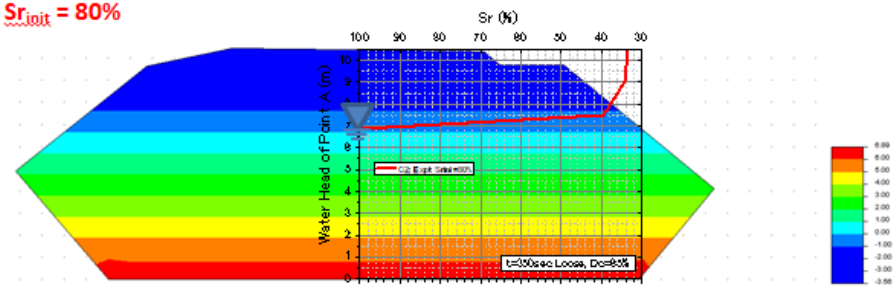

Sr_{init} = 90%

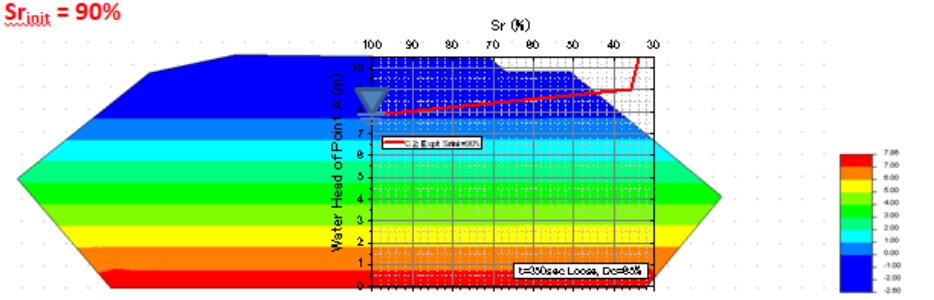

C-3. Seepage Analysis Runs Bauxite (Medium Dense; Dc=80%) at t=57.5 hrs

Case 1: Experimental Results; Pervious Side Boundary

Sr_{init} = 55%

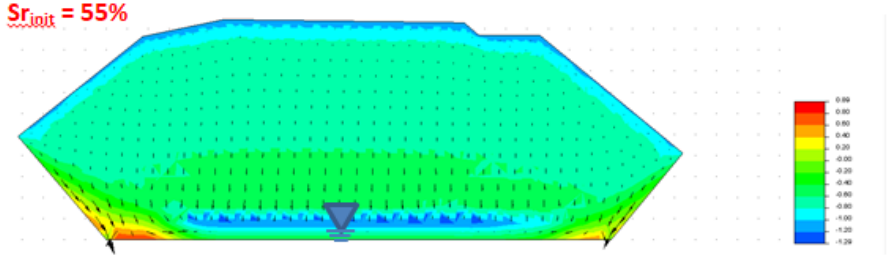

Sr_{init} = 60%

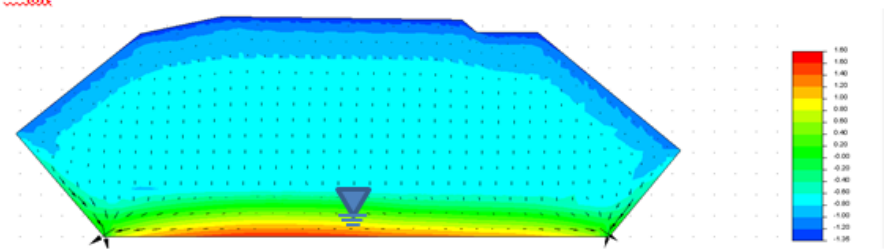

Sr_{init} = 70%

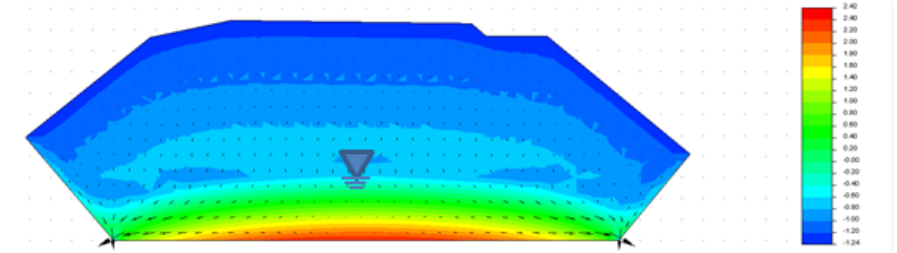

Sr_{init} = 80%

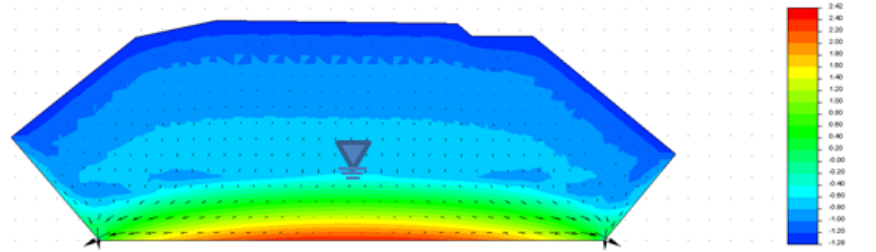

Sr_{init} = 90%

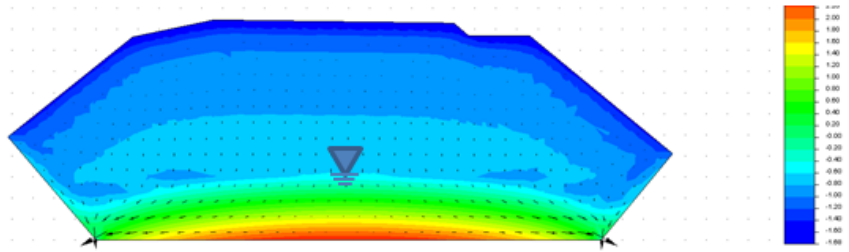

Case 2: Experimental Results; Impervious Side Boundary

Sr_{init} = 55%

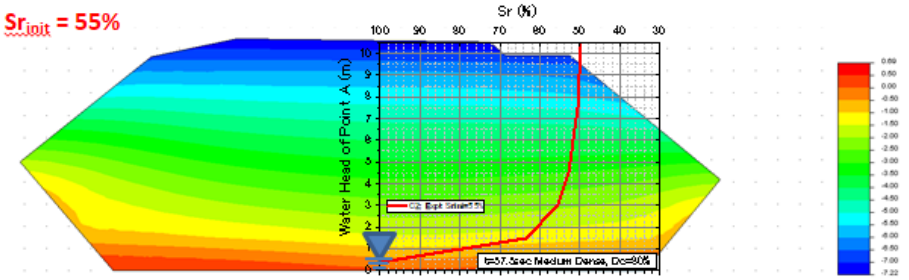

Sr_{init} = 60%

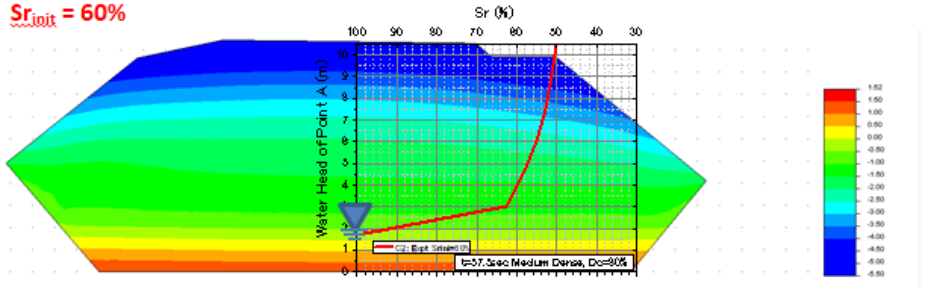

Sr_{init} = 70%

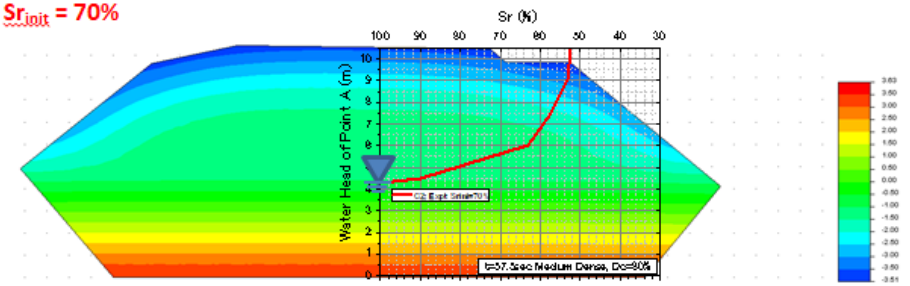

Sr_{init} = 80%

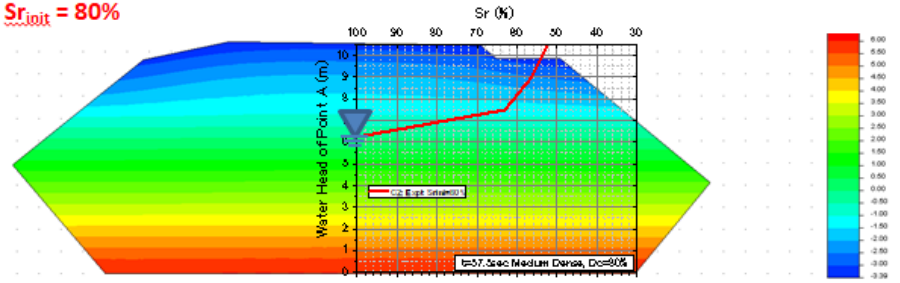

Sr_{init} = 90%

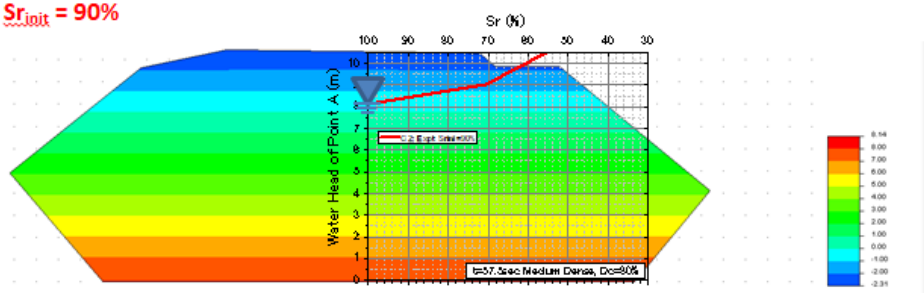

C-4. Seepage Analysis Runs Bauxite (Medium Dense; Dc=80%) at t=350 hrs

Case 1: Experimental Results; Pervious Side Boundary

Sr_{init} = 55%

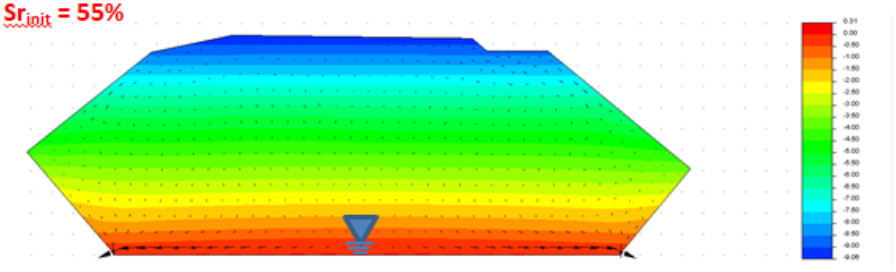

Sr_{init} = 60%

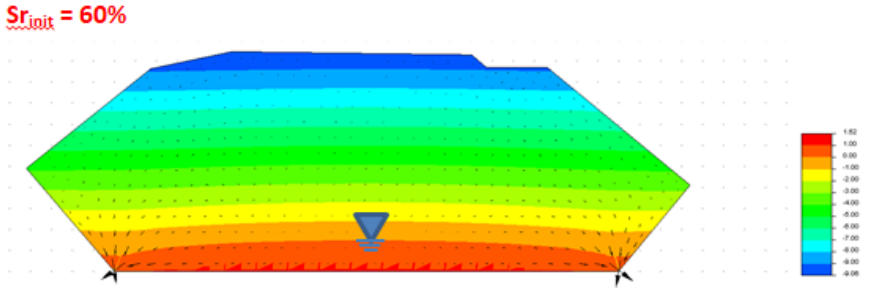

Sr_{init} = 70%

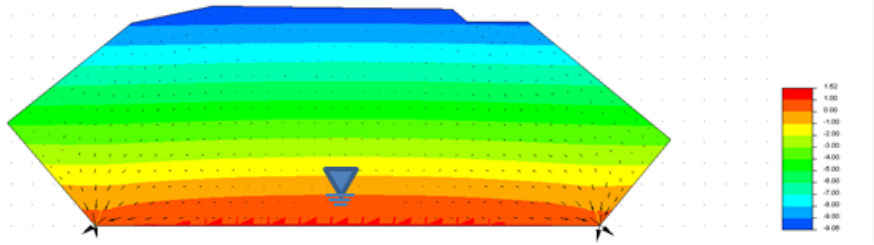

Sr_{init} = 80%

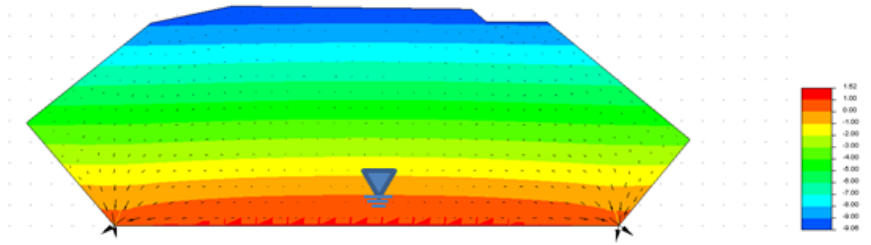

Sr_{init} = 90%

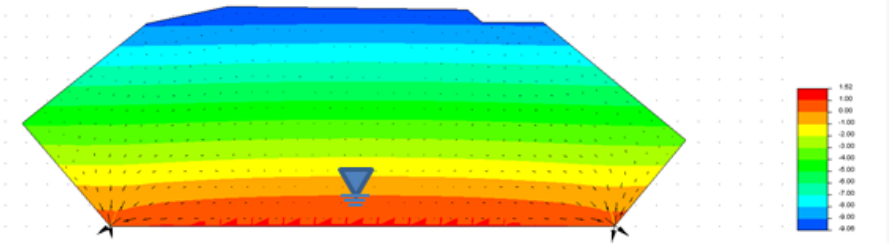

Case 2: Experimental Results; Impervious Side Boundary

Sr_{init} = 55%

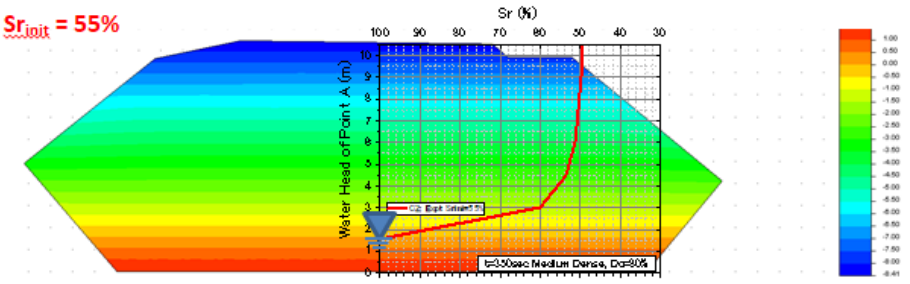

Sr_{init} = 60%

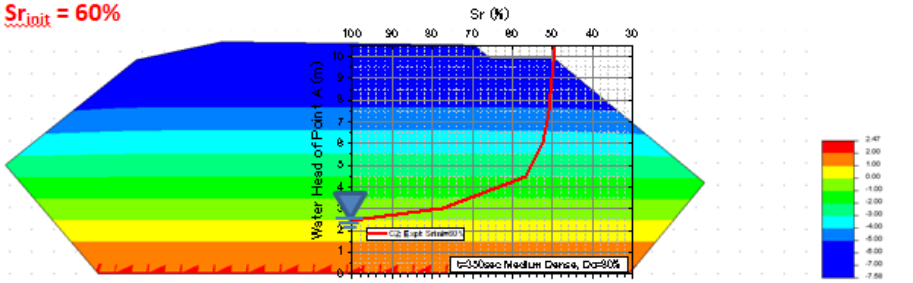

Sr_{init} = 70%

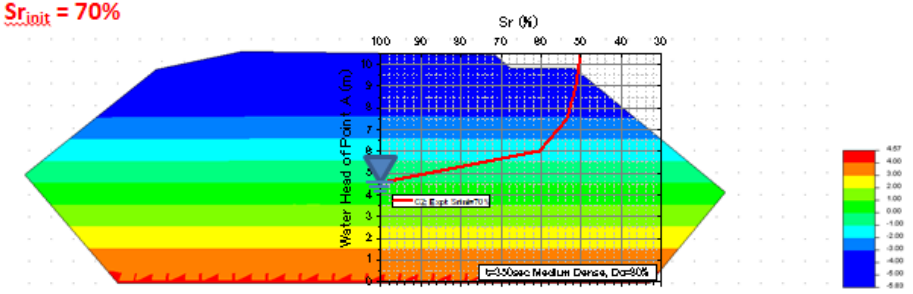

Sr_{init} = 80%

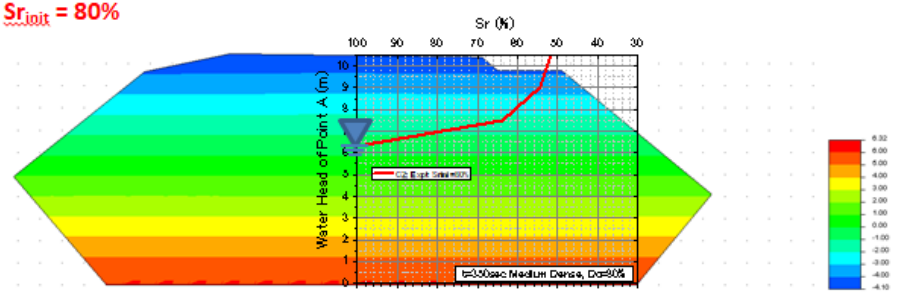

Sr_{init} = 90%

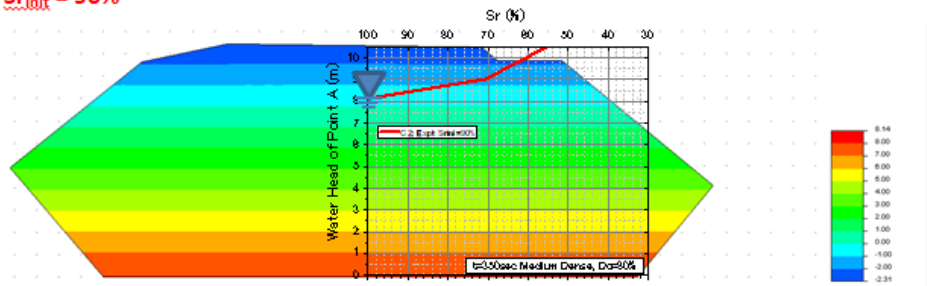

C-5. Seepage Analysis Runs Bauxite (Dense; Dc=90%) at t=57.5 hrs

Case 1: Experimental Results; Pervious Side Boundary

Sr_{init} = 55%

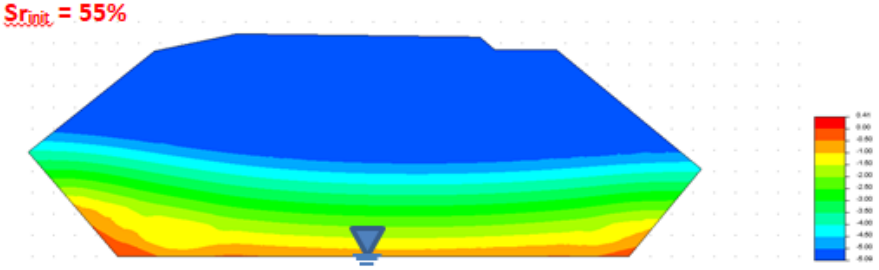

Sr_{init} = 60%

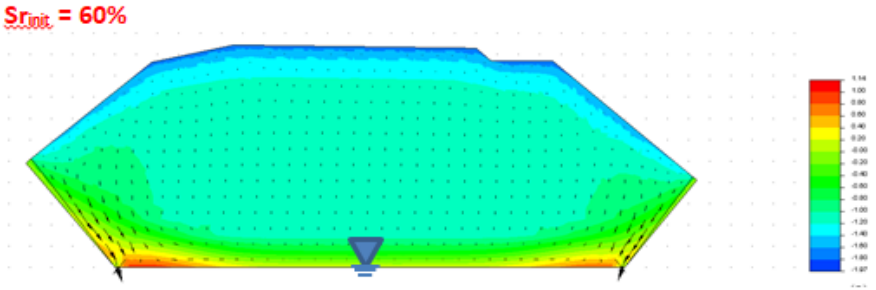

Sr_{init} = 70%

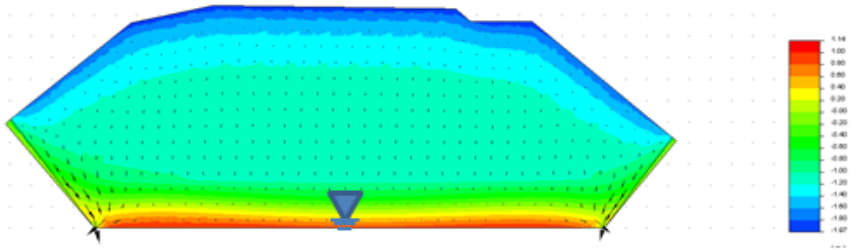

Sr_{init} = 80%

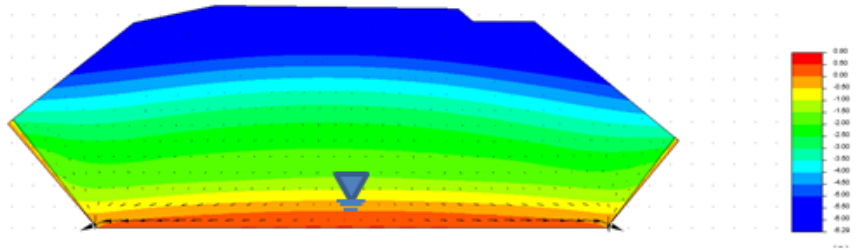

Sr_{init} = 90%

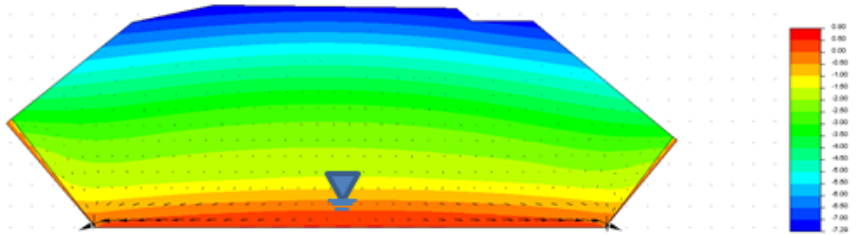

Case 2: Experimental Results; Impervious Side Boundary

Sr_{init} = 55%

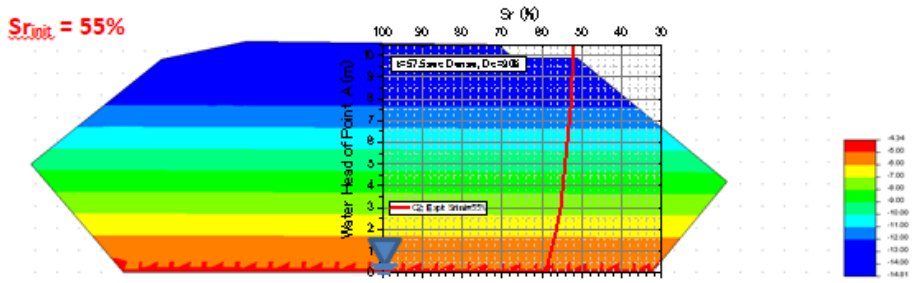

Sr_{init} = 60%

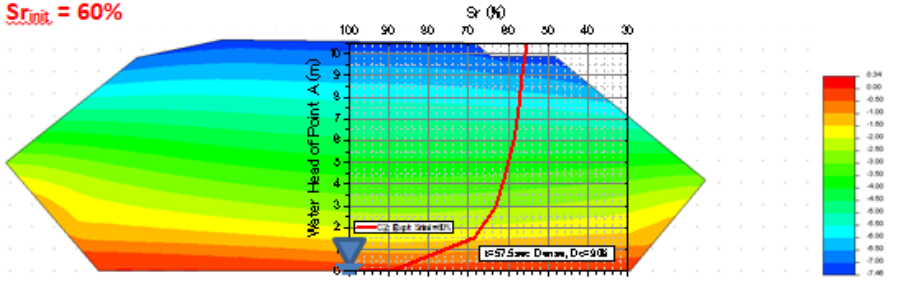

Sr_{init} = 70%

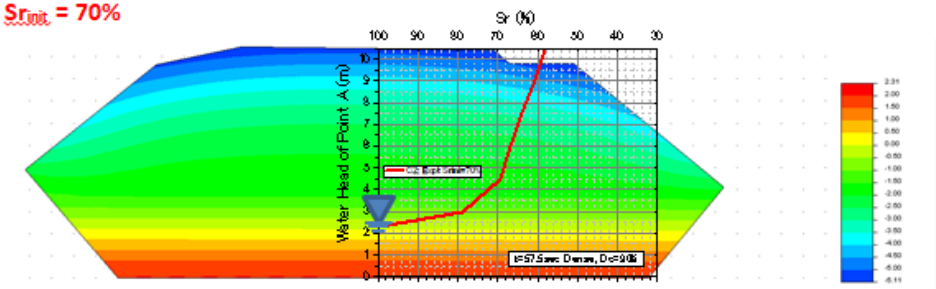

Sr_{init} = 80%

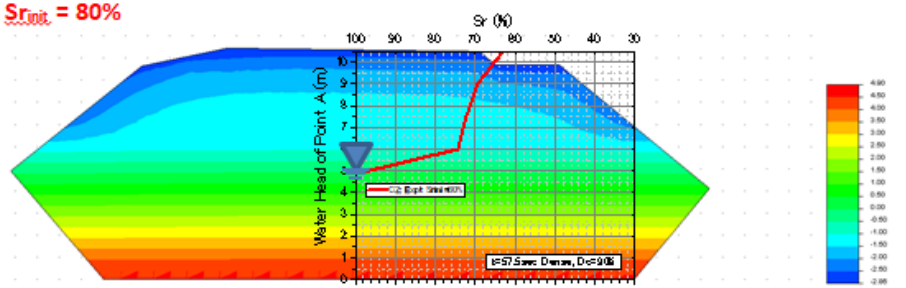

Sr_{init} = 90%

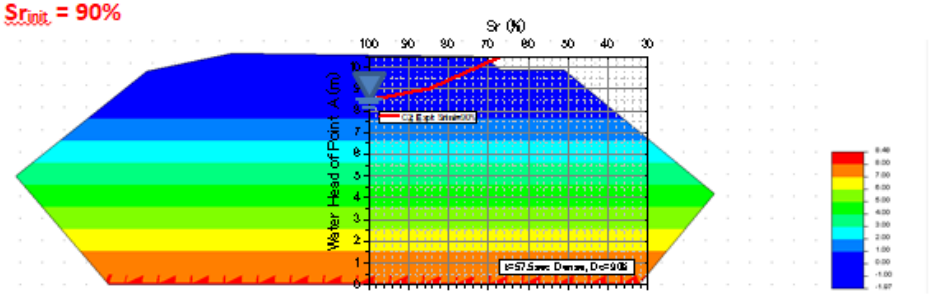

C-6. Seepage Analysis Runs Bauxite (Dense; Dc=90%) at t=350 hrs

Case 1: Experimental Results; Pervious Side Boundary

Sr_{init} = 55%

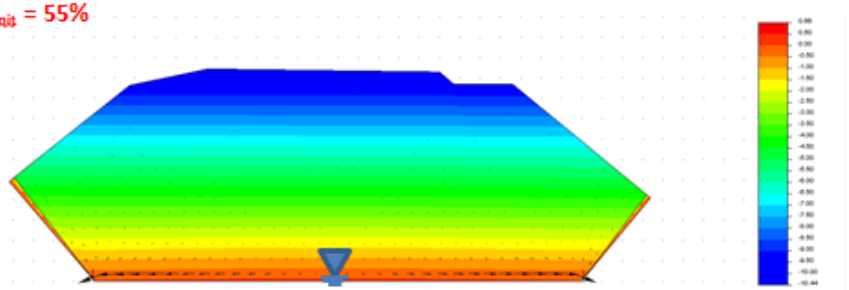

Sr_{init} = 60%

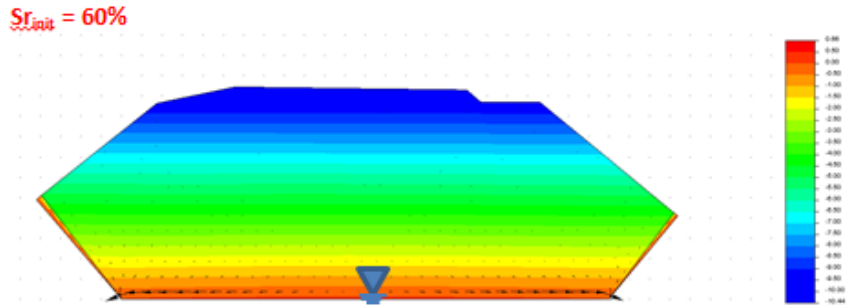

Sr_{init} = 70%

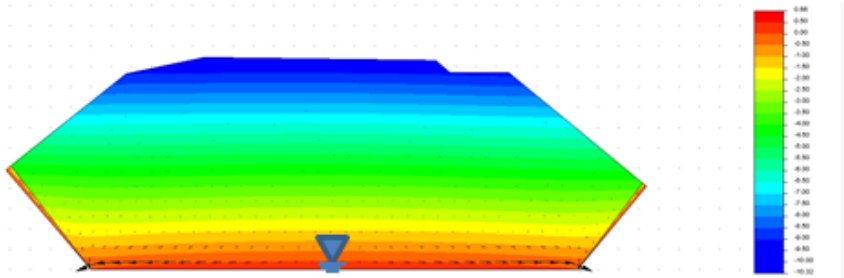

Sr_{init} = 80%

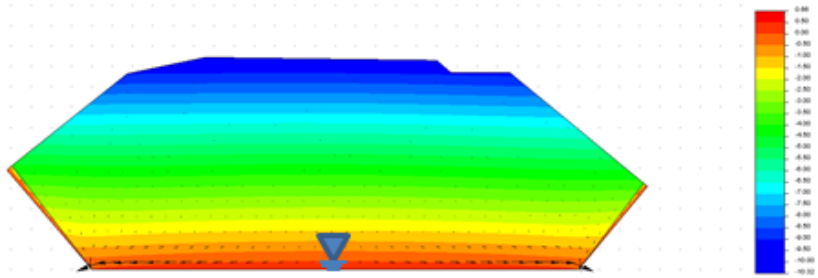

Sr_{init} = 90%

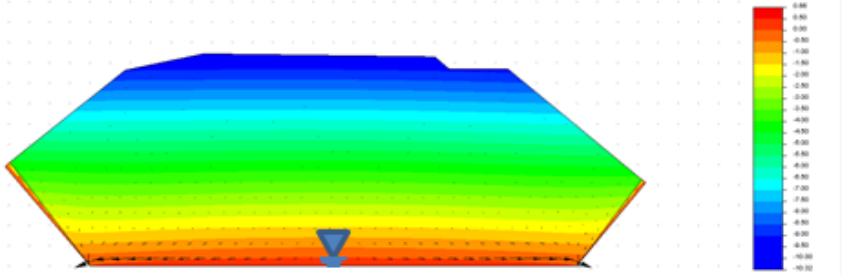

Case 2: Experimental Results; Impervious Side Boundary

Sr_{init} = 55%

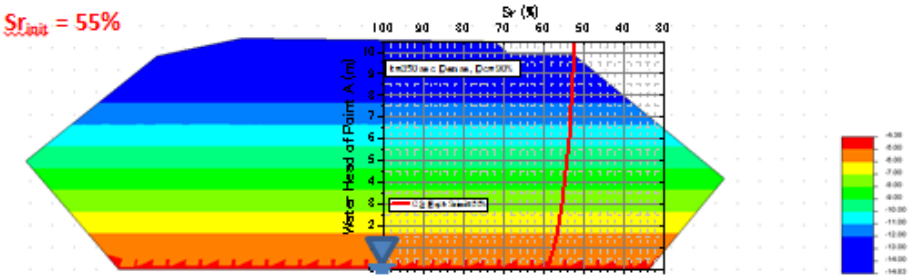

Sr_{init} = 60%

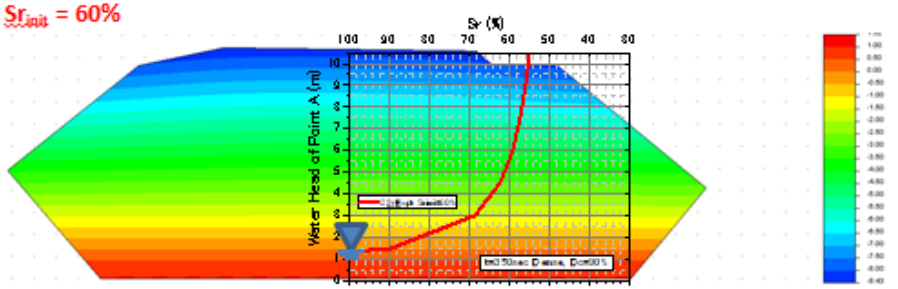

Sr_{init} = 70%

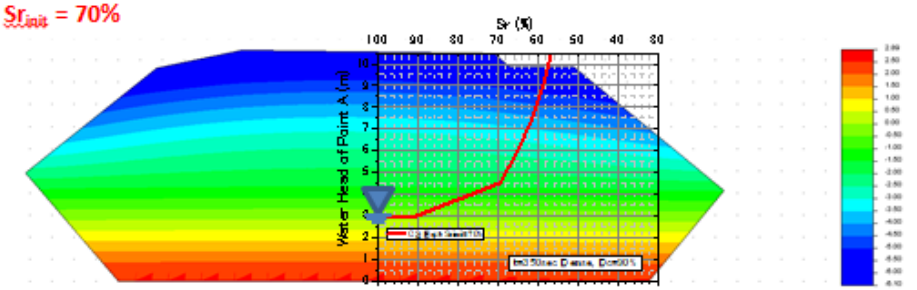

Sr_{init} = 80%

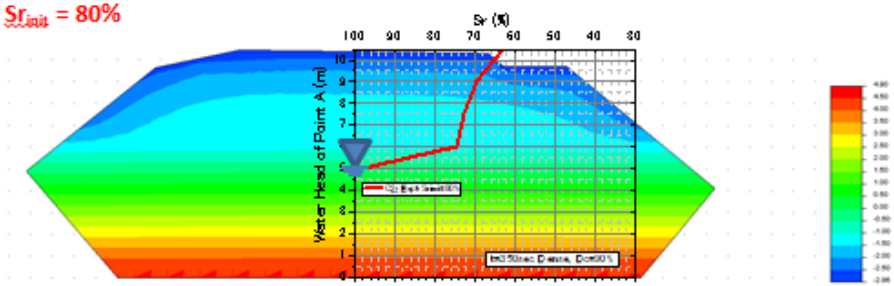

Sr_{init} = 90%

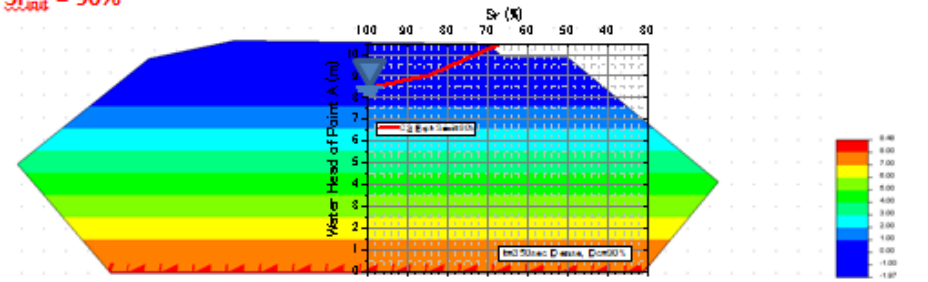

C-7. Seepage Analysis Runs Iron Ore (Dense; Dc=90%) at t=57.5 hrs

Case 1: Experimental Results; Pervious Side Boundary

Sr_{init} = 55%

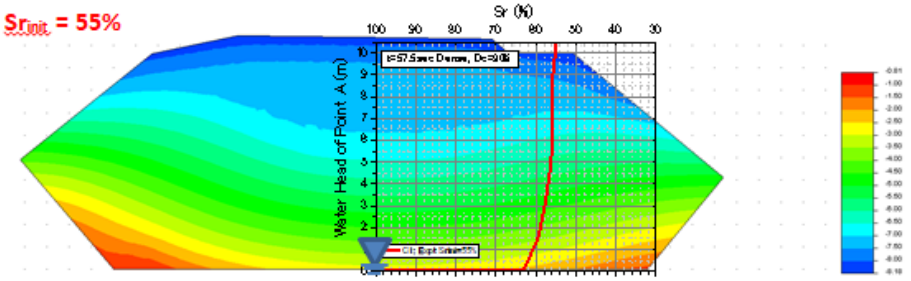

Sr_{init} = 60%

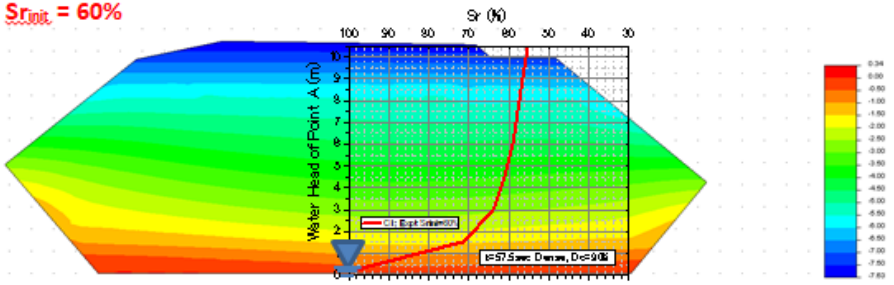

Sr_{init} = 70%

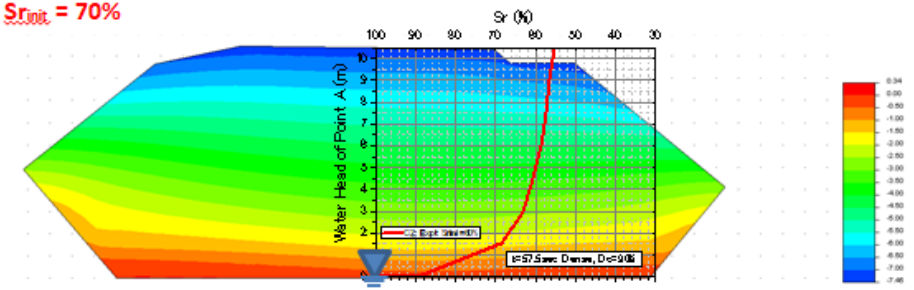

Sr_{init} = 80%

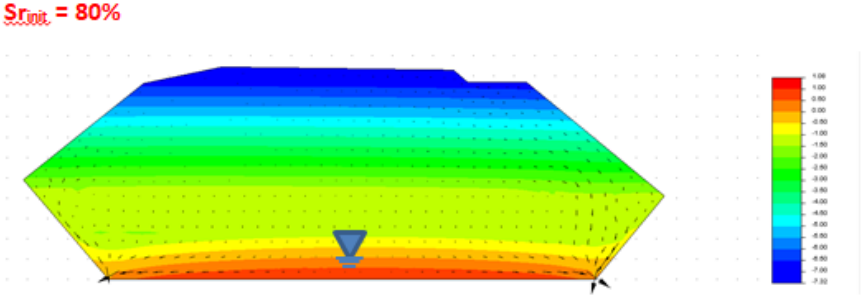

Sr_{init} = 90%

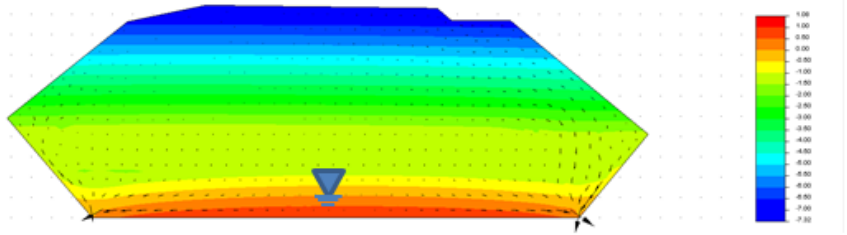

Case 2: Experimental Results; Impervious Side Boundary

Sr_{init} = 55%

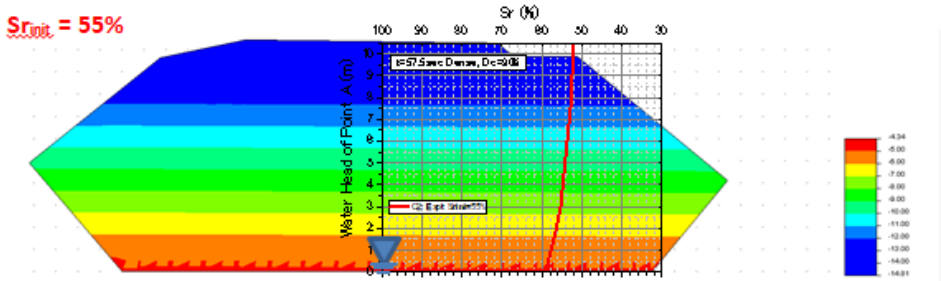

Sr_{init} = 60%

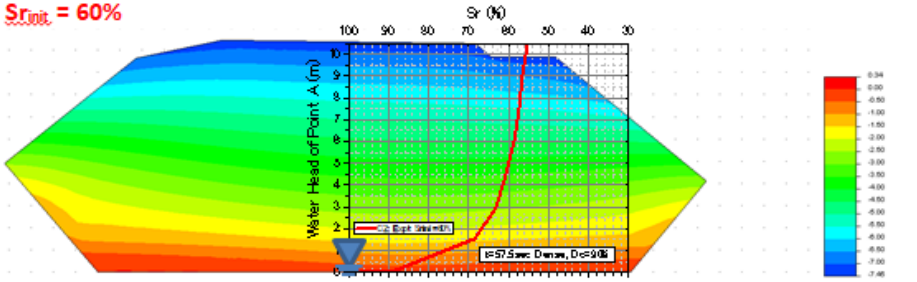

Sr_{init} = 70%

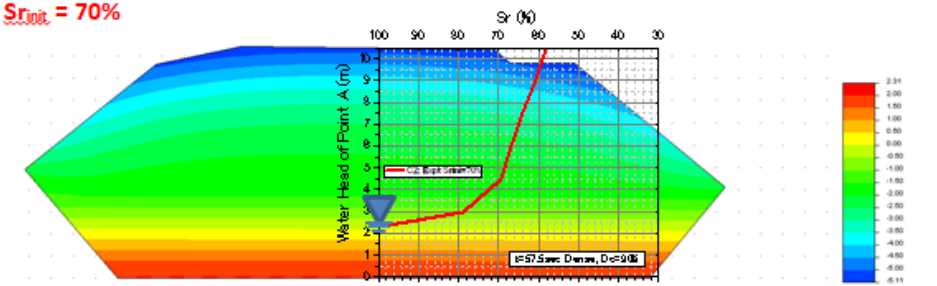

Sr_{init} = 80%

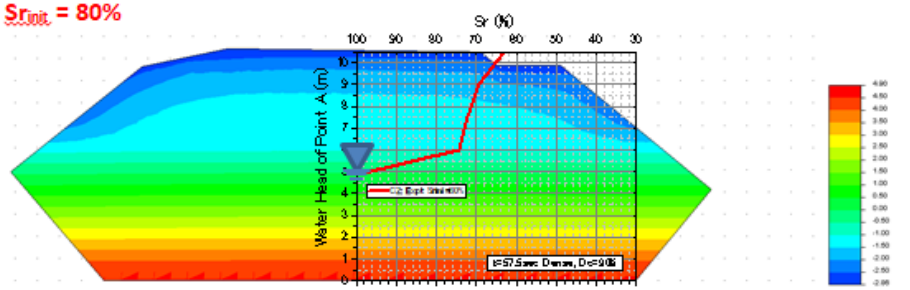

Sr_{init} = 90%

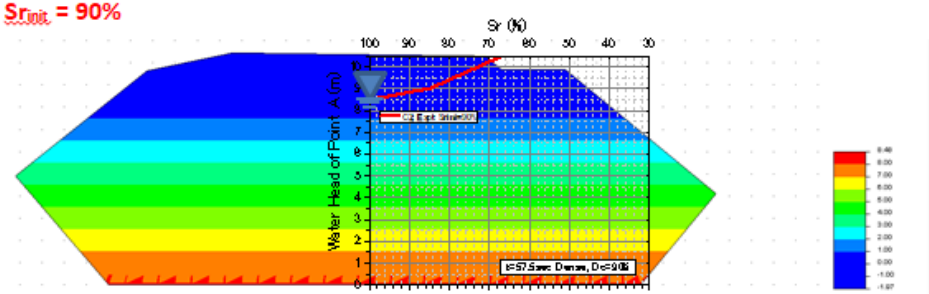

C-8. Seepage Analysis Runs Iron Ore (Dense; Dc=90%) at t=350 hrs

Case 1: Experimental Results; Pervious Side Boundary

Sr_{init} = 55%

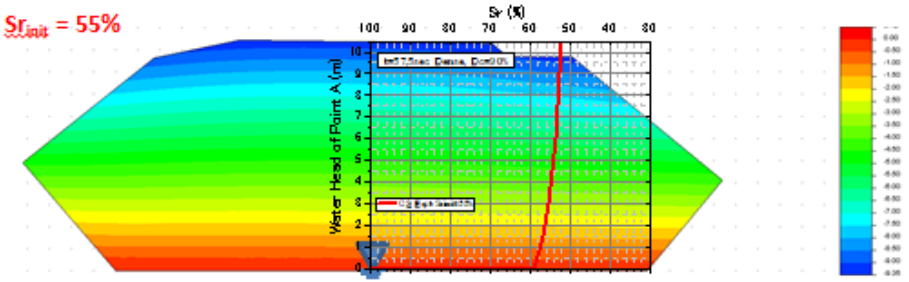

Sr_{init} = 60%

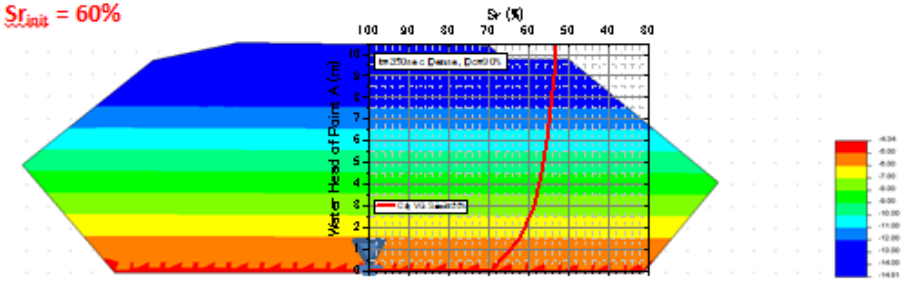

Sr_{init} = 70%

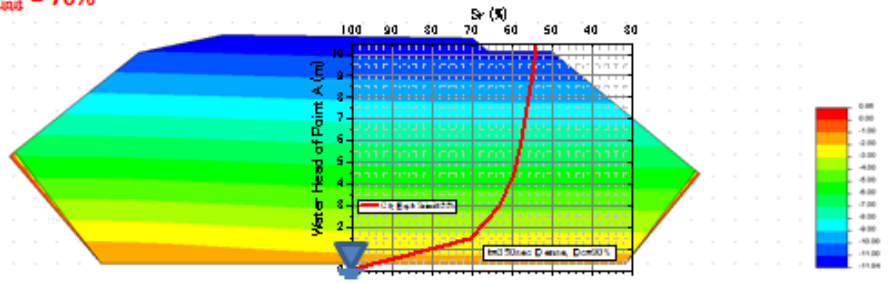

Sr_{init} = 80%

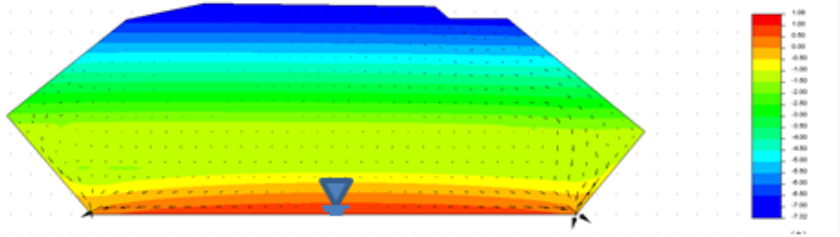

Sr_{init} = 90%

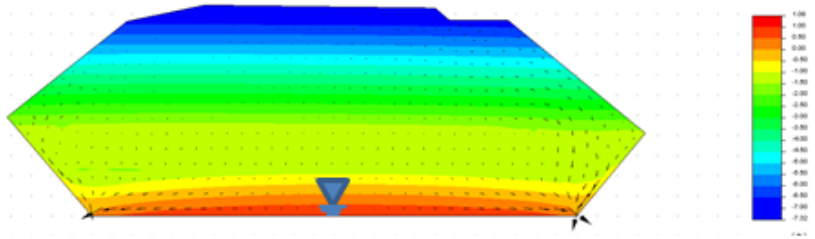

Case 2: Experimental Results; Impervious Side Boundary

Sr_{init} = 55%

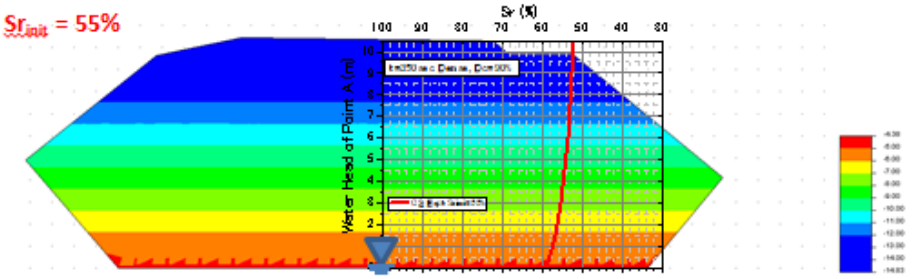

Sr_{init} = 60%

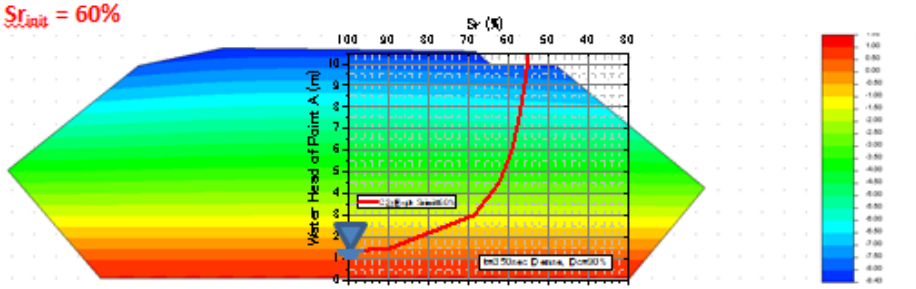

Sr_{init} = 70%

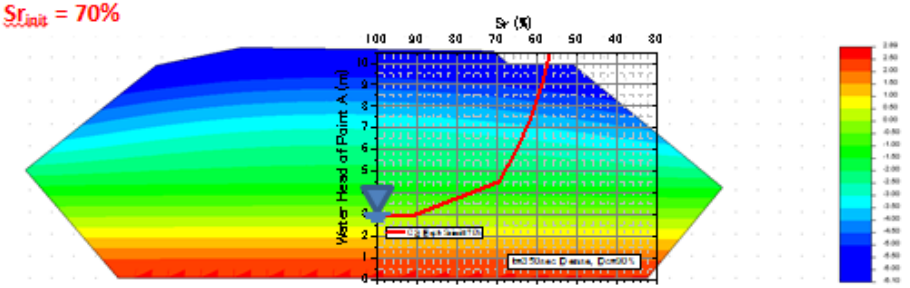

Sr_{init} = 80%

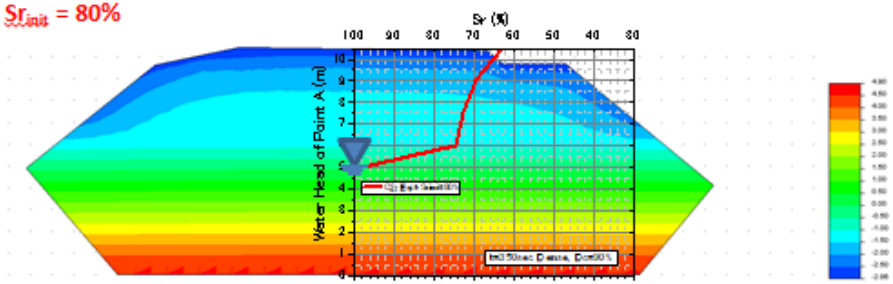

Sr_{init} = 90%

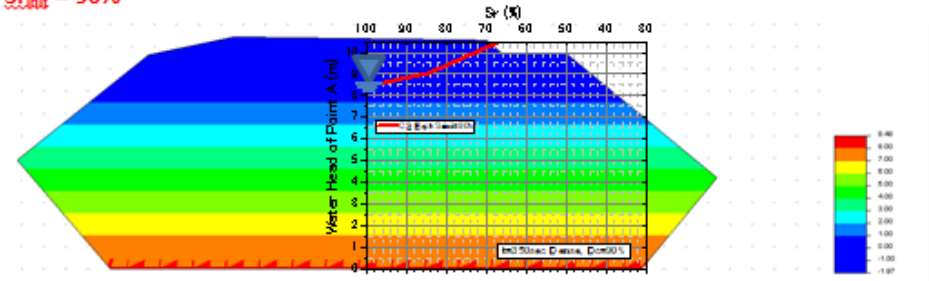

C-9. Seepage Analysis Runs Inagi Sand (Loose; Dc=65%) at t=57.5 hrs

Case 1: Experimental Results; Pervious Side Boundary

Sr_{init} = 55%

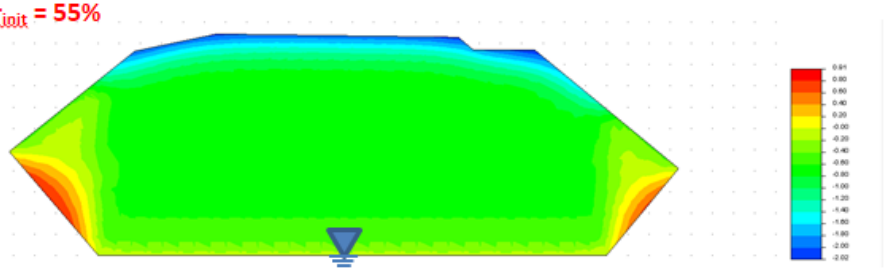

Sr_{init} = 60%

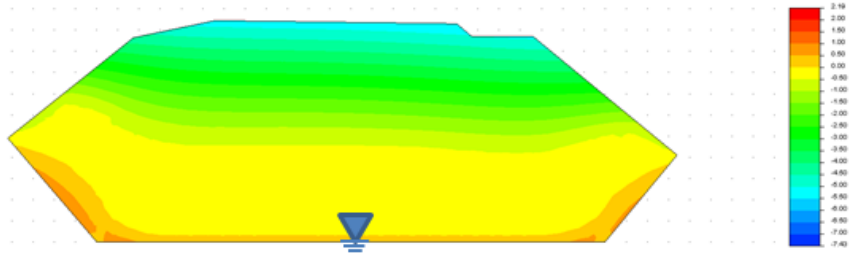

Sr_{init} = 70%

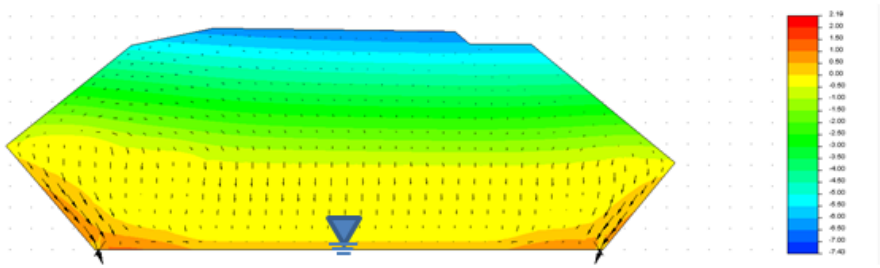

Sr_{init} = 80%

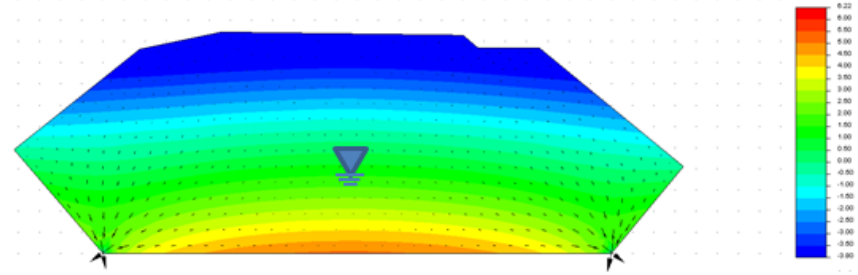

Sr_{init} = 90%

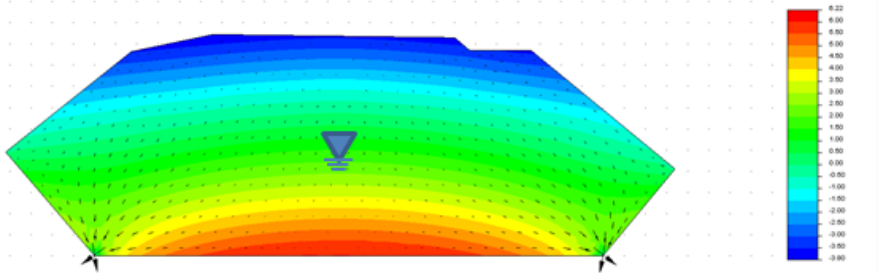

Case 2: Experimental Results; Impervious Side Boundary

Sr_{init} = 55%

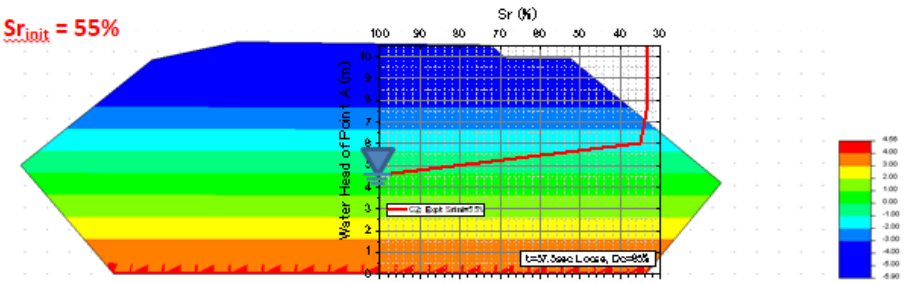

Sr_{init} = 60%

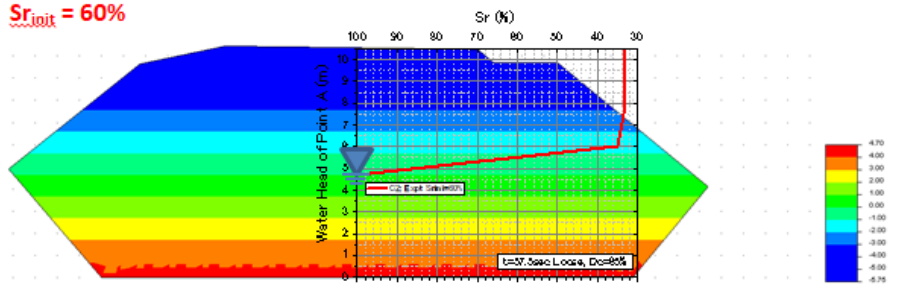

Sr_{init} = 70%

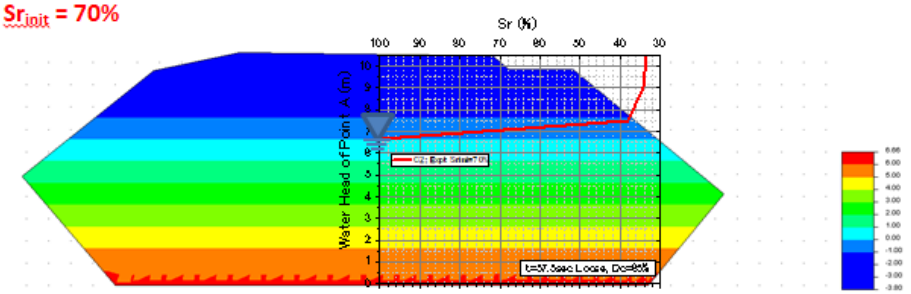

Sr_{init} = 80%

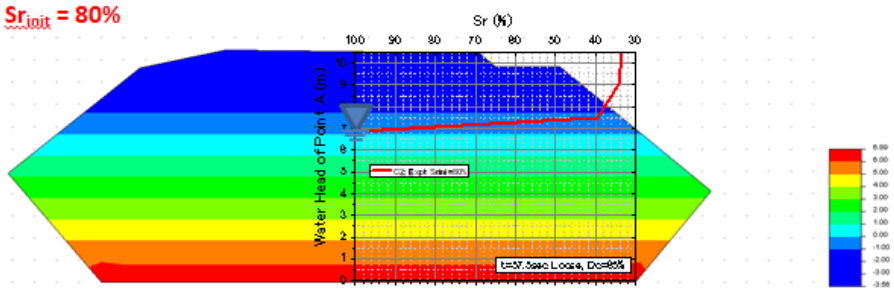

Sr_{init} = 90%

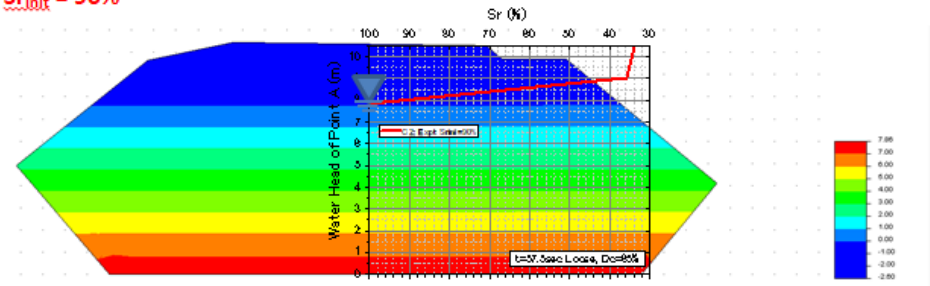

C-10. Seepage Analysis Runs Inagi Sand (Loose; Dc=65%) at t=350 hrs

Case 1: Experimental Results; Pervious Side Boundary

Sr_{init} = 55%

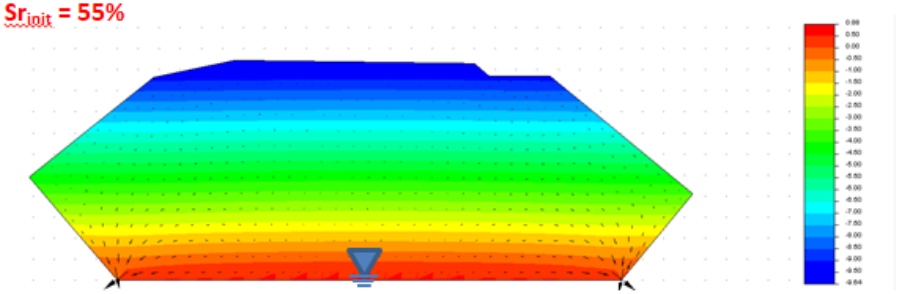

Sr_{init} = 60%

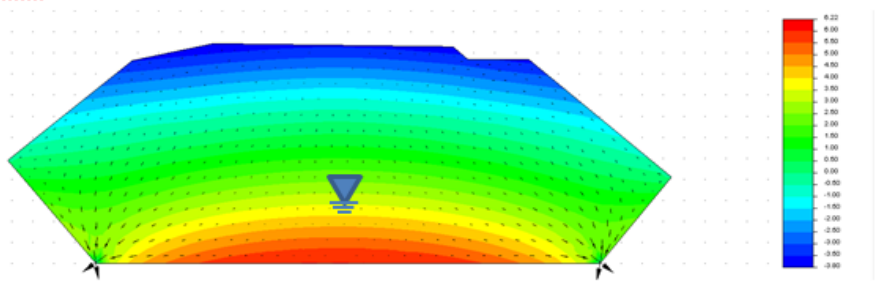

Sr_{init} = 70%

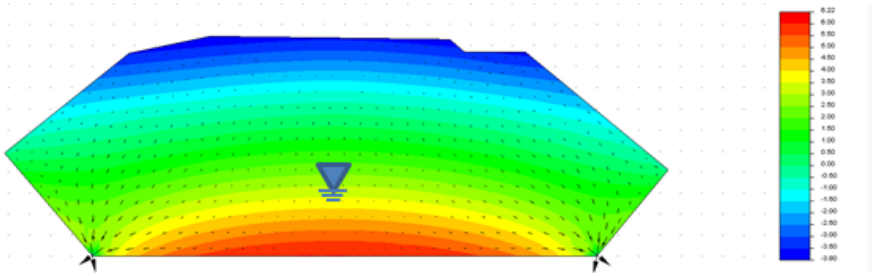

Sr_{init} = 80%

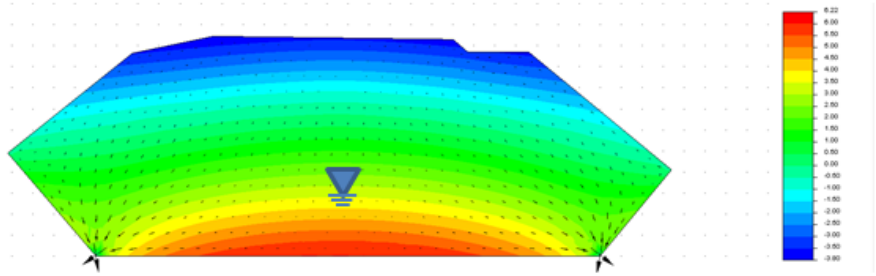

Sr_{init} = 90%

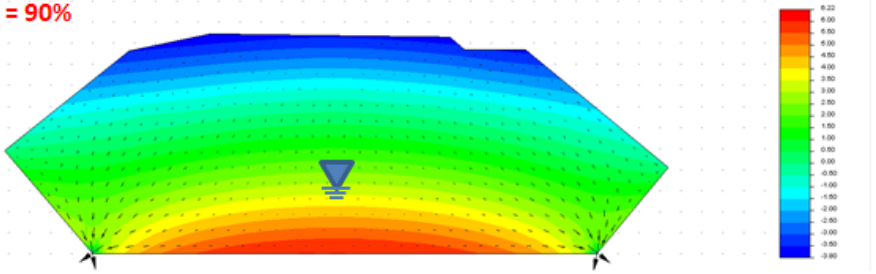

Case 2: Experimental Results; Impervious Side Boundary

Sr_{init} = 55%

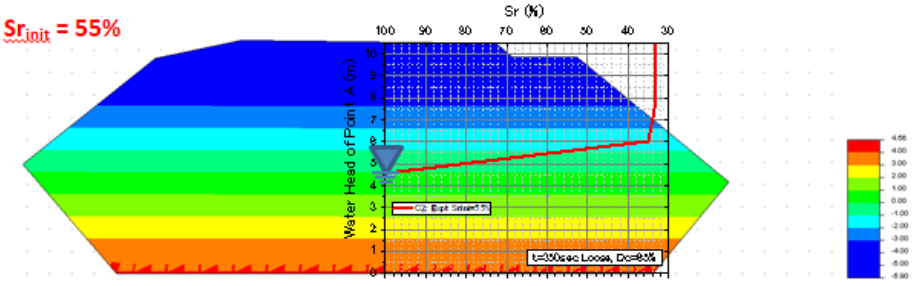

Sr_{init} = 60%

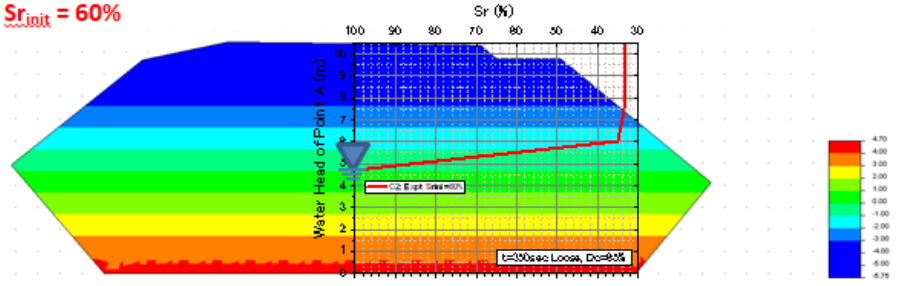

Sr_{init} = 70%

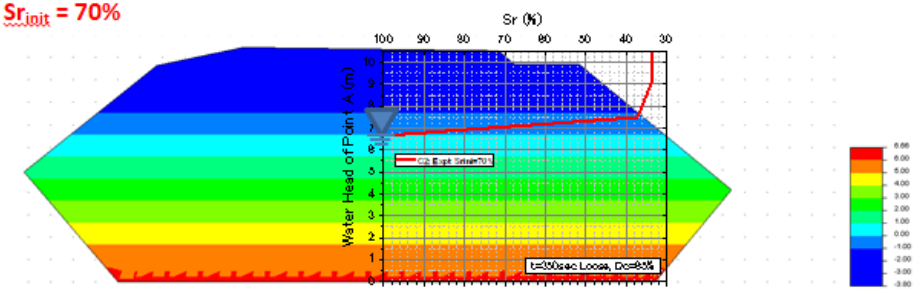

Sr_{init} = 80%

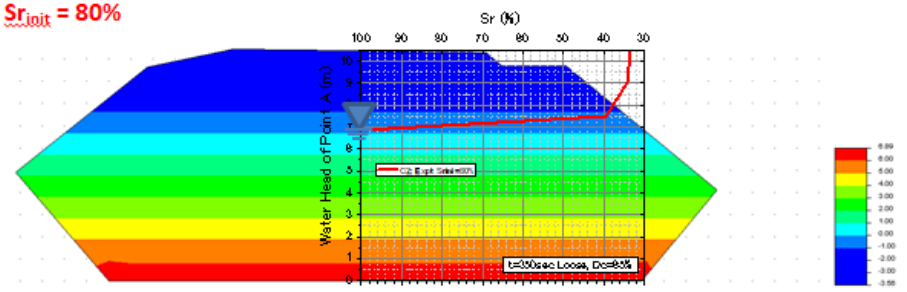

Sr_{init} = 90%

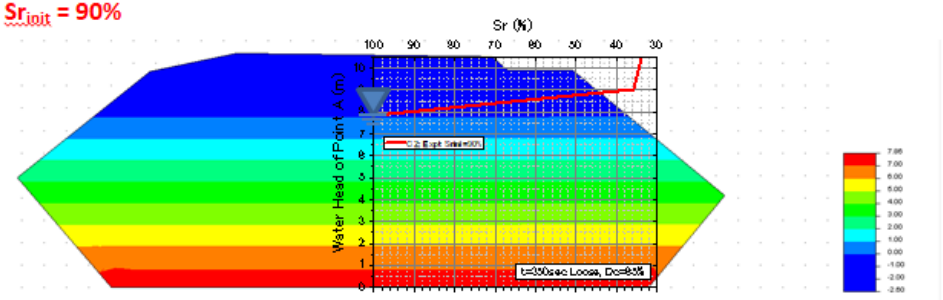

Appendix D: Dynamic Response Analysis

Contents

D-1. Bauxite (Case 1)

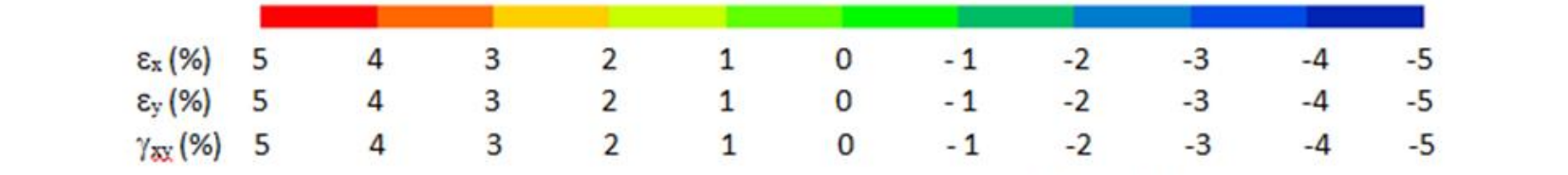

a.) ε_x @5° rolling b.) ε_y @5° rolling c.) γ_{xy} @5° rolling

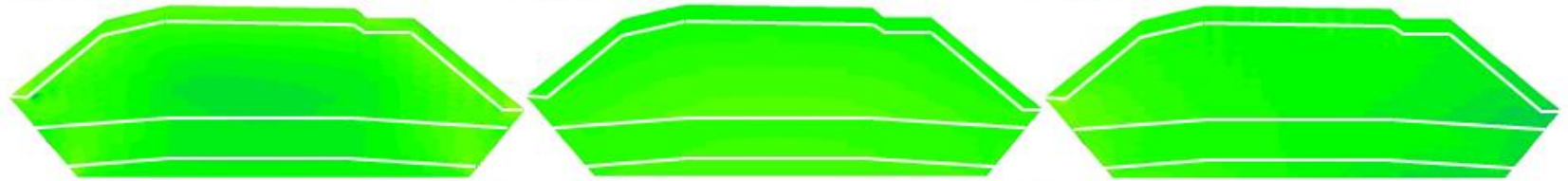

Contour of strains at failure under 5° rolling (bauxite, dense, Case 1)

a.) ε_x @10° rolling b.) ε_y @10° rolling c.) γ_{xy} @10° rolling

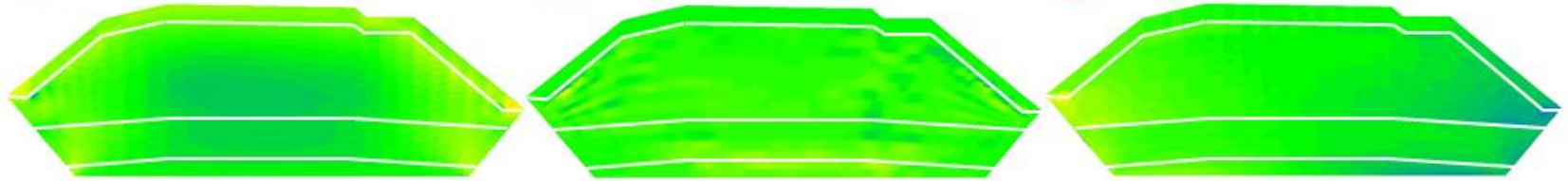

Contour of strains at failure under 10° rolling (bauxite, dense, Case 1)

a.) ε_x @15° rolling b.) ε_y @15° rolling c.) γ_{xy} @15° rolling

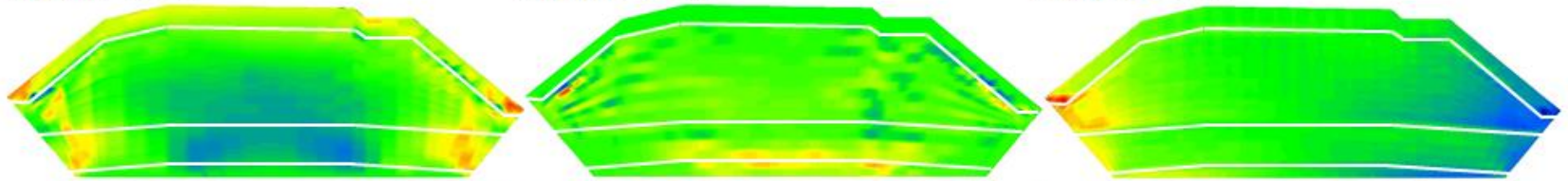

Contour of strains at failure under 15° rolling (bauxite, dense, Case 1)

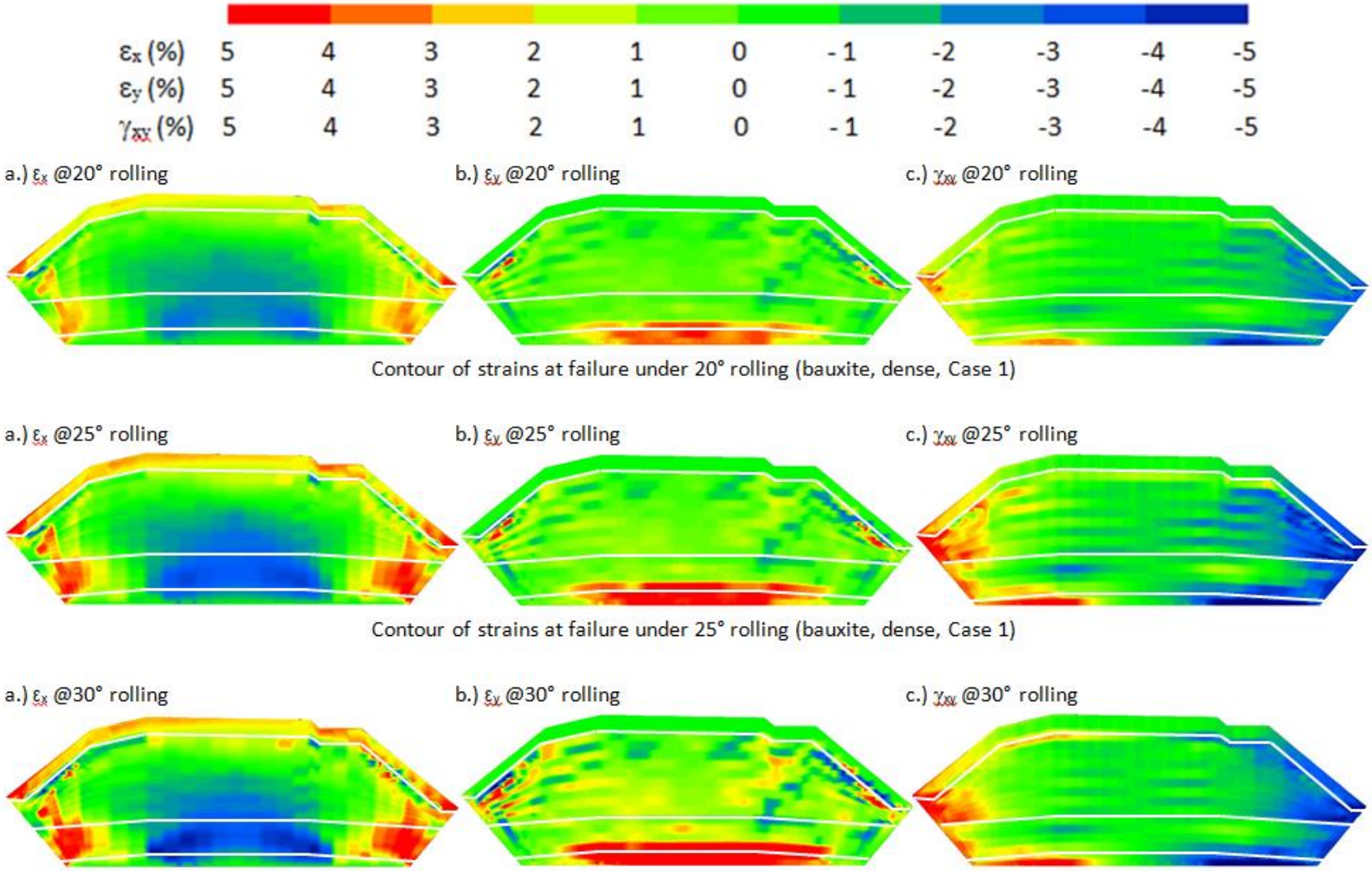

Contour of strains at failure under 20° rolling (bauxite, dense, Case 1)

Contour of strains at failure under 25° rolling (bauxite, dense, Case 1)

Contour of strains at failure under 30° rolling (bauxite, dense, Case 1)

D-2. Bauxite (Case 2)

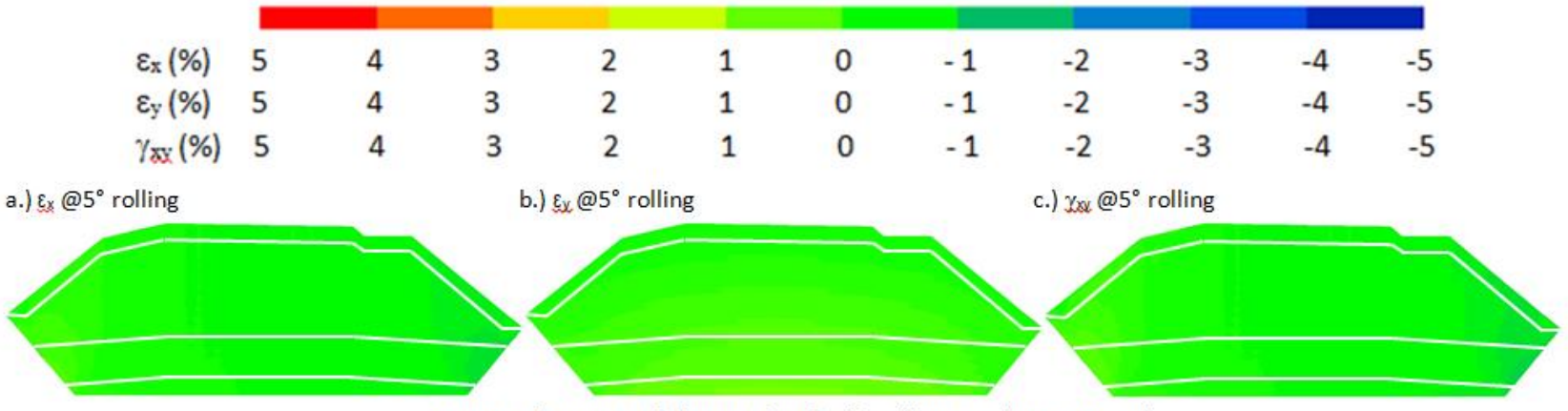

Contour of strains at failure under 5° rolling (bauxite, dense, Case 2)

Contour of strains at failure under 10° rolling (bauxite, dense, Case 2)

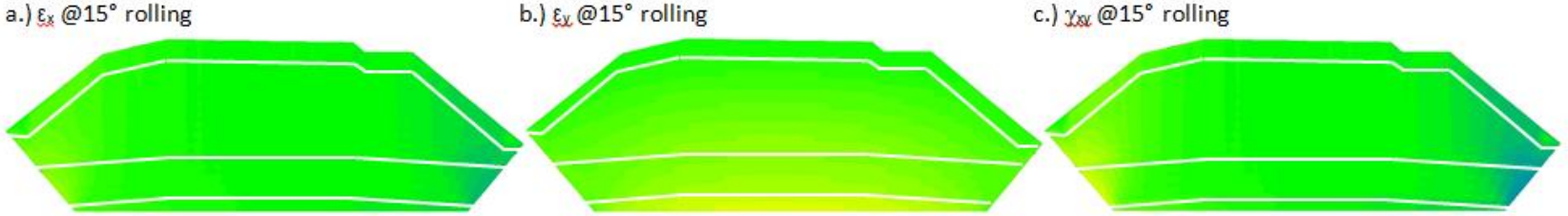

Contour of strains at failure under 15° rolling (bauxite, dense, Case 2)

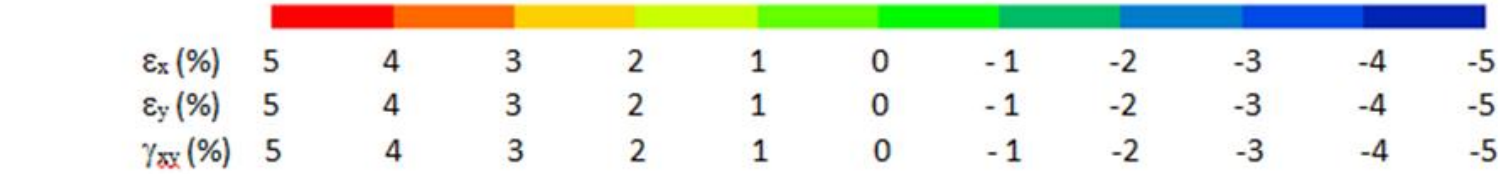

a.) ε_x @20° rolling b.) ε_y @20° rolling c.) γ_{xy} @20° rolling

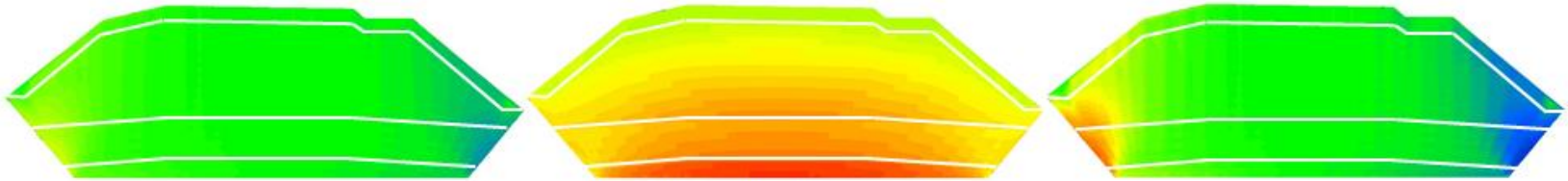

Contour of strains at failure under 20° rolling (bauxite, dense, Case 2)

a.) ε_x @25° rolling b.) ε_y @25° rolling c.) γ_{xy} @25° rolling

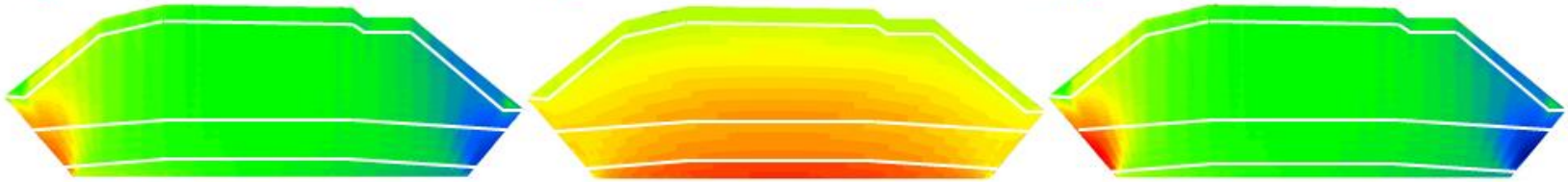

Contour of strains at failure under 25° rolling (bauxite, dense, Case 2)

a.) ε_x @30° rolling b.) ε_y @30° rolling c.) γ_{xy} @30° rolling

Contour of strains at failure under 30° rolling (bauxite, dense, Case 2)

D-3. Bauxite (Case 3)

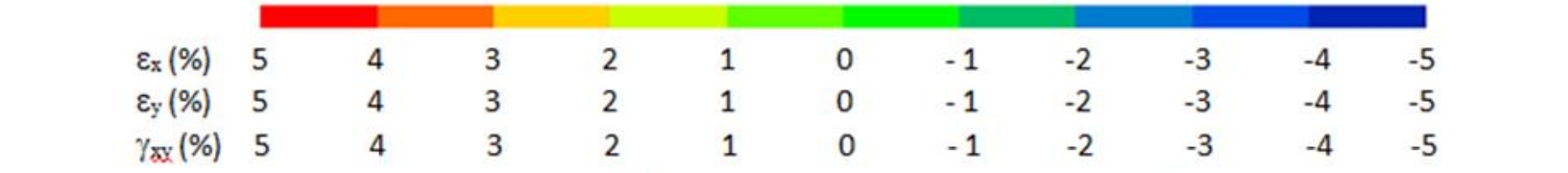

a.) ε_x @5° rolling b.) ε_y @5° rolling c.) γ_{xy} @5° rolling

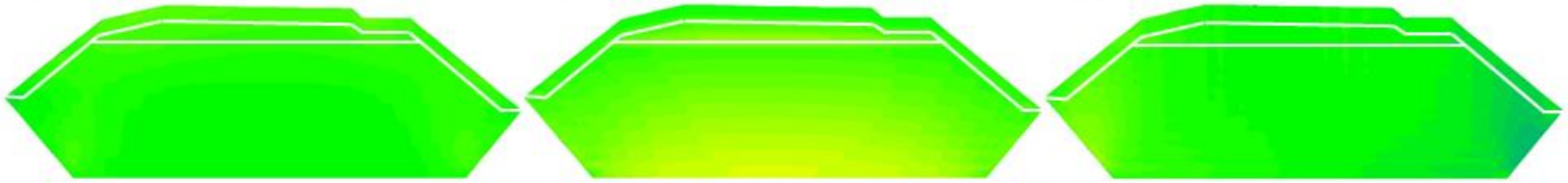

Contour of strains at failure under 5° rolling (bauxite, dense, Case 3)

a.) ε_x @10° rolling b.) ε_y @10° rolling c.) γ_{xy} @10° rolling

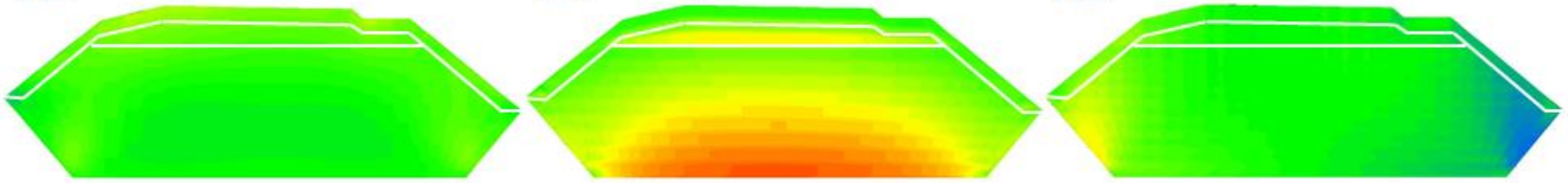

Contour of strains at failure under 10° rolling (bauxite, dense, Case 3)

a.) ε_x @15° rolling b.) ε_y @15° rolling c.) γ_{xy} @15° rolling

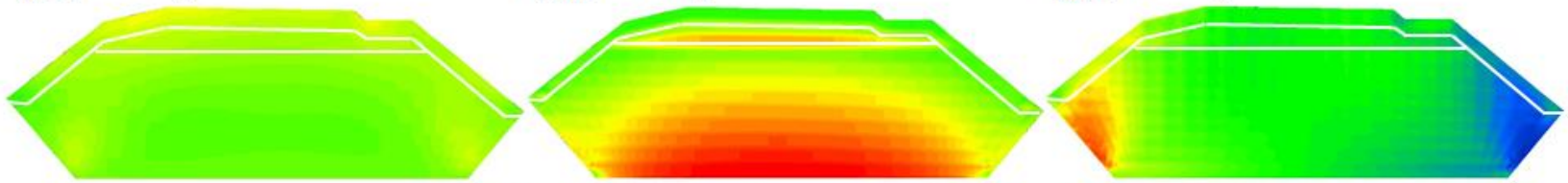

Contour of strains at failure under 15° rolling (bauxite, dense, Case 3)

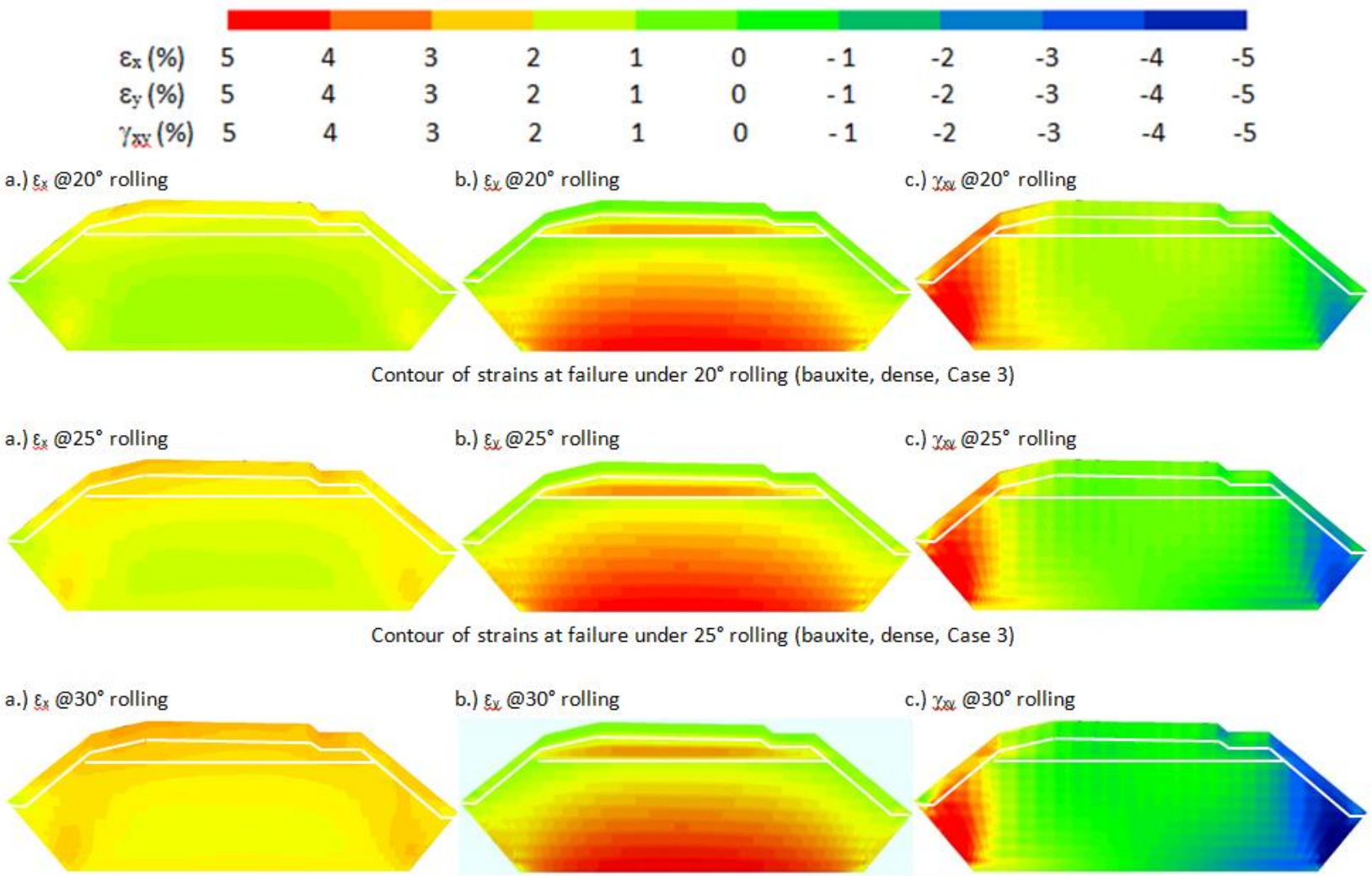

Contour of strains at failure under 20° rolling (bauxite, dense, Case 3)

Contour of strains at failure under 25° rolling (bauxite, dense, Case 3)

Contour of strains at failure under 30° rolling (bauxite, dense, Case 3)

D-4. Iron Ore (Case 1)

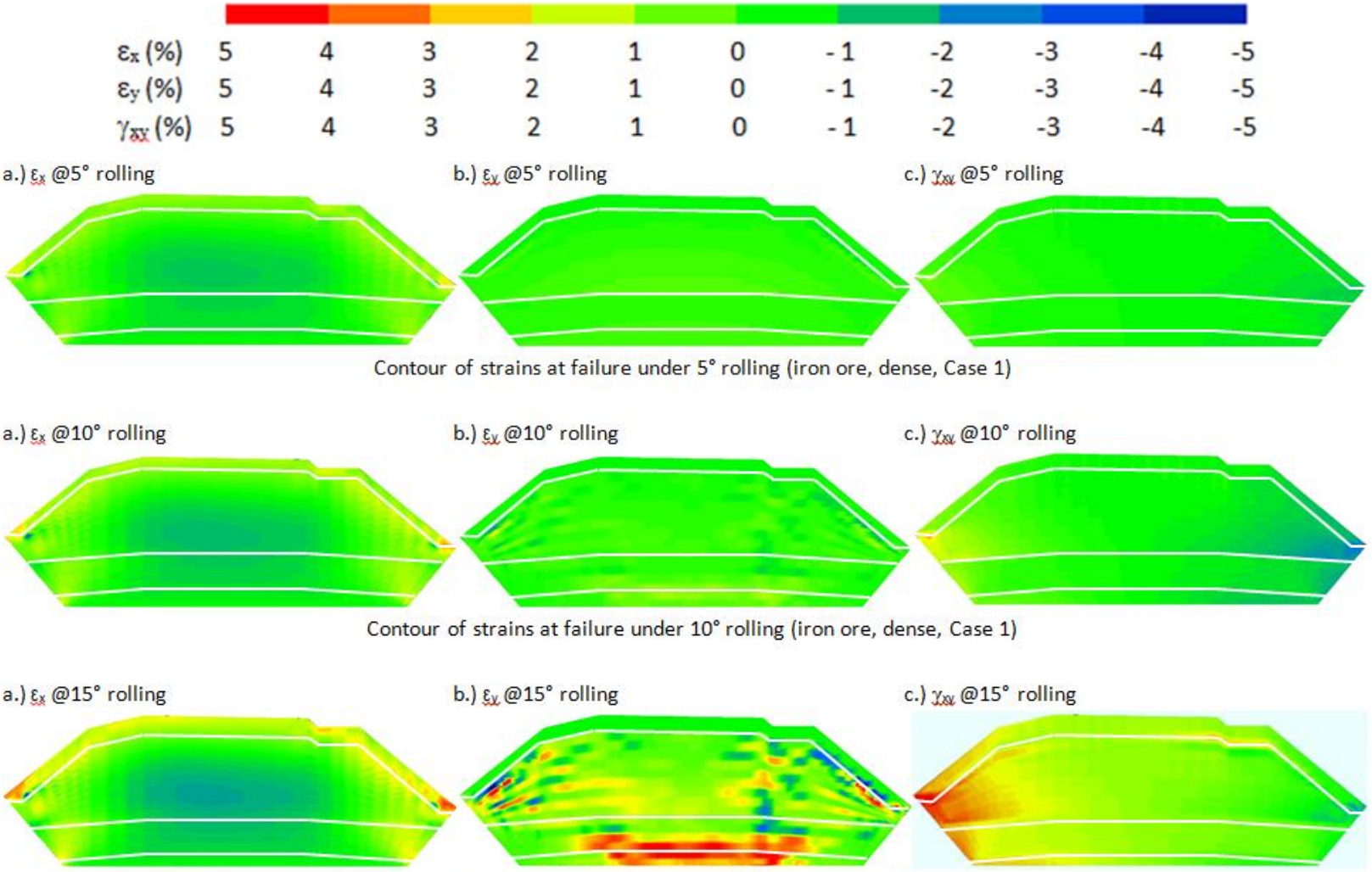

Contour of strains at failure under 5° rolling (iron ore, dense, Case 1)

Contour of strains at failure under 10° rolling (iron ore, dense, Case 1)

Contour of strains at failure under 15° rolling (iron ore, dense, Case 1)

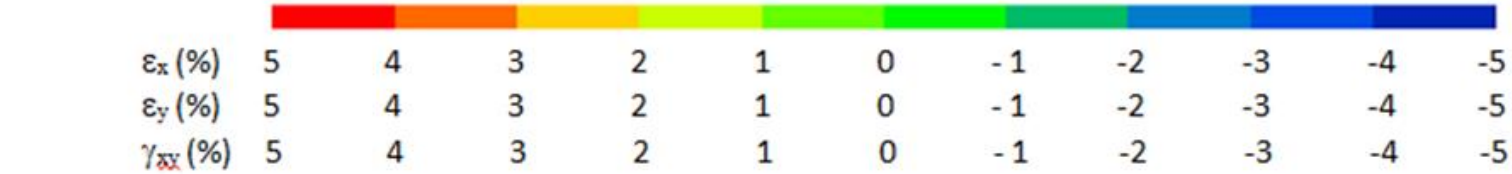

a.) ε_x @20° rolling b.) ε_y @20° rolling c.) γ_{xy} @20° rolling

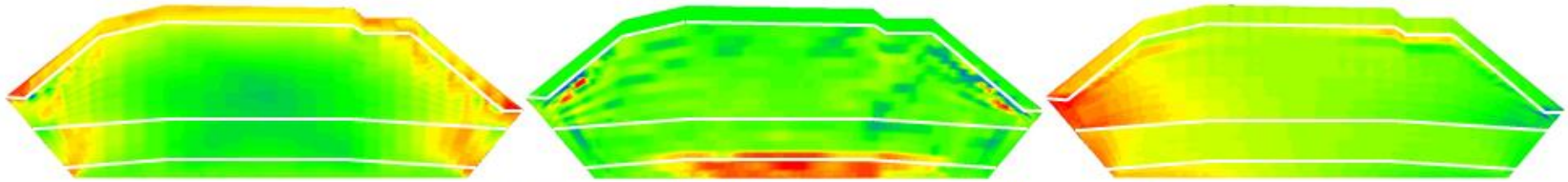

Contour of strains at failure under 20° rolling (iron ore, dense, Case 1)

a.) ε_x @25° rolling b.) ε_y @25° rolling c.) γ_{xy} @25° rolling

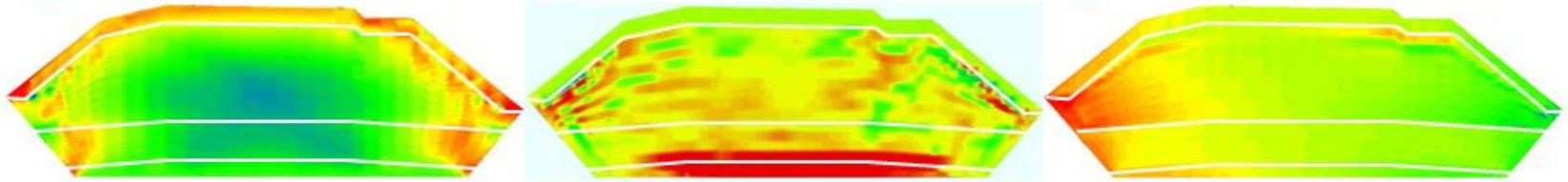

Contour of strains at failure under 25° rolling (iron ore, dense, Case 1)

a.) ε_x @30° rolling b.) ε_y @30° rolling c.) γ_{xy} @30° rolling

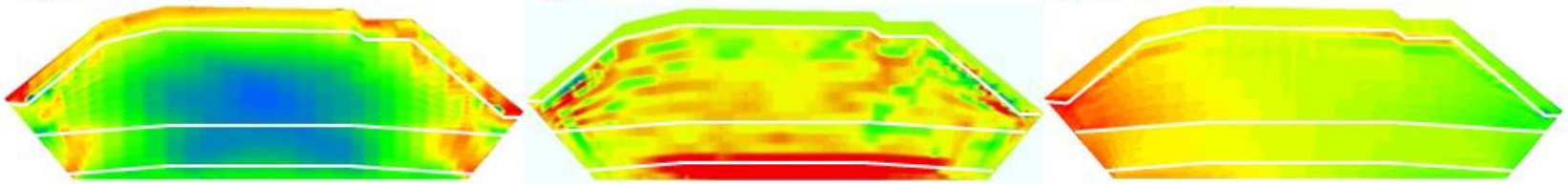

Contour of strains at failure under 30° rolling (iron ore, dense, Case 1)